Quantification of Constraint in Three-Dimensional Fracture Mechanics

By

Osama Abdulhamid Terfas

Submitted in fulfilment of the requirements for the Degree of Doctor of Philosophy

Department of Mechanical Engineering
School of Engineering
College of Science and Engineering
University of Glasgow

September 2010

Abstract

The role of crack tip constraint in three dimensional fracture mechanics has been investigated under elastic-plastic conditions using finite element techniques. Out-of-plane constraint loss has been identified by comparing the mean stress of the three dimensional cracked body with a reference plane strain configuration. This has allowed the quantification of constraint loss due to thickness. This is important for fitness-for-service procedures where the use of standard thick deeply cracked samples inherently leads to conservative assessments. The proximity to plane–strain conditions was investigated, as well as the J-integral along the crack fronts of typical fracture mechanics specimens. It was shown that deep cracks (a/w=0.5) were significantly affected by out-of-plane constraint loss, while the effect was smaller for shallow cracks (a/w=0.1) when in-plane effects were dominant, where a is the crack length and w is the width of the specimen. The out-of-plane effect was confirmed experimentally with a series of fracture mechanics tests on thin and thick deeply cracked fracture mechanics samples. Computational and experimental studies showed that geometries with B/w=0.2 maintained high constraint conditions at the centre plane and exhibited a low fracture toughness, where B is the thickness of the specimen. As such they can be used to measure the plane strain fracture toughness (J_{Ic}) as long as the thickness and the ligament exceed $20J/\sigma_0$. The increased slope of the resistance J_R curve and enhanced fracture toughness were correlated to the loss of out-of-plane constraint that developed in thinner samples (B/w=0.1). A procedure to incorporate the effects of out-of-plane constraint in the R6 failure assessment diagram was proposed.

A procedure was developed to determine ductile crack growth of semi-elliptical surface cracks in flat plates. The procedure used the J-Δa resistance curve developed from standard high and low constraint geometries in conjunction with an analysis of the crack tip stress field using finite element modelling. This allowed the evolution of crack shape under ductile tearing to be modelled. The majority of the work was devoted to the study of surface breaking semi-elliptical cracks subject to bending, uniaxial tension or biaxial loading.

Both the mean stress and J-integral were geometry and load dependent, and were non-uniformly distributed around the crack front. Crack growth was dependent on the level of crack tip constraint, and the original crack shape was generally not retained after ductile tearing. In bending the crack growth was suppressed in the thickness direction and the crack extended significantly sub-surface in a stable manner so that the crack adopted a boat shape. In tension the crack extended through the thickness and this was accompanied with extensive growth in the angular range 45°-70°. In biaxial loading higher constraint levels were observed, however the overall trend of crack growth was similar to uniaxial tension.

Finally, the results from the finite element modelling and the crack growth procedure were verified with experimental data. Excellent agreement in the crack shape patterns was observed between the test data and the crack growth models.

Acknowledgements

I would like to express my grateful acknowledgement to my principal supervisor Dr. Bostjan Bezensek for his supervision and support. I wish to thank my second supervisor Prof. John Hancock for his support, encouragement during my study. I am also grateful to Prof. Margaret Lucas for her support.

I also acknowledge the financial support granted by Libyan government throughout the course of my study.

I am most appreciative of my father, mother, brothers and sisters for their continuing support. Special thanks to my wife for her patience and providing me comfort and my son for giving me all the joy.

Above all, I thank Allah almighty for his unlimited blessings.

Dedicated to my parents, wife and son

Declaration

This thesis is entirely my own work. This work has not been previously submitted for any other degree or qualification in any university.

Osama Abdulhamid Terfas
September 2010

Table of Contents

List of Figures

List of Abbreviations

K	Stress intensity factor
J	J-integral
K_{Ic}	Fracture toughness under small scale yielding conditions
J_{Ic}	Fracture toughness under ductile tearing
T	Elastic T-stress (the 2^{nd} parameter in Williams expansion)
Q	Q-stress (the 2^{nd} parameter in the non-linear series)
J_R	Resistance curve
a	Crack length
w	Width of the specimen
B	Thickness
Δa	Crack extension
b	Uncracked ligament in surface cracks
c	Uncracked ligament in single edge cracked bars
T_i	Traction vector
F_i	Force vector
A_i	Area vector
n_j	Unit vector
σ_{ij}	2^{nd} order stress tensor
ε_{ij}	2^{nd} order strain tensor
ui	Displacement vector
E	Young`s modulus
υ	Poisson`s ratio
G	Shear modulus
S_{ij}	Stress deviator
e_{ij}	Strain deviator
δ_{ij}	Kronecker delta
σ_{kk}	Hydrostatic stress

ε_{kk}	Hydrostatic strain
$\bar{\sigma}$	Von-Mises stress
σ_0	Yield stress
k	Maximum shear stress
$\sigma_1,\sigma_2,\sigma_3$	Principal stresses
$\bar{\varepsilon}^p$	Equivalent plastic strain
$\varepsilon_1^p, \varepsilon_2^p, \varepsilon_3^p$	Principal plastic strain
γ_{ij}	Shear strain
$\bar{\varepsilon}$	Equivalent strain
σ_a	Remote applied stress
W	Work
U	Total energy of a system
U_0	Total energy of the whole system without a crack
U_a	The change in the elastic energy due to the crack
U_γ	Surface energy
G	Energy release rate
σ_f	Fracture stress
γ_p	Specific surface energy associated with plastic deformation
r	Radial distance a head of the crack tip
θ	Angle defining position along the crack front of a surface crack
Y	Dimensional factor of geometry and loading
r_p	Plastic zone radius
δ	Crack tip opening displacement, CTOD
n	Strain hardening exponent
α	Material constant
Π	Potential energy
[K]	Stiffness matrix
[F]	Nodal force vector
[u]	Nodal displacement vector
Φ	Yield function of Gurson`s model
f	Void volume fraction

$\dot{\delta}$	The rate of crack opening displacement
$\dot{J}$	The rate of change of J-integral
β	Biaxiality parameter
f_k	Line-load magnitude
$\mu(s)$	Direction normal to the crack front
$\sigma_{\theta\theta}$	Opening stress
σ_m	Mean stress
A_2	Constraint parameter of J-A_2 concept
T_z	Constraint parameter factor through thickness
σ_{zz}	Out-of-plane stress
$\dot{\varepsilon}_{kk}^{p}$	Plastic strain rate of volume change
$\dot{\varepsilon}_{eq}^{p}$	Equivalent plastic strain rate
Λ	Scaling coefficient
f_N	Volume function of nucleating voids
S_N	Standard deviation
ε_m	Mean strain
$\dot{f}$	The rate of void growth
q_1, q_2, q_3	Gurson`s model coefficients
$\bar{\sigma}$	Flow stress
σ_e	Equivalent stress
f_c	Critical void volume fraction
f_F	Void volume at final failure
T_R	Tearing modulus
U_e	Elastic energy
U_p	Plastic energy
η_e,η_p	Geometry dependent constants
δ_{el}, δpl	Elastic and plastic crack tip opening displacement
δ_{corr}	Crack tip opening displacement taking account of stable crack extension
ν_p	Plastic component of the notch opening displacement
Z	Thickness of knife edges

$(\sigma_m)^{ssy}$	Mean stress under small scale yielding conditions
$(\sigma_m)^{HRR}$	Mean stress of HRR field
χ	Measure of deformation
ΔG_m^{Gb}	Global bending effect
$\Delta \sigma_m^{op}$	Out-of-plane effect, O_p
Δ	Lateral contraction
PE	Plane strain
PS	Plane stress
z	Half thickness
R	Stress ratio
F	Force
V	Notch opening displacement
K_r	Measure of proximity to fracture
K_{mat}	Material toughness
K_{app}	Applied stress intensity factor
L_r	Measure of proximity to plastic collapse
K_{mat}^c	Constraint based material toughness
P	Applied load
P_0	Limit load
σ_{uts}	Ultimate tensile stress
J_{el}	Elastic component of J-integral
J_{pl}	Plastic component of J-integral
ε_{ref}	Reference true strain
$J_c(T)$	Fracture toughness as a function of constraint
$J_c(T=0)$	Fracture toughness for fully constrained solution
J_{mat}	Fracture toughness of the material
m	Constraint sensitivity of material fracture toughness
f(Lr)	Curve function of the failure assessment diagram
P_Q	Critical load on load-displacement curve for K_{IC} determinations
K_Q	Provisional fracture toughness
f(a/w)	Non-dimensional function of a/w

1. Introduction

Engineering structures may contain cracks or flaws which arise from manufacture or service. Under applied loads possibly combined with aggressive environmental conditions, these cracks may grow and potentially cause a catastrophic failure. Fracture mechanics provides quantitative methodologies to evaluate how cracks affect the integrity of structural components. Ensuring the fitness for service of structures containing cracks or flaws is the central theme of fracture mechanics.

Under linear elastic conditions crack tip fields are controlled by a parameter such as the stress intensity factor (K) (Irwin, 1957), and under plastic conditions by the J-integral (Rice, 1968). Consequently a critical value of the stress intensity factor K_{Ic} or the J-integral J_{Ic} is used as a measure of fracture toughness of the material. Hutchinson (1968), Rice and Rosengren (1968) showed that the crack tip stress field in elastic-plastic materials can be characterised by a single parameter, such as the J-integral. The corresponding crack tip field is known as the HRR singular field. Singular parameter characterisation of fracture toughness implies geometry independent and allowing data to be transferred from small laboratory specimens to real structures. However, McClintock (1971) argued that under fully plastic conditions the crack tip field is not unique, and in the limit of non hardening plasticity J no longer characterises all crack tip fields. Two parameter fracture mechanics J-T (Betegón and Hancock, 1991) and J-Q (O'Dowd and Shih, 1991, 1992) was introduced to quantify in-plane constraint loss. One parameter quantifies the deformation and the second quantifies the crack tip constraint. The term constraint is used as a measure of the level of hydrostatic or mean stress that develops at a crack tip as a result of geometry and loading. High constraint geometries are associated with highly triaxial local stress fields, while low constraint geometries have lower stress triaxiality and exhibit higher fracture toughness in fracture mechanics tests.

Until recently two-dimensional plane–strain models have been widely used to quantify the stress and deformation fields at the crack tip, but in fact these fields are three-dimensional. The understanding of constraint effects in three-dimensional crack

configurations (such as surface cracks) under elastic-plastic conditions is still not clear. The present research focuses on three-dimensional analysis of crack tip fields for both surface cracks and single edge cracked bend bars, in order to quantify constraint effects associated with realistic structural defects.

The resistance to fracture of a given material is quantified by experimental values of fracture toughness. Fracture toughness testing is described in standards such as ASTM E1737-96 or BS7448-97. These are usually based on square or rectangular deep cracked geometries with thickness to width ratio in the range 1:1 to 1:2 and are necessarily conservative. In reality many structures have thin-walls and may contain shallow flaws which may exhibit low constraint. To reduce the cost of unnecessary replacement and to provide an accurate margin of safety, fracture toughness data relevant to the thickness of the particular geometry is needed. In the present work the effect of thickness was examined using finite element analysis and fracture experiments to determine tearing resistance and fracture toughness in the context of the standard test procedures.

However in the context of realistic defects in engineering structures predictions of crack growth and crack shape development under ductile tearing have yet to be established. This is an issue for defect assessments in engineering components such as pressure vessels where a surface crack may develop through a different sequence of shapes compared with fatigue and stress intensity factor driven failure. The development of the crack shape becomes important when considering the stability of crack growth as well as in a Leak-Before-Break (LBB) methodology (Brocks et al, 1990, Brickstad and Sattari-Far, 2000). In LBB applications the crack shape development is important, as this governs the estimate of the crack opening area or leak rate at breakthrough. It is therefore important to investigate the crack shape development under ductile tearing.

To investigate the behaviour of surface cracks and to understand the role of constraint in three-dimensional cracks under elastic-plastic conditions, a detailed study was undertaken to quantify constraint in a wide range of semi-elliptical surface cracks subject to bending, uniaxial tension and biaxial loading. A procedure based on constraint, the J-integral, the tearing modulus and fracture toughness of the material was developed to determine crack extension of surface cracked geometries.

The research begins with a literature review of the fundamentals of fracture mechanics in chapter two. Linear elastic fracture mechanics is reviewed in chapter three, then elastic-plastic fracture mechanics is presented in chapter four. This is followed by a chapter discussing constraint effects due to in-plane (T/Q) effects, out-of-plane and global bending effects. Experimental determination of the plane strain fracture toughness (K_{Ic}), J-integral and crack tip opening displacement CTOD are reviewed in chapter six.

Following the literature review, a detailed study on single edge cracked bend specimens carried out in the present work, is described. Chapter seven examines the out-of-plane constraint associated with thickness effects in shallow and deep cracked geometries (a/w=0.1, 0.2, 0.35 and 0.5) with different specimen thicknesses (B/w=0.5, 0.3 0.2, 0.1). The aim was to determine the effect of out-of-plane constraint on the crack tip field and to correlate the loss of out-of-plane constraint with the enhanced fracture toughness. This allows the failure assessment diagram (FAD) to be modified in a similar way to the constraint modified FAD based on the in-plane effect in R6.

Chapter eight presents an experimental investigation of J-Δa resistance curves in geometries of various thicknesses, B/w=0.5, 0.2 and 0.1. The purpose is to investigate the dependence of the fracture toughness on thickness in a systematic way. The enhanced fracture toughness was correlated to the loss of constraint arising through the thickness of the sample. In order to establish a correlation between out-of-plane and in-plane effects shallow cracked specimens were also tested.

In chapter nine a new procedure was developed to predict ductile crack extension in semi-elliptical surface cracked plates. The procedure is based on the ductile tearing resistance curves of high and low constraint fracture mechanics specimens. The procedure combines both constraint and the J-integral to determine crack growth under ductile tearing. Re-meshing was also used to determine crack shape development under incremental ductile tearing. This was applied to a range of surface cracks under bending, uniaxial and biaxial loads in subsequent chapters.

Chapter ten presents the stress fields of deep semi-elliptical surface cracks with different aspect ratios (a/c) in bending using finite element technique. The plastic zone, the mean

stress, J-dominance and plane strain conditions ahead of the crack at different parametric angles are investigated. The findings were combined with the new procedure of chapter nine to determine the crack growth and crack shape evolution under ductile tearing. Force and moment redistributions were also investigated.

Chapter eleven examines shallow semi-elliptical surface cracks in bending using finite element techniques. The aim is to investigate how shallow cracks in full plasticity behave compare to deep cracks. It also aims to investigate how the crack configuration can affect the constraint and determine the crack extension for a range of surface cracks in bending. To validate the finite element calculations, four surface cracked samples with part-through semi-elliptical cracks were also tested under three point bending. Excellent agreement between the crack growth procedure of chapter nine and the test data were observed.

Chapter twelve and thirteen quantify crack tip constraint, J-integral and crack growth in deep and shallow semi-elliptical surface cracks under elastic-plastic conditions in tension. These factors determine crack shape development under ductile tearing. Force and moment redistributions were also investigated.

The effect of biaxial load on the crack tip field was investigated in chapter fourteen. The proximity to plain strain conditions, crack tip constraint, J-integral, crack growth and the crack shape evolution were determined.

Finally the main conclusions are summarised in chapter fifteen.

2. Fundamentals of mechanics

2.1 Stress

The fundamental concepts of stress and strain in deformable bodies, which underpin the current research are reviewed in standard texts, such as McClintock and Argon (1966), Timoshenko and Goodier (1971), Knott (1974), and Gere and Timoshenko (1991). The concept of stress can be illustrated by considering an elemental cube cut from a body subject to arbitrary forces using a right handed Cartesian co-ordinate system (x_i, i=1, 2, 3) as shown in Figure (2.1). Two types of forces can be distinguished: surface forces which are distributed over the surface, and body forces which distributed through the volume of the body. Each force is a vector, denoted F_i represented by components in the x_i directions (i=1, 2, 3). Consider an area A which is normal to a unit vector n_j as shown in Figure (2.2). If a force F_i acts on the area, the traction vector T_i is defined as:

$$T_i = F_i / A \qquad (i = 1, 2, 3) \qquad (2.1)$$

The area may also be written in a vector notation, A_j as:

$$A_j = A\, n_j \qquad (j = 1, 2, 3) \qquad (2.2)$$

Stress may now be defined as a second order tensor σ_{ij} which relates the two first order tensors (vectors), force and area (Nye 1964).

$$\sigma_{ij} = F_i / A_j \qquad (i, j = 1, 2, 3) \qquad (2.3)$$

The stress tensor and the traction vector are simply related by:

$$T_i = \sigma_{ij}\, n_j \qquad (2.4)$$

Two suffices describe the components of the stress. The first suffix denotes the outer normal to the plane on which the component of stress acts, while the second suffix denotes the direction in which the stress acts. The normal component of stress acts on the faces which are perpendicular to coordinate axes x_i. By convention normal stress takes a positive sign when force acts outward from the plane and a negative sign when acting towards the plane. Shear stresses arise when ($i \neq j$), that is stress component acting in the respective planes. From the figure, it can be seen that there are nine stress components of a second order stress tensor (σ_{ij}):

$$\sigma_{ij} = \begin{bmatrix} \sigma_{11} & \sigma_{12} & \sigma_{13} \\ \sigma_{21} & \sigma_{22} & \sigma_{23} \\ \sigma_{31} & \sigma_{32} & \sigma_{33} \end{bmatrix} \tag{2.5}$$

Equilibrium through the sum of moments about body axes to zero reduces the number of stresses to six independent components for homogeneous isotropic materials:

$$\sigma_{11},\ \sigma_{22},\ \sigma_{33}, \sigma_{12} = \sigma_{21},\ \sigma_{13} = \sigma_{31},\ \sigma_{23} = \sigma_{32} \tag{2.6}$$

If the element is in static equilibrium the components of stress must satisfy differential equations of equilibrium which may be written as:

$$(\sigma_{ij}, x_j) + F_i = 0 \quad , \quad i=1, 2, 3 \tag{2.7}$$

Where the comma denotes differentiation, F_i are the body forces in the x_i directions.

The stress components can be changed from one coordinate system to another by transformation equations, which are now derived for a two dimensional state of stress. Consider an infinitesimal element cut from a deformable body which is rotated by an angle θ about the x_3 direction as shown in Figure (2.3a,b) in the x_1, x_2 system. The element has the two normal σ_{11}, σ_{22} and a shear component σ_{12} acting on it. Due to equilibrium the forces associated with all components of the stress sum to zero. From this the normal and shear stresses in another co-ordinate system rotated at an angle θ to x_i

system can be derived. For the polar co-ordinate system (r, θ) the relevant transformation equations (Gere and Timoshenko, 1991):

$$\sigma_{rr} = \sigma_{11}\cos^2\theta + \sigma_{22}\sin^2\theta + 2\sigma_{12}\sin\theta\cos\theta \tag{2.8a}$$

$$\sigma_{\theta\theta} = \sigma_{11}\sin^2\theta + \sigma_{22}\cos^2\theta - 2\sigma_{12}\sin\theta\cos\theta \tag{2.8b}$$

$$\sigma_{r\theta} = (\sigma_{22} - \sigma_{11})\sin\theta\cos\theta + \sigma_{12}(\cos^2\theta - \sin^2\theta) \tag{2.8c}$$

The maximum normal and shear stresses are particularly important. In the coordinate system in which there are no shear stresses acting on the faces of the infinitesimal element the normal stresses are called principal stresses. The planes on which these stresses act are principal planes. From Mohr's Circle, which is a graphical interpretation of the stress transformation equations and shown in Figure (2.4), the principal stresses σ_i can be determined from equation of a circle (Gere and Timoshenko, 1991):

$$\sigma_{1,2} = \frac{1}{2}(\sigma_{11} + \sigma_{22}) \pm \sqrt{\left(\frac{\sigma_{11} - \sigma_{22}}{2}\right)^2 + {\sigma_{12}}^2} \tag{2.9}$$

Their orientation can be obtained by

$$\tan 2\theta_p = \frac{2\sigma_{12}}{\sigma_{11} - \sigma_{22}} \tag{2.10}$$

Where the suffix p denotes the axes of principal stresses.

The maximum shear stress is the radius of the circle:

$$\tau_{\max} = \sqrt{\left(\frac{\sigma_{11} - \sigma_{22}}{2}\right)^2 + {\sigma_{12}}^2} \quad = \left|\frac{\sigma_1 - \sigma_2}{2}\right| \tag{2.11}$$

The normal stresses which act on planes of maximum and minimum shear stresses can be written as

$$\sigma_n = \frac{\sigma_{11} + \sigma_{22}}{2} \tag{2.12}$$

Equation 2.8c can be re-written in the form:

$$\sigma_{r\theta} = -\frac{\sigma_{11} - \sigma_{22}}{2} \sin 2\theta + \sigma_{12} \cos 2\theta \tag{2.13}$$

To obtain the maximum shear stress, the derivative of $\sigma_{r\theta}$ respect to the angle θ is taken and gives:

$$\tan 2\theta_s = -\frac{\sigma_{11} - \sigma_{22}}{2\sigma_{12}} \tag{2.14}$$

Where, θ_s is the orientation of the planes of maximum shear stress. Comparing equation (2.14) with the orientation of principal stresses given by equation (2.10):

$$\tan 2\theta_s = -\frac{1}{\tan 2\theta_p} = -\cot 2\theta_p \tag{2.15}$$

From trigonometry:

$$\tan(\alpha \pm 90^\circ) = -\cot \alpha$$

Hence $\alpha = 2\theta_p$ and $2\theta_s = 2\theta_p \pm 90^\circ$ or $\theta_s = \theta_p \pm 45^\circ$ (2.16)

Thus the planes of maximum shear stress occur at 45° to the principal planes.

2.2 Strain

The deformation of a body is described by a non-dimensional second order tensor known as strain, ε_{ij}, associated with a set of displacement, u_i. Using a framework of small deformation theory, the strains can be expressed (McClintock, 1971):

$$\varepsilon_{ij} = \frac{1}{2}\left(u_{i,j} + u_{j,i}\right) \tag{2.17}$$

Where the comma denotes differentiation.

Direct or normal strains occur when i=j, and can be understood as non-dimensional extensions of edges of the elementary cube, cut virtually from a deformable body.

$$\varepsilon_{11} = \frac{\partial u_1}{\partial x_1} \quad , \quad \varepsilon_{22} = \frac{\partial u_2}{\partial x_2} \quad , \quad \varepsilon_{33} = \frac{\partial u_3}{\partial x_3} \tag{2.18}$$

Shear strains occur when $i \neq j$:

$$\varepsilon_{12} = \frac{1}{2}\left(\frac{\partial u_1}{\partial x_2} + \frac{\partial u_2}{\partial x_1}\right)$$

$$\varepsilon_{13} = \frac{1}{2}\left(\frac{\partial u_1}{\partial x_3} + \frac{\partial u_3}{\partial x_1}\right) \tag{2.19}$$

$$\varepsilon_{23} = \frac{1}{2}\left(\frac{\partial u_2}{\partial x_3} + \frac{\partial u_3}{\partial x_2}\right)$$

It should be noted that an alternative notation γ_{ij} (engineering shear strain) is frequently used for shear strains with the relation ($\gamma_{ij} = 2\varepsilon_{ij}$).

The components of the strain must satisfy compatibility conditions to ensure the field of displacement is valid and consistent with strains through a set of differential equations, which have two forms (Rice, 1968a):

$$\frac{\partial^2 \varepsilon_{11}}{\partial x_2^2} + \frac{\partial^2 \varepsilon_{22}}{\partial x_1^2} = 2\frac{\partial^2 \varepsilon_{12}}{\partial x_1 \partial x_2} \tag{2.20}$$

and

$$\frac{\partial^2 \varepsilon_{11}}{\partial x_2 \partial x_3} = \frac{\partial}{\partial x_1}\left(-\frac{\partial \varepsilon_{23}}{\partial x_1} + \frac{\partial \varepsilon_{13}}{\partial x_2} + \frac{\partial \varepsilon_{12}}{\partial x_3}\right) \tag{2.21}$$

The full set of equations can be compactly written using tensor notation (Rice, 1968a):

$$\frac{\partial^2 \varepsilon_{ij}}{\partial x_k \partial x_l} + \frac{\partial^2 \varepsilon_{kl}}{\partial x_i \partial x_j} = \frac{\partial^2 \varepsilon_{ik}}{\partial x_j \partial x_l} + \frac{\partial^2 \varepsilon_{jl}}{\partial x_i \partial x_k} \tag{2.22}$$

Strains and stresses are related through constitutive laws, such as Hook's law for linear elastic materials.

2.3 Elasticity

At small loads most engineering materials exhibit a linear relationship between stress and strain. It is experimentally observed that the strain is recovered when the applied load is removed before the yield point as shown in figure (2.5a). The main feature of elastic deformation is that it is reversible and that the stress and strain are uniquely related. In uni-axial tension (or compression) the stress and strain is written as:

$$\sigma = E\varepsilon \tag{2.23}$$

This known as Hooke's law, and the constant of proportionality E is Young's modulus, which is a material property. If a body is subjected to a uniaxial load in the x_2 direction, the corresponding strain can be written (Timoshenko and Goodier, 1971):

$$\varepsilon_{22} = \frac{\sigma_{22}}{E} \tag{2.24}$$

The longitudinal extension of the body will be accompanied by transverse contractions through a relation using Poisson's ratio, υ:

$$\varepsilon_{11} = \frac{-\upsilon\sigma_{22}}{E}$$
$$\varepsilon_{33} = \frac{-\upsilon\sigma_{22}}{E} \tag{2.25}$$

Poisson's ratio is defined as the negative of the transverse strain divided by axial strain in a uni-axially loaded body:

$$\upsilon = \frac{-\varepsilon_{11}}{\varepsilon_{22}} = \frac{-\varepsilon_{33}}{\varepsilon_{22}} \tag{2.26}$$

If an isotropic body is subjected to multi-axial loading, the direct components of strain can be expressed using the full Hooke's law, and including contribution from thermal dilatations:

$$\varepsilon_{11} = \frac{1}{E}[\sigma_{11} - \upsilon(\sigma_{22} + \sigma_{33})] + \alpha\Delta T$$
$$\varepsilon_{22} = \frac{1}{E}[\sigma_{22} - \upsilon(\sigma_{11} + \sigma_{33})] + \alpha\Delta T \tag{2.27}$$
$$\varepsilon_{33} = \frac{1}{E}[\sigma_{33} - \upsilon(\sigma_{11} + \sigma_{22})] + \alpha\Delta T$$

Where α is coefficient of thermal expansion and ΔT is the change in temperature.

The shear stress-strain relationship is described by:

$$\varepsilon_{12} = \frac{\sigma_{12}}{2G}, \quad \varepsilon_{23} = \frac{\sigma_{23}}{2G}, \quad \varepsilon_{31} = \frac{\sigma_{31}}{2G} \tag{2.28}$$

Where G is known as the shear modulus. The relationship between Young's and shear modulus (McClintock, 1971):

$$G = \frac{E}{2(1+\upsilon)} \tag{2.29}$$

It is often convenient to identify deformation with and without volume change. In this respect it is useful to introduce the stress and strain deviators, S_{ij} and e_{ij} (Rice, 1968a):

$$S_{ij} = \sigma_{ij} - \delta_{ij}\sigma_{kk}/3 \tag{2.30}$$

$$e_{ij} = \varepsilon_{ij} - \delta_{ij}\varepsilon_{kk}/3 \tag{2.31}$$

Where δ_{ij} is the Kronecker delta:

$$\delta_{ij} = \begin{bmatrix} 1 & 0 \\ 0 & 1 \end{bmatrix} \tag{2.32}$$

And σ_{kk} and ε_{kk} are the volumetric/hydrostatic stress and strain respectively. The elastic strains can then be written in terms of volumetric and deviatoric components (Rice, 1968a):

$$\varepsilon_{ij} = \frac{(1-2\upsilon)}{E}\delta_{ij}\sigma_{ij} + \frac{S_{ij}}{2G} \tag{2.33}$$

The stresses can also be written in terms of the strain:

$$\sigma_{ij} = 2G\left(\varepsilon_{ij} + \frac{\upsilon}{1-2\upsilon}\delta_{ij}\varepsilon_{kk}\right) \tag{2.34}$$

2.4 The Yield Criterion

Plastic deformation is irreversible and occurs at a constant volume (effectively Poisson's ratio equals a half), whereby any change of dimension (i.e. elongation) in a major direction must be accompanied with opposite change (i.e. reduction) in other two directions. Consider a bar subject to a tensile force in which the load is removed beyond yield point of the material. The behaviour of the material under σ-ε curve will return by different path parallel to the original portion of the curve at some value of plastic strain as shown in Figure (2.5.b). It should be noted that there is no distinction between plastic deformation and non-linear elastic deformation when unloading or rotation of the loads is not allowed (proportional loading). This is known as deformation plasticity as opposed to incremental plasticity in which unloading or rotations are allowed.

The condition which characterises the transition state of a material beyond the elastic limit to cause permanent deformation is known as the yield criteria. Yield criteria for isotropic materials must be independent of the co-ordinate system and a function of the stress invariants. The two common yield criteria for metals are the Von-Mises criterion (1913) and Tresca criterion (1864). The concept of yielding in both is based on assumption that the hydrostatic stress component does not produce plastic flow, and therefore the combination of stresses which produce yielding must involve the shear stresses in the system.

In the Von-Mises criteria, yielding occurs in multi-axial loaded material when the equivalent stress $\bar{\sigma}$ reaches the uniaxial yield strength of the material σ_0 (Knott, 1974):

$$\bar{\sigma} = \sigma_0$$

$$\bar{\sigma} = \sqrt{\frac{1}{2}\left[(\sigma_1 - \sigma_2)^2 + (\sigma_2 - \sigma_3)^2 + (\sigma_3 - \sigma_1)^2\right]} \tag{2.35}$$

where σ_1, σ_2, σ_3 are the principal stresses.

The equivalent stress can be written in a general Cartesian system as:

$$\bar{\sigma} = \sqrt{\frac{1}{2}\left[(\sigma_{11} - \sigma_{22})^2 + (\sigma_{22} - \sigma_{33})^2 + (\sigma_{33} - \sigma_{11})^2\right] + 3(\sigma_{12}^2 + \sigma_{23}^2 + \sigma_{31}^2)} \qquad (2.36)$$

and more compactly in terms of the stress deviators:

$$\bar{\sigma} = \sqrt{\frac{3}{2} S_{ij} S_{ij}} \qquad (2.37)$$

For the biaxial case where $\sigma_3=\sigma_{13}=\sigma_{23}=0$, this plots as an ellipse, in the $\sigma_1\sigma_2$ plane as shown in Figure (2.6). This gives:

$$\sigma_0^2 = \sigma_1^2 - \sigma_1\sigma_2 + \sigma_2^2$$

For the case of yield in pure shear:

$$\sigma_1 = -\sigma_2 = k$$

Thus,

$$k = \frac{\sigma_0}{\sqrt{3}} \qquad (2.38)$$

Therefore, the von Mises yield criterion may be written in terms of the uniaxial yield stress ($\bar{\sigma} = \sigma_0$) or in terms of the yield stress in shear ($k=\sigma_0/\sqrt{3}$).

The Tresca criterion suggests that yielding in multi-axial states of stress occurs when the difference between the maximum and minimum principal stresses equals the yield strength of the material, and that occurs when the maximum shear stress equals half the yield strength in simple tension:

$$\sigma_1 - \sigma_3 = \sigma_0 = 2k \qquad (\sigma_1 \geq \sigma_2 \geq \sigma_3) \qquad (2.39)$$

It is observed that the yield surface of the Tresca criterion is surrounded by the von Mises' surface as shown in Figure (2.7). For a plastic material subjected to combined stresses Tresca's criterion is therefore more conservative.

Most materials strain or work harden, so that the equivalent stress to cause yield depends on the associated plastic strain. Thus, plastic strain must be quantified by a parameter which corresponds to equivalent stress, this parameter is known as equivalent plastic strain $\bar{\varepsilon}^{p}$ (McClintock, 1971):

$$\bar{\varepsilon}^{p} = \sqrt{\frac{2}{9}\left[\left(\varepsilon_1^p - \varepsilon_2^p\right)^2 + \left(\varepsilon_2^p - \varepsilon_3^p\right)^2 + \left(\varepsilon_3^p - \varepsilon_1^p\right)^2\right]} \tag{2.40}$$

Where $\varepsilon_1^p, \varepsilon_2^p, \varepsilon_3^p$ are the principal plastic strains. The numerical factor 2/9 makes the equivalent plastic strain equal the uniaxial strain ε^p in a uni-axial tensile test of an incompressible material. The equivalent strain can be written in terms of non-principal strains:

$$\bar{\varepsilon}^{p} = \sqrt{\frac{2}{9}\left[\left(\varepsilon_{11}^p - \varepsilon_{22}^p\right)^2 + \left(\varepsilon_{22}^p - \varepsilon_{33}^p\right)^2 + \left(\varepsilon_{33}^p - \varepsilon_{11}^p\right)^2\right] + \frac{1}{3}(\gamma_{12}^p)^2 + \frac{1}{3}(\gamma_{23}^p)^2 + \frac{1}{3}(\gamma_{31}^p)^2} \tag{2.41}$$

2.5 Plasticity

Non-linear elastic relations can be expressed in similar way to linear elastic relations. If deformation occurs at a constant volume, Poisson's ratio is a half and by replacing the Young's modulus (E) by the ratio of the equivalent stress to the equivalent strain, $E = \bar{\sigma}/\bar{\varepsilon}$, the direct strains can be written as:

$$\varepsilon_{11} = \frac{\bar{\varepsilon}}{\bar{\sigma}}\left[\sigma_{11} - \frac{1}{2}(\sigma_{22} + \sigma_{33})\right]$$

$$\varepsilon_{22} = \frac{\bar{\varepsilon}}{\bar{\sigma}}\left[\sigma_{22} - \frac{1}{2}(\sigma_{11} + \sigma_{33})\right] \tag{2.42}$$

$$\varepsilon_{33} = \frac{\bar{\varepsilon}}{\bar{\sigma}}\left[\sigma_{33} - \frac{1}{2}(\sigma_{22} + \sigma_{11})\right]$$

and by substituting $G = \frac{E}{3}$ the shear strain can be written as:

$$\gamma_{12} = \frac{3\sigma_{12}\,\bar{\varepsilon}}{\bar{\sigma}}, \qquad \gamma_{23} = \frac{3\sigma_{23}\,\bar{\varepsilon}}{\bar{\sigma}}, \quad \gamma_{31} = \frac{3\sigma_{32}\,\bar{\varepsilon}}{\bar{\sigma}} \tag{2.43}$$

In deformation plasticity loads must always increase in same ratio and are not allowed to rotate while in incremental plasticity loads need not increase in proportion and may also rotate. Thus, in incremental plasticity the history of strain must be considered. The total plastic strain is the sum of the plastic strain increments:

$$\varepsilon^p = \int d\varepsilon^p \tag{2.44}$$

For instance, if a body has been subject to a tensile strain of $\bar{d\varepsilon}^p$ = 0.01 followed by a compressive strain $\bar{d\varepsilon}^p$ = -0.01 there would be no net shape change but the accumulated plastic strain would be $\bar{d\varepsilon}^p$ = 0.02. Equations (2.42), (2.43) can be written in terms of increments as:

$$d\varepsilon_{11}^{p} = \frac{\bar{d\varepsilon}^{p}}{\bar{\sigma}}\left[\sigma_{11} - \frac{1}{2}(\sigma_{22} + \sigma_{33})\right]$$
$$d\varepsilon_{22}^{p} = \frac{\bar{d\varepsilon}^{p}}{\bar{\sigma}}\left[\sigma_{22} - \frac{1}{2}(\sigma_{11} + \sigma_{33})\right] \tag{2.45}$$
$$d\varepsilon_{33}^{p} = \frac{\bar{d\varepsilon}^{p}}{\bar{\sigma}}\left[\sigma_{33} - \frac{1}{2}(\sigma_{22} + \sigma_{11})\right]$$

$$d\gamma_{12} = \frac{3\sigma_{12}\, d\bar{\varepsilon}}{\bar{\sigma}}, d\gamma_{23} = \frac{3\sigma_{23}\, d\bar{\varepsilon}}{\bar{\sigma}}, d\gamma_{31} = \frac{3\sigma_{32}\, d\bar{\varepsilon}}{\bar{\sigma}} \tag{2.46}$$

In elastic-plastic deformation the total strain is the sum of the current elastic strain and the plastic strain and takes the form:

$$\varepsilon_{11} = \frac{1}{E}[\sigma_{11} - \upsilon(\sigma_{22} + \sigma_{33})] + \frac{\bar{\varepsilon}^{p}}{\bar{\sigma}}\left[\sigma_{11} - \frac{1}{2}(\sigma_{22} + \sigma_{33})\right]$$
$$\varepsilon_{22} = \frac{1}{E}[\sigma_{22} - \upsilon(\sigma_{11} + \sigma_{33})] + \frac{\bar{\varepsilon}^{p}}{\bar{\sigma}}\left[\sigma_{22} - \frac{1}{2}(\sigma_{11} + \sigma_{33})\right] \tag{2.47}$$
$$\varepsilon_{33} = \frac{1}{E}[\sigma_{33} - \upsilon(\sigma_{11} + \sigma_{22})] + \frac{\bar{\varepsilon}^{p}}{\bar{\sigma}}\left[\sigma_{33} - \frac{1}{2}(\sigma_{11} + \sigma_{22})\right]$$

For the shear strains:

$$\gamma_{12} = \frac{\sigma_{12}}{G} + \frac{3\sigma_{12}\,\bar{\varepsilon}^{p}}{\bar{\sigma}}$$
$$\gamma_{23} = \frac{\sigma_{23}}{G} + \frac{3\sigma_{23}\,\bar{\varepsilon}^{p}}{\bar{\sigma}} \tag{2.48}$$
$$\gamma_{31} = \frac{\sigma_{31}}{G} + \frac{3\sigma_{32}\,\bar{\varepsilon}^{p}}{\bar{\sigma}}$$

For incremental plasticity, the incremental strains are:

$$d\varepsilon_{ij} = \frac{(1-2\upsilon)}{3E}\delta_{ij}d\sigma_{kk} + \frac{ds_{ij}}{2G} + \frac{3\bar{d}\varepsilon^{p}}{2\bar{\sigma}}s_{ij} \tag{2.49}$$

2.6 Plane Stress and Plane Strain

Full three dimensional problems are frequently intractable for close form analytical solutions and two dimensional idealisations can be used. If the thickness of a body in the x_3 direction is small relative to the in-plane dimensions, (x_1, x_2), the normal and shear stress and their gradients $\partial\sigma_{33}/\partial x_3$ are often assumed to be zero in the x_3-direction and the stress state is called plane stress. The plane stress condition can be formally expressed as:

$$\sigma_{3i} = 0\,, \quad and \frac{\partial\sigma_{3i}}{\partial x_3} = 0 \qquad (i = 1, 2, 3) \tag{2.50}$$

Conversely, a state of plane strain exists when the thickness is very large compared to all other dimensions. Under plane strain conditions, the material is not allowed to contract in the through-thickness direction (x_3-direction), which requires that the components of strain in that direction are zero $\varepsilon_{3i} = 0$ and ε_{3i}, $x_3 = 0$. The requirement that $\varepsilon_{33} = 0$ leads to the normal stress in third direction:

$$\sigma_{33} = \upsilon(\sigma_{11} + \sigma_{22}) \tag{2.51}$$

It should be noted these are simplified states of stress which bound real three-dimensional states of stress.

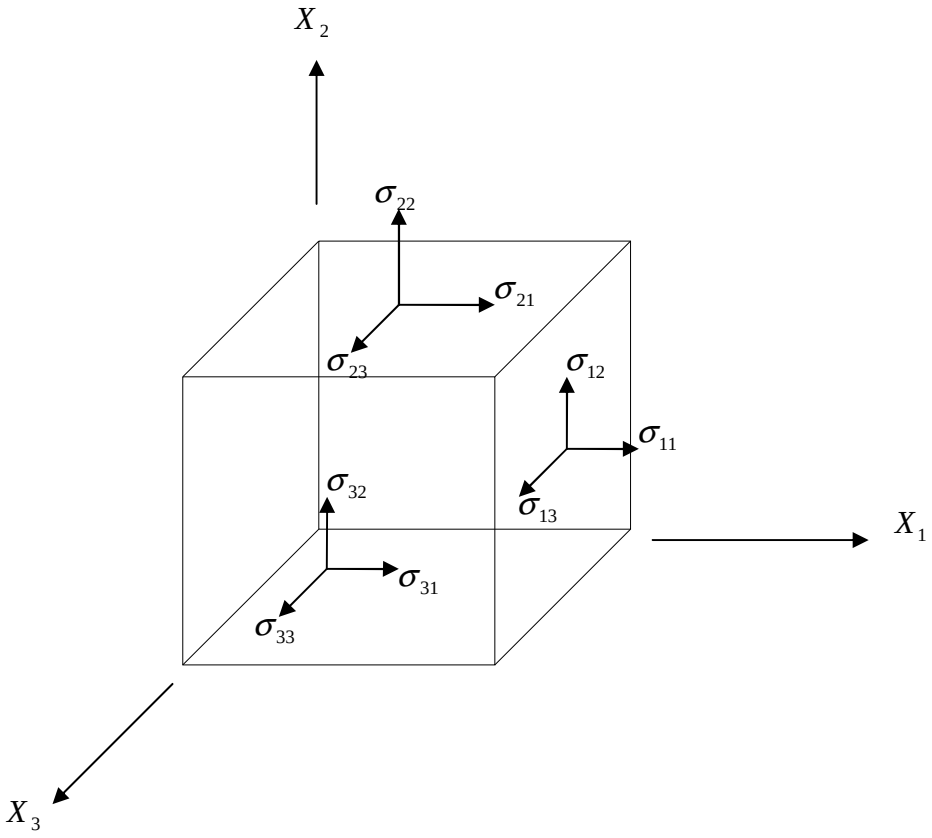

Figure 2.1 Components of stress referred to a Cartesian co-ordinate system.

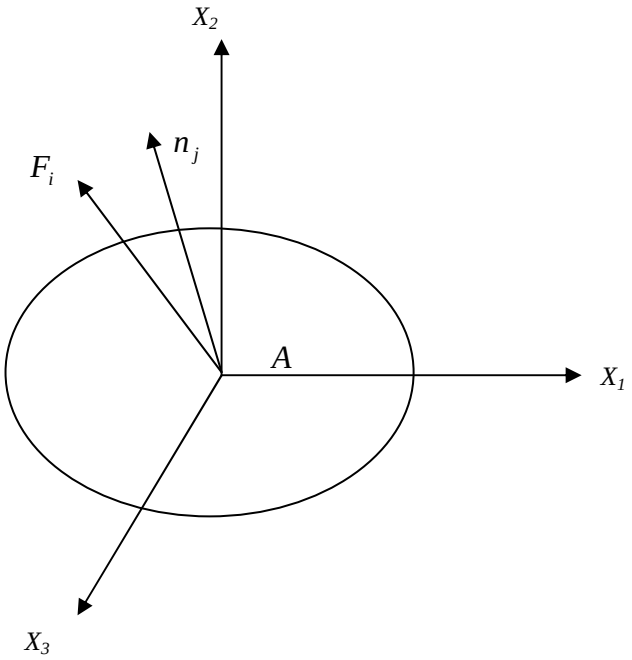

Figure 2.2 A unit vector n_j, and a force F_i acting on an area A.

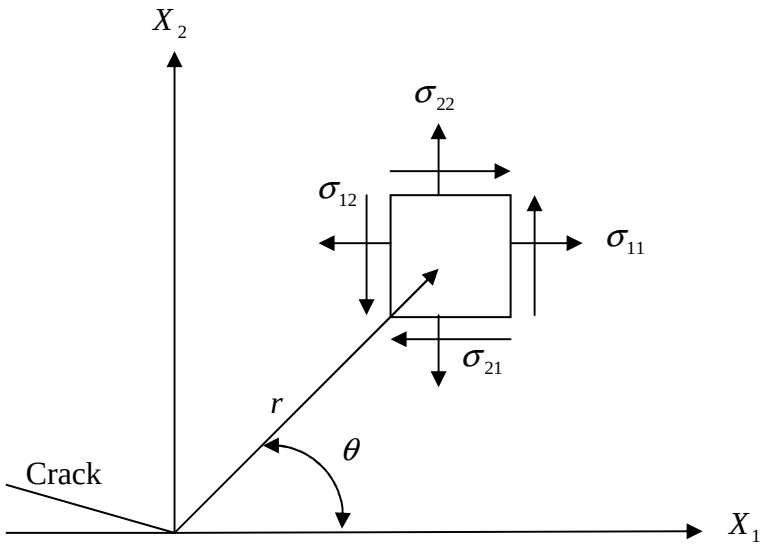

(a)

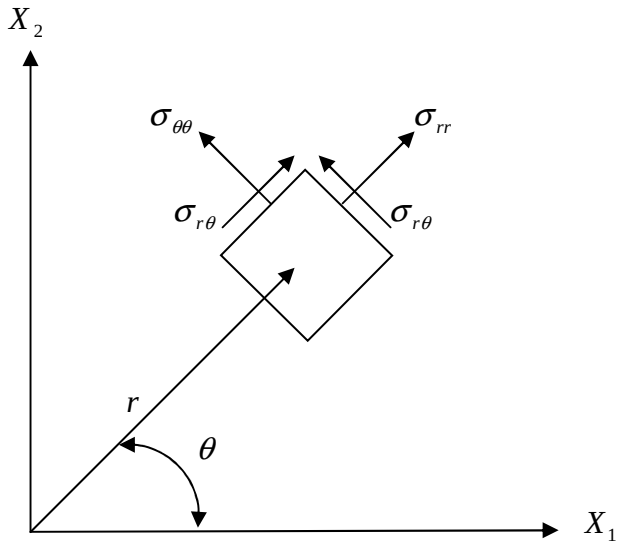

(b)

Figure 2.3 The normal and shear stresses in: (a) Cartesian co-ordinate system (b) polar co-ordinate system.

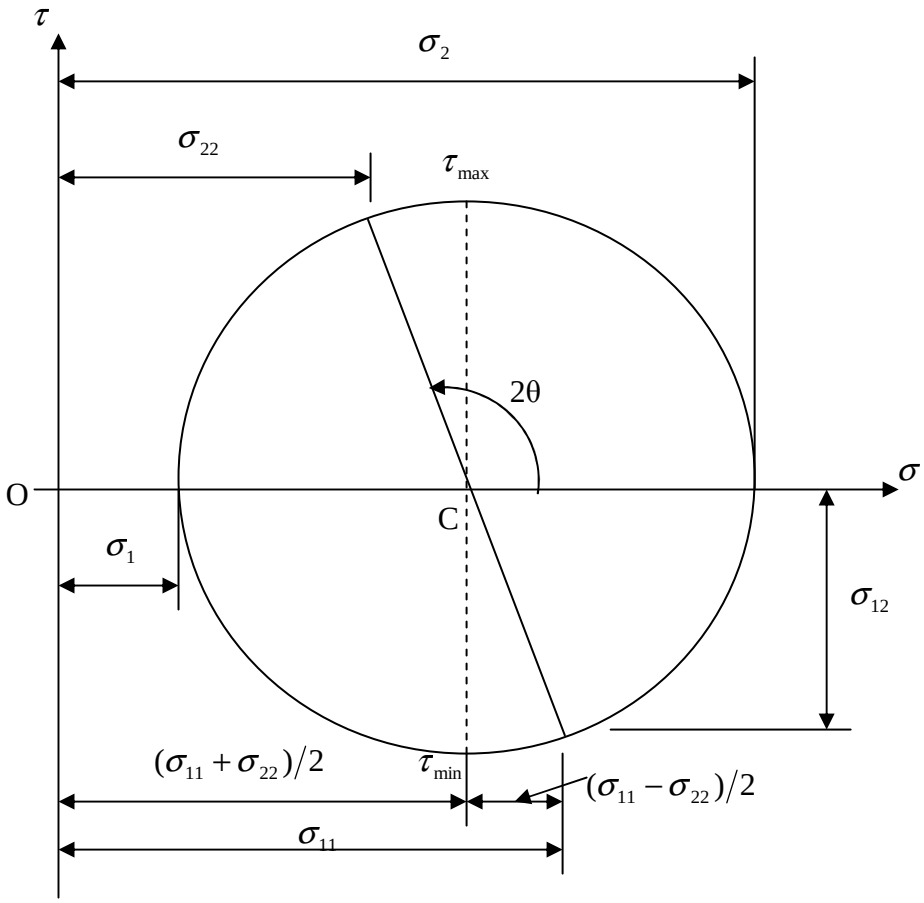

Figure 2.4 Stresses represented by a Mohr's Circle.

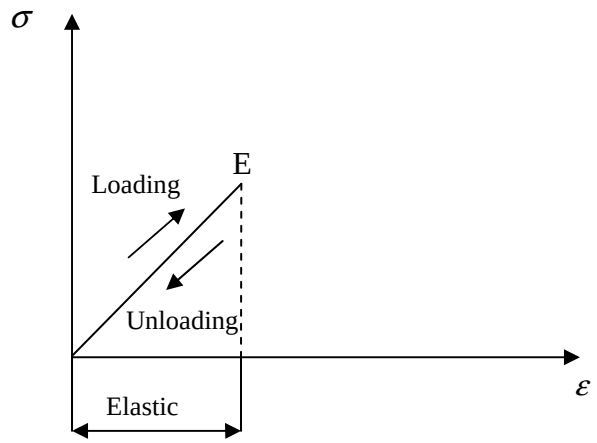

(a)

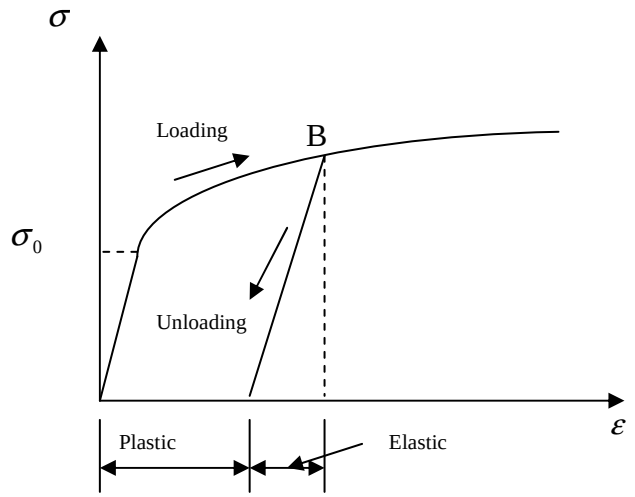

(b)

Figure 2.5 Stress-strain relation in: (a) elastic behaviour (b) plastic deformation

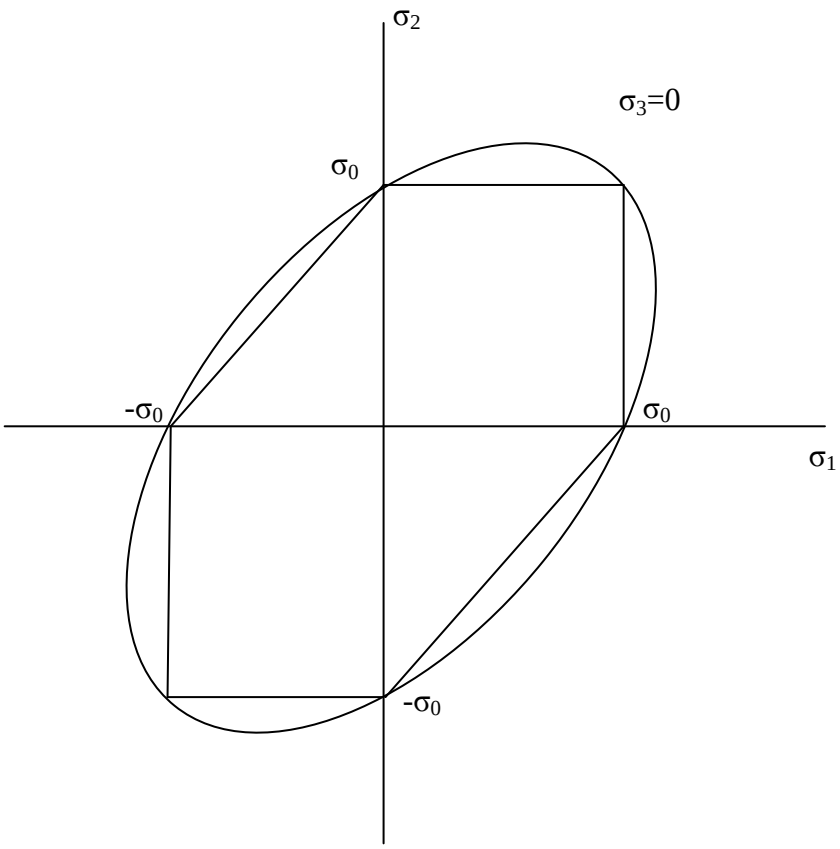

Figure 2.6: von Mises ellipse in plane stress.

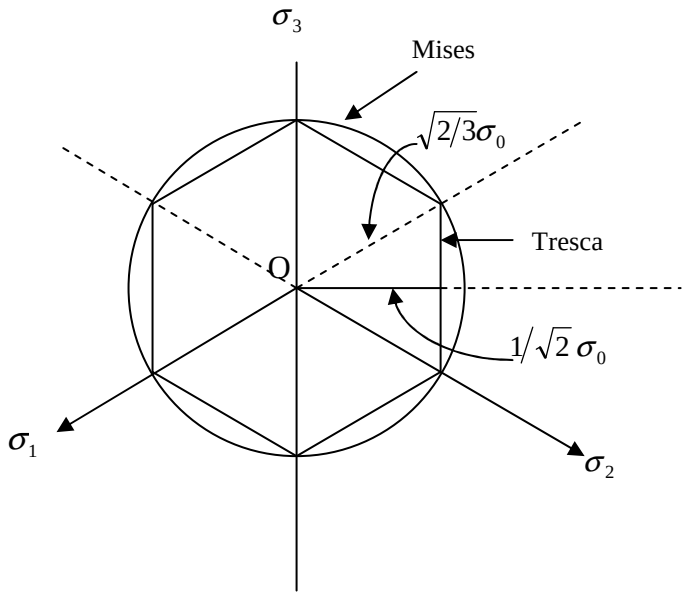

Figure 2.7 Illustration of yielding criterion in 3D: von Mises cylinder and Tresca hexagon.

3. Linear elastic fracture mechanics

3.1 Introduction

Fracture mechanics is intended to assure the integrity of structures which may contain cracks or defects, and is reviewed in standard texts such as Knott (1974), Anderson (1995) and Janssen et al (2002). The fundamental concepts are based on the nature of the stress and strain fields close to the crack front. Linear elastic fracture mechanics (LEFM) attempts to describe the fracture behaviour of a material that behaves largely elastically. The concepts of LEFM were initially introduced by Inglis (1913), and developed by Griffith (1921), Westergaard (1939) and Irwin (1957), and are introduced in the following sections.

3.2 Stress concentration factor

Inglis (1913) considered the effect of stress concentrations, focusing on an infinite plate under tensile stress σ_a with a central elliptical crack, with semi-axes a and c as shown in Figure (3.1a). The maximum stress occurs at the end of the major axis and can be expressed simply as:

$$\sigma_{\max} = \sigma_a (1 + \frac{2c}{a}) \tag{3.1}$$

When σ_a is a remote applied stress. When a = c (a circular hole) the maximum stress will occur at the edges of the hole and is three times the applied stress ($\sigma_{max} = 3\sigma_a$). The Inglis solution is particularly important because in the limit it addresses the stress distribution associated with a sharp crack (a=0) when the stress concentration becomes infinite. The implication is that in a perfectly elastic plate containing a sharp crack the failure will occur at an infinitesimal small stress. It should also be noted that the stress concentration is independent of the crack length.

3.3 Energy balance approach

In order to resolve the dilemma presented by the infinite stress concentration factor, Griffith (1921) considered the energy balance associated with fracture of brittle materials. Crack propagation was assumed to occur when elastic energy released during the crack extension was greater than the surface energy required for formation of a new surface. The idea is derived from a fundamental concept of thermodynamics which states that the change from non-equilibrium state to equilibrium is accompanied by a loss in potential energy.

The total energy of a system U which consists of a plate with a crack subjected to remote loading can be written (Janssen et al, 2002):

$$U=U_0+U_a+U\gamma-W \tag{3.2}$$

Where, U_0 is the total energy of the whole system without a crack, U_a is the change in the elastic energy of the plate due to the presence of the crack, $U\gamma$ is change in surface energy due to the crack, and W is work performed by the loading system during introducing the crack.

When the total energy U reaches a maximum value the crack is no longer stable, thus:

$dU/da < 0$

Since U_0 is constant, then

$$\frac{d}{da}(U_a + U_\gamma - W) < 0$$

After rearranging the equation becomes:

$$\frac{d}{da}(W - U_a) > \frac{dU_\gamma}{da} \tag{3.3}$$

The potential energy U_p to introduce a crack:

$U_p = U_0 + U_a - W$

$$G = \frac{-dU_p}{da} = \frac{d}{da}(W - U_a) \tag{3.4}$$

Where, G is the energy release rate. Substituting G, in equation (3.3), this gives:

$$\frac{-dU_p}{da} > \frac{dU_\gamma}{da} = R \tag{3.5}$$

This indicates that increasing the crack length by Δa leads to a decrease in the potential energy, and an increase in the surface energy.
Where, R is defined as the energy required to resist crack growth, and can be related to the energy release rate:

$G > R$

for a crack to propagate.

Consider an infinite solid plate containing a centre crack of length 2a as illustrated in Figure (3.1b). For a crack extending under fixed displacement, the force-displacement diagram is shown in Figure (3.2a). The strain energy accumulated for a crack length 2a is:

$$U_{strain} = \frac{F_1 u}{2} \tag{3.6}$$

Where u is fixed displacement, and F_1 is the load corresponding to the crack length 2a. If the same displacement is applied to a plate with a longer crack of length 2(a+da), the

strain energy is decreased by $\frac{1}{2}$.u(F_1-F_2). Since the work (W) done by external force is zero, (W = F.Δu = F.0 = 0). The whole potential energy of the system U_T is:

$$U_T = U_{strain} - W = \frac{Fu}{2} \tag{3.7}$$

Similar results are obtained under fixed load conditions as shown in Figure (3.2b). The work done by external force is:

$$W = Fu \tag{3.8}$$

And the potential energy of the system as crack extends by da is:

$$\begin{aligned} U_T &= U_{strain} - W \\ &= \frac{1}{2}Fu - Fu = -\frac{Fu}{2} \end{aligned} \tag{3.9}$$

It can be seen that the magnitude of change in potential energy is the same whether the crack is extended under fixed displacement or fixed load conditions.

Based on Inglis' (1913) results, the elastic energy released by introducing a central crack of length 2a can be written as:

$$U_{strain} = \pi a^2 t \frac{\sigma_a^2}{E'} \tag{3.10}$$

In plane stress E`=E, whereas in plane strain $E' = \frac{E}{1-\upsilon^2}$. Here υ is Poisson's ratio and t is the thickness of the plate.

The increase in surface energy due to introducing the crack is:

$$U_{surface} = 4at\gamma_s \tag{3.11}$$

Where γ_s is the surface energy of the material per unit area and (4at) is the area of the two surfaces that are created by the crack.

The net change in potential energy of the system can be written as:

$$U_T = U_{surface} - U_{strain}$$

$$U_T = 4at\gamma_s - \frac{\pi\sigma_a^2 a^2 t}{E'}$$

Based on the hypothesis that crack extension occurs when the potential energy of the system remains constant or decreases:

$$\frac{dU_T}{da} = 0$$

$$4t\gamma_s - 2\frac{\pi a\sigma_a^2 t}{E'} = 0 \tag{3.12}$$

The fracture criteria can now be expressed by a critical remote stress ($\sigma_a = \sigma_f$) which is a function of crack length (Griffith, 1921):

$$\sigma_f = \sqrt{\frac{2\gamma_s E'}{\pi a}} \tag{3.13}$$

Equation (3.13) depends on the assumption that fracture occurs under perfectly elastic conditions. Irwin (1948) and Orowan (1952), argued that the fracture process occurring at the crack tip is associated with plasticity even in very brittle materials. Thus the energy absorbed by plastic deformation γ_p must be considered, and the fracture stress can be approximated (Irwin, 1948) and Orowan, 1952):

$$\sigma_f = \sqrt{\frac{2E'\left(\gamma_s + \gamma_p\right)}{\pi a}} \tag{3.14}$$

Where, γ_p is the specific surface energy associated with plastic deformation.

Irwin (1956) formalised this concept by arguing that the rate of change of potential energy characterises crack extension. This is defined as a critical energy release rate, G_c:

$$G_c = \frac{\pi \sigma_f^2 a}{E'} \tag{3.15}$$

3.4 Stress intensity factor and crack tip singularity

An alternative approach to fracture is to consider the crack tip stresses and associated crack tip singularity. Consider a cylindrical coordinate system (r,θ) centred at the crack tip in an isotropic elastic material as illustrated in Figure (3.3). Westergaard (1939) gave an asymptotic solution for the stresses and displacements close to the crack tip. For Mode I loading, the leading stress term can be written as:

$$\begin{aligned}
\sigma_{x_1} &= \frac{\sigma\sqrt{\pi a}}{\sqrt{2\pi r}} \cos\frac{\theta}{2}\left(1 - \sin\frac{\theta}{2}\sin\frac{3\theta}{2}\right) + \text{..... ...} \\
\sigma_{x_2} &= \frac{\sigma\sqrt{\pi a}}{\sqrt{2\pi r}} \cos\frac{\theta}{2}\left(1 + \sin\frac{\theta}{2}\sin\frac{3\theta}{2}\right) + \text{..... ...} \qquad (r << a) \\
\sigma_{x_1 x_2} &= \frac{\sigma\sqrt{\pi a}}{2\pi r} \sin\frac{\theta}{2}\left(\cos\frac{\theta}{2}\cos\frac{3\theta}{2}\right) + \text{..... .....}
\end{aligned} \tag{3.16}$$

Where (r,θ) are polar coordinates centred at the crack tip, and the radial distance r is very small compared to the crack length a.

Irwin (1957) showed that the magnitude of stress at a crack tip can be characterized by a single parameter, the stress intensity factor, K:

$$\sigma_{ij} = \frac{K}{\sqrt{2\pi r}} f_{ij}(\theta) \tag{3.17}$$

The stress intensity factor depends on the type, the level of loading and the geometry and may be rewritten in form:

$$K = \sigma\sqrt{\pi a}\, Y$$

Where Y is the dimensionless factor of geometry and loading. Stress intensity factors for many crack problems are tabulated by Rooke and Cartwright (1976), and Murakami (1987).

The associated displacements (u_1,u_2) in (x_1,x_2) co-ordinate system can be written (Anderson, 1995):

$$u_1 = \frac{K_I}{2G}\sqrt{\frac{r}{2\pi}}\left\{\cos\frac{\theta}{2}\left[k - 1 + 2\sin^2\frac{\theta}{2}\right]\right\}$$
$$u_2 = \frac{K_I}{2G}\sqrt{\frac{r}{2\pi}}\left\{\sin\frac{\theta}{2}\left[k + 1 - 2\cos^2\frac{\theta}{2}\right]\right\} \tag{3.18}$$

Where k = (3-4υ) for plane strain and k = (3-υ)/(1+ υ) for plane stress.

The stress field near the sharp crack is also described by Williams' (1957) asymptotic expansion:

$$\sigma_{ij} = A_{ij}(\theta) r^{\frac{-1}{2}} + B_{ij}(\theta) r^0 + C_{ij}(\theta) r^{\frac{1}{2}} + \ldots\ldots\ldots \tag{3.19}$$

As r approaches the crack tip (r→0) the leading term is singular, but the second term is finite, and the remaining high order terms in the series approach zero at the crack tip.

Three types of loading can be considered on the crack as illustrated in Figure (3.4). Mode I is an opening loading, where load acts normal to the crack plane, Mode II (in-plane

shear) when the load acts parallel to the crack plane and perpendicular to the crack front, such that one crack surface slides on the other. Mode III (out-of-plane) loading is associated with torsional loading or shear parallel to the crack front.

3.5 Crack tip plasticity

The elastic stress singularity at the crack tip which is predicted by the linear elastic fracture mechanics can not exist in real materials due to localised plastic deformation when stresses exceed the yield strength. A simple approximation to the plastic zone size can be given by Irwin's approximation (1960):

$$r_p = \frac{1}{\alpha\pi}\left(\frac{K}{\sigma_0}\right)^2 \tag{3.20}$$

Where α is 2 for plane stress and 6 for plane strain, and the shape of the plastic zone is assumed to be circular.

The shape of the crack tip plastic zone can be approximated by combining Westergaard`s equations with the yield criteria. Westergaard`s equations written in terms of the principal stresses are:

$$\sigma_1 = \frac{K_I}{\sqrt{2\pi r}}\cos\frac{\theta}{2}(1+\sin\frac{\theta}{2})$$
$$\sigma_2 = \frac{K_I}{\sqrt{2\pi r}}\cos\frac{\theta}{2}(1-\sin\frac{\theta}{2}) \tag{3.21}$$

The third principal stress in plane stress is:

$$\sigma_3 = 0 \tag{3.22}$$

and for plane strain:

$$\sigma_3 = \frac{2\upsilon K_I}{\sqrt{2\pi r}}\cos\frac{\theta}{2} \tag{3.23}$$

Using the Tresca criteria, the radius of the plastic zone ahead of the crack in plane stress as a function of (θ) can be given as:

$$r_p(\theta) = \frac{K^2}{2\pi\sigma_0^2}\left[\cos\frac{\theta}{2}(1+\sin\frac{\theta}{2})\right]^2 \tag{3.24}$$

and in plane strain:

$$r_p(\theta) = \frac{K^2}{2\pi\sigma_0^2}\cos^2\frac{\theta}{2}\left[(1-2\upsilon+\sin\frac{\theta}{2})\right]^2 \tag{3.25}$$

Using the von Mises criteria, the shape of the plastic zone for plane stress can be written (Anderson, 1995):

$$r_p(\theta) = \frac{K^2}{4\pi\sigma_0^2}\left[1+\cos\theta+\frac{3}{2}\sin^2\theta\right] \tag{3.26}$$

and in plane strain:

$$r_p(\theta) = \frac{K^2}{4\pi\sigma_0^2}\left[(1-2\upsilon)^2(1+\cos\theta)+\frac{3}{2}\sin^2\theta\right] \tag{3.27}$$

It should be noted that the plastic zone size in plane stress is significantly bigger than in plane strain as shown in Figure (3.5).

3.6 Validity of linear elastic fracture mechanics (LEFM)

Linear elastic fracture mechanics is valid as long as the size of the plastic zone ahead of a crack tip is very small compared to the body dimensions. Consequently, the stress

intensity factor alone fully characterises the stress field under conditions of small scale yielding and the critical value K_{Ic} is a measure of fracture toughness. In order to ensure the validity of LEFM, the specimen size requirements for valid K_{Ic} fracture test are given by standards such as ASTM E 399-90 (1997) on a standard geometry containing a deep crack as shown in Figure (3.6), with width (w), crack length (a), thickness (B) and uncracked ligament (w-a). These requirements are:

$$a, B, (w-a) \geq 2.5\left(\frac{K_{Ic}}{\sigma_0}\right)^2 \tag{3.28}$$

Where σ_0 is the uniaxial yield stress.

The thickness requirement ensures plane strain conditions, while the crack length (a) and the ligament (w-a) requirements ensure that the near tip stress field is characterized by K.

3.7 The effect of specimen thickness on fracture toughness K_{Ic}

Fracture toughness (K_{Ic}) is influenced by the specimen thickness (Irwin and Kies, 1954, Irwin et. al., 1958, and Wallin, 2001). In thick specimens plane strain conditions prevail across the majority of the thickness, and a lower bound fracture toughness is observed. This plane strain fracture toughness is denoted as K_{Ic}, which is argued to be a material property. If the specimen is thin compared to the size of the plastic zone where plane stress conditions exist, higher fracture toughness is obtained. Figure (3.7) shows the relationship between fracture toughness and specimen thickness. The fracture toughness decreases as thickness increases until plateau is reached where further increase in thickness does not affect the toughness.

3.8 Determination of stress intensity factor *K*

The domain integral method developed and discussed by (DeLorenzi, 1985 and Li, Shih and Needleman, 1985, Shih, Moran and Nakamura, 1986) has been used to determine the

stress intensity factor. Nakamura, et. al, (1989), and Zhao, et. al, (2001) extended these expressions to general three-dimensional problems.

A local stress intensity factor K(s) at point (s) can be defined in the plane perpendicular to the crack front and relates to the local energy release rate J(s) (Zhao, Tong and Byrne, 2001):

$$K(s)=\sqrt{\frac{E.J(s)}{(1-\upsilon^2)}} \tag{3.29}$$

J(s) at point s is determined by a domain integral (Nakamura and Parks, 1989):

$$J(s)=\frac{1}{A_c}\int_{V(s)}(\sigma_{ij}.\frac{\partial u_i}{\partial x_k}.\frac{\partial q_k}{\partial x_j}-w.\frac{\partial q_k}{\partial x_k}).dV \tag{3.30}$$

Where, A_c is the increase in cracked area and the domain V(s) encloses the crack front.

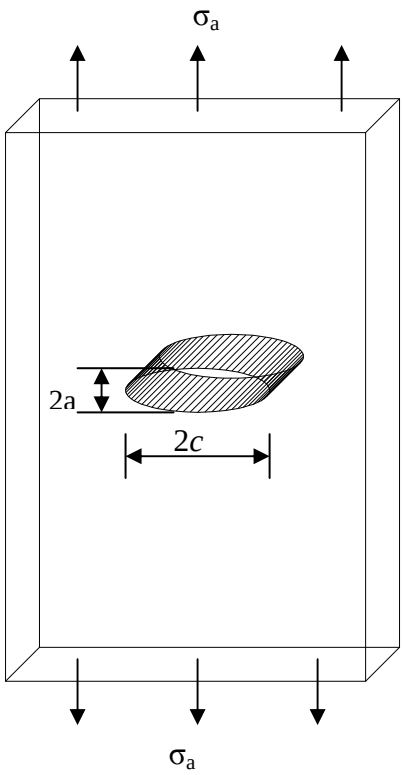

Figure 3.1a: Infinite plate with a central elliptical crack.

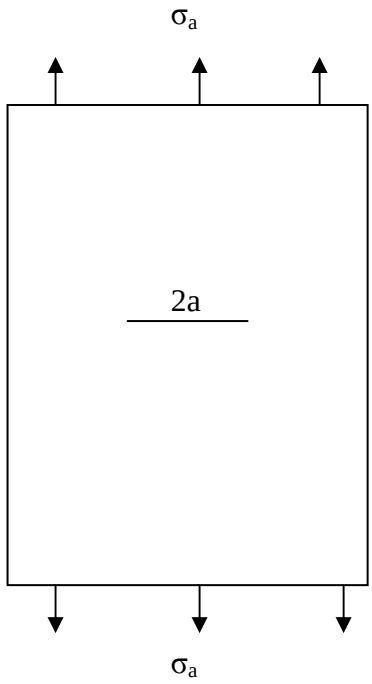

Figure 3.1b: Infinite plate with a central sharp crack.

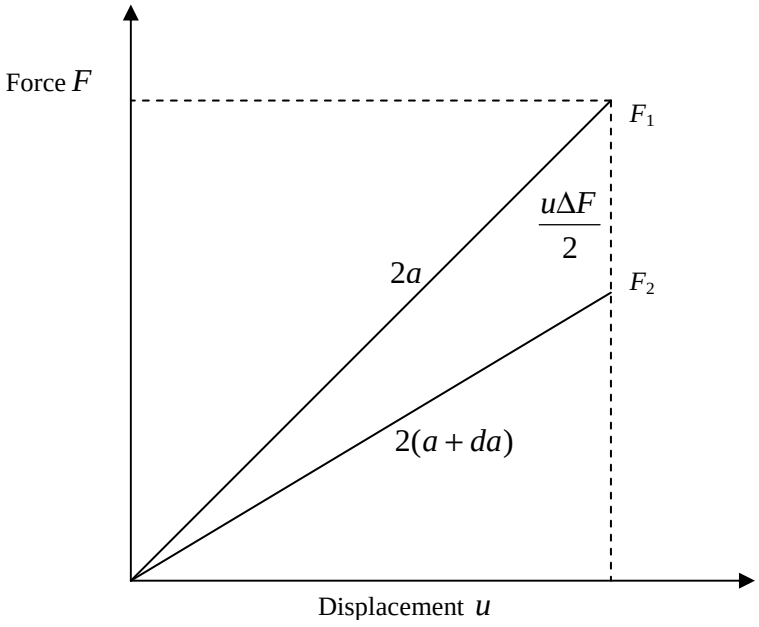

(a)

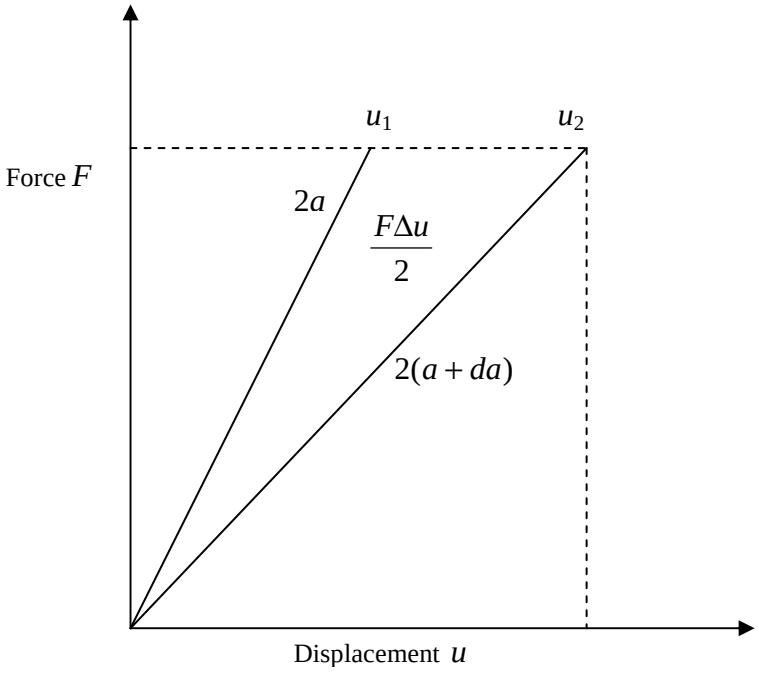

(b)

Figure 3.2: A crack extended under fixed displacement (a), and under fixed load (b).

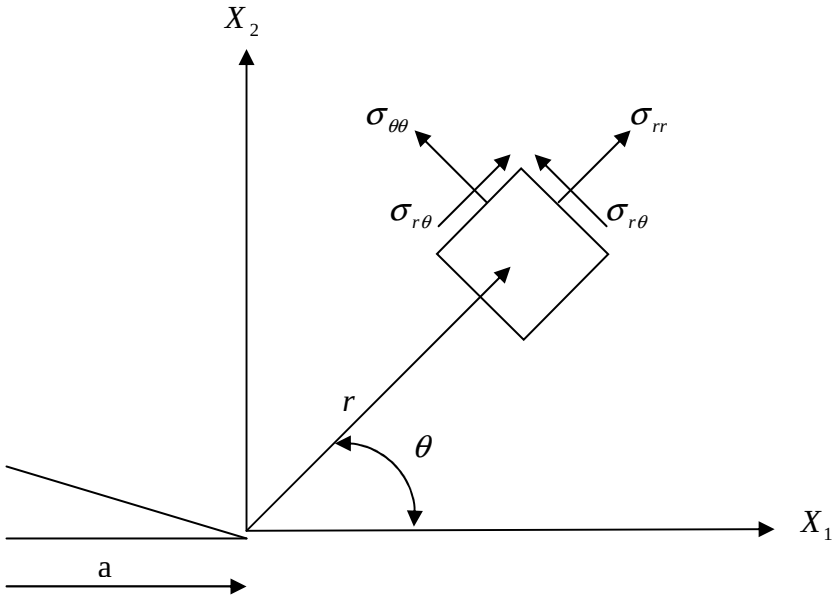

Figure 3.3 Stresses in polar co-ordinate system ahead of the crack.

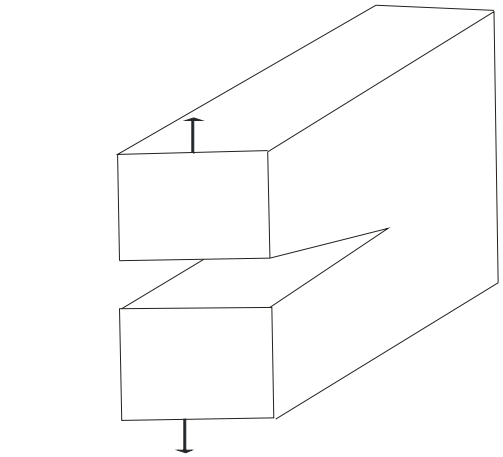

I

(a)

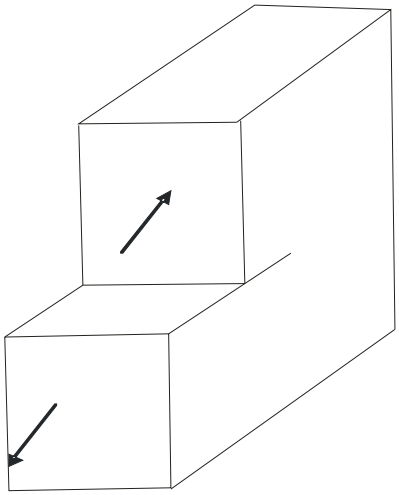

II

(b)

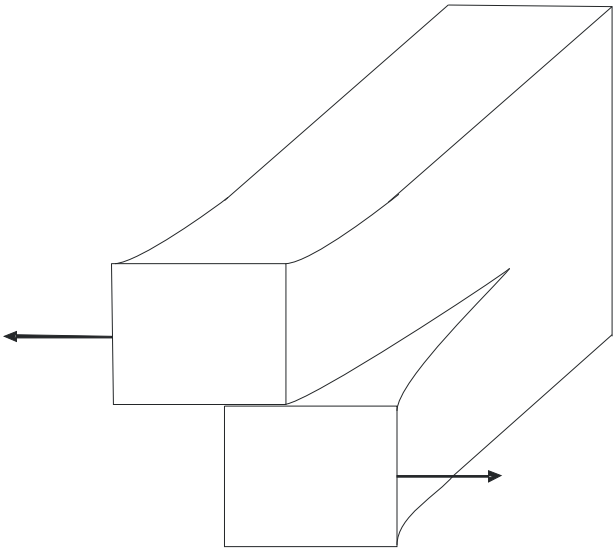

III

(c)

Figure 3.4: Modes of loading: (a) opening (b) in-plane shear (c) out-of-plane

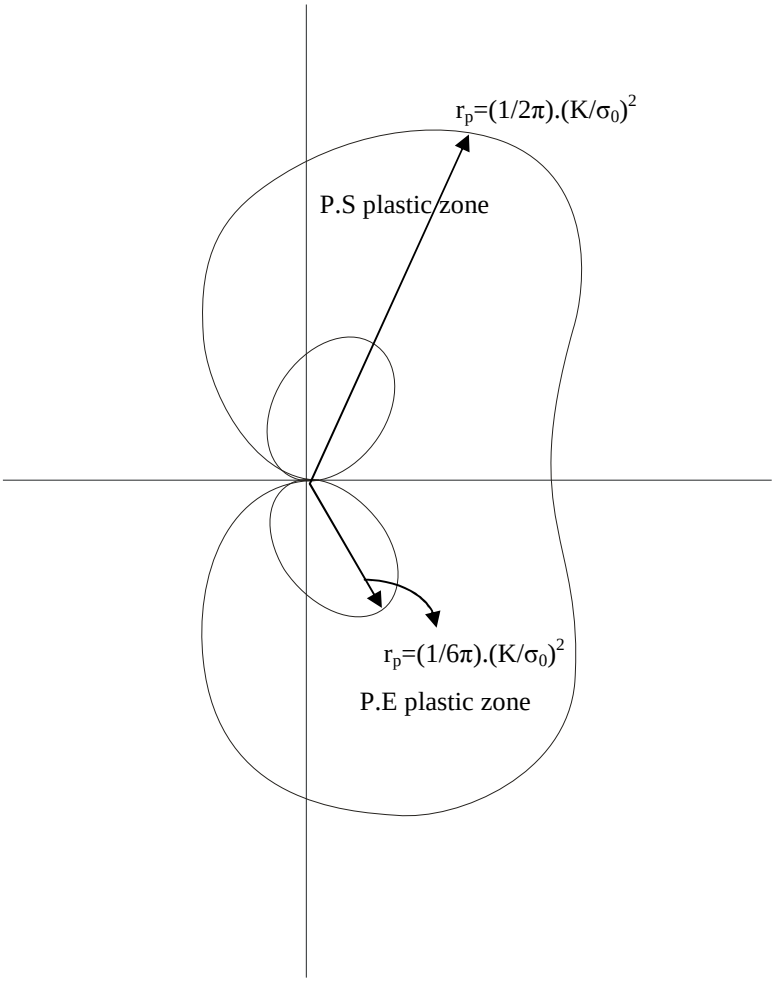

Figure 3.5: Plastic zone size in plane stress and plane strain conditions.

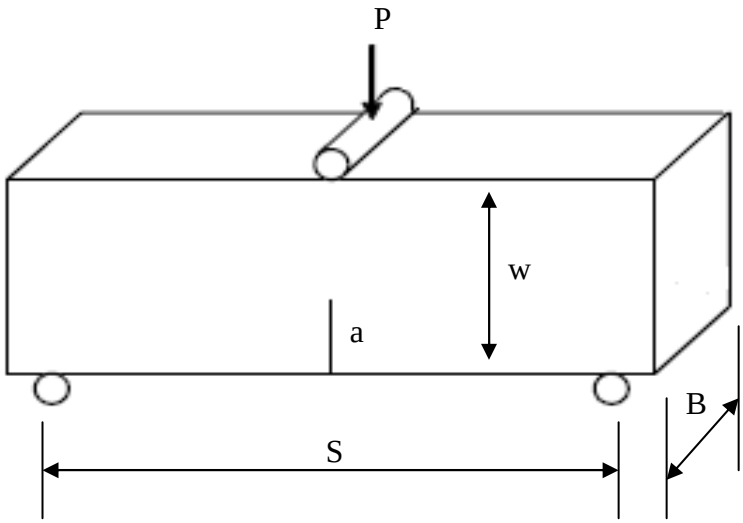

Figure 3.6: A standard specimen of ASTM for plane strain fracture toughness (Single edge cracked bend bar).

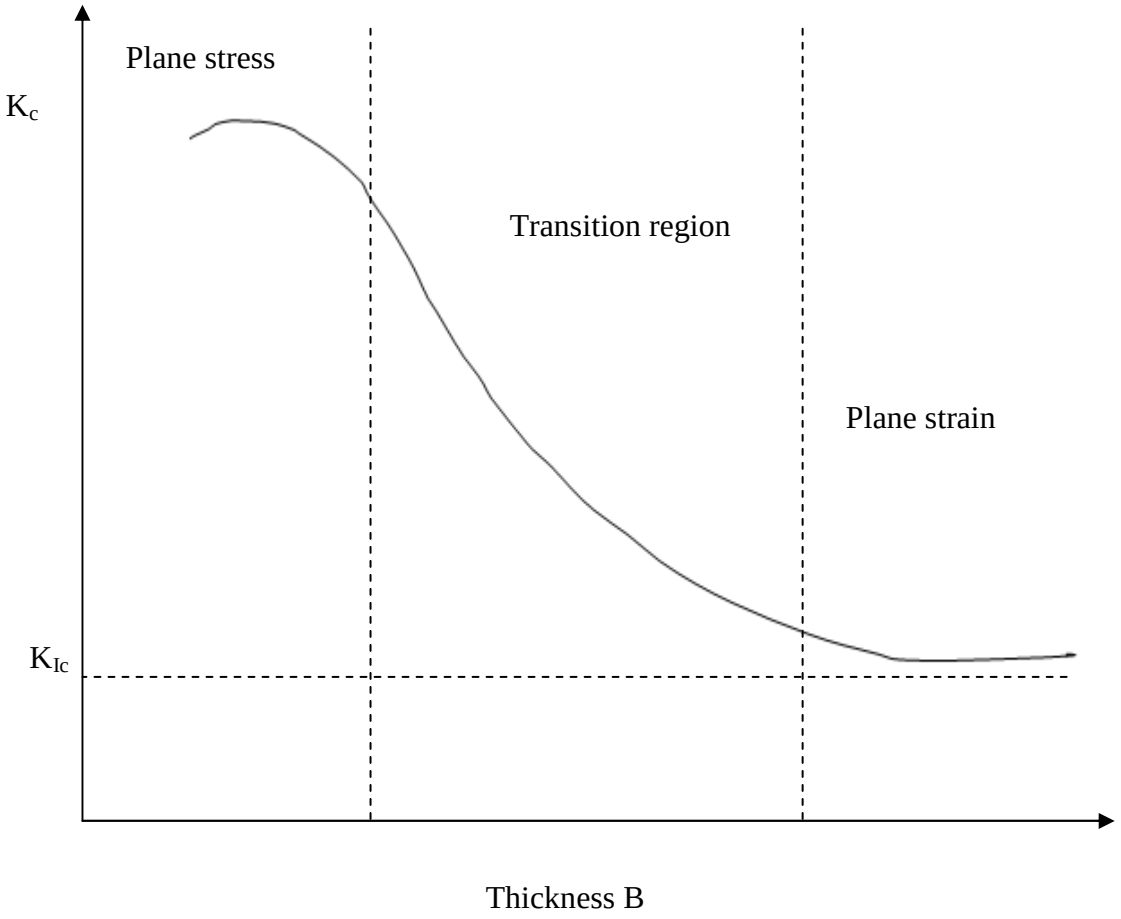

Figure 3.7: Toughness-thickness relationship.

4. Elastic-plastic fracture mechanics

4.1 Introduction

The concept of linear elastic fracture mechanics is no longer valid once the plastic zone around the crack tip becomes comparable in size with other body dimensions. Under these conditions elastic-plastic fracture mechanics uses the crack tip opening displacement (CTOD) and the J-integral to measure crack tip loading.

4.2 Crack tip opening displacement (CTOD)

As plastic deformation develops with increased load the crack tip starts to open and blunt prior to fracture. Wells (1961) introduced the crack tip opening displacement as a measure of the crack tip loading. The CTOD is the distance at which two perpendicular lines originating at crack tip intersect the crack flanks, as shown in Figure (4.1), (Shih, 1981 and Kumar et. al, 1981). It can also be defined as the displacement of the crack flanks of a blunting crack measured at the original crack tip. Wells (1961) observed that the fracture will occur at the critical value of CTOD, δ_c, which is considered to be a material property. In small scale yielding the CTOD, δ, can be related to the stress intensity factor, K, and the energy release rate, G:

$$\delta = \frac{4K_I^2}{E'\sigma_0} = \frac{4G}{\sigma_0} \tag{4.1}$$

This relation is for a non-hardening material under plane stress conditions. The general relation is given (Anderson, 1995):

$$\delta = \frac{K_I^2}{mE'\sigma_0} = \frac{G}{m\sigma_0} \tag{4.2}$$

Where, m is a dimensionless constant taken approximately as unity for plane stress and 2 for plane strain.

4.3 The J-Integral

Cherepanov (1967), Eshelby (1968) and Rice (1968) independently introduced a line integral which characterises stress singularities: the J-integral. They showed that J-integral is path independent on a path surrounding the crack tip, starting from the lower surface to the upper surface in an anti-clockwise direction as shown in Figure (4.2). J-integral sums the change in the energy in the volume enclosed by the path Γ (Rice, 1968):

$$J = \int_{\Gamma} w dy - T_i \frac{\partial u_i}{\partial x} ds \tag{4.3}$$

Here Γ is the length of the path contour. The first term (w) denotes the strain energy density (work of deformation per unit volume) which can be written as:

$$w = \int \sigma_{ij} d\varepsilon_{ij} \tag{4.4}$$

The second term represents work done by external forces where the components of traction vector T_i are:

$$T_i = \sigma_{ij}\, n_j \tag{4.5}$$

Where n_j is the unit vector perpendicular to the contour. u_i is the displacement vector and ds is the increment of length along the contour.

In order to develop a physical interpretation, consider a situation in which the crack is virtually extended by an incremental distance da as illustrated in Figure (4.3). Consequently, the path Γ moves and takes a new position, and the strain energy is released. During the process, work is done by the traction which is described by the

second term in the integral, while the change in strain energy is described by the first term.

In non-linear elastic materials J-integral can be interpreted in terms of the change in potential energy per unit area for a virtual crack extension da. This is identical to the energy release rate G in linear elastic materials (Janssen et al, 2002):

$$J = G = \frac{-1}{B}\left(\frac{dU}{da}\right) \tag{4.6}$$

The J-integral requires that no unloading may occur within the contour Γ. Therefore the J-integral is applicable to materials obeying a deformation theory of plasticity. In this case, the stress-strain curve is conveniently described by the Ramberg-Osgood relation:

$$\frac{e}{e_0} = \frac{\sigma}{\sigma_0} + \alpha\left(\frac{\sigma}{\sigma_0}\right)^n \tag{4.7}$$

Where α is a material constant and n is the strain hardening exponent, ranging from 1 in elastic conditions to ∞ for a non-hardening plastic material. Since the elastic strain at the crack tip is very small compared to the plastic strain, the stress-strain relation can be further simplified:

$$\frac{e}{e_0} = \alpha\left(\frac{\sigma}{\sigma_0}\right)^n \tag{4.8}$$

4.4 Numerical determination of J-integral

The J-integral is widely applied as a fracture mechanics parameter. In non-linear elastic materials the J-integral is identified with the energy release rate during crack advances. While in the linear elastic materials it is correlated with the stress intensity factor. In order to provide an accurate evaluation of J-integral using the finite element technique, a domain integral method is often adopted. The J-integral is associated with the change in

potential energy due to a virtual extension of a crack front as shown in Figure (4.4), as introduced independently by Hellen (1975) and Parks (1974, 1977). The technique is based on calculations of the variation in potential energy due to a virtual change of crack length. The technique is applicable to both two and three-dimensional problems. Hellen (1975) initially addressed linear elastic materials, while Parks (1974, 1977) extended the technique to include nonlinear material behaviour.

The potential energy of the body, in terms of the finite element technique using stiffness derivative formulation is given by (Parks 1974, Hellen 1975):

$$\Pi = \frac{1}{2}[u]^T[K][u] - [u]^T[F] \tag{4.9}$$

Where u is a vector with the nodal displacement, [K] is stiffness matrix and F is a vector with applied nodal force.

The energy release rate can be related to the stiffness derivative matrix with respect to crack length (Parks (1974), Hellen (1975)):

$$G = -\frac{d\Pi}{da} = -\frac{1}{2}[u]^T \frac{\partial[K]}{\partial a}[u] \tag{4.10}$$

The implementation of this equation requires moving only the elements within a domain at the crack tip. As the elements are distorted, their stiffness changes and the corresponding energy release rate can be written as

$$G = -\frac{1}{2}[u]^T \left(\sum_{i=1}^{N_C} \frac{\partial[K_i]}{\partial a} \right)[u] \tag{4.11}$$

Where $[K_i]$ are the stiffness matrices of the element and N_C is the elements number within the domain integral.

Li, Shih and Needleman, (1985), and Shih, Moran and Nakamura, (1986), generalised a domain integral method to determine the energy release rate. The domain A is an area

around the crack tip which enclosed by the contours Γ_0 and Γ_1 as shown in Figure (4.5). In Abaqus the domain is identified as rings of elements surrounding the crack tip. The expression of J-integral in terms of domain integral in two-dimensional problems can be written (Shih, Moran and Nakamura, 1986):

$$J = \int_A \left[\sigma_{ij} \frac{\partial u_i}{\partial x_1} - W\delta_{1j} \right] \frac{\partial q_1}{\partial x_j} dA. \tag{4.12}$$

Where A is the surface of the component under consideration, while u_i and σ_{ij} are the components of the displacement vector and the stress tensor, w is strain energy density, and q_1 is the weight function, δ_{1j} is the Kronecker delta.

In three-dimensional analysis the crack front is described by a continuously turning tangent as shown in Figure (4.6a). The energy release rate (J-integral) at point s can be expressed as a domain integral (Zhao, Tong and Byrne, 2001):

$$J(s) = \frac{1}{A_C} \int_{V(s)} (\sigma_{ij} \cdot \frac{\partial u_i}{\partial x_k} \cdot \frac{\partial q_k}{\partial x_j} - w. \frac{\partial q_k}{\partial x_k}) . dV \tag{4.13}$$

Where, A_C the increase in cracked area, V(s) the domain encloses the crack front segment between (s-ε) and (s+ε) as shown in Figure (4.6b).

4.5 HRR Field

Hutchinson (1968a) and Rice and Rosengren (1968) independently analysed asymptotic crack tip fields under elastic plastic conditions and showed that the J-integral quantifies the amplitude of the near stress field in a similar way to the stress intensity factor in an elastic stress field. The HRR field assumes that the crack remains sharp during deformation and that finite geometry changes associated with the crack tip blunting are neglected. Formally this implies a framework of small deformation theory where the stresses at the crack tip can be described by the HRR fields using the J-integral (Rice and Rosengren, 1968):

$$\frac{\sigma_{ij}}{\sigma_0} = \left(\frac{J}{\varepsilon_0 \sigma_0 \alpha I_n r} \right)^{\frac{1}{1+n}} \tilde{\sigma}_{ij}(n,\theta) \tag{4.14}$$

$$\frac{\varepsilon_{ij}}{\varepsilon_0} = \frac{\alpha}{E} \left(\frac{J}{\varepsilon_0 \sigma_0 \alpha I_n r} \right)^{\frac{n}{1+n}} \tilde{\varepsilon}(n,\theta) \tag{4.15}$$

Here r is the radial distance from a crack tip, $\tilde{\sigma}_{ij}(n,\theta)$, $\tilde{\varepsilon}(n,\theta)$ and I_n are tabulated functions of strain hardening exponent n and the parametric angle θ. If n=1 the HRR field reduces to the Westergaard equations (i.e. $\sigma_{ij} \alpha r^{-1/2}$) for linear elasticity. Conversely, if n=∞ (perfect plasticity) the stress field σ_{ij} is independent of r, and the crack tip stresses are finite.

It should be noted that in order for J to be a path independent σ_{ij} e_{ij} must exhibit a r^{-1} singularity (Anderson, 1995). In a linear elastic material σ_{ij} and e_{ij} vary as $r^{-1/2}$ so that the product of stress and strain has a r^{-1} singularity. Similarly in non-linear material σ_{ij} and e_{ij} must vary as $r^{-1/n+1}$ and $r^{-n/n+1}$ respectively, and the product of stress and strain again exhibits an r^{-1} singularity.

4.6 J-Dominance

McClintock (1971) examined different cracked geometries, in fully plastic condition and observed that the crack tip field is not unique. Consequently in the limit of non hardening plasticity J no longer uniquely characterise all crack tip fields. He demonstrated that the stress fields depend on geometry and loading mode.

The conditions under which a unique crack tip field evolves at the crack tip are known as the J-dominance conditions. To establish these conditions McMeeking and Parks (1979) carried out a detailed study on a deeply cracked plane strain bend bar and a centre crack panel for a low and non hardening material. They compared the small scale yielding field with that in large scale yielding and concluded that fields were similar as long as the uncracked ligament is greater than $200J/\sigma_0$ in tension and $25J/\sigma_0$ in bending.

Shih and German (1981) confirmed the calculations of McMeeking and Parks by comparing the full field small geometry change solution with HRR field at $r \geq 2J/\sigma_0$. They showed that the size of the region dominated by HRR singularity is a small fraction of the uncracked ligament length in low hardening materials. Using the criteria that the stress must be within 90% of the HRR value at a distance ($r=2J/\sigma_0$), Shih and German suggested that the uncracked ligament must exceed $25J/\sigma_0$ to ensure J-dominance of deeply edge crack bar subject to bending while $200J/\sigma_0$ for centre cracked panel subjected to tension to maintain J-dominance.

A detailed study was carried out by Al-Ani and Hancock (1991) on short cracks in edge cracked bar in bending and tension. They showed that plastic zone extended backward to encompass the cracked face, and J-dominance is controlled by the crack length (a) and lost at a $>200J/\sigma_0$.

4.7 Micromechanics of ductile tearing and cleavage

The process of ductile fracture of most metals and alloys includes void nucleation, growth and coalescence. Void nucleation normally occurs in the presence of second phase particles or inclusions and is caused by either the debonding of the particles from the matrix material or by particle fracture. Following void nucleation, the voids grow, interact, and eventually coalesce in the applied deformation field. The main characteristic of ductile fracture is that a lot of energy is consumed by the extensive plastic deformation. The ductile fracture process is driven by high stress triaxiality (McClintock, 1968, Rice and Tracey, 1969). Rice and Johnson (1970) showed that finite plastic deformation is necessary for void growth combined with high stress triaxiality. Under mode I loading the maximum triaxiality exists at approximately a distance 2 CTOD (Crack tip opening displacement) from the crack tip (Brocks and Schmitt, 1995). High stress triaxiality nucleates microvoids and plastic strain is necessary for growth and coalescence (McMeeking and Parks, 1979, Hancock and Cowling, 1980). Figure (4.7) shows the growth and coalescence of microvoids. If a cracked plate is loaded local strains and stresses at the crack tip will nucleate voids. Then the crack blunts and the voids grow and coalesce, and eventually form a continuous fracture surface as shown in Figure (4.8).

In fracture samples the crack may extend in a thumbnail fashion in which the greatest extension occurs at the centre of the specimen while the free surface edges fail by shear lip formation (Delorenzi and Shih, 1983). Under mode I load the maximum plastic strain occurs at 45-degree from the crack plane and causes hole coalescence in a zig-zag manner (Hancock and Cowling, 1980, Anderson, 1995). At the microscale level this is the preferred path for void coalescence, and zigzag often occurs even if the crack appears to be flat at macroscale level (Beachem and Yoder, 1973).

The process of void growth and coalescence can be modelled using a continuum mechanics approach using Gurson model (Gurson, 1977) which introduces damage through the constitutive relation. The Gurson-Tvergaard porous plasticity model (Gurson, 1977, Tvergaard 1981, 1982) assumes voids are spherical in materials and remain spherical in the growth process. A critical void volume fraction (f_c) is often used to designate material failure (e.g. Needleman and Tvergaard, 1987). Important modifications have been made to the Gurson model. Yamamoto (1978) introduced flow stress to include the effect of strain hardening. Tvergaard improved the accuracy of the Gurson model by adjusting the numerical coefficients. Tvergaard and Needleman (1984) associated the model with complete loss of stress carrying capacity. Although the flow potential proposed by Gurson does permit a complete loss of stress carrying capacity at a critical void volume fraction, this critical void volume fraction is unrealistically high (Tvergaard and Needleman, 1984, Zhang and Niemi, 1995).

The Gurson-Tvergaard model derived from a rigid-plastic limit analysis of a solid containing a spherical void and the yield function is given (Tvergaard, 1982):

$$\Phi = \left(\frac{\sigma_e}{\bar{\sigma}}\right)^2 + 2q_1.f.\cosh\left(\frac{3q_2\sigma_m}{2\bar{\sigma}}\right) - (q_3 f^2 + 1) = 0 \qquad (4.16)$$

Where σ_e is the Mises effective stress, σ_m is the hydrostatic stress and $\bar{\sigma}$ is the flow stress of the material. Values of q_1=1.5, q_2=1.0 and q_3=q_1^2 are used for metals, while f is the void volume fraction. The rate of the void growth is given by:

$$\dot{f} = (1-f)\dot{\varepsilon}_{kk}^{p} + \Lambda \dot{\varepsilon}_{eq}^{p} \tag{4.17}$$

Where $\dot{\varepsilon}_{kk}^{p}$ is the plastic strain rate of volume change, and $\dot{\varepsilon}_{eq}^{p}$ is the equivalent plastic strain rate. The first term is the growth rate of pre-existing voids and the second term is the contribution of new voids that are nucleated with plastic strain. Λ is the scaling coefficient which is applied to the plastic strain rate of the matrix material (Anderson, 1995):

$$\Lambda = \frac{f_N}{S_N\sqrt{2\pi}} . \exp\left(-\frac{1}{2}\left[\frac{\varepsilon_{eq}^{p} - \varepsilon_N}{S_N} \right]^2 \right) \tag{4.18}$$

The plastic strain range for the nucleation of new voids can be described by a normal distribution with a mean value ε_N, S_N is the standard deviation and f_N is the volume fraction of nucleating voids.

It is often assumed that the failure occurs when the void fraction (f) reaches a critical value (f_c). Tvergaard and Needleman (1984) introduced an effective void volume fraction (f^*) instead of (f) to include void coalescence:

$$f^* = f \quad \text{for} \quad f \le fc \quad \text{or}$$
$$f^* = f_c + \frac{f_u^* - f_c}{f_F - f_c}(f - f_c) \qquad \text{for} \quad f > fc \tag{4.19}$$

Where f_c, f_u^* and f_F are fitting parameters. The effect of hydrostatic stress is amplified when $f > f_c$ which accelerates the onset of a plastic instability.

In contrast cleavage fracture occurs due to the direct separation of low index crystallographic planes. Little energy is consumed and usually accompanied by modest levels of plastic deformation. Cleavage fracture occurs due to the local plastic flow required for inducing dislocations to nucleate microcracks in the second phase particle or carbides. These then cleave crystal grains and propagate through the adjacent grains due

to the effect of stresses of the macroscopic crack (Bowen et al, (1987), Wang et al, (2002a,b)). Ritchie, Knott and Rice (1973) (henceforth RKR) introduced a model to relate the fracture stress to the fracture toughness. They stipulated that fracture occurs when the stress ahead of the crack tip exceeds the fracture stress over a characteristic distance r_c and regardless of the specimen size and crack length. A finite volume of material must be sampled ahead of the crack tip to include a particle that is sufficiently large to nucleate cleavage (Curry and Knott, 1979). Thus a critical volume over which the opening stress exceeds the fracture stress is required for failure. It was confirmed that the distribution of the crack opening stress over the ligament is almost the same for different SENB specimens at critical fracture toughness, (Kim et al., 2003), in accord with the RKR model.

4.8 Ductile-brittle transition

The mechanism of fracture in ferritic steels can change from ductile to cleavage as the temperature decreases. At low temperatures, steel fails by cleavage due to the increase in the yield stress and the local fracture stress is reached before extensive plasticity can develop. At high temperatures, the material is ductile and fails by void nucleation and coalescence. In transition region both micromechanisms cleavage and ductile can occur. Figure (4.9) shows the schematic toughness-temperature curve for ductile-brittle transition. At low temperatures the cleavage mechanism prevails and the toughness reaches the lower-shelf region. At higher temperature the toughness becomes higher at the upper shelf where the ductile fracture dominates. In the lower transition region the fracture mechanism is pure cleavage, but with an increase in temperature the toughness increases and cleavage becomes more difficult. In the upper transition region crack growth initiates by void coalescence but final fracture occurs by cleavage (Wallin, 1989). On initial loading in the upper transition region cleavage does not occur because there are no critical particles near the crack tip. As the crack advances by ductile tearing, the growing crack samples a critical particles and cleavage occurs (Dodds, et al., 1991 and Anderson, 1995).

4.9 Crack instability controlled by J

The material resistance to ductile crack growth is usually expressed in terms of the resistance curve, J-Δa, as shown in Figure (4.10), where the fracture toughness increases with increasing crack extension. Depending on the material response, geometry and loading conditions ductile instability may occur after a certain amount of crack extension. The fracture toughness J_{Ic} on the J-Δa resistance curve is measured near the initiation of stable crack growth, however the exact point at which the crack initiates is often difficult to define. In consequence an arbitrary crack extension of 0.2mm extension is adopted. The slope of the resistance curve dJ/da describes the stability of the crack growth, in which a material with a high slope will experience more stable crack growth. This slope is usually described by a nondimensional tearing modulus (Paris et al., 1979, Hutchinson and Paris, 1979), T_R:

$$T_R = \frac{E.dJ}{\sigma_0^2.da} \tag{4.20}$$

The crack is stable as long as the slope of the applied driving force is less than that for the material curve (i.e. at b_1) as shown in Figure (4.11). However further increase in the driving force at point b_2 the crack becomes instable. Since the slope of R-curve is presented by a non-dimensional tearing modulus, instability occurs when the applied tearing modulus reaches the material tearing modulus:

$$T_{app} \geq T_R \tag{4.21}$$

4.10 Crack tip fields in a growing crack.

The asymptotic crack tip fields for a stationary crack under elastic plastic conditions can be quantified by the single parameter, J-integral, (Hutchinson, 1968a and Rice and Rosengren, 1968). In the limit of non-hardening the HRR field is consistent with the Prandtl field (1920) where the complete plasticity is assumed to surround the crack tip

Hutchinson (1968b). The Prandtl field consists of three regions as shown in Figure (4.12), two diamond-shaped regions (I, III) and centre fan region (II) between the diamond regions. The stress field in diamond regions is constant, but in the centre fan regions the field changes corresponding to the angle θ.

In contrast, Rice, Drugan and Sham (1980) analysed the crack tip stress field in a growing crack under small scale yielding conditions and in non-hardening materials. They proposed stress discontinuity around the tip of a growing crack. They also showed that the continued plastic response around the crack tip assumed in a growing crack is relaxed, and an elastic sector confined between the fan sector and the trailing plastic sector of a moving crack is necessary. The rate of opening displacement, δ, associated with a moving crack can be expressed (Rice, Drugan and Sham, 1980):

$$\dot{\delta} = \alpha \frac{\dot{J}}{\sigma_0} + \beta \frac{\sigma_0}{E} \dot{a} \ln\left(\frac{R}{r}\right) \tag{4.22}$$

Where $\dot{\delta}$ is the rate of opening displacement at a distance R behind the crack tip. $\dot{J}$ is the rate of change in J-integral and $\dot{a}$ is the rate of a growing crack. A and β are constants. R scales approximately with the size of the plastic zone and is estimated by:

$$R = \frac{\lambda E J}{\sigma_0^2} \quad \text{where} \quad \lambda=2.0 \tag{4.23}$$

The constant α is approximately equal to that in stationary cracks and can be estimated by:

$$\delta = \alpha \frac{J}{\sigma_0} \tag{4.24}$$

Drugan, Rice and Sham (1982) showed that the crack tip field includes more than the three sectors observed in a stationary crack. This field includes a plastic sector of non-constant stress, an elastic unloading sector and a trailing plastic sector of the same type as that directly preceding the elastic sector in addition to the two plastic sectors exist as constant stress and centre fan sector, as shown in Figure (4.13). Varias and Shih (1993)

showed that the loading and geometry effects on the growing crack are different from that in a stationary crack. They showed non-zero T-stress (positive or negative) reduces the stress triaxiality in a growing crack, which contrasts to a stationary crack where the negative T-stress lower the stress triaxiality and positive T-stress increases slightly the triaxiality near the crack tip (Betegón and Hancock, 1991). They also showed higher stress triaxiality for zero T-stress than the HRR field for a stationary crack. Beardsmore et al (2009) showed that the crack tip J-integral and constraint for a growing crack depend on the way in which the crack is introduced into the computational model.

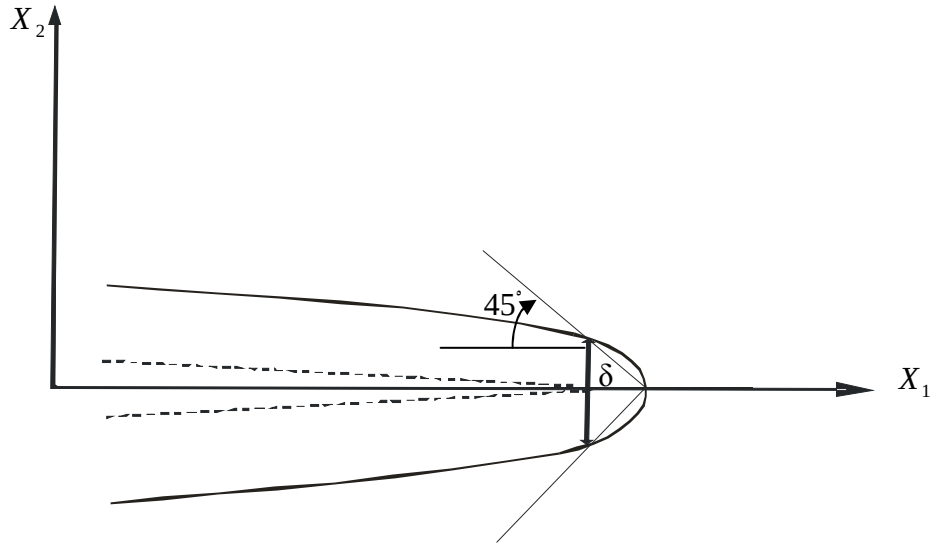

Figure 4.1: Two definitions of the crack tip opening displacement CTOD, δ.

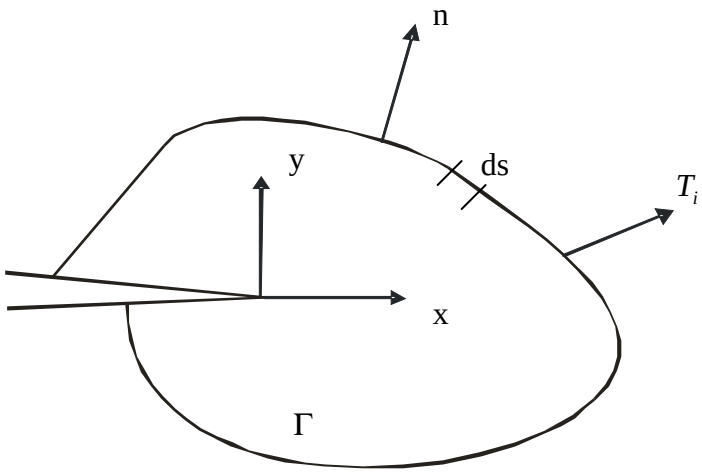

Figure 4.2: An arbitrary path, Γ, surrounding a crack front giving rise to the definition of J-integral.

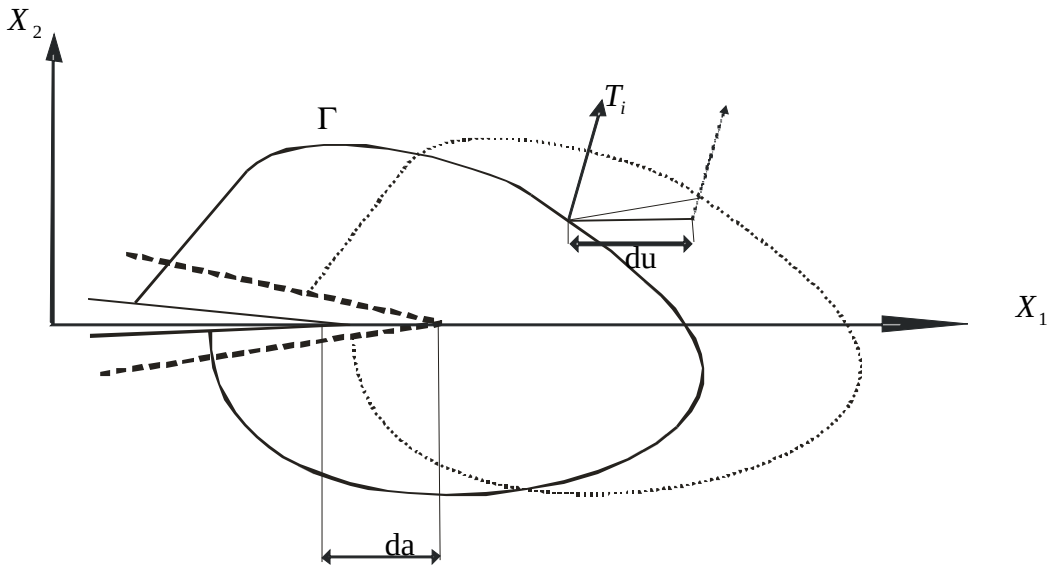

Figure 4.3: Contour integral associated with a virtually extended crack.

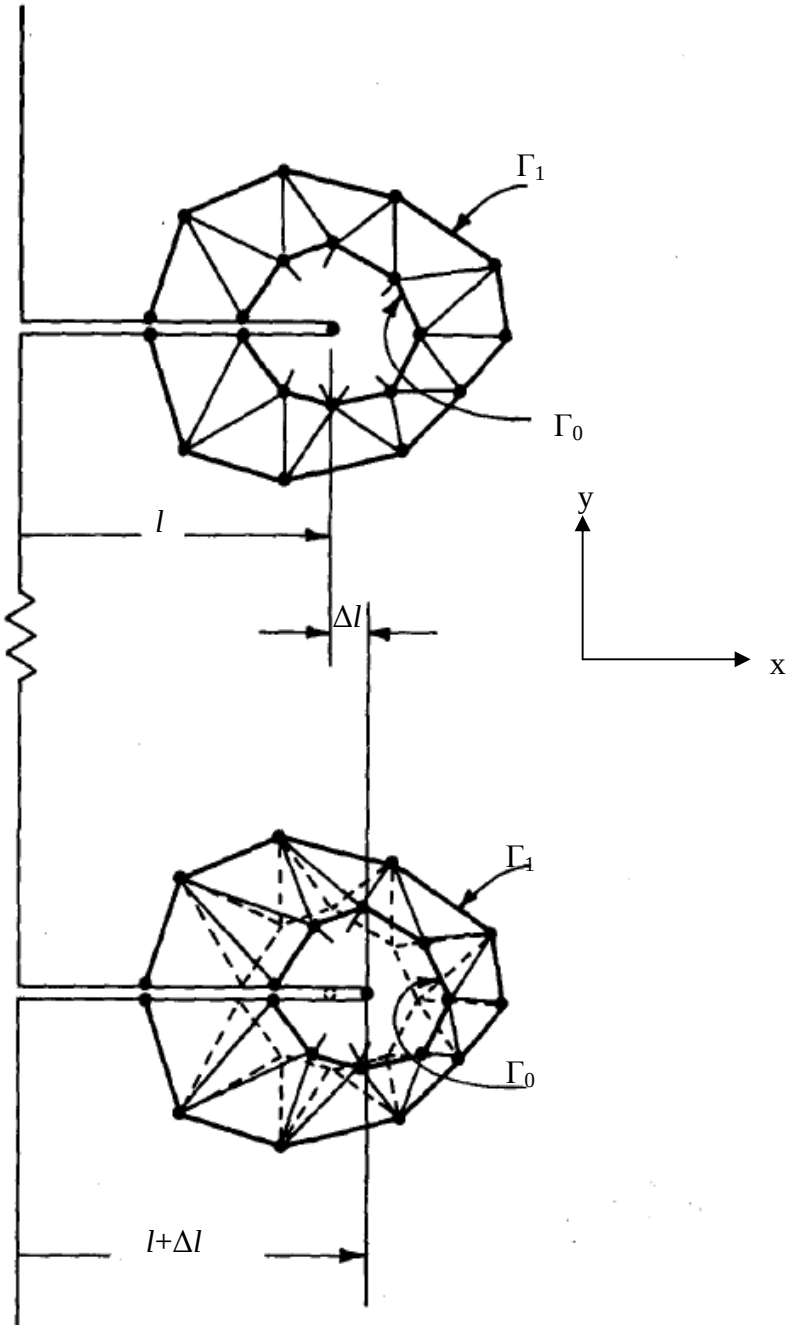

Figure 4.4: Illustration of virtual extension technique after Parks (1974, 1977) and Hellen (1975).

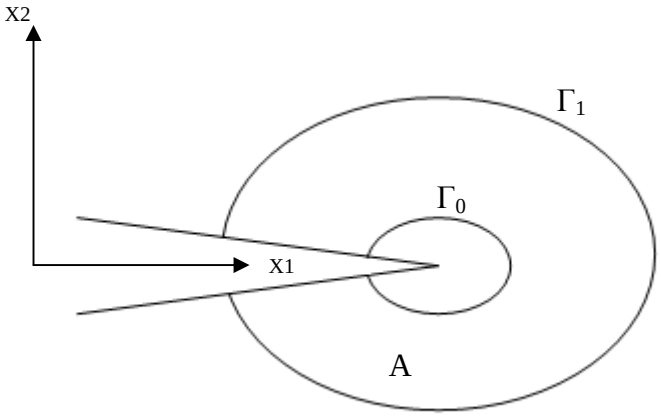

Figure 4.5: Domain integral enclosed by paths Γ_0 and Γ_1.

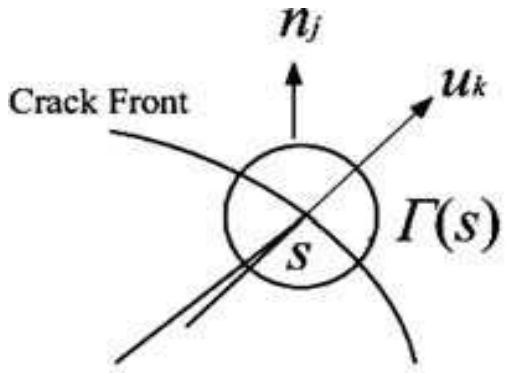

(a)

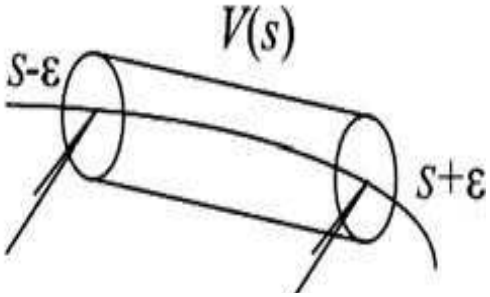

(b)

Figure 4.6: Schematic of elements used in the definition of the J-integral and the interaction integral: (a) Crack tip contour Γ (b) Volume V(s) encloses the crack front (Zhao, et al. 2001).

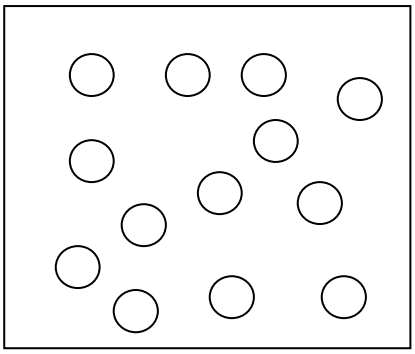

a. Nucleation

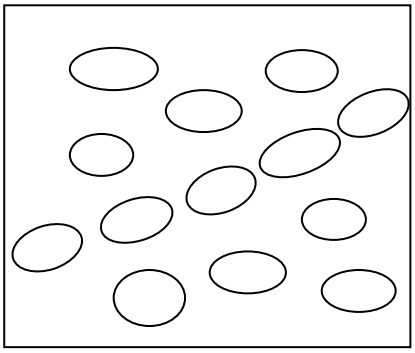

b. Growth

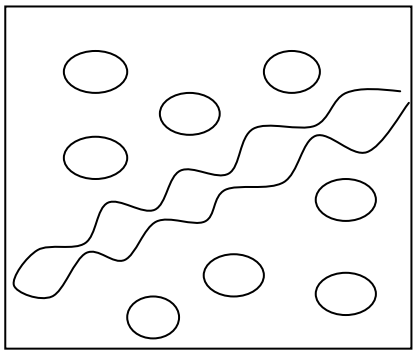

c. Coalescence

Figure 4.7: Ductile fracture by void nucleation, growth and coalescence.

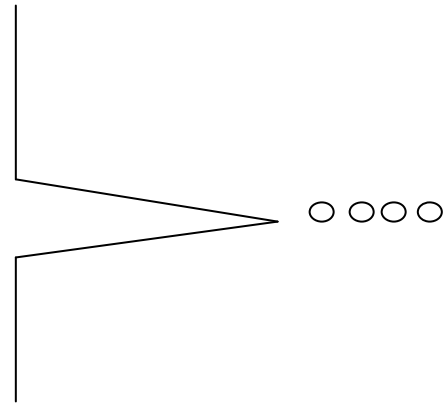

a. Void nucleation

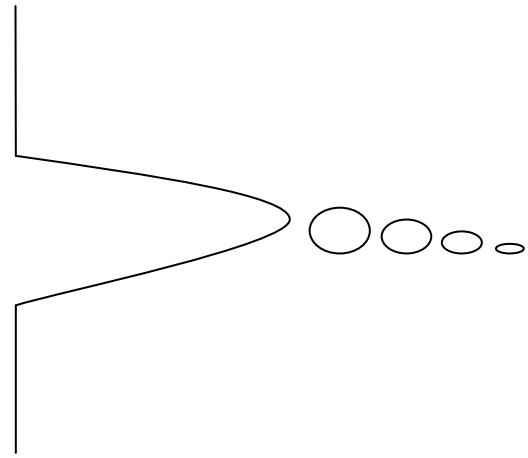

b. Crack blunts

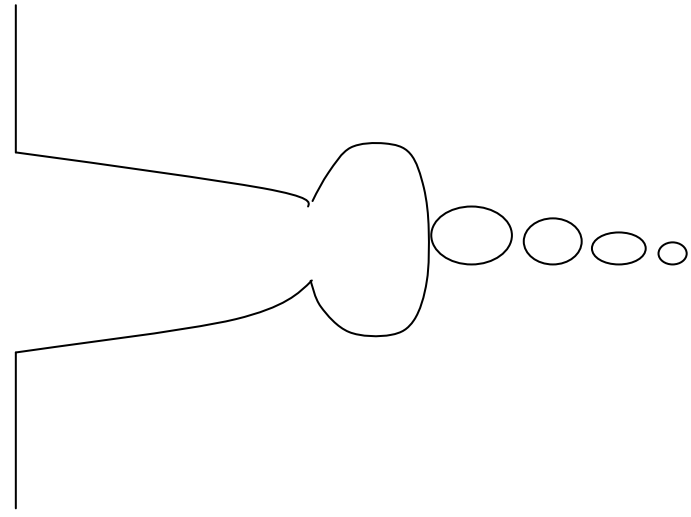

c. Coalescence

Figure 4.8: Ductile fracture by coalescence of voids with the crack.

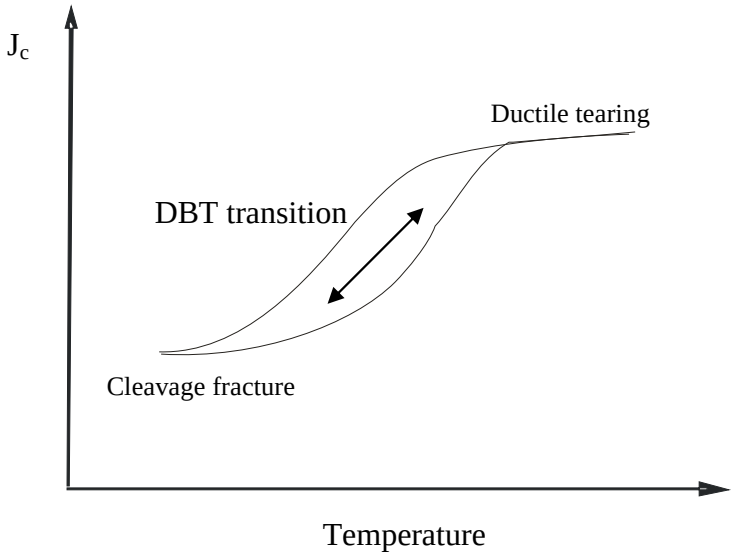

Figure 4.9: J-Temperature curve showing the ductile-brittle transition.

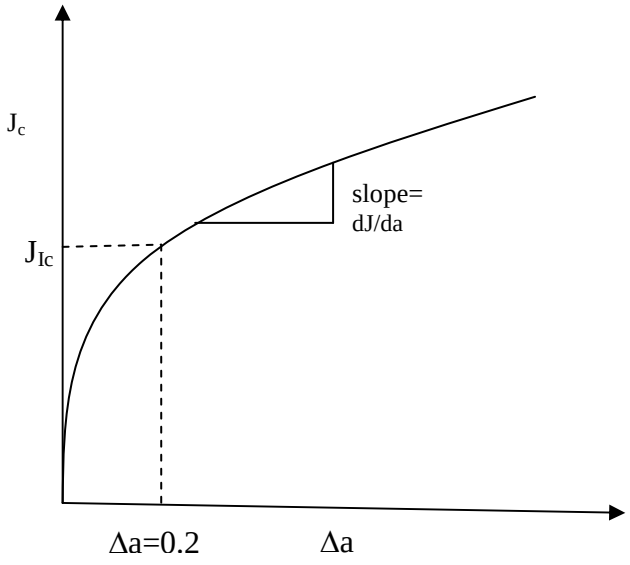

Figure 4.10: The J-Δa curve in a ductile material.

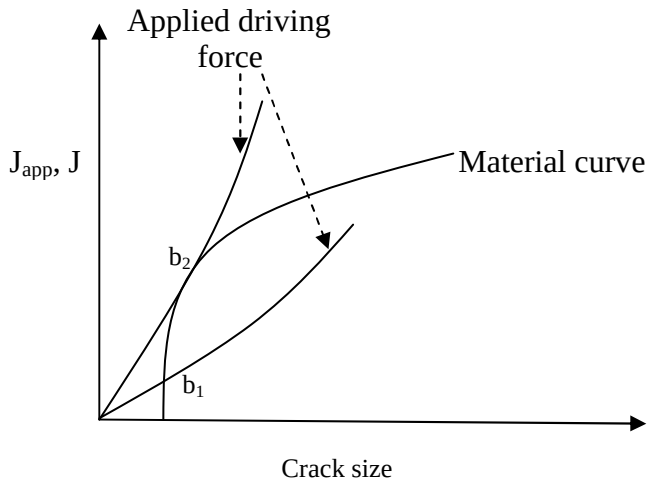

Figure 4.11: Schematic of ductile instability controlled by J-integral, b_1 and b_2 are the intersection points of the applied driving force with the material curve.

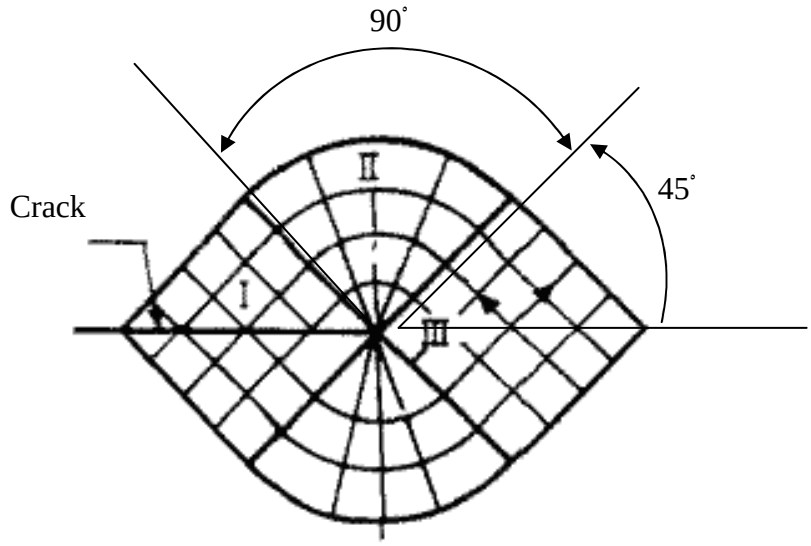

Figure 4.12: The Prandtl stress field represented by slip lines as a near tip solution for a stationary crack.

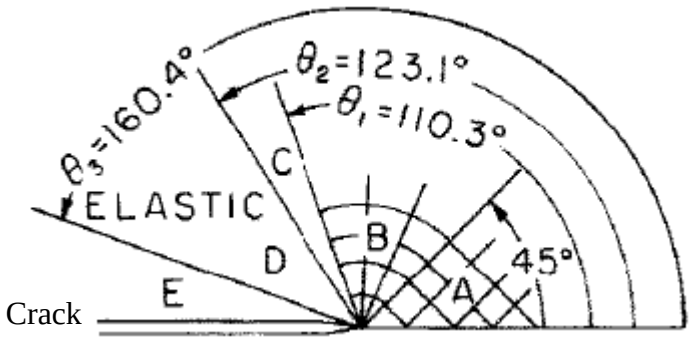

Figure 4.13: The near tip fields with an elastic unloading sector for a growing crack in a material with v=0.3, (after Drugan et al. 1982).[A-constant stress plastic sector, B-centre fan sector, C-a non-constant stress plastic sector, D-an elastic unloading sector, E-a non-constant stress plastic sector].

5. Constraint effects

5.1 Introduction

A single parameter (J-integral) uniquely characterises the crack tip field is associated for highly constrained geometries such as deeply cracked bend bars. However single parameter characteristic is limited by geometry and loading mode, since the stress at the crack tip can be relaxed. Therefore two parameter approaches J-T (Du and Hancock, 1991), J-Q (O'Dowd and Shih 1991, 1992) and J-A_2 (Chao et al., 1993, 1994) were introduced to quantify the stress field near a crack tip, and thus remove some conservatism inherent in a single parameter approach. This chapter discusses two parameter (T/Q) characterisation in plane strain conditions. This is followed by a discussion of the out-of-plane due to thickness effect.

5.2. Two parameter characterisation of the crack tip field

5.2.1 Elastic T-Stress

Larsson and Carlsson (1973) demonstrated that the second term in William's expansion has a significant effect on the shape and size of the plastic zone ahead of the crack tip. Rice (1974) pointed out that the second term in the series is independent of distance and corresponds to a uni-axial stress, which is parallel to the crack flank. This term is denoted as T-stress which has dimensions of stress and depends on geometry and the applied load. The stress series near the crack tip described by Rice (1974) then becomes:

$$\begin{bmatrix} \sigma_{11} & \sigma_{12} \\ \sigma_{21} & \sigma_{22} \end{bmatrix} = \frac{K}{\sqrt{2\pi r}} \begin{bmatrix} f_{11}(\theta) & f_{12}(\theta) \\ f_{21}(\theta) & f_{22}(\theta) \end{bmatrix} + \begin{bmatrix} T & 0 \\ 0 & 0 \end{bmatrix} \tag{5.1}$$

The T-stress can be calculated directly on the crack flank at $\theta=\pm\pi$ by finite element analysis from the expression:

$$T = \lim_{r \to 0} \sigma_{11}(\theta = \pm\pi) \quad \text{since} \quad f_{ij}(\theta = \pm\pi) = 0 \tag{5.2}$$

The T-stress can also be defined by a load independent bi-axiality parameter β introduced by Leevers and Radon (1983).

$$\beta = \frac{T\sqrt{\pi a}}{K} \tag{5.3}$$

The T-stress has been tabulated for a wide range of cracked geometries in tension and bending given by Leevers and Radon (1983), Sham (1991), Wang et al (1992) and Sherry et. al (1995).

Bilby et al (1986) first showed a two parameter solution (J-T) of the stress field is necessary in some configuration. Du and Hancock (1991) found that compressive T-stresses enlarge the plastic zone and cause the plastic lobes to swing forward, while tensile T-stresses exhibit smaller plastic zone and the lobes swing backward. They showed that the full Prandtl field only develops when the T-stress is positive and plasticity encompasses the full crack tip zone as shown in Figure (5.1). Conversely, with negative T-stress incomplete plasticity develops around the crack tip. Betegón and Hancock (1991) showed that J-dominance is maintained and the stress fields hold close to the HRR field for geometries that exhibit positive or zero T-stress. The loss of J-dominance was associated with compressive T-stress which introduces a corresponding second order term into the nonlinear asymptotic expansion. This term causes the stress ahead of the crack to reduce, and thus a two parameter characterisation (J and T) is needed to describe the stress field. They pointed out the loss of constraint ahead of the crack in any geometry within contained yielding can be determined by comparison with a reference stress (i.e. SSY) and the loss of constraint parameterised with T-stress. Sumpter and Hancock (1991) showed the effect of compressive T-stress on fracture toughness. They showed that increased toughness in cleavage is associated with compressive T-stress for shallow cracks. Hancock, Reuter and Parks (1993) quantified the crack tip constraint and fracture toughness by the T-stress parameter in full plasticity in ductile tearing. They showed the geometry independent toughness is associated with positive T-stress, and the geometry dependant toughness is associated with negative T-stresses. Low

constraint geometries (e.g. centre cracked panels) exhibit much higher toughness than constrained geometries (e.g. deeply cracked bend bar) as shown in Figure (5.2). They also correlated the constraint effect with the slope of the resistance curves dJ/da as shown in Figure (5.3) with large resistance to ductile tearing offered by geometries with a more negative T-stress. Kim et al. (1996) and Zhu and Chao (2000) showed the crack-tip constraint remain 'almost' constant for all range of deformation levels in deeply cracked SENB and DECP specimens under small scale yielding conditions. With the decrease of constraint levels in low constraint geometries, the hydrostatic stress ahead of the crack tip decreased from the Prandtl field and an elastic sector occurred on the crack flanks.

5.2.3 Determination of the elastic T-stress

Kfouri (1986) introduced an interaction J-integral based on Eshelby`s theorem to extract the T-stress parameter in two-dimensional crack problems. Nakamura, et al (1992) introduced the interaction integral method to extract the elastic T-stress in three dimensional solution. This has been reviewed widely in the literature (Zhao, 2001, Wang, 2003, Zhao, et al, 2007).

The interaction integral method is used to determine the elastic T-stress using the line-load solution. The line load with a magnitude of $f_k = f\mu(s)$ is applied on the crack front as illustrated in Figure (5.4), where (f) represents the force per unit length and $\mu(s)$ defines the direction normal to the crack front at point s in the crack plane. The solution is a special case of a plane strain semi-infinite crack with a point force, f, applied at the crack tip in the direction parallel to the crack plane. The crack-tip stress field is given by Nakamura and Parks (1992):

$$\sigma_{11}^{L} = \frac{f}{\pi r}\cos^3\theta, \qquad \sigma_{22}^{L} = \frac{f}{\pi r}\cos\theta\sin^2\theta, \qquad \sigma_{33}^{L} = \frac{f}{\pi r}\upsilon\cos\theta,$$

$$\sigma_{12}^{L} = \frac{f}{\pi r}\cos\theta^2\sin\theta, \qquad \sigma_{13}^{L} = \sigma_{23}^{L} = 0$$

Where, r and θ are the local polar coordinates in the plane perpendicular to the crack plane. σ_{ij} is the stress field in the crack tip region, and the superscript (L) designates the field as that of the line-load solution.

Cardew et al, (1985) used this solution to extract the T-stress for two-dimension crack problems by interaction J-integral based on Eshelby's theorem. For three-dimension crack problems, Nakamura et al, (1992) extracted the T-stress at point s on the crack front as:

$$T(s)=\frac{E}{(1-\upsilon^2)}\left[\frac{I(s)}{f}+\upsilon\varepsilon_{33(s)}\right] \tag{5.4}$$

Where, $\varepsilon_{33}(s)$ describes the extensional strain at point s in the direction tangential to the crack front. The interaction integral I(s) can be determined by means of the same domain integral method used for J-integral determination.

5.2.4 J-Q Approach

For non-linear deformation, the crack tip fields can be represented by asymptotic series in a similar way as the Williams expansion in linear elasticity. The leading term is the HRR field, and the higher order terms can be written as an asymptotic series (Sharma and Aravas, 1991):

$$\sigma_{ij} = A_{ij} r^{-\frac{1}{1+n}} \tilde{\sigma}^{(1)}(\theta,n)+B_{ij} r^{t} \sigma^{(2)}(\theta,n)+C_{ij} r^{u} \tilde{\sigma}^{(3)}(\theta,n)+\ldots\ldots \tag{5.5}$$

Where $\frac{1}{1+n} < t < u$. A_{ij}, B_{ij} and C_{ij} are the dimensionless amplitudes, and $\tilde{\sigma}^{(I)}(\theta,n)$ are angular functions.

O'Dowd and Shih (1991, 1992) defined the second term in the series as the Q-Parameter, a quantitative measure of crack tip constraint, and the series can be rewritten in the form:

$$\sigma_{ij} = \sigma_0 \left(\frac{J}{\alpha \sigma_0 e_0 I_n r} \right)^{\frac{1}{1+n}} \tilde{\sigma}\ (\theta, n) + Q \left(\frac{r}{J/\sigma_0} \right)^{t} \tilde{\sigma}\ (\theta, n) + \ldots\ldots\ldots\ldots\ldots \quad (5.6)$$

The Q-Parameter is a distance independent when the exponent t is zero. This simplification allows the crack tip fields to be written as:

$$\sigma_{ij} = (\sigma_{ij})_{HRR} + Q \sigma_0\ \delta_{ij} \quad (5.7)$$

Where $(\sigma_{ij})_{HRR}$ is the reference field, and δ_{ij} is the Kronecker delta.

The field can also be described using the small scale yielding (T=0) field as the reference field:

$$\sigma_{ij} = (\sigma_{ij})_{T=0} + Q \sigma_0\ \delta_{ij} \quad (5.8)$$

Q-Parameter can be derived from subtracting the reference stress field for T=0 or HRR field:

$$Q = \frac{\sigma_{\theta\theta} - (\sigma_{\theta\theta})_{T=0}}{\sigma_0} \quad \text{or} \quad Q = \frac{\sigma_{\theta\theta} - (\sigma_{\theta\theta})_{HRR}}{\sigma_0} \quad \text{for} \quad \frac{r\sigma_0}{J} = 2\,, \theta = 0 \quad (5.9)$$

A relationship between the second order terms in linear and non-linear expansions was given in the literature, (Betegón and Hancock, 1991, O`Dowd and Shih, 1994). Betegón and Hancock (1991) used the modified boundary layer formulations to suggest the Q-T relationship in contained yielding as:

$$Q = 0.64 \left(\frac{T}{\sigma_0} \right) - 0.4 \left(\frac{T}{\sigma_0} \right)^2 \quad , \qquad \frac{T}{\sigma_0} \leq 0,\ n = 13 \quad (5.10)$$

$$Q = 0.6 \left(\frac{T}{\sigma_0} \right) - 0.75 \left(\frac{T}{\sigma_0} \right)^2 \quad , \qquad \frac{T}{\sigma_0} \leq 0,\ n = \infty \quad (5.11)$$

The development of J-T/Q toughness loci is important for structural integrity assessments. The conditions at failure are derived from specific geometry and load dependent toughness values by matching the constraint at fracture with the laboratory tests at the same constraint level. Figure (5.5) shows the J-T/Q toughness locus scheme. Failure is predicted when the applied driving force curve passes through the toughness locus region bounded by upper and lower limit.

5.2.5 J-A_2 approach

J-A_2 approach of Chao has been widely discussed in the literature. Yang et al, (1993), Chao et al. (1994), Chao and Zhu, (1998) proposed a three term solution J-A_2 based on a dominant singularity characterised by J and higher order terms by a parameter A_2. The A_2-parameter quantifies the level of constraint at the crack tip. The three-term asymptotic crack tip solution can be written (Chao and Zhu, 1998):

$$\frac{\sigma_{ij}}{\sigma_0} = A_1\left[\left(\frac{r}{L}\right)^{S1} \tilde{\sigma}_{ij}^{(1)}(\theta,n) + A_2\left(\frac{r}{L}\right)^{S2} \tilde{\sigma}_{ij}^{(2)}(\theta,n) + A_2^2\left(\frac{r}{L}\right)^{S3} \tilde{\sigma}_{ij}^{(3)}(\theta,n)\right] \tag{5.12}$$

Where A_1 and s_1 are given by the HRR fields:

$$A_1 = \left(\frac{J}{\alpha\varepsilon_0\sigma_0 I_n L}\right)^{-S1}, \quad s_1 = -\frac{1}{n+1} \tag{5.13}$$

Where the angular functions $\tilde{\sigma}_{ij}^{(k)}$, the dimensionless integration constant I_n and the exponents (s_1, s_2 and s_3) are tabulated by Chao and Zhang (1997). L is the characteristic length (i.e. crack length). σ_0 is a reference stress and $\varepsilon_0 = \sigma_0/E$ is a reference strain with E as Young`s modulus. The value of the constraint parameter, A_2, can be determined by matching the stress component (i.e $\sigma_{\theta\theta}$) in equation (5.12) with that from finite element analysis at a point (r,θ).

Zhu and Chao (1999) showed that the J-A_2 approach is appropriate for low and high constraint geometries, however the J-A_2 solution is limited to small scale yielding for

high constraint geometries under bending. The J-A_2 solution can be applied in hardening and low hardening materials (i.e. n=30).

5.3 Out-of-plane effects

The stress field in a three dimensional body can also be affected by the out-of-plane effects associated with the thickness. The through-thickness stress in a three-dimensional geometry can be described by out-of-plane constraint factor, T_z, (Guo, 1995, Neimitz, 2004, Guo et al., 2007). This factor is defined as the ratio of the out-of-plane stress to the sum of in-plane stresses, $T_z= \sigma_{zz}/(\sigma_{xx}+\sigma_{yy})$. The value of T_z varies from 0.5 in plane strain to zero in plane stress. Near the crack tip at centre of the geometry the constraint level reaches plane strain, and reduces as the radial distance increases. It is also shown that the constraint maintains plane strain condition over the majority of the thickness, but decreases to zero at the free surface.

Newman and Bigelow (1993) examined constraint variations through the opening and hydrostatic stress along the crack front in thick and thin specimens. They showed that thick specimens maintain high constraint at the crack front through the thickness but that the constraint level reduces sharply near the free surface. However, thin specimens appear significantly less constrained even at the mid-plane. Yuan and Brocks (1998) quantified the in-plane and out-of-plane constraint effects under small scale and large scale yielding conditions. They showed under very small loads when the plastic zone is significantly smaller compared to the other geometry dimensions, the stress fields for high constraint geometry can be quantified by the plane strain solution. As the deformation increases the full field stress ahead of the crack front is no longer accurately characterised by the J-Q parameterisation in the three-dimensions. They observe that the Q factor varies significantly for different specimen thickness. For thin specimen the Q factor reduces significantly compared to the thick one.

Kim et al (2001) extended the J-A_2 three term solution to quantify the constraint effect for an elastic-plastic three-dimensional crack front. They showed that the crack tip constraint can be described by the J-A_2 parameter in moderate hardening materials (n=3) in thin plates under both low and high loading conditions. Kim et al (2004a) quantified

the out-of-plane constraint effect in terms of the stress triaxiality parameter (σ_m/σ_e), where σ_e is the equivalent von-Mises stress. They found that the out-of-plane constraint is related to in-plane constraint for low constraint geometry, and the effect of thickness is pronounced for high constraint geometries. Kim et al (2003) showed in the rectangular deep cracked bend specimen (SECB) there is no relaxation of crack tip constraint even as the load increases. They point out the effect of thickness and magnitude of loading on the crack tip constraint can be ignored and well described by two-dimensional solution under small scale yielding conditions. However in deep square specimens the stress field deviates from plane strain solution as load increases. In shallow square specimens the constraint reduces at much lower load levels.

Hebel et al (2007) utilized several two-parameter descriptions J-T, J-Q, J-A_2 and J-h (h is the stress triaxiality parameter) onto various specimens configuration. They observed that the concepts of two-parameters yielded similar results under small scale yielding. However in full plastic deformation the loss of constraint is not captured by J-T, J-A_2 concepts. A good quantification of out-of-plane constraint is achieved by the triaxiality parameter h and relatively well by J-Q concept.

It has been also shown that for bending dominated specimens the two-parameter characterisation the crack tip field is limited (Wei and Wang, 1995a,b, Chao and Zhu, 1998, Chao et al, 2004). This is because the crack tip field is significantly affected by the global bending moment under full plastic deformation. Wei and Wang (1995a,b) modified the J-Q approach by adding a third parameter k_2 to quantify the loss of constraint in deep cracked bend bar under full plastic deformation condition. Karstensen (1996) modified the J-Q solution by decomposing the parameter Q into two parts: elastic Q_T which is a distance independent and associated with T-stress, and Q_p which is a distance dependent and associated with the global bending field, and regarded as the difference between the total loss of constraint given by Q and the loss of constraint given by a negative T-stress. Chao et al (2004) introduced an additional term to the J-A_2 three term solution to quantify the global bending effect. Likewise Zhu et al (2006) developed the J-Q theory by introducing an additional linear stress term to characterise the influence of global bending under large scale yielding.

5.4 The effect of specimen dimension and crack size on fracture toughness

Material resistance to ductile crack growth is usually expressed in terms of the resistance curve, J-Δa. Sumpter and Hancock (1991) showed the crack tip triaxiality reduces, and fracture toughness increases, in shallow cracked specimens failing by cleavage in HY80 welds. Dodds et al (1991) examined the fracture toughness of A36-Steel in lower transition region and pointed out that the fracture toughness J_c in shallow cracks is about two-three times that observed for deep cracks. This increase of toughness appears as a result of loss of constraint due to the spread of the plastic zone to the back surface.

Cotterell et al (1985) studied the effect of plastic constraint on the initiation of ductile tearing in an Australian Steel 1204-350. They pointed out the critical crack tip opening displacement δ_{Ic} for shallow cracks are about twice that for deep cracks. Hancock, Reuter and Parks (1993) showed the geometry dependency of crack tip constraint and fracture toughness in full plasticity under ductile tearing in A710-Steel. They showed that there is a significant effect of constraint on toughness for crack extension, and the fracture toughness in centre cracked panel (CCP) is four times greater than that in deep cracked specimens. Also showed there is a strong effect of constraint on the slope of the resistance curves. Burstow et al (1996) examined A508-Steel and showed that the effect of constraint on crack initiation of ductile fracture is insignificant. However the loss of constraint associated with shallow cracks results increase in the slope of the resistance curve. Joyce and Link (1997) showed that the toughness of HY80-Steel under ductile tearing at initiation is almost constant for a wide range of crack depth ratio, but the slope of the J-R curves varies significantly after the initiation and becomes higher for shallower cracks. Chao and Zhu (2000), and Lam et al (2003) modified the concept of J-R curve for small amount of ductile tearing (1.5mm). They showed that the J-R curve is strongly dependent on specimen and crack size, and the constraint effect on J-R curve can be quantified by the J-A_2 concept. Ostby et al. (2007a) examined hardening materials with strain exponents, n, 5, 10 and 20 under ductile fracture. They showed that the stress level ahead of the crack tip increases as a ductile crack grows, and is pronounced for small amounts of crack growth. The local fracture strain decreases for small amounts of ductile crack growth, which changes the local crack tip geometry. There is a significant

effect of specimen size on the level of stress. This effect is due to the different constraint levels in the specimens at the initiation of ductile crack growth and becomes nearly constant with further crack growth. They showed that both geometry and size effects are material hardening dependent. Ostby et al. (2007b) pointed out that the J-R curves reveal little dependence on the specimen size for small amount of ductile crack growth in bend and tensile specimens. The size effect becomes more significant with further crack growth in small specimens and increases in low hardening materials. For shallow cracked tensile specimens the crack growth resistance decreases in small specimens for large crack growth, while the opposite is the case for deeply cracked bend specimens. Zhu et al (2007) showed that J-R curves for HY80-Steel are strongly dependent on the crack size, and shallow cracks give higher resistance curves, and the fracture toughness under ductile fracture at initiation, J_{Ic}, is weakly dependent on the crack tip constraint, and the critical fracture toughness after initiation $J_{(1mm)}$ is strongly dependent on the level of constraint. Smith et al (2008) examined the thickness effect on fracture toughness in specimens with widths w=20, 40 and 80mm, and thickness B=10, 20 and 40mm for A508-Steel. These experiments showed that the effect of thickness in small specimens (w=20) on the J-Δa curves under ductile tearing is relatively small compared to the increase in toughness for larger crack extensions. They also showed larger specimens (w=80) exhibit a significant reduction of the slope of the J-Δa curve, and are less resistant to ductile tearing.

5.5 Part-through surface cracks

Part through-wall flaws are often encountered in an engineering practice and have to be considered in flaw evaluations. Under elastic conditions Zhang and Guo (2005, 2006) examined the T_z-constraint for a semi-elliptical surface crack in an elastic plate subjected to uniform tension. T_z is defined as the ratio of the out-of-plane stress (σ_{zz}) to sum of the opening and normal to the crack front stresses ($\sigma_{\theta\theta}+\sigma_{rr}$). They showed that T_z reduces from Poisson's ratio at the crack tip to approach zero as radial distance increases. The T_z-constraint decreases gradually from the deepest point at the same radial distance to the free surface.

Under ductile tearing, Brocks and Noack (1988) examined an inner surface flaw in a pipe under increasing internal pressure up to yielding of the ligament. They considered a deep flaw with depth ratio of a/w=0.59 and aspect ratio of a/c 0.35. The material stress-strain curve used describes the German standard steel 20 MnMoNi 55. They showed that the maximum J-integral occurs at the deepest point while the stresses are below the HRR solution. They showed that the stresses approach the HRR value at 75° as shown in Figure (5.6). Brocks et al. (1990) tested a vessel with a surface flaw under combined load and ductile tearing. They tested two German steels 20 MnMoNi 55 and StE 460. They observed that the canoe-shape crack front occurred when the crack grew with a greater rate in the axial direction than the growth in the thickness direction as shown in Figure (5.7).

Faleskog (1994) examined ductile fracture in a pressure vessel steel 2¼ Cr 1 Mo. They tested a large surface cracked plate under combined load and small compact tension specimens. It was shown that ductile tearing initiation is insensitive to the level of constraint; however the increase of toughness after initiation is significantly affected by the level of constraint. Moussavi (1995) showed that in geometry containing a semi-elliptical surface crack under tension the decrease in stress triaxiality increases tearing modulus T_r implying the J-R curve under ductile tearing is constraint dependent as shown in Figure (5.8).

Gao et al. (1998) used the computational cell model to predict the ductile tearing in deep surface cracks introduced into 2¼ Cr 1 Mo steel plates. They showed that surface flaws under combined tension and bending the maximum crack growth occurs at the deepest point, while in pure bending the maximum growth occurs below the surface. Brickstad et al. (2000) showed that the maximum J-integral values in full plasticity occur near to the surface and decrease towards the deepest points in deep semi-elliptical surface cracks a/w=0.9, a/c=0.9 in tension under ductile tearing as shown in Figure (5.9). For cracks with a/c=0.15 the J-integral was maximum at 60° measured from the deepest point but was suppressed at the free surface as shown in Figure (5.10).

Kim et al. (2004b) examined the effect of biaxial loading on the J-integral and crack tip constraint under elastic-plastic conditions. The material chosen was hardening material

with strain exponent of n=5 and 10. The biaxial loading was defined as B= $\sigma_x^{\infty}/\sigma_y^{\infty}$ and ranging from 0 to 1 was applied to the plate as shown in Figure (5.11). They pointed out that the effect of biaxial loading was more pronounced for semi-circular surface cracks (a/c=1) and was minimal for semi-elliptical surface cracks (a/c=0.2). They also showed that the effect of the biaxiality became more significant near the free surface.

Chen et al. (2005) studied stress triaxiality and plastic deformation in deep semi-elliptical surface cracks a/w>0.5 under ductile tearing. The material studied was API-X70 pipeline steel. They showed that non-uniform values of stress triaxiality were observed under tension. The crack grows the most at the deepest segment on the crack front and the least at the surface. Berg et al. (2008) investigated the effect of circumferential crack growth in a surface cracked pipe under ductile tearing. The material behaviour was assumed to be hardening material associated with strain exponent of n=15 which corresponds to X65 steel. They showed that the crack grows in the circumferential direction in cracks with short crack length, while for longer crack lengths circumferential growth is insignificant.

Wang (2009) examined the effect of biaxial loading in surface cracked plates under elastic-plastic conditions. Two loadings conditions λ=0 and 1 were considered as shown in Figure (5.12). He showed that there is no significant difference in the constraint level at the deepest point of semi-circular surface cracks (a/c==1) under both uniaxial (λ=0) and biaxial loadings (λ=1). He also showed that a more uniform crack tip constraint level occurs along the crack front under uniaxial loading, however under biaxial loading the constraint level increases and reaches the maximum at 70° measured from the deepest point, then decreases towards the free surface as shown in Figures (5.13) and (5.14).

In leak-before-break applications the crack shape during propagation is important as it determines crack opening area and leak rate at breakthrough (Brickstad and Sattari-Far, 2000). It is necessary to prove that the crack will breakthrough in a stable mode by fatigue, tearing or creep and that the leak is detected before the fracture instability occurs (Brocks et al, 1990). The crack size at detectable-leakage is compared with the critical size and the leak before break is satisfied when the critical size is larger than the detectable leakage crack.

Predictions of the crack shape development have been made for fatigue and stress intensity factor driven failure (Brickstad and Sattari-Far, 2000, Hodulak et al., 1978, Newman and Raju, 1981, Carpinteri, 1993, Lin and Smith, 1999, a, b). Such calculations show flaw size, shape and a loading mode effects on the subsequent flaw development. For example, in tension dominated geometries surface flaws tend to acquire a near semi-circular profile until the flaw breaks-through the vessel wall as shown in Figure (5.15) (Scott and Thorpe, 1981). Conversely under bending dominant loading the flaw evolution is more complex and is a competition between the extension through the thickness and growth on the surface. However a preferred shape through decrease in the a/c ratio (a-the crack depth, c-the major length at surface) as the crack advances is adopted regardless of the original crack shape as shown in Figure (5.16). Brickstad and Sattari (2000) showed that under bending the crack grows more rapidly at the free surface than at the deepest point under sub-critical crack propagation (i.e. fatigue). They also showed the crack does not change its shape for short surface cracks, while the crack grows mainly at the deepest point for longer cracks in tension.

It may be concluded that both J-integral and constraint vary along the crack front of surface cracks and show geometry and load dependent under ductile tearing. The maximum crack growth occurs at the deepest point of semi-elliptical surface crack under combined tension and bending, while the maximum crack growth was below the surface under pure bending. However, a full detailed study for a range of surface cracks taking account of both J-integral and constraint as well as crack growth and under different types of loading is still required.

5.6 Failure assessment diagram

Failure assessment diagram is an approach used for elastic-plastic fracture mechanics analysis of structural components. Strength based assessment ensures that the strength of the material is higher than the maximum applied stress in service but does not account for flaws or defects. One of the purposes of defect assessment is to predict failure in real structures containing cracks. Therefore, it is necessary to have some guidance in the form of a defect acceptance curve.

Dowling and Townley (1975) proposed a two criteria approach for failure assessment in the form of failure assessment diagram (FAD). It is based on the assumption that failure occurs when the applied load reaches the fracture toughness under linear elastic condition, or the collapse load of the structure containing crack under completely plastic conditions. The diagram is shown in Figure (5.17) which represents two failure modes: on the ordinate fracture under small scale yielding represented by K_r which is the ratio of applied stress intensity factor to fracture toughness $K_r = K_{app}/K_{mat}$, and plastic collapse L_r on the abscissa which is the ratio of applied load to the limit load $L_r = P/P_0$. Limit load expressions for a wide range of geometries can be found in assessment codes such as BS 7910, R6 or obtained from FEA. The point $L_r = L_r^{\max}$ corresponds to the maximum allowable plastic deformation:

$$L_r^{\max} = \frac{\sigma_0 + \sigma_{uts}}{2\sigma_0} \tag{5.14}$$

Here σ_0 is the yield stress and σ_{uts} is the ultimate tensile stress. It should be noted that $\sqrt{J_r}$ which is regarded as $\sqrt{J_{el}/J_{Ic}}$ can also be used instead of K_r. The assessment point (K_r, L_r) is placed on the diagram. If the point lies inside the region under the curve, the structure is safe, otherwise the structure is unsafe.

Three options of decreasing conservation are available in the diagram:

Option1 is a general curve which is suitable for all materials that do not exhibit a yield discontinuity in stress-strain relationships and is described by:

$$K_r = [1 - 0.14L_r^2]\,[0.3 + 0.7\exp(-0.65L_r^6)] \qquad \text{For} \quad L_r \le L_r^{\max} \tag{5.15}$$

$$K_r = 0 \qquad \text{For } L_r > L_r^{\max} \tag{5.16}$$

Option2 is a material specific curve which is suitable for materials with known of stress-strain relationship:

$$K_r = \left[\frac{E.\varepsilon_{ref}}{L_r.\sigma_0} + \frac{L_r^3.\sigma_0}{2E.\varepsilon_{ref}} \right]^{-\frac{1}{2}} \qquad \text{For } L_r \le L_r^{\max} \qquad (5.17)$$

Where ε_{ref} is the reference true strain.

Option3 is a curve derived from a detailed analysis of a specific geometry and material and is the least conservative. The J-integral is decomposed into an elastic part J_{el} which is proportional to $(P/P_0)^2$ and a plastic part J_p proportional to $(P/P_0)^{n+1}$. The equation of the assessment curve is:

$$K_r = \left(\frac{J_e}{J} \right)^{\frac{1}{2}} \qquad \text{For } L_r \le L_r^{\max} \qquad (5.18)$$

5.7 Constraint based failure assessment diagram

The conventional failure assessment diagram is developed for high constrained geometries, and the effects of constraint loss are not accounted for. MacLennan and Hancock (1995), and Ainsworth and O'Dowd (1995) developed a modified failure assessment diagram to take advantage of enhanced fracture toughness associated with constraint loss. The constraint loss is quantified by MacLennan and Hancock (1995):

$$\frac{J_c(T)}{Jc(T=0)} = \left[\frac{1}{\exp(\frac{T}{\sigma_0})} \right]^m \qquad T/\sigma_0 < 0 \qquad (5.19a)$$

$$\frac{J_c(T)}{Jc(T=0)} = 1 \qquad T/\sigma_0 > 0 \qquad (5.19b)$$

Constraint sensitivity of fracture is defined by the exponent *m*. *m*=0 for materials showing constraint insensitivity that characterised by critical fracture toughness and non zero values of *m* correspond to unconstrained materials. $J_c(T)$ denotes the critical values of J and is now a function of the constraint parameter T. $J_c(T=0)$ denotes a fully

constrained solution for a deeply cracked specimen with T≥0. Ainsworth and O`Dowd (1995) included the constraint effects in the failure assessment diagram. They describe the fracture toughness J_{mat} or K_{mat} as the fracture toughness measured on highly constrained specimens, while the enhanced fracture toughness K^c_{mat} which is a constraint dependent can be written (Ainsworth and O`Dowd, 1995):

$$K^c_{mat} = K_{mat}[1+\alpha(\beta L_r)^m] \tag{5.20}$$

Where the parameter β is a function of constraint, (β = Q/L_r, or T/L_r), while α and m are material constants. This enables the failure assessment line to be modified (Ainsworth and O`Dowd, 1995):

$$f_c = f(L_r).[1+\alpha(\beta L_r)^m] \tag{5.21}$$

Where $f(L_r)$ in the original failure assessment curve.

In R6, the failure assessment diagram was modified to include constraint effects. This can be performed in two procedures: Procedure I modifies the failure assessment curve to account for constraint and retains the material fracture toughness K_{mat} unchanged as shown in Figure (5.18a):

$$K_r = f(L_r)[1+\alpha(-\beta L_r)^m] \tag{5.22}$$

Where α and m are material parameters which quantify the constraint effects on toughness. β is a measure of constraint, (β = Q/L_r, or T/L_r).

In procedure II, the fracture toughness K_{mat} used to define K_r is modified to account for constraint, K^c_{mat} and retains the failure assessment curve unchanged as shown in Figure (5.18b):

$$K^c_{mat} = K_{mat} \quad \text{for} \quad T/\sigma_0,\ Q \geq 0 \tag{5.23a}$$

$$K^c_{mat} = K_{mat}[1+\alpha(\beta L_r)^m] \quad \text{for} \quad T/\sigma_0,\ Q < 0 \tag{5.23b}$$

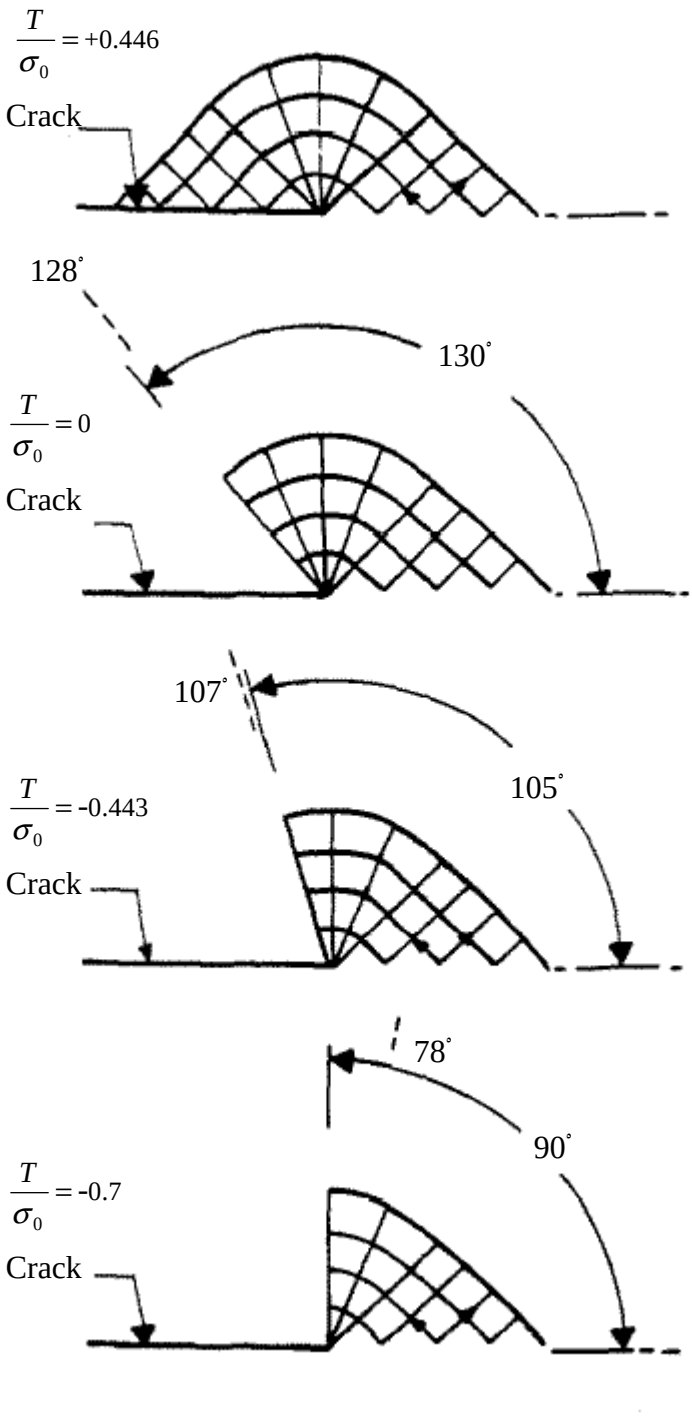

Figure 5.1: The effect of the T-stress on the plastic zone shape, after Du and Hancock (1991).

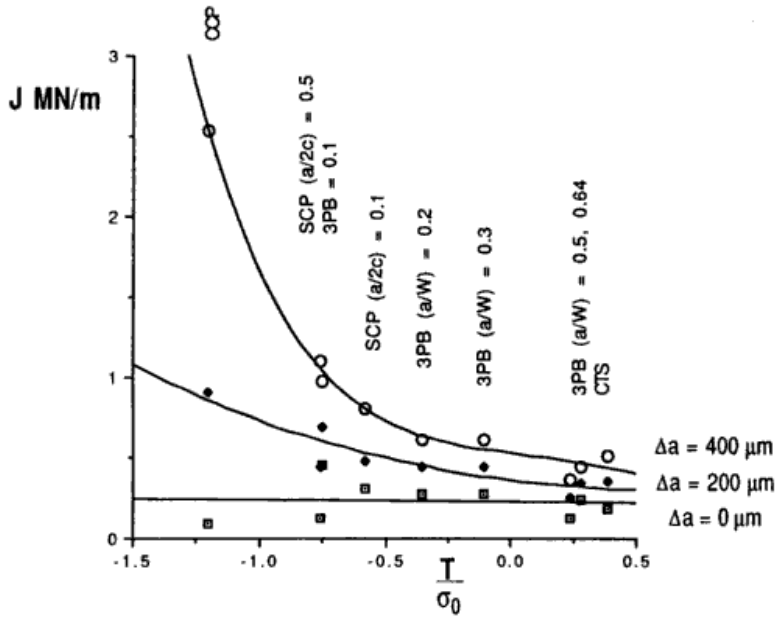

Figure 5.2: J as a function of the T stress at crack extension of 0, 200 and 400μm, after Hancock et al, (1993).

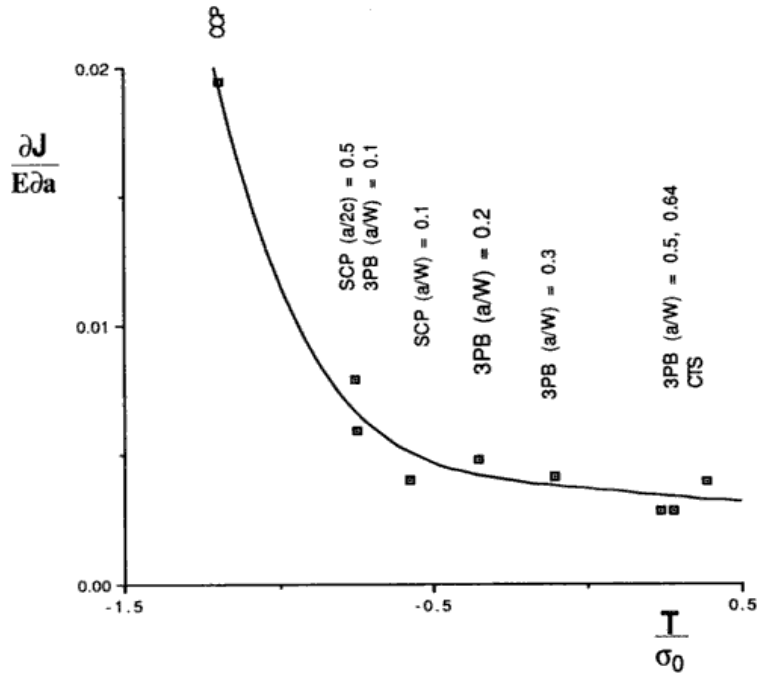

Figure 5.3: The slope of the J-Δa resistance curve as a function of T, after Hancock et al, (1993).

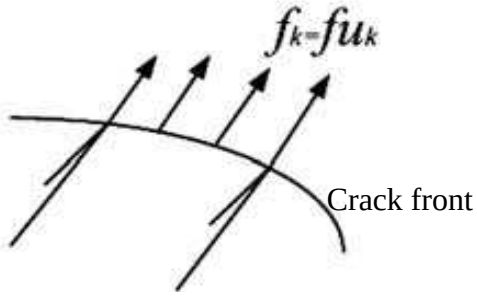

Figure 5.4: Line load along the crack front.

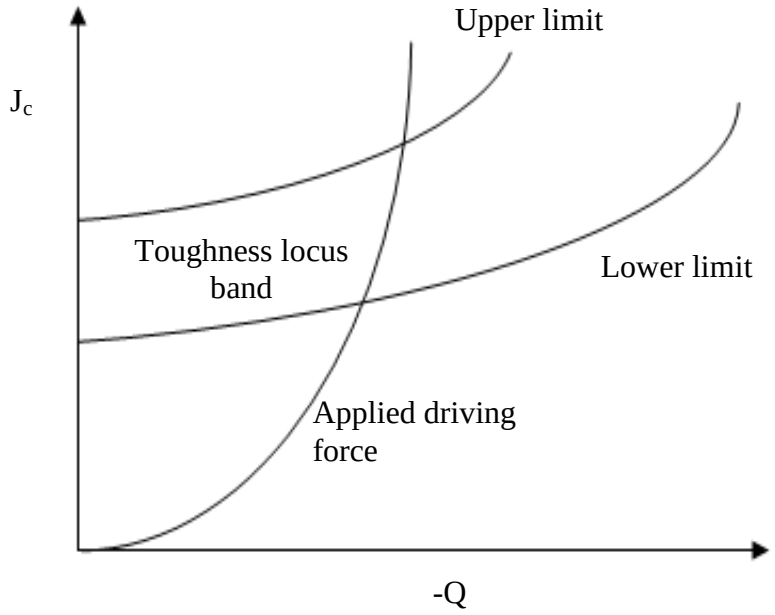

Figure 5.5: Application of the J-Q toughness locus

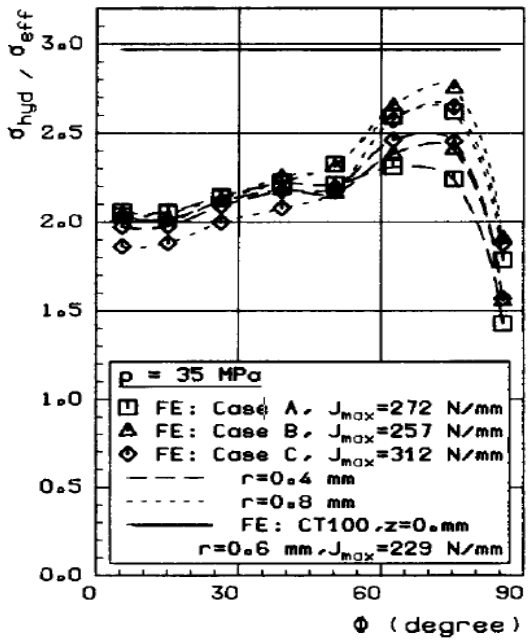

Figure 5.6: The triaxiality of stress along the crack front of the semi-elliptical surface flaw after Brocks and Noak (1988).

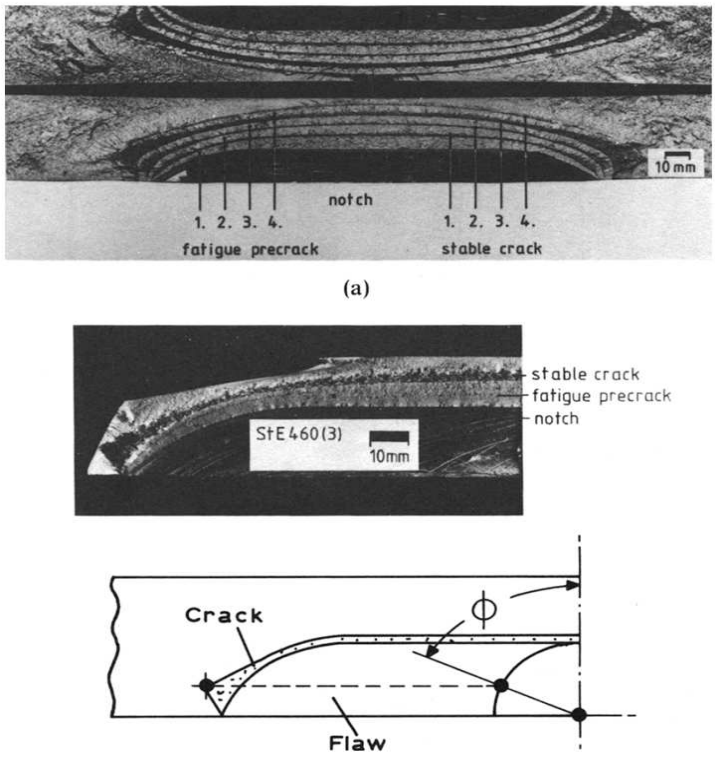

Figure 5.7: Fracture surface of fatigue and ductile tearing of surface flaws (a) 20 MnMoNi 55 and (b) StE 460 after Brocks et al (1990).

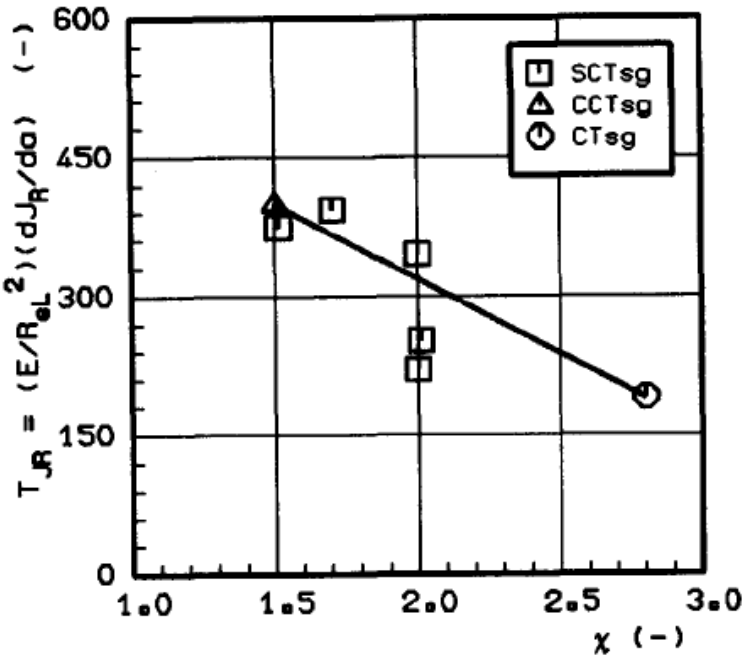

Figure 5.8: The relation between the tearing modulus T_{JR} and stress triaxiality χ after Moussavi (1995).

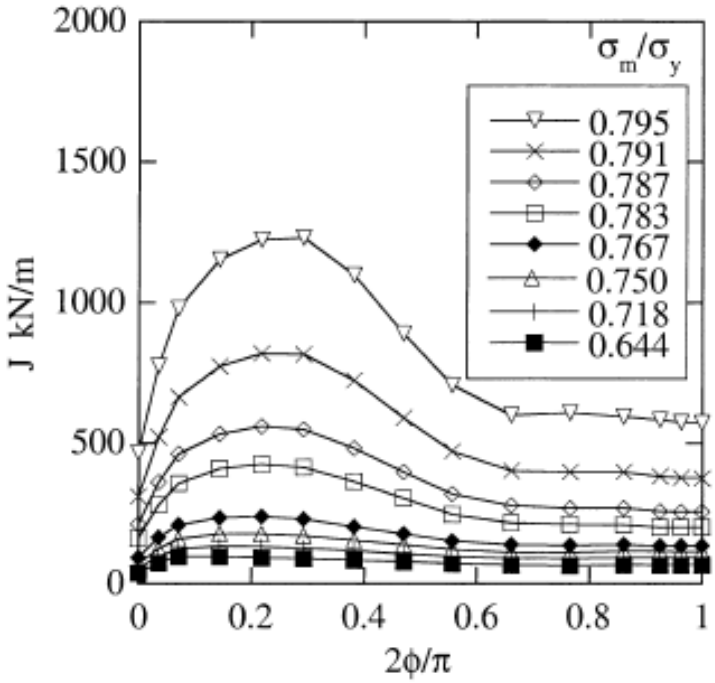

Figure 5.9: Distribution of J-integral along the crack front for a surface crack a/c=0.9 in tension after Brickstad et al (2000).

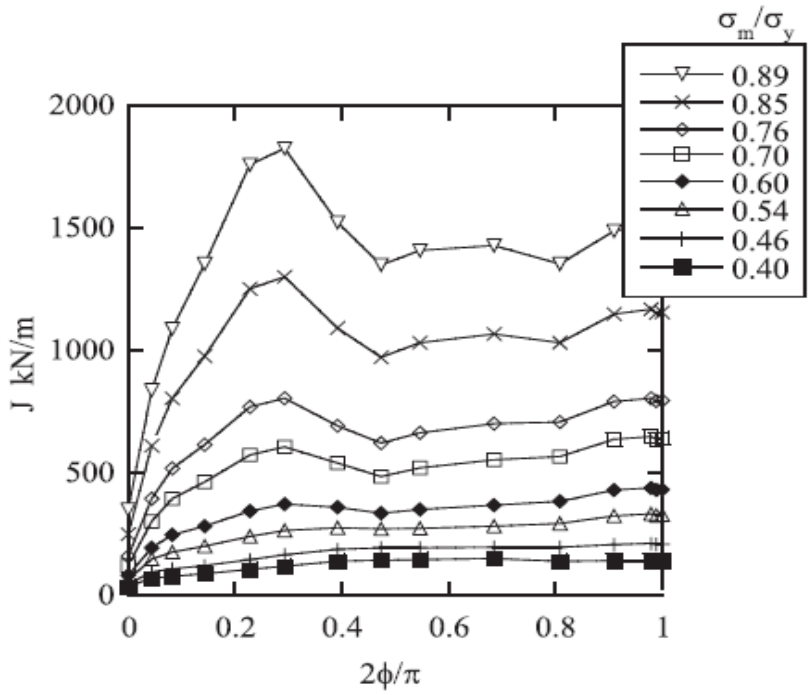

Figure 5.10: Distribution of J-integral along the crack front for a surface crack a/c=0.15 in tension after Brickstad et al (2000).

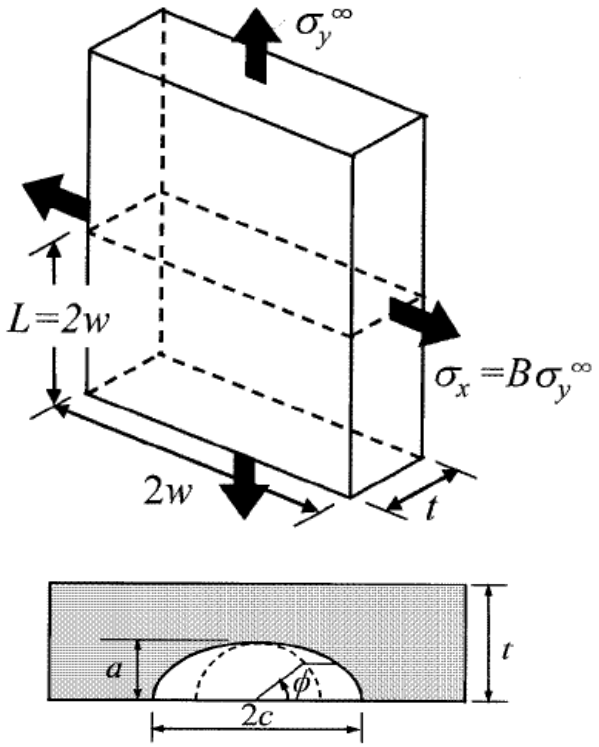

Figure 5.11: Illustration of a surface cracked plate under biaxial loading (Kim et al 2004b).

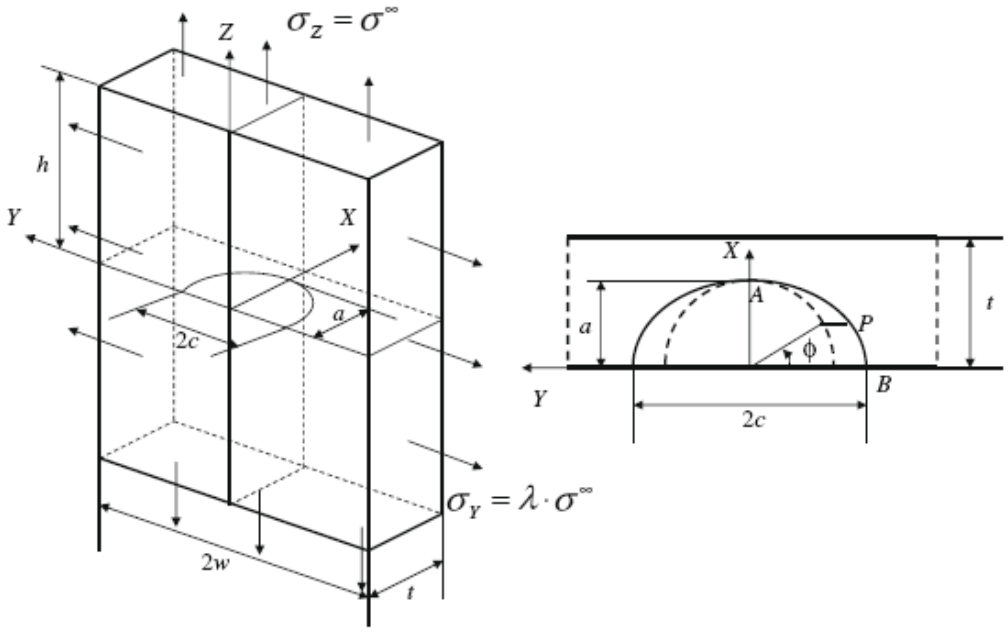

Figure 5.12: Illustration of a surface cracked plate under biaxial loading (Wang 2009).

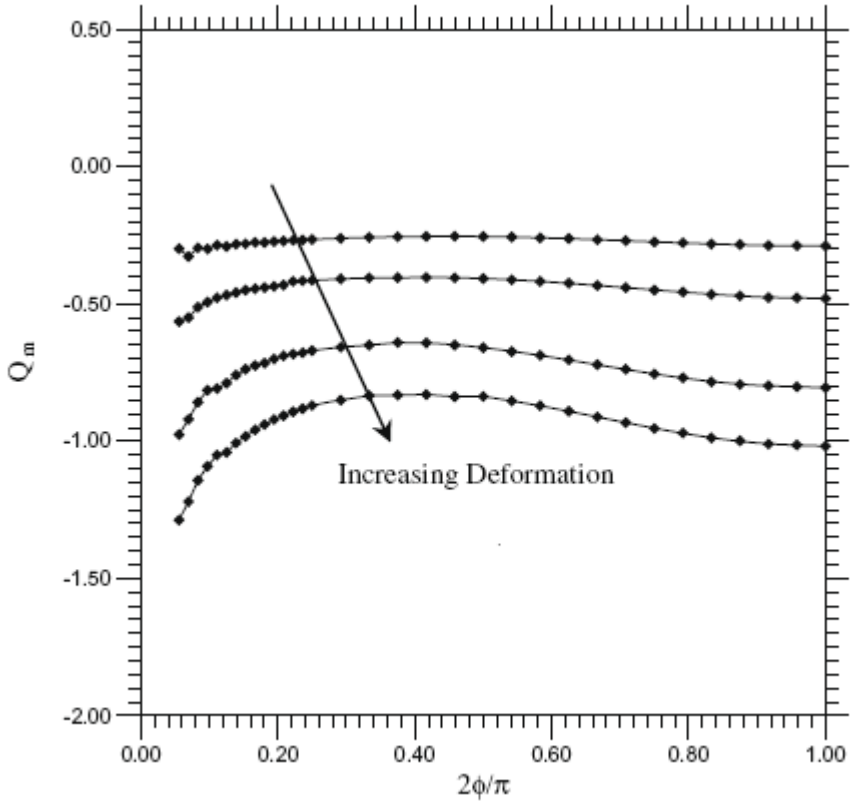

Figure 5.13: Distribution of Q-stress along the crack front of deep surface crack a/w=0.6, a/c=1 under uniaxial tension after Wang (2009).

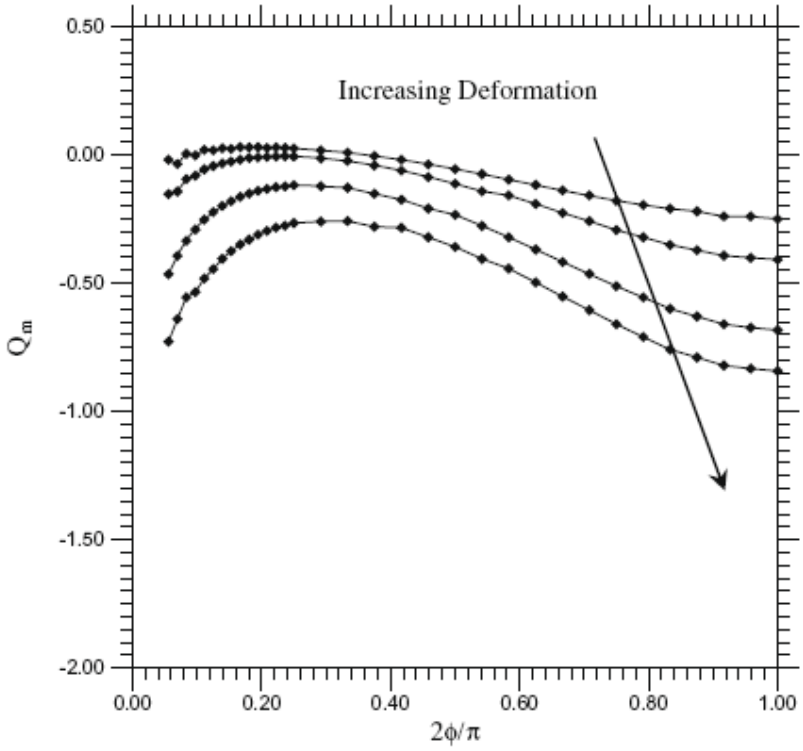

Figure 5.14: Distribution of Q-stress along the crack front of deep surface crack a/w=0.6, a/c=1 under uniaxial tension after Wang (2009).

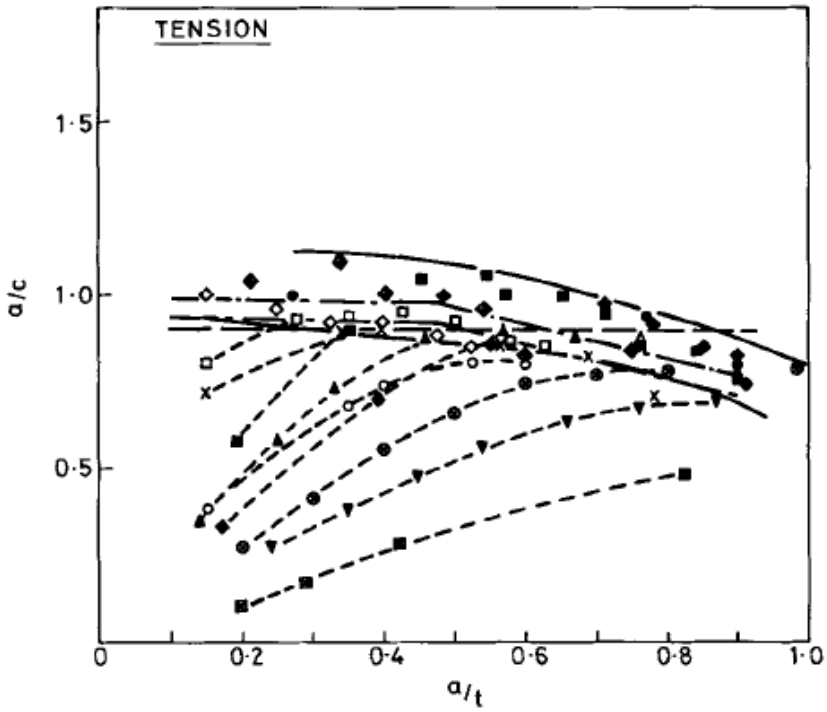

Figure 5.15: Development of crack shape under fatigue in tension after Scott and Thorpe (1981).

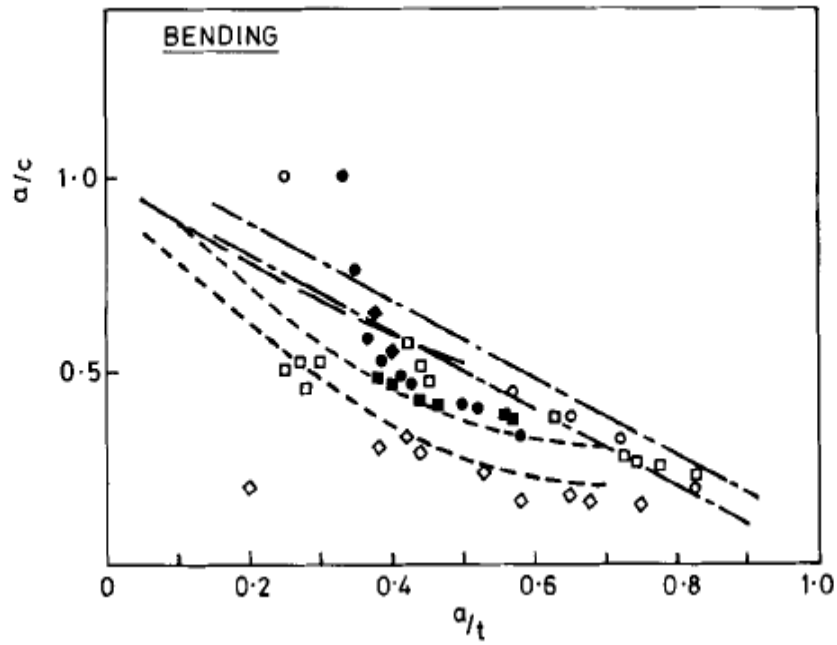

Figure 5.16: Development of crack shape under fatigue in bending after Scott and Thorpe (1981).

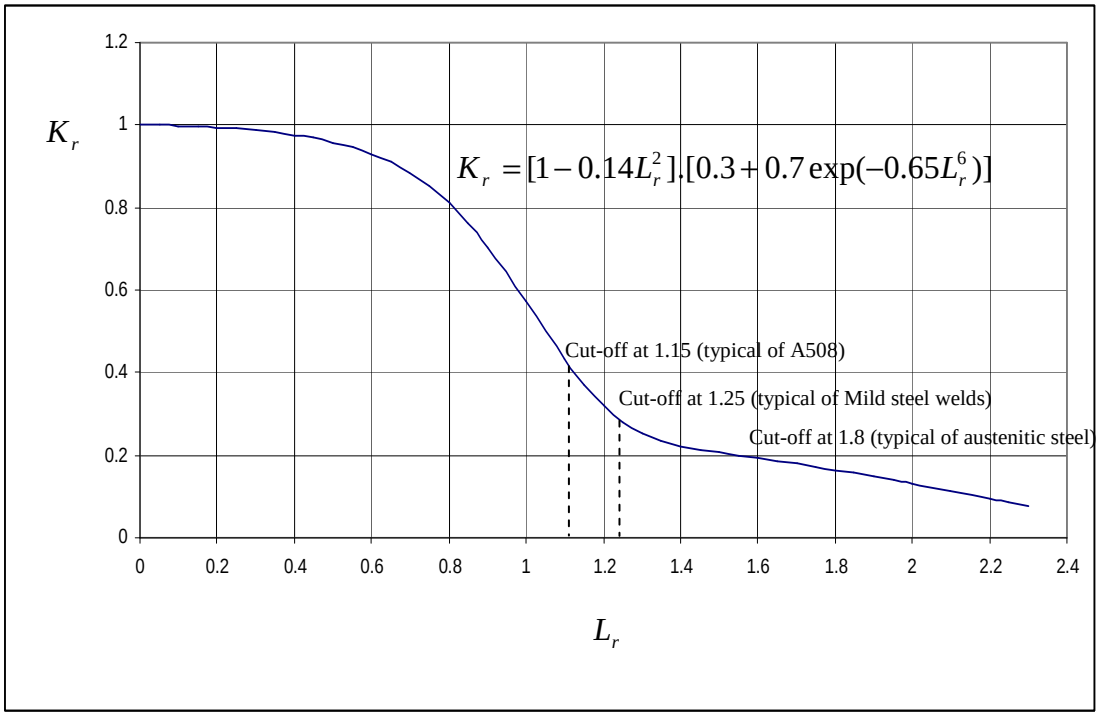

Figure 5.17: The general failure assessment diagram.

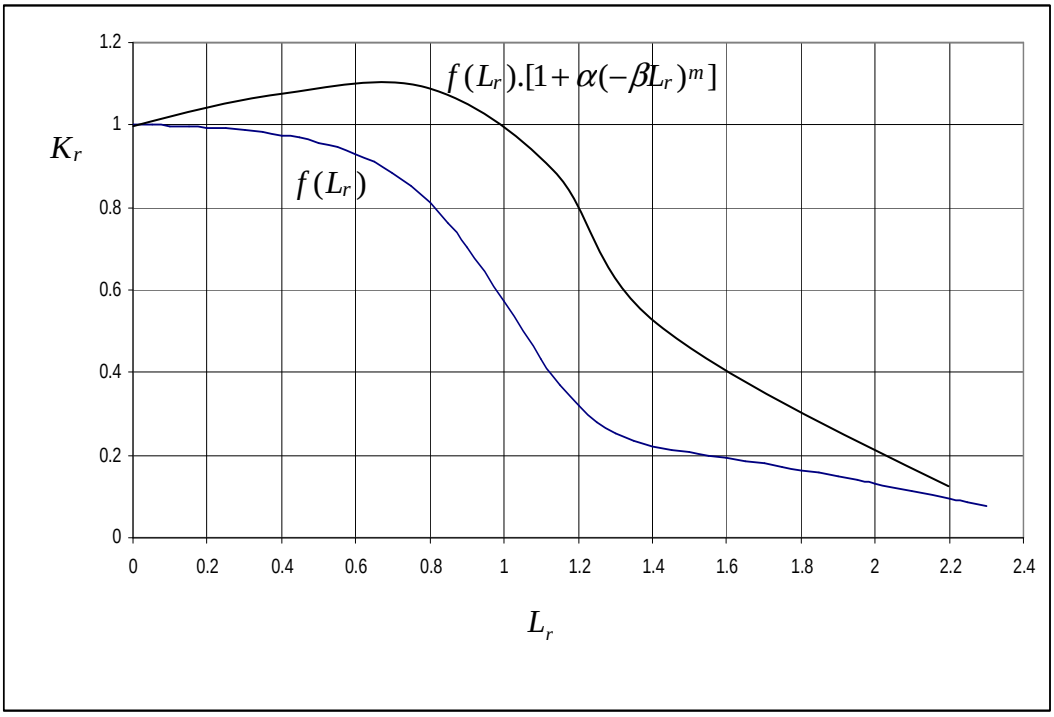

a-Procedure I

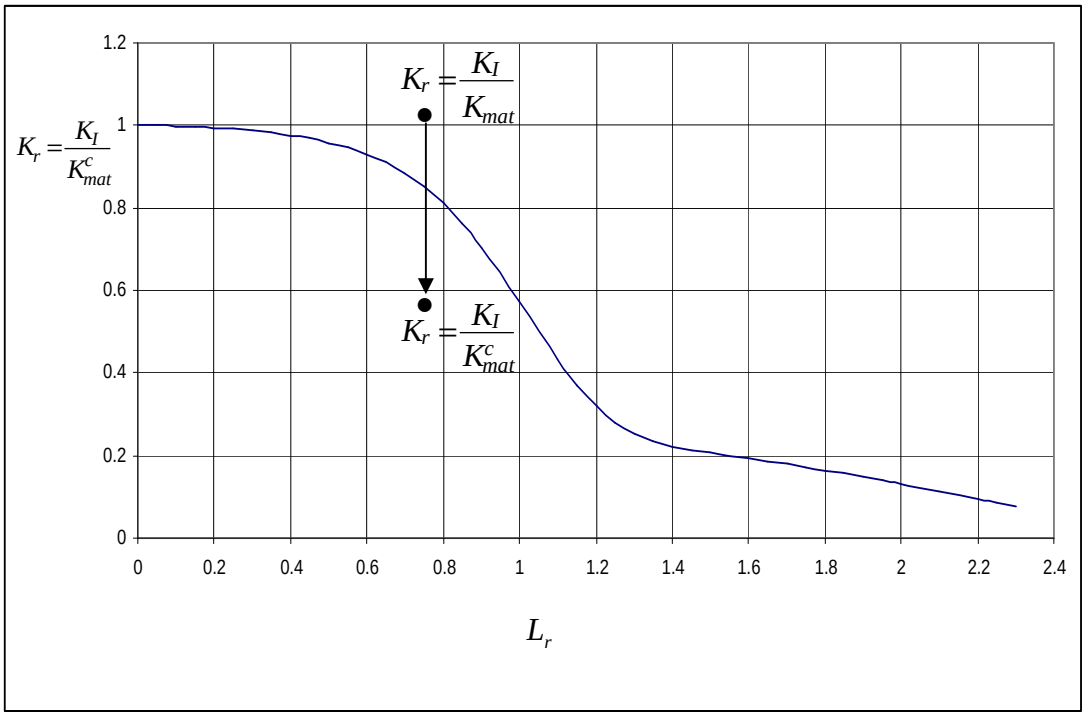

b-Procedure II

Figure 5.18: Constraint based failure assessment diagram.

6. Experimental determination of fracture toughness

6.1 Plane strain fracture toughness K_{Ic}

The purpose of determining plane strain fracture toughness K_{Ic} is to characterise the resistance of a material to fracture under small scale yielding. A valid K_{Ic} is a lower bound fracture toughness and is a key parameter in estimating the critical defect size for a material in service conditions.

Experimental determinations of K_{Ic} involve testing pre-cracked specimens by either tension or three point bending. Two kinds of specimen configurations are commonly used: single edge cracked bend and compact tension specimens as shown in Figure (6.1). The ratio of crack depth to width (a/w) must lie in range of 0.45 to 0.55. During the test, a monotonically increasing load is applied on a specimen until it fails or the crack extends. The load and displacement are monitored. Three principal types of load-displacement curves can be identified to calculate a critical load P_Q as illustrated in Figure (6.2). The crack length (a) is measured by taking the average of eight measurements across crack front, and in order to ensure limited plasticity at the crack tip and in a valid test, the ratio of P_{max}/P_Q must not exceed 1.10. Once the crack length and the critical load are computed, provisional fracture toughness K_Q can be calculated from the expression (ASTM E399):

$$K_Q = \frac{P_Q}{B\sqrt{w}}\ f(a/w) \tag{6.1}$$

Where, f(a/w) is a non dimensional function of (a/w) for particular geometry given in ASTM E399. If the validity requirements given in chapter (3) are satisfied, K_Q can be regarded as K_{Ic}. However, if the validity requirements are not satisfied the test must be repeated with a larger specimen, or fracture toughness determined by using the crack tip opening displacement or the J-integral discussed next.

It should be noted that the validity requirements of the test are particularly restrictive for tough materials and for small specimens with a plastic zone comparable to the body dimensions. The requirements are difficult to satisfy in tough materials used in real engineering structures where fracture occurs with a large plastic zone and impracticably larger specimens may be needed.

6.2 J-integral fracture toughness J_c

The fracture toughness (J_c) test places lower demands on size requirements as opposed to those demanded in ASTM for plane strain fracture toughness, K_{Ic}. The size requirements at fracture demand the ligament, b, and the thickness, B, must exceed $20J/\sigma_0$ for bend dominated geometries. The testing is typically performed on a specimen of thickness up to that of the real structure. The standard toughness testing procedure ensures sufficiently high crack tip stress or high constraint, and thus provides conservative (lower bound) estimates of toughness. Kumar, Shih and German (1981), established a method to characterise the J-integral where the body is completely yielded. The J-integral is decomposed into elastic and plastic parts, J^e, J^p respectively.

$$J = J^e + J^p \tag{6.2}$$

In an elastic body, the stress intensity factor is determined from the applied load, and J^e can be simply determined from the stress intensity factor:

$$J^e = \frac{K^2}{E'} \tag{6.3}$$

or

$$J^e = \sigma_0 e_0 a \left(\frac{P}{P_0}\right)^2 f(a/w) \tag{6.4}$$

Where P is the applied load, P_0 is the limit load, and f(a/w) is a non-dimensional function which depends on configuration (ASTM E399).

In a fully plastic material, the J-integral can be determined (Kumar, Shih and German, 1981):

$$J^p = \alpha\ \sigma_0 e_0 a \left(\frac{P}{P_0}\right)^{n+1} h(a/w, n) \tag{6.5}$$

Where, α is a material property, h is a tabulated value depends upon configuration (a/w) and hardening exponent n. The complete form suggested by Kumar, Shih and German (1981) may be written as:

$$\frac{J}{\sigma_0 e_0 a} = f(a/w)\left(\frac{P}{P_0}\right)^2 + \alpha\ h(a/w, n)\left(\frac{P}{P_0}\right)^{n+1} \tag{6.6}$$

The procedure is applicable in hardening and relatively low hardening materials. However, it becomes less accurate in non-hardening materials (n=∞) and causing J-integral to be highly sensitive.

Sumpter and Turner (1977) developed the relation between the J-integral and the absorbed energy in elastic and plastic manner. The energy represented by the area under the load-displacement curve is decomposed into elastic and plastic components as illustrated in Figure (6.3). The relevant expression developed by Sumpter and Turner (1977) can be written as:

$$J = \frac{\eta^e U^e}{(W-a)B} + \frac{\eta^p U^p}{(W-a)B} \tag{6.7}$$

Where the elastic and plastic energy are U^e and U^p respectively, and η^e, η^p are geometry dependent constants.

According to British Standard BS 7448-4:1997, the total J-integral (J_0) is also given as a sum of the elastic and plastic components:

$$J_0=\left[\frac{FS}{(BB_N)^{0.5}W^{1.5}}.f\left(\frac{a_0}{W}\right)\right]^2\frac{(1-\nu^2)}{E}+\frac{\eta_p U_p}{B_N(w-a_0)} \tag{6.8}$$

Where, U_p is the absorbed energy and determined from the area under load vs. load line displacement curve. B_N is the effective thickness if a side-grooved specimen is used.

The corrected J-integral accounting for ductile crack extension is determined to be:

$$J_{corr}=J_0\{1-\frac{(0.75\eta_p-1)}{(w-a_0)}\Delta a\} \tag{7.9}$$

The J-integral can also be determined using the experimental load-crack mouth opening displacement (CMOD) curve (Sumpter, 1987, Kirk and Dodds, 1993, Sreenivasan and Mannan, 2000, Kim and Schwalbe, 2001, Kim, 2002, Kim, et al., 2004a, Zhu and Joyce, 2007). The elastic and plastic energy U^e and U^p in equation (6.7) are determined from the area under the load-CMOD curve. The plastic geometry factor Eta (η^p) is different from η^p using load-line displacement curve. Expressions to determine the plastic geometry factor Eta (η^p) for deep and shallow cracks are available in the literature.

6.3 Crack tip opening displacement CTOD fracture toughness, δ_c

Wells (1961) developed the concept of the crack tip opening displacement as a fracture mechanics parameter and is used in (BS 7448-4:1997, ASTM E399) standards of fracture toughness test.

The purpose of the CTOD (δ) test is to determine the critical δ_c on δ-R curve that is associated with the onset of the crack growth in ductile materials. The CTOD calculation is based on the plastic hinge model. The two rigid arms rotate around the hinge point which is located at position r_p (w-a) in the ligament ahead of the crack tip, where r_p is plastic rotational factor. During the test both load and notch opening displacement are recorded. The plastic component of the notch opening displacement V_p is measured at the termination of the test by drawing the parallel line to the elastic tangential line, OA as shown in Figure (6.4).

The crack tip opening displacement consists of elastic and plastic parts:

$$\delta=\delta_{el}+\delta_{pl} \tag{6.10}$$

The elastic part is calculated as

$$\delta_{el}=\left[\frac{FS}{(BB_N)^{0.5}W^{1.5}}.f\left(\frac{a_0}{W}\right)\right]^2\frac{(1-\nu^2)}{2\sigma_{YS}E} \tag{6.11}$$

Where, F is the load, S is the bending span, B and B_N are the thickness of non-side grooved and side-grooved specimens, respectively, and $f(a_0/w)$ is the non-dimensional function depends on the configuration and is obtained from the tables or from the equation given in BS7448-4:97, σ_{YS} is the yield strength, E is the Young's modulus, and ν is the Poisson's ratio.

The plastic part is estimated as

$$\delta_{pl}=\frac{0.6\Delta a+0.4(W-a_0)}{0.4W+0.6(a_0+\Delta a)+z}V_P \tag{6.12}$$

The total crack tip opening displacement is defined to take account of stable crack extension, δ_{corr} (BS 7448-4:1997):

$$\delta_{corr}=\left[\frac{FS}{(BB_N)^{0.5}W^{1.5}}.f\left(\frac{a_0}{W}\right)\right]^2\frac{(1-\nu^2)}{2\sigma_{YS}E}+\frac{0.6\Delta a+0.4(W-a_0)}{0.4W+0.6(a_0+\Delta a)+z}V_P \tag{6.13}$$

Where V_p is the plastic component of the notch opening displacement and z is the thickness of a knife edge. The value of 0.4 presents the rotational factor (r_p) based on the plastic hinge model in deep cracked specimens. The rotation factor r_p identifies the location of the centre of a plastic hinge and is widely discussed in the literature for different kinds of crack lengths, (Xiao and Huang, 1982, Wu, 1983, Sumpter, 1987, Zhang and Wang, 1987, Wu et al., 1988, Zhang and Zhu, 1988, Tang and Shi, 1992, and Kirk and Dodds, 1993).

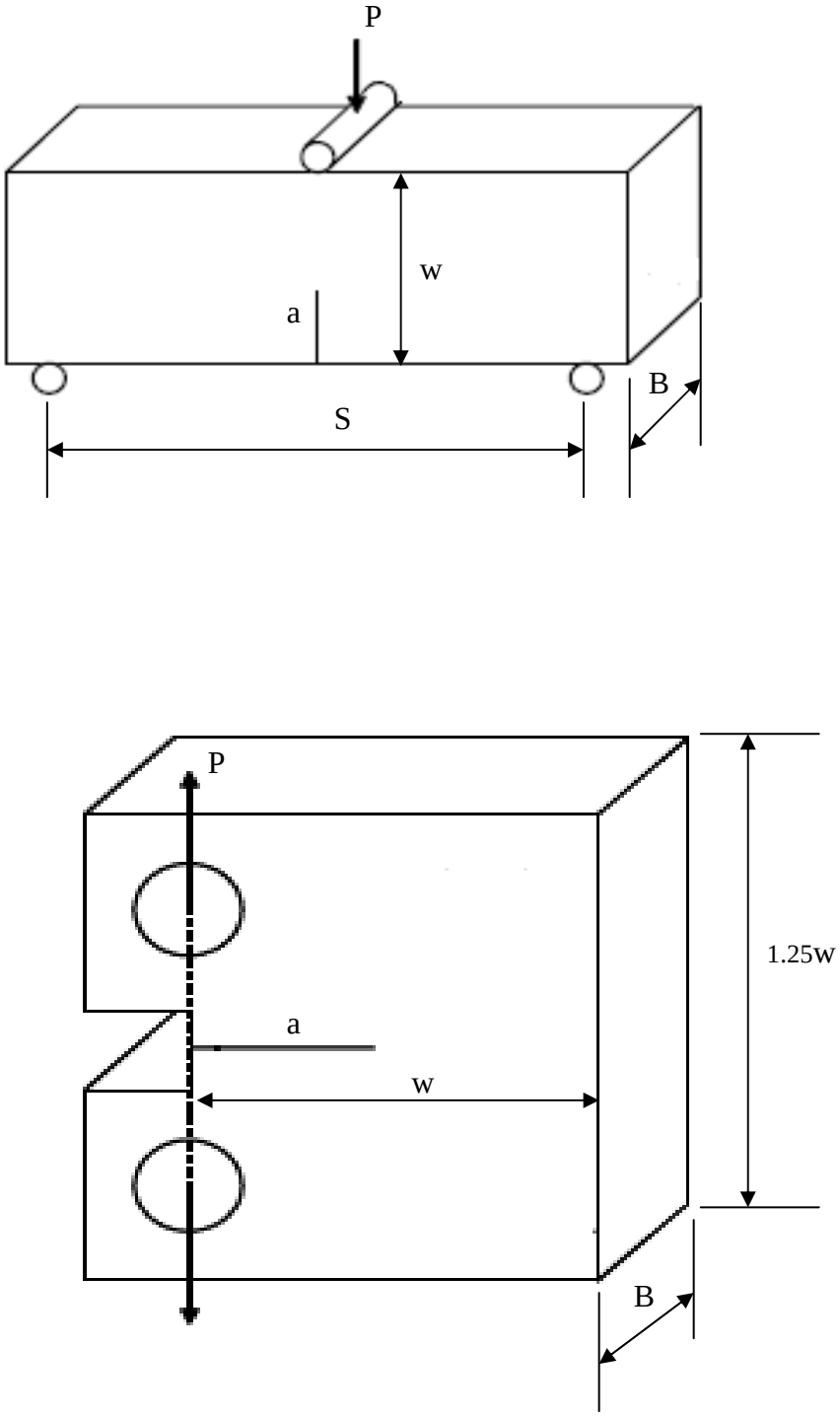

Figure 6.1: Standard specimens for plane strain fracture toughness, (a) Single edge cracked bend bar (b) Compact tension specimen.

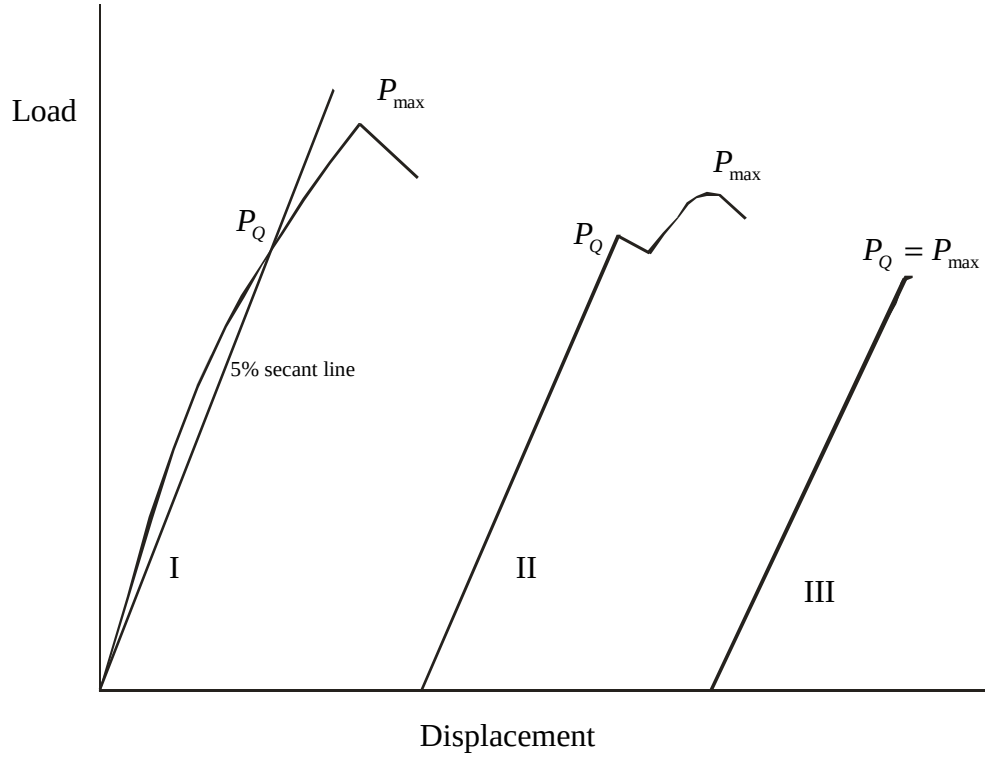

Figure 6.2: The principal types of load-displacement curves in standard test of plane strain fracture toughness, K_{Ic}.

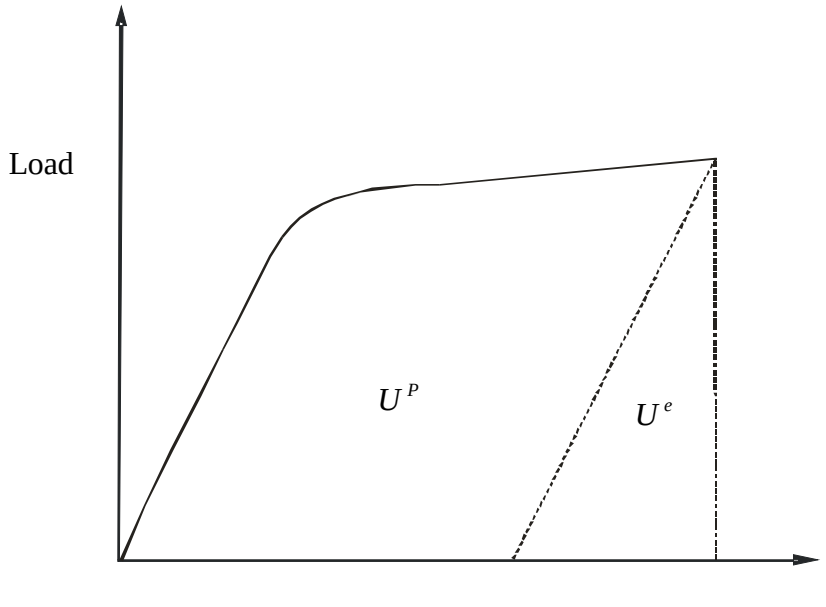

Figure 6.3: Plastic and elastic energy represents the area under the Load-displacement curve.

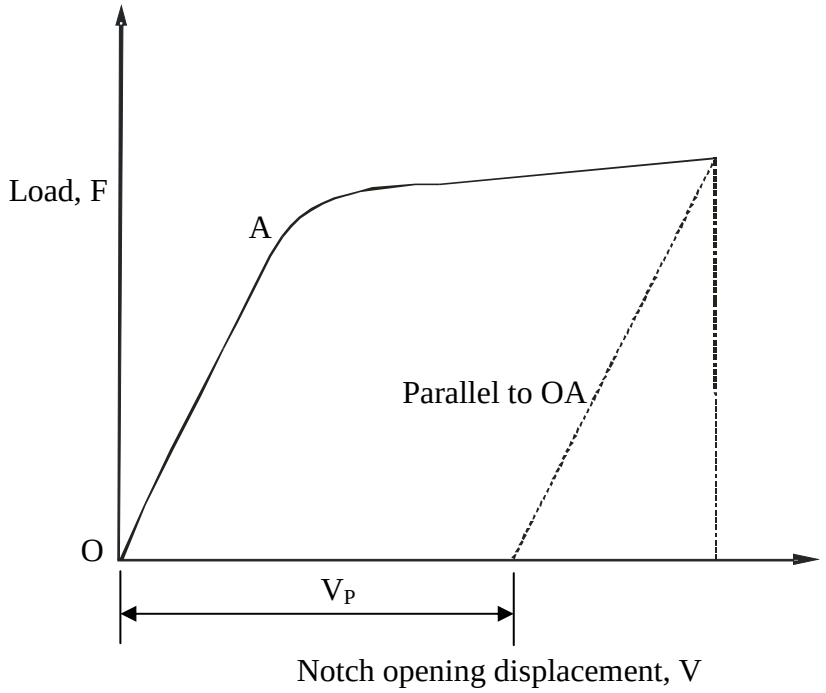

Figure 6.4: Load-notch opening displacement diagram.

7. A study of out-of-plane effects in edge cracked bend bars

7.1 Introduction

The stresses near the crack tip in an edge cracked bar are affected by the thickness of the bar. The effect is particularly significant in full plasticity. Conventional fracture assessment based on a single parameter J-integral and the modified approach based on in-plane constraint (T/Q-effect) tends to underestimate the fracture resistance of the material in three-dimensional structures. In this chapter the mean stress is systematically decomposed into contributions from the: in plane (T/Q-effect), out-of-plane, and global bending effects. The objective is to identify any systematic trends in the out-of-plane constraint due to the geometry. The mean stress was calculated on the mid-plane at a distance $2J/\sigma_0$ such that the blunting effects vanish and both small geometry change solution and large geometry change solution are consistent.

7.2 Geometry and Material

Table (7.1) shows the size of plane and side-grooved single edge cracked bend specimens considered in this study in both dimensional and non-dimensional formats.

	Plane specimens for out-of-plane examinations					The geometry of side-grooves examinations				
	Dimensional (mm)			Non-dimensional		Dimensional (mm)			Non-dimensional	
1-Deep cracks	w	a	B	a/w	B/w	w	a	B	a/w	B/w
	10	5	5	0.5	0.5	50	25	25	0.5	0.5
	10	5	3	0.5	0.3	50	25	10	0.5	0.2
	10	5	2	0.5	0.2	50	25	5	0.5	0.1
	10	5	1	0.5	0.1					
	10	3.5	5	0.35	0.5					
	10	3.5	2	0.35	0.2					
	10	3.5	1	0.35	0.1					
2-Shallow cracks	10	2	5	0.2	0.5					
	10	2	3	0.2	0.3					
	10	2	2	0.2	0.2					
	10	2	1	0.2	0.1					
	10	1	5	0.1	0.5					
	10	1	3	0.1	0.3					
	10	1	2	0.1	0.2					
	10	1	1	0.1	0.1					

Table (7.1): The geometry of the edge cracked bend bars examined in this work.

The material response was defined as isotropic elastic-perfectly plastic with Young's modulus of 200 GPa, Poisson's ratio of 0.49, and a yield strength of 300 MPa. However in general non-dimensional results are presented. The material yields following a Mises yield criterion and plastically obeys an associated flow rule.

7.3 Finite element model

Finite element analyses were conducted to obtain accurate crack-tip stress fields for specimens without side grooves. The finite element model is shown in Figure (7.1a). The crack was modelled as a sharp crack with no radius at the tip employing that the numerical models use small geometry change solution. The elements used were continuum three-dimensional with reduced integration, C3D8R. Thirty concentric rings of elements surrounded the crack tips. The innermost ring contains collapsed elements with coincident but independent nodes as shown in Figure (7.1b). Size of the elements increases with the increase of distance from the crack tip, r.

To benchmark the three-dimensional model the stress intensity factor, K obtained from the finite element model under elastic conditions was benchmarked against a non-dimensional geometry factor $Y=K/(\sigma_{app}\sqrt{\pi a})$ published by Newman and Raju (1981). The value of the mid-plane was used for verification and was Y=1.437 which is in agreement with Newman and Raju solution of Y=1.416. As a further check of the model the elastic T-stress at the mid-plane was $T/\sigma_{app}=0.32$ close to the Sham`s (1991) solution with a value of 0.317.

Due to the symmetry conditions, only a quarter of the SECB specimen was modelled and appropriate symmetry boundary conditions were applied on the planes of symmetry. The load was applied as displacement boundary condition as shown in Figure (7.2). The J-integral was evaluated with the virtual crack extension technique adopted in ABAQUS using a contour defined in the far field where J-integral is still path-independent. This was done by creating different contours around the crack tip. The first contour which consists of elements directly connected to crack tip nodes was defined first. Then Abaqus adds subsequent rings of elements (contours) that share nodes with the elements in the previous contour up to a defined contour (n) where J-integral is measured. For side-

grooved specimens the side groove with an angle of 45˚was cut to a depth of 10 % of the thickness on each lateral face to obtain 80% net thickness of the full thickness, and the finite element model is shown in Figure (7.3).

7.4 Full stress field in an edge cracked bend bar

7.4.1 Two-dimensional model

In-plane constraint can be quantified by performing elastic-plastic modified boundary layer calculations in contained yielding (Betegón and Hancock, 1991, O'Dowd and Shih 1991, 1992):

$$\sigma_m^{2D} = \sigma_m^{SSY} + Q(\chi).\sigma_0 \tag{7.1}$$

Where σ_m^{SSY} is the mean stress in small scale yielding and χ is a measure of deformation ($c\sigma_0/J$).

The parameter Q of O'Dowd and Shih (1991, 1992) scales the mean stress for the in-plane constraint effect, which depends on geometry and loading in a non-linear manner, and is largely distance independent.

The full field solution in plane strain can be written as:

$$\sigma_m^{2D}(r,\chi) = \sigma_m^{SSY} + Q(\chi).\sigma_0 + \Delta\sigma_m^{Gb}(r,\chi) \tag{7.2}$$

Where, $\Delta\sigma_m^{Gb}$ is contribution from global bending, χ is a measure of deformation ($c\sigma_0/J$), and r is a distance from the crack tip which is taken here equal to $2J/\sigma_0$. The global bending effect in plane strain can then be defined as:

$$G_b(r,\chi) = \frac{\sigma_m^{2D} - \sigma_m^{SSY} - Q\sigma_0}{\sigma_0} \tag{7.3}$$

The assumption is made that higher order terms can be added by linear superposition. These additives terms are consistent with the literature (e.g. Karstensen 1996).

7.4.2 Three-dimensional model

It is hypothesised that the stresses near the crack tip in three-dimensional full field solutions can be written as:

$$\sigma_m^{3D}(r,\chi) = \sigma_m^{SSY} + Q(\chi).\sigma_0 + \Delta\sigma_m^{Gb}(r,\chi) + \Delta\sigma_m^{Op}(r,\chi) \tag{7.4}$$

Where σ_m^{SSY} is the mean stress under high constraint small scale yield conditions, Q is the O'Dowd and Shih in-plane constraint parameter, $\Delta\sigma_m^{Gb}$ is the reduction in the mean stress due to global bending and $\Delta\sigma_m^{Op}$ is the reduction in the mean stress due of out-of-plane effects ($O_p = \Delta\sigma_m^{Op}/\sigma_0$). The mean stress ($\sigma_m^{3D}$) derived from the FE model was measured at a distance of $2J/\sigma_0$ using local J-integral at the mid-plane. To investigate the out-of-plane constraint effect, the reference full field solution was obtained from a two-dimensional plane strain geometry identical to the three-dimensional geometry in all respects other than the thickness. The reference solution was then subtracted from the 3-D full field solution of the single edge cracked bend bar at a matching $\chi = c\sigma_0/J$ using the average J-integral:

$$O_p(r,\chi) = \frac{\sigma_m^{3D} - \sigma_m^{2D}}{\sigma_0} \tag{7.5}$$

In principle equation (7.4) may also be solved for the global bending term $\Delta\sigma_m^{Gb}(r,\chi)$, if the remaining terms are known:

$$G_b(r,\chi) = \frac{\sigma_m^{3D} - \sigma_m^{SSY} - Q\sigma_0 - O_P\sigma_0}{\sigma_0} \tag{7.6}$$

7.5 Out-of-plane constraint in non-hardening materials

The mean stress for deeply cracked geometries (a/w=0.5) of different thicknesses (B/w=0.5, 0.3, 0.2 and 0.1) is shown in Figure (7.4). For a thick specimen B/w=0.5 the mean stress maintained high levels of constraint within 10% of HRR field up to a large level of deformation ($c\sigma_0/J = 30$). The geometry with B/w=0.3 also exhibited high levels of constraint in contained yielding but the mean stress reduced in full plasticity starting from $c\sigma_0/J = 80$. For thin specimens (B/w=0.2) the mean stress reduced at a lower level of deformation compared to the thick specimens. Thinnest geometries B/w=0.1 showed the largest constraint loss.

In shallow cracked geometries (a/w=0.2) the mean stress for thick specimens (B/w=0.5) was below the HRR field even in small scale yielding, and reduced further with increasing in deformation as shown in Figure (7.5). A similar observation holds for thinner cracked specimens with an additional loss of constraint.

Figure (7.6) shows the mean stress for the shallowest cracks (a/w=0.1) at different specimen thickness. The mean stress was below the HRR field for all levels of deformation and all thicknesses. Importantly the magnitude of the mean stress was largely independent of the thickness. The effect of thickness in very shallow cracked bars (a/w= 0.1) was very small.

The out-of-plane term for a deeply cracked (a/w=0.5) geometry is shown in Figure (7.7). For thick geometries (B/w=0.5) the out-of-plane constraint loss was insignificant at all observable deformation levels. In geometries with B/w=0.3 the out-of-plane effect was significant at deformation levels higher than $c\sigma_0/J=70$. For thin geometries (B/w=0.2) the out-of-plane effect became even more pronounced early in the deformation history ($c\sigma_0/J=200$). For thinnest specimens (B/w=0.1) the out-of-plane effect became significant in small scale yielding and increased massively in full plasticity.

A similar trend to deeply cracked geometries (a/w=0.5) was observed for relatively shallow cracks (a/w=0.2) as shown in Figures (7.8). However in shallowest cracked

geometries (a/w=0.1) the out-of-plane effect was significantly less pronounced compared to that observed in deep cracked geometries and became notable only at very large deformations ($c\sigma_0/J<100$) as shown in Figure (7.9). Conclusion can be made that in shallow cracked geometries the in-plane effect dominates the out-of-plane effect.

The effect of the crack depth on the mean stress is shown in Figures (7.10) to (7.12). Figure (7.10) shows the mean stress at the mid-plane for thick specimens (B/w=0.5) as a function of deformation. The biggest stress was observed for highly constrained geometries (a/w=0.5), while smaller values were observed for shallow cracked geometries (a/w=0.2 and 0.1). It is clear that the mean stress decreased as the crack depth became shallower, but for the most part up to (a/w=0.35) remained within the limits of the highly constrained geometry (HRR-field). Thin specimens (B/w=0.2) with a/w=0.5 maintained high levels of mean stress, however a big loss of constraint was observed for shallow cracked specimens $a/w\leq0.2$ as shown in Figure (7.11). Further reductions in the mean stress were observed for the thinnest geometries as shown in Figure (7.12).

Figure (7.13) shows the out-of-plane constraint parameter (O_p) for thick rectangular specimens (B/w=0.5) with different crack depths. The overall trend of the out-of-plane effect for different depths was insignificant even in full plasticity. For thin specimens B/w=0.2, 0.1 the out-of-plane effect was more pronounced than in thicker specimens particularly for a/w=0.5 and 0.35 geometries as shown in Figures (7.14) and (7.15). The (O_p) term had a big effect in deep cracks while the effect reduced in shallow cracks. This is because shallow cracked geometries were highly affected by the in-plane effect (T-stress) and less affected by the out-of-plane effect and global bending. The plastic zone developed rapidly in shallow cracks which reduced the mean stress before the effect of thickness became significant.

The out-of-plane constraint as a function of radial distances ($r\sigma_0/J=2,4,6,8$) for thin geometries (a/w=0.5, B/w=0.2) is shown in Figure (7.16) for non-hardening materials. The O_p term increased with the increase in the radial distance ahead of the crack tip. Figure (7.17) shows the O_p constraint loss in very thin geometries (B/w=0.1) is significantly influenced by the radial distance. This confirms the out-of-plane effect is distance dependent. In contrast, the O_p in hardening material (n=10) was less sensitive to

the radial distance, in geometries with a ratio of B/w=0.2 as shown in Figure (7.18). The thinnest geometries B/w=0.1 showed a greater dependence on the radial distance (r) as shown in Figure (7.19), however they were less distance dependent compared to non-hardening materials.

7.6 Surface contraction

Surface contraction is a feature in fracture mechanics samples in full plasticity. Lateral contraction becomes significant when estimating fracture toughness under ductile tearing using the nominal thickness. This section examines the out-of-plane contraction in the thickness direction for single edge cracked bend bars. Deep and shallow cracked geometries (a/w=0.1 and 0.5) with different thicknesses (B/w=0.5, 0.3, 0.2, 0.1) were examined. The contraction was measured at the crack tip (r=0) on the surface node in the FE model under different levels of deformation. The corresponding plastic zones are also shown. The plastic zone size was measured at the centre-plane from the crack tip in the same direction of maximum plastic strain and the preferred path for fracture at the microscopic level (θ=45˚).

Figure (7.20) shows the contraction ratio (Δ/B) as a function of deformation in deeply cracked geometries (a/w=0.5) for different thicknesses (B/w=0.1, 0.2, 0.3, 0.5). The out-of-plane contraction increased with deformation. In small scale yielding the contraction was insignificant, however increased significantly in full plasticity ($c\sigma_0/J \leq 100$) for all geometries. The largest contraction ratio (Δ/B) was found in thin geometries B/w=0.1, and much less for thick geometries B/w=0.5. Figure (7.21) shows the size of the plastic zone at the mid-plane as a function of surface contraction. The plastic zone developed rapidly in thin geometries B/w=0.1. The contraction was insignificant when a small plastic zone surrounded the crack tip, however the contraction increased markedly when the plastic zone encompassed significant fraction of the ligament. In thin geometries B/w=0.2, 0.1 the contraction became significant when the radius of the plastic zone was approximately equal to the thickness. In thick geometries B/w=0.5 the contraction became significant when the plastic zone radius reached approximately half the thickness.

Figure (7.22) shows the surface contraction ratio (Δ/B) in shallow cracked geometries (a/w=0.1). Thin geometries showed larger contraction ratio (Δ/B) compared to the thick ones. Figure (7.23) shows Δ/B as a function of the plastic zone. The surface contraction in thin geometries B/w=0.2 became significant when the radius of the plastic zone was approximately twice the specimen thickness. Thinnest geometries B/w=0.1 showed the contraction was significant when the size of the plastic zone r_p was approximately 3-4 times the specimen thickness, as shown in Figure (7.23). In thick geometries B/w=0.5 the contraction became significant when the plastic zone was approximately equal to the thickness. Thin-shallow cracked geometries showed a rapid development in the plastic zone size. The size of the plastic zone in shallow cracked geometries was about twice the plastic zone in deep cracked geometries. Figure (7.24) shows the contraction is insignificant when plane strain conditions dominate, however as plane strain conditions are lost at the centre of the specimen, the surface contraction increases. In conclusion, shallow crack geometries contracted more in comparison with deep cracked geometries of the same thickness. The contraction ratio (Δ/B) also increased for thinner geometries.

7.7 The effect of side-grooves in fracture mechanics samples

One of the major features associated with standard fracture samples in ductile tearing is that the crack tends to extend in a thumbnail fashion where the crack extends largely at the centre-plane compare to the free surface. Researchers have considered this feature and performed analysis by using side-grooves. Delorenzi and Shih (1983) observed uniform stress intensity factor and energy release rate across the thickness in compact tension with 25% side-grooves of the total thickness. Nevalainen and Dodds (1995) showed that there is no significant effect on the mid-plane stresses in side-grooved specimens with groove angle of 45˚and depth of 20% of the total thickness.

As shown previously the contraction became significant at high deformation levels required for ductile tearing, and this may affect the constraint levels across the thickness and the fracture toughness in test specimens. Therefore to define a programme for fracture tests on edge cracked bend samples the effect of side-grooving on the constraint and J-integral was examined. This section presents a comparison between side-grooved and non-side grooved geometries. The distribution of the mean stress, σ_m/σ_0, and J-

integral ($J/c\sigma_0 e_0$) along the crack front were examined. σ_0 is the yield stress, $e_0=\sigma_0/E$ and c is the ligament, (w-a). The proximity to plane strain conditions was examined using the plane strain constraint parameter, T_z, which was defined as the ratio of out-of-plane stress to the sum of in-plane stresses, $T_z=\sigma_{zz}/\sigma_{rr}+\sigma_{\theta\theta}$. The angle of the side groove assessed in this study was 45˚and the depth was 10 % of the thickness on each lateral face to obtain 80% net thickness of the full thickness.

7.7.1 Thick, deeply cracked bend bars (a/w=0.5, B/w=0.5).

The distribution of the mean stress along the crack front for non side-grooved geometries is shown in Figure (7.25). It can be seen that the mean stress maintained a high level of constraint from the mid-plane (z/(B/2)=0) to quarter-plane and reached the HRR field at low deformation levels. With increasing deformation ($c\sigma_0/J<100$) the loss of constraint became significant around the quarter-plane region (z/(B/2)=0.5). At the free surface the stresses cluster around the plane stress solution at low deformation levels, and reduced further at the high deformation level of $c\sigma_0/J=38$. This contrasts with the side-grooved geometries shown in Figure (7.26) where uniformity of the mean stress was observed across most of the thickness. At the mid-plane the side grooves did not elevate the crack tip constraint, however at the root of the V-grooves (free surface) the mean stress remained significantly elevated and was consistent across the crack plane. This result is similar to that obtained by Nevalainen and Dodds (1995).

Figure (7.27) shows the plane strain constraint, $T_z=\sigma_{zz}/(\sigma_{rr}+\sigma_{\theta\theta})$, maintains the theoretical value, 0.5, over the majority of the thickness at low deformation levels ($c\sigma_0/J>375$), and reduces at the free surface to zero. This is in contrast to the side-grooved geometry when the plane strain conditions were maintained across the thickness as shown in Figure (7.28). Figure (7.29) shows non-dimensional J-integral ($J/c\sigma_0 e_0$) along the crack front from the mid-plane to the free surface for a non side-grooved geometry. A big variation was observed in J-integral values across the thickness and the maximum value at the mid-plane decreased gradually towards the free surface. The J-integral distribution in side-grooved geometries was more uniform across the thickness as shown in Figure (7.30). This is in good agreement with results of Delorenzi and Shih, (1983), and

Nevalainen and Dodds (1995). In summary, the introduction of side-grooves establishes a more uniform stress field across the crack front.

7.7.2 Thin, deeply cracked bend bars (a/w=0.5, B/w=0.2).

Figure (7.31) shows the distribution of the mean stress across the thickness (along the crack front) as a function of dimensionless half thickness for a thin deeply cracked geometry (B/w=0.2, a/w=0.5) without side grooves. At the mid-plane (z/(B/2)=0) the mean stress remained close to the HRR solution at low deformation level and reduced towards the free surface at a faster rate than in the thicker geometry.

In geometries with side grooves, the overall trend in the mean stress was much more uniform across the majority of the thickness except at positions very close to the free surface (the V-groove) as shown in Figure (7.32). At the mid-plane, both geometries with and without side grooves had a similar magnitude of mean stress, but towards the free surface the grooved geometry retained higher stress levels than the non-grooved geometry.

Figure (7.33) shows that the plane strain conditions are maintained across the thickness up to a distance of 1.25mm (z/(B/2)=0.75) from the surface at low deformation level $c\sigma_0/J>326$ and that constraint reduced markedly as deformation increased. In side-grooved specimens the plane strain conditions maintained along the crack front as shown in Figure (7.34).

The J-integral along the crack front for this geometry with and without side grooves is shown in Figures (7.35) and (7.36). The J-integral rapidly reduced near the free surface in the non-side grooved geometry as shown in Figure (7.35). In contrast the side-grooved geometry retained the values of J-integral across the thickness resulting in a more uniform distribution as shown in Figure (7.36).

7.7.3 Very thin, deeply cracked bend bars (a/w=0.5, B/w=0.1).

The mean stress along the crack front in a very thin deeply cracked geometry B/w=0.1 is shown in Figure (7.37). The mean stress maintained high levels of constraint at low

deformation levels at the mid-plane but rapidly reduced through the thickness towards the free surface. The significant loss of constraint at the centre of the specimen appeared as deformation progressed beyond $c\sigma_0/J<183$. In contrast side-grooved geometries showed a more uniform mean stress and no significant increase in the stress value at the mid-plane. However, side grooves had a big effect on the mean stress at root of the groove as shown in Figure (7.38). Figures (7.39) and (7.40) show that the proximity to plane strain in both geometries, non-side grooved and side-grooved, respectively. At the mid-plane in both geometries plane strain conditions were maintained a value of 0.4 close to the Poisson's ratio value of 0.5 under small scale yielding condition, and reduced significantly at large scale yielding. The J-integral distribution in non-side grooved geometries decreased sharply from the maximum value at the mid-plane to the minimum at the free surface as shown in Figure (7.41). The calculations confirmed that the distribution of J-integral was uniform across the thickness in side-grooved geometries as shown in Figure (7.42).

7.7.4 Thick, shallow cracked bend bars (a/w=0.1, B/(w-a)=1).

Figure (7.43) shows the mean stress across the half thickness from the mid-plane to the free surface for a shallow crack geometry (a/w=0.1). It can be seen that in a non-grooved geometry the mean stress was below the HRR field and maintained the same level along the crack front except at a position close to the surface where the mean stress reached the plane stress value. For a side-grooved geometry, the distribution of the mean stress was constant across the thickness as shown in Figure (7.44). The plane strain parameter maintained a value of 0.4 only at low deformation level $c\sigma_0/J \geq 254$ over the majority of the crack front but reduced to zero at the free surface as shown in Figure (7.45). In side-grooved geometries plane strain constraint was maintained at 0.4 across the thickness even at the root of the V-notch (free surface) and reduced gradually as deformation increased as shown in Figure (7.46). It is interesting to observe that the J-integral maintained the maximum value along the majority of the crack front up to a distance of (z/(B/2)=0.75) from the mid-plane where the J-integral reduced, with slightly higher values at the quarter of the plane as shown in Figure (7.47). The J-integral again

increased in side grooved geometry across the thickness as shown in Figure (7.48) and the overall distribution was uniform.

7.8 Discussion

At the centre plane of deeply cracked geometries a/w=0.5, the out-of-plane effect was insignificant under small scale yielding conditions, but became very significant under large scale yielding for B/w≥0.2. Thinnest geometries (B/w=0.1) showed the out-of-plane effect became significant in contained yielding compared to thicker ones. In specimens with B/w=0.2, a/w=0.5 the out-of-plane effect became significant when the plastic zone size was approximately equal the thickness as shown in Figure (7.49). For shallow cracked geometries a/w=0.1, the out-of-plane effect at the centre plane was very small compared to deep cracks, and appeared when the plastic zone was twice the thickness. It may be concluded that as the in-plane constraint is the dominant effect in shallow cracks, and out-of-plane constraint loss is the important effect in deep cracks (a/w=0.5).

Figure (7.50) shows the relationship between the out-of-plane effect at the centre plane and the surface contraction. In thick geometries there was little effect of the out-of-plane constraint. The effect became dominant in thin geometries in conjunction with the increase in surface contraction, both of which were significant in full plasticity.

The average mean stresses at a distance of $2J/\sigma_0$ for side-grooved and non-side grooved thick and thin geometries are shown in Figures (7.51), (7.52) and (7.53). It is clear the average mean stress in side-grooved specimens was higher than in non-side grooved specimens. This may indicate that ductile tearing in side-grooved specimens may initiate at lower deformation levels than in non-side grooved specimens, as a result the fracture toughness J_{Ic} tends to be smaller in side grooved specimens.

The mean stress (σ_m/σ_0) at the free surface maintained at approximately 0.33 which is below plane stress value at high deformation levels in all specimens regardless of the specimen thickness. This observation occurred due to the radial stress (σ_{rr}) at (θ=0, $r\sigma_0/J$=2) decreased significantly and became close to zero at high deformation levels beside the out-of-plane stress which was also zero at the free surface. This is similar to a

uni-axial stress state when both transverse stresses are zero and the axial stress equal to yield stress, then $\sigma_m=(1/3)\sigma_0$.

7.9 Conclusion

It may be concluded that the out-of-plane effect at the mid-plane in deeply cracked specimens (a/w=0.5) was pronounced only at high deformation levels in geometries with thickness ratios of B/w≥0.2, while constraint loss occurred at lower deformation levels in very thin geometries B/w=0.1. The out-of-plane effect became significant as the plastic zone became large compared to the specimen dimensions. For example, in geometries with B/w=0.2 the Op-term was significant when the plastic zone size reached approximately the specimen thickness. The constraint levels in deeply cracked specimens showed a significant dependence on out-of-plane effects and thin-deeply specimens showed a more severe loss of out-of-plane constraint than shallow cracked specimens. The out-of-plane effect varied significantly with the distance (r) from the crack tip as the specimen became thinner, and was more pronounced in non-hardening materials. The engineering implications of this analysis can be discussed in terms of a failure assessment diagram since the loss of constraint due to thickness effect increases the margin of safety of the defect components, as discussed in chapter (8).

It was also shown that the surface contraction increased with deformation, with largest contraction (Δ/B) being observed in thin geometries B/w=0.1, and less for thick geometries B/w=0.5. Deep geometries (a/w=0.5) with B/w≤0.2 contracted significantly when the plastic zone size equal to the thickness. In thick geometries (a/w=0.5, B/w=0.5) the contraction became significant when the plastic zone radius reached around half the thickness. The contraction can be related to the proximity to plane strain conditions.

The comparison between side-grooved and non-side grooved specimens revealed that a non-uniform stress field and J-integral occur along the crack front in non-side grooved specimens. The variation along the crack front increased as the thickness decreased. In contrast, more uniform mean stress and J-integral distributions occurred across the thickness of side-grooved specimens, and plane strain conditions were also maintained across the crack front even in relatively thin specimens B/w=0.2.

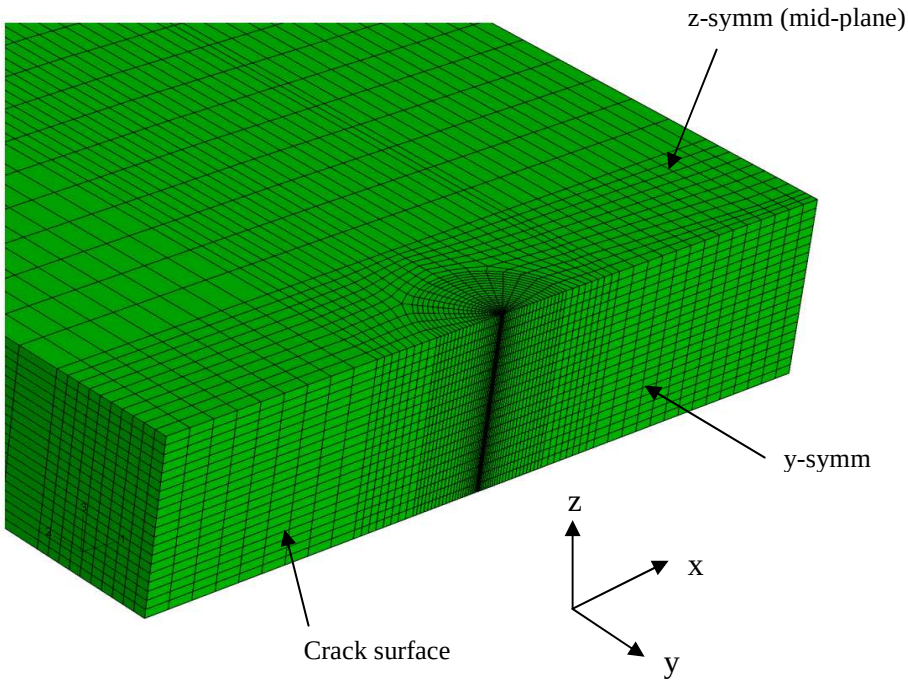

Figure 7.1a: Finite element model for an edge cracked bend bar.

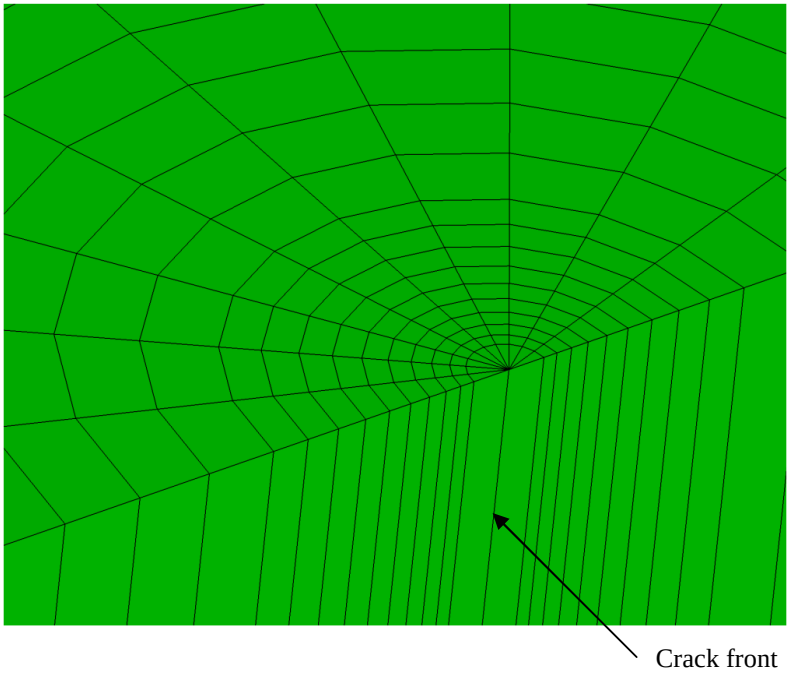

Figure 7.1b: Close-up of mesh at the crack tip.

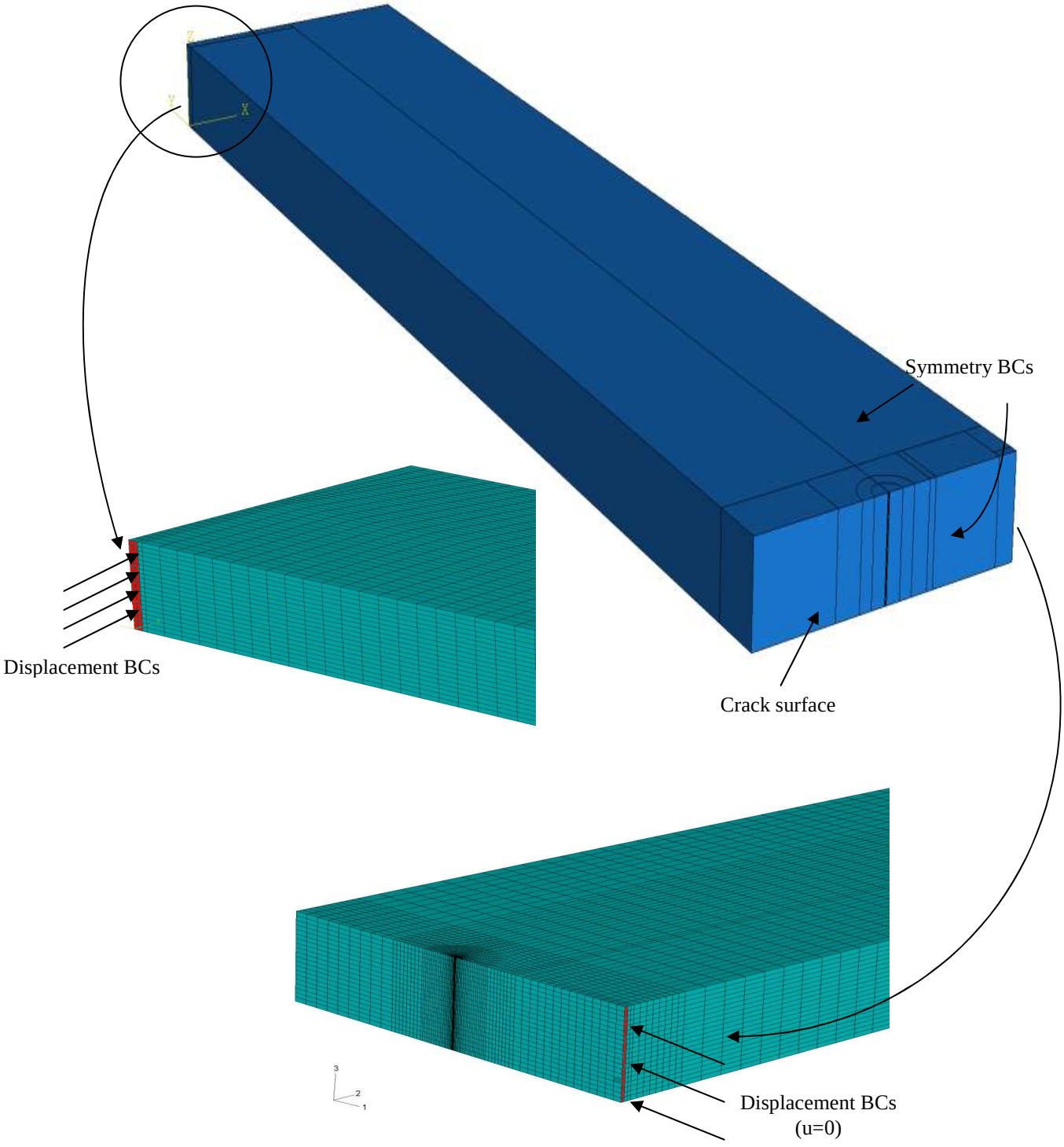

Figure 7.2: Illustration of the SECB model and boundary conditions for elastic-plastic analysis.

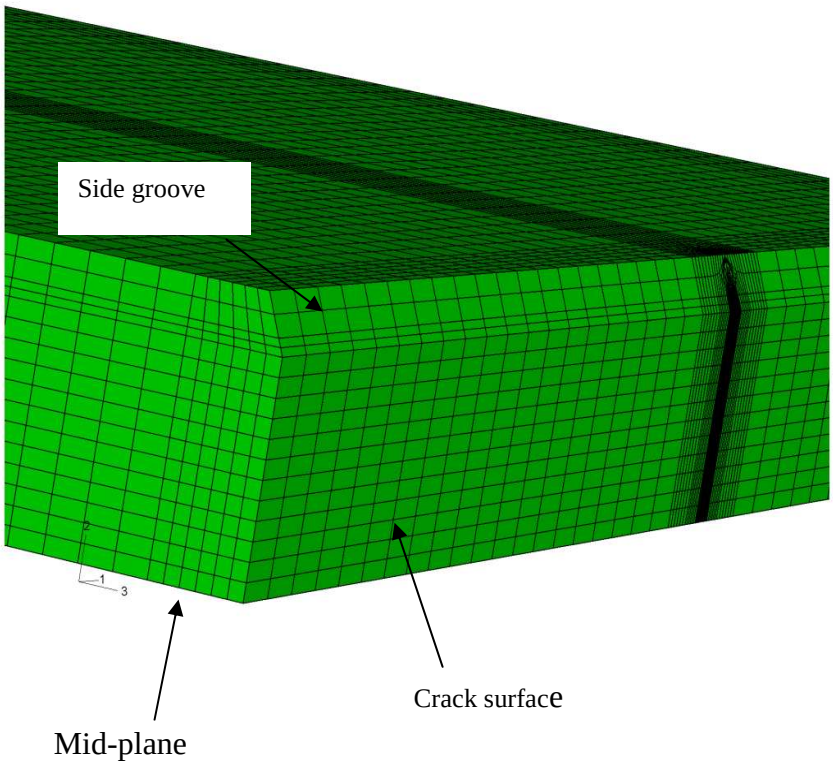

Figure 7.3: Finite element model for a side grooved specimen.

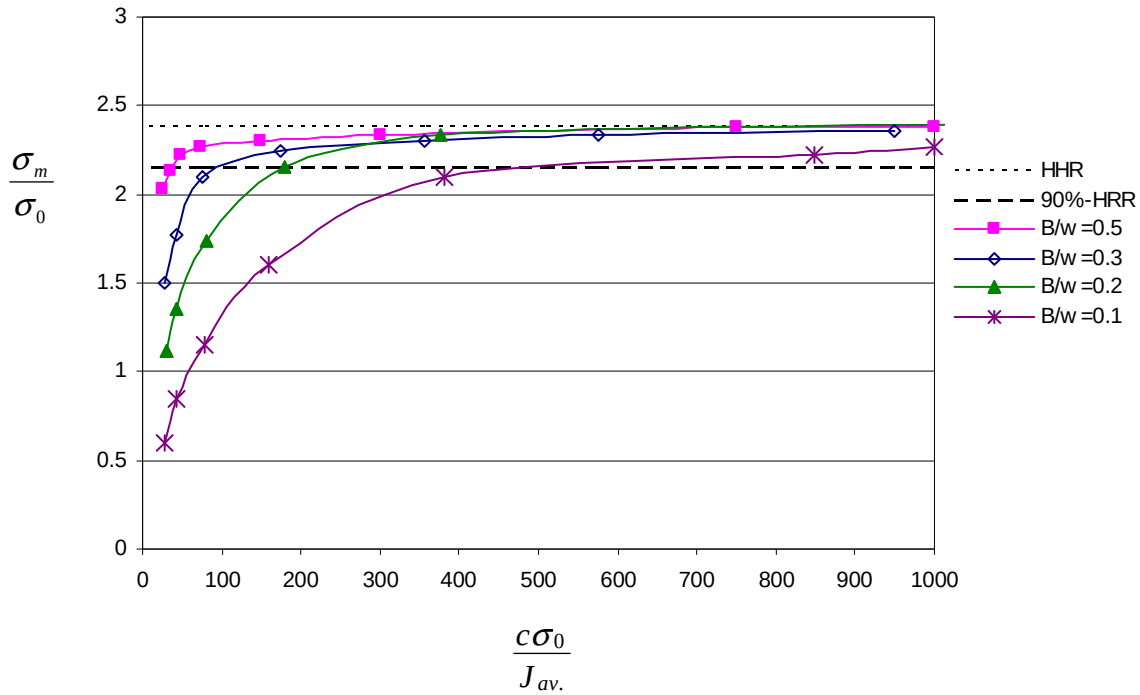

Figure 7.4: The mean stress at a distance $2J/\sigma_0$ at the mid-plane for a deeply SECB-3D bar (a/w=0.5, B/w=0.5, 0.3, 0.2 and 0.1), c is the uncracked ligament.

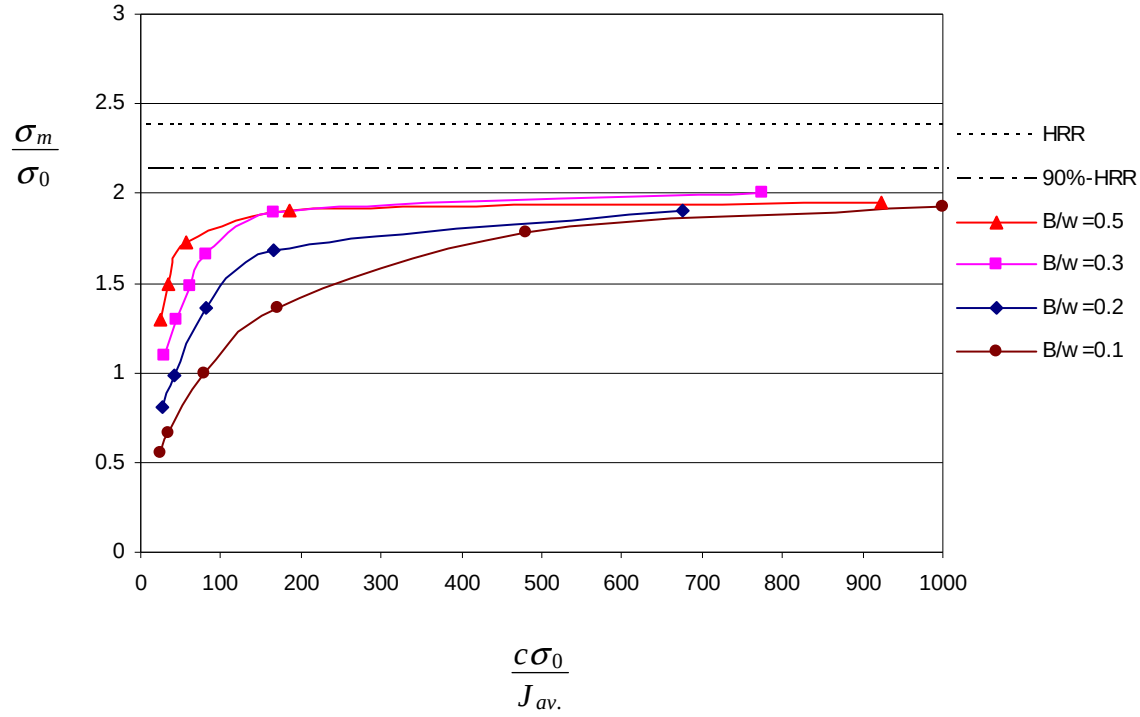

Figure 7.5: The mean stress at a distance $2J/\sigma_0$ at the mid-plane for a shallow SECB-3D bar (a/w=0.2, B/w=0.5, 0.3, 0.2 and 0.1), c is the uncracked ligament.

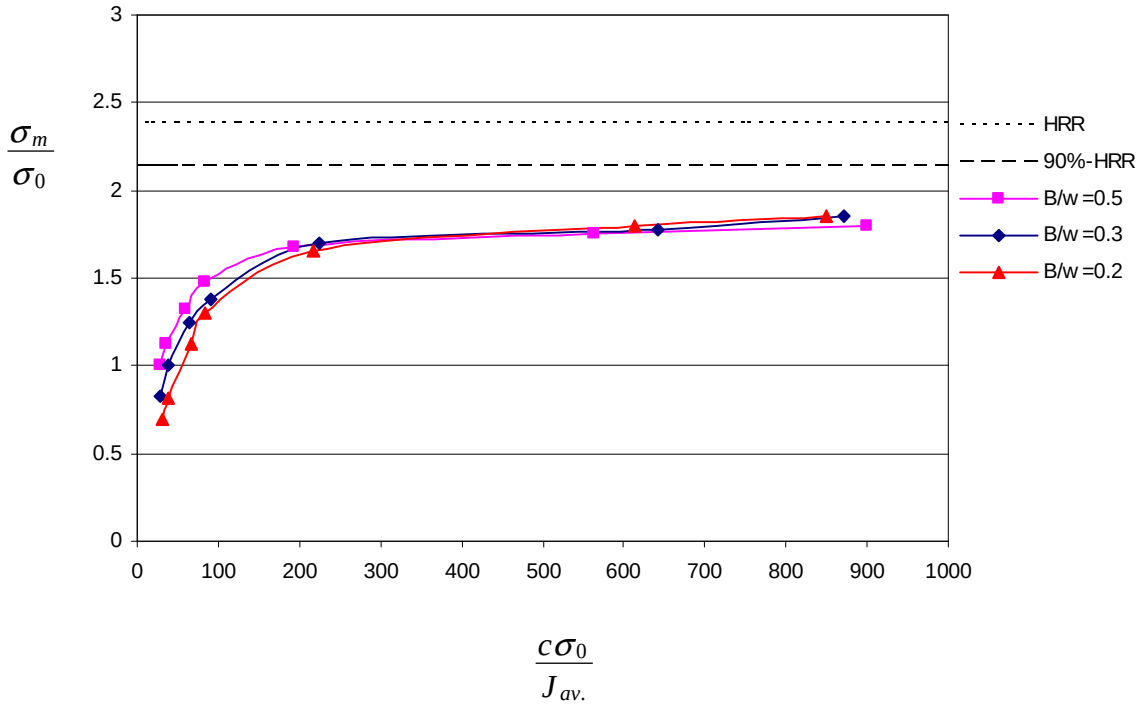

Figure 7.6: The mean stress at a distance $2J/\sigma_0$ at the mid-plane for a shallow SECB-3D bar (a/w=0.1, B/w=0.5, 0.3, 0.2 and 0.1), c is the uncracked ligament.

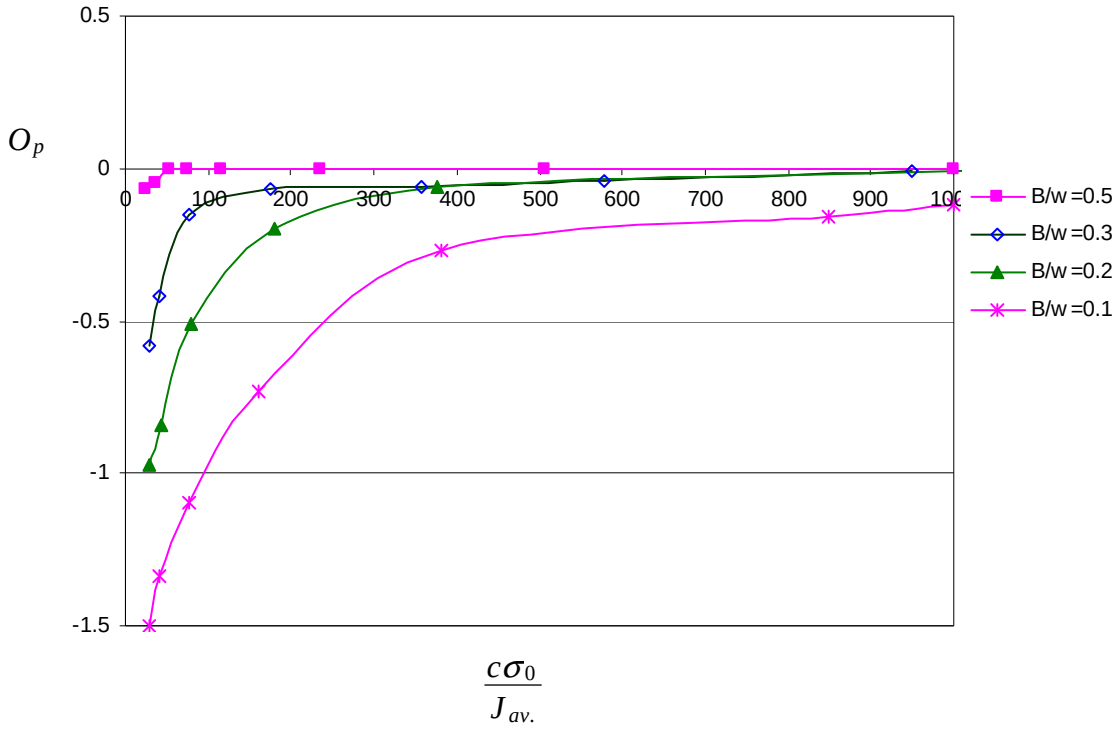

Figure 7.7: Out-of-plane effect at a distance $2J/\sigma_0$ at the mid-plane for deeply cracked geometries with a/w=0.5 as a function of thickness ratio, B/*w*, c is the uncracked ligament.

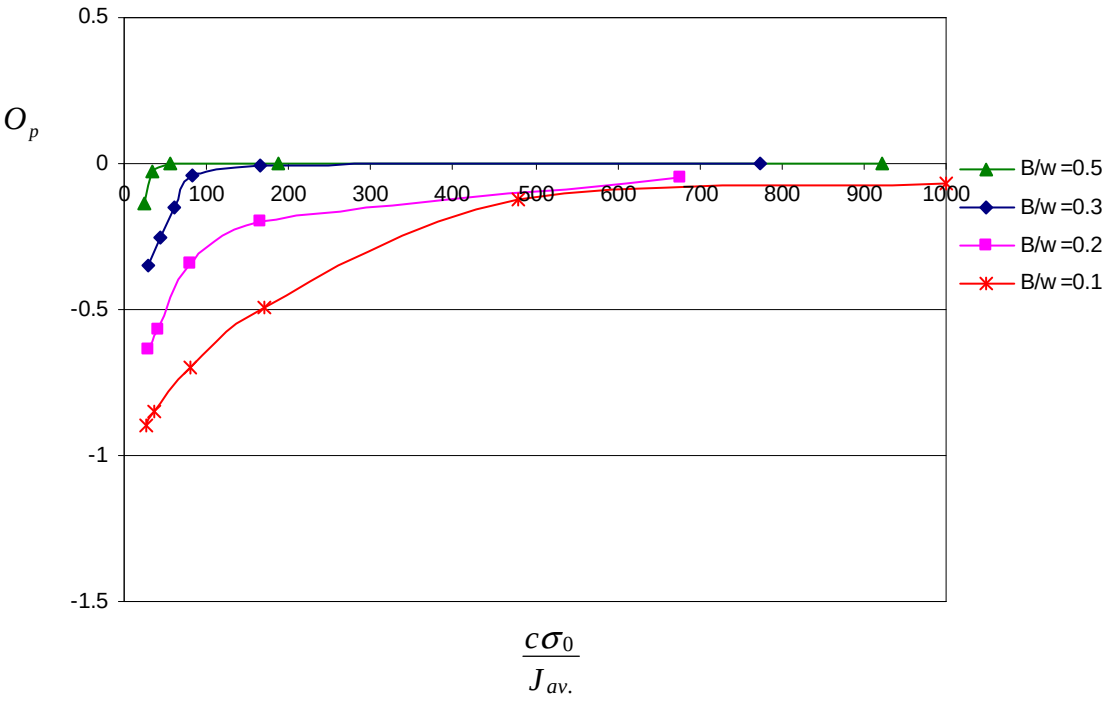

Figure 7.8: Out-of-plane effect at a distance $2J/\sigma_0$ at the mid-plane for cracked geometries with a/w=0.2 as a function of thickness ratio, B/*w*, 0.1, 0.2, 0.3, 0.5, c is the uncracked ligament.

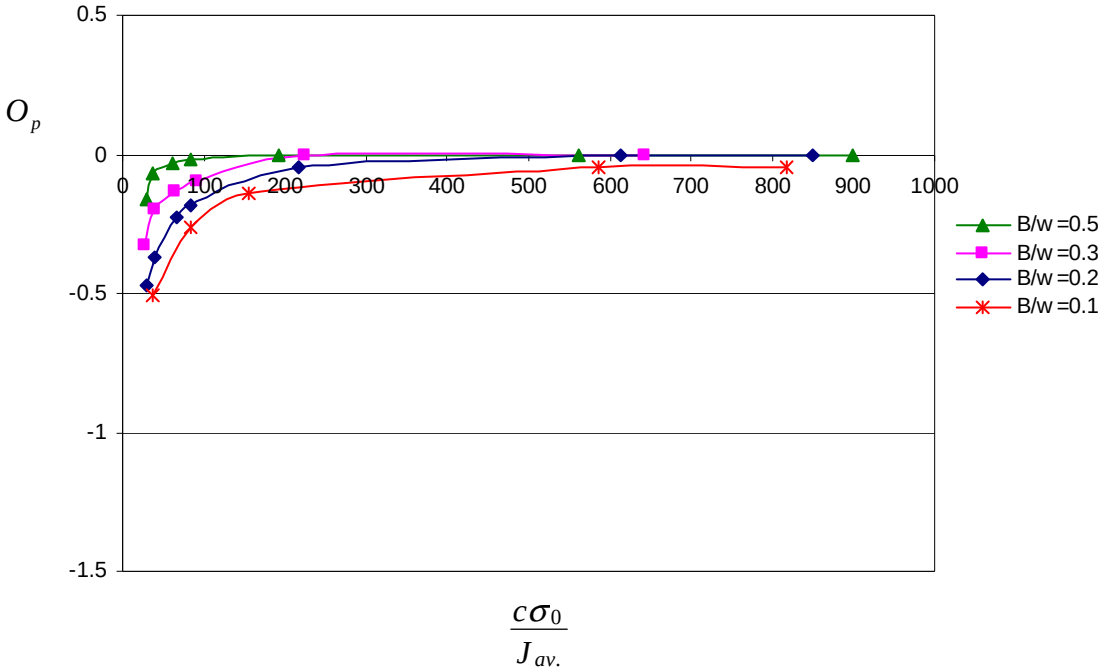

Figure 7.9: Out-of-plane effect at a distance $2J/\sigma_0$ at the mid-plane for shallow cracked geometries with a/w=0.1 as a function of thickness ratio, B/*w*, c is the uncracked ligament.

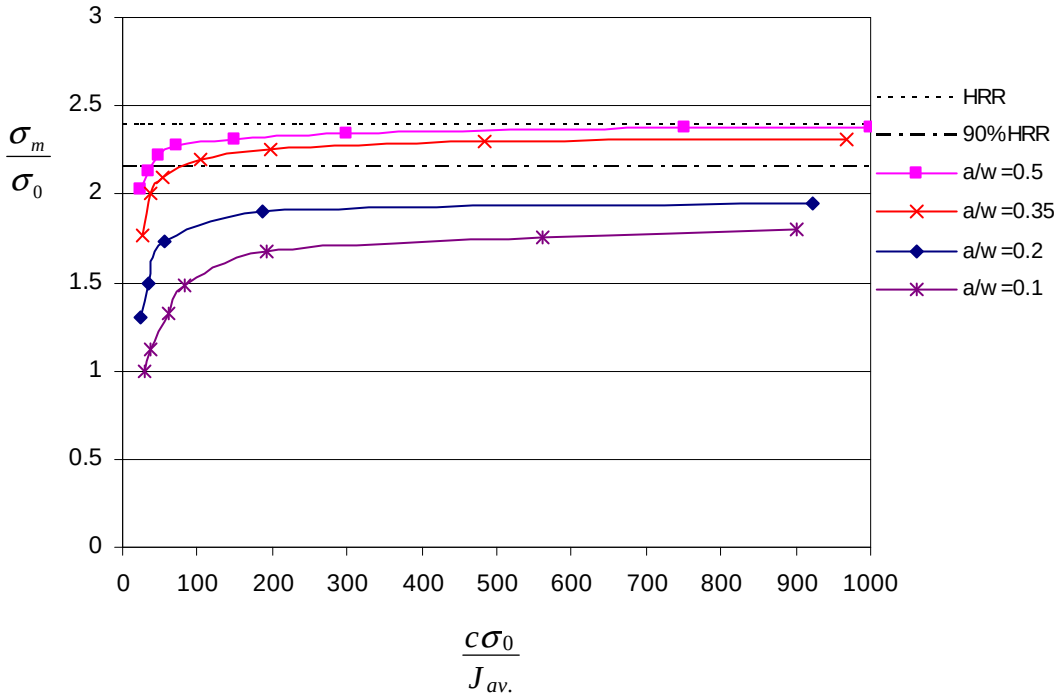

Figure 7.10: The mean stress at a distance $2J/\sigma_0$ at the mid-plane for SECB-3D bars (B/w=0.5, a/w=0.1, 0.2, 0.35 and 0.5) , c is the uncracked ligament.

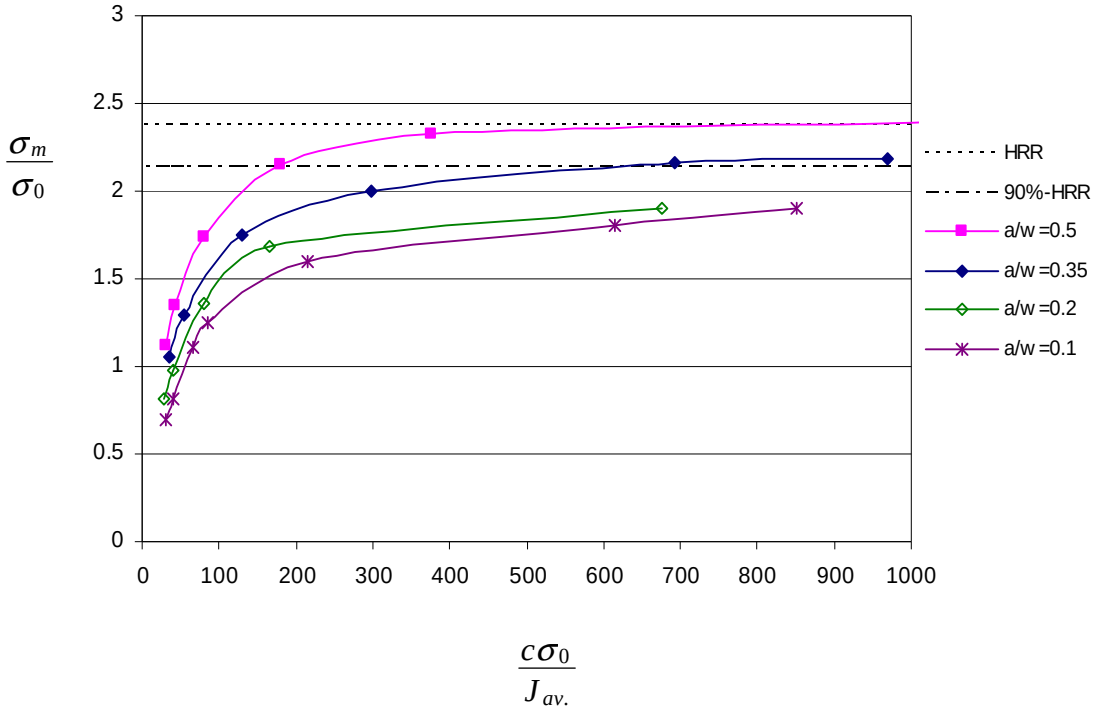

Figure 7.11: The mean stress at a distance $2J/\sigma_0$ at the mid-plane for SECB-3D bars (B/w=0.2, a/w=0.1, 0.2, 0.35 and 0.5), c is the uncracked ligament.

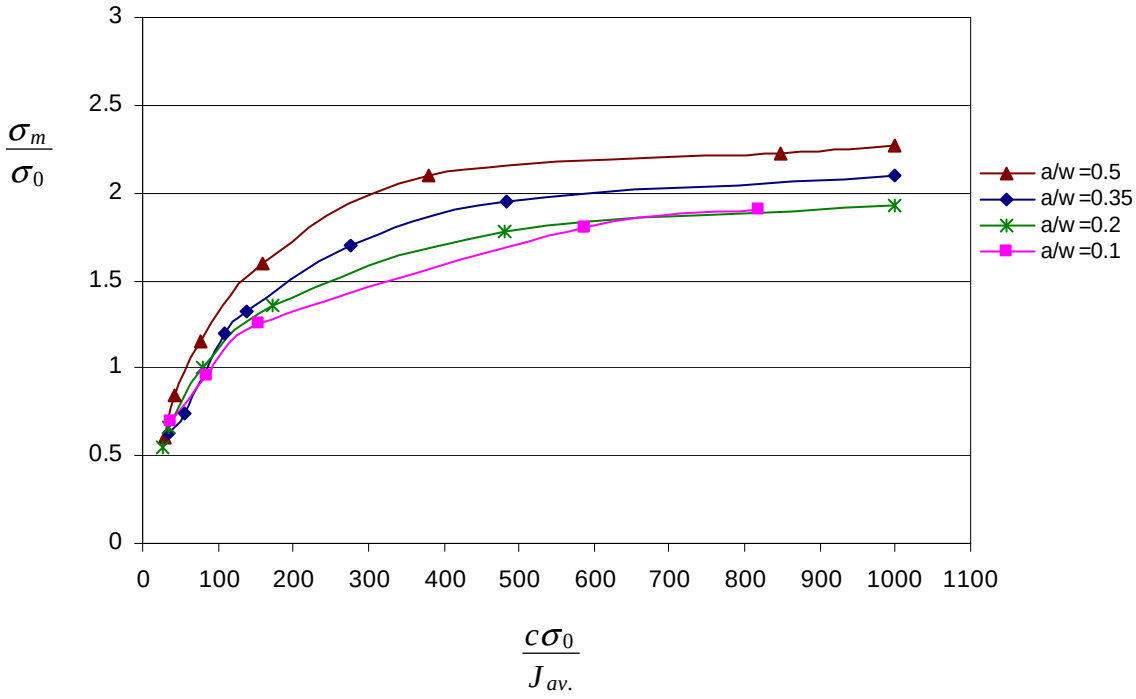

Figure 7.12: The mean stress at a distance $2J/\sigma_0$ at the mid-plane for SECB-3D bars (B/w=0.1, a/w=0.1, 0.2, 0.35 and 0.5), c is the uncracked ligament.

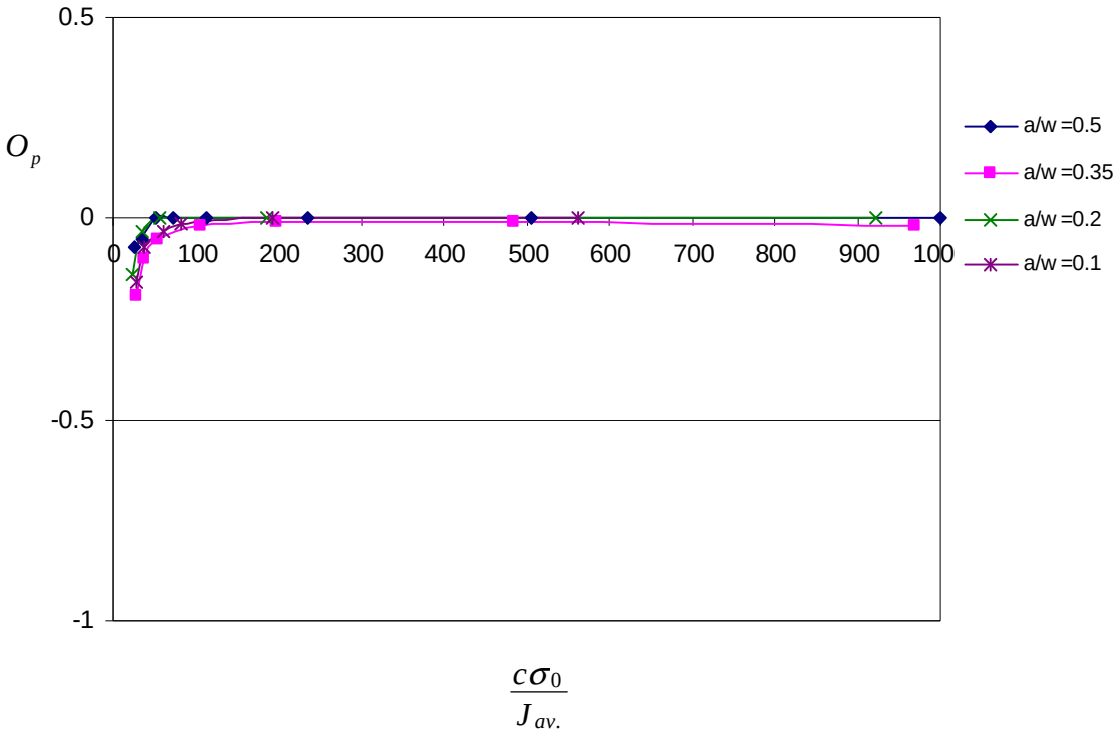

Figure 7.13: Out-of-plane effect at a distance $2J/\sigma_0$ at the mid-plane for geometries with *B/w*=0.5 as a function of crack depth ratio, a/w, c is the uncracked ligament.

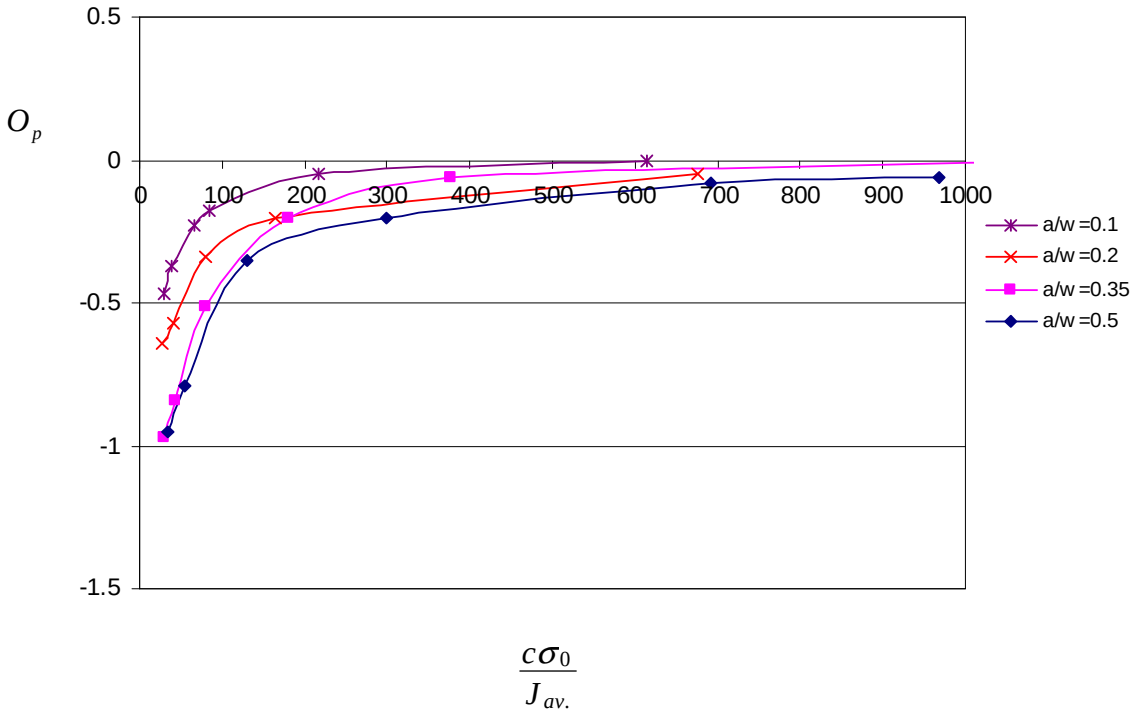

Figure 7.14: Out-of-plane effect at a distance $2J/\sigma_0$ at the mid-plane for geometries with B/*w*=0.2 as a function of crack depth ratio, a/w, c is the uncracked ligament.

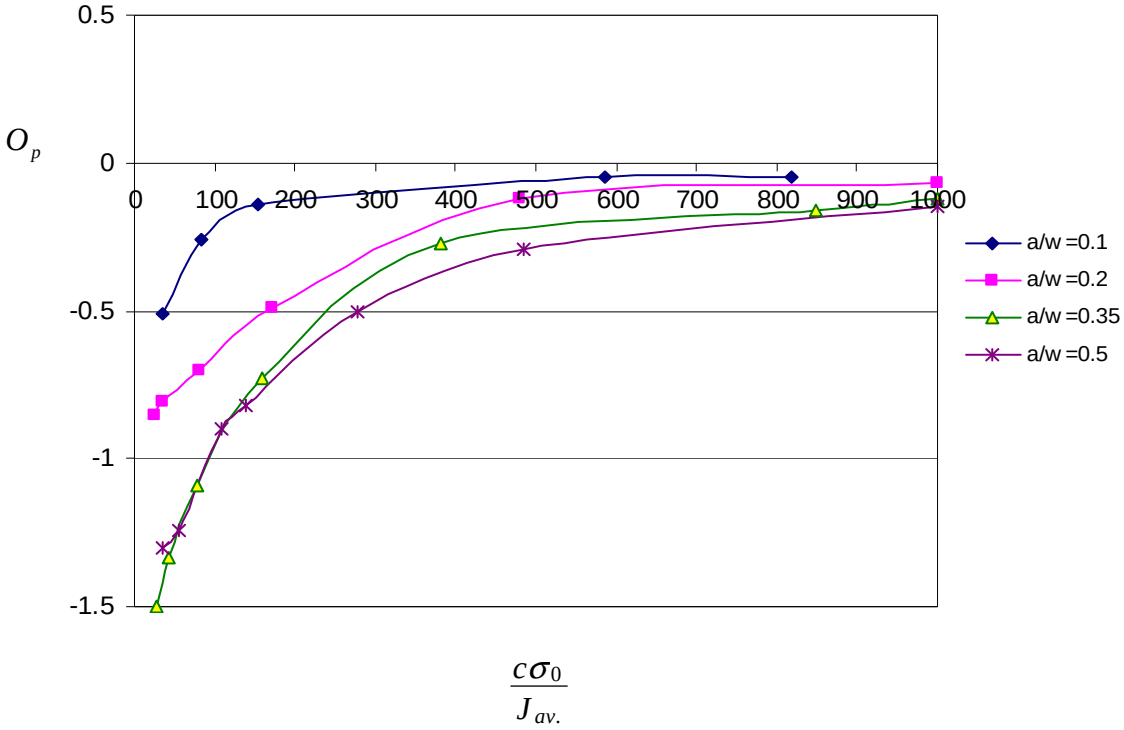

Figure 7.15: Out-of-plane effect at a distance $2J/\sigma_0$ at the mid-plane for geometries with B/*w*=0.1 as a function of crack depth ratio, a/w, c is the uncracked ligament.

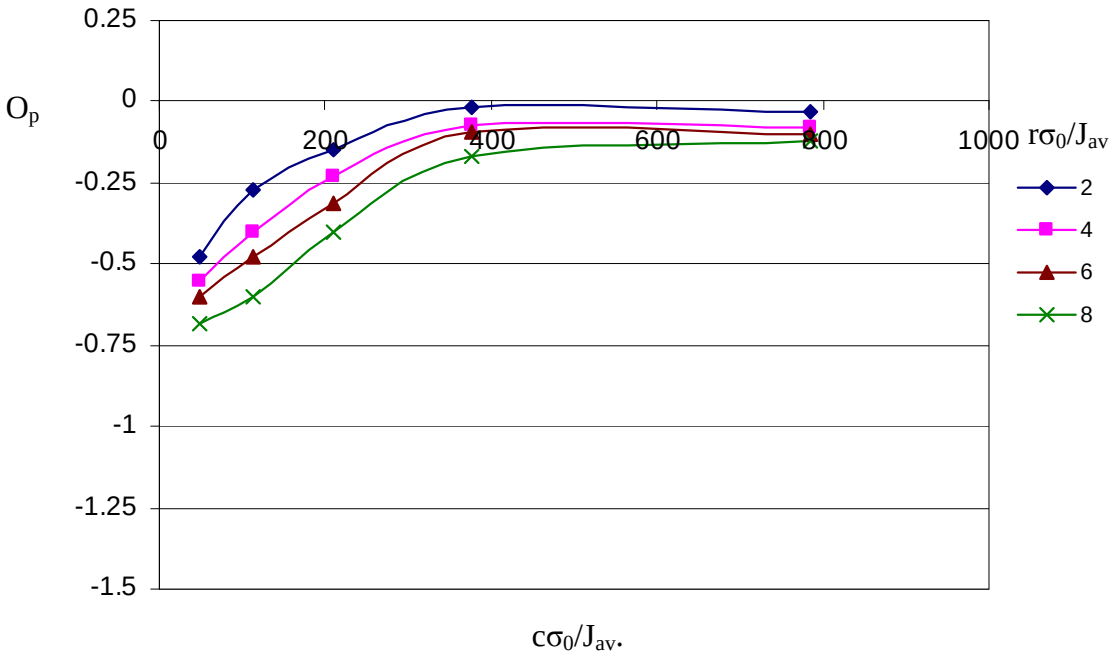

Figure 7.16: The effect of out-of-plane at the mid-plane in a deeply SECB bar a/w=0.5 and B/w=0.2 at distance $r\sigma_0/J$= 2, 4, 6 and 8, in non-hardening materials, c is the uncracked ligament.

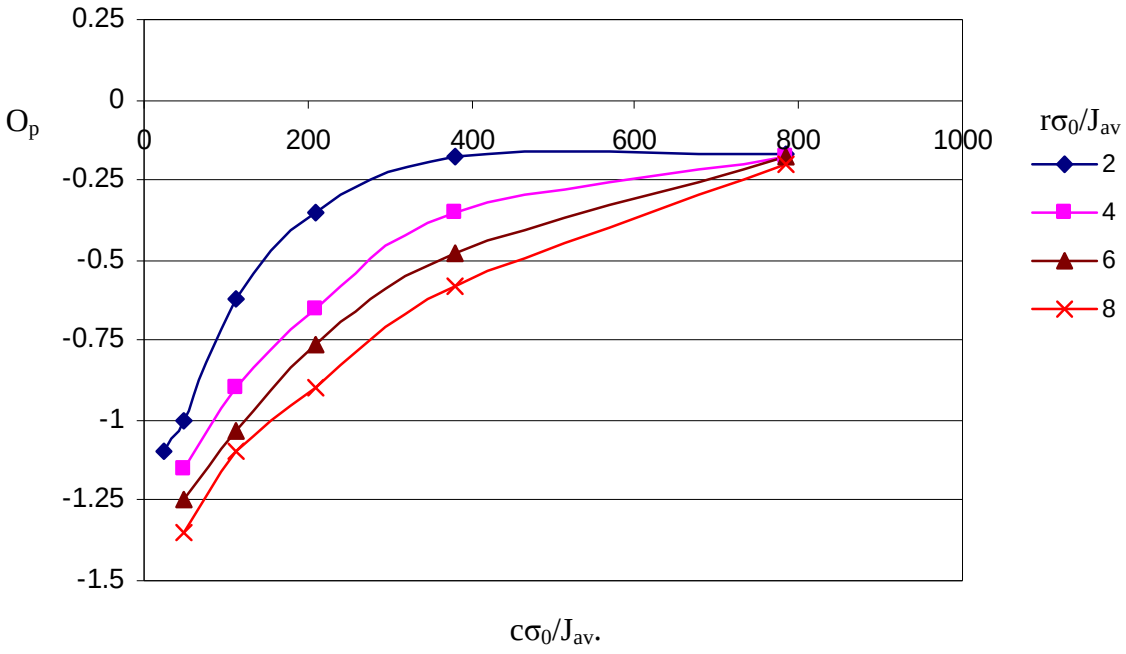

Figure 7.17: The effect of out-of-plane at the mid-plane in a deeply SECB bar a/w=0.5 and B/w=0.1 at distance $r\sigma_0/J$= 2, 4, 6 and 8, in non-hardening materials, c is the uncracked ligament.

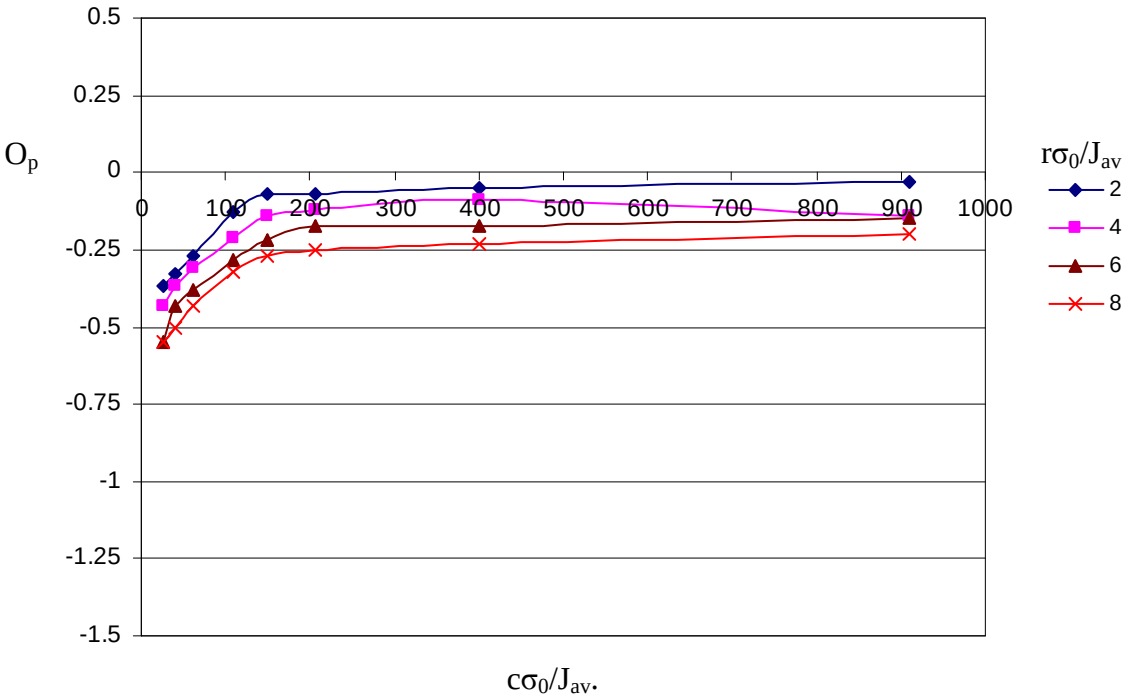

Figure 7.18: The effect of out-of-plane at the mid-plane in a deeply SECB bar a/w=0.5 and B/w=0.2 at distance $r\sigma_0/J$= 2, 4, 6 and 8, in hardening materials n=10, c is the uncracked ligament.

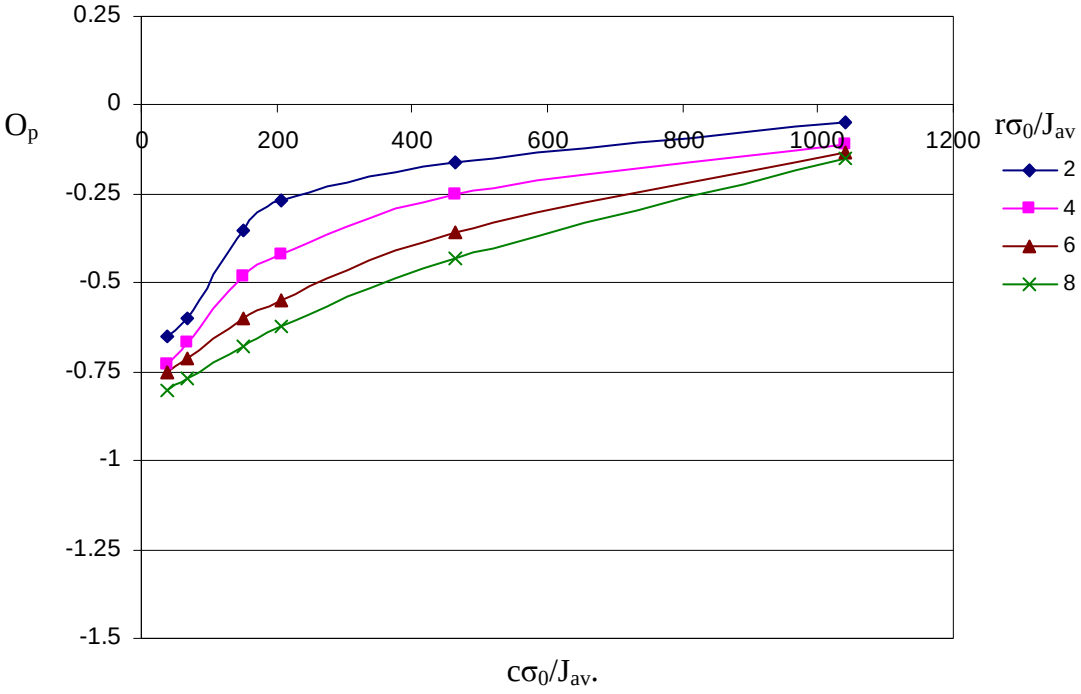

Figure 7.19: The effect of out-of-plane at the mid-plane in a deeply SECB bar a/w=0.5 and B/w=0.1 at distance $r\sigma_0/J$= 2, 4, 6 and 8, in hardening materials n=10, c is the uncracked ligament.

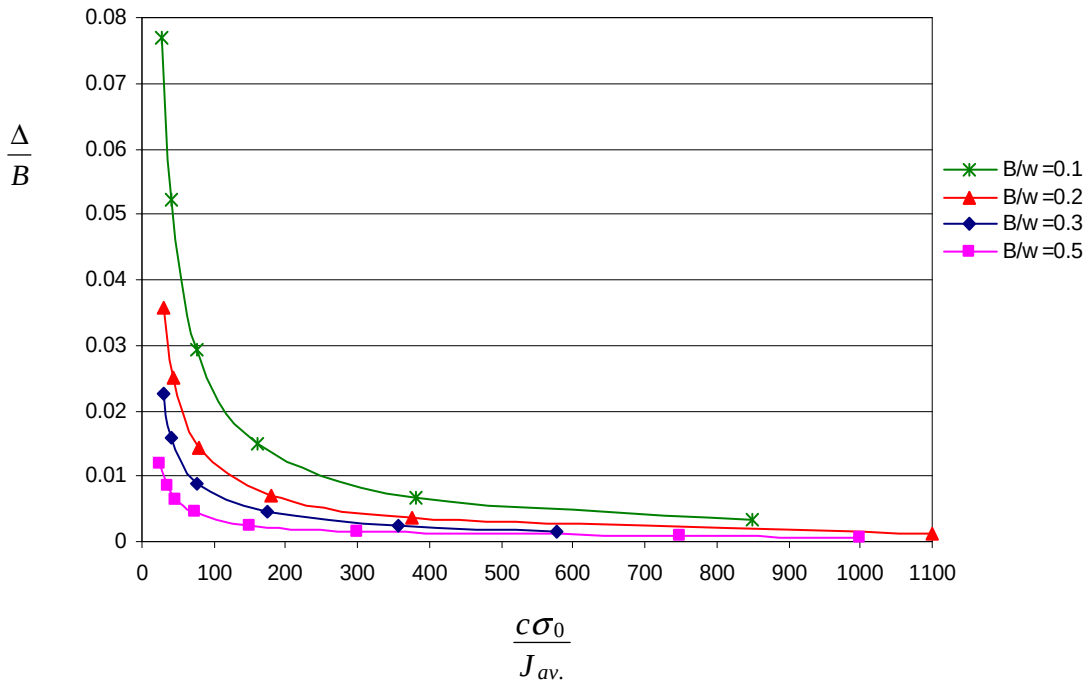

Figure 7.20: Out-of-plane contraction as a function of deformation level for deeply cracked specimens a/w=0.5 for different thickness, c is the uncracked ligament.

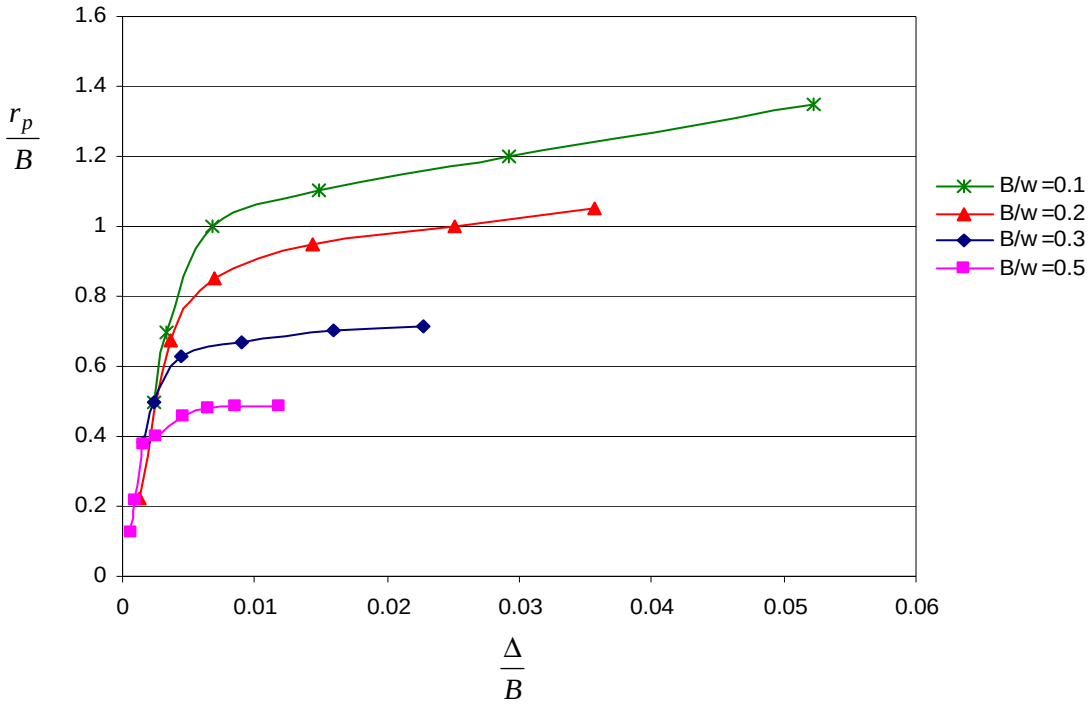

Figure 7.21: The size of the plastic zone as a function of out-of-plane contraction for deeply cracked specimens a/w=0.5 for different thickness.

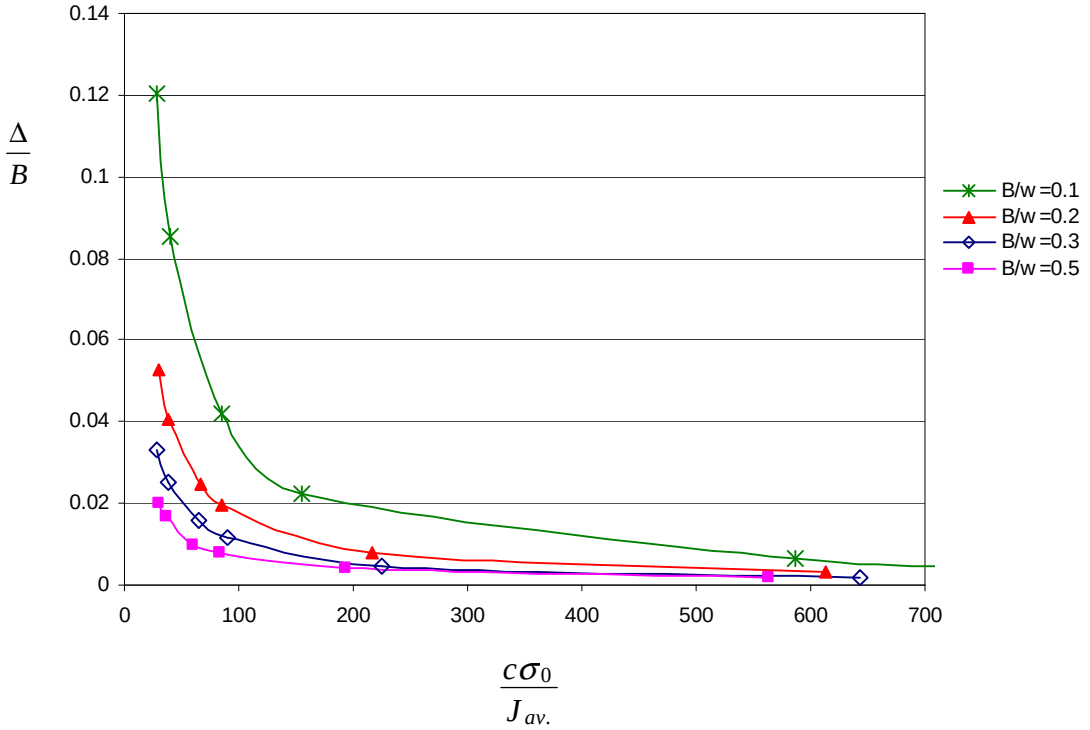

Figure 7.22: Out-of-plane contraction as a function of deformation level for shallow cracked specimens a/w=0.1 for different thickness, c is the uncracked ligament.

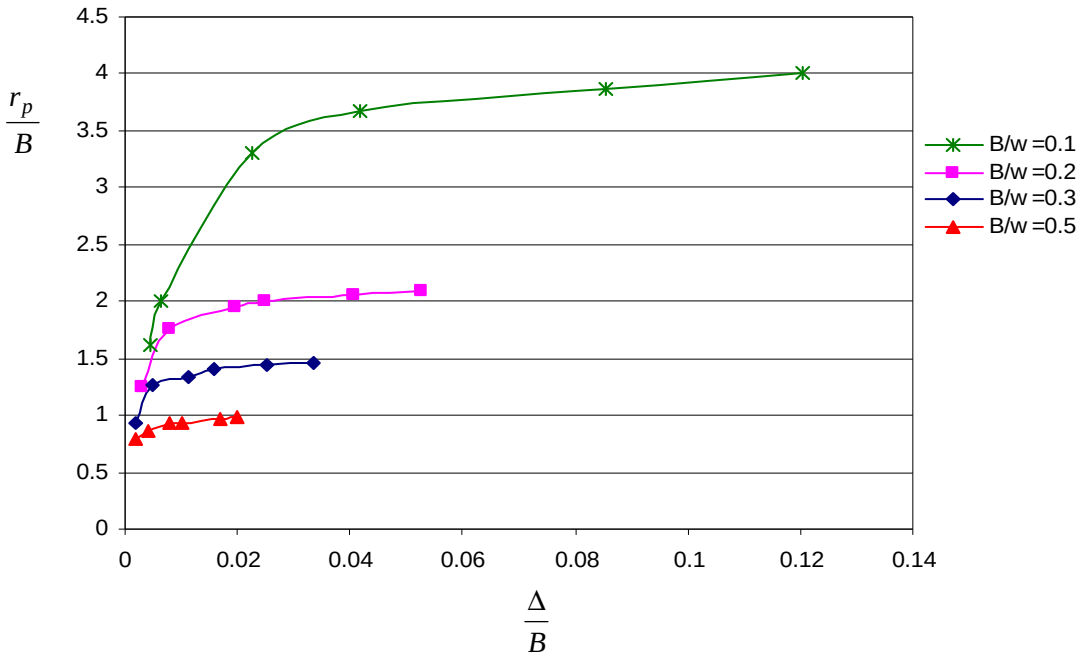

Figure 7.23: The size of the plastic zone as a function of out-of-plane contraction for shallow cracked specimens a/w=0.1 for different thickness.

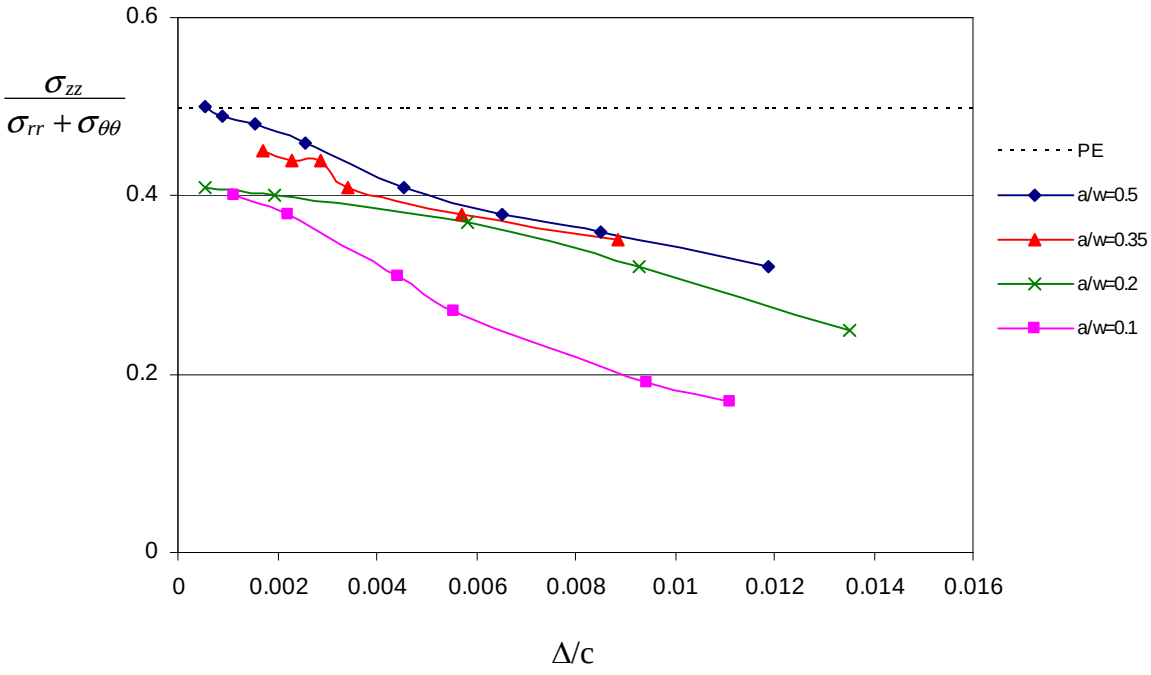

Figure 7.24: The proximity to plane strain at a distance $2J/\sigma_0$ at the centre plane as a function of contraction for thick geometries B/w=0.5 with different crack depths in 3-D SECB, (PE is the plane strain value of 0.5), c is the uncracked ligament.

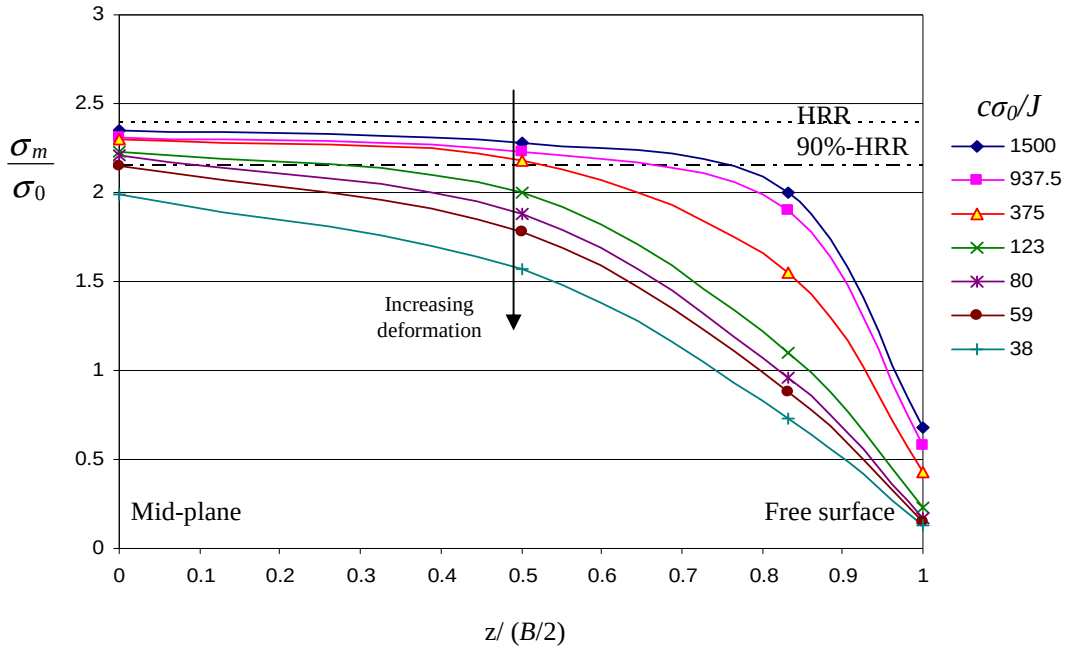

Figure 7.25: The mean stress at a distance $2J/\sigma_0$ along the crack front from the mid-plane to the free surface for non-grooved specimens (a/w=0.5, B/w=0.5), c is the uncracked ligament.

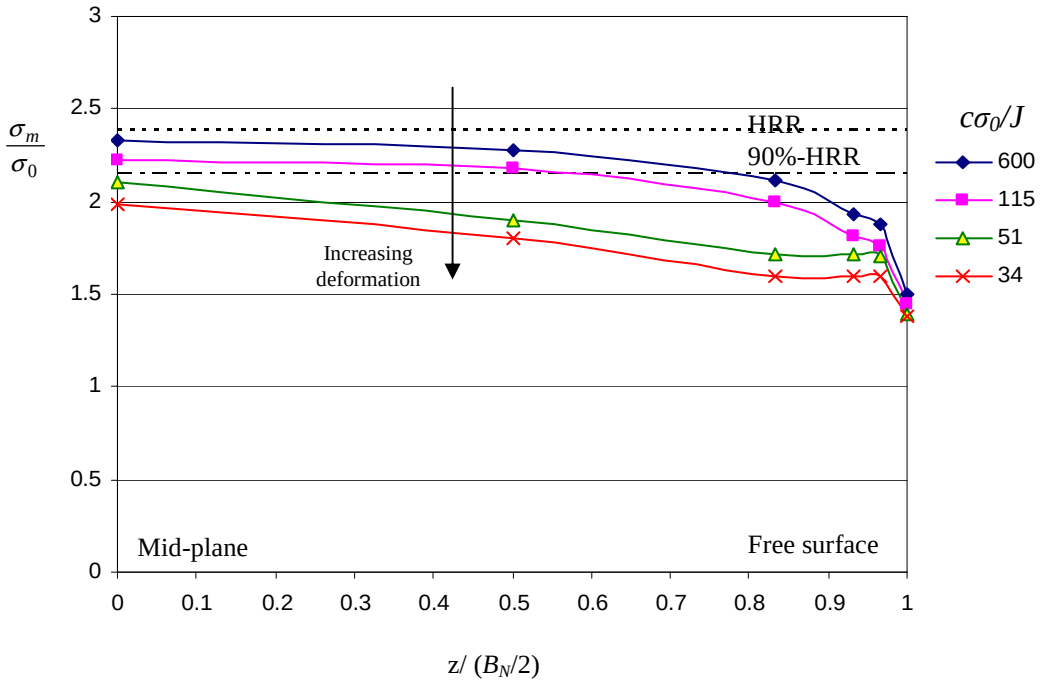

Figure 7.26: The mean stress at a distance $2J/\sigma_0$ along the crack front from the mid-plane to the free surface for side-grooved specimens, (a/w=0.5, B/w=0.5), c is the uncracked ligament.

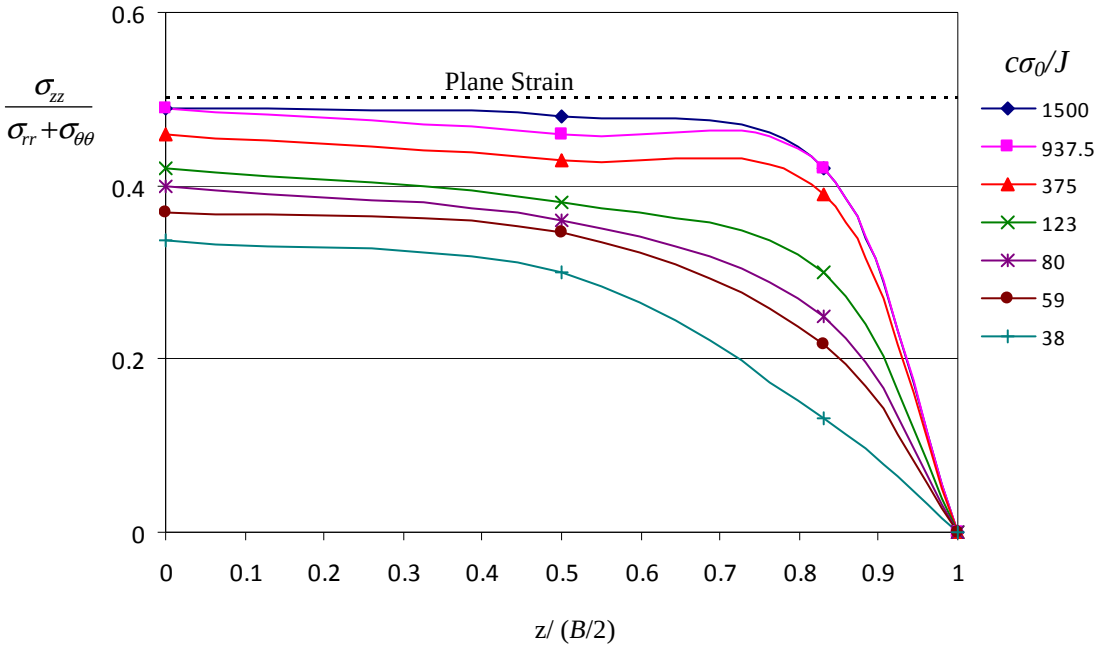

Figure 7.27: The proximity to plane strain at a distance $2J/\sigma_0$ across the thickness from the mid-plane to the free surface for non-grooved specimens, (a/w=0.5, B/w=0.5), c is the uncracked ligament.

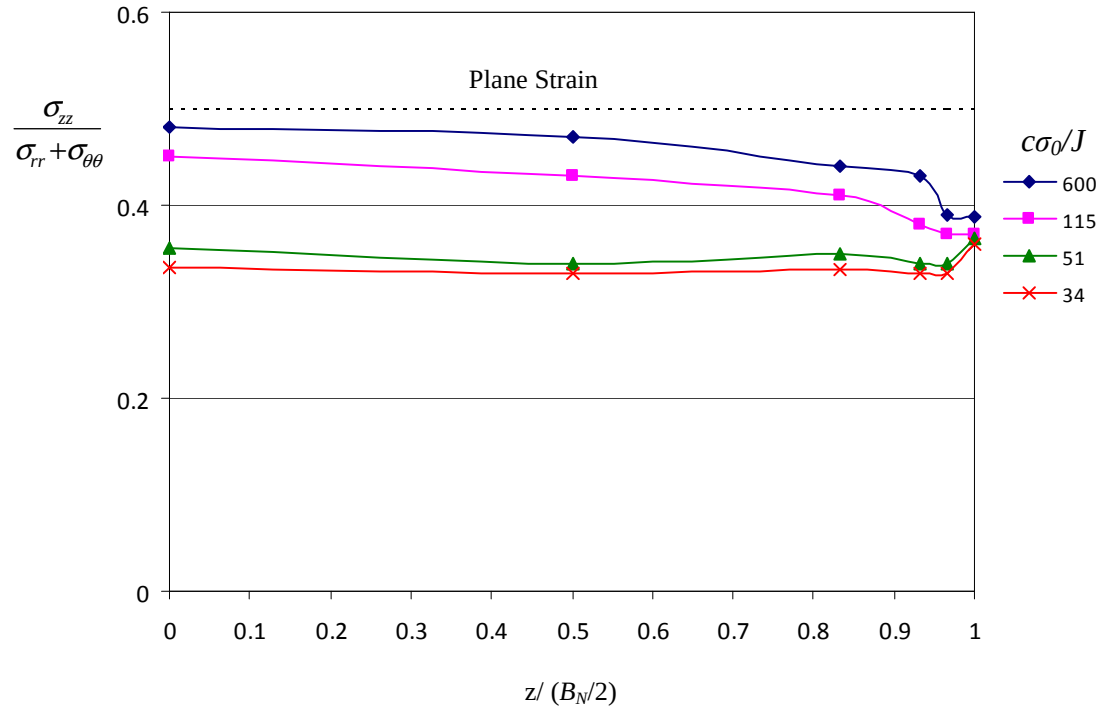

Figure 7.28: The proximity to plane strain at a distance $2J/\sigma_0$ across the thickness from the mid-plane to the free surface for side-grooved specimens, (a/w=0.5, B/w=0.5), c is the uncracked ligament.

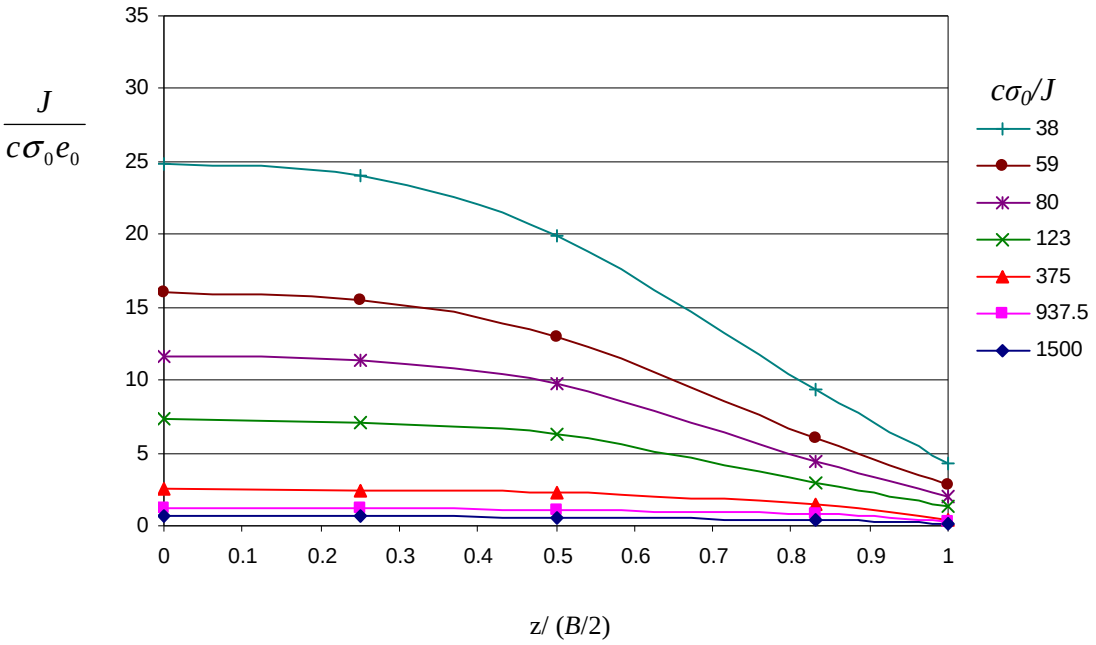

Figure 7.29: The non-dimensional J-integral along the crack front from the mid-plane z/(*B/2)*=0 to the free surface for non-grooved specimens (a/w=0.5, B/w=0.5), c is the uncracked ligament.

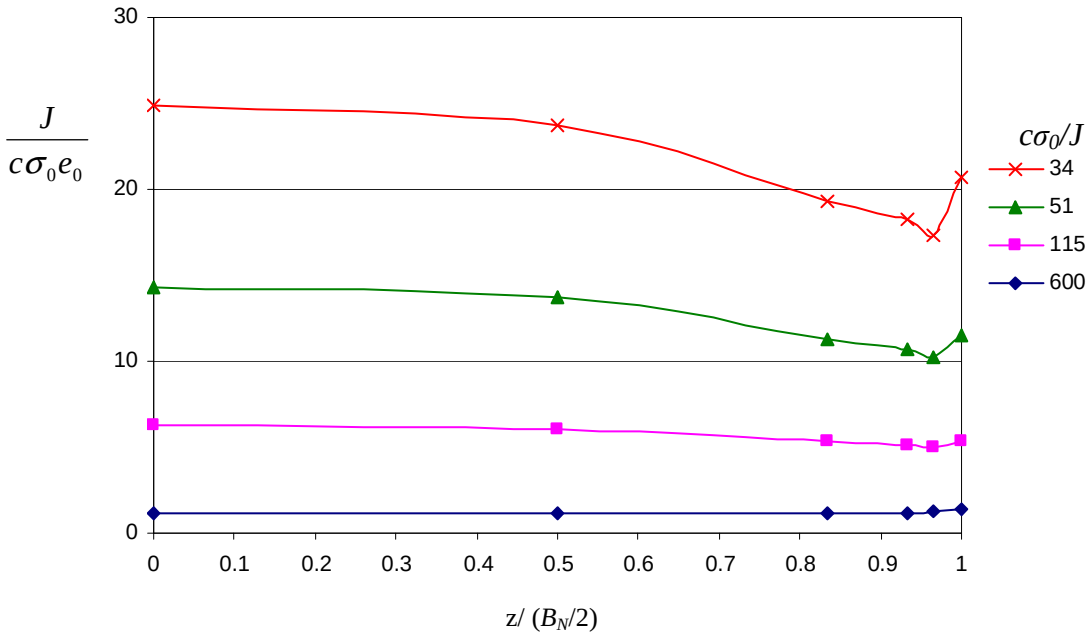

Figure 7.30: The non-dimensional J-integral along the crack front from the mid-plane z/(B_N/*2)*=0 to the free surface for side-grooved specimens, (a/w=0.5, B/w=0.5), c is the uncracked ligament.

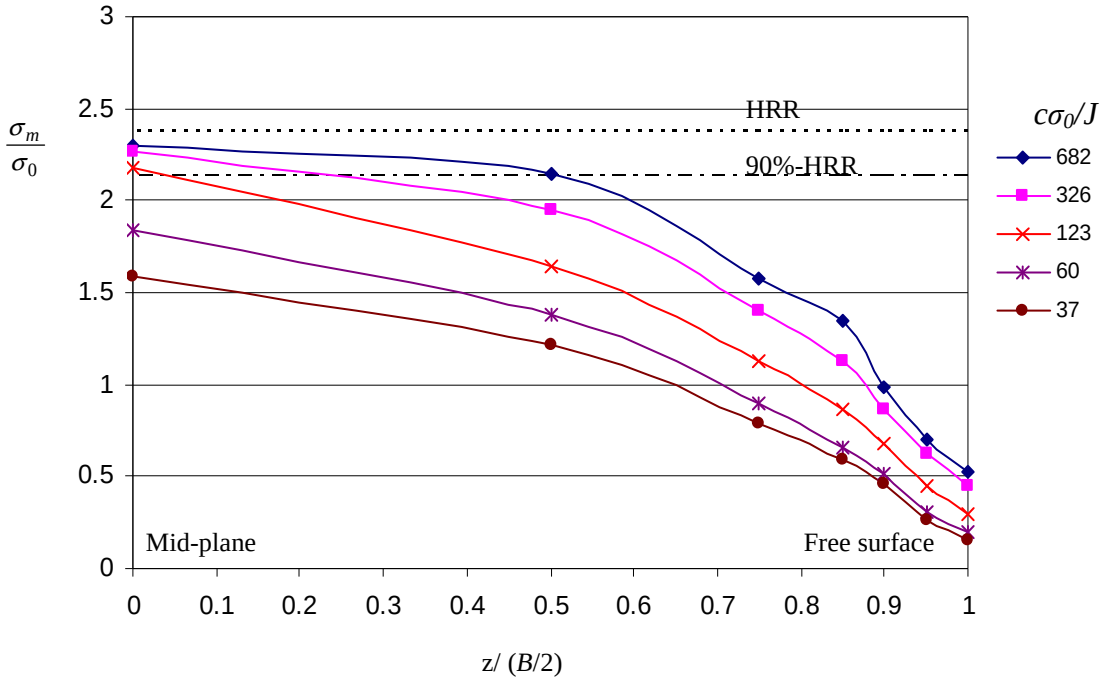

Figure 7.31: The mean stress at a distance $2J/\sigma_0$ along the crack front from the mid-plane to the free surface for non-grooved specimens (a/w=0.5, B/w=0.2), c is the uncracked ligament.

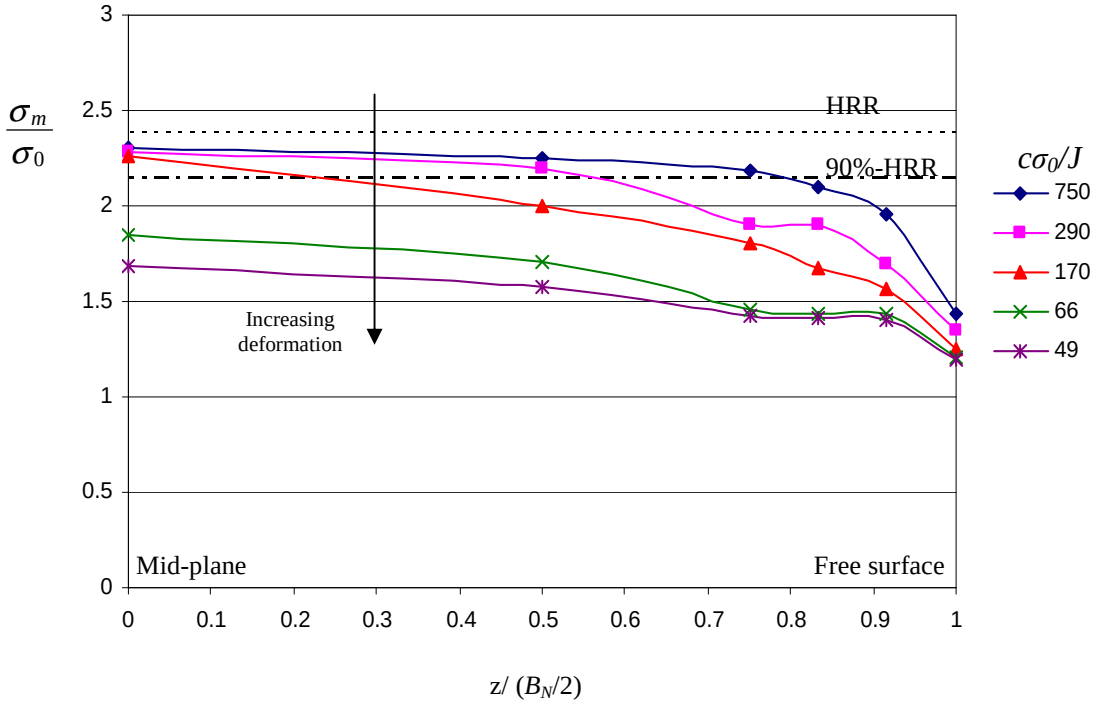

Figure 7.32: The mean stress at a distance $2J/\sigma_0$ along the crack front from the mid-plane to the free surface for side-grooved specimens (a/w=0.5, B/w=0.2), c is the uncracked ligament.

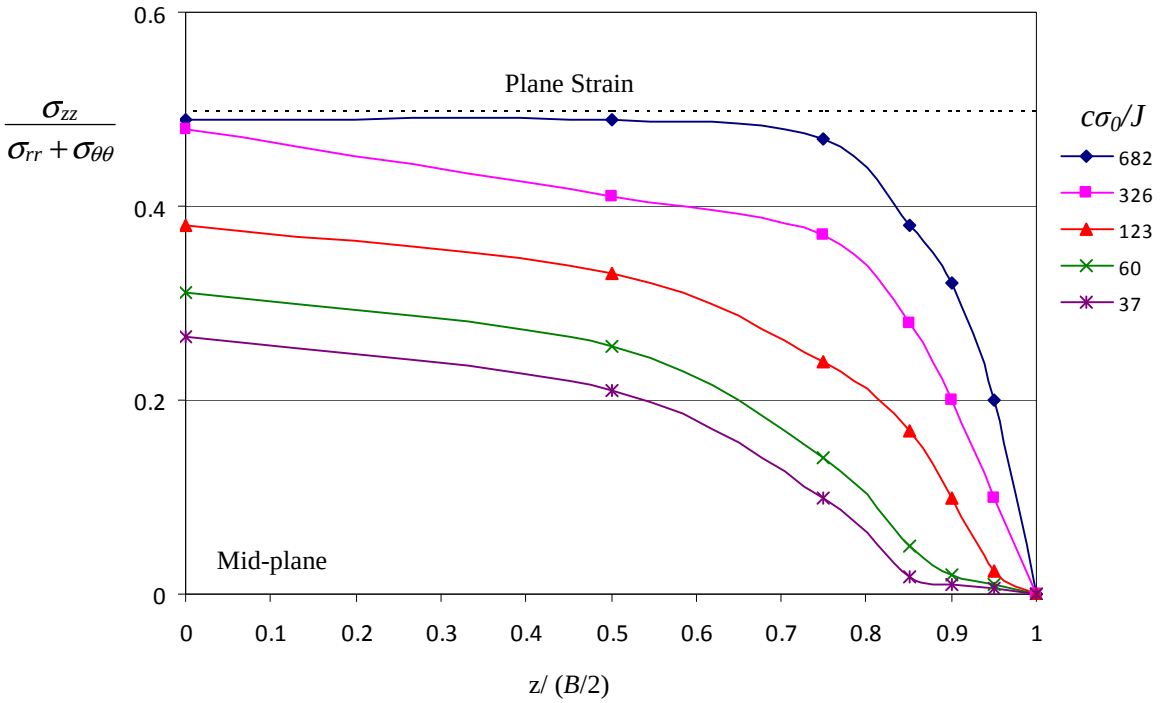

Figure 7.33: The proximity to plane strain at a distance $2J/\sigma_0$ across the thickness from the mid-plane to the free surface for non-grooved specimens (a/w=0.5, B/w=0.2), c is the uncracked ligament.

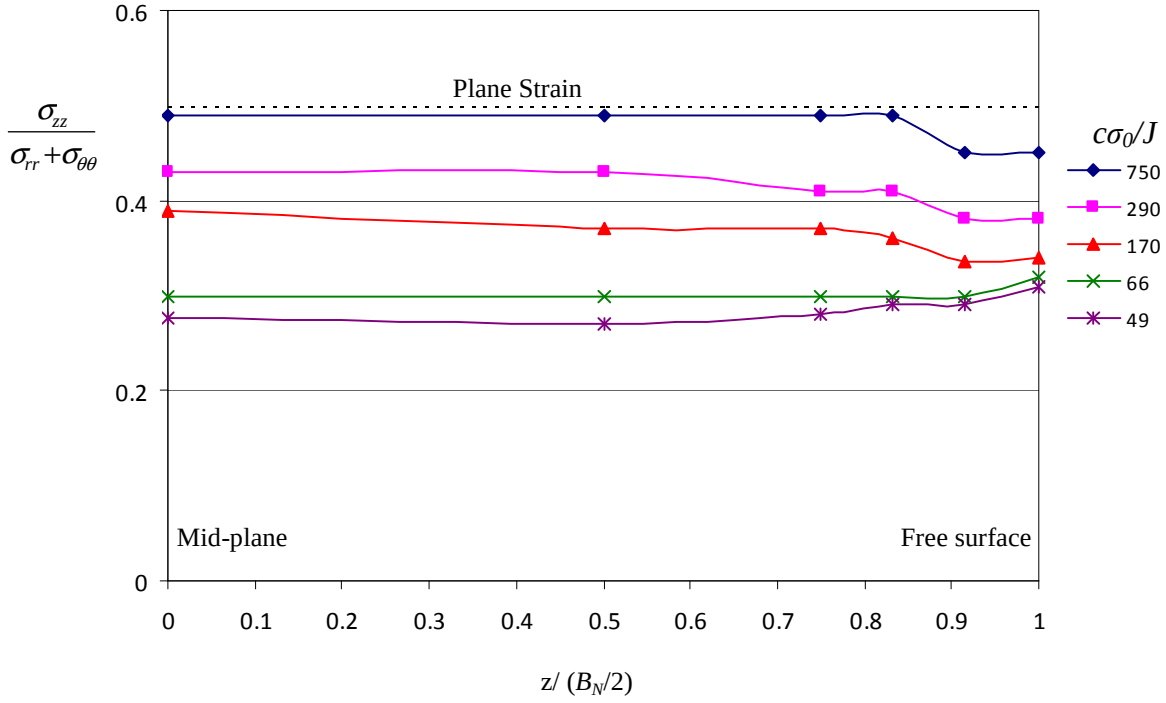

Figure 7.34: The proximity to plane strain at a distance $2J/\sigma_0$ across the thickness from the mid-plane to the free surface for the side-grooved specimen (a/w=0.5, B/w=0.2), c is the uncracked ligament.

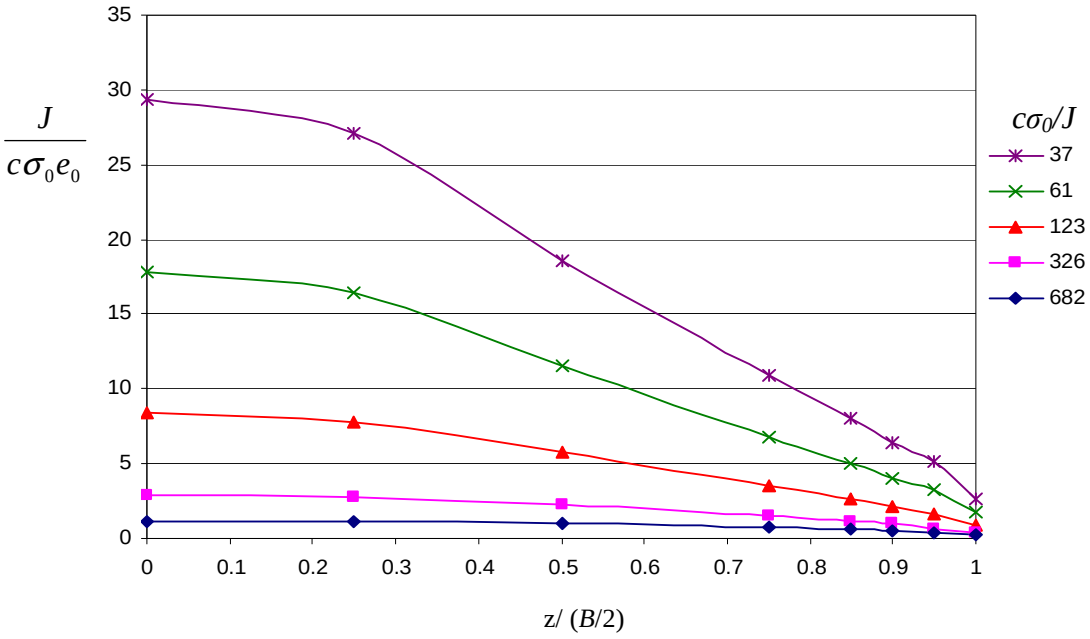

Figure 7.35: The non-dimensional J-integral along the crack front from the mid-plane z/(*B/2)*=0 to the free surface for non-grooved specimens (a/w=0.5, B/w=0.2), c is the uncracked ligament.

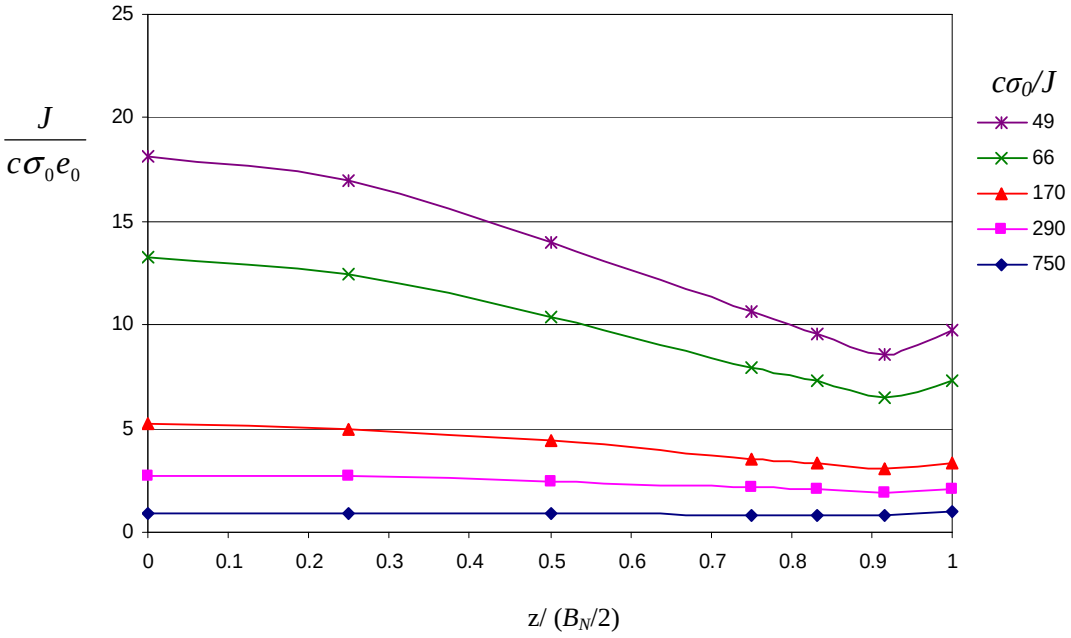

Figure 7.36: The non-dimensional J-integral along the crack front from the mid-plane z/(B_N/*2)*=0 to the free surface for the side-grooved specimen (a/w=0.5, B/w=0.2), c is the uncracked ligament.

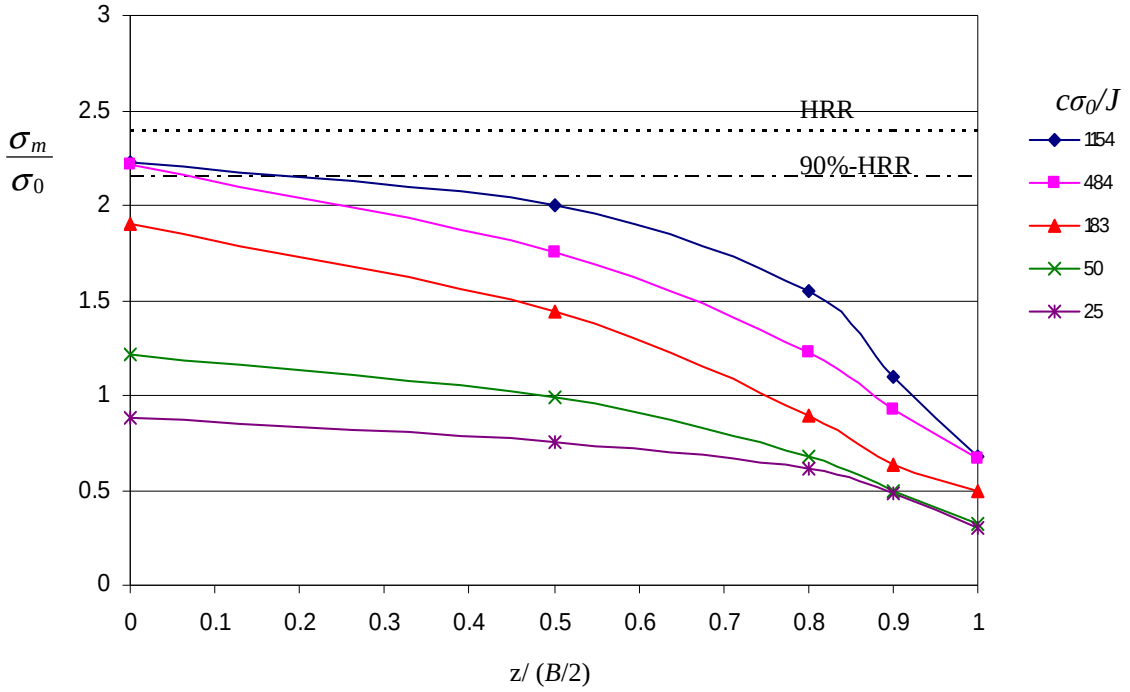

Figure 7.37: The mean stress at a distance $2J/\sigma_0$ along the crack front from the mid-plane to the free surface for non-grooved specimens (a/w=0.5, B/w=0.1), c is the uncracked ligament.

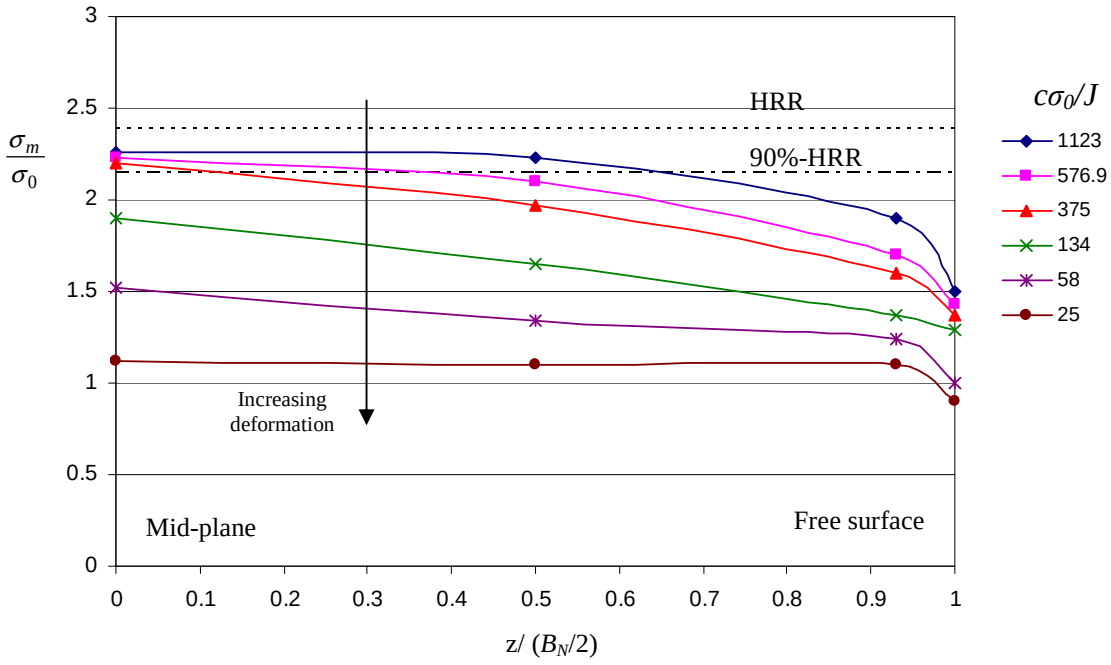

Figure 7.38: The mean stress at a distance $2J/\sigma_0$ along the crack front from the mid-plane to the free surface for the side-grooved specimen (a/w=0.5, B/w=0.1), c is the uncracked ligament.

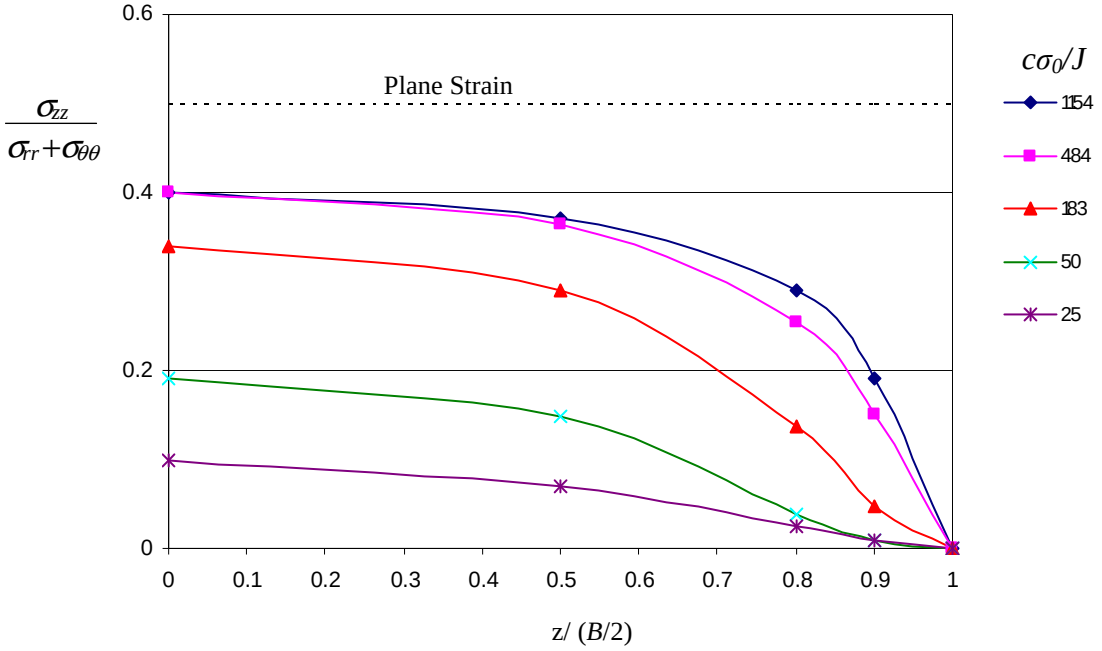

Figure 7.39: The proximity to plane strain at a distance $2J/\sigma_0$ across the thickness from the mid-plane to the free surface for non-grooved specimens (a/w=0.5, B/w=0.1), c is the uncracked ligament.

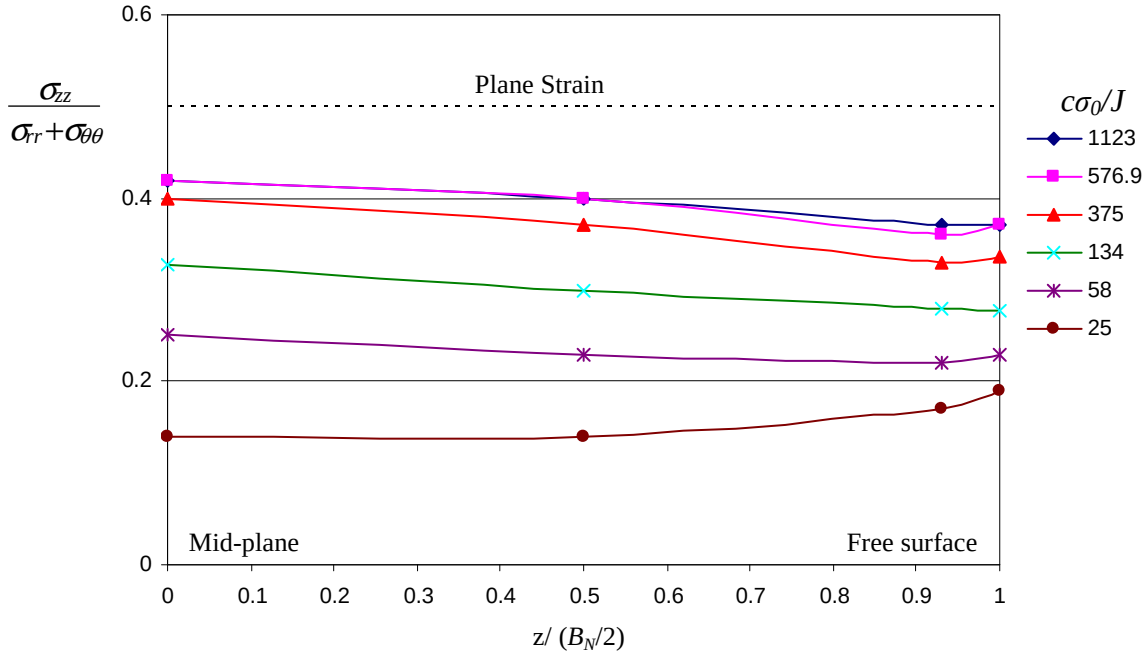

Figure 7.40: The proximity to plane strain at a distance $2J/\sigma_0$ across the thickness from the mid-plane to the free surface for the side-grooved specimen (a/w=0.5, B/w=0.1), c is the uncracked ligament.

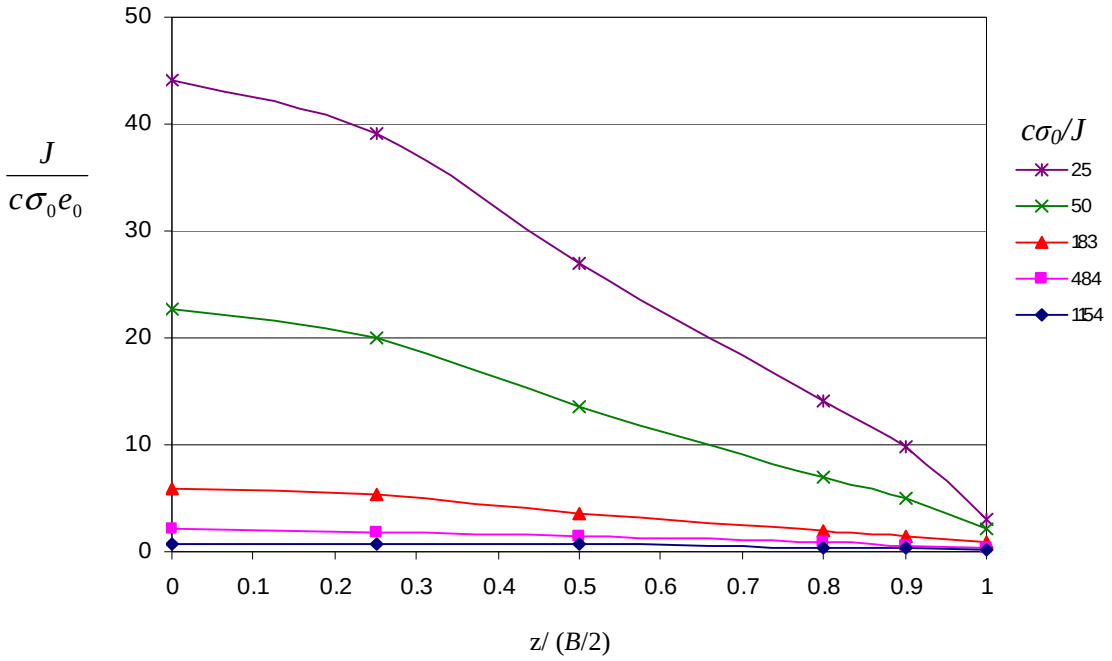

Figure 7.41: The non-dimensional J-integral along the crack front from the mid-plane to the free surface for non-grooved specimens (a/w=0.5, B/w=0.1), c is the uncracked ligament.

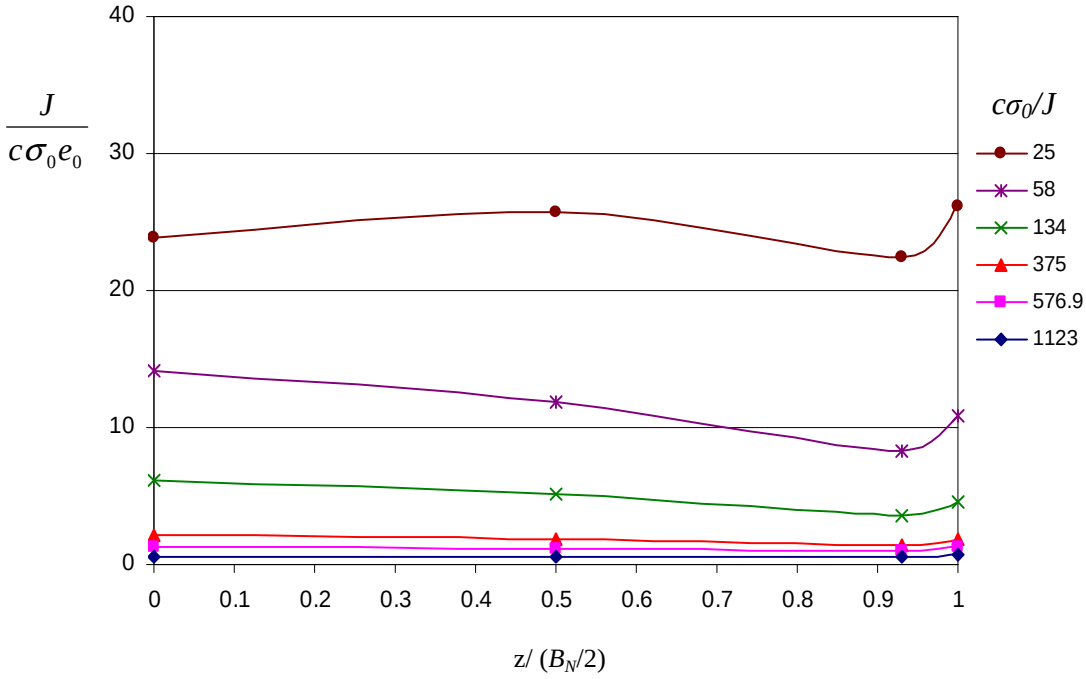

Figure 7.42: The non-dimensional J-integral along the crack front from the mid-plane to the free surface for the side-grooved specimen (a/w=0.5, B/w=0.1), c is the uncracked ligament.

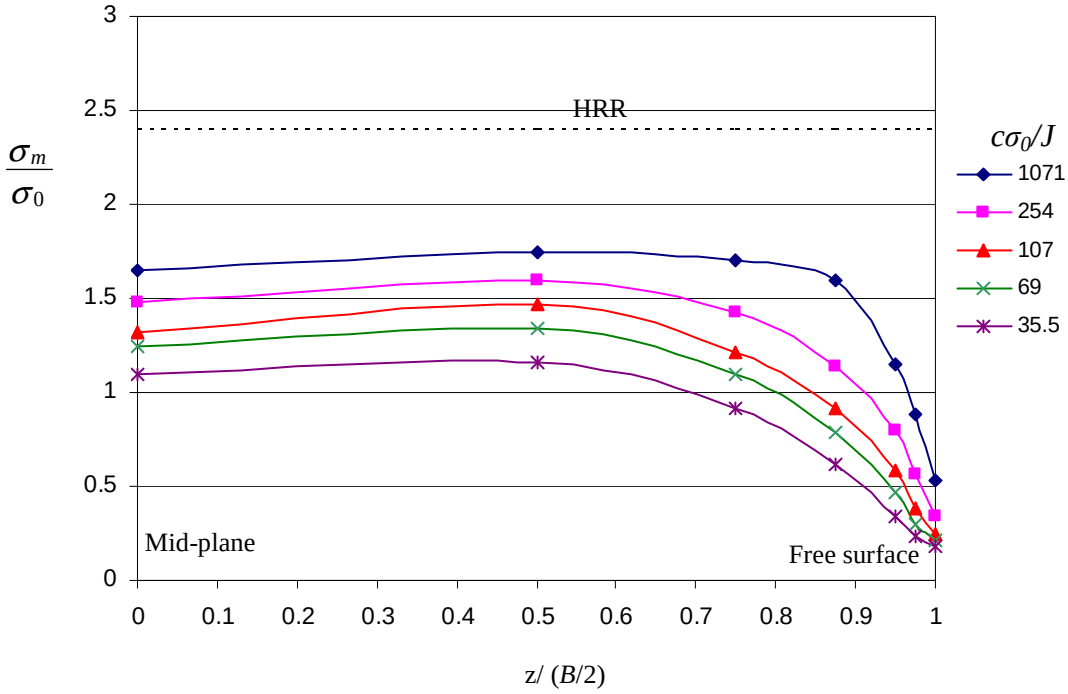

Figure 7.43: The mean stress at a distance $2J/\sigma_0$ along the crack front from the mid-plane to the free surface for a non-grooved specimen (a/w=0.1, B/(w-a)=1), c is the uncracked ligament.

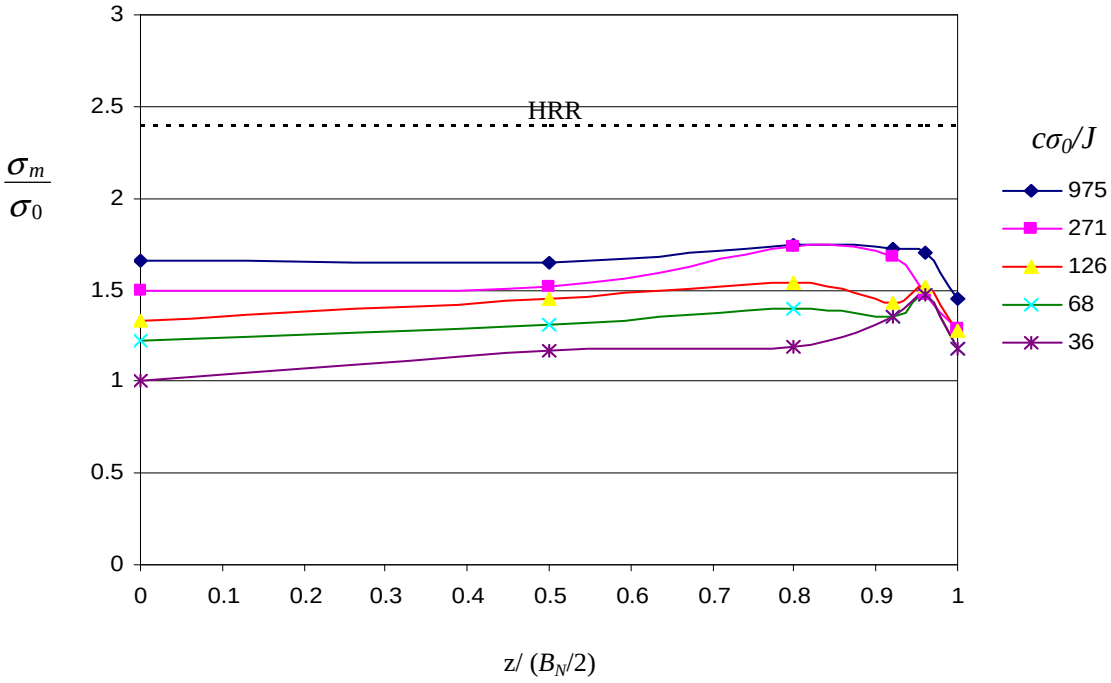

Figure 7.44: The mean stress at a distance $2J/\sigma_0$ along the crack front from the mid-plane to the free surface for the side grooved specimen (a/w=0.1, B/(w-a)=1), c is the uncracked ligament.

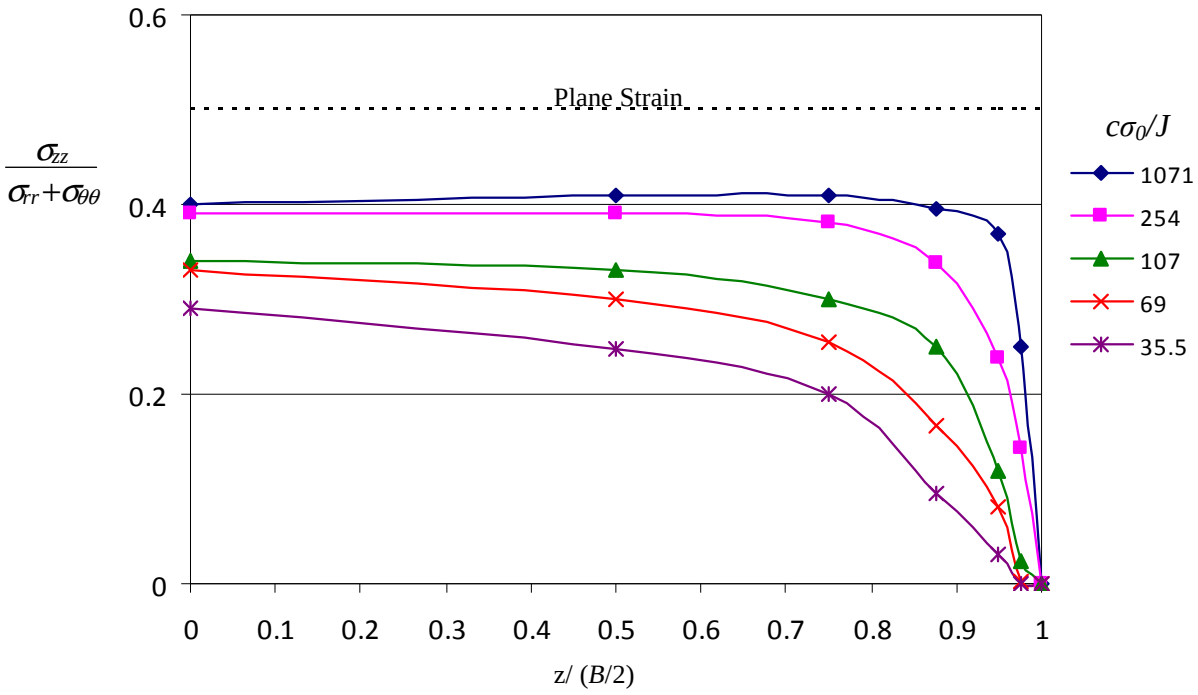

Figure 7.45: The proximity to plane strain at a distance $2J/\sigma_0$ across the thickness from the mid-plane to the free surface for the SECB without side grooves, (a/w=0.1, B/(w-a)=1), c is the uncracked ligament.

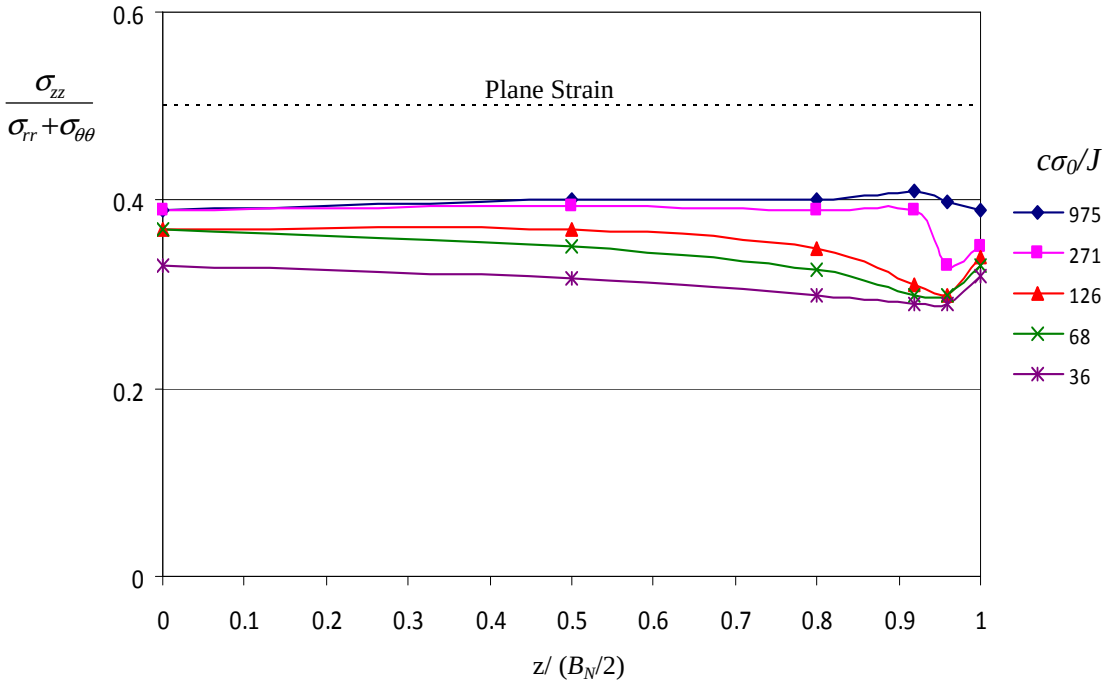

Figure 7.46: The proximity to plane strain at a distance $2J/\sigma_0$ across the thickness from the mid-plane to the free surface for the SECB with side grooves, (a/w=0.1, B/(w-a)=1), c is the uncracked ligament.

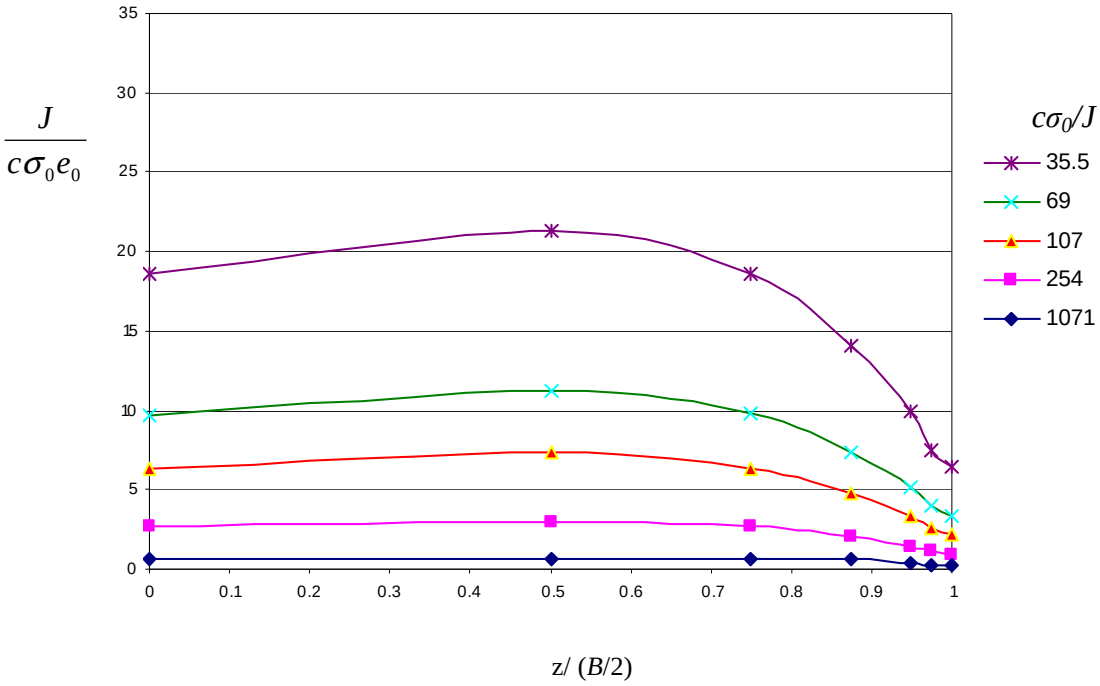

Figure 7.47: The non-dimensional J-integral along the crack front from the mid-plane z/(B/2)=0 to the free surface for the non-grooved specimen (a/w=0.1, B/(w-a)=1), c is the uncracked ligament.

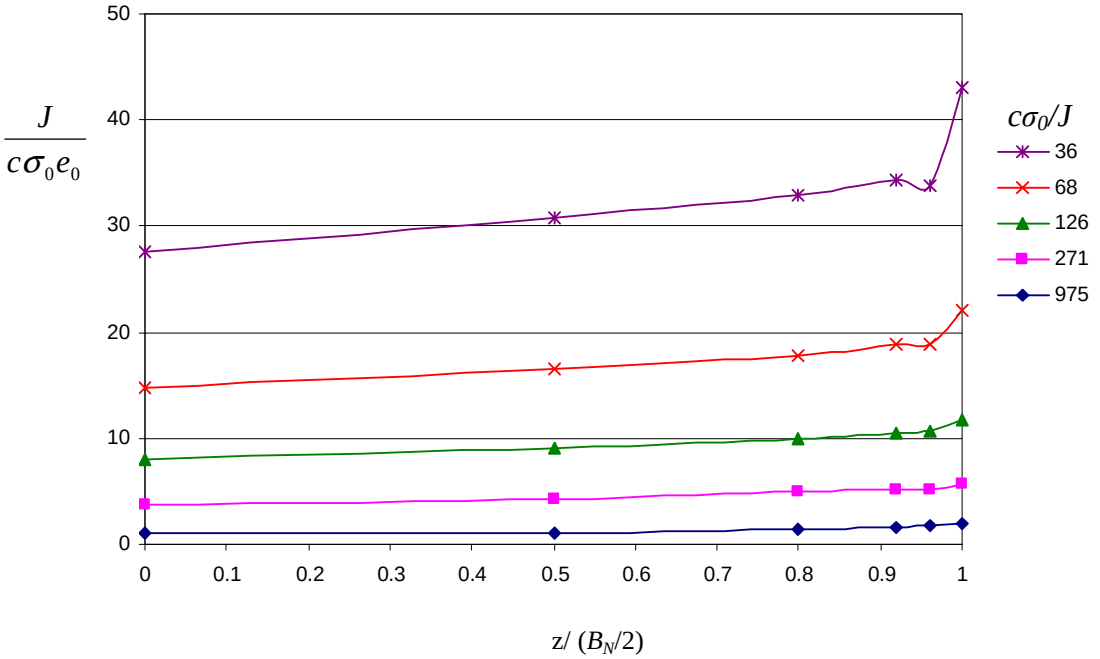

Figure 7.48: The non-dimensional J-integral along the crack front from the mid-plane z/(B_{eff}/2)=0 to the free surface for the side-grooved specimen (a/w=0.1, B/(w-a)=1), c is the uncracked ligament.

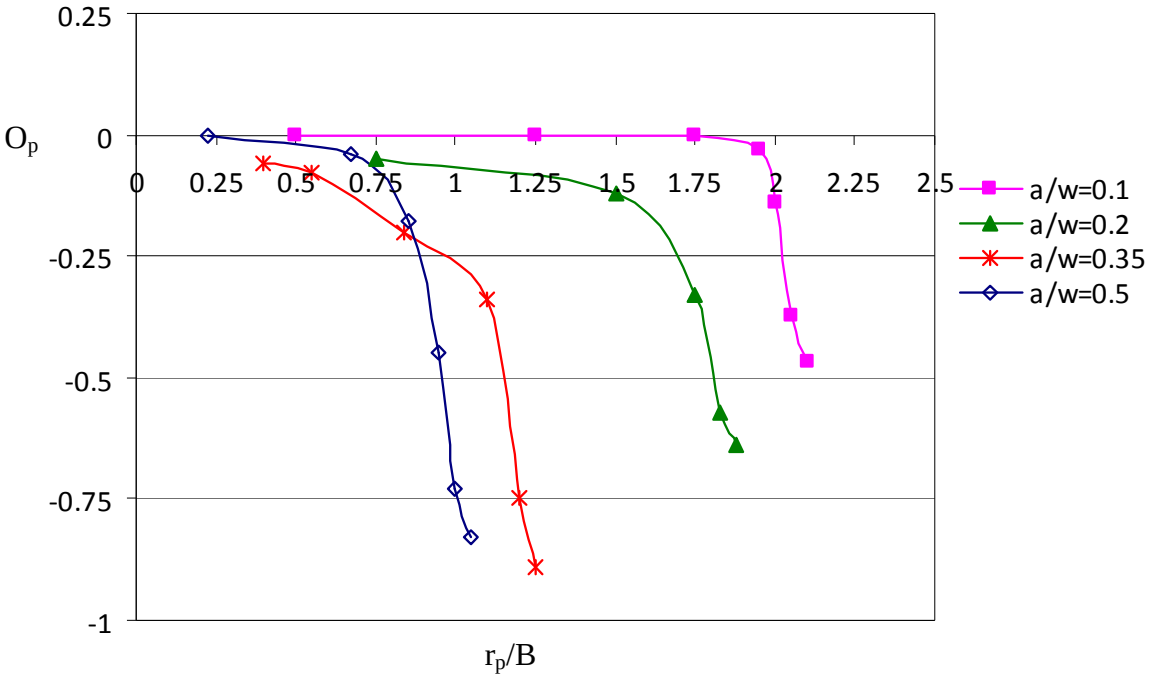

Figure 7.49: Out-of-plane constraint as a function of the plastic zone size in thin specimens (B/w=0.2) in non-hardening materials.

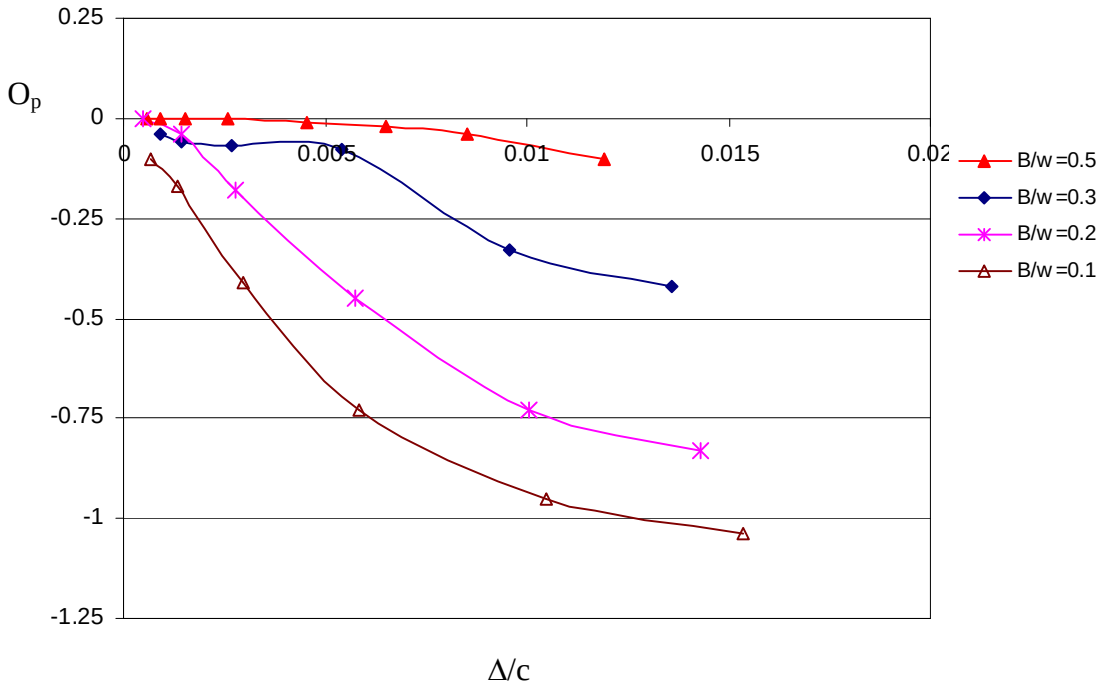

Figure 7.50: Relationship between the surface contraction and out-of-plane effect in deeply cracked geometries.

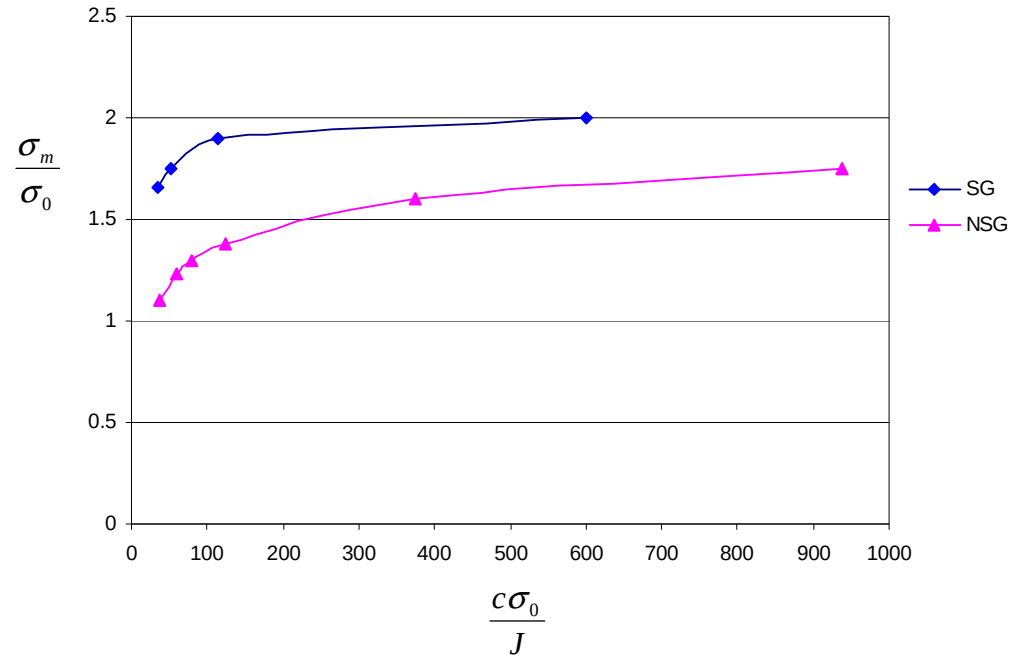

Figure 7.51: The mean stress at a distance $2J/\sigma_0$ across the thickness in side-grooved (SG) and non-side grooved (NSG) specimens with (a/w=0.5, B/w=0.5), c is the uncracked ligament.

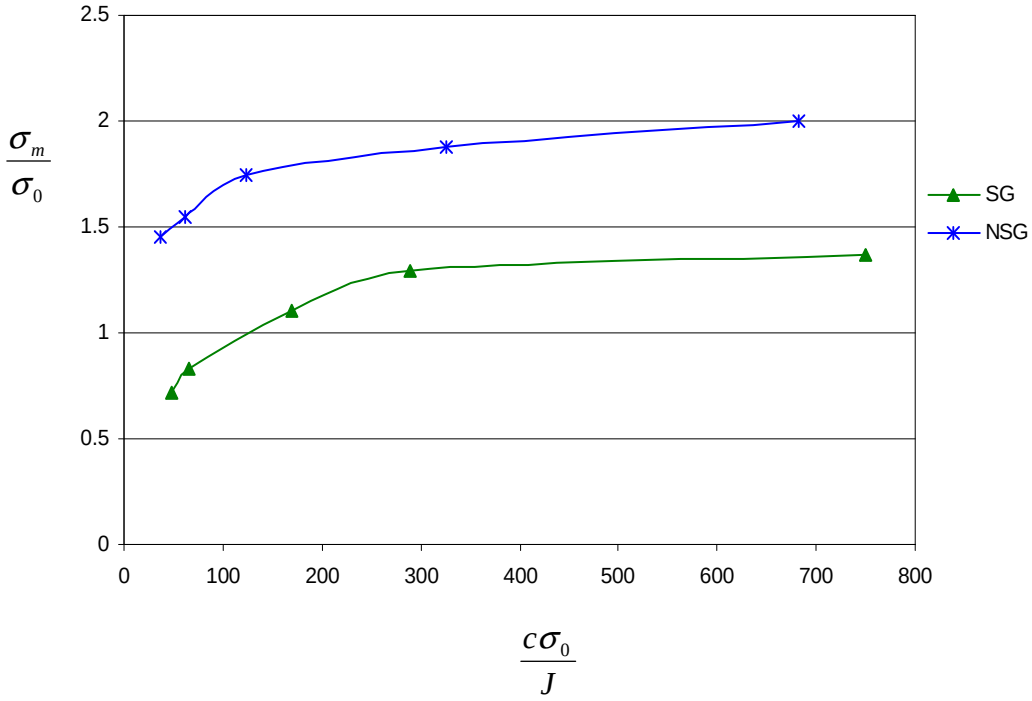

Figure 7.52: The mean stress at a distance $2J/\sigma_0$ across the thickness in side-grooved (SG) and non-side grooved (NSG) specimens with (a/w=0.5, B/w=0.2), c is the uncracked ligament.

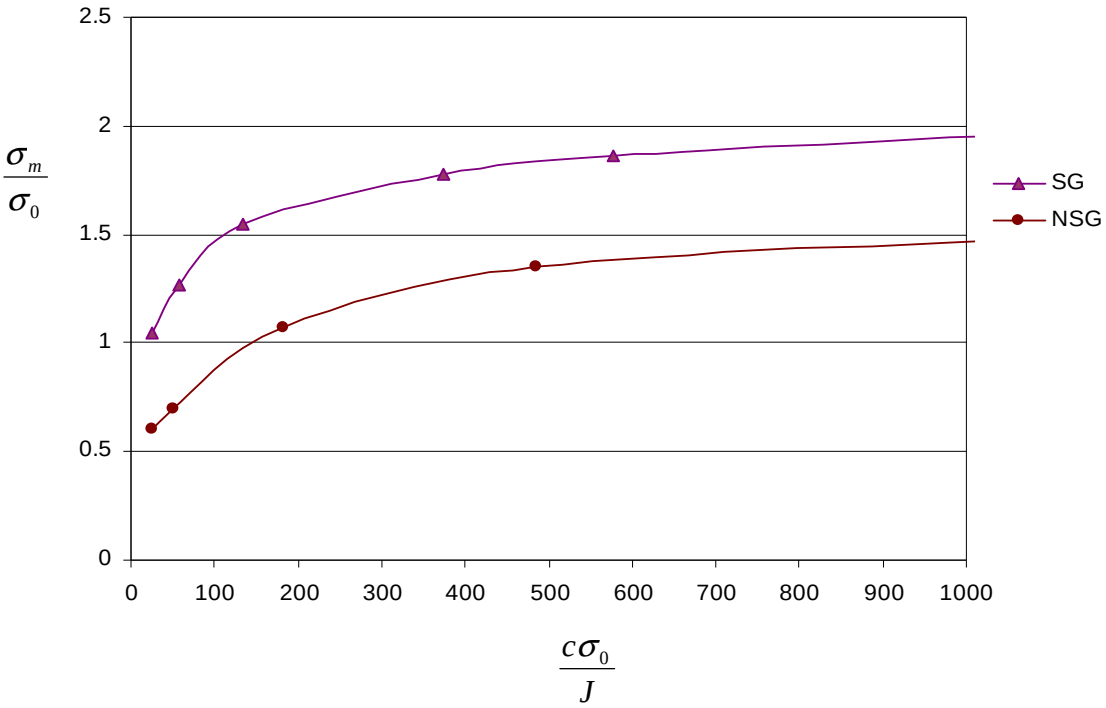

Figure 7.53: The mean stress at a distance $2J/\sigma_0$ across the thickness in side-grooved (SG) and non-side grooved (NSG) specimens with (a/w=0.5, B/w=0.1), c is the uncracked ligament.

8. Constraint based fracture toughness: an experimental study

8.1 Introduction

This chapter describes an experimental programme to measure the fracture toughness and crack growth resistance curves of a plain carbon steel at room temperature on a series of side-grooved samples with varying thickness and crack depths. Single edge cracked bend specimens were used as recommended by ASTM E1737 and BS7448-4:97, as shown in Figure (8.1). To generate the crack growth resistance curve the multiple specimen method was adopted. In this method a number of specimens were tested to different amounts of crack extension, Δa. Deeply cracked (a/w=0.5) thick and thin specimens were examined, (B/w=0.5, 0.2 and 0.1). In order to establish a correlation between out-of-plane and in-plane effects shallow cracked specimens were also tested (a/w=0.16, B/(w-a)=1) and (a/w=0.1, B/(w-a)=1).

8.2 Material

The material chosen was mild carbon-manganese steel complying with the designation, 50D under BS4360. Tensile tests were performed using cylindrical tensile specimens with a diameter of 5.64mm and a 32mm gauge length at 20° C to determine the mechanical properties. The true stress versus true strain curve was derived from the engineering stress-strain relation as shown in Figure (8.2). The material behaves as an intermediate hardening material which is described by a hardening exponent n=10. Young's modulus was 210 GPa, Poisson's ratio of 0.3, a yield strength of 400 MPa, and the ultimate tensile stress was 626 MPa.

8.3 Test preparation

Fracture mechanics samples were cut from a large 25mm thick rolled plate. Samples were notched with a cutter such that the crack plane contained the rolling direction and the short transverse direction, T-L.

Samples were first fatigue pre-cracked in three point bending according to BS 7448. During the fatigue precracking the load was periodically reduced with fatigue crack growth to keep the maximum stress intensity factor below 30MPa√m. Fatigue precracking was done at room temperature using a servohydraulic machine at a frequency of 3-4Hz and a stress ratio (R) of 0.1. This was repeated until the ratio of crack depth to width (a/w) in range of 0.45 to 0.55 was obtained. The specimens were side grooved in order to maintain the uniformity of the stress and strain fields across the thickness, and keeping the crack front straight as discussed in the preceding section. The grooves were cut to a depth of 10 % of the thickness on each lateral face to obtain 80% net thickness of the whole thickness.

8.4 Test procedure

Fracture tests were performed on a universal testing machine equipped with three point bending set-up. A multiple specimen technique was used. Samples were tested under displacement control at a cross-head speed of 0.5mm/min. Each specimen was subjected to a chosen amount of displacement and the amount of crack extension associated with this loading was measured after the test. The first specimen was used to determine the full force-notch opening displacement (F-V) curve and the test was stopped at the maximum load. Subsequent tests were stopped at progressively smaller clip-gauge displacements. All tests were performed at room temperature at ambient conditions.

To measure the notch opening displacement (V) a clip gauge was placed on the sample using a set of 3mm high knife edges, as shown in Figure (8.3). The load line displacement was measured by the movement of the crosshead. The test set-up is shown in Figure (8.3). During the test, both the applied load and notch opening displacement

were recorded. The plastic component of the notch opening displacement Vp was measured graphically at the termination of the test.

The plastic energy absorbed in the material U_p was determined for each test by measuring the area under the Force-crosshead displacement curve. The J-integral and the crack tip opening displacement CTOD were calculated in accord with British Standard BS 7448-4:1997 as discussed in chapter (6).

8.5. Measurements of the initial crack length and the amount of ductile tearing

After the test, the specimens were cooled in a liquid nitrogen bath and broken open, and the initial fatigue pre-crack length a_0 and stable crack growth Δa were measured at nine equally spaced points through the thickness. This was done first by averaging the two side surface crack lengths, and then averaging this value with the other seven points and dividing by eight. The ductile crack extension was measured from the end of the fatigue pre-crack to the final extension, at the same nine equally spaced points along the crack front and averaged in the same manner. The original length of the fatigue crack a_0 for all specimens was in the range of 0.47-0.55w, and almost uniform crack extension was obtained for all specimens tested.

8.6 δ-Δa Resistance curve and determination of ($\delta_{0.2}$) in deeply cracked bend specimens (a/w=0.5, B/w=0.5, 0.2, 0.1).

The thickness (B) and ligament (c) requirements ($c\sigma_0/J>20$ and $B\sigma_0/J>20$) were maintained in most tests. However the thinnest specimens B/w=0.1 met only the ligament requirements but did not meet the thickness requirements. The experimental data were used to construct a δ-Δa curve. The value of the crack tip opening displacement (δ) for each specimen was plotted versus the amount of crack tip extension Δa. The curve fit was constructed through the data points and the fracture toughness corresponding to crack extension of 0.2 mm was determined. $\delta_{0.2}$ was used here as the crack tip opening displacement at the initiation of the crack growth.

Figure (8.4) shows the crack opening displacement (δ) as a function of ductile tearing Δa in thick and thin specimens, a/w=0.5, B/w=0.5, 0.2 and 0.1 respectively (Terfas and Bezensek, 2009b). The slope of the δ-Δa curve increased as the crack extension increased. The δ at Δa=0.2mm in thick specimen (B/w=0.5) was at approximately 0.1 mm. The δ-Δa data can be approximated by a linear relationship:

$$\delta=0.0891(\Delta a)+0.089 \quad mm \tag{8.1}$$

In thin specimens (B/w=0.2) the intersection of the constructed line $\delta_{0.2}$ with a curve fitting showed the fracture toughness at 0.115 mm. The δ-Δa relationship can be presented as:

$$\delta=0.1132(\Delta a)+0.0922 \quad mm \tag{8.2}$$

The fracture toughness was significantly increased with further reduction in the specimens thickness, (B/w=0.1). Using curve fitting the fracture toughness at Δa=0.2mm was approximately $\delta_{0.2}$=0.14 mm and the equation is described as:

$$\delta=0.2109(\Delta a)+0.095 \quad mm \tag{8.3}$$

High constraint associated with thick specimens tended to have lower crack growth resistance curve compared to less constrained thin specimens. The tearing resistance increased with the decreasing constraint level associated with thin specimens.

8.7 J-Δa Resistance curve and determination of ($J_{0.2}$) in deeply cracked bend specimens (a/w=0.5, B/w=0.5, 0.2, 0.1).

A similar procedure was used to construct J-Δa curves. Figure (8.5) shows J-integral values obtained experimentally as a function of the crack extension for thick and thin specimens (a/w=0.5, B/w=0.5, 0.2 and 0.1). It can be seen that the fracture toughness, $J_{0.2}$ was approximately 82 N/mm for thick specimens B/w=0.5, and a fitted curve gives:

$$J=68.5(\Delta a)+68.22 \quad N/mm \tag{8.4}$$

For thin specimens B/w=0.2 the crack resistance increased and the intersection of the crack initiation line with the fitted curve showed the fracture toughness reached $J_{0.2}$ = 88 N/mm. This value is slightly larger than that fracture toughness observed for thick specimens. The J-Δa relationship can be represented by curve fitting as:

$$J=92.02(\Delta a)+70.5 \quad N/mm \tag{8.5}$$

With a further decrease in thickness to B/w=0.1 a significant increase in fracture toughness was observed $J_{0.2}$= 105 N/mm and the data can be represented by:

$$J=150.94(\Delta a)+75 \quad N/mm \tag{8.6}$$

The experimental values of J-integral and crack tip opening displacement at the same amount of crack extension are plotted in Figure (8.6). The relationship between the J-integral and the crack tip opening displacement may be written in terms of a coefficient, M, as:

$$J=M\sigma_0\delta \tag{8.7}$$

The coefficient value (M) in thick specimens (B/w=0.5) was approximately 1.95 close to the plane strain value of 2 (Shih, 1981). For thin specimens (B/w=0.2) the coefficient, M, was 1.90, which is still close to the value observed in thick specimens. However the M coefficient became considerably smaller with a further reduction in thickness (B/w=0.1) and reached a value of 1.70.

8.8 Fracture toughness in shallow cracked specimens (a/w=0.16, 0.1, B/(w-a)=1

The finite element analysis presented in previous chapters showed the strong dependence of the constraint level on the crack geometry. Therefore it is important to correlate the enhanced fracture toughness with the constraint loss experimentally using different crack

depths to obtain different crack tip constraint levels. This is then compared to the J-O_p locus which is based on the thickness effect.

Due to the dependency of the fracture toughness on the geometry, the plastic geometry factor (η_{pl}) to determine J-integral was determined using finite element analysis. The η_{pl} values were equal to 3.1 in a/w=0.16 and 3.3 in a/w=0.1, and agree with data given by Kirk and Dodds (1993). The J-integral was determined from the experimental load-crack mouth opening displacement (CMOD) curve, which provides a more accurate J-estimation in comparison with the LLD based J-estimation particularly in shallow cracked SE(B) specimens (Sumpter, 1987, Kirk and Dodds, 1993, and Kim and Schwalbe, 2001, Kim, 2002, Kim, et al., 2004).

An increase in fracture toughness ($J_{0.2}$) was observed for very shallow cracks a/w=0.1, as shown in Figure (8.7). Deeply cracked specimens attained $J_{0.2}$=82 N/mm while shallow cracked specimens $J_{0.2}$=102 and 116 N/mm for a/w=0.16 and a/w=0.1, respectively. It may be concluded that the constraint levels associated with deep cracked specimens tended to cause a lower crack growth resistance curve compared to shallow cracked specimens.

8.9 Discussion

Figure (8.8) shows that the increase in toughness associated with thin specimens is due to the reduction in the mean stress ahead of the crack tip compared to high mean stress levels maintained in the thick specimens (Terfas and Bezensek, 2009b). Using the criterion of 10% of HRR field to maintain J-dominant (Shih and German 1981), the thickness and ligament size of thick specimens (B/w=0.5) agreed with the ASTM requirements. For the B/w=0.2 specimens, the thickness requirements met the ASTM standard but the ligament requirements demanded by the current calculations suggest a more severe requirement ($c \geq 50J/\sigma_0$). The thinnest specimens did not satisfy either the thickness nor ligament size requirements and showed that both thickness (B) and the ligament (c) must be larger than $35J/\sigma_0$ and $175J/\sigma_0$, respectively.

Plane strain constraint was also examined for the three test geometries and is shown in Figure (8.9). Thick geometries maintained plane strain conditions even under large scale yielding. There was no significant loss in plane strain constraint at fracture in thin geometries (B/w=0.2), however a significant deviation from plane strain conditions was observed in the thinnest specimens (B/w=0.1).

Figure (8.10) shows the out-of-plane constraint measured at $r\sigma_0/J=2$ at the mid-plane using finite element analysis. Thick specimens B/w=0.5 maintained high levels of constraint even at high deformation levels. For specimens with B/w=0.2 a small loss of constraint appeared only at high deformation levels $c\sigma_0/J<100$. Thinnest specimens showed significant loss of constraint due to the thickness effect. This results in the enhanced fracture toughness observed in thin specimens B/w=0.1. This indicates that the toughness is dependent on the B/w ratio as shown in Figure (8.11). The loss of constraint associated with decrease in thickness results in increase in toughness (J_c).

The engineering implications of the current findings can be discussed in terms of the failure assessment diagram. The loss of constraint due to the thickness effect increased the fracture toughness, subsequently increased the margin of safety of components containing defects.

ASTM (1998) and BS7448 (1997) suggest J_c at an extension of $\Delta a=0.2$mm to define initiation toughness. Figure (8.12) shows J-O_p locus for crack extensions $\Delta a=0.2$mm and 0.4mm. This thickness enhanced toughness can be included in failure assessment schemes by defining a J-O_p failure loci in the form $J_{Op}=f(J_{Ic},O_p)$. A linear fit to toughness data can be written:

$$J_{Op}=J_{Ic}(1-\alpha O_p) \qquad (8.8)$$

Here J_{Ic} represents the plane strain fracture toughness measured on deeply cracked thick samples. α is a constant and equal to 0.54 for $\Delta a=0.2$mm, and 0.73 for $\Delta a=0.4$mm. The modified failure assessment line can be constructed in a similar manner to that used by Ainsworth and O`Dowd (1995) by modifying the failure assessment line for the out-of-

plane constraint (i.e thickness effect) and retaining the plane strain J_{Ic} value for normalising the ordinate.

In shallow cracked geometries in-plane effects dominated and the out-of-plane effect was very small, and the modified assessment curve can be expressed as Kr= f(Lr).[1+α(-$\beta L_r)^m$], (Ainsworth and O`Dowd, 1995) . In deeply cracked geometries only the out-of-plane was significant. Therefore the assessment can be performed using the modified Kr=f(Lr).[$\sqrt{(1-\alpha O_p)}$]. Where f(Lr) is the original failure assessment curve, and the second term is $\sqrt{J_{Op}/J_{Ic}}$ that represent the increase in toughness based on the out-of-plane constraint which is given by Eq. (8.8) and is shown in Figure (8.13).

Figures (8.14) and (8.15) show the J-Op locus compared to J-Q locus at crack extensions of Δa=0.2 and 0.4mm. It can be seen that the increase in toughness due to the in-plane constraint loss was in general similar to the increase in toughness due to the out-of-plane effect.

8.10 Conclusion

Tests on thick and thin specimens showed that the fracture toughness J_{Ic} at Δa=0.2mm was dependent on the specimen thickness with thin specimens having a higher fracture toughness compared to the thick specimens. In the ASTM E1737 the recommended specimen size for single edge cracked bars is B/w=0.5, however the standard allows alternative specimens in the range 1≤B/w>0.25 to be used. In this work specimens with B/w=0.2 maintained high constraint conditions and low fracture toughness close to the values observed in the standard specimens. This indicates that standard requirements can now be relaxed to B/w=0.2 and can be used to determine the plane strain fracture toughness (Terfas and Bezensek, 2009b). A quantitative relation between the thickness and fracture toughness was established in a similar manner to the toughness – constraint relations developed for shallow cracks, on the basis of constraint levels in thick and thin fracture mechanics samples. A procedure to incorporate thickness related constraint loss in the R6 FAD was also proposed, however a further investigation may be required.

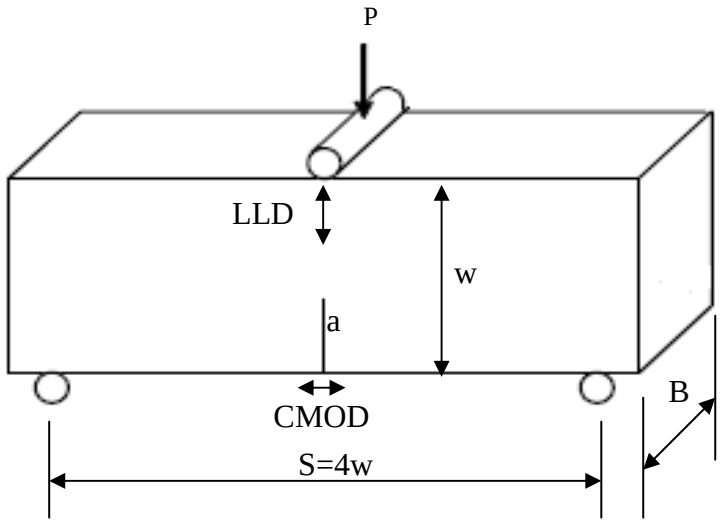

Figure 8.1: A standard single edge cracked bend specimen for fracture toughness.

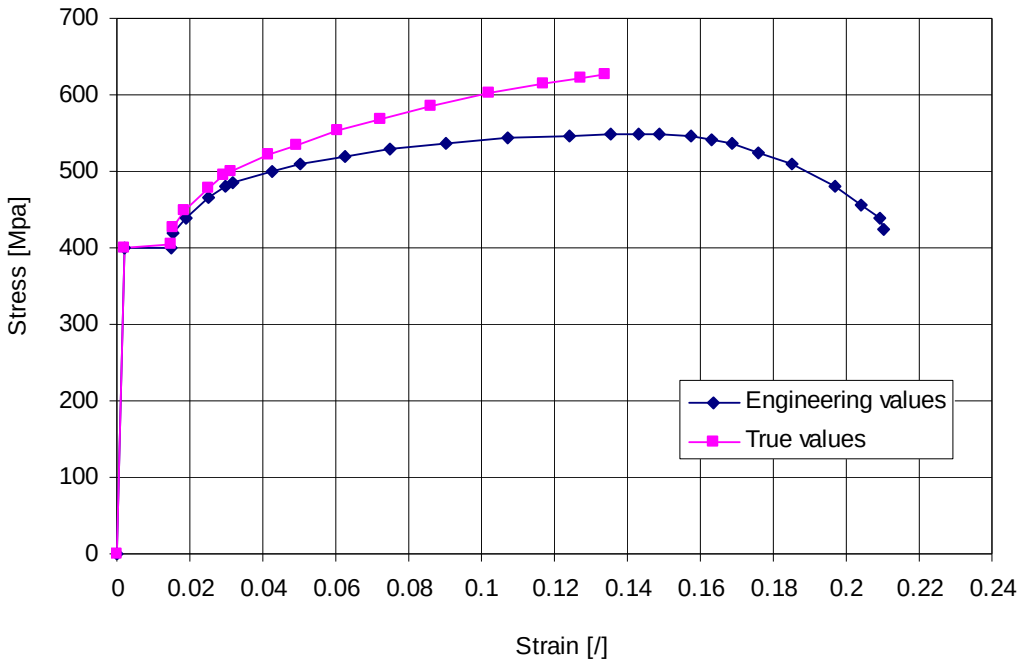

Figure 8.2: Stress-strain curves for materials used in fracture tests.

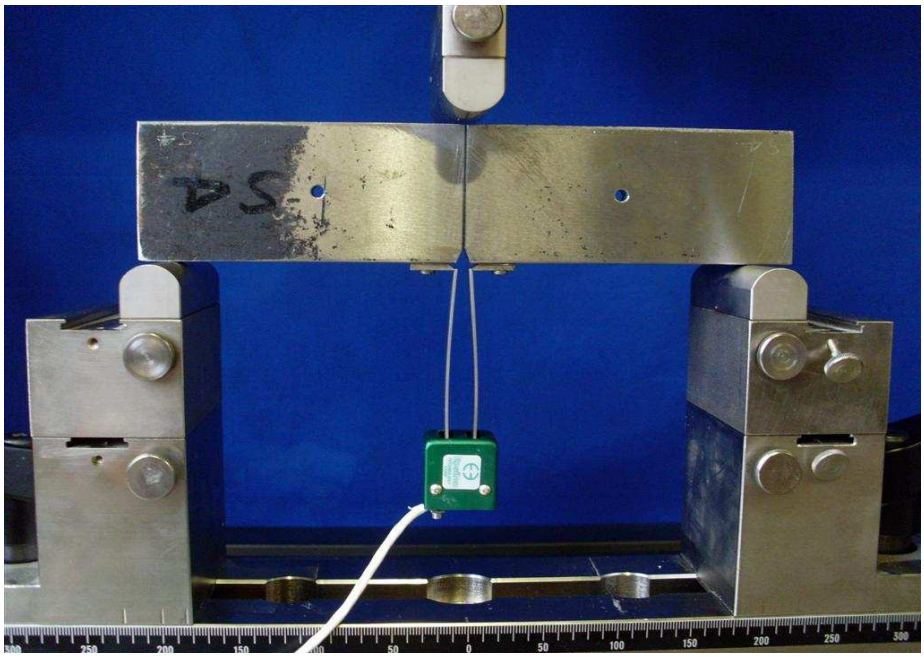

Figure 8.3: Clip gauge used in the three point bend specimen.

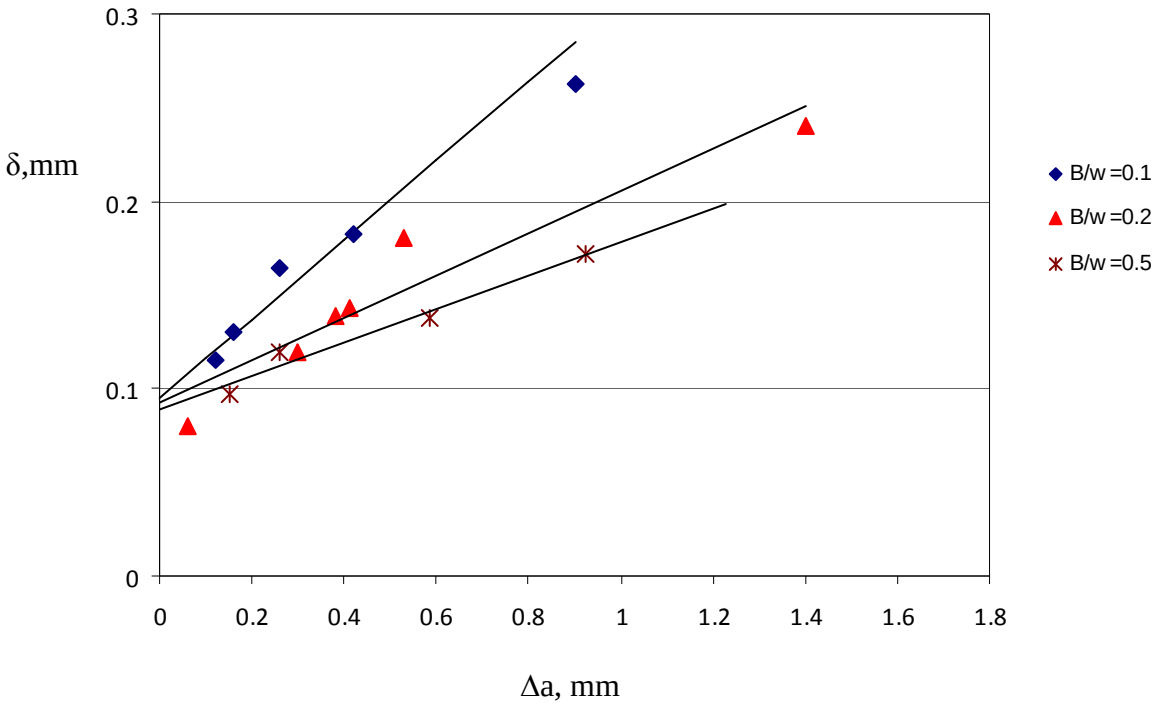

Figure 8.4: The fracture resistance curve (δ-Δa curve) for thick and thin single edge notched bend specimens with a/w=0.5 and B/w=0.5, 0.2 and 0.1 (Terfas and Bezensek, 2009b).

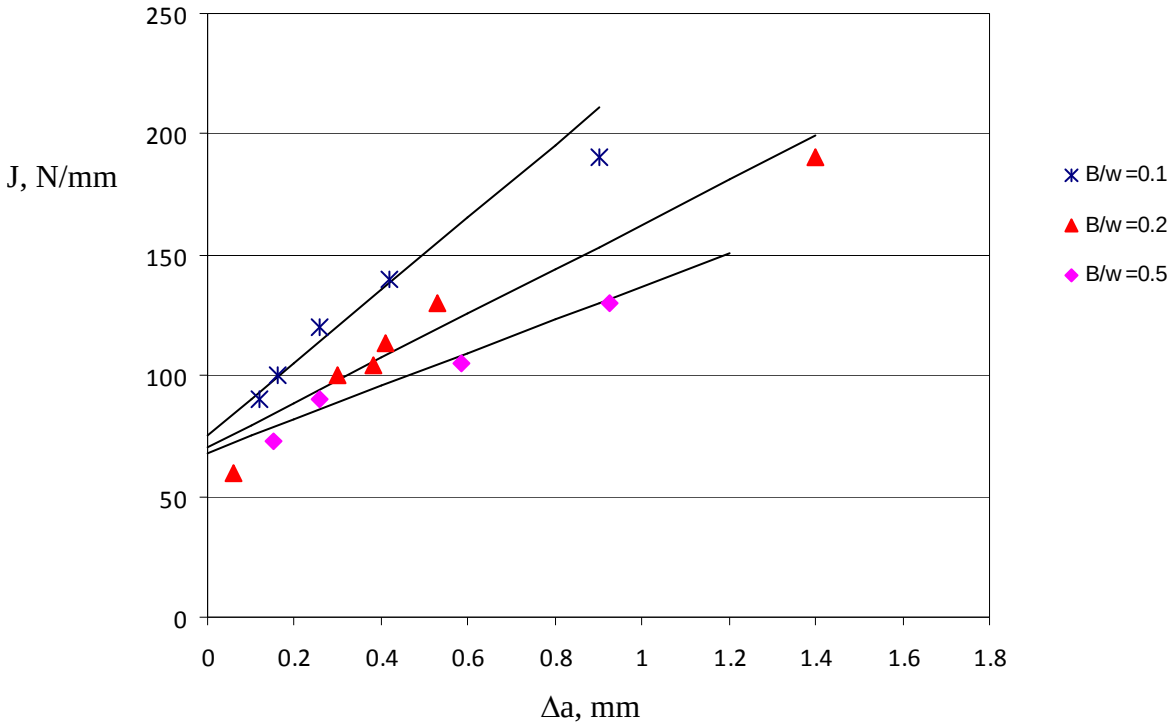

Figure 8.5: The fracture resistance curve (J-Δa curve) for thick and thin single edge notched bend specimens with a/w=0.5 and B/w=0.5, 0.2 and 0.1.

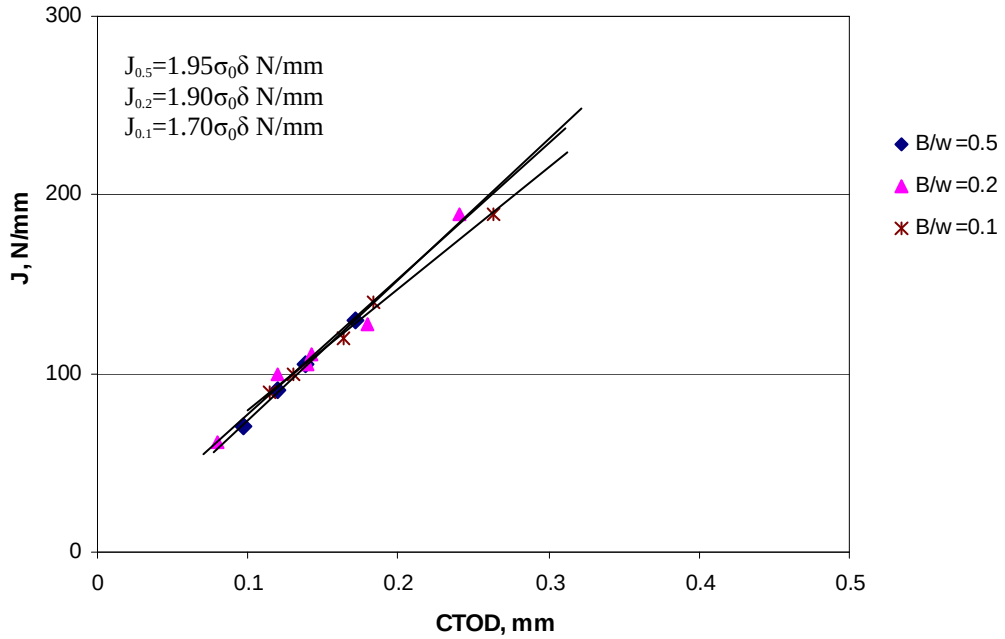

Figure 8.6: Fracture toughness J-integral and crack tip opening displacement relationship in thick and thin single edge notched bend specimens with a/w=0.5 and B/w=0.5, 0.2 and 0.1.

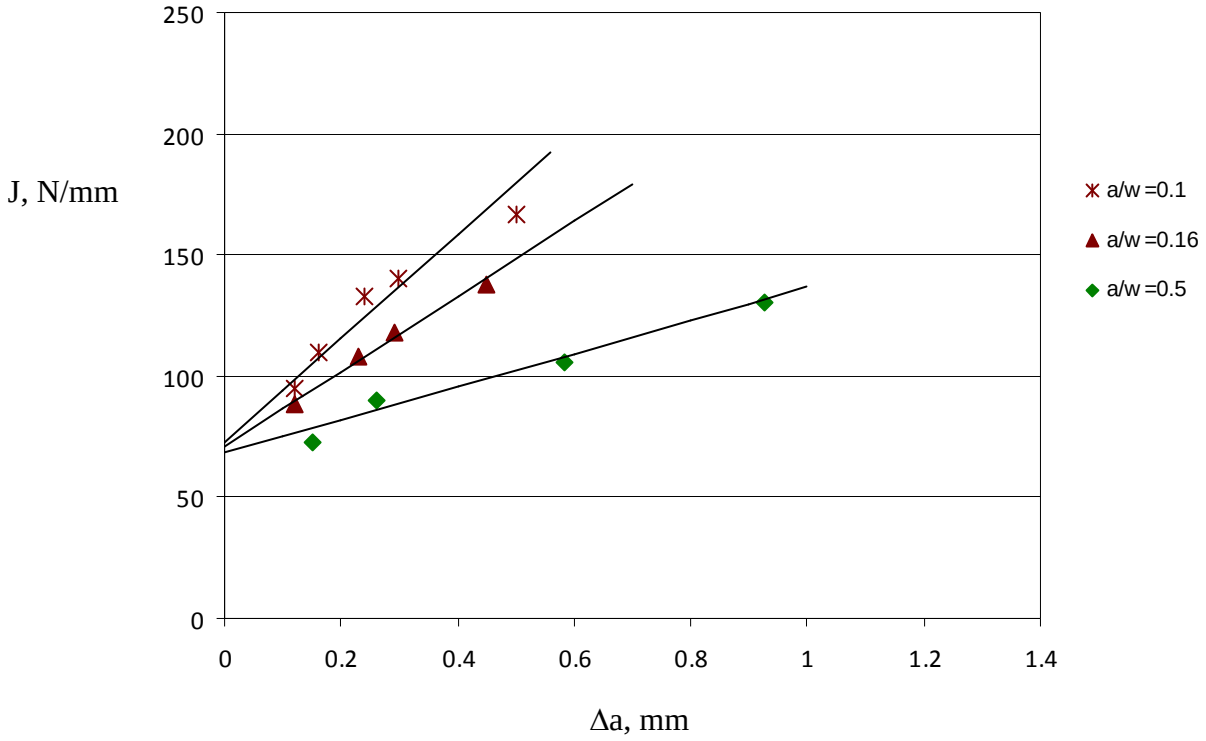

Figure 8.7: The fracture resistance curve (J-Δa curve) for deep and shallow cracked specimens a/w=0.5, 0.16 and 0.1.

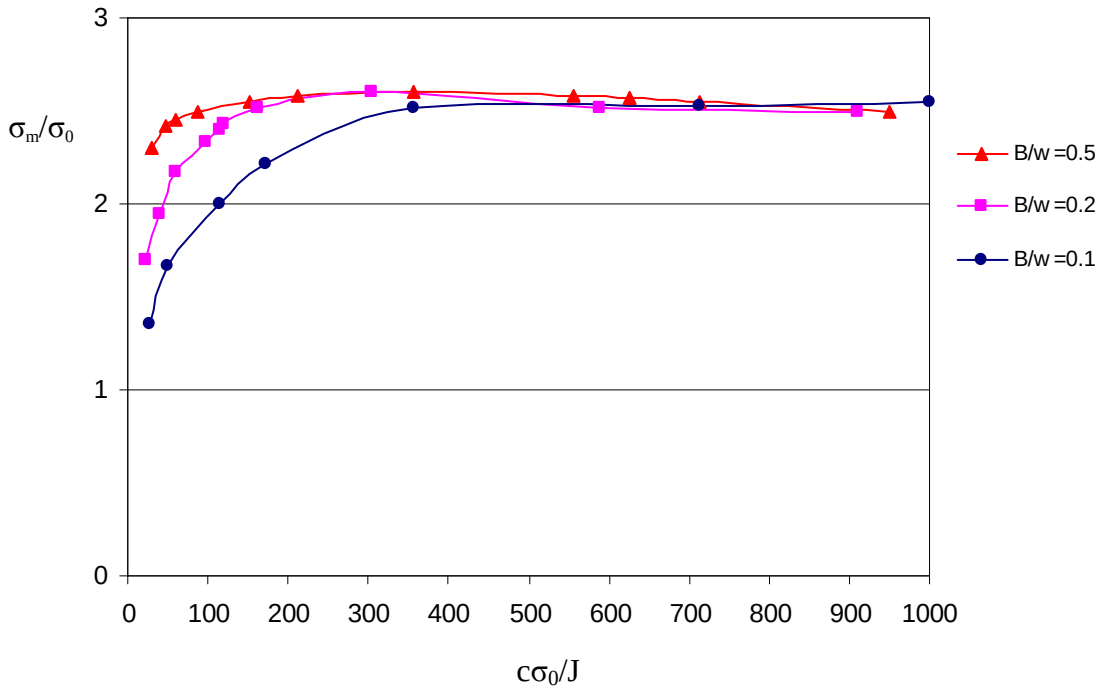

Figure 8.8: The mean stress at $r\sigma_0/J=2$ at mid-plane as a function of deformation in single edge bend specimens with a/w=0.5 and B/w=0.5, 0.2 and 0.1 (Terfas and Bezensek, 2009b).

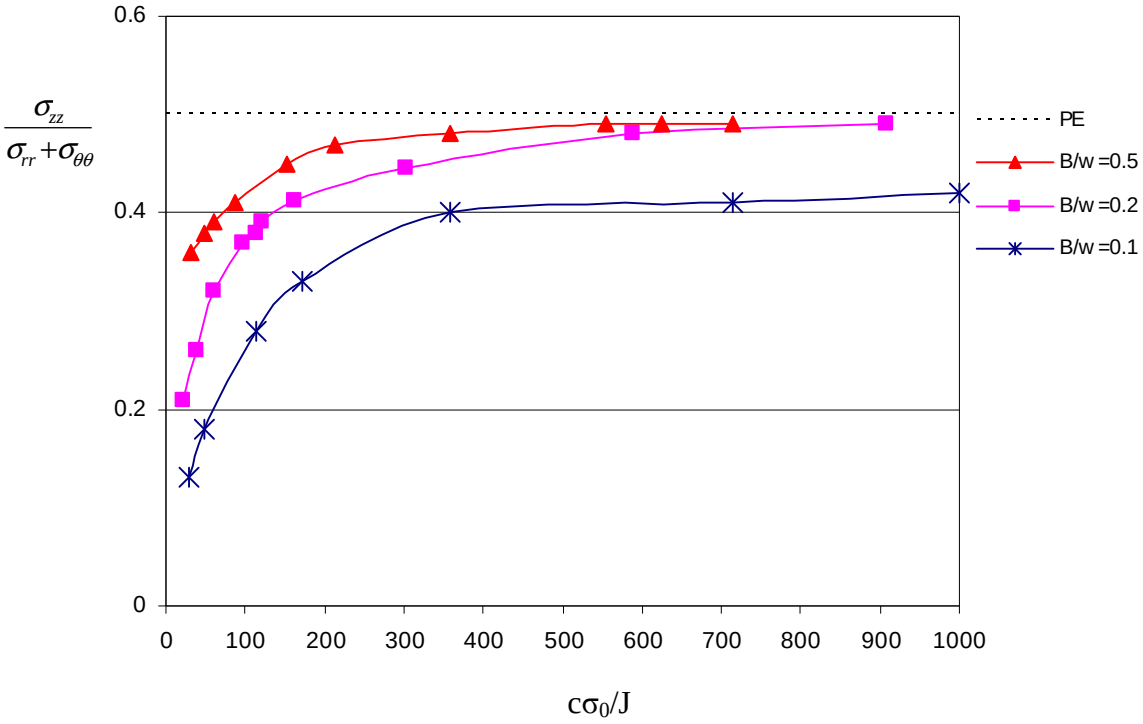

Figure 8.9: Plane strain conditions as a function of deformation in single edge bend specimens with a/w=0.5 and B/w=0.5, 0.2 and 0.1.

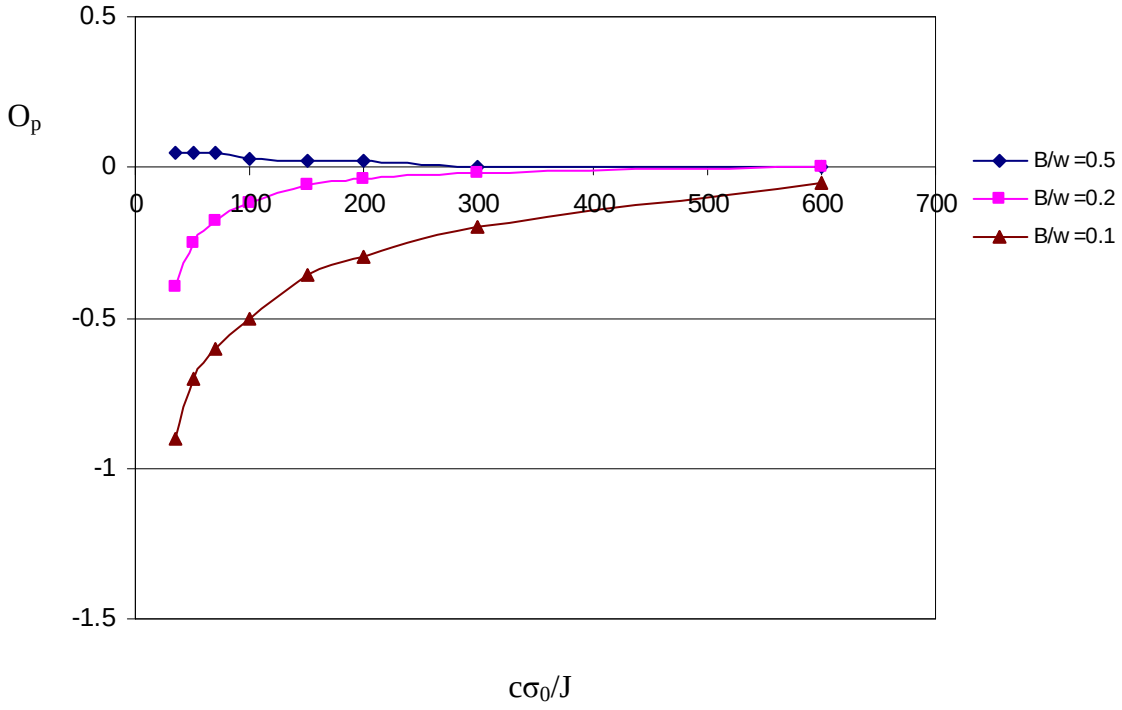

Figure 8.10: Out-of-plane effect at $r\sigma_0/J=2$ at mid-plane for geometries, a/w=0.5, B/*w*=0.5, 0.2 and 0.1 according to the test samples, n=10.

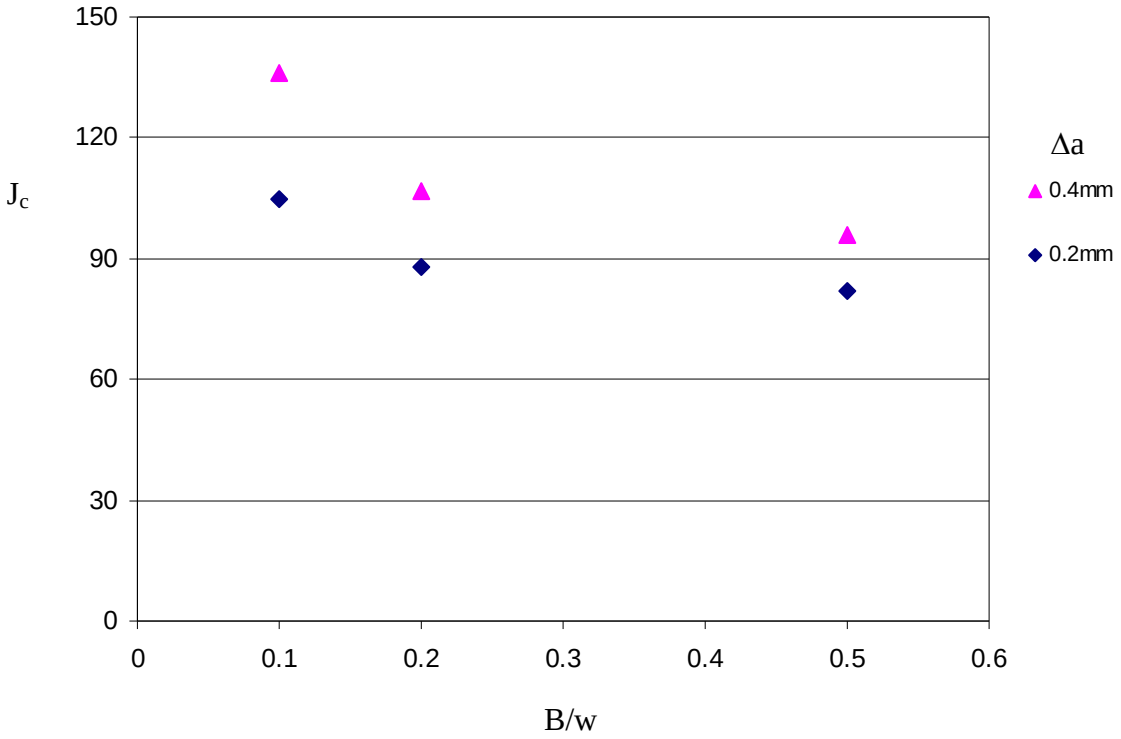

Figure 8.11: Toughness as a function of the B/w ratio of edge cracked bend bars.

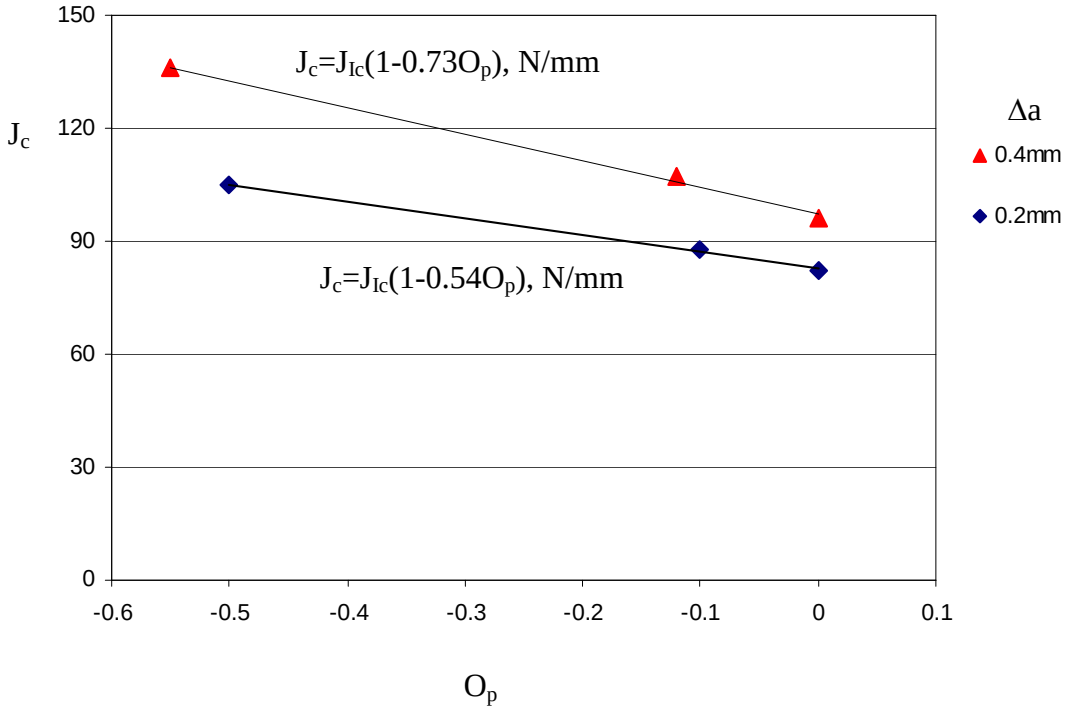

Figure 8.12: Toughness at Δa=0.2mm and Δa=0.4mm as a function of out-of-plane constraint (at $r\sigma_0/J=2$).

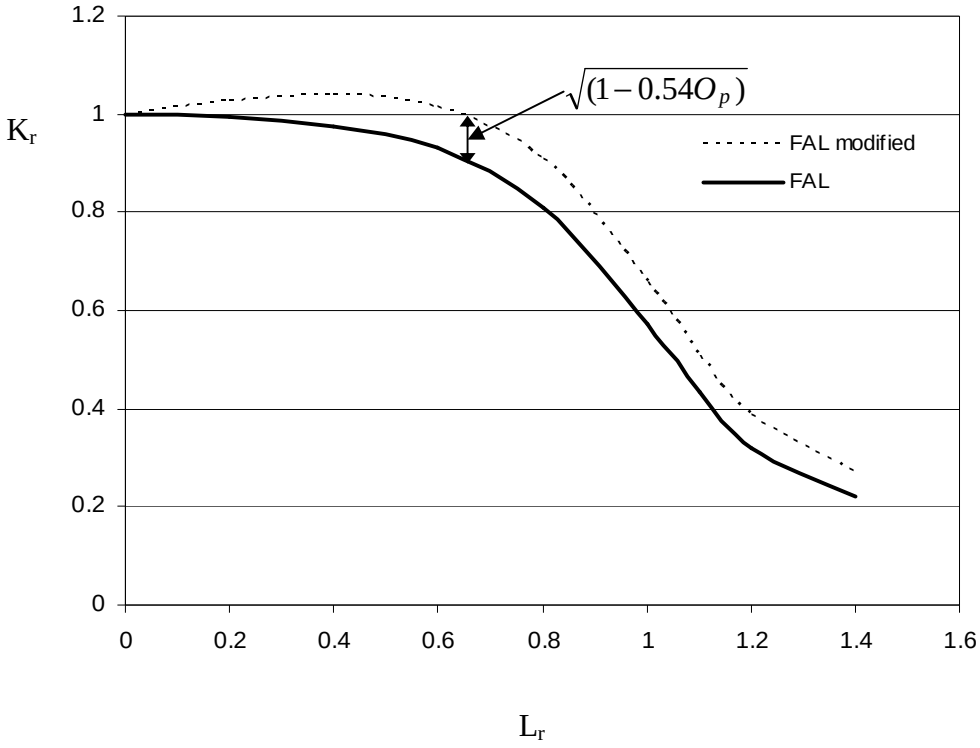

Figure 8.13: Modified failure assessment diagram based on out-of-plane constraint.

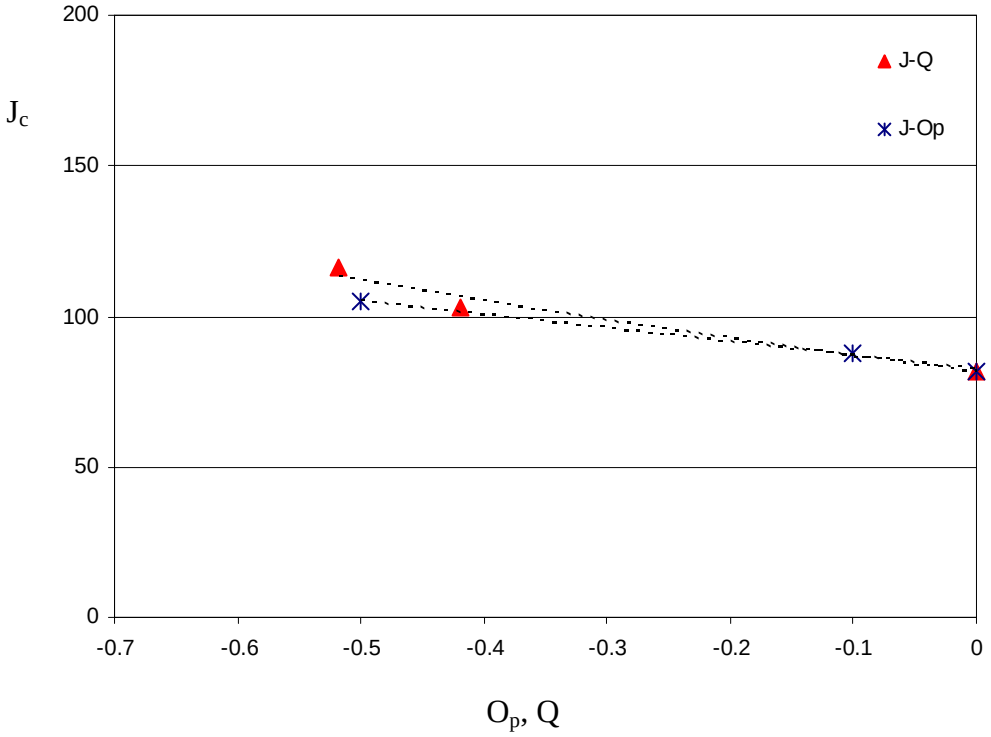

Figure 8.14: A comparison between J-Op and J-Q locus (J_c at Δa=0.2mm, Op and Q at $r=2J/\sigma_0$).

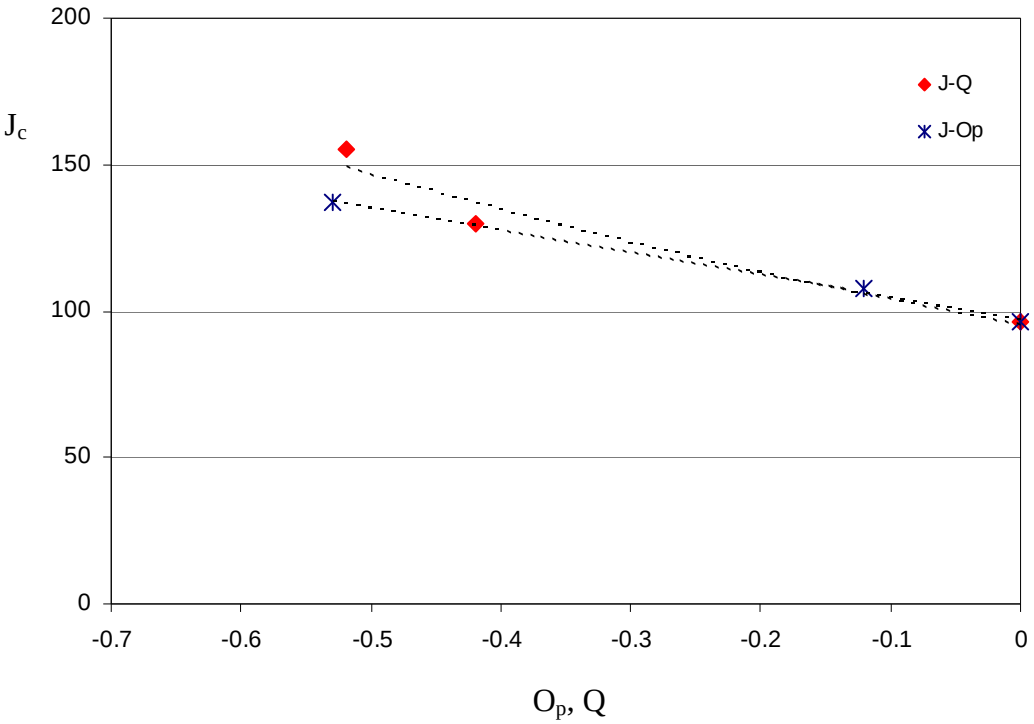

Figure 8.15: A comparison between J-Op and J-Q locus (J_c at Δa=0.4mm, Op and Q at $r=2J/\sigma_0$).

9. A procedure to determine ductile crack extension

A new procedure was developed to determine the ductile crack extension of semi-elliptical surface cracks in flat plates. The method is based on experimental ductile tearing resistance curves obtained from plane strain fracture mechanics specimens with a range of crack tip constraints. The resistance curve J-Δa depends on the mean stress which for plane strain specimens can be expressed as a function of the T-stress. The J-Δa resistance curves of Hancock, Reuter and Parks (1993) derived from deep and shallow edge cracked bend bars, CTS specimens, centre cracked panels and surface cracked panels shown in Figure (9.1) were used as the base data. This data was used to derive a relationship between the mean stress which is a function of the T-stress, and the tearing modulus $T_r=\partial J/E\partial a$. The mean stress can be simply written as a function of the T-stress:

$$\frac{\sigma_m}{\sigma_0} = 2.39 + \frac{T}{\sigma_0} = 2.39 + Q \qquad (9.1)$$

The term 'T/σ_0' quantifies the level of constraint at the crack tip in a similar way to the Q-parameter of O'Dowd and Shih (1991, 1992). The tearing modulus $T_r=(\partial J/(E\partial a))$ derived from Figure (9.1) is plotted as a function of the mean stress (Eq. 9.1) and is shown in Figure (9.2).

A reduction in the mean stress increases the slope of the J-Δa curve (hence increases the tearing modulus). A curve-fitting procedure gives the relation:

$$T_r = 0.0658 - 0.0557\left(\frac{\sigma_m}{\sigma_0}\right) + 0.0125\left(\frac{\sigma_m}{\sigma_0}\right)^2 \qquad (9.2)$$

The tearing modulus is thus taken to be a function of the current level of constraint, but to be independent of deformation level. That is to say the J-Δa curves are taken to be linear. The experimental data of Hancock et al (1993) was obtained under plane strain conditions and measured at limited deformation levels, so that constraint is only lost by in-plane effects. However for surface cracked panels it is clear that constraint can be lost by in-plane effects, by proximity to a free surface, and loss of plane strain conditions as well as effects due to the global bending impinging on the near tip field. It is now assumed that the tearing modulus only depends on the current level of mean stress through equation (9.2) for all mechanisms of constraint loss.

The applied J to cause a defined amount of crack extension Δa can then be written in terms of the tearing modulus which is a function of the mean stress:

$$J = J_{Ic} + \left(\frac{\partial J}{E\partial a}\right).\Delta a.E \tag{9.3}$$

Here it is convenient to define J_{Ic} as the applied value of J corresponding to the initiation of crack extension (Δa=0). This may be contrasted with the definition used in experimental programmes in which it is convenient to define J_{Ic} at a small amount of crack extension (i.e. Δa=0.2mm).

By rearranging equation (9.3), the crack extension can be in terms of plane strain fracture toughness and the tearing modulus as:

$$\Delta a = \left(\frac{J}{J_{Ic}} - 1\right) \Big/ \left(\frac{T_r.E}{J_{Ic}}\right) \qquad J \geq J_{Ic} \tag{9.4}$$

In order to present non-dimensional results the crack extension is normalised on the smallest uncracked ligament, b. Eq. (9.4) can then be re-written in a non-dimensional manner:

$$\frac{\Delta a}{b} = \left(J - J_{Ic}\right).\frac{1}{T_r.E.b} \qquad \text{For} \qquad J \geq J_{Ic} \tag{9.5}$$

Using equation (9.5) an estimate of the crack extension around the crack front can be made from a knowledge of J_{Ic}, the local values of J and the mean stress (at $2J/\sigma_0$) around the crack front, which defines the tearing modulus T_r.

To determine the crack shape pattern associated with continued ductile tearing from surface cracks, the initial crack shape was modelled and analysed for the local J-integral and the mean stress around the crack front. Although non-dimensional results are presented, the material used was assumed to be isotropic elastic-perfectly plastic with Young's modulus of 200 GPa, Poisson's ratio of 0.49, and a yield strength of 300 MPa. J_{Ic} was taken to be $b\sigma_0/100$ so that crack extension occurred in fully plastic conditions. Crack growth was then estimated using equation (9.5).

This procedure captures many of the key features of crack extension in surface cracked panels, notably crack extension depends on both the local J value and the local level of constraint. However in order to capture the effects of finite geometry changes a remeshing procedure was introduced. Following the first estimate of crack extension (defined as step zero) a new crack front was created by extending the original crack front by a small increment using equation (9.5). The crack growth increment at the point of the maximum growth on the crack front was chosen for convenience. The crack extensions at the other points around the crack front were scaled to be proportional to the extension at this point. A new finite element mesh was then created for each increment of crack growth and the new crack shape was re-analysed for the mean stress and the J-integral. As the material response was idealised as perfectly plastic, strain hardening does not raise the flow stress and the applied load changes only as the geometry changes the limit load. As the tearing-resistance curves are linear the increment ΔJ in each numerical step is related to the increment of local crack extension Δa.

The total value of J at each point around the crack front represents the sum of the increments of J:

$$J = \sum \Delta J \tag{9.6}$$

Similarly, the total crack extension at each point around the crack front is the sum of the increments of crack extension.

$$a = \sum \Delta a \tag{9.7}$$

This procedure was used to predict the ductile crack extension and crack shape sequences in a wide range of surface cracks shown in Table (9.1). All cracks were introduced in a large flat plate and subject to bending, uniaxial and biaxial tension. The results are presented in subsequent chapters for bending, uniaxial loading and biaxial loading, respectively.

	Dimension (mm)			Non-dimensional	
1-Deep cracks	W	a	c	a/W	a/c
	10	5	15	0.5	0.33
	10	5	10	0.5	0.5
	10	5	5	0.5	1
2- Shallow cracks	10	2	6	0.2	0.33
	10	2	4	0.2	0.5
	10	1	1	0.1	1

Table (9.1): The geometry of the surface cracks examined in this work.

Here a is the crack depth, c is the major axis of the semi-elliptical crack, the thickness was W, and b=W-a is the ligament at the deepest point. The width and length of the model were 2B, 2H respectively.

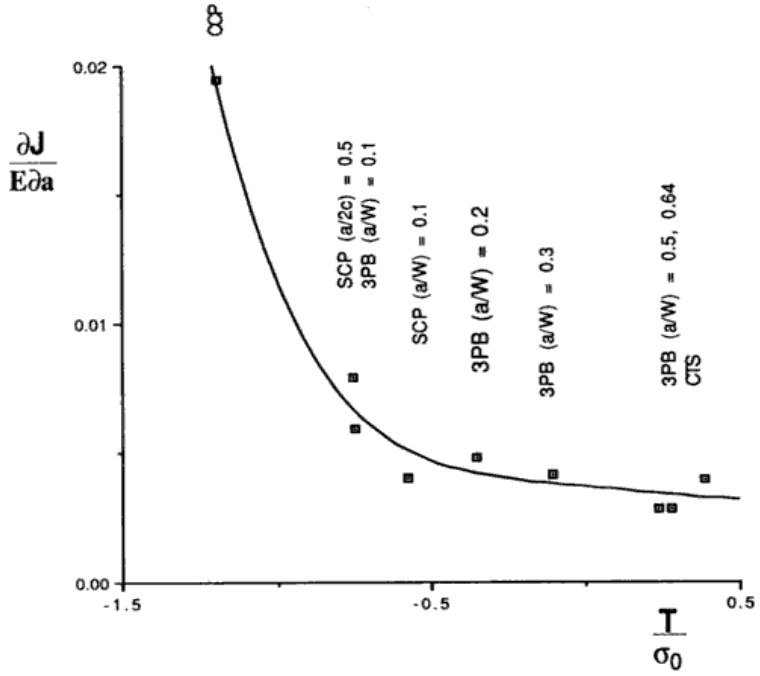

Figure 9.1: The slope of the J-Δa resistance curve as a function of T, after Hancock et al, (1993).

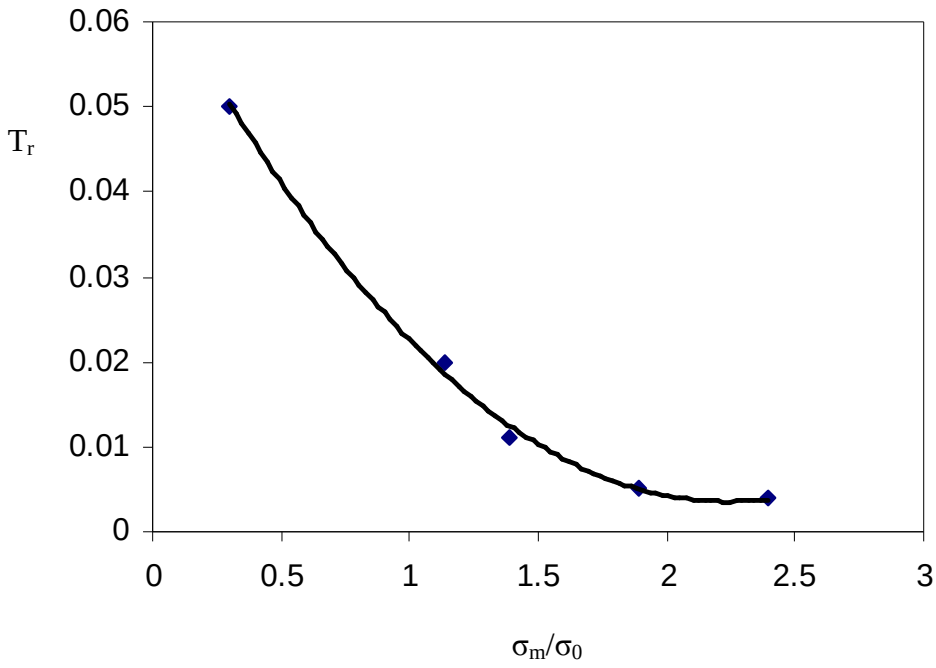

Figure 9.2: Tearing modulus as a function of the mean stress.

10. Deep semi-elliptical surface cracks in bending

10.1 Introduction

The effect of constraint on the three-dimensional cracks encountered in engineering practice is still problematic. The crack shape, size and type of loading all play a substantial role in the failure processes. Solutions for ductile crack growth taking account of constraint for surface cracks are not yet available in the literature. The shape of the advancing crack during ductile tearing needs to be understood in flaw evaluation procedures. Similarly it is important to determine the location where the crack growth initiates around the crack front. This identifies the corresponding toughness to be used in defect assessment procedures. In order to demonstrate the role of constraint in controlling the crack tip field a wide range of surface cracks were examined. The geometries studied are given in Table (9.1).

The chapter presents results from modelling semi-elliptical surface cracks subject to bending using finite element techniques. The material data, geometry and finite element model are initially presented. In order to validate the finite element model the stress intensity factor and elastic T-stress solutions were compared to the solutions available in the literature. A detailed study under elastic-plastic condition was then carried out. Initially the development of the plastic zone around the crack at both low deformation levels and in full plasticity is shown. Next, the mean stress, J-dominance conditions and proximity to plane strain at different parametric angles are discussed. The procedure developed in the Chapter (9) was then used to estimate the crack extension, and the evolution of the crack shape. Finally, force and moment redistribution were also investigated.

10.2 Material data

The material was taken to be isotropic elastic-perfectly plastic (n=∞) with Young's modulus of 200 GPa, Poisson's ratio of 0.49, and a yield strength of 300 MPa. However in general, non-dimensional results are presented. The material followed the Mises yield criterion and obeyed an associated flow rule. The notation is based on the cylindrical co-ordinate system shown in Figure (10.1).

10.3 Finite element model

To capture an accurate stress profile near the crack tip a very refined mesh was used close to the crack front. To allow for the correct form of stress singularity at the stationary crack tip under elastic-plastic conditions, collapsed three dimensional continuum hexahedral elements with reduced integration C3D8R with coincident but independent nodes were used. To ease meshing, a mesh for a semi-circular cut-out encompassing the crack front was created. Then a Matlab routine was developed to collapse the ring of nodes from the cut-out to the crack tip. The average element size was in the range of w/1000-2000 along the crack front, where w is the plate thickness. The elements were biased towards the free surface to accommodate stress gradients. Due to symmetry only one quarter of the geometry was modelled and symmetry boundary conditions were imposed on the appropriate surfaces as shown in Figure (10.2). The load was applied as displacement boundary condition. The J-integral was evaluated with the domain integral technique adopted in ABAQUS using a contour defined in the far field where J-integral is still path-independent.

For deep semi-elliptical cracks (a/w=0.5, a/c=1) thirty concentric rings of elements extended radially from the crack tip. Each ring contained 400 elements: 40 elements along the crack front and 10 around the half circumference. The total number of elements was 107,672. The mesh is shown in Figure (10.3). For deep semi-elliptical surface cracks (a/c=0.5) forty concentric rings of elements were created around the crack tip. Each ring contained 300 elements: 30 elements along the crack front and 10 around the half circumference. The total number of elements was 132,153. The mesh is shown in Figure (10.4). For deep semi-elliptical surface cracks (a/c=0.3) thirty concentric rings of

elements were created around the crack tip. Each ring contained 450 elements: 45 elements along the crack front and 10 around the half circumference. The total number of elements was 95,494. The mesh is shown in Figure (10.5).

10.4 Deep semi-elliptical surface crack in bending (a/c=1, a/w=0.5)

10.4.1 Benchmark results

The stress intensity factor was first determined from the finite element model of a deep semi-circular surface crack and benchmarked with published results by Newman and Raju (1981). The stress intensity factor was normalised by the applied stress and the square root of the crack length at the deepest point, a, and is plotted as a function of the parametric angle θ as shown in Figure (10.6). Good agreement was observed between the two data sets.

Figure (10.7) compares the elastic T-stress with the three dimensional solution by Wang (2003), and the two dimensional solution of Sham (1991). Values of the T-stress for a single edge notched bar in three point bending in the range a/w=0.1-0.5 were used for comparison. The comparison was made by considering the depth ratio a/w in two dimensional solution to be the same as depth ratio a`/w in the three dimensional model where a` = a cos(θ), as shown in the Figure (10.7). It can be seen that the T-stress in the 3-D solution in both the current analysis and Wang's solution exhibited negative values for ratios a`/w < 0.34 and became more negative as the surface was approached. The T-stress was positive at the deepest point. It should be noted that the solution given by Wang (2003) does not include the elastic T-stress at the free surface, and thus the value of T-stress at the surface may be unreliable. It is interesting to note that the T-stress distribution in 3-D was similar to 2-D in the range ($0.15 \geq a`/w \leq 0.5$). However a difference between the 2-D and the 3-D solutions occurred at a/w less than 0.15 or $\theta \geq 72.5^{\circ}$ and became significant at the free surface where the T-stress was highly compressive. The difference arises as the T-stress at the free surface in 3-D is perpendicular to the surface but in 2-D is parallel.

10.4.2 Crack tip stress fields in full plasticity

Figure (10.8) shows that plasticity developed from the crack near free surface and reduced towards the deepest point. This is due to the largest stress intensity factor which was located at the free surface. Figure (10.9) shows that plasticity develops across most of the cross section of the plate at a deformation level of $b\sigma_0/J\approx220$. Here b is the minimum uncracked ligament (w-a) and J is the J-integral, taken at the deepest point. Even at this deformation level a narrow elastic segment was confined to the centre of the plate along the neutral axis. As a result the deepest point of the crack remained elastic due to its proximity to the neutral axis. In the ligament at the deepest segment an elastic hinge was observed. The body had completely yielded at a deformation level of approximately $b\sigma_0/J \approx 25$ as shown in Figure (10.10).

The mean stress at the crack tip (r=0) and at a distance $r=2J/\sigma_0$ at the deepest point ($\theta=0^{\circ}$) is shown in Figure (10.11).The figure shows that the mean stress at the crack tip (r=0) reaches the HRR field value ($2.39\sigma_0$), and that a highly constrained J-dominant field was maintained at the crack tip at all deformation levels. At a distance $r=2J/\sigma_0$ J-dominance was lost at a deformation level $b\sigma_0/J$ =110, and the mean stress, which was distance independent at low deformation levels became distance dependent.

Using the co-ordinate system shown in Figure (10.1), the ratio of the out of plane to the sum of in-plane stresses, $T_z = \sigma_{zz}/(\sigma_{rr}+\sigma_{\theta\theta})$ was used to measure the proximity to plane strain conditions. Figure (10.12) shows that the ratio $\sigma_{zz}/(\sigma_{rr}+\sigma_{\theta\theta})$ at the crack tip (r=0) is largely independent of the deformation level and reaches the value of plane strain (0.5). For finite radial distances, the proximity to plane strain became dependent on the deformation level. At low deformation levels plane-strain conditions were maintained. However as deformation increased ($b\sigma_0/J\leq110$) plane strain conditions were lost.

It is of interest to determine the specimen size requirement to maintain J-dominance in the near tip field. In Figure (10.13) the mean stress is plotted as a function of the non-dimensional distance $r\sigma_0/J$ from the crack tip. The J-dominance criterion used here is that of Shih and German (1981), which requires that the mean stresses are within 90 % of HRR field. At low levels of deformation ($b\sigma_0/J\approx936$), a J-dominant field was maintained even at relatively large distances from the crack tip ($r\sigma_0/J=16$). With increased levels of

deformation, the J-dominant field shrank. In full plasticity ($b\sigma_0/J \leq 220$) a J-dominant field was limited to distances less than $4J/\sigma_0$. Figure (10.14) shows the relationship between the level of deformation and the non-dimensional distance from the crack tip, at which J-dominance is maintained. At low deformation levels a J-dominant field was established over large crack tip distances. With increased levels of deformation the extent of the high mean stress (hence J-dominant region) reduced to $r\sigma_0/J \leq 2$ at $b\sigma_0/J \approx 110$. A single parameter is insufficient to describe the crack tip fields at $2J/\sigma_0$ at deformation levels of $b\sigma_0/J < 110$. This broadly coincides with development of large scale plasticity across the uncracked ligament as shown in Figures (10.9) and (10.10).

Figure (10.15) shows the mean stress at the crack tip (r=0) and at a distance $2J/\sigma_0$ as a function of deformation at the parametric angle of 45˚. The mean stress at the crack tip (r=0) reached the HRR field ($2.39\sigma_0$) for all levels of deformation. At $2J/\sigma_0$ the mean stress was within 90 % of the HRR field up to a deformation level of $b\sigma_0/J \approx 60$. This may be compared to a significant loss of constraint at the deepest point in full plasticity. Figure (10.16) shows that the proximity to plane strain conditions at the crack tip (r=0) and at $r=2J/\sigma_0$ were maintained at low and high deformation levels.

At θ=70˚the mean stress at the crack tip (r=0) and at $2J/\sigma_0$ fell below the plane strain HRR field value even at low deformation levels as shown in Figure (10.17). The low value of mean stress could be due to the effect of the compressive T-stress (Fig. 10.7) at this location which caused in-plane constraint loss. To investigate this further, the mean stress is plotted in Figure (10.18), and compared to the mean stress obtained from a 2D solution using the Q-parameter, derived from the T-stress (Karstensen 1996):

$$\frac{\sigma_m}{\sigma_0} = \left(\frac{\sigma_m}{\sigma_0}\right)_{SSY} + 0.83\left(\frac{T}{\sigma_0}\right) - 0.88\left(\frac{T}{\sigma_0}\right)^2 \qquad (10.1)$$

This relationship was derived for a non-hardening material under contained yielding using a plane strain modified boundary layer model and is valid at distances in the range $1 < r\sigma_0/J < 5$ for a negative T-stress. In-plane constraint loss at 70˚still did not explain the

difference between the SSY solution and the full three-dimension stress in full plasticity ($J/b\sigma_0$>0.01). This is due to other effects such as out-of-plane effect or change in the force to moment ratio which may affect the crack tip field in full plasticity. The proximity to plane strain was maintained at (0.37) which is below the plane strain level of (0.5) as shown in Figure (10.19). The force to moment ratio is examined in section (10.4.4).

Figure (10.20) shows that the mean stress at distances $r=2J/\sigma_0$ and r=0 reaches the plane stress value (0.577) at the free surface. However the mean stress at $2J/\sigma_0$ reduced with increase in deformation to uni-axial stress (0.3).

Figure (10.21) shows the mean stress at a distance $r=2J/\sigma_0$ around the crack front, from contained yielding to fully plasticity. The largest mean stress under contained yielding ($b\sigma_0/J$> 110) occurred at the deepest point and the mean stress decreased gradually around the crack circumference reaching its smallest value at the free surface. In full plasticity ($b\sigma_0/J$<100), a significant reduction in the mean stress was observed at the deepest point, and the greatest mean stress was located at $\theta=45^{\circ}$.

Figure (10.22) shows that plane strain conditions were maintained at low deformation levels along the crack front from the deepest point to 70°. In full plasticity, plane strain conditions were lost at the deepest point, as well as the free surface. Figure (10.23) shows the non-dimensional J-integral along the crack front. The J-integral was largest at 70° rather than at the deepest point or the free surface (Terfas, 2009, and Terfas and Bezensek, 2009a).

10.4.3 Determination of crack growth of a deep semi-circular surface crack under bending.

Crack growth around the semi-circular crack (a/c=1) was predicted using the procedure described in Chapter (9). Figure (10.24) shows crack growth around the crack front from the deepest point to the free surface. It can be seen that the crack is predicted to extend most in the angular range 45° - 70° compared to the deepest point or the free surface. This reflects the observation that the mean stress and the J-integral were largest in this angular range at high deformation levels (Terfas 2009, Terfas and Bezensek 2009a). For crack

shape sequence, the results show a consistent trend for the mean stress and J-integral around the crack front, and the largest crack extension was consistently at 45°, as shown in Figure (10.25). Figure (10.26) shows the steps of crack growth for a deep semi-circular surface crack under bending. It can be seen that the crack is predicted to extend sub-surface and to be suppressed at the deepest point and the free surface resulting a boat shape. This is a different profile to that develops in fatigue where the crack grows through the thickness and a semi-elliptical shape is maintained (Scott and Thorpe, 1981). Figure (10.27) shows the crack surface area as a function of global deformation, here taken as the deflection normalised by the span.

10.4.4 Force-moment redistribution along a deep semi-circular surface crack a/c=1, a/w=0.5 in bending.

This section investigates how the force to moment ratio changes with deformation and how this affects the crack tip conditions. The opening stress $\sigma_{\theta\theta}$ was extracted from the model through thickness paths originating on the crack front and extending to the remote face as shown in Figure (10.28). Four such paths were considered, at θ=0°, 45°, 70° and 90°. The paths are designated as (1), (2), (3) and (4).

The local forces per unit thickness, F, were calculated from the area under the stress-distance curve by integrating:

$$F = \int \sigma_{\theta\theta}(y).dy \tag{10.2}$$

The moment per unit thickness, M, was calculated as:

$$M = \int \sigma_{\theta\theta}(y).y.dy \tag{10.3}$$

Initially the non-dimensional force ($F/b\sigma_0$) and moment ($M/b^2\sigma_0$) redistributions are shown, followed by the force-moment ratio, F.b/M, where b is the uncracked ligament at the deepest point (a constant) and σ_0 is the yield stress.

Figure (10.29) shows the distribution of opening stress $\sigma_{\theta\theta}$ at the deepest point (path1) as a function of a non-dimensional distance (d/w) from the crack front through the thickness. The figure shows that at deformation levels ($b\sigma_0/J=936$) the stress field is predominantly elastic. At higher deformation levels ($b\sigma_0/J=32$) in the ligament the compressive field grew at the expense of the tensile field, resulting in the ligament being subject to an opening moment and a closing force.

Figure (10.30) shows the opening stress for the parametric angle 45˚(path2) at low and high levels of deformation $b\sigma_0/J=936$ and 32. In both cases the tensile field was larger than at the deepest point ($\theta=0$˚). Figure (10.31) shows the opening stress for a parametric angle 70˚(path3) as a function of a distance (d/w). At low deformation levels $b\sigma_0/J=936$ the tensile stress was similar to the compressive stress. As the deformation increased the near tip field was subjected to an enlarged tensile field, and a compressive field on the back face.

The force and moment redistribution are shown in Figures (10.32) to (10.36). Figure (10.32) shows a gradual increase in the moment at the deepest point ($\theta=0$˚, path1) compared to a significant increase in the compressive force as deformation increases. The ligament was thus subject to an opening moment and closing compressive force. Figure (10.33) shows the force and moment at 45˚(path2) change very little with deformation. The compressive force at 45˚was small compared to the deepest point. At 70˚(path3) the ligament was subject to an opening moment and a tensile force as shown in Figure (10.34). The tensile force and the opening moment both increased particularly in full plasticity. The tensile force and opening moment caused the significant increase in the J-integral at this angle as observed in the previous section. A fully tensile field occurred at the free surface ($\theta=90$˚, path4) as shown in Figure (10.35).

Figure (10.36) shows the force-moment ratio (F.b/M) plotted as a function of deformation for the paths shown in Figure (10.28). It can be seen that the uncracked

ligament at the deepest point was subjected to opening bending moment and compressive force. The compressive force reduced both the mean stress and the J-integral, and consequently the crack no longer extended at this position in full plasticity. At the parametric angle 45˚ the ratio was slightly negative and smaller than at deepest point. At 70˚ the ligament was subjected to a tensile force and an opening bending moment, which increased with deformation. At the free surface (θ=90˚, path4) the force-moment ratio was also positive.

10.5 A deep semi-elliptical surface crack (a/w=0.5, a/c=0.33) in bending

10.5.1 Crack tip stress field

Figure (10.37) shows that plasticity initially developed from the crack at the free surface but was suppressed at the deepest point. The plastic zone also developed from the back face towards the crack front in the uncracked ligament.

Figure (10.38) shows the mean stress at the crack tip (r=0) and at $2J/\sigma_0$ as a function of deformation at the deepest point (θ=0˚). At the crack tip, a high level of constraint was observed at all levels of deformation. At $2J/\sigma_0$ a high level of constraint was maintained up to $b\sigma_0/J=80$. This may be compared with the semi-circular crack when J-dominance was lost at a lower deformation level of $b\sigma_0/J=110$ as shown in Figure (10.39).

Figure (10.40) shows the mean stress at $2J/\sigma_0$ around the crack front from the deepest point to the free surface. The mean stress reached the highest values at θ=0˚ and 22.5˚ in contained yielding, however as deformation increased ($b\sigma_0/J<80$) the mean stress reduced to less than 90% of the plane strain HRR value. At 45˚ a high mean stress was maintained even at high deformation levels ($b\sigma_0/J=60$). At 70˚ and 77.5˚ the mean stress reduced significantly with deformation. At the free surface the mean stress exhibited the plane stress value ($0.577\sigma_0$). Figure (10.41) shows the largest J-integral occurs at 70˚, and the smallest values are located at the deepest point and the free surface.

The proximity to plane strain conditions at the crack tip (r=0) and at $2J/\sigma_0$ is shown in Figures (10.42) and (10.43). At the crack tip, plane strain conditions were maintained between the deepest point and 77.5˚ at all deformation levels. However, at $2J/\sigma_0$ plane

strain conditions were lost at high deformation levels over the most of the crack front but remained close to the plane strain value at the parametric angle θ=45°.

10.5.2 Crack growth

The procedure described in Chapter (9) was applied for a semi-elliptical surface crack (a/c=0.33) to predict ductile crack growth. Crack growth as a function of a parametric angle θ is shown in Figure (10.44). It can be seen that growth occurred with a higher rate at θ=45° than at the deepest point, where crack growth was suppressed. To establish a crack shape sequence, two more steps were determined after the initial crack extension. Figures (10.45) and (10.46) show that the maximum crack growth for the first and the second steps also occurred at 45°. Crack growth was suppressed at the deepest point and at the free surface, and the crack grew beneath the surface as shown in Figure (10.47). Figure (10.48) shows the crack surface area as a function of deflection normalised by the span.

10.5.3 Force-moment redistribution along semi-elliptical surface cracks (a/c=0.33, a/w=0.5) in bending.

Figures (10.49) to (10.52) show the force and moment redistribution for a deep semi-elliptical surface crack (a/c=0.33, a/w=0.5). Figure (10.49) shows an increase in both the opening moment and the compressive force as the deformation increases at the deepest point (θ=0°, path1). Little change in the force and moment was observed at 45°(path2) as shown in Figure (10.50). At 70°(path3) both the tensile force and moment increased with deformation as shown in Figure (10.51), and a tensile force dominated the ligament. Figure (10.52) shows the force to moment ratio as a function of deformation. It can be seen that the force-moment ratio changed along the crack in a similar manner to that observed for a deep semi-circular crack. At the deepest point the ratio became more negative due to the compressive force, while the ratio was close to zero at 45°. At 70°the force to moment ratio was positive due to the presence of a tensile force. This indicates the loss of constraint at the deepest point was due to the compressive force which inhibited crack growth, while at 45°-70°constraint was maintained due to the tensile field combined with an opening moment.

10.6 Deep semi-elliptical crack (a/w=0.5) in bending with aspect ratio a/c=0.5.

The plastic zone for deep surface cracks with a/c=0.5 developed initially at the free surface as shown in Figure (10.53). It then developed across the uncracked ligament due to the effect of bending moment on the uncracked section. Figure (10.54) shows the non-dimensional J-integral as a function of the parametric angle, θ. The maximum J-integral was located in the angular range 45° - 70°, while the smallest J was at the deepest point and at the free surface.

The mean stress at $r\sigma_0/J=2$ around the crack is shown in Figure (10.55). High constraint levels were maintained at the deepest point under small scale yielding, and lost in full plasticity ($b\sigma_0/J=100$). However the mean stress remained high at 45° and at 70°. Figure (10.56) shows the proximity to plane strain as a function of deformation. It can be seen that plane strain conditions were maintained along the crack front from the deepest point to 70°. However plane strain conditions were lost at the deepest point in large scale yielding and the associated J-dominance was lost as well. The results in Figure (10.57) show that the largest crack extension occurred at 45° as deformation increases and crack growth decreases at the deepest point due to the global bending effect.

10.7 Discussion

Deep surface cracks in bending initially exhibited a highly constrained J-dominant field under small scale yielding conditions at the deepest point; however the constraint was lost in full plasticity. The loss of a single parameter characterisation (J-dominance) occurred at approximately $b\sigma_0/J=110$ for semi-circular cracks (a/c=1), and increased as the value of a/c decreased reaching $b\sigma_0/J=80$ for semi-elliptical cracks (a/c=0.33) as shown in Figure (10.58). The loss of J-dominance could be due to the effect of the compressive force that dominated the ligament at the deepest point in full plasticity. Surface cracks have curved crack fronts that feature big variations in the stress triaxiality and J-integral along the crack front. Therefore the fracture toughness determined from

the standard J-test is generally conservative when apply to components containing surface cracks.

The largest mean stresses under small scale yielding conditions occurred at the deepest point and decreased gradually towards the free surface. In full plasticity ($b\sigma_0/J<100$) global bending and out-of-plane effects reduced crack tip constraint at the deepest point, and the maximum mean stress occurred at $\theta=45^{\circ}$.

Plane strain conditions were maintained at low deformation levels along the crack front from the deepest point to approximately 70°. In fully plasticity plane strain conditions were lost at the deepest point and near the free surface but were maintained in the range 45°-70°. The high levels of crack tip constraint located in the angular range 45°-70° caused maximum crack growth at this range, while growth suppressed at the deepest point due to the compressive force which dominated the ligament.

Figure (10.58) shows that the mean stress at the deepest point increases as a/c ratio reduces. This effect was not observed at the other positions on the crack, 45° and 70°, as shown in Figures (10.59) and (10.60), where the same mean stress developed irrespective of the crack aspect ratio.

It was also shown that the force-moment ratio became negative as deformation increased with a closing force and an opening moment at the deepest point ($\theta=0^{\circ}$, path1). The closing force reduced the crack tip constraint and caused loss of J-dominance at the deepest point, consequently crack extension stopped. At 45° (path2) the force-moment ratio was close to zero. However at 70° (path3) the ratio became positive and increased with deformation due to the presence of a highly tensile force. The tensile field combined with an opening moment caused a high constraint and a significant growth in the angular range (45°-70°). As a result the crack was predicted to grow sub-surface developing a boat shape which agrees with Gao et al (1998) who predicted that the maximum crack growth under pure bending occurs below the surface.

10.8 Conclusion

It can be concluded that a J-dominant field was maintained at the deepest point and at 45° at low deformation levels ($b\sigma_0/J>100$). At 70° the mean stress was below the HRR field. The loss of J-dominance at the deepest point in the three dimensional surface configuration was observed at much lower deformation levels ($b\sigma_0/J=110$) than for the 2-D plane strain edge cracked bend bar where the J-dominance was lost at $b\sigma_0/J<25$ (Shih and German, 1981, McMeeking and Parks, 1979).

The distributions of crack tip constraint and J-integral around the crack front at large deformation levels were different from that at small deformation levels. This emphasises that both, the mean stress and the J-integral were geometry and load dependent, and consequently have a strong effect on ductile crack growth. The J-integral alone can not control crack growth and crack tip constraint must also be accounted for. Deeply surface cracked geometries tended to grow sub-surface developing a boat shape. Current findings provide detailed solutions of the constraint and the J-integral for semi-elliptical surface cracks, and identify the segment around the crack front that has the lowest resistance to ductile tearing and the segment where crack growth is inhibited.

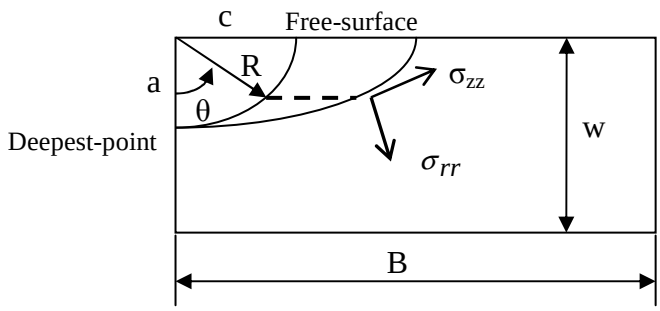

Figure 10.1: Illustration of the notation and the cylindrical coordinate system.

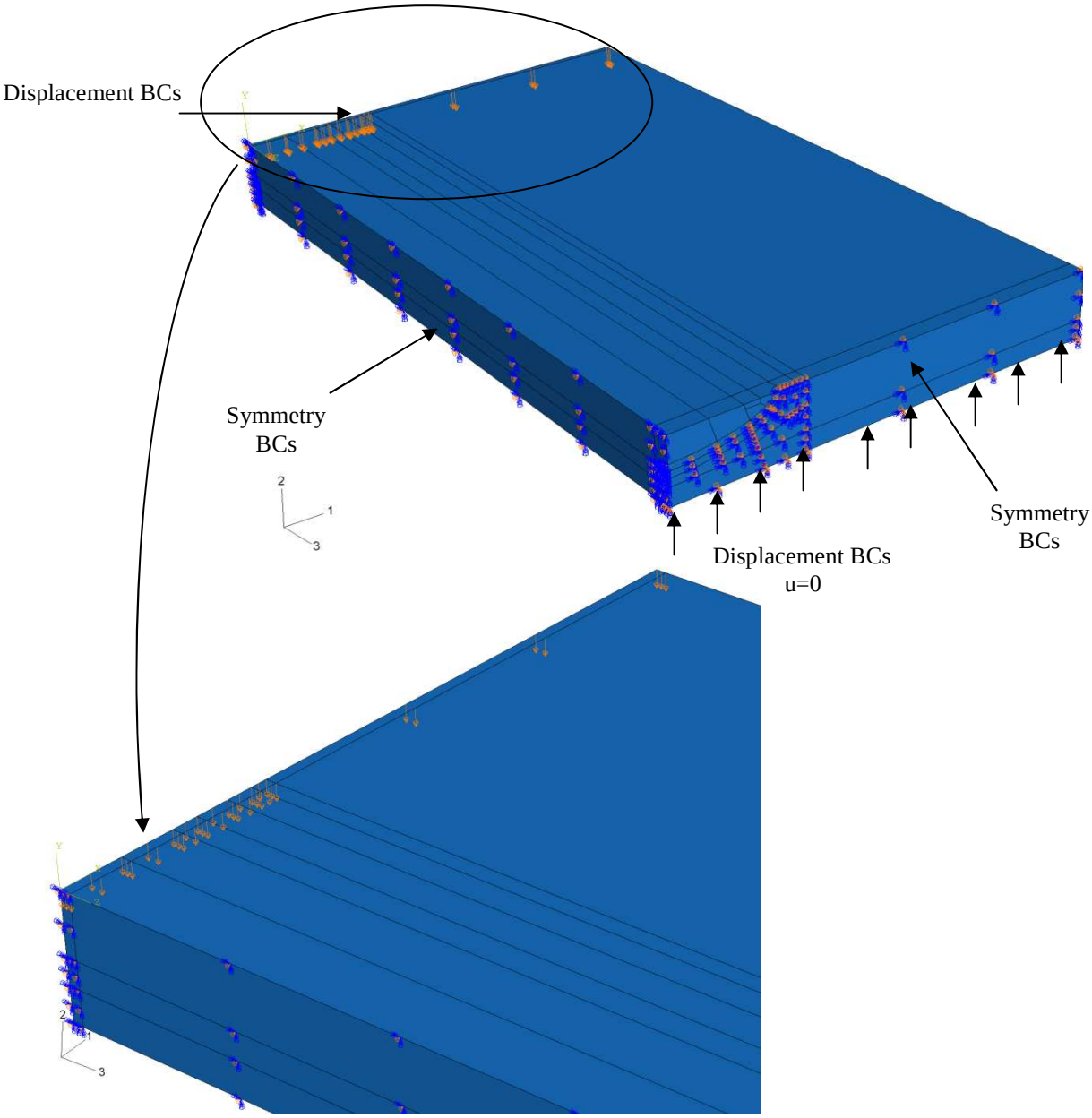

Figure 10.2: Quarter model and boundary conditions for elastic-plastic analysis.

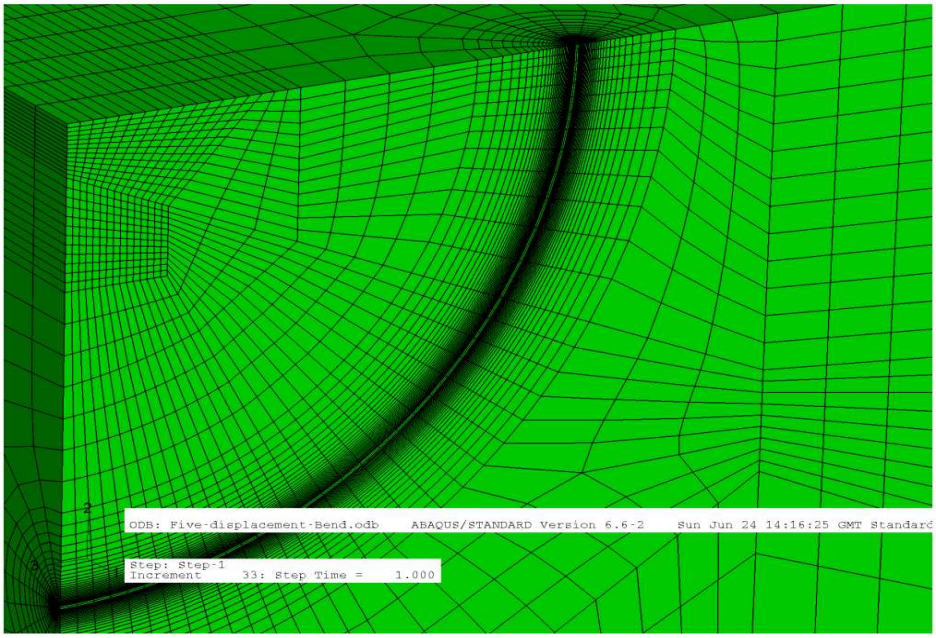

Figure 10.3: The mesh of a deep semi-circular surface crack (a/w=0.5, a/c=1).

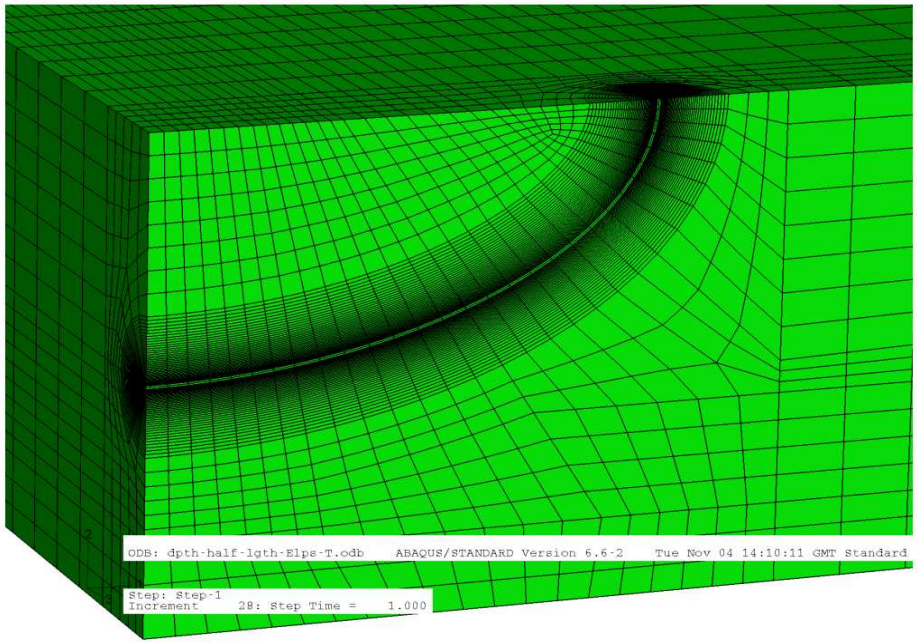

Figure 10.4: The mesh for a deep semi-elliptical surface crack with a/w=0.5, a/c=0.5

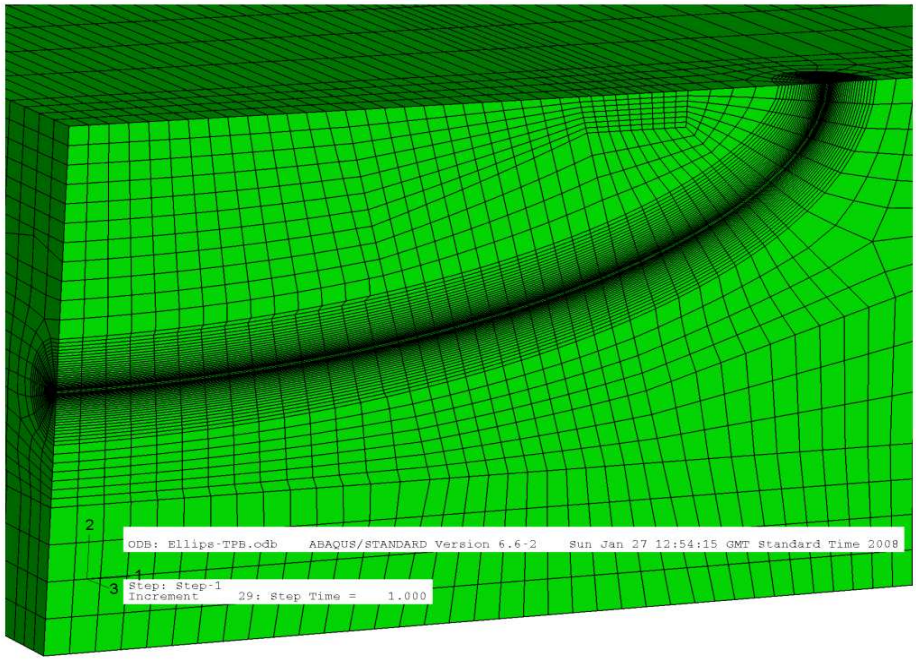

Figure 10.5: The mesh for a deep semi-elliptical surface crack with a/w=0.5, a/c=0.3

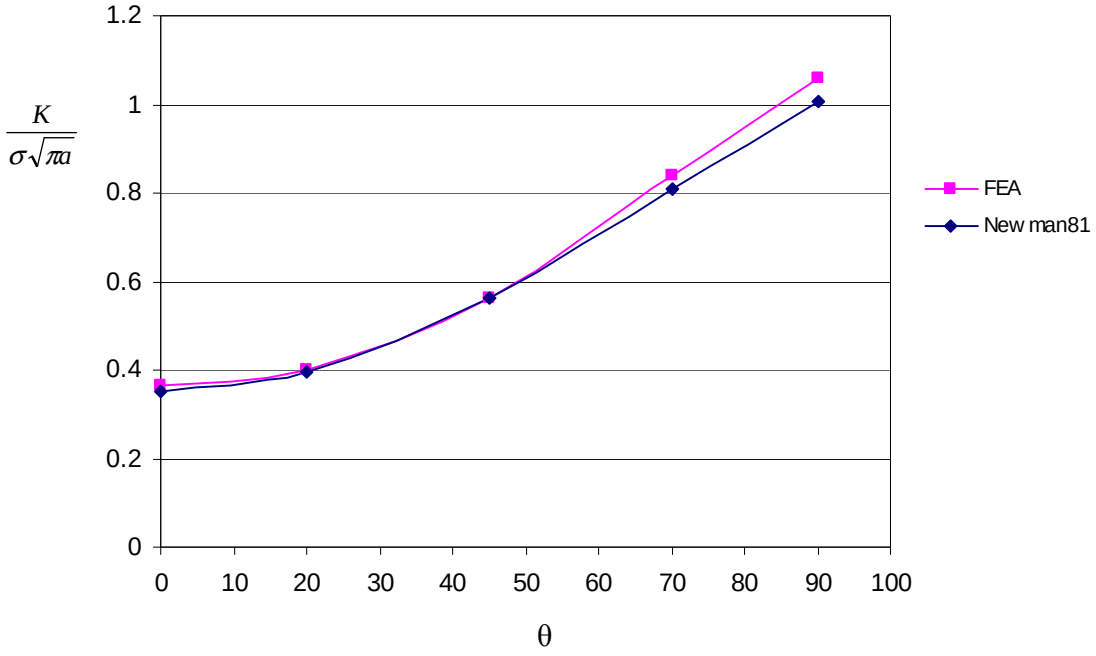

Figure 10.6: Benchmark of the stress intensity factor K in a semi-circular surface crack (a/w=0.5, a/c=1) under bending with Newman and Raju solution (1981).

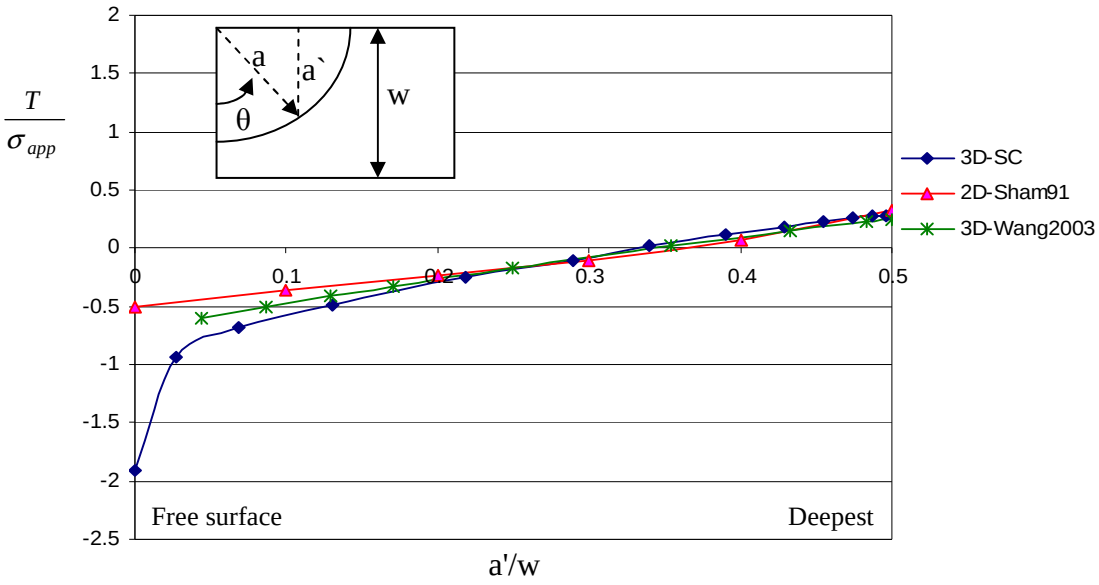

Figure 10.7: Benchmark of the elastic T- stress in a deep semi-circular surface crack with Wang's solution (2003), and compared with two dimensional solution (Sham, 1991).

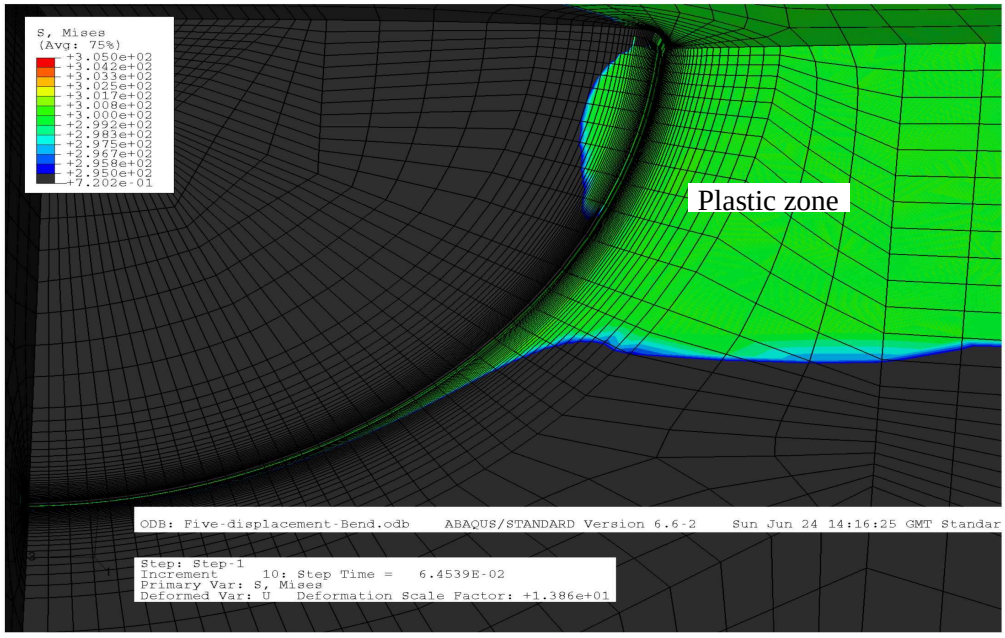

Figure 10.8: A small plastic zone developed at the deepest point (θ=0˚) compared to the plastic zone in the angular range θ=70˚-90˚($b\sigma_0/J$ =936, at θ=0˚), (a/w=0.5, a/c=1).

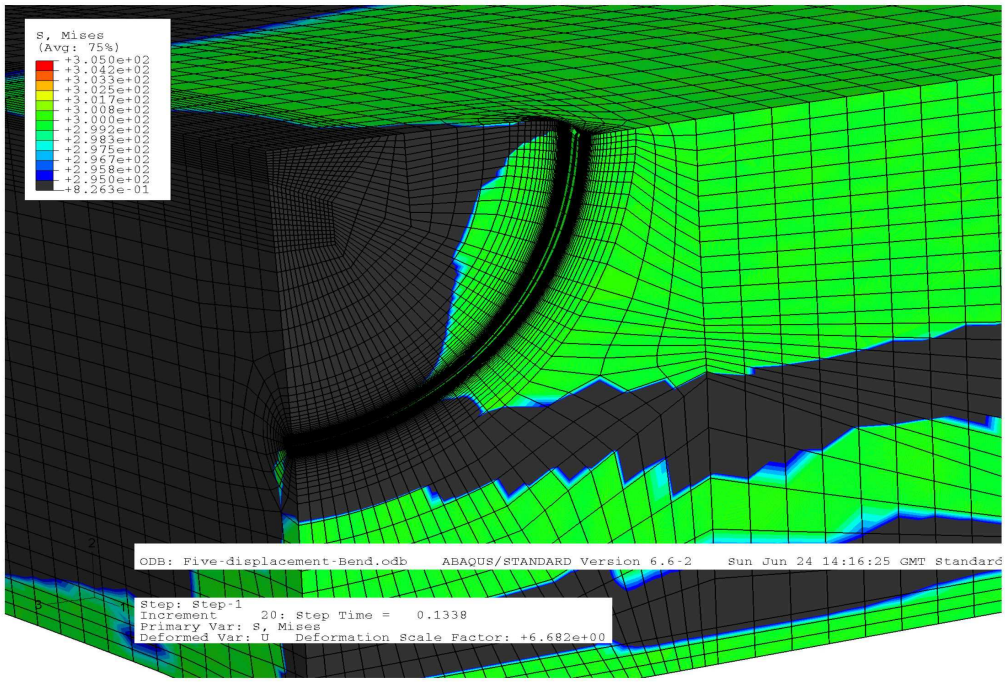

Figure 10.9: An increase in plasticity in the angular range 45˚-90˚ compared to the deepest point ($b\sigma_0/J=220$, at $\theta=0$˚), ($a/w=0.5$, $a/c=1$).

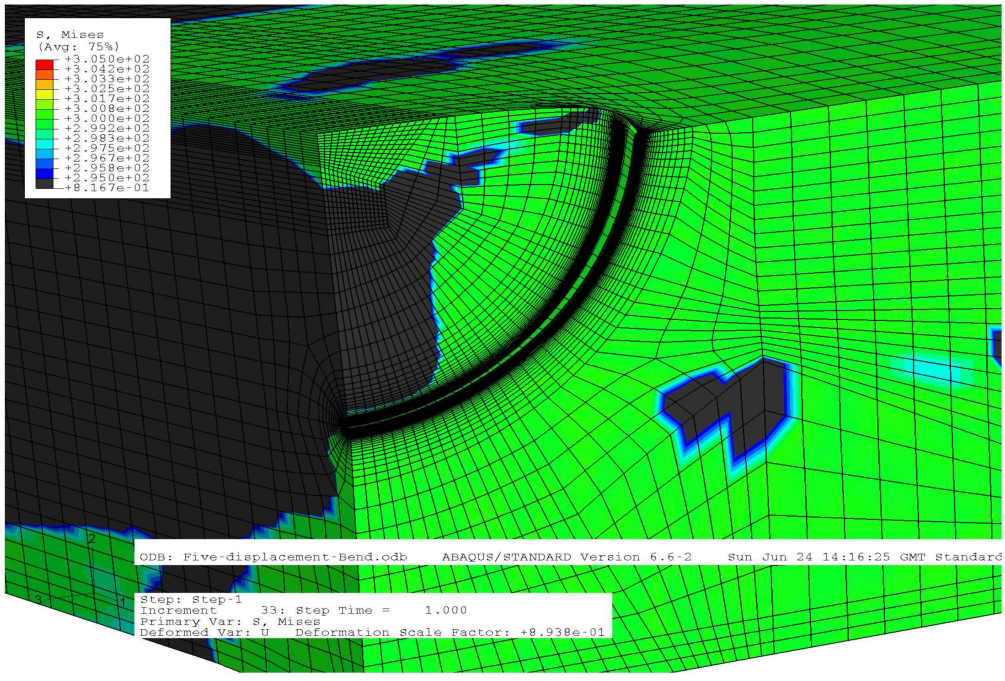

Figure 10.10: Full plasticity across the entire body ($b\sigma_0/J=25$, at $\theta=0$˚), ($a/w=0.5$, $a/c=1$).

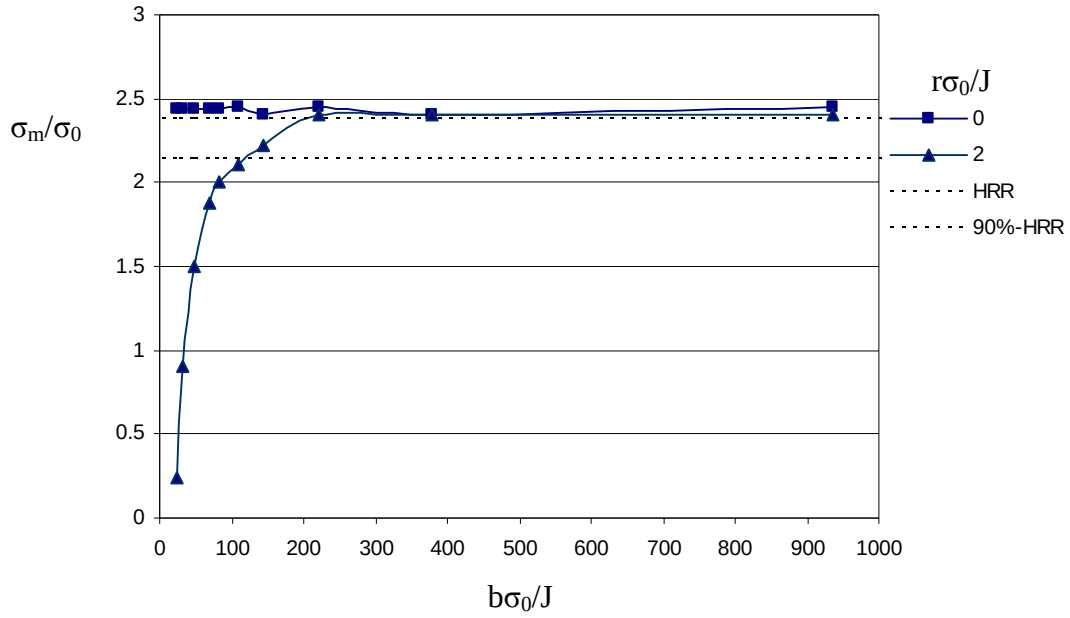

Figure 10.11: The mean stress as a function of the level of deformation for θ=0˚, at the tip (r=0) and at a distance $r\sigma_0/J=2$, (a/w=0.5, a/c=1).

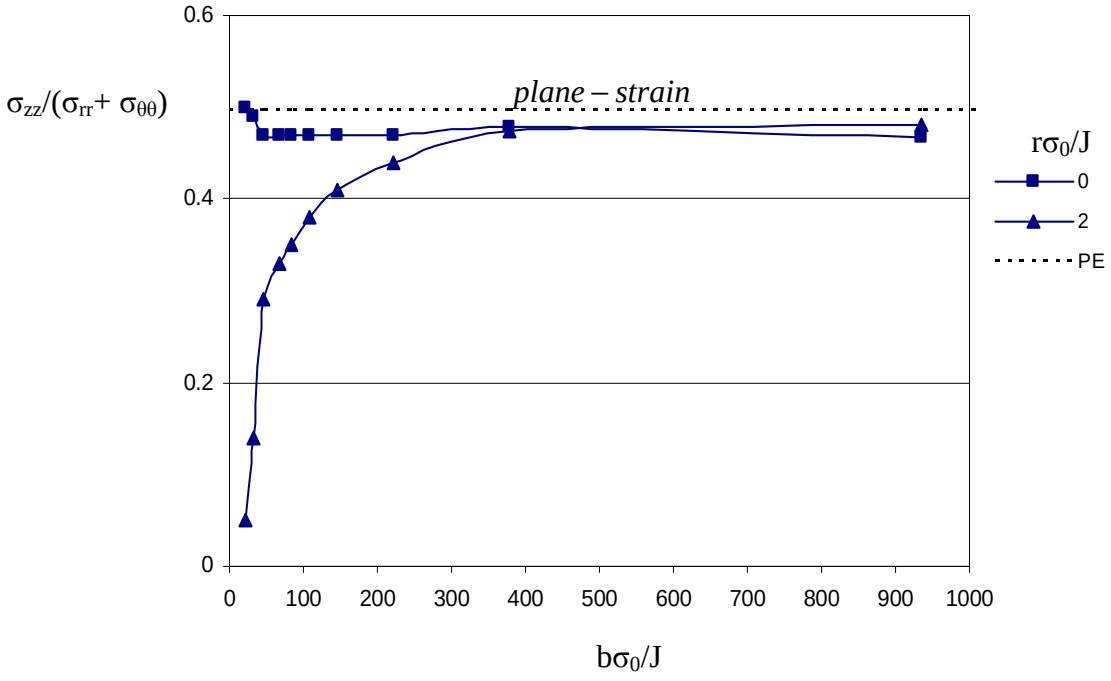

Figure 10.12: Proximity to plane strain conditions at the deepest point (θ=0˚) as a function of the level of deformation at the tip (r=0) and at ($r\sigma_0/J=2$), (a/w=0.5, a/c=1).

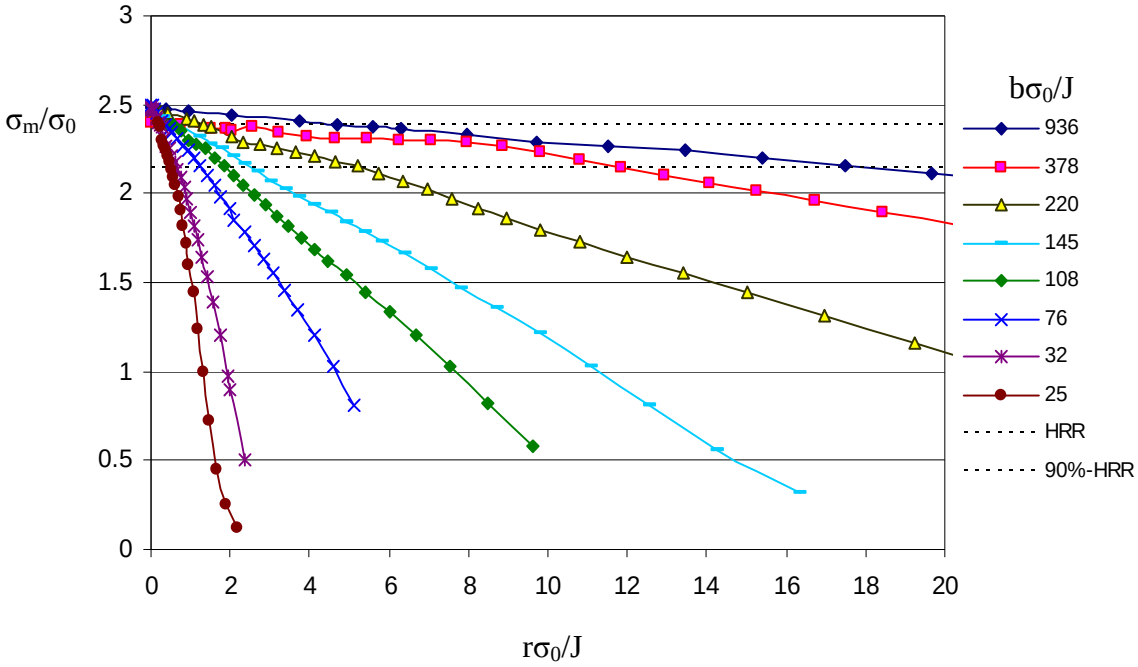

Figure 10.13: The mean stress at the deepest point (θ=0̊) as a function of the non-dimensional distance for a deep semi-circular surface crack (a/w=0.5, a/c=1).

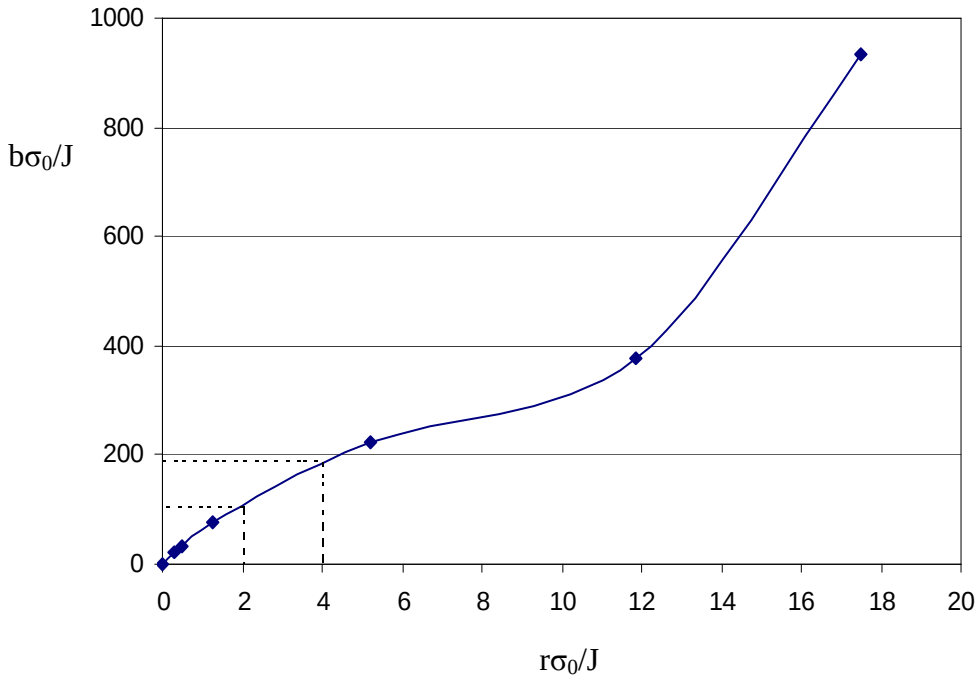

Figure 10.14: The size requirement for the J-Dominance at the deepest point (θ=0̊) of a deep semi-circular surface crack (a/w=0.5, a/c=1).

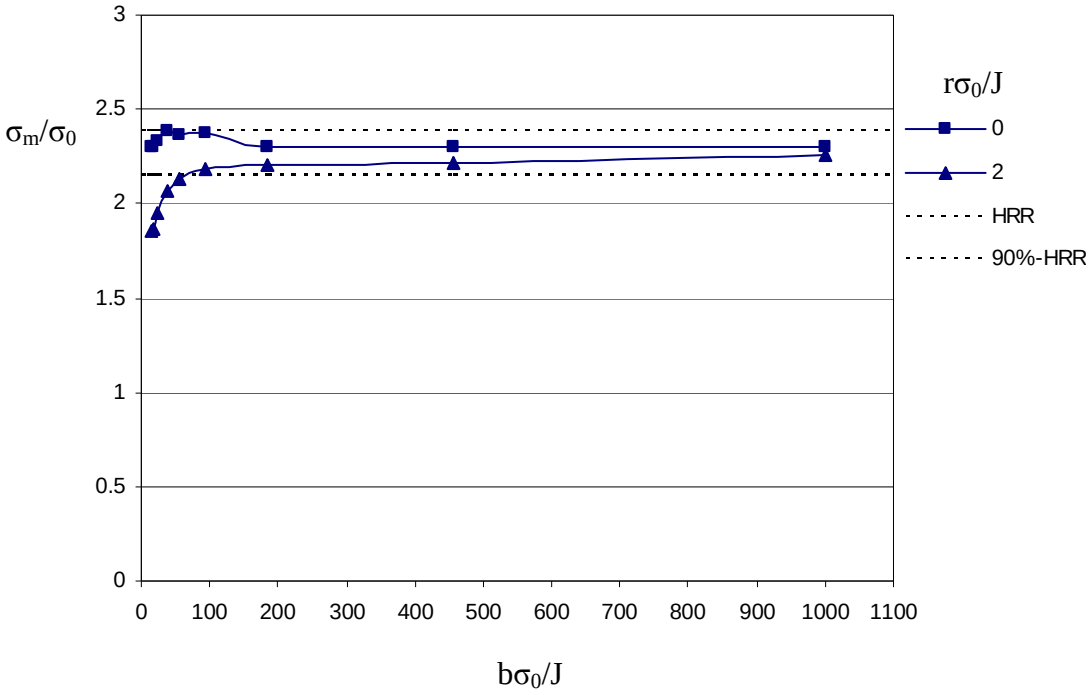

Figure 10.15: The mean stress as a function of the level of deformation at θ=45˚ at the tip (r=0) and at a distance $r\sigma_0/J=2$ for a deep semi-circular surface crack (a/w=0.5, a/c=1).

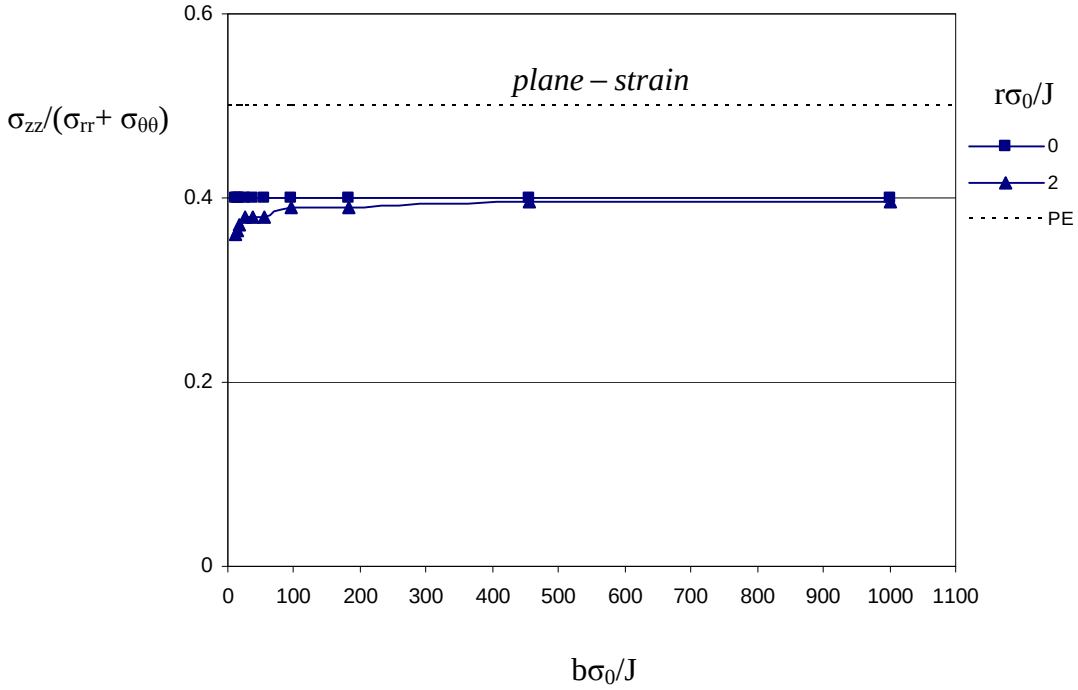

Figure 10.16: Proximity to plane strain conditions at θ=45˚ as a function of deformation at the tip (r=0) and at $r\sigma_0/J=2$ for a deep semi-circular surface crack (a/w=0.5, a/c=1).

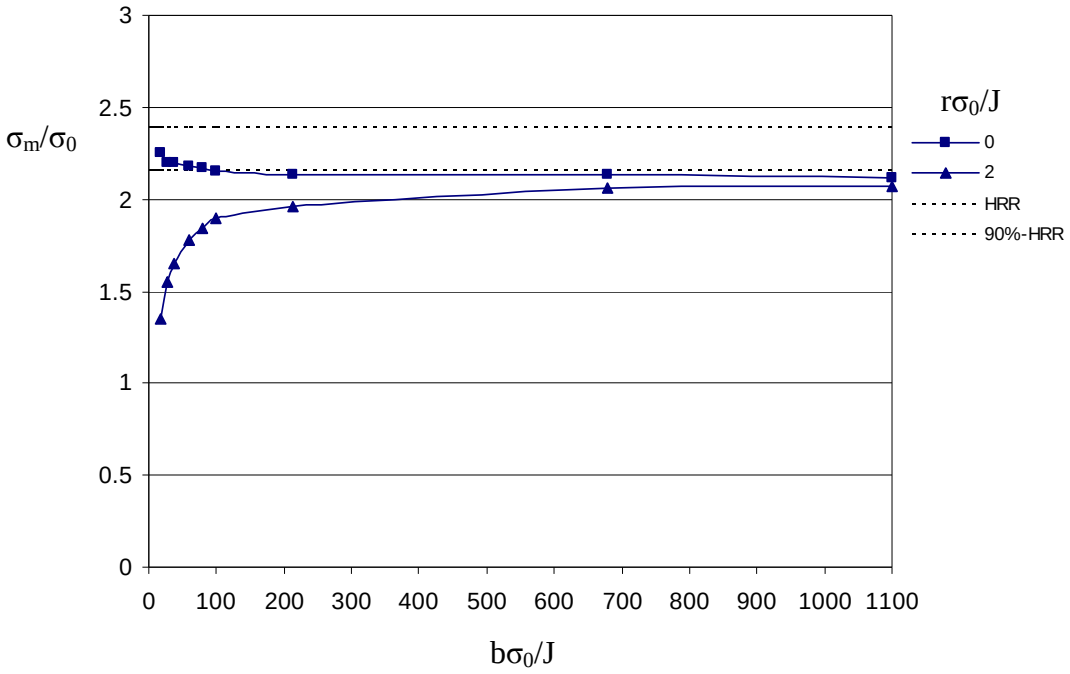

Figure 10.17: The mean stress as a function of the level of deformation at θ=70˚at the tip (r=0) and at a distance rσ$_0$/J=2 and compared with the HRR field in a deep semi-circular surface crack (a/w=0.5, a/c=1).

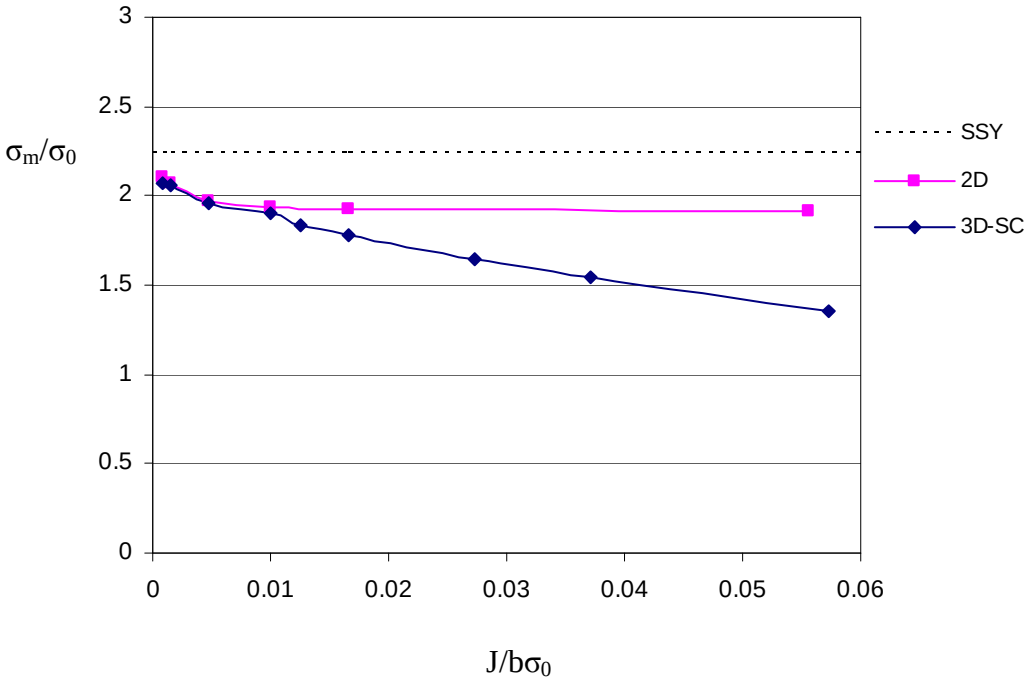

Figure 10.18: The mean stress at (r=2J/σ$_0$) at θ =70˚in a deep semi-circular (SC) surface crack (a/w=0.5, a/c=1) compared to 2-D solution.

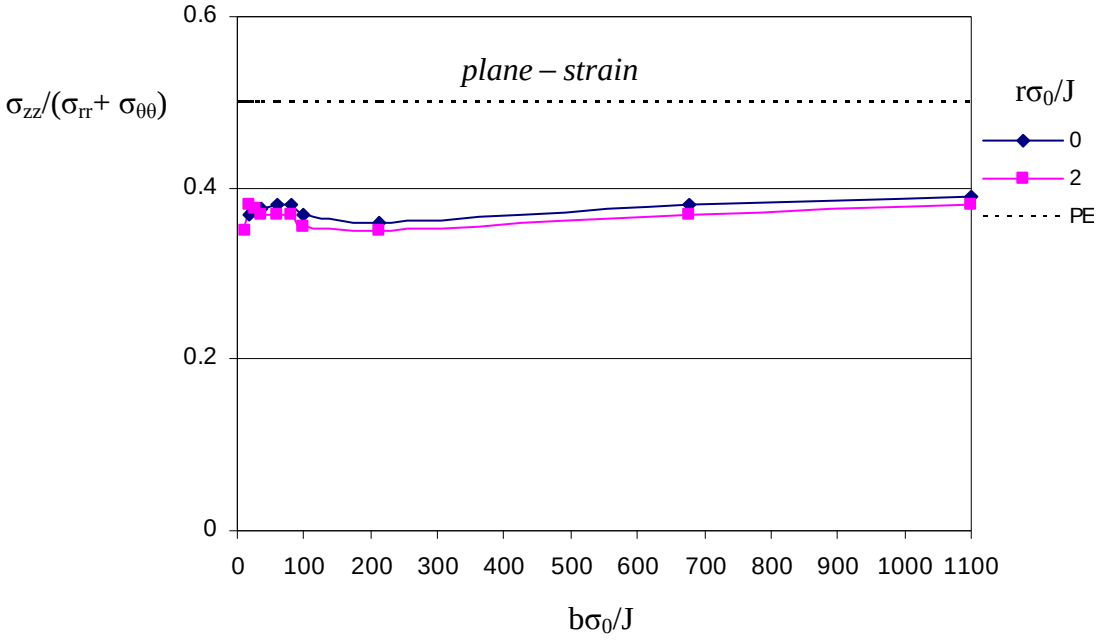

Figure 10.19: Proximity to plane strain conditions at θ=70˚as a function of deformation at $r\sigma_0/J=2$ in a semi-circular surface crack (a/w=0.5, a/c=1).

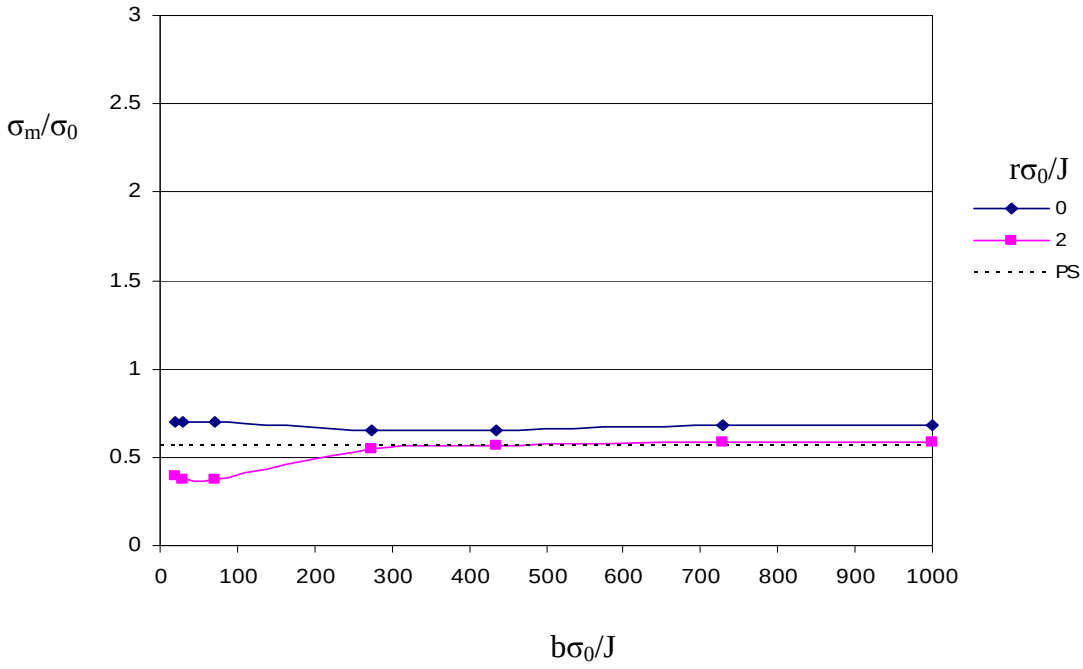

Figure 10.20: Mean stress as a function of the level of deformation at θ=90˚at the tip (r=0) and at a distance $r\sigma_0/J=2$ in a semi-circular surface crack (a/w=0.5, a/c=1).

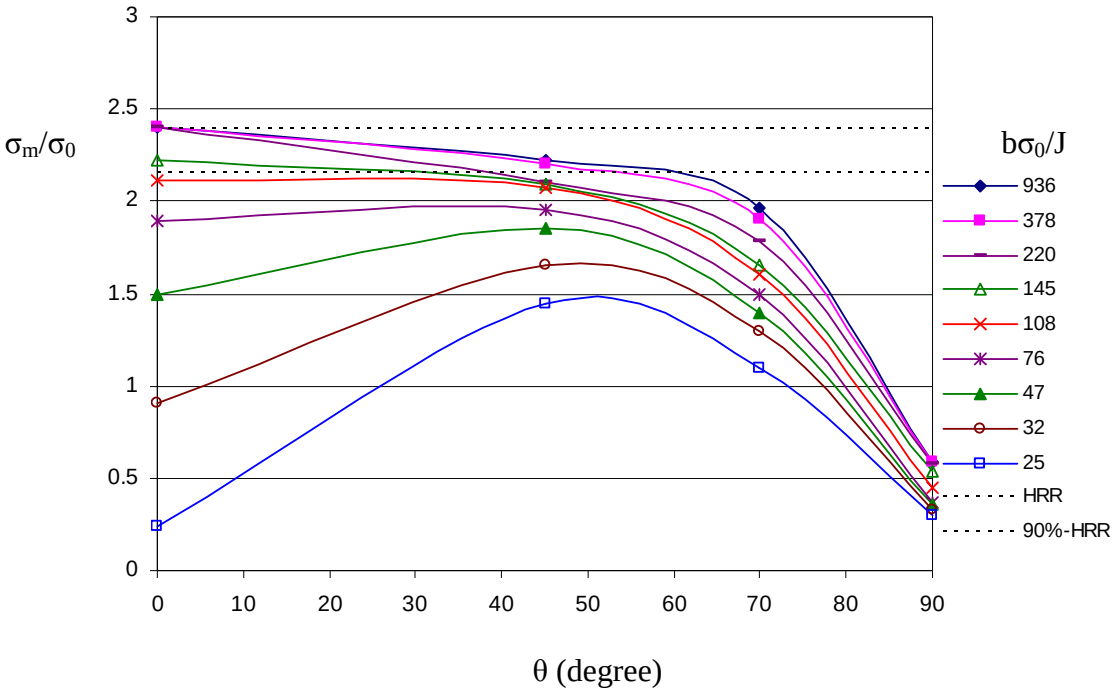

Figure 10.21: Mean stress at $r\sigma_0/J=2$ as a function of the parametric angle θ along the crack at different levels of deformation for a semi-circular surface crack (a/w=0.5, a/c=1).

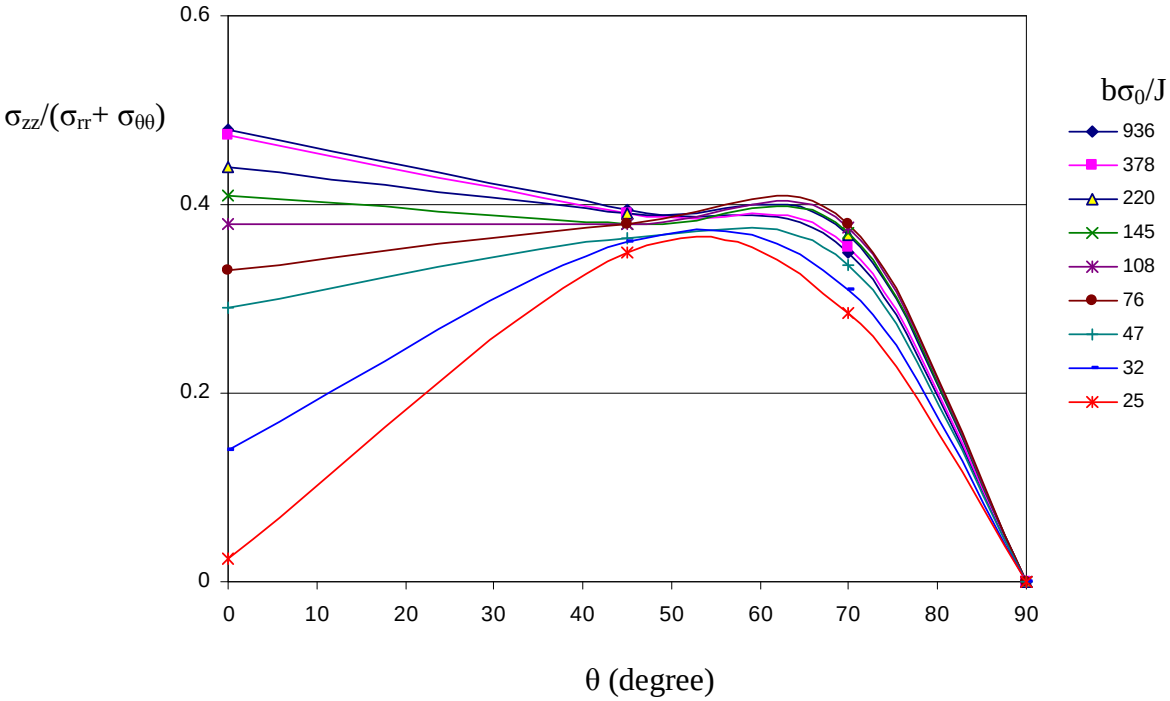

Figure 10.22: Proximity to plane strain conditions as a function of the parametric angle θ along the crack front for a semi-circular surface crack (a/w=0.5, a/c=1).

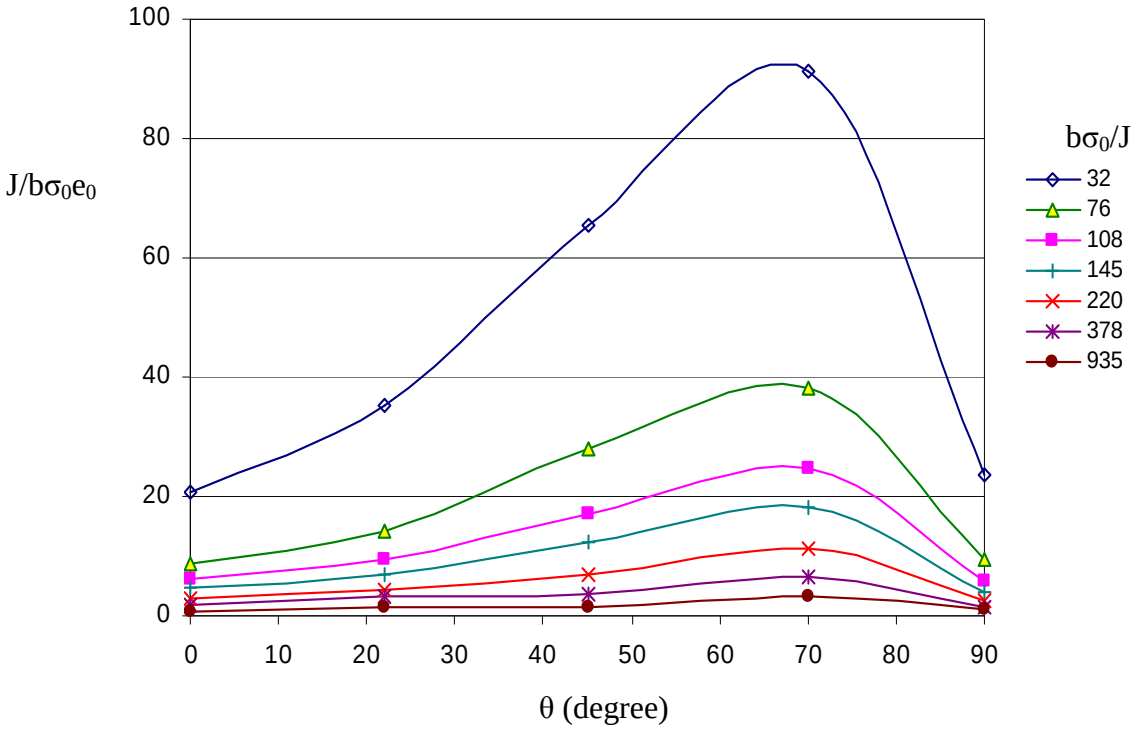

Figure 10.23: Non-dimensional J-integral along the crack front from the deepest θ=0˚ to the free surface θ=90˚ in a semi-circular surface crack (a/w=0.5, a/c=1) (Terfas, 2009, and Terfas and Bezensek, 2009a).

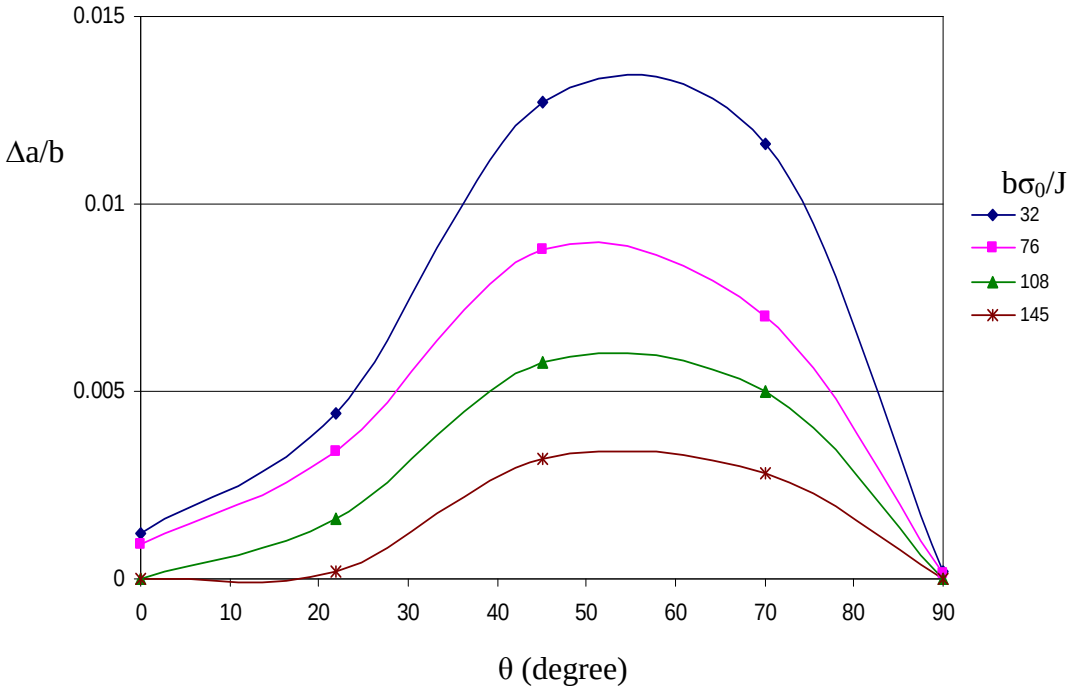

Figure 10.24: Crack growth as a function of the parametric angle θ from the deepest point to the free surface in a semi-circular surface crack (a/w=0.5, a/c=1) (Terfas 2009, Terfas and Bezensek, 2009a).

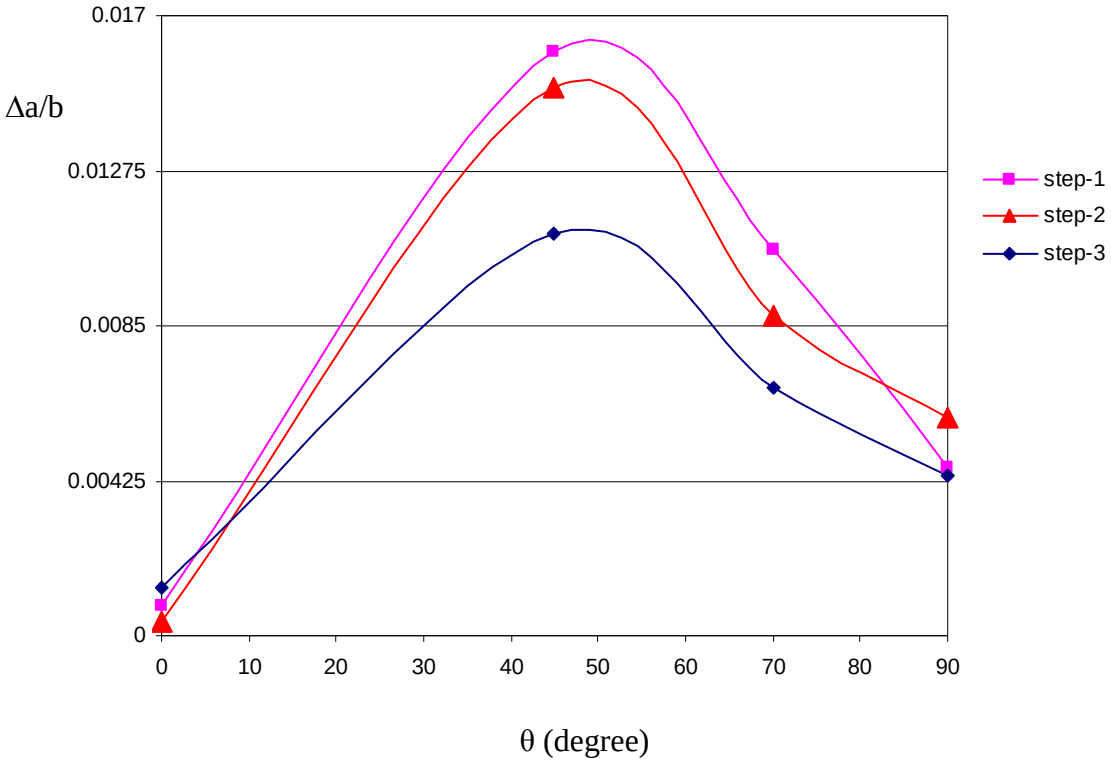

Figure 10.25: Crack extension steps at $b\sigma_0/J=25$, 20 and 15 for a deep semi-circular surface crack along the crack front under bending.

Figure 10.26: Crack shape development of a deep semi-circular crack (a/w=0.5, a/c=1) in bending (Terfas 2009, Terfas and Bezensek, 2009a).

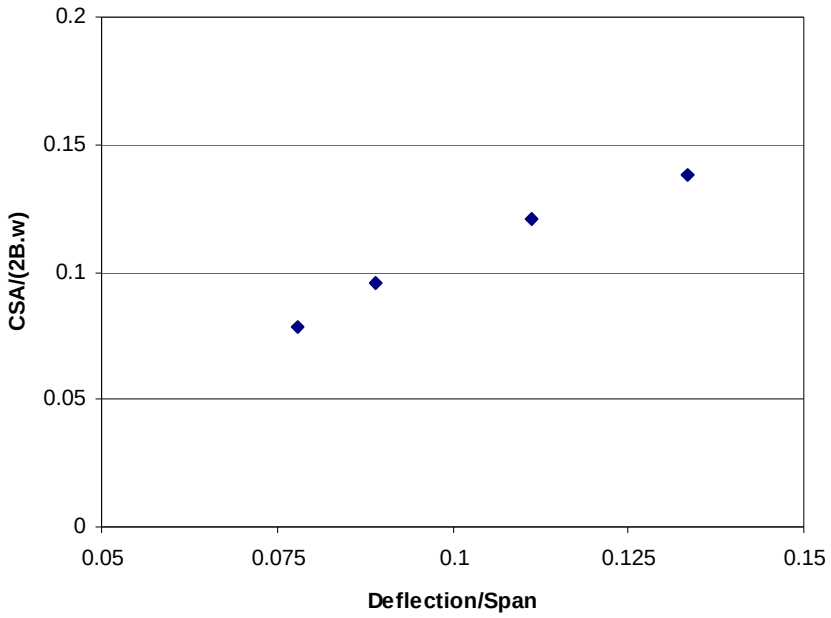

Figure 10.27: Crack surface area normalised by cross section area as a function of deflection.

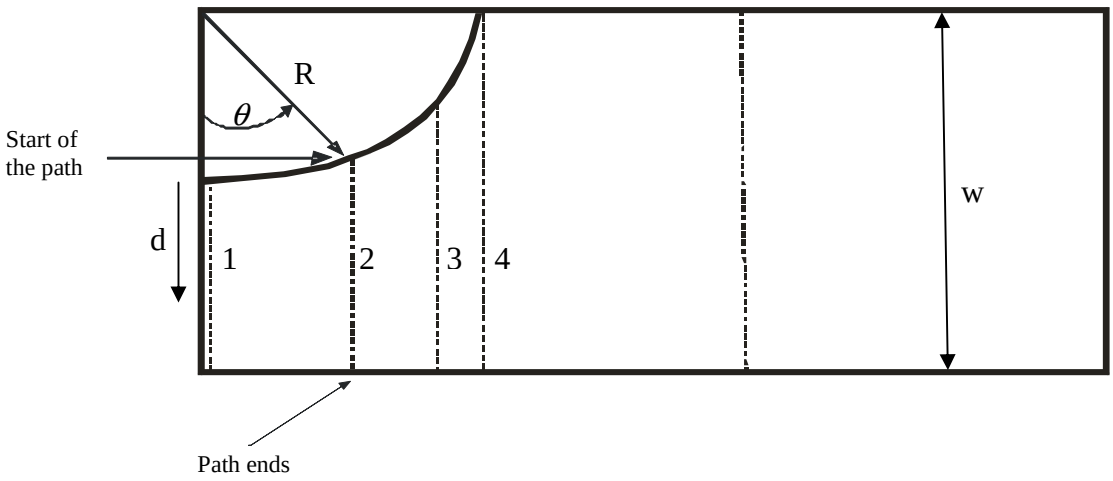

Figure 10.28: Paths used to determine local force and moment.

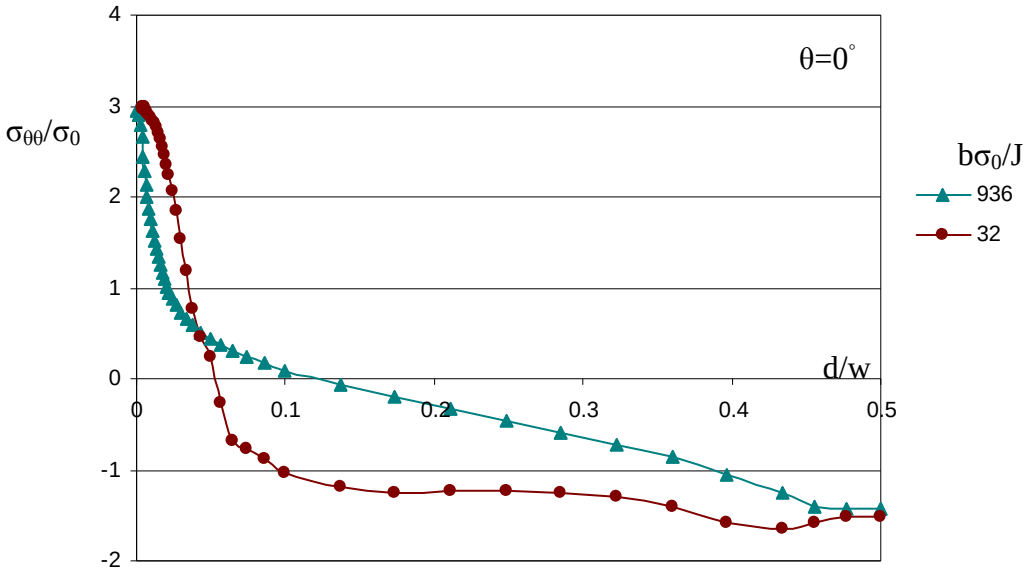

Figure 10.29: The opening stress $\sigma_{\theta\theta}$ at the deepest point ($\theta=0^{\circ}$, path1) as a function of a distance (d/w) for a deep semi-circular surface crack (a/w=0.5, a/c=1) in bending.

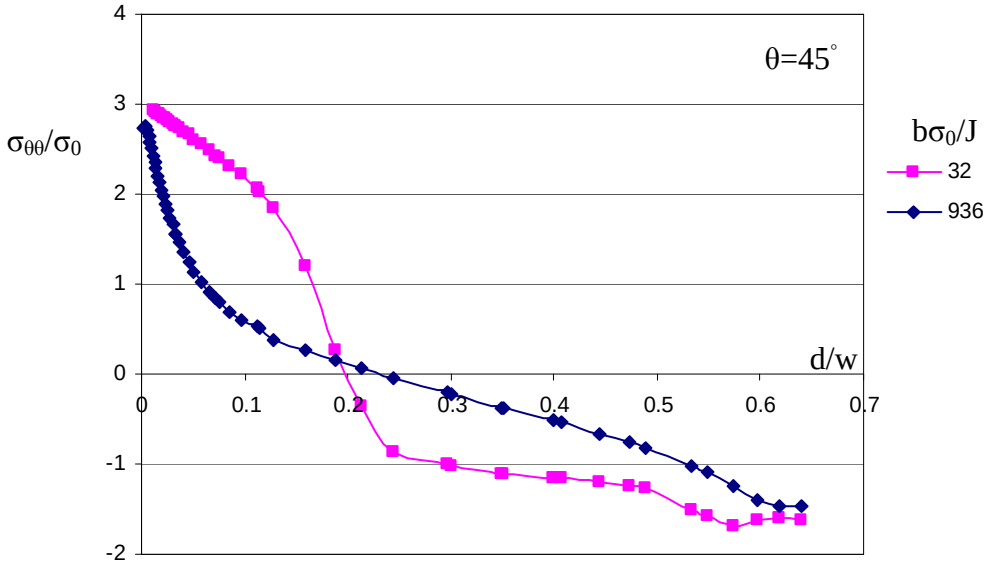

Figure 10.30: The opening stress $\sigma_{\theta\theta}$ at $\theta=45^{\circ}$(path2) as a function of a distance (d/w) for a deep semi-circular surface crack (a/w=0.5, a/c=1) in bending.

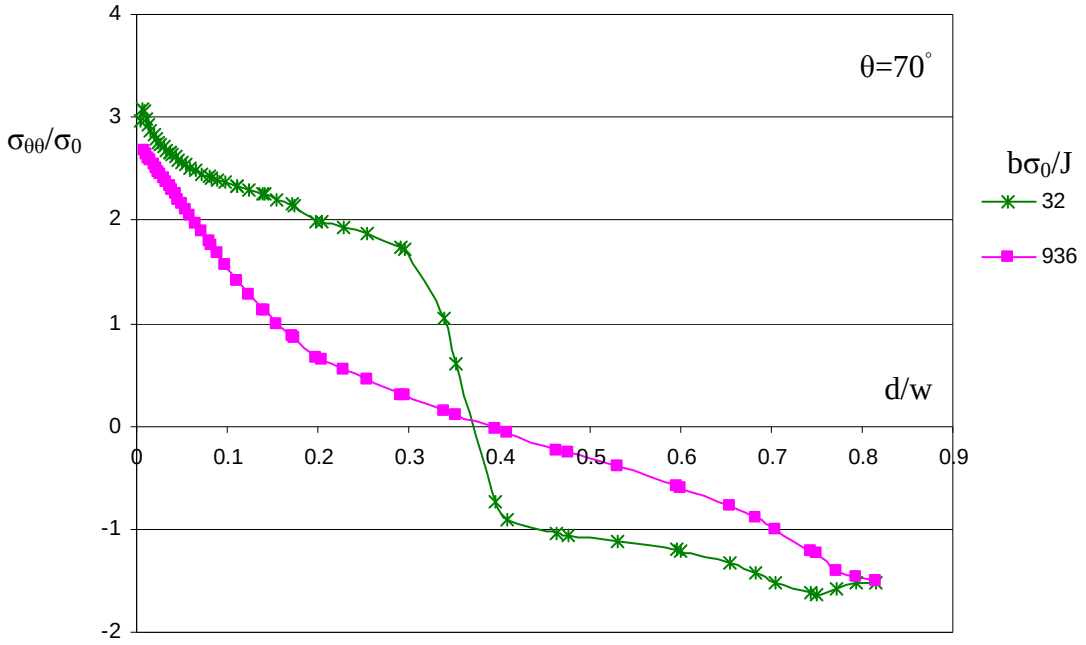

Figure 10.31: The opening stress $\sigma_{\theta\theta}$ at $\theta=70^{\circ}$(path3) as a function of a distance (d/w) for a deep semi-circular surface crack (a/w=0.5, a/c=1) in bending.

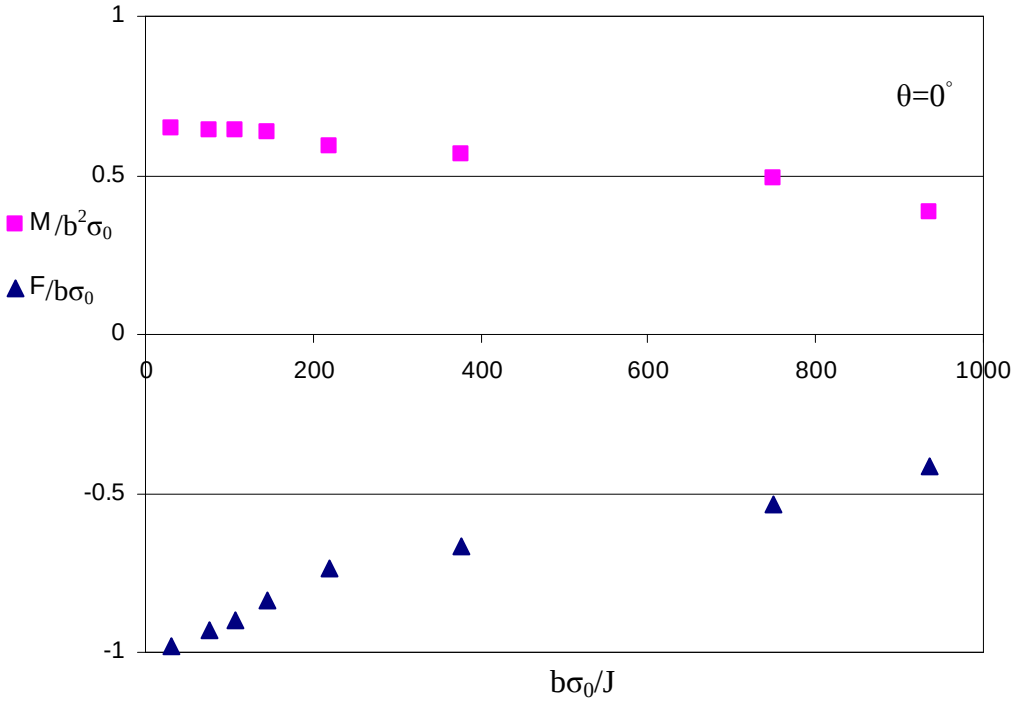

Figure 10.32: Force and moment redistribution along the uncracked ligament at the deepest point (path1) as a function of deformation for a deep semi-circular surface crack (a/w=0.5, a/c=1) in bending.

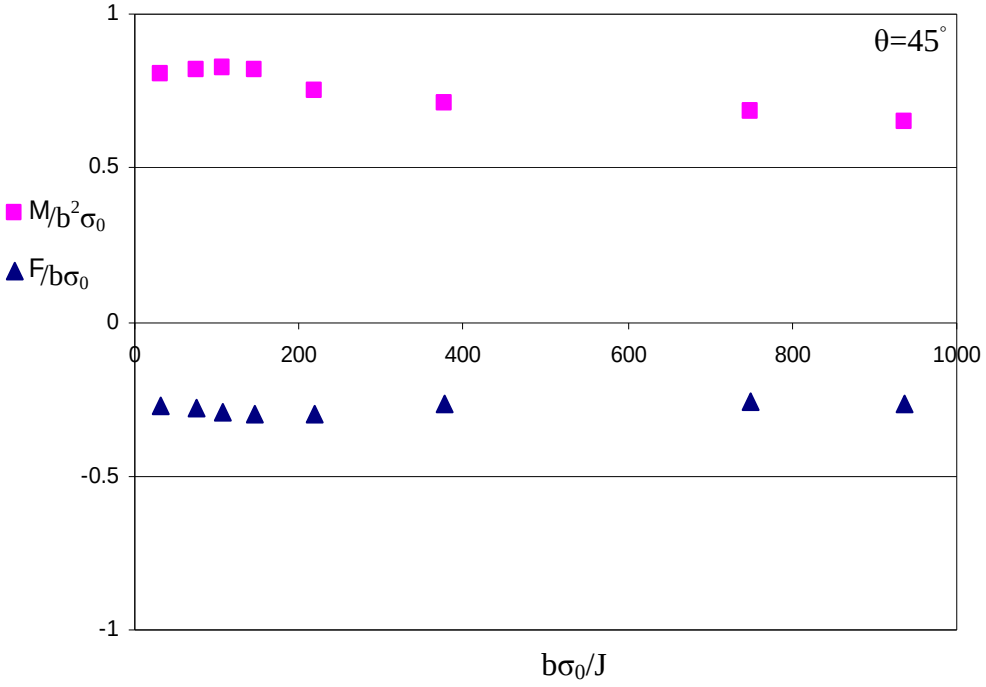

Figure 10.33: Force and moment redistribution along the uncracked ligament at 45° (path2) as a function of deformation for a deep semi-circular surface crack (a/w=0.5, a/c=1) in bending.

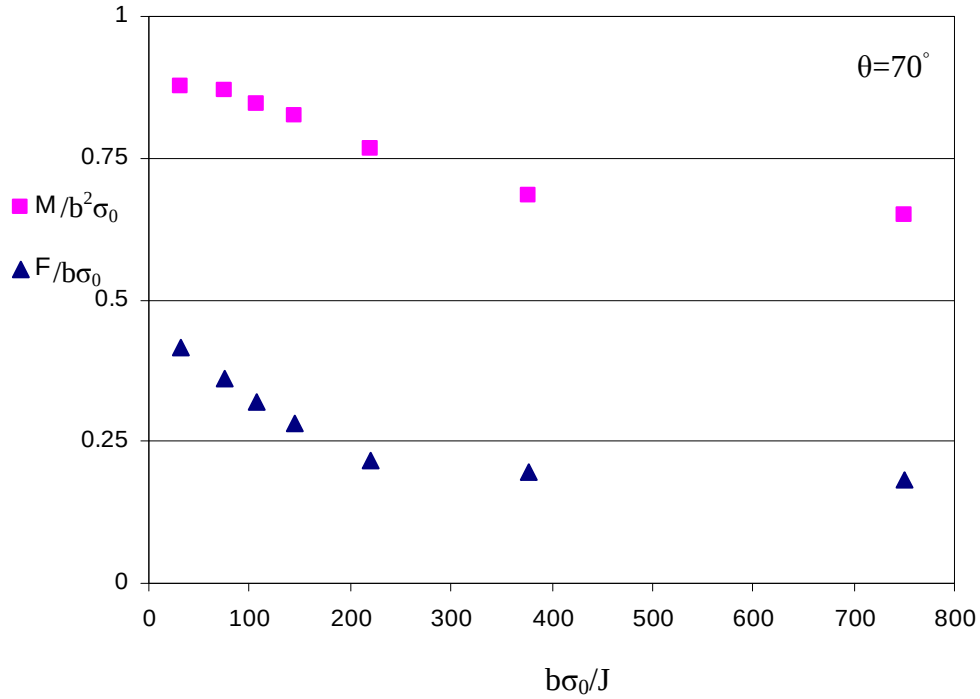

Figure 10.34: Force and moment redistribution along the uncracked ligament at 70° (path3) as a function of deformation for a deep semi-circular surface crack (a/w=0.5, a/c=1) in bending.

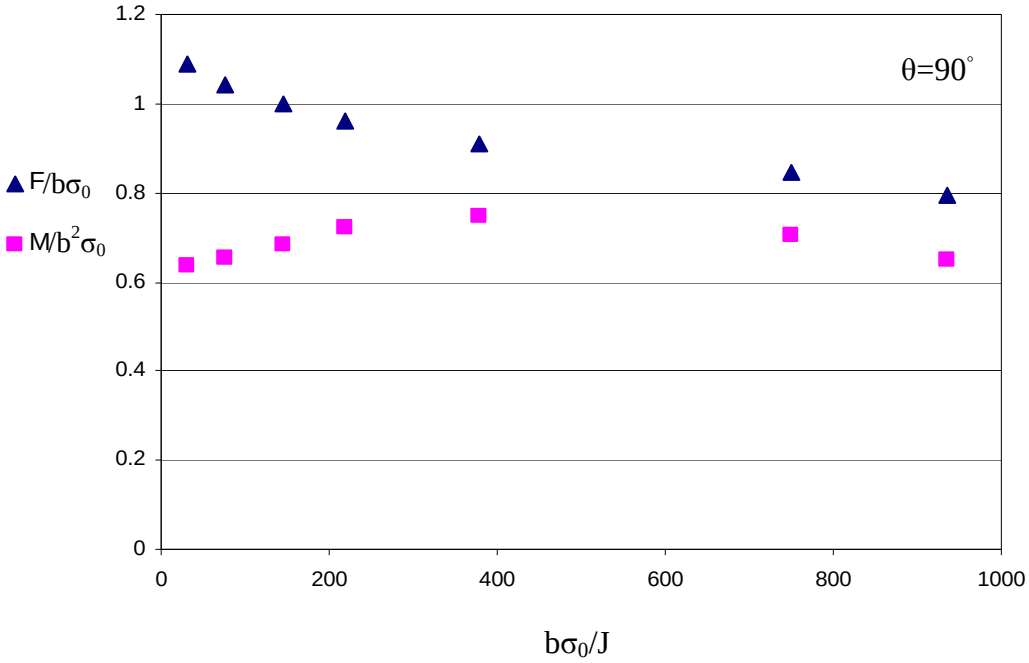

Figure 10.35: Force and moment redistribution along the uncracked ligament at 90° (path4) as a function of deformation for a deep semi-circular surface crack (a/w=0.5, a/c=1) in bending.

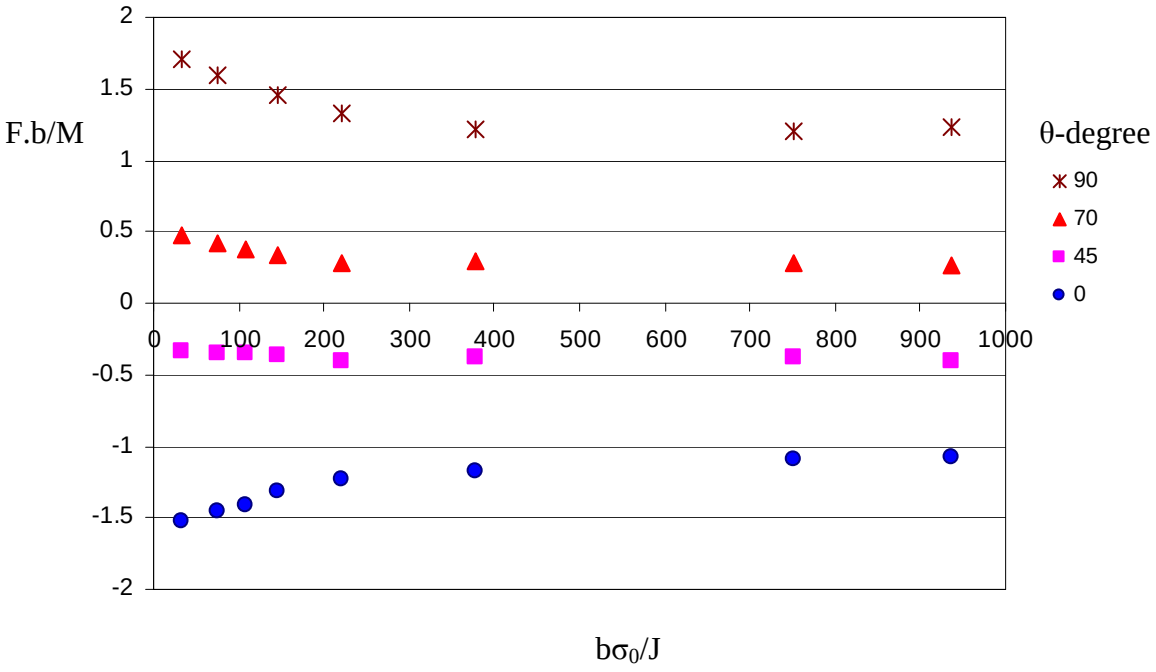

Figure 10.36: Force-moment ratio on the uncracked ligament ahead of the crack in a deep semi-circular surface crack (a/w=0.5, a/c=1) in bending.

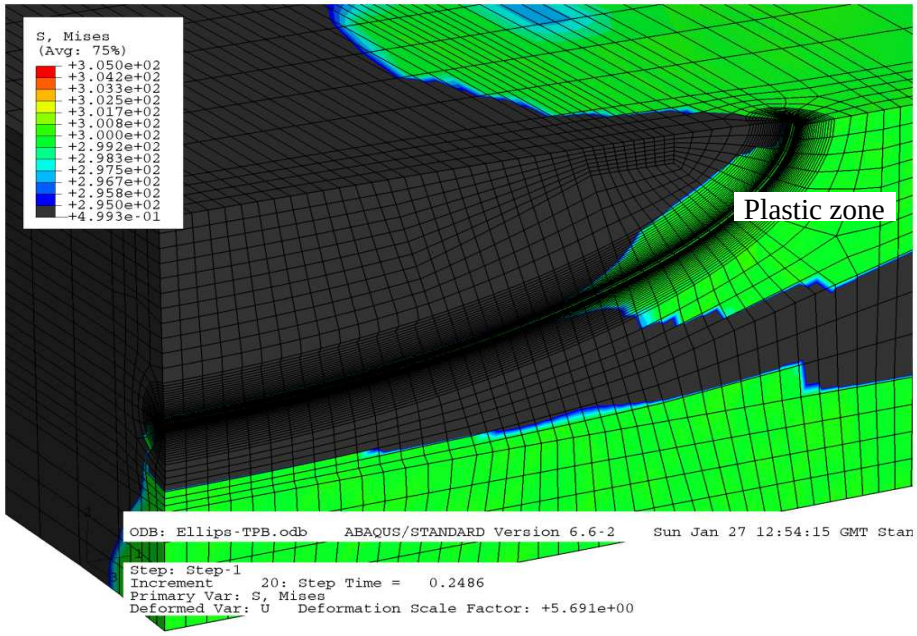

Figure 10.37: Development of the plastic zone around a semi-elliptical surface crack (a/w=0.5, a/c=0.33) at deformation level of $b\sigma_0/J=200$ (at $\theta=0^\circ$).

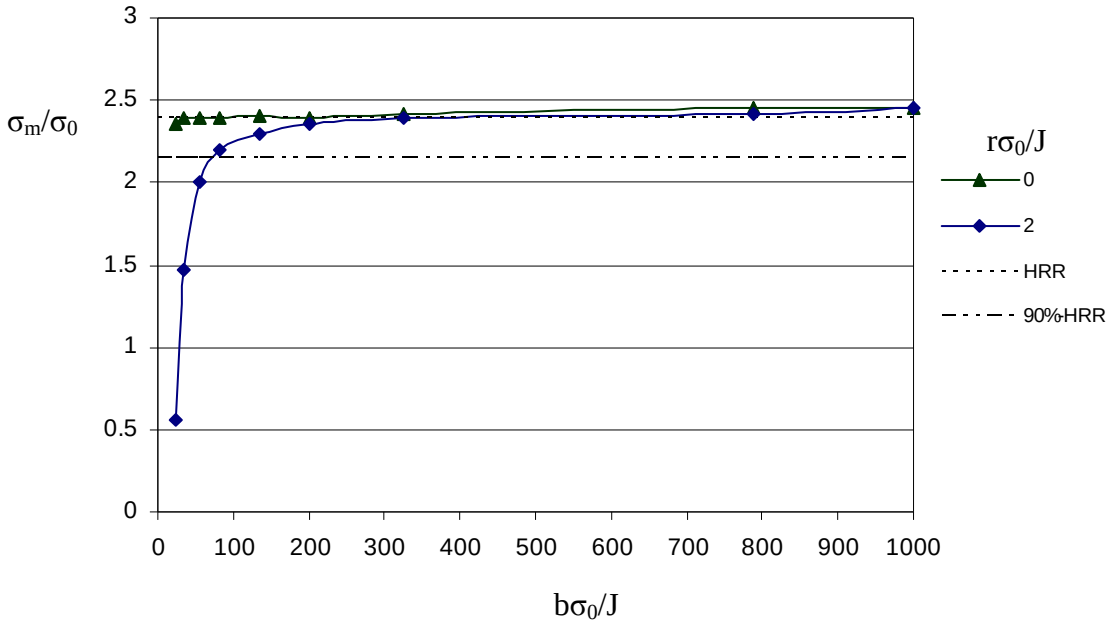

Figure 10.38: Mean stress as a function of the level of deformation for $\theta=0^\circ$ at a distance $r\sigma_0/J=0$ and 2 for a deep semi-elliptical crack (a/w=0.5, a/c=0.33).

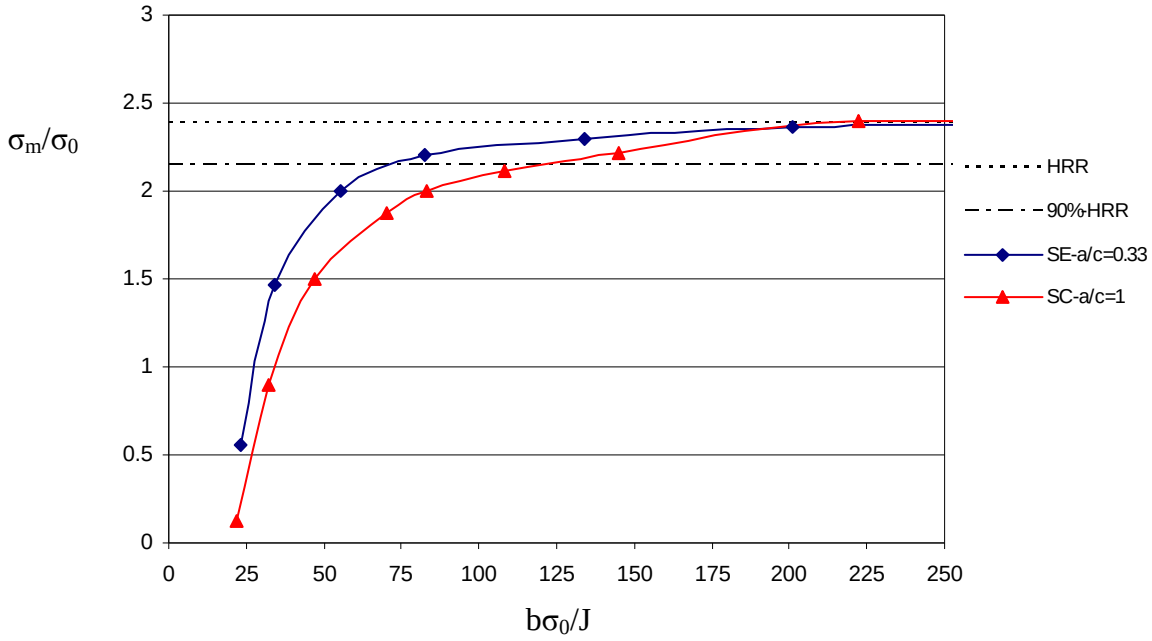

Figure 10.39: The mean stress as a function of the level of deformation for θ=0˚ at a distance rσ$_0$/J=2 for deep semi-circular (SC-a/c=1) and semi-elliptical (SE-a/c=0.33) cracks.

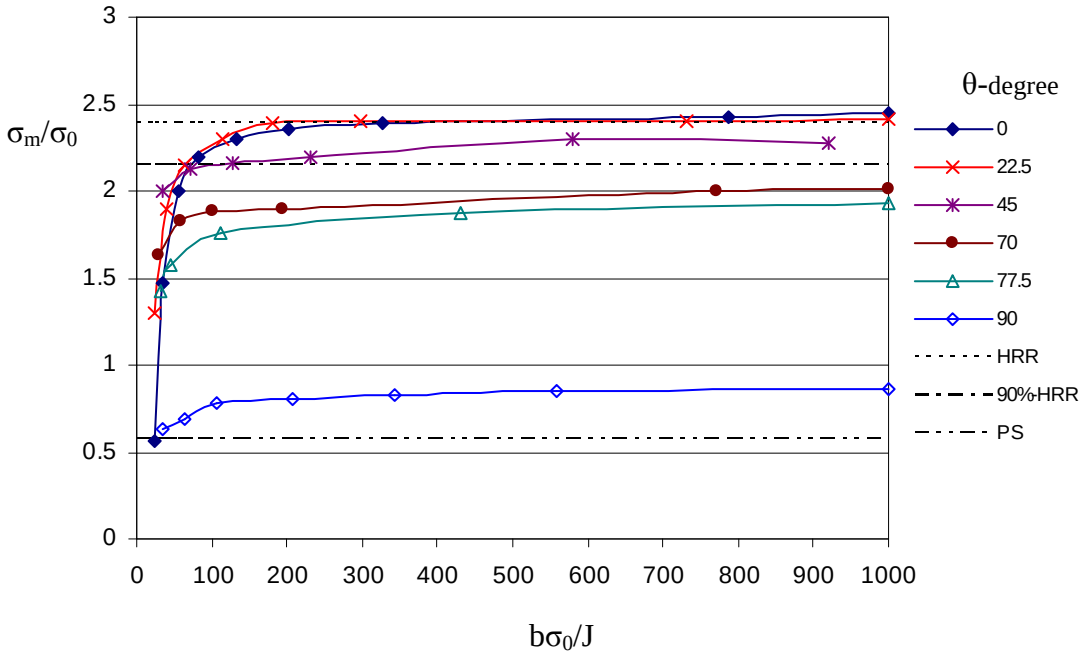

Figure 10.40: The mean stress as a function of the level of deformation for (θ=0˚, 22.5˚, 45˚, 70˚, 77.5˚, 90˚) at a distance rσ$_0$/J=2 for a deep semi-elliptical surface crack (a/c=0.33, a/w=0.5).

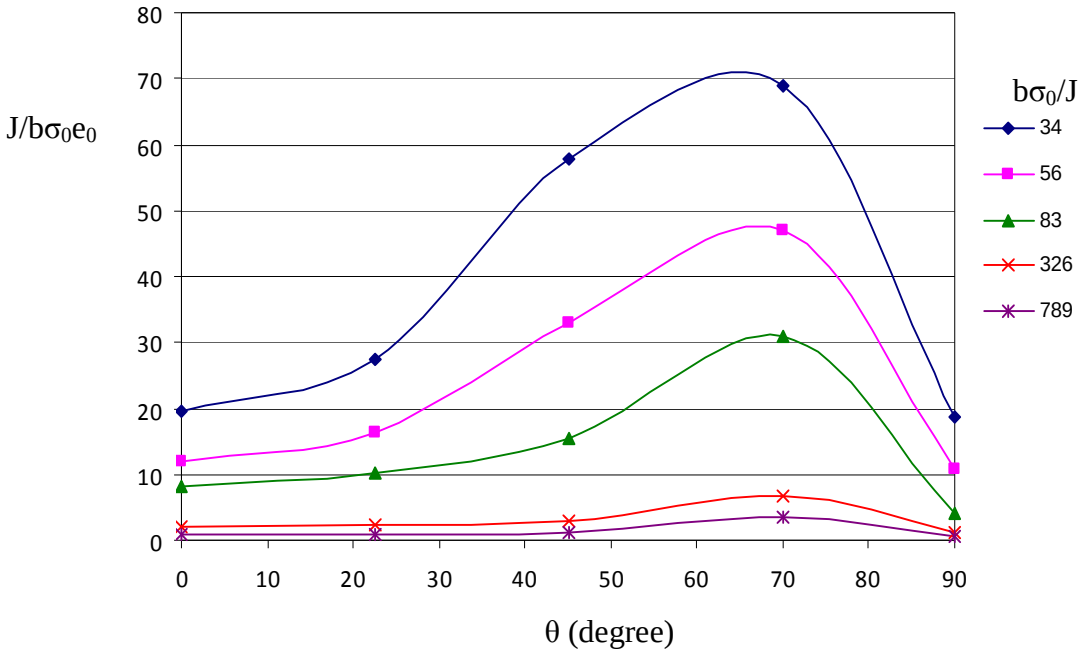

Figure 10.41: J-integral along the crack front for a deep semi-elliptical surface crack (a/w=0.5, a/c=0.33) in bending.

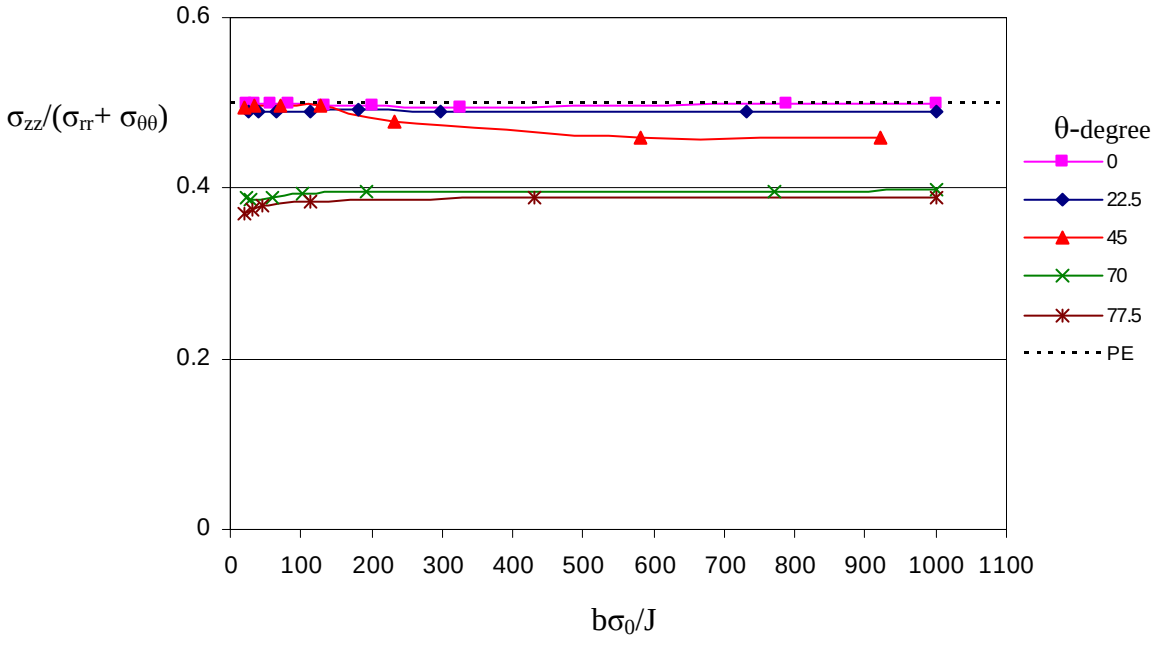

Figure 10.42: Proximity to the plane strain conditions along the crack front as a function of the level of deformation at the tip (r=0) in a semi-elliptical surface crack (a/w=0.5, a/c=0.33).

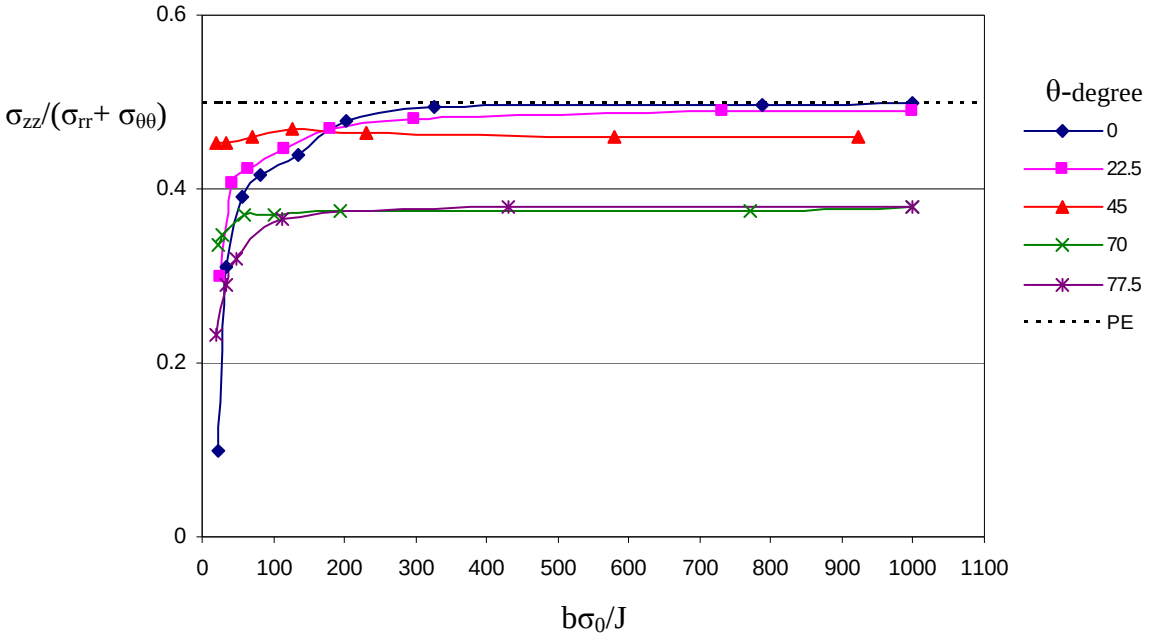

Figure 10.43: Proximity to the plane strain conditions along the crack front as a function of the level of deformation at a distance $2J/\sigma_0$ in a deep semi-elliptical surface crack (a/c=0.33, a/w=0.5).

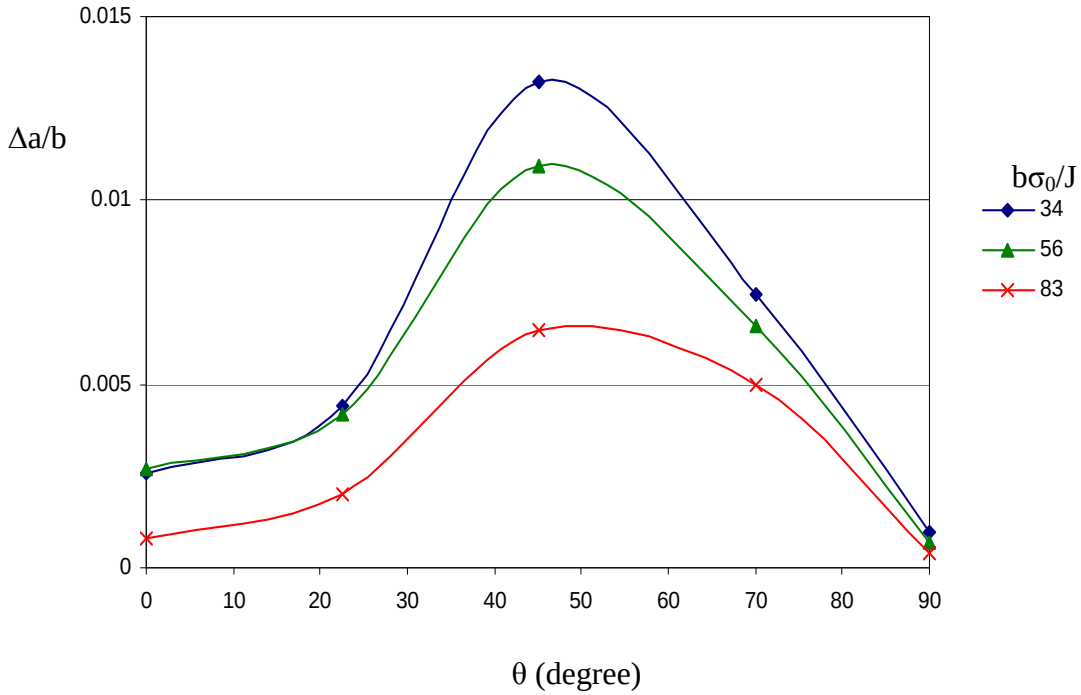

Figure 10.44: Crack growth around the crack front as a function of the parametric angle θ for a deep semi-elliptical surface crack (a/c=0.33, a/w=0.5) in bending.

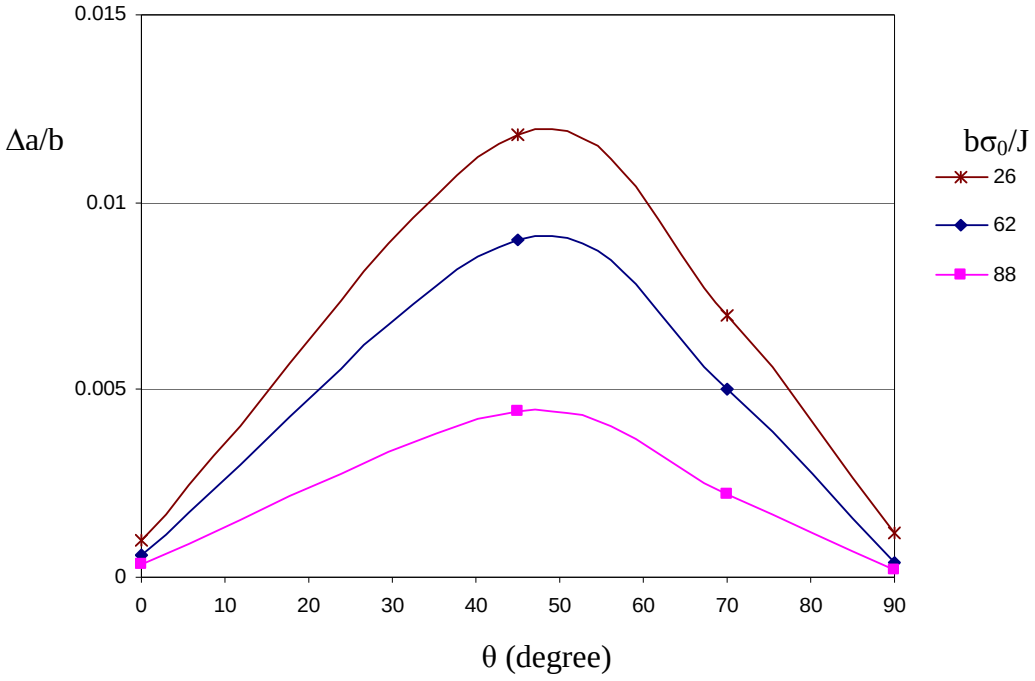

Figure 10.45: Crack growth for the first step of a deep semi-elliptical surface crack (a/c=0.33, a/w=0.5) in bending.

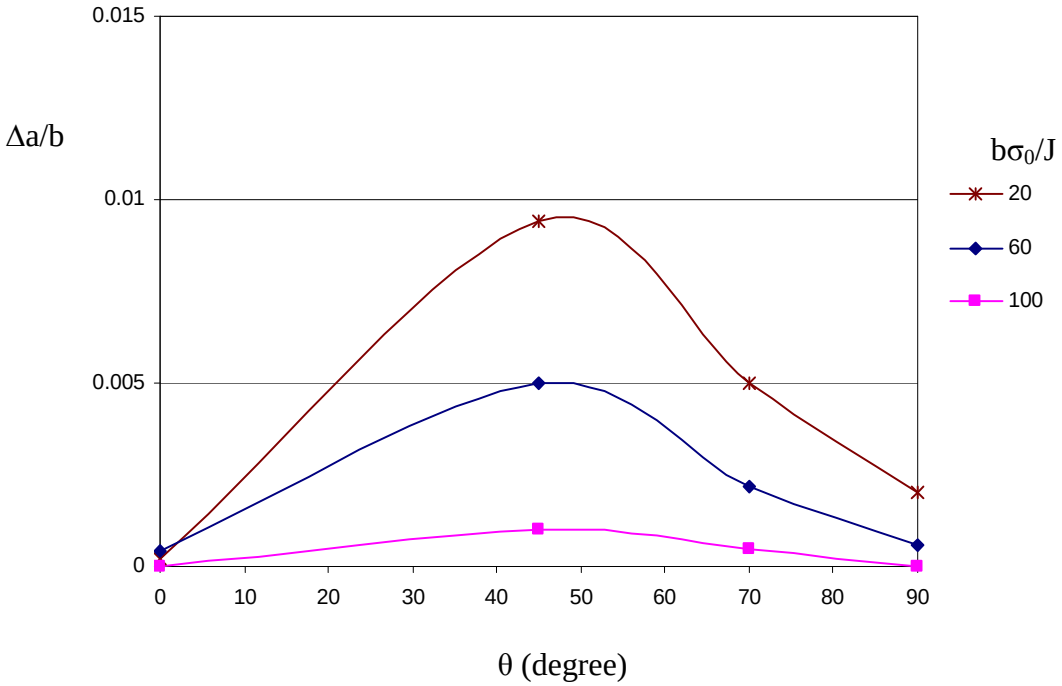

Figure 10.46: Crack growth for the second step of a deep semi-elliptical surface crack (a/c=0.33, a/w=0.5) in bending.

Figure 10.47: Crack shape sequence for a deep semi-elliptical surface crack under bending (a/w=0.5, a/c=0.33).

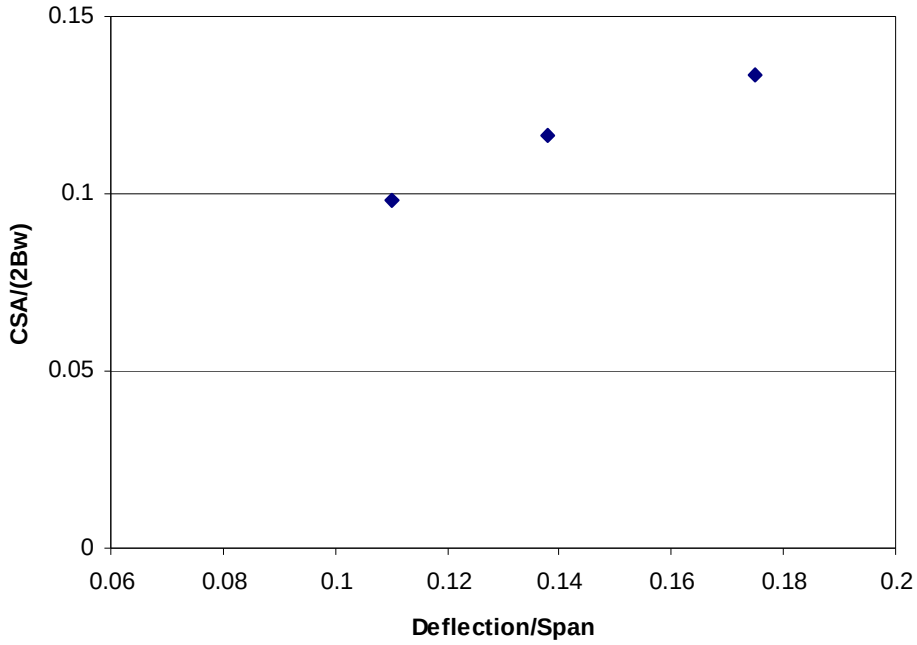

Figure 10.48: Crack surface area normalised by cross section area as a function of deflection.

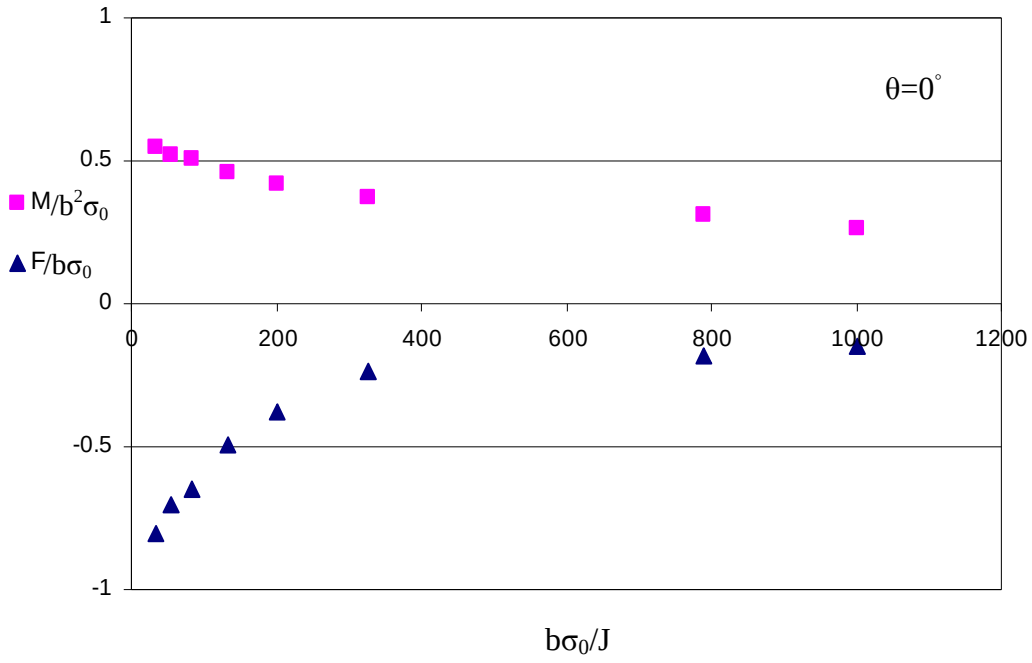

Figure 10.49: Force and moment redistribution along the uncracked ligament at the deepest point (path1) as a function of deformation in a deep semi-elliptical (a/w=0.5, a/c=0.33) surface crack in bending.

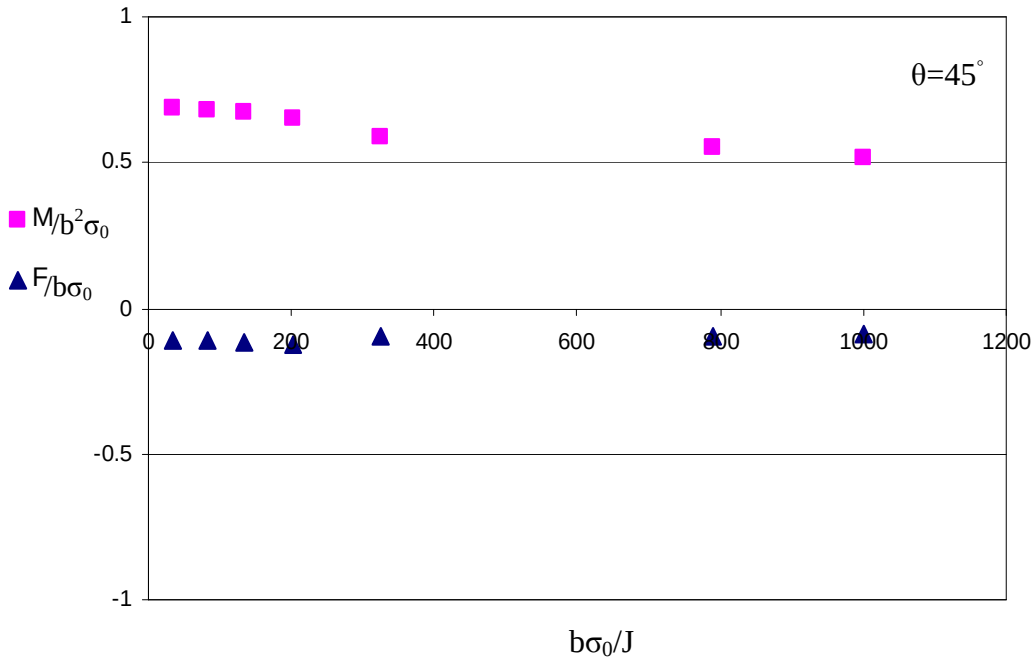

Figure 10.50: Force and moment redistribution along the uncracked ligament at 45° (path2) as a function of deformation in a deep semi-elliptical (a/w=0.5, a/c=0.33) surface crack in bending.

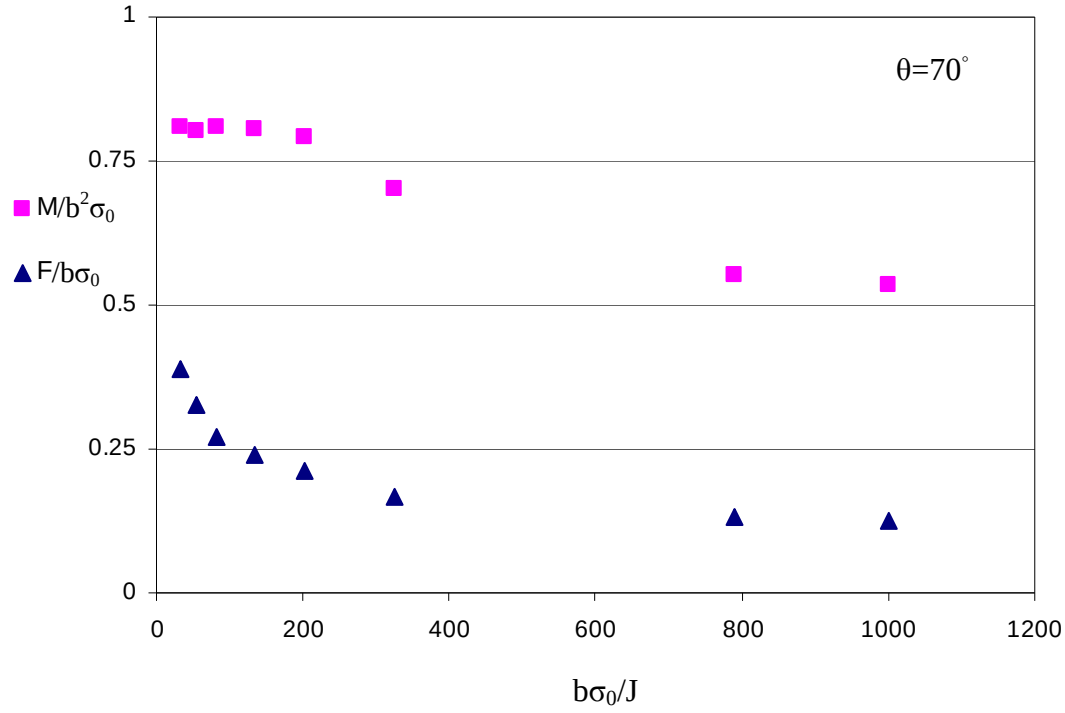

Figure 10.51: Force and moment redistribution along the uncracked ligament at 70° (path3) as a function of deformation in a deep semi-elliptical (a/w=0.5, a/c=0.33) surface crack in bending.

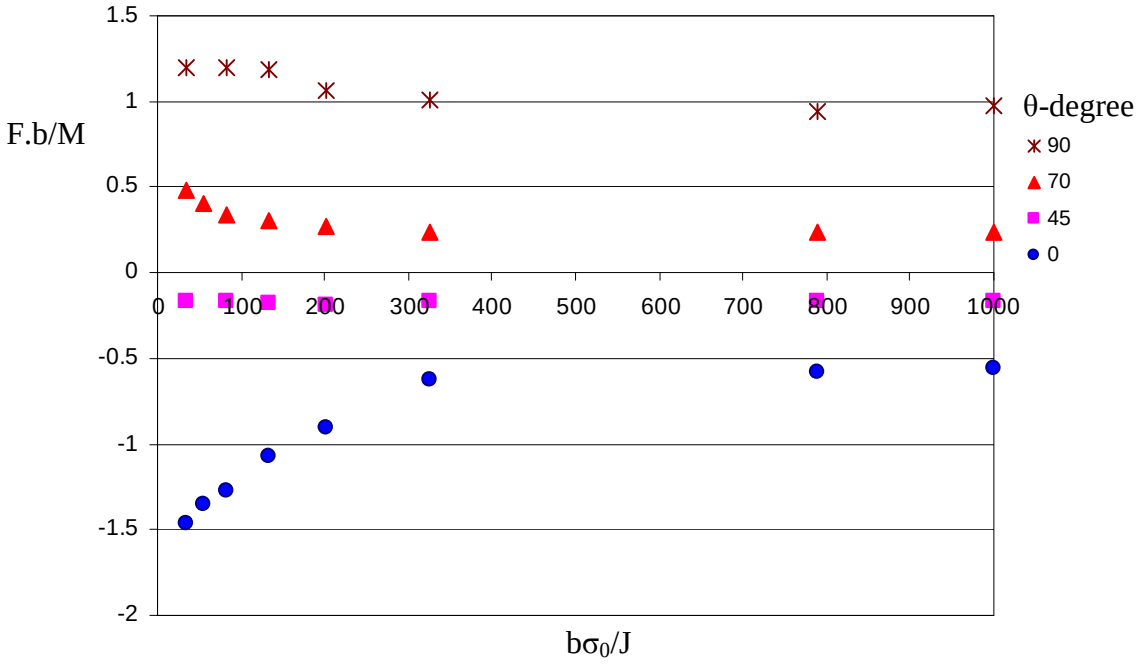

Figure 10.52: Force-moment ratio on the uncracked ligament ahead of the crack in a deep semi-elliptical surface crack (a/w=0.5, a/c=0.33) in bending.

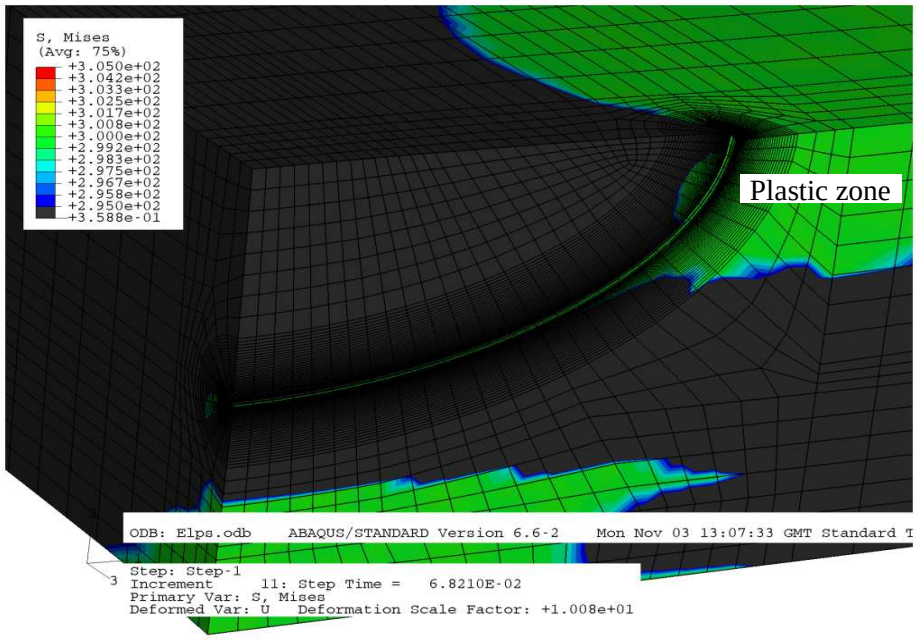

Figure 10.53: Development of the plastic zone around the crack front in a deep semi-elliptical surface crack a/w=0.5 with aspect ratio of a/c=0.5 in three point bending.

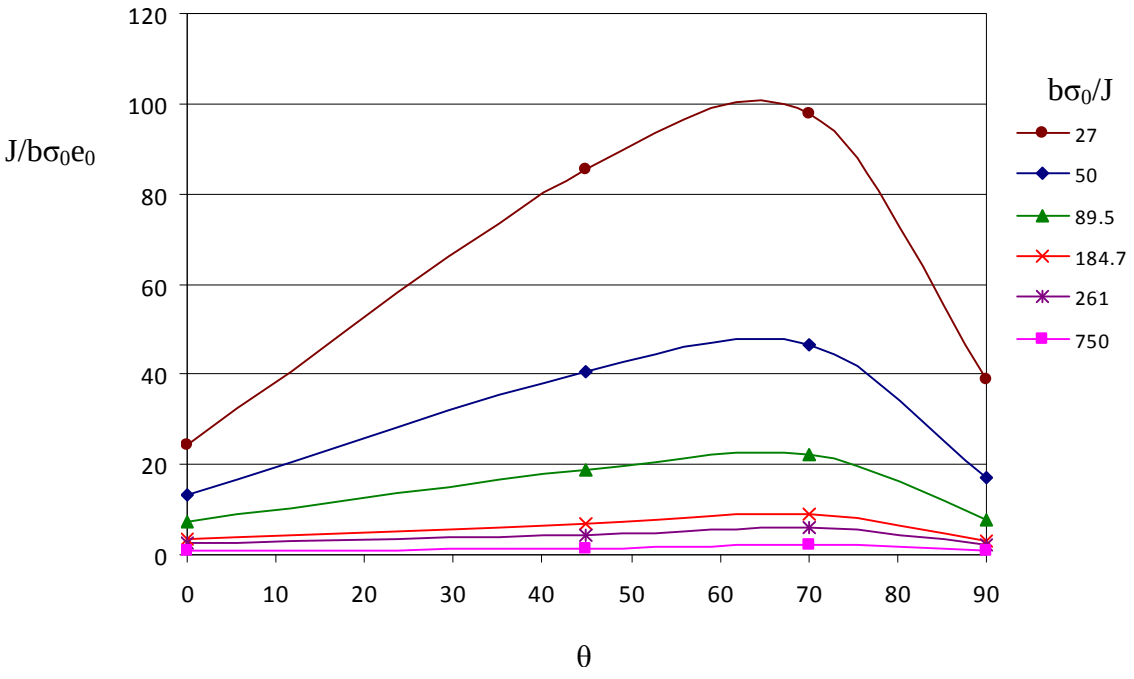

Figure 10.54: J-integral along the crack front for a deep semi-elliptical surface crack in bending, (a/c=0.5, a/w=0.5).

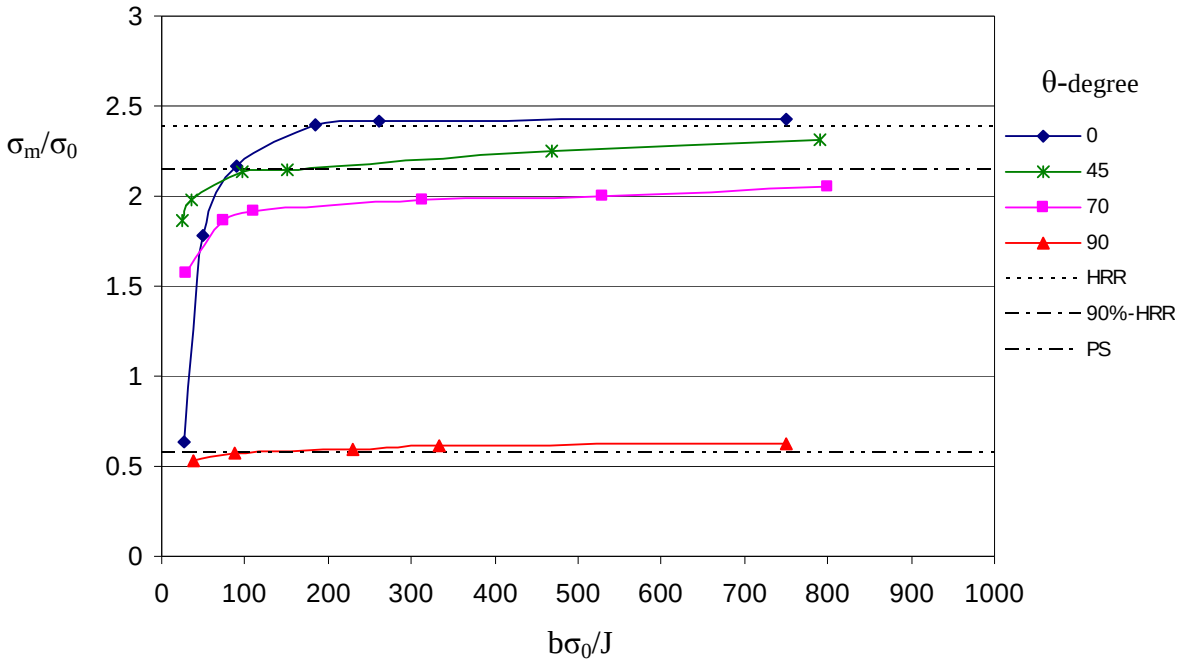

Figure 10.55: The mean stress at a distance $r\sigma_0/J=2$ as a function of the deformation level around the crack front for a deep semi-elliptical surface crack in bending. (a/c=0.5, a/w=0.5).

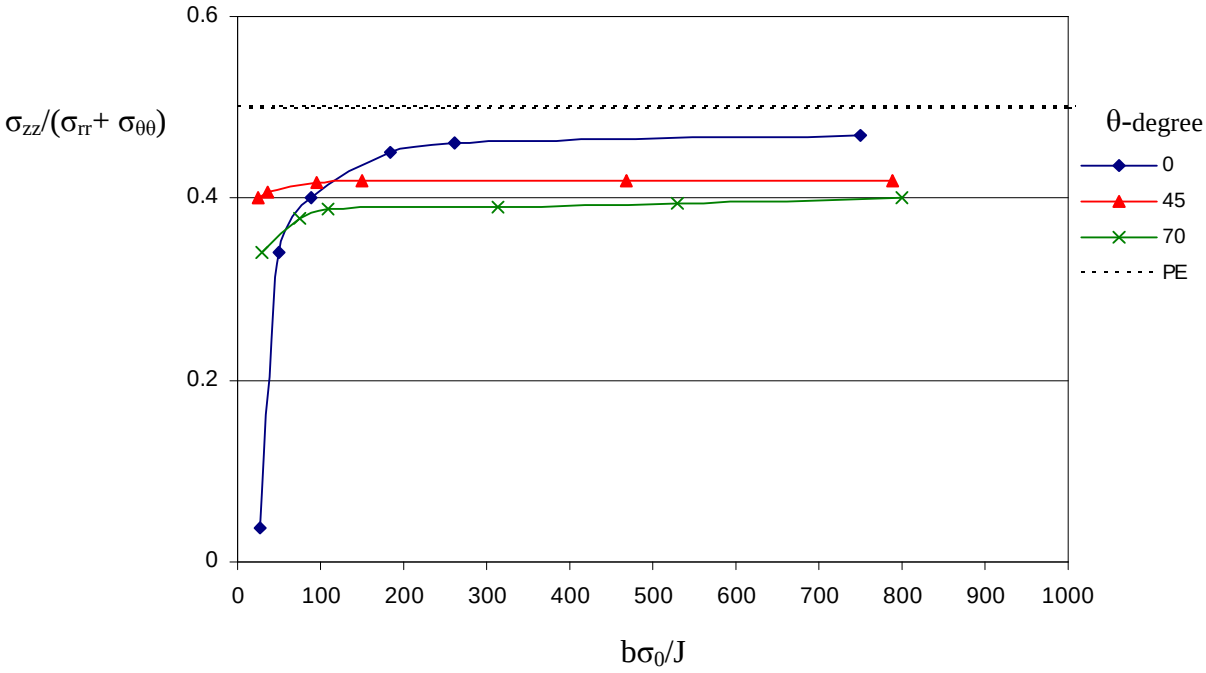

Figure 10.56: Proximity to plane strain conditions around the crack front for a deep semi-elliptical surface crack in bending (a/c=0.5, a/w=0.5).

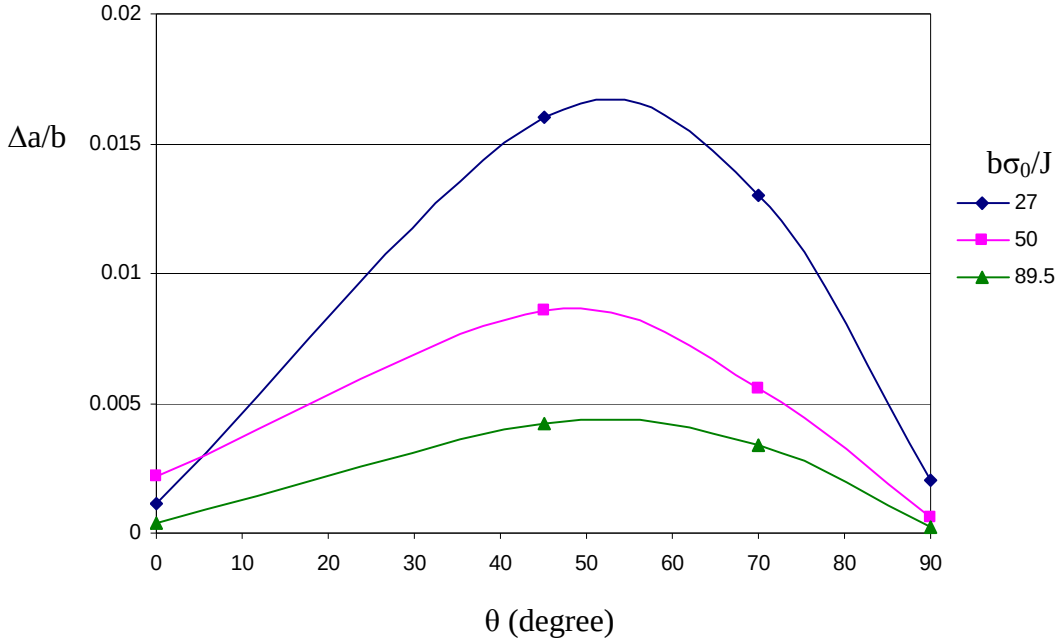

Figure 10.57: Crack growth as a function of the parametric angle θ for a deep semi-elliptical surface crack in bending. (a/c=0.5, a/w=0.5).

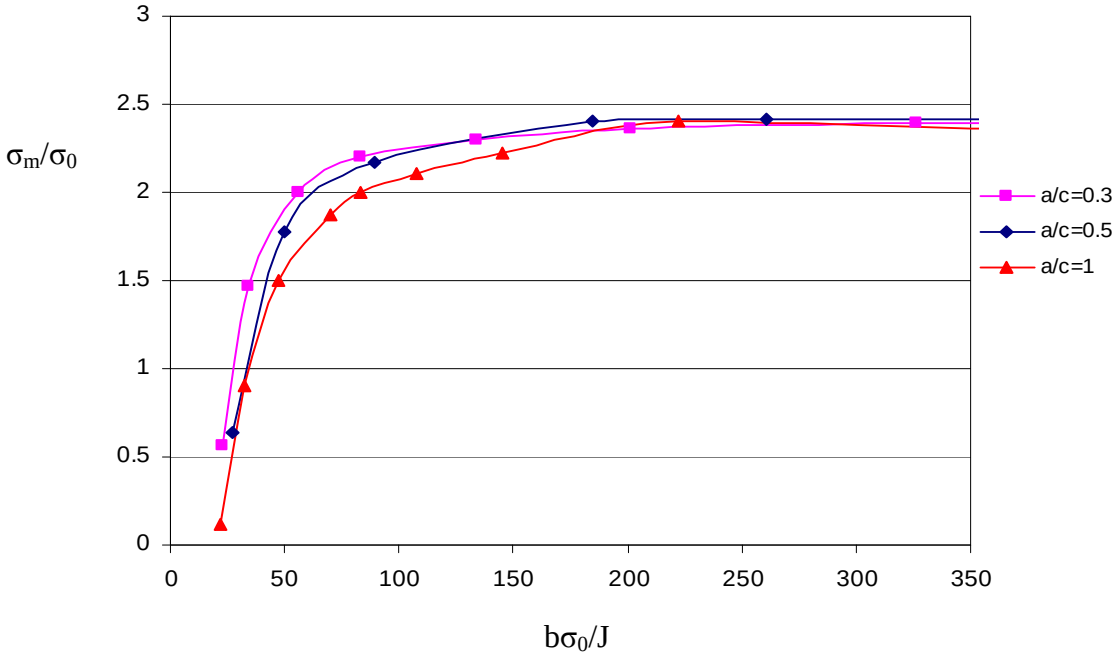

Figure 10.58: The mean stress at a distance rσ0/J=2 as a function of deformation level at the deepest point for a deep semi-elliptical surface crack, a/w=0.5, with different aspect ratios in bending (a/c=0.33, 0.5 and 1).

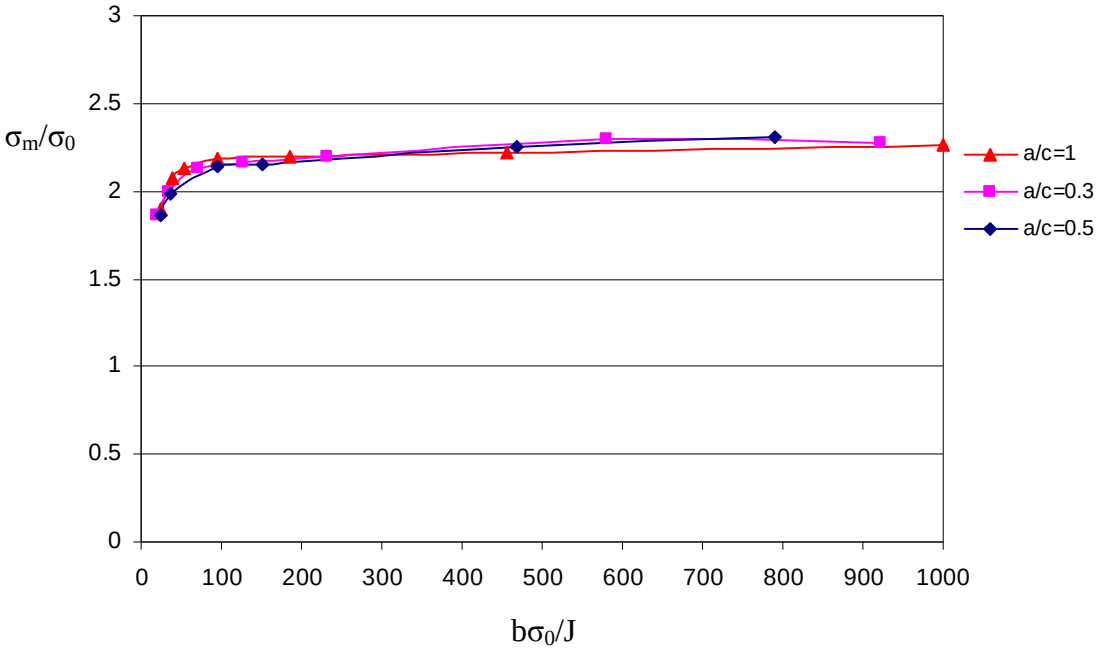

Figure 10.59: The mean stress at a distance $r\sigma_0/J=2$ as a function of deformation level at 45° for a deep semi-elliptical surface crack, a/w=0.5, with different aspect ratios in bending (a/c=0.33, 0.5 and 1).

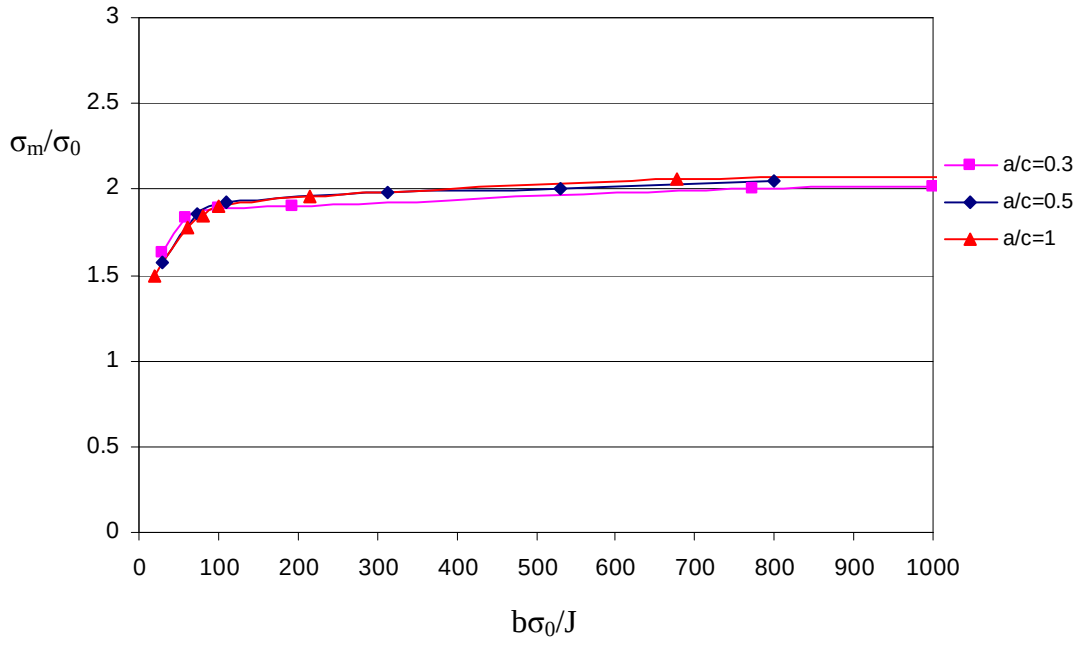

Figure 10.60: The mean stress at a distance $r\sigma_0/J=2$ as a function of the deformation level at 70° for a deep semi-elliptical surface crack, a/w=0.5, with different aspect ratios in bending (a/c=0.33, 0.5 and 1).

11. Shallow semi-elliptical surface cracks in bending

11.1 Introduction

This chapter presents results of modelling shallow semi-elliptical surface cracks. The aim is to investigate whether shallow cracks behave in a similar manner to deep cracks. It also investigates how the crack configuration affects crack tip constraint. The material data was described in Chapter (10). The geometry and finite element model are initially presented. A detailed elastic-plastic solution is then described. Initially the development of the plastic zone around the crack at both low deformation and fully plastic condition is shown. The mean stress, J-dominance conditions and plane strain constraint ahead of the crack at different parametric angles are then examined. Finally, the procedure proposed in Chapter (9) was used to estimate the amount and the direction of the maximum crack extension.

11.2 Finite element model

For shallow semi-elliptical cracks (a/w=0.1, a/c=1), thirty concentric rings of elements were focused around the crack tip. Each ring contained 312 elements: 26 elements along the crack front and 12 around the half circumference, as shown in Figure (11.1). The total number of elements was 120,000. In the shallow semi-elliptical surface crack with a/c=0.5 the total number of elements was 60,305. Forty five rings with 9900 elements were created; each ring contained 220 elements distributed as 22 elements along the crack and 10 elements around the half circumference. The final mesh is shown in Figure (11.2). For a semi-elliptical surface crack with a/c=0.3 the number of elements was 109,388. Twenty seven rings were created around the crack front and the number of elements in each ring was 280. A portion of the mesh is shown in Figure (11.3).

11.3 Shallow semi-circular surface crack in bending (a/c=1, a/w=0.1)

11.3.1 Crack tip stress field

Figures (11.4) to (11.6) show the development of the plastic zone around the crack. The largest plastic zone developed in the angular range 60˚-90˚ and reduced towards the deepest point as shown in Figures (11.4) and (11.5). The development of the plastic zone started at a very low deformation levels ($b\sigma_0/J=4390$) where b is the uncracked ligament and J is the local J-integral at the deepest point. Figure (11.6) shows that plasticity encompasses most of the cross section at a deformation level $b\sigma_0/J=192$. A small elastic segment was confined in the middle of the bar along the neutral line of the body. The plastic zone at the deepest point in a shallow crack was larger and developed earlier than in the deep crack configuration.

The mean stress at the crack tip (r=0) and at a distance $r=2J/\sigma_0$ for the deepest position ($\theta=0$˚) is shown in Figure (11.7). Low mean stresses occurred even at low deformation levels ($b\sigma_0/J\approx2000$) as anticipated. The reduction in the mean stress in contained yielding was caused by in-plane constraint loss (compressive T-stress) as shown in Figure (11.8). To investigate the effect of T-stress the Karstensen`s equation (1996) was used as described in Chapter (10) and the resultant mean stress are shown in Figure (11.7). In-plane constraint loss (T/Q) reduced the mean stress within contained yielding. However in-plane constraint loss (T/Q effect) still did not fully explain the difference between the reference plane strain solution and the full three-dimension solution. In fully plastic deformation ($b\sigma_0/J<200$) the mean stress was distance dependent and an additional reduction was observed. The plane strain condition $\sigma_{zz}/(\sigma_{rr}+\sigma_{\theta\theta})$ was maintained at all deformation levels at both distances, r=0 and $2J/\sigma_0$ as shown in Figure (11.9). This differs from the deep crack results where the plane strain parameter at $r=2J/\sigma_0$ collapsed at deformation levels of $b\sigma_0/J\approx200$.

Figure (11.10) shows the mean stress at $\theta=45$˚ as a function of deformation level. At the tip the mean stress was $1.75\sigma_0$ at all observable levels of deformation. At $r=2J/\sigma_0$ the mean stress collapsed markedly when a deformation of $b\sigma_0/J=200$ was approached. The mean stress was distance independent at low deformation levels and became distance dependent at high deformation levels ($b\sigma_0/J\leq200$). The proximity to plane strain

conditions is shown in Figure (11.11). At $\theta=45^{\circ}$ the ratio was close to 0.4 until large deformations ($b\sigma_0/J=100$). However for the deep crack there was no loss of plane strain constraint at this angle.

Figure (11.12) shows the mean stress directly ahead of the crack at $\theta=70^{\circ}$ as a function of deformation. At the tip the mean stress was approximately $1.75\sigma_0$ for all deformation levels, but at a distance $r=2J/\sigma_0$ the mean stress again reduced in full plasticity ($b\sigma_0/J\leq 300$). The plane strain parameter is shown in Figure (11.13). The ratio at the tip was close to the theoretical value for plane strain. However it significantly reduced at $b\sigma_0/J\leq 300$. The reduction in the mean stress and plane strain parameter at a distance two crack tip openings could be due to the proximity to the free surface. The distinction is obvious given that the plane strain parameter was retained for deep crack configurations at both, $r=0$ and $r=2J/\sigma_0$. At the free surface the mean stress exhibited the same value as the deep crack at a plane stress value of (0.577) as shown in Figure (11.14).

Figure (11.15) summarises the mean stress as a function of the parametric angle. It shows that the mean stress distribution is almost uniform along the crack front with slightly elevated values at 45°. This contrasts to deep cracks when the mean stress rose significantly at 45°-70° as deformation increased, while collapsing at the deepest point. This is because the deepest point of the deep crack is close to the neutral axis. At the free surface plane stress conditions prevail in both configurations.

Plane strain conditions were maintained around the majority of the crack front up to ($\theta=70^{\circ}$) in small scale yielding ($b\sigma_0/J\geq 713$) as shown in Figure (11.16). In large plastic deformation ($b\sigma_0/J\leq 192$) plane strain conditions were lost at 70° and became zero at the free surface. It should be noted that at this particular position $\theta=70^{\circ}$, the crack depth ratio is a`/w= 0.034 which is very close to the free surface when the mean stress was lost and a plane stress state was encountered. Figure (11.17) shows the non-dimensional J-integral as a function of the parametric angle. The maximum values of the J-integral were in the region 45°-70°, and decreased at the deepest point and the free surface.

11.3.2 Determination of crack growth in a shallow semi-circular surface crack a/c=1, a/w=0.1 in bending.

To calculate crack extension the procedure of Chapter (9) was used. The results in Figure (10.18) show that the crack extends in full plasticity in the 45°-70° segment, but also continues growing at the deepest point. This is different to deep cracks where the crack no longer grows at the deepest point. For crack shape sequence, the maximum values of J-integral and mean stress occurred in the angular range 45°-70°. Subsequently the crack grew at higher rate at 45° than at the deepest point as shown in Figure (11.19). The crack maintained this shape until the crack depth approaches the half thickness (a/w=0.5) then the growth restricted to 45°-70° since the global bending effect suppressed the growth at the deepest point as shown in Figure (11.20).

11.3.3 Force-moment redistribution around a shallow semi-circular surface crack front a/c=1, a/w=0.1 in bending.

Figure (11.21) shows the distribution of the opening stress $\sigma_{\theta\theta}$ at the deepest point (θ=0°) as a function of a distance from the tip towards the back face (d/w) for a shallow semi-circular crack. The tensile stress on the ligament was equivalent to the compressive stress at low and high deformation levels. This contrasts with deep cracks where a large compressive field was established across most of the ligament as shown in Figure (10.29). Similar stress profiles were observed at the other positions around the crack tip as shown in Figures (11.22) and (11.23) for 45° and 70° respectively.

Figure (11.24) shows the way in which a compressive force and tensile moment develop at the deepest point (θ=0°) for this configuration. There was no significant change in the force or moment in the transition from small scale yielding to full plasticity. This behaviour is also shown at 45° and 70° as illustrated in Figures (11.25) and (11.26).

Figure (11.27) shows the force-moment ratio at low and high deformation levels. It can be seen that the ratio was almost independent of deformation at all angles considered. At the deepest point the ratio was negative due to the compressive force, however the force-

moment ratio was close to zero in the angular region 45°-70°. The force-moment ratio at the deepest point (θ=0°) was less negative than the force-moment ratio at the same angle in a deep crack.

11.4 Shallow semi-elliptical crack a/w=0.2, a/c=0.33 in bending

11.4.1 Stress fields

Figures (11.28) and (11.29) show the development of the plastic zone around a shallow semi-elliptical crack in bending. Plasticity developed initially at the free surface and then extended towards the deepest point.

Figure (11.30) shows the distribution of the J-integral along the crack front. The J-integral values were similar for all positions on the crack front up to the parametric angle of 70°, measured from the deepest point. At the free surface the J-integral was significantly lower.

The mean stress around the crack front is shown in Figure (11.31). This was determined at a radial distance of $2J/\sigma_o$ ahead of the crack tip, normal to the crack front. The largest stresses were observed at the deepest point and systematically reduced when approaching the free surface, where stresses matched the plane stress state $0.577\sigma_0$. The plane strain constraint at the deepest point retained the plane strain value 0.5 as shown in Figure (11.32). At 45° the constraint was approximately 0.43 which is close to plane strain value. However, the constraint collapsed considerably at 70° at high deformation levels ($b\sigma_0/J<100$).

11.4.2 Determination of crack growth of a shallow semi-elliptical surface crack a/c=0.33, a/w=0.2 under bending.

The results of the procedure described in Chapter (9) are shown in Figure (11.33). The largest crack extension is predicted to occur for the deepest segment of the crack front (θ=0°), due to the combination of a high mean stress and a high J-integral at this location

(Terfas and Bezensek, 2009a). Approximately the same amount of ductile crack growth is predicted for the first half of the crack front (up to the 45°). As the free surface was approached, both the mean stress and the J-integral reduced, thus indicating less crack growth.

To determine the crack shape the mean stress and the J-integral were determined for a series of crack shapes and used in conjunction with the procedure of Eq. (9.5) to evolve the crack through a sequence of shapes. The resulting sequence of crack shapes is shown in Figure (11.34) for the three steps considered. In the first step the crack growth was dominant from the deepest point to 45°, with only a very small extension predicted for the free surface.

After the first step of crack extension, the crack growth retarded at the deepest segments and became largest in the region of 45°. After the second step the crack shape started to deviate significantly from the semi-elliptical shape. With the increase in crack depth, the mean stresses and the J-integral departed from the initial trend. The mean stress collapsed below the highly constrained value for the deepest point, while the J-integral attained its largest value in the angular range 45°-70°. The net result of these two changes was the largest ductile crack extension occurred at 45° and reduced gradually towards the free surface and the deepest segment. At the deepest point crack growth was almost suppressed due to the effect of the global bending moment impinging on the local crack tip field. On the surface the mean stress was low. Figure (11.35) summarises the growth of an initial shallow semi-elliptical surface crack under bending (Terfas and Bezensek, 2009a). Figure (11.36) shows the crack surface area as a function of global deformation, here taken as the deflection normalised by the span.

Figure (11.37) shows the force-moment ratio in a shallow semi-elliptical surface crack a/c=0.33, a/w=0.2. The force-moment ratio along the crack in shallow cracks was significantly smaller than that observed in deep semi-elliptical surface cracks, and was weakly dependent on the deformation level.

11.5 A shallow semi-elliptical surface crack in bending, (a/w=0.2, a/c=0.5)

The plastic zone for (a/c=0.5) developed in a similar way to that for (a/c=0.33), in that a bigger plastic zone developed in the surface direction (i.e. at deformation level of $b\sigma_0/J=439$), as shown in Figure (11.38), where b and J are both measured at the deepest point. Figure (11.39) shows the normalised J-integral at different levels of deformation as a function of parametric angle θ for the shallow semi-elliptical surface crack in bending. The distribution of J-integral shows less variation from the deepest point to 70° compared to the large variation observed for the deep cracks discussed in the previous chapter. It can also be seen that the values of J-integral show a slight reduction at the deepest point in comparison to a similar crack with higher aspect ratio (a/c=0.33).

The mean stress was almost uniform around the crack except at the free surface, and remained high at the deepest point as well as at 45° as shown in Figure (11.40). Figure (11.41) shows the proximity to plane strain along the crack at different deformation levels. The plane strain parameter remained high at about 0.47 and close to the theoretical value of plane strain of 0.5 at the deepest point, and at about 0.4 at 45°. Constraint loss started at 70° as plastic deformation increased. The crack grew most between the deepest point and 45° as shown in Figure (11.42).

11.6 Surface cracked panel experiments under bending

The material chosen was a plain carbon-manganese steel described as grade 50D under BS4360. Tensile tests were performed using specimens with 5.64mm diameter and 32mm original gauge length at room temperature 20° C to determine the mechanical properties. The material behaves as an intermediate hardening material with a hardening exponent n=10. Young's modulus was 210 GPa, Poisson's ratio 0.3, the yield strength of 400 MPa, and the ultimate tensile stress was 626 MPa.

Four surface cracked plates with length of 220mm, 60mm width and 10mm thick were machined from a 25mm thick plate. A semi-elliptical notch with depth ratio of a/w=0.2

and aspect ratio of a/c=0.2 was machined in the surface with a cutter as shown in Figure (11.43). Fracture tests were performed on a universal testing machine equipped with three-point bending, and the test set-up is shown in Figure (11.44). Samples were tested under displacement control at a cross-head speed of 2mm/min. Each specimen was subjected to a large displacement to ensure crack growth. It should be mentioned that the cracks were introduced into plates with a cutter and there was no fatigue pre-cracked performed.

Figures (11.45) to (11.48) show the force-crosshead displacement curve for each test sample with different amounts of displacement. The experimental observations on shallow semi-elliptical notches were consistent with the FEA results. The crack grew at the deepest point by 1-2mm and growth reduced towards the free surface as shown in Figures (11.49) and (11.50). For larger displacements crack growth increased along the crack front including the deepest point up to about half thickness. Then the crack stopped growing at the deepest point and extended at 45°-70° under the surface and a boat shape appeared as shown in Figures (11.51) and (11.52). Figure (11.53) shows the steps of crack growth of the test samples as deformation increases. This observation emphasises that ductile tearing was strongly affected by the level of local constraint in the vicinity of the crack tip. After significant amount of the crack growth constraint was lost at the deepest point due to bending moment impinging on the crack tip field. The bending moment effects reduced at 45°-70° and allowed the crack to extend at this point and beneath the surface. This indicates that crack growth under bending is a relatively stable process.

11.7 Discussion

In shallow semi-circular cracks (a/w=0.1, a/c=1) the mean stress distribution was almost uniform along the crack front with slightly elevated values at 45°. The maximum J-integral occurred in the angular region 45°-70°. This contrasts to deep cracks when the mean stress was elevated significantly at 45°-70° as deformation increased, and collapsed rapidly at the deepest point. Crack growth occurred along the crack front including the deepest point and was larger in the angular range 45°-70° at high deformation levels. This

is different to the behaviour of deep cracks where the crack stops growing at the deepest point.

In shallow semi-elliptical surface cracks (a/w=0.2, a/c=0.33) the maximum mean stress occurred at the deepest point and systematically reduced when approaching the free surface, where stresses matched the plane stress value $0.577\sigma_0$. This contrasts to the behaviour of deep cracks where the mean stress reduced at the deepest point at high deformation levels. The local field at the deepest point allows the crack to grow in the deepest direction. However for semi-circular surface cracks (a/c=1) the largest crack growth was found in the angular range 45° to 70°. Decreasing a/c develops higher constraint and J-integral values at the deepest point, subsequently more growth is expected.

It has been shown that two different initial shapes (a/w=0.5, a/c=1) and (a/w=0.2, a/c=0.33) showed similar behaviour in bending. For deep cracks the loss of constraint at the deepest point and the low stress triaxiality at the free surface increases the resistance to ductile tearing at these segments. The largest crack extension was thus observed for 45° to 70° segments. This growth was however confined to subsurface due to very low stress triaxialities at the surface which suppress crack growth. In shallow surface cracks the local tension field causes crack growth at the deepest point in the early stages. However as the flaw depth approaches half the thickness (a/w=0.5) a similar sequence of crack shapes was observed to those in deep cracks with crack extension largely confined to the 45° to 70° segments. This results in crack tunnelling with limited ductile tearing on the surface. In bending, the flaws do not seem to propagate readily in the through-thickness direction due to the global bending field suppressing the local crack tip field at the deepest segments, thus promoting the flaw extension along the width direction. This result is consistent with results obtained by Brocks et al (1990) who tested a surface flaw in a pipe under combined bending and tension. They observed that the crack grew with a greater rate in the axial direction than growth through the thickness adopting the canoe-shape.

11.8 Conclusion

Non-uniform levels of constraint and J-integral occur around the crack front of a semi-elliptical crack at large deformation levels. This emphasises that both, the mean stress and J-integral are geometry and load dependent, and both have a major effect on the direction and extent of ductile crack growth. The amount of crack extension around the crack front is dependent on the initial crack shape and type of loading. Shallow semi-elliptical surface cracks (a/c=0.33, 0.5) exhibit uniform crack tip constraint and values of the J-integral along the crack front between the deepest point and 70°. Semi-circular surface cracks (a/c=1) showed an increase in crack tip constraint and J-integral in the angular range 45°-70° compared to the deepest point and the free surface. Consequently more ductile tearing occurred in the angular region 45°-70° than at the deepest point and the free surface. The initial crack shape was no longer maintained as the crack developed under ductile tearing. It can be concluded that deeply cracked geometries tend to grow significantly in the angular region 45°-70°, while shallow cracks grow most at the deepest point.

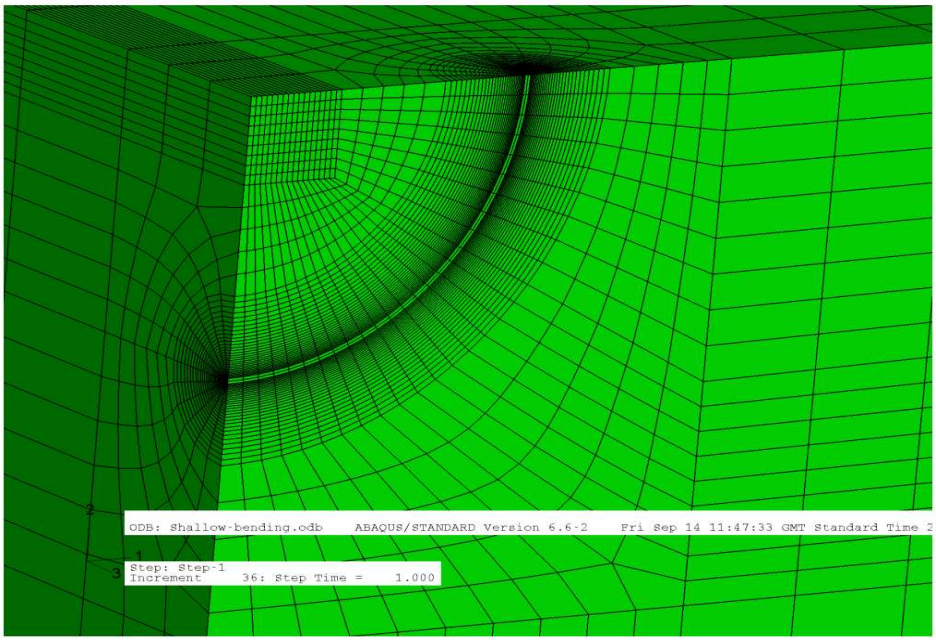

Figure 11.1: The mesh of the shallow semi-circular surface crack model, (a/w=0.1, a/c=1).

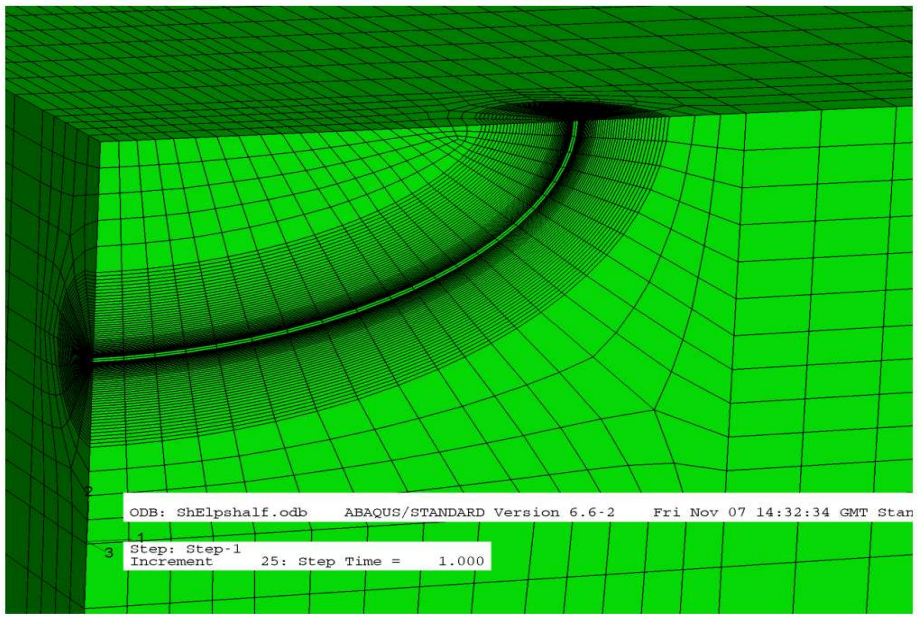

Figure 11.2: The mesh for a shallow semi-elliptical surface crack with a/w=0.2, a/c=0.5.

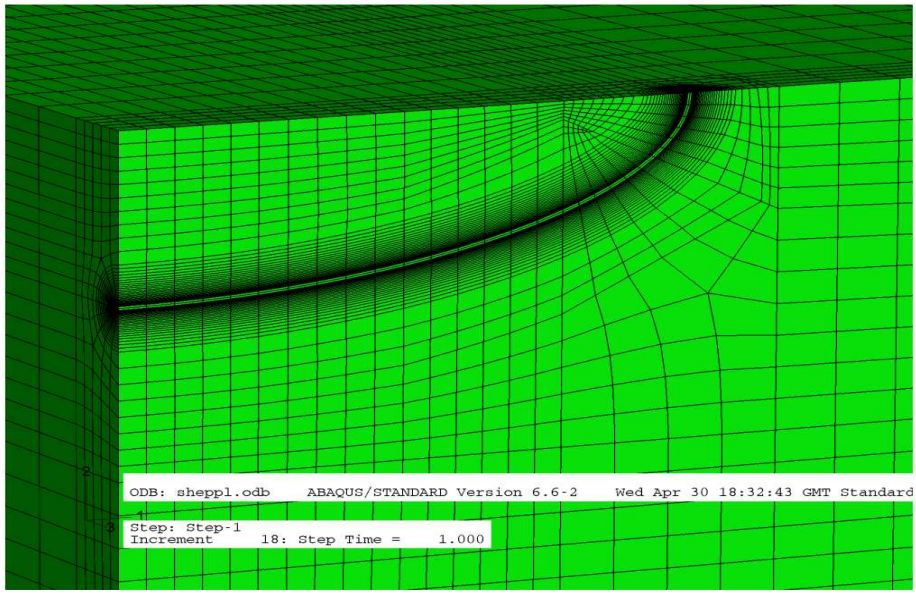

Figure 11.3: The mesh for a shallow semi-elliptical surface crack with a/w=0.2, a/c=0.3

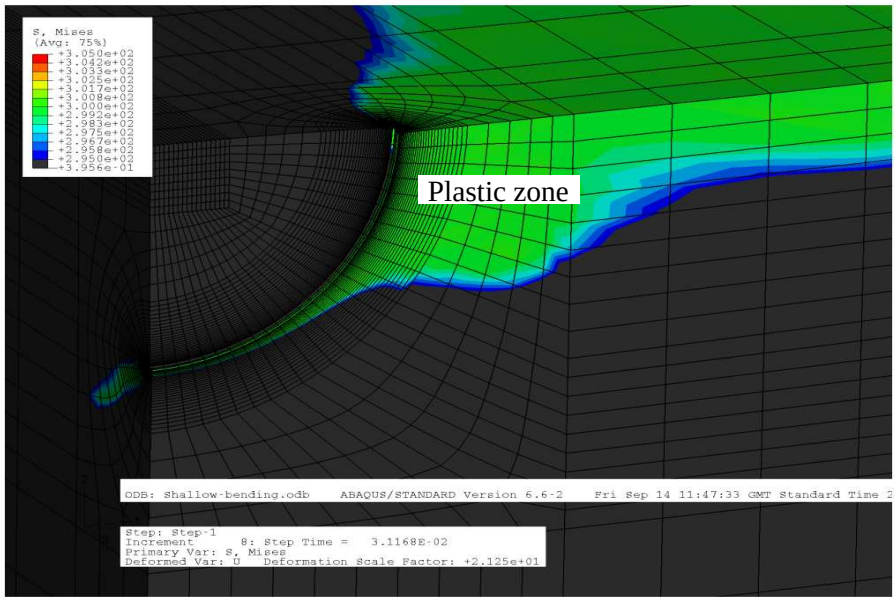

Figure 11.4: Development of the plastic zone along the crack at $b\sigma_0/J$= 4390, J was taken at $\theta=0^{\circ}$, (a/w=0.1, a/c=1).

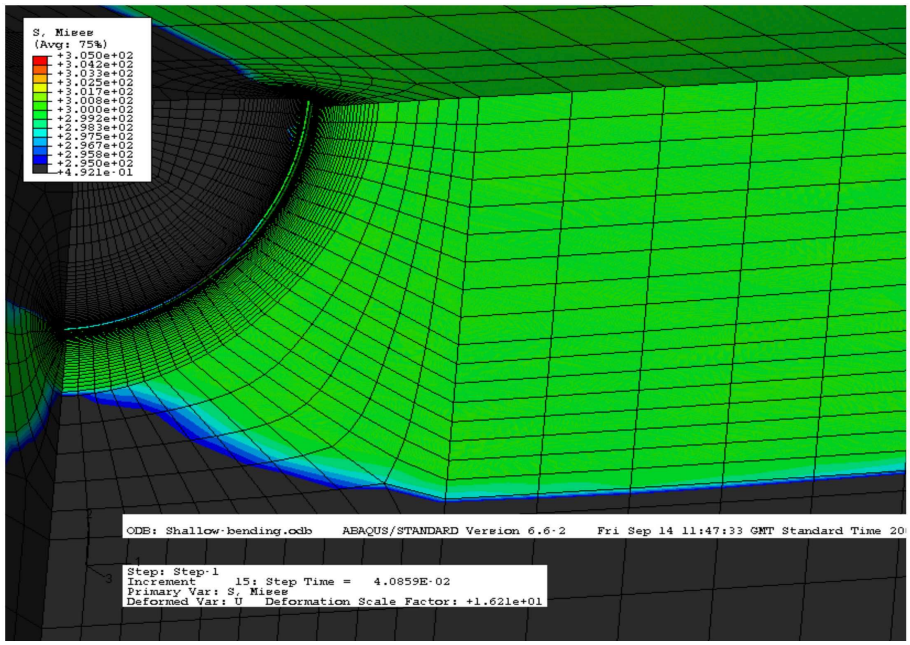

Figure 11.5 Extent of the plasticity through the body at $b\sigma_0/J$= 2061, J was taken at θ=0˚, (a/w=0.1, a/c=1).

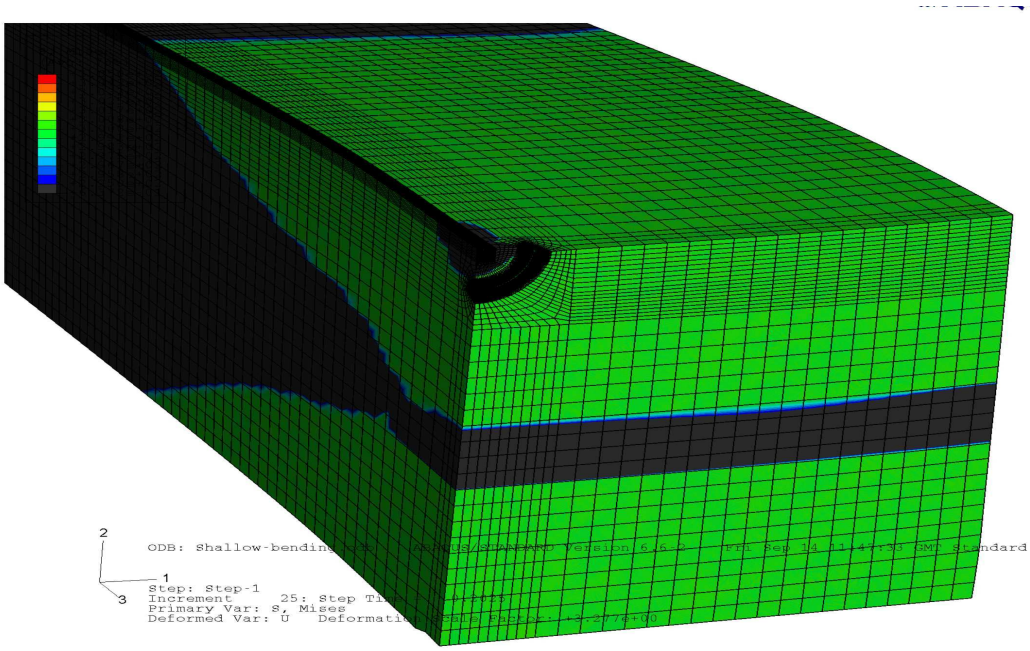

Figure 11.6: Full plasticity at ($b\sigma_0/J$=192, J was taken at θ=0˚), (a/w=0.1, a/c=1).

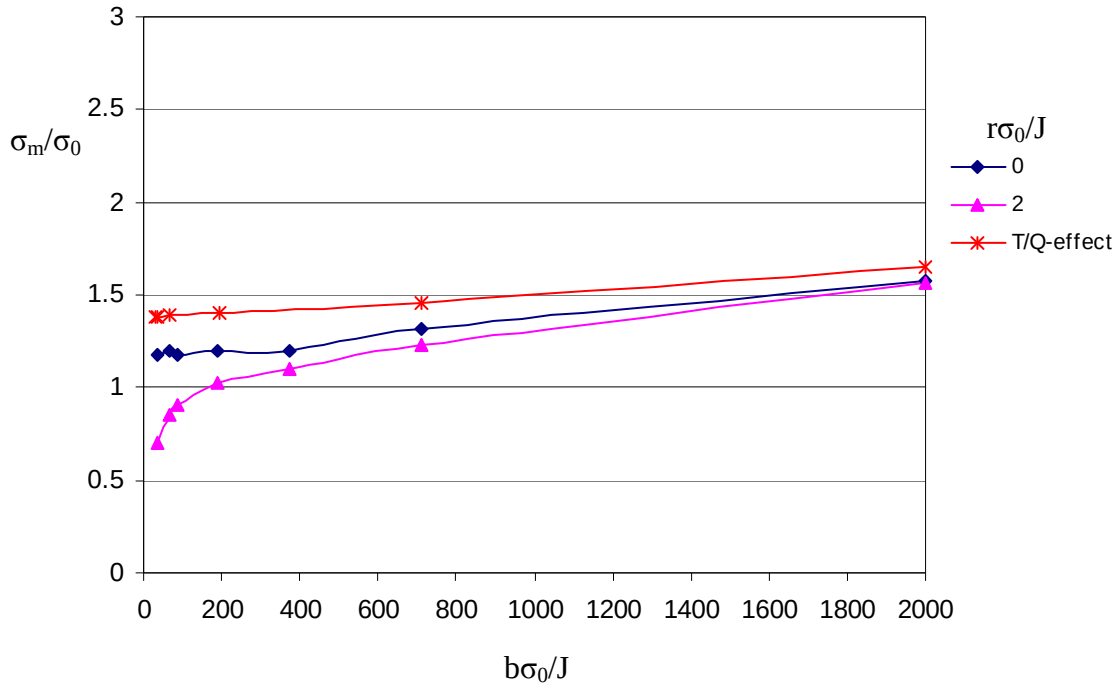

Figure 11.7: The mean stress at the deepest point of a shallow semi-circular surface crack (a/w=0.1, a/c=1) as a function of deformation level at the crack tip and at $r=2J/\sigma_0$, and compared to in-plane effects.

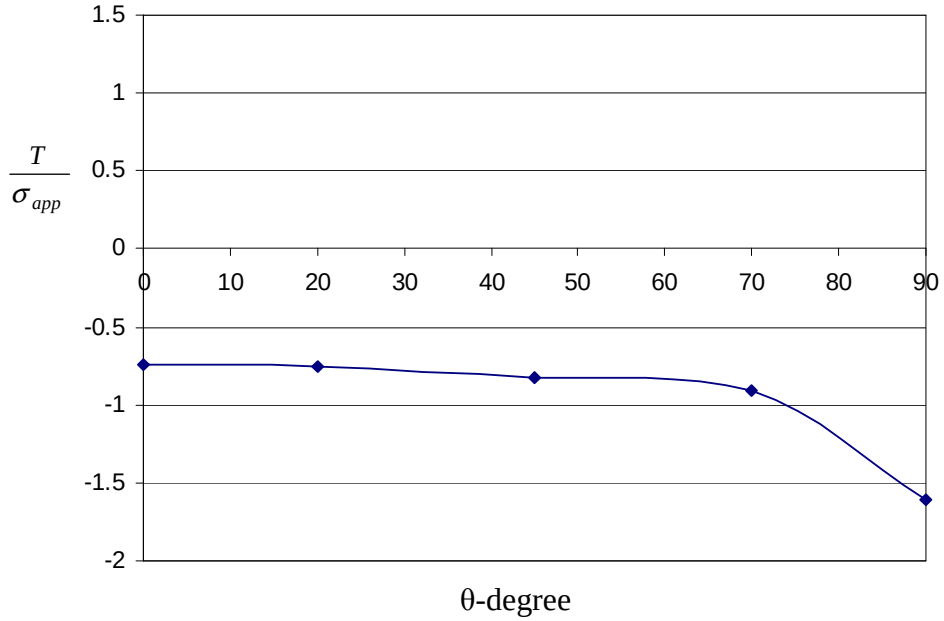

Figure 11.8: Elastic T- stress as a function of parametric angle (θ) in a shallow semi-circular surface crack (a/w=0.1, a/c=1).

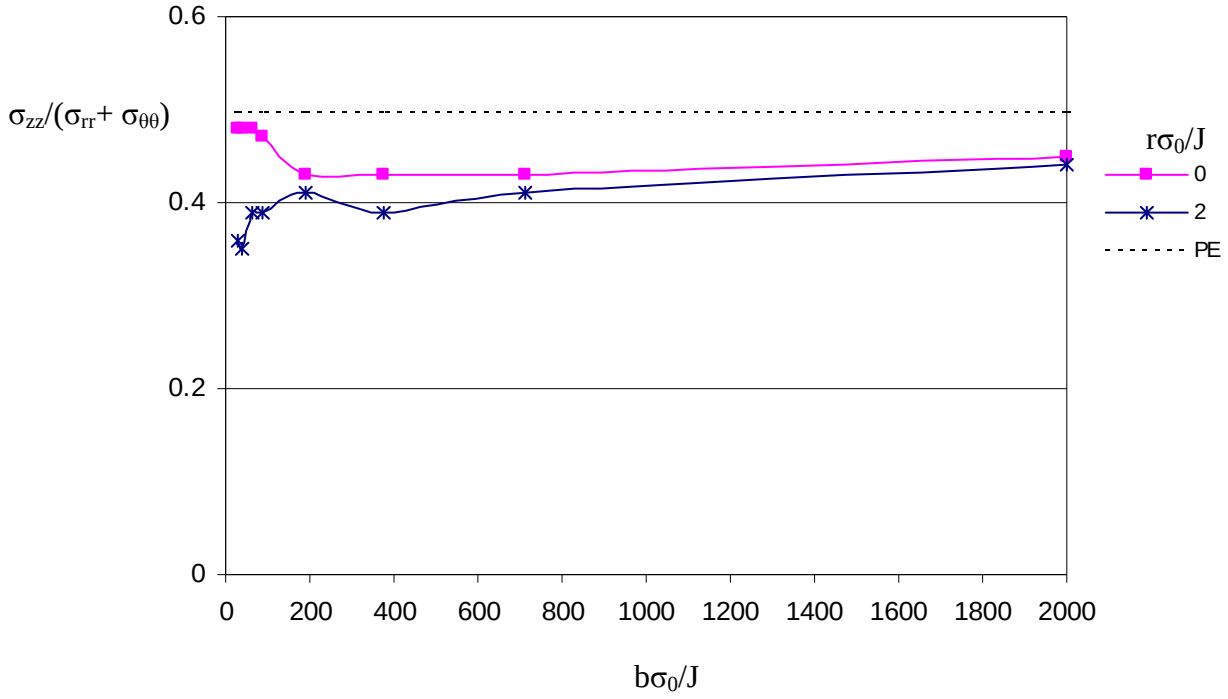

Figure 11.9: The proximity to plane strain at the deepest point as a function of deformation levels for a shallow semi-circular surface crack a/c=1, a/w=0.1, (PE is the plane strain value, 0.5).

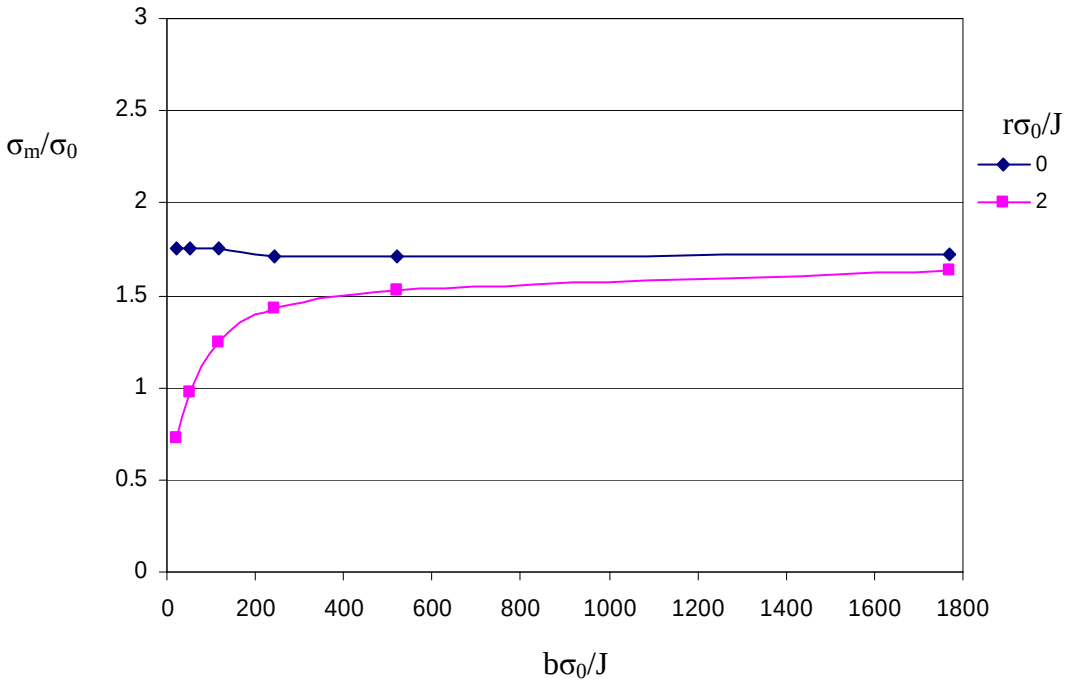

Figure 11.10: The mean stress at θ=45˚as a function of deformation levels at the tip and at r=2J/σ_0.

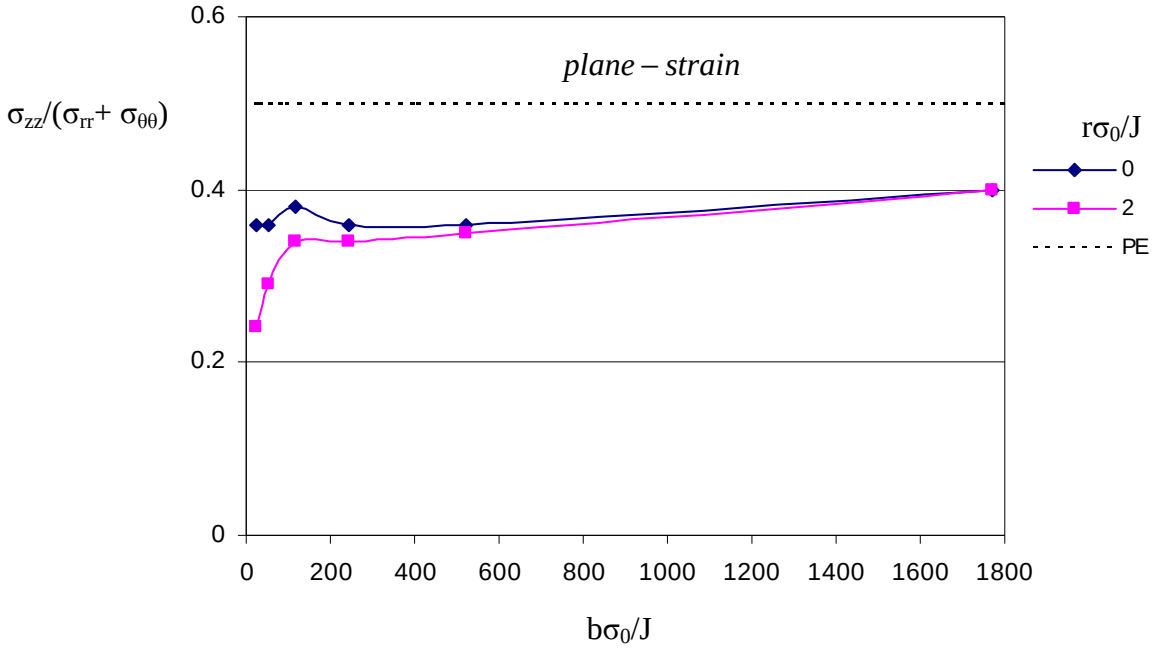

Figure 11.11: The proximity to plane strain as a function of levels of deformation for $\theta=45^{\circ}$ in the shallow semi-circular surface crack (a/w=0.1, a/c=1).

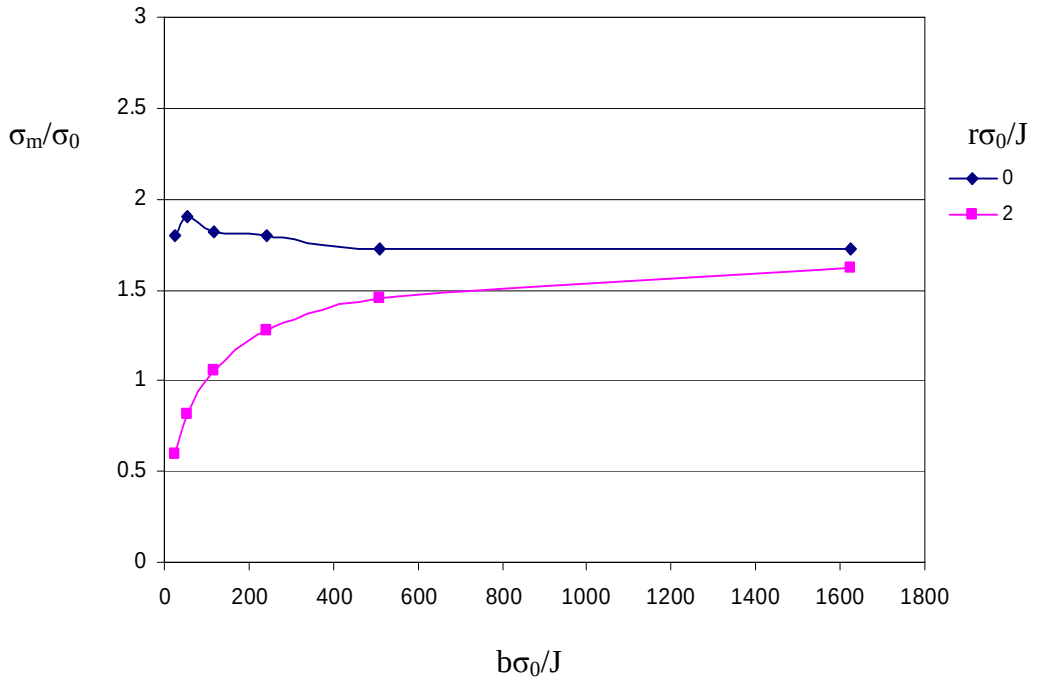

Figure 11.12: The mean stress at $\theta=70^{\circ}$ as a function of deformation at the tip and at $r=2J/\sigma_0$.

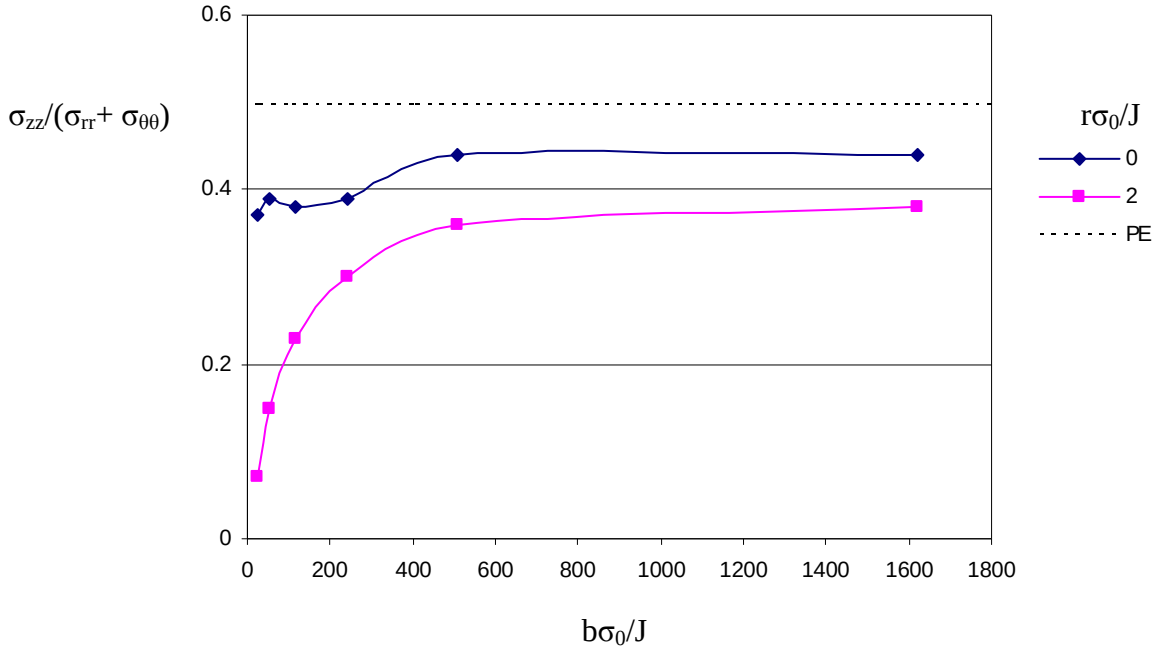

Figure 11.13: The proximity to plane strain as a function of levels of deformation for $\theta=70^{\circ}$.

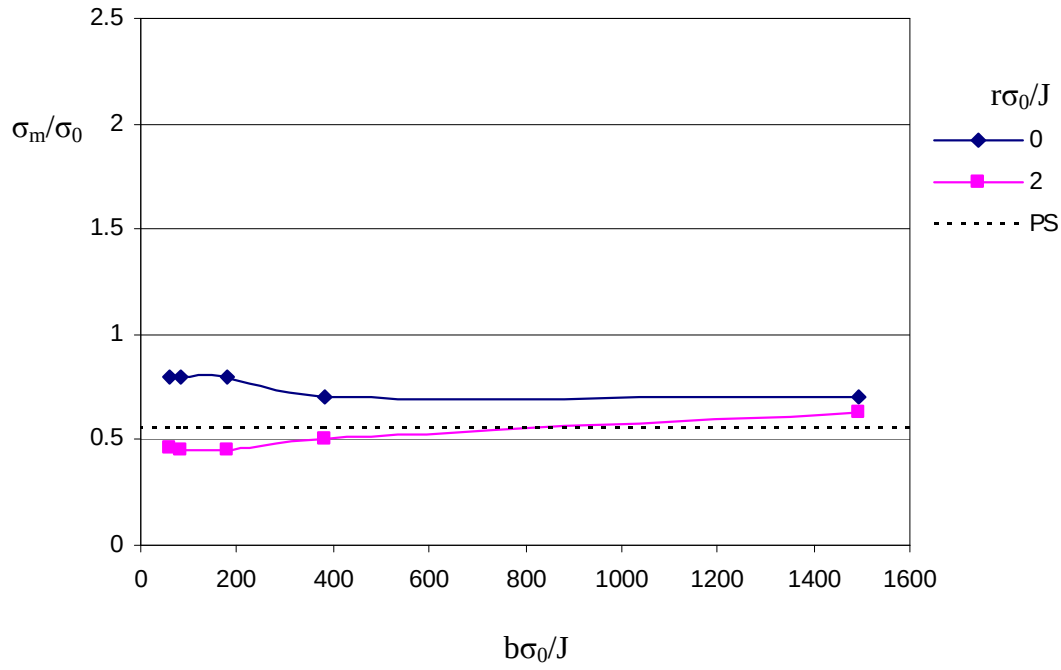

Figure 11.14: The mean stress at the free surface as a function of deformation at the tip and $r=2J/\sigma_0$ for a shallow semi-circular surface crack.

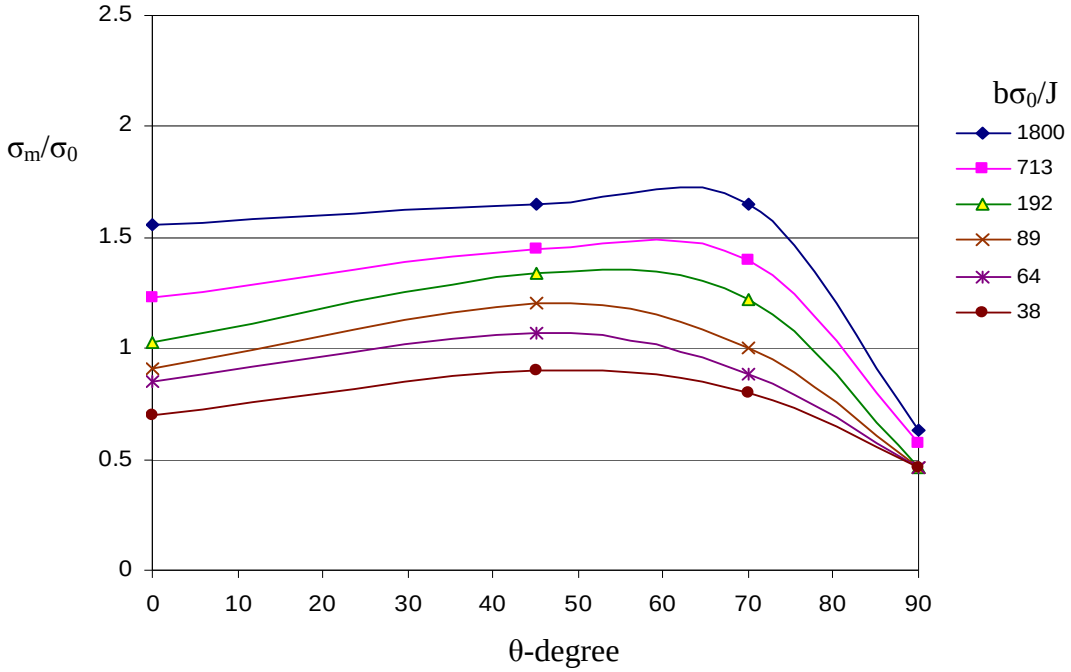

Figure 11.15: The mean stress at $r=2J/\sigma_0$ as a function of the parametric angle θ along the crack for a shallow semi-circular surface crack (a/w=0.1, a/c=1) in bending.

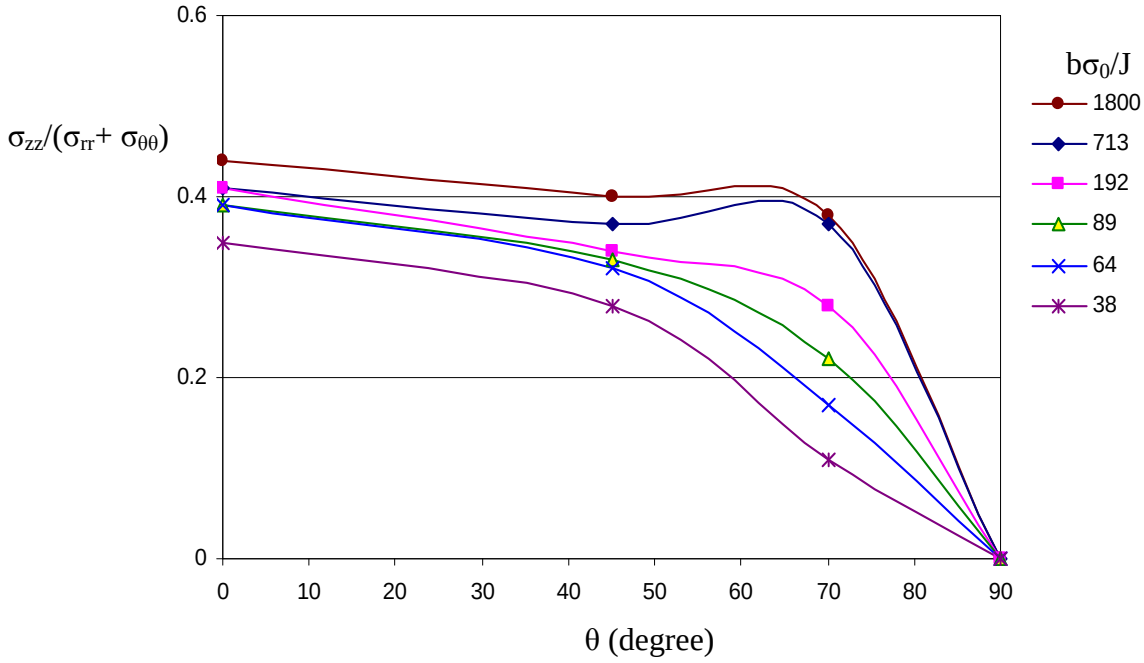

Figure 11.16: The proximity to plane strain at $r=2J/\sigma_0$ as a function of the parametric angle θ along the crack for a shallow semi-circular surface crack (a/w=0.1, a/c=1) in bending.

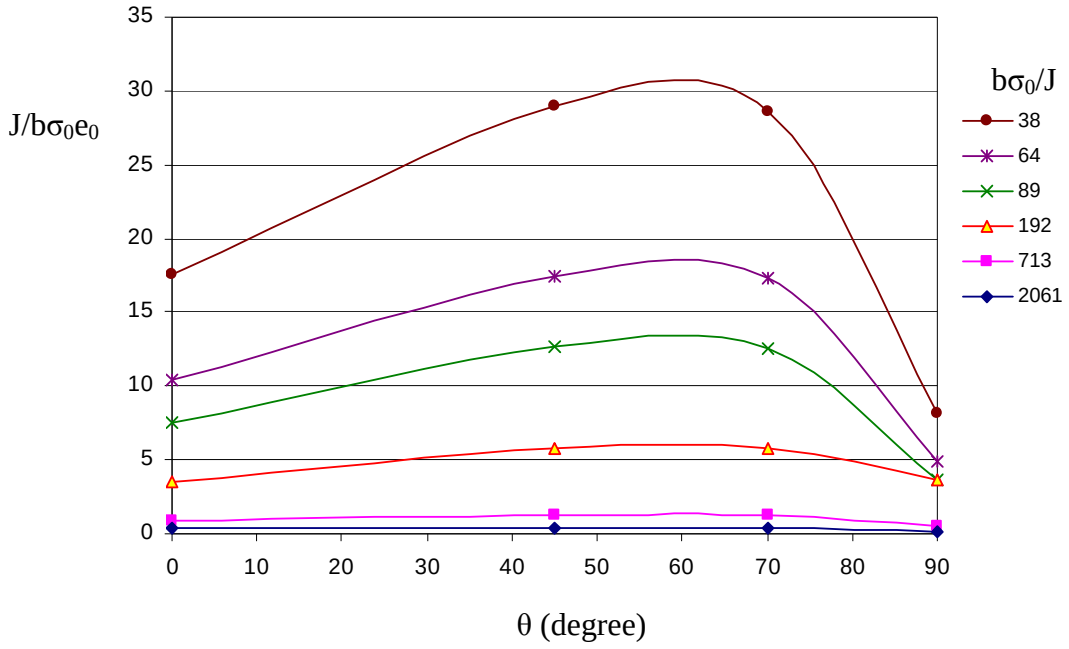

Figure 11.17: Non-dimensional J-integral distribution along the crack front from the deepest point (θ=0˚) to the free surface (θ=90˚) for a shallow semi-circular surface crack (a/w=0.1, a/c=1).

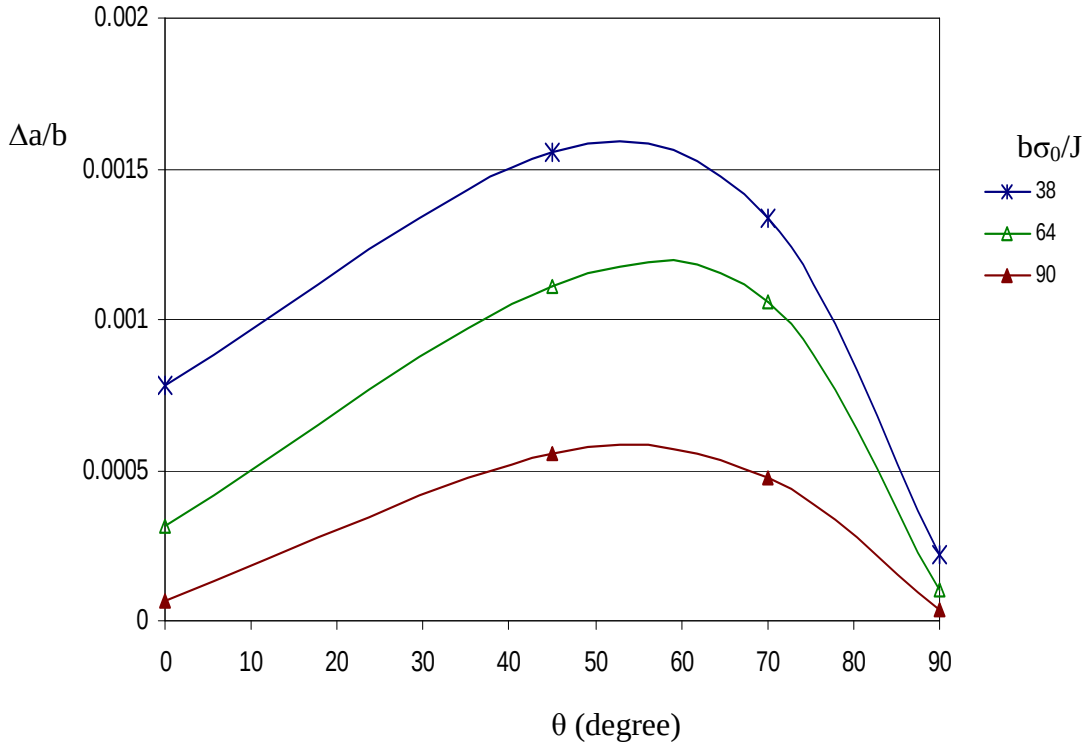

Figure 11.18: Crack growth as a function of parametric angle from the deepest point to the free surface for a shallow semi-circular surface crack (a/w=0.1, a/c=1).

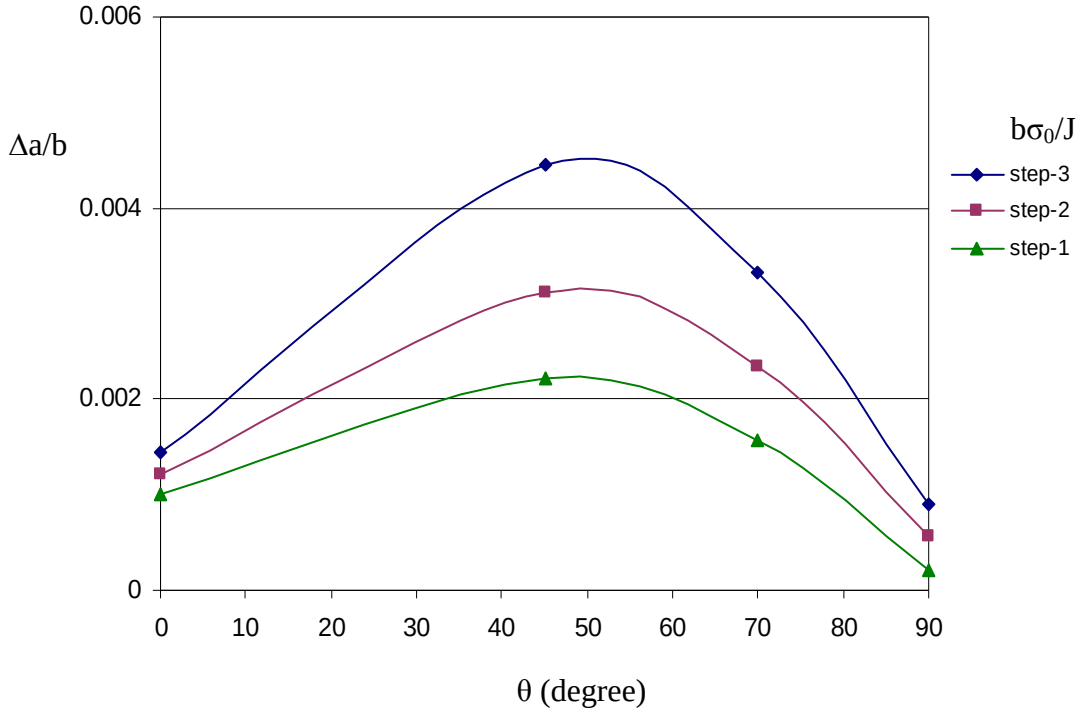

Figure 11.19: Crack growth steps at $b\sigma_0/J$=30, 25 and 20 for a shallow semi-circular surface crack a/c=1, a/w=0.1 in bending.

Figure 11.20: The crack shape development of a shallow semi-circular surface crack (a/w=0.1, a/c=1) under full plastic deformation in bending.

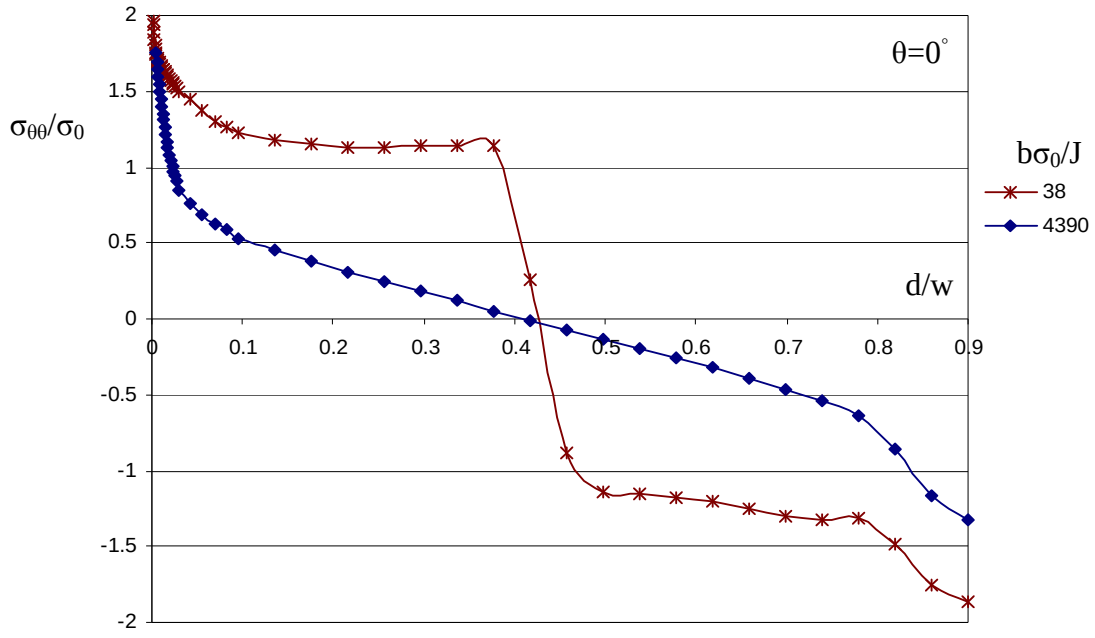

Figure 11.21: The opening stress $\sigma_{\theta\theta}$ at the deepest point $\theta=0^{\circ}$ as a function of a distance d/w for a shallow semi-circular surface crack (a/w=0.1, a/c=1) in bending.

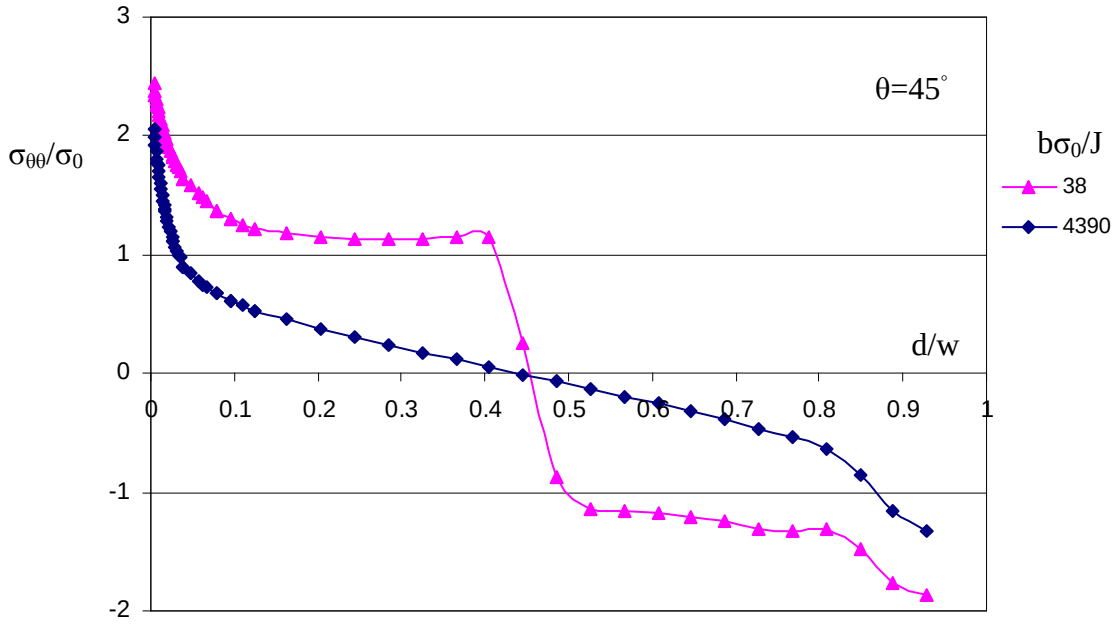

Figure 11.22: The opening stress $\sigma_{\theta\theta}$ at $\theta=45^{\circ}$ as a function of a distance d/w for a shallow semi-circular surface crack (a/w=0.1, a/c=1) in bending.

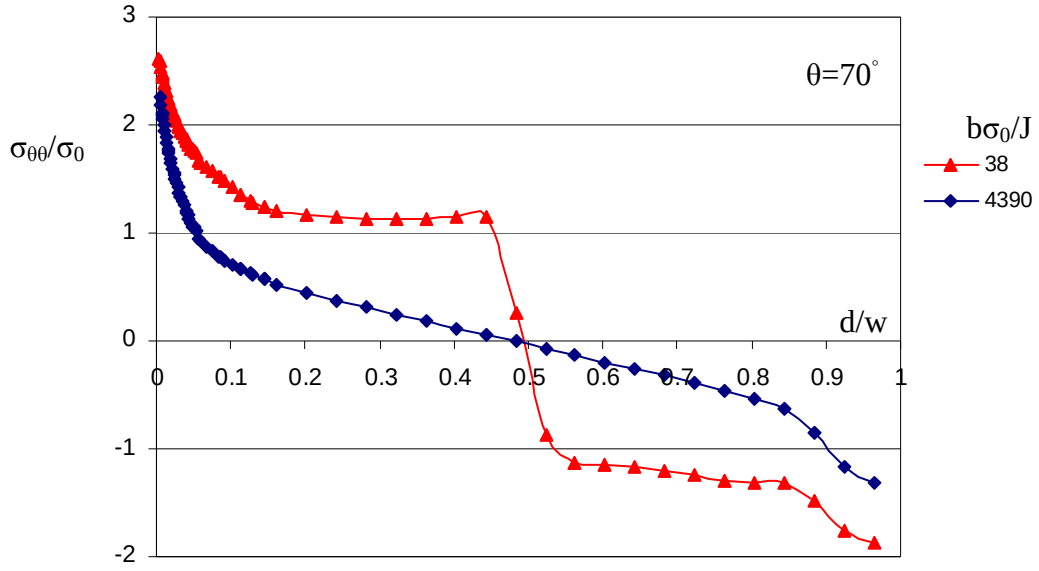

Figure 11.23: The opening stress $\sigma_{\theta\theta}$ at $\theta=70^{\circ}$ as a function of a distance d/w for a shallow semi-circular surface crack (a/w=0.1, a/c=1) in bending.

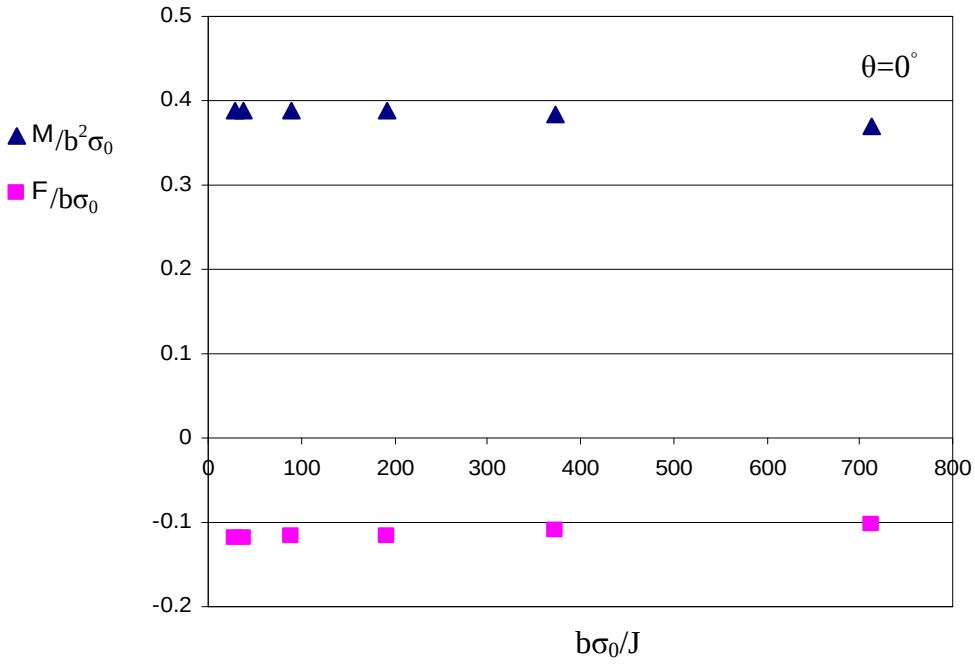

Figure 11.24: Force and moment redistribution along the uncracked ligament at the deepest point as a function of deformation for a shallow semi-circular surface crack (a/w=0.1, a/c=1) in bending.

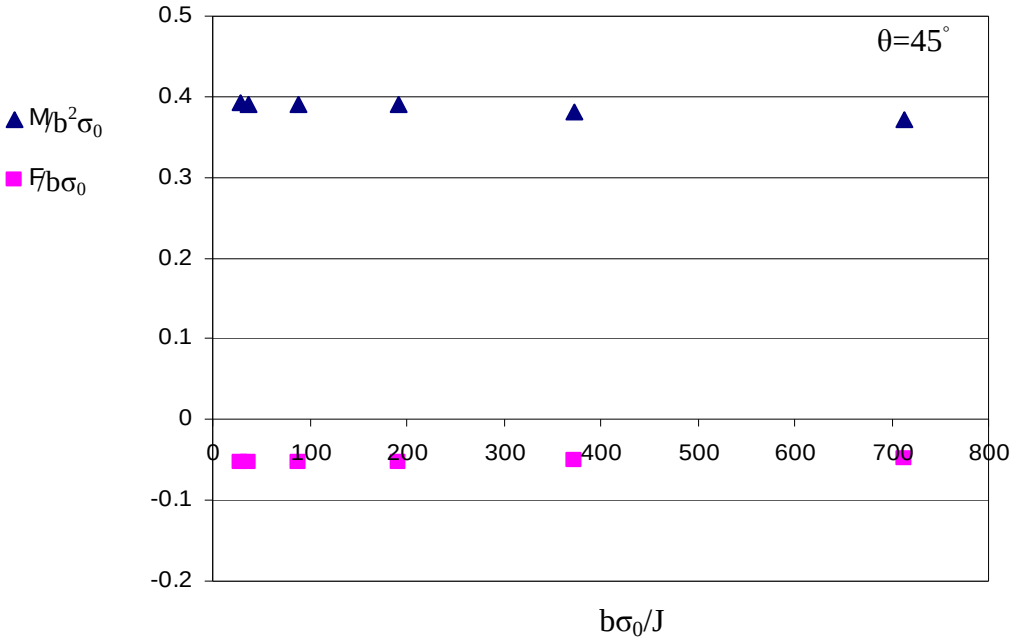

Figure 11.25: Force and moment redistribution along the uncracked ligament at 45° as a function of deformation for a shallow semi-circular surface crack (a/w=0.1, a/c=1) in bending.

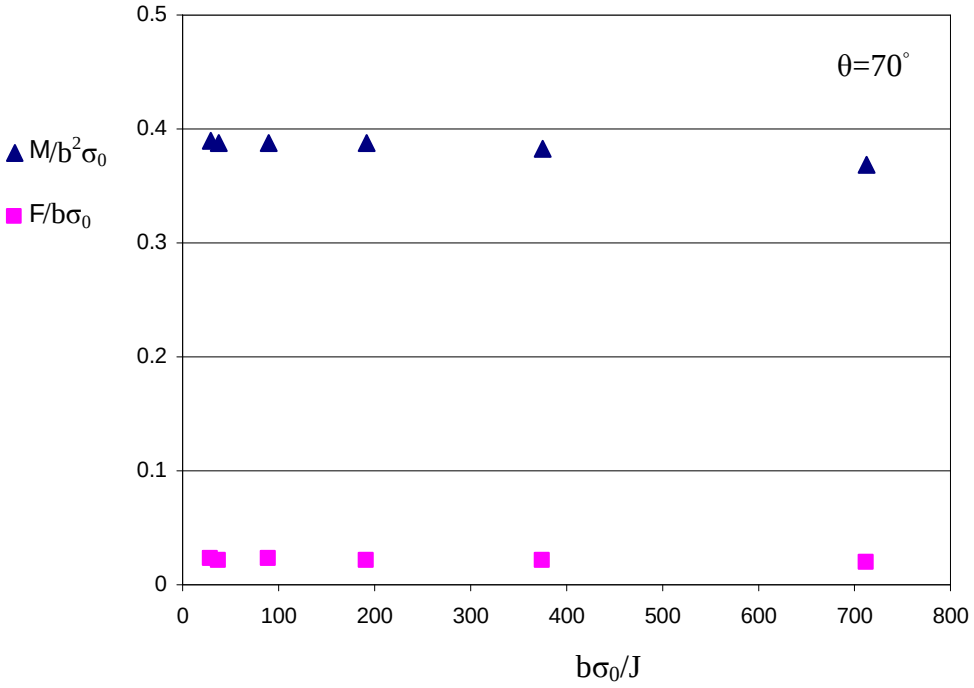

Figure 11.26: Force and moment redistribution along the uncracked ligament at 70° as a function of deformation for a shallow semi-circular surface crack (a/w=0.1, a/c=1) in bending.

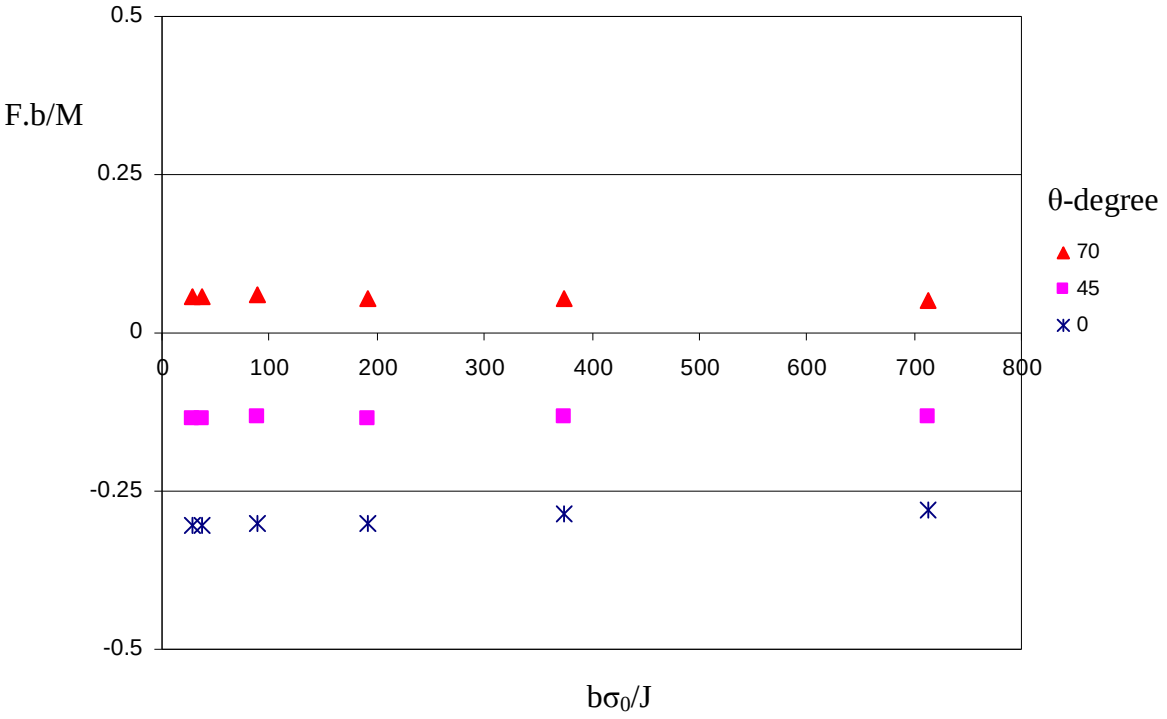

Figure 11.27: Force-moment ratio on the uncracked ligament ahead of the crack in a shallow semi-circular surface crack (a/w=0.1, a/c=1) in bending.

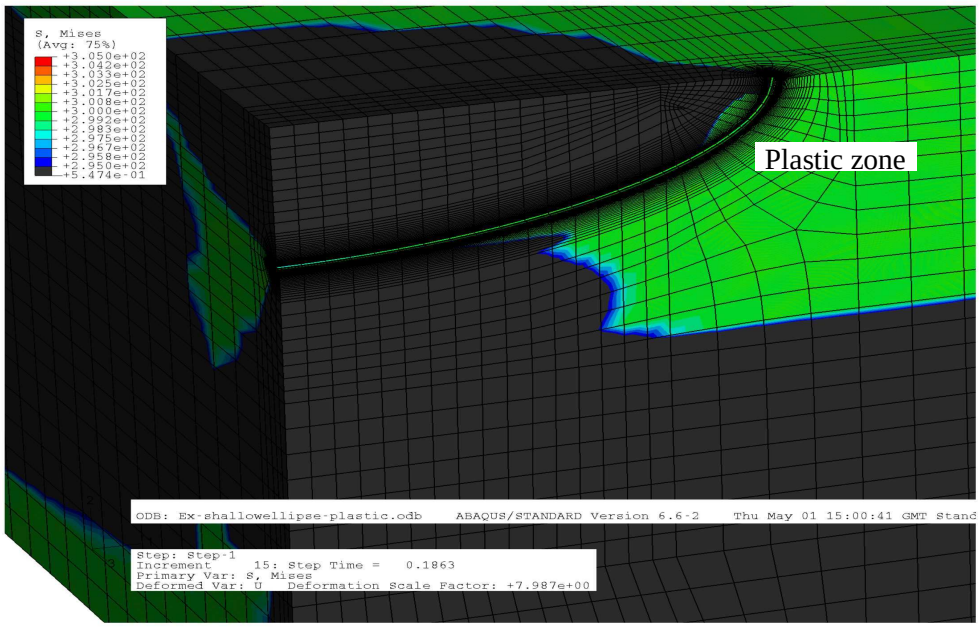

Figure 11.28: Plastic zone development around the crack front in a shallow semi-elliptical surface crack (a/c=0.33, a/w=0.2) in bending.

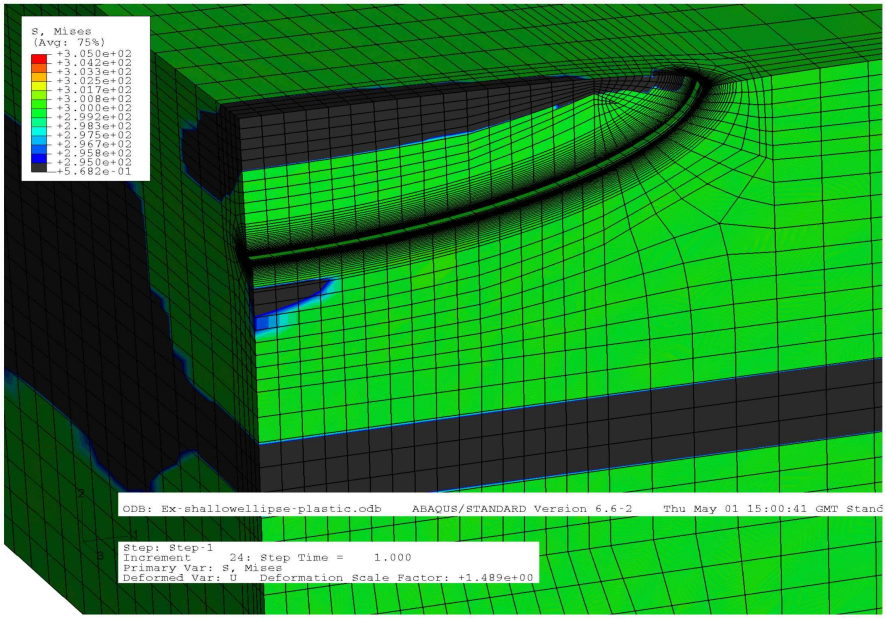

Figure 11.29: The plastic hinge centred at the body in a shallow semi-elliptical surface crack (a/c=0.33, a/w=0.2) in bending.

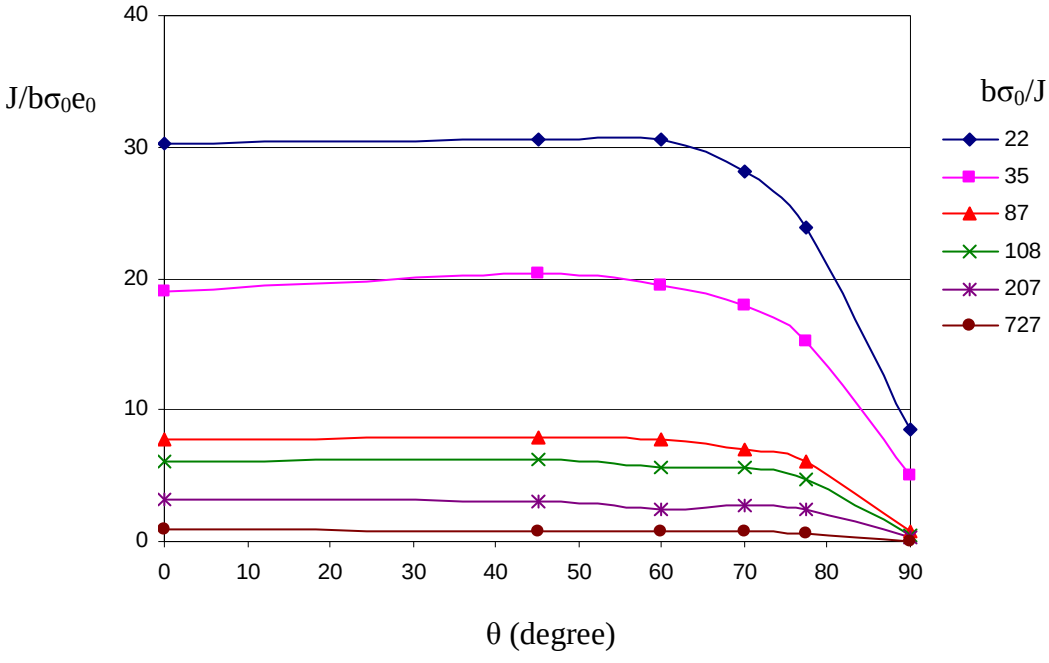

Figure 11.30: J-integral along the crack front in a shallow semi-elliptical surface crack (a/c=0.33, a/w=0.2) in bending (Terfas and Bezensek, 2009a).

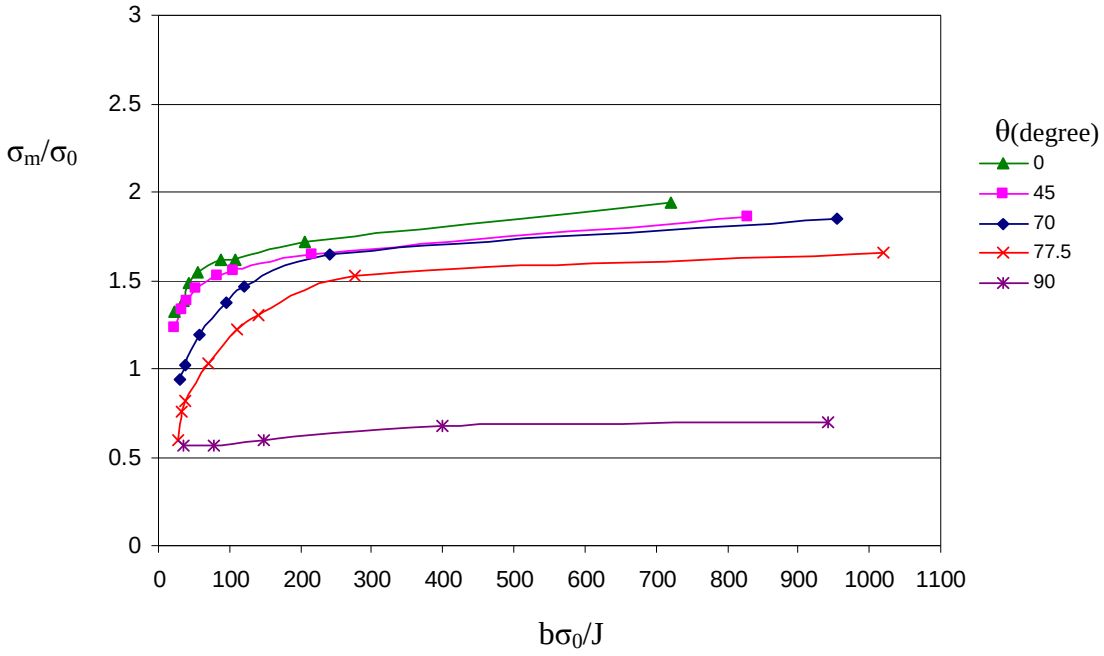

Figure 11.31: The mean stress at a distance $r\sigma_0/J=2$ as a function of deformation levels in a shallow semi-elliptical surface crack (a/c=0.33, a/w=0.2) in bending (Terfas and Bezensek, 2009a).

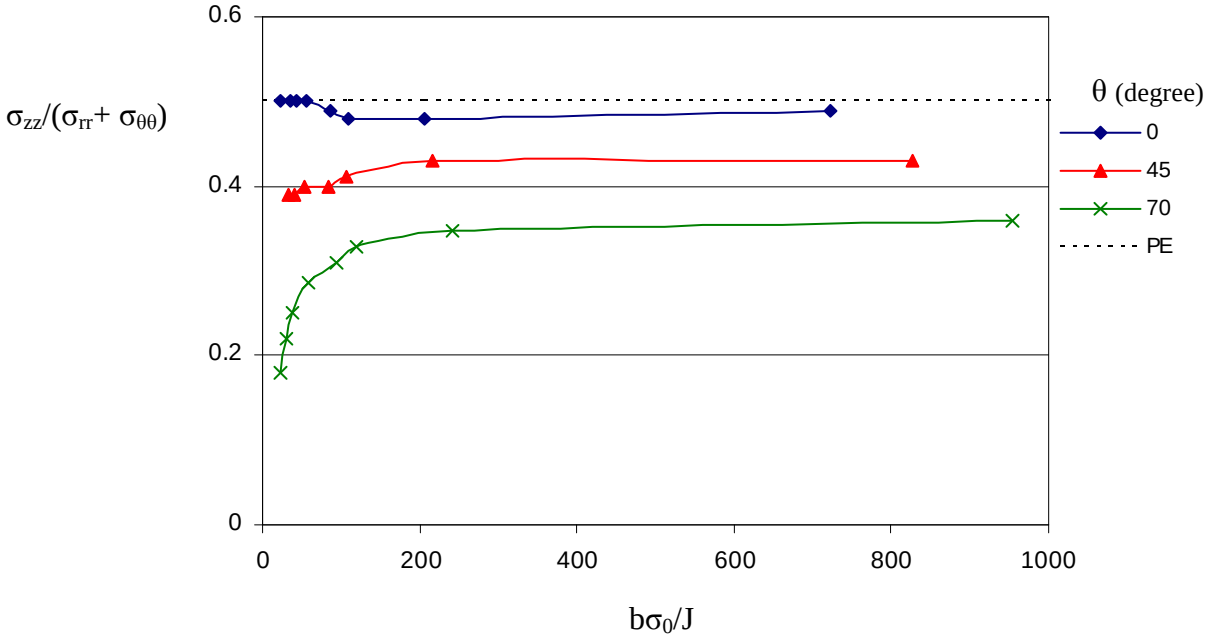

Figure 11.32: The proximity to plane strain around the crack front for a shallow semi-elliptical crack (a/c=0.33, a/w=0.2) in bending.

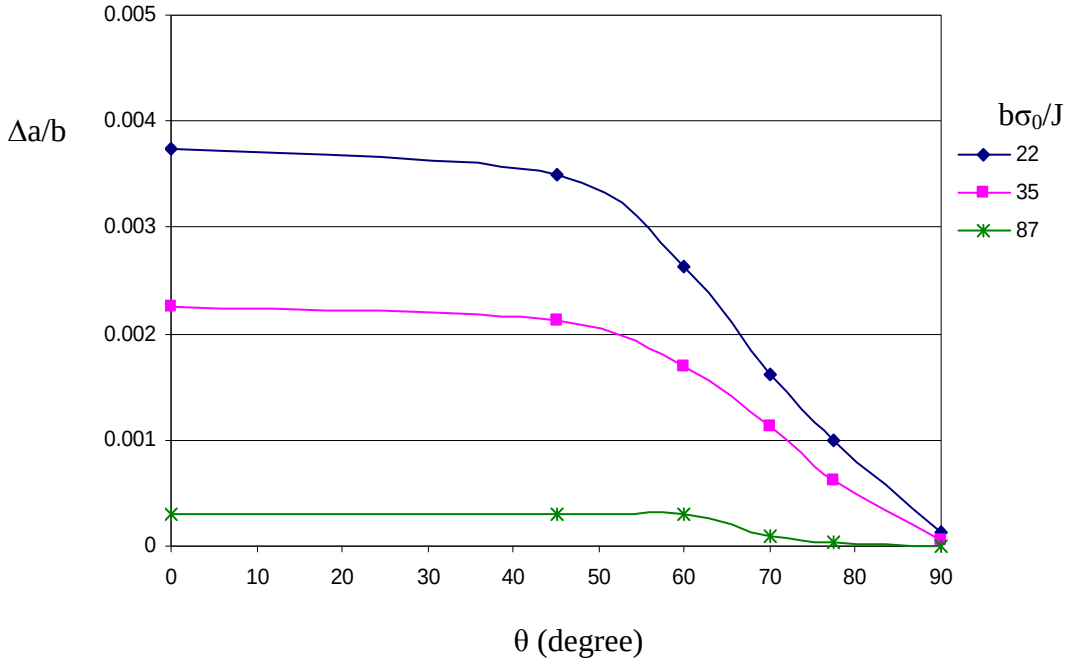

Figure 11.33: Crack growth around the crack front as a function of the parametric angle θ in bending (a/c=0.33, a/w=0.2) (Terfas and Bezensek, 2009a).

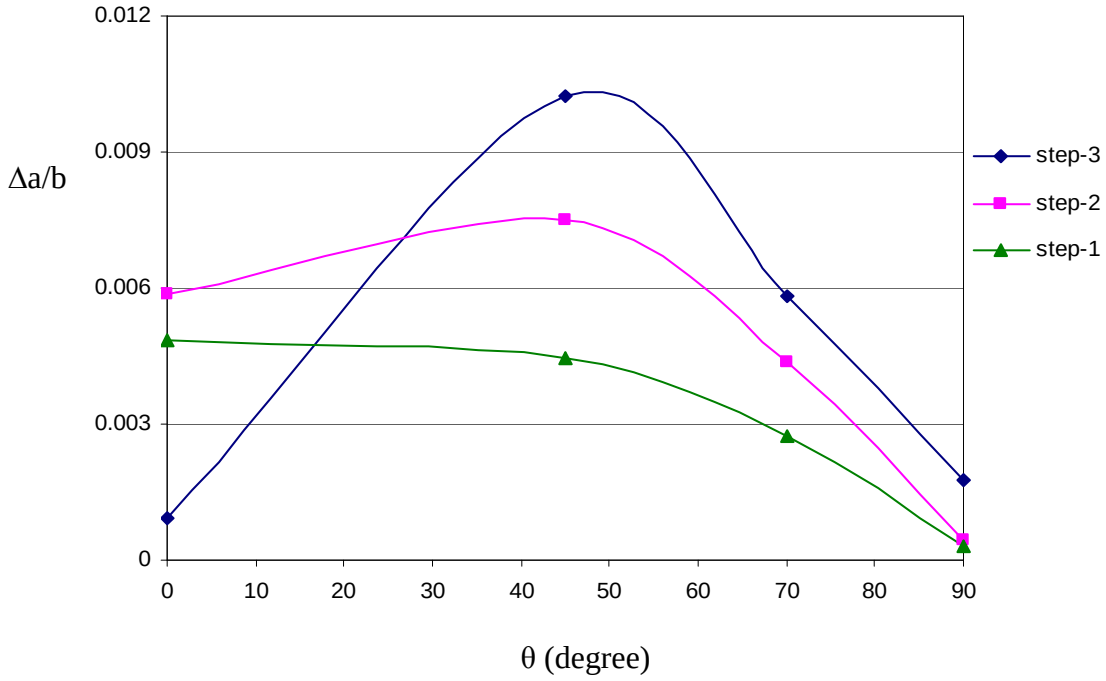

Figure 11.34: Crack growth steps at bσ0/J= 20, 15 and 10 as a function of the parametric angle θ along the crack front.

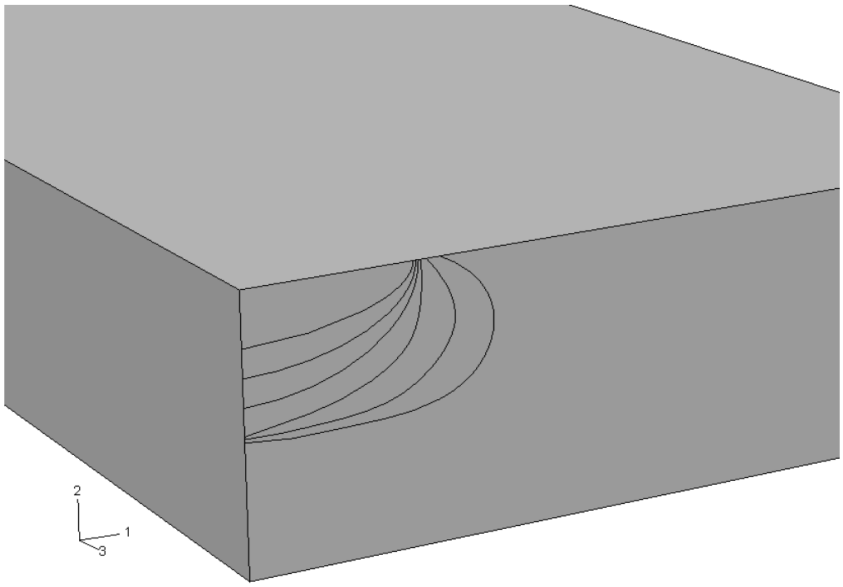

Figure 11.35: Illustration of the growth of a shallow semi-elliptical surface crack (a/w=0.2, a/c=0.33) in bending (Terfas and Bezensek, 2009a).

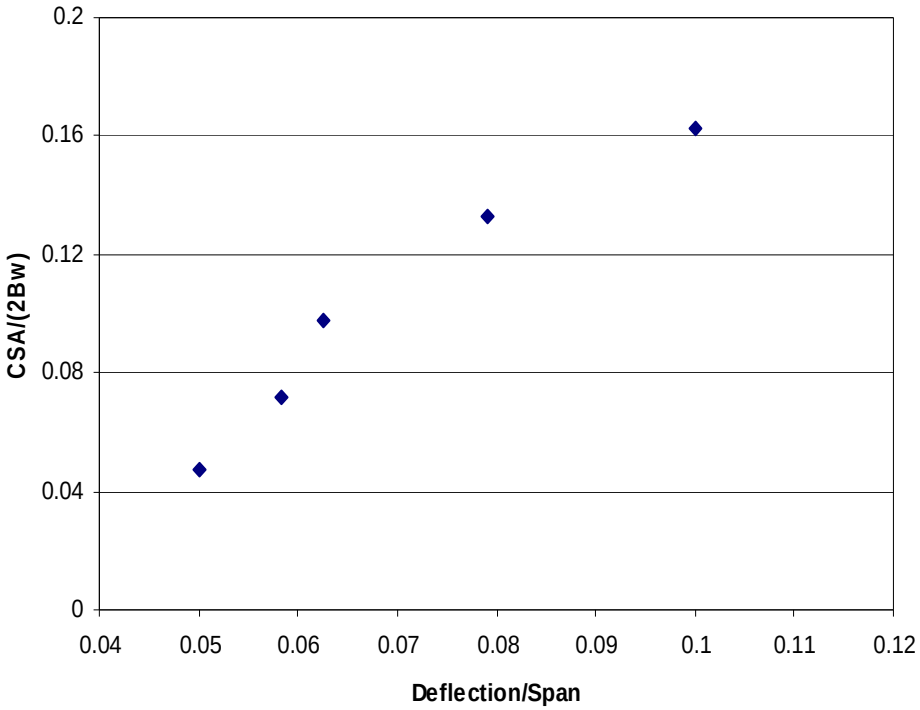

Figure 10.36: Fracture surface area normalised by cross section area of the plate as a function of deflection.

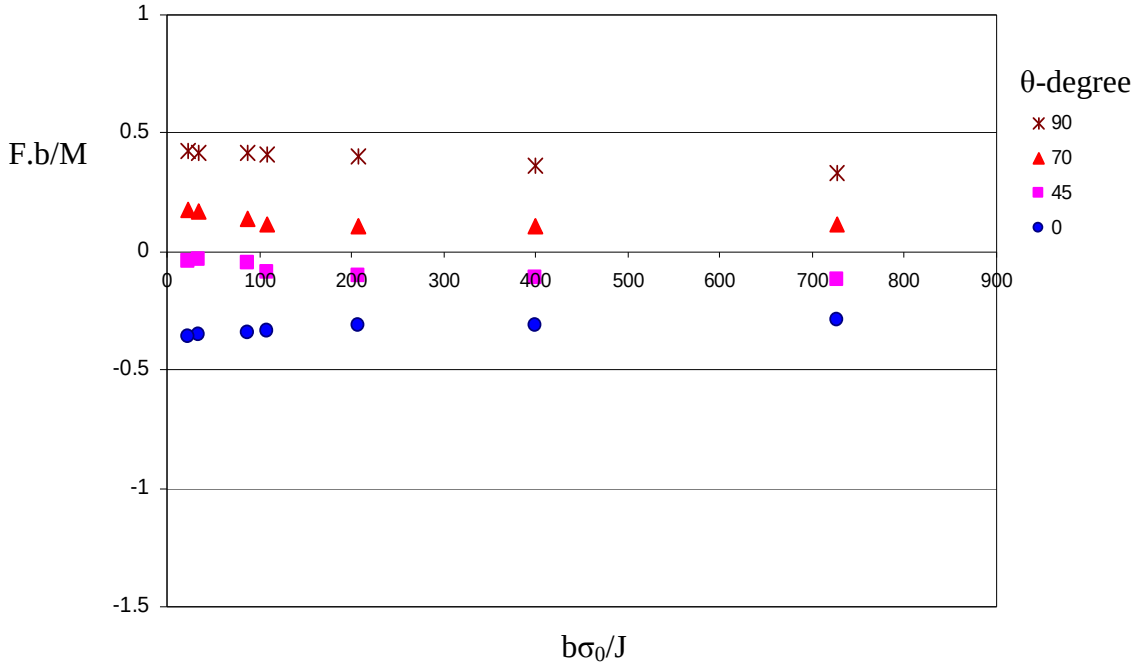

Figure 11.37: Force-moment ratio on the uncracked ligament ahead of the crack in a shallow semi-elliptical surface crack (a/w=0.2, a/c=0.33) in bending.

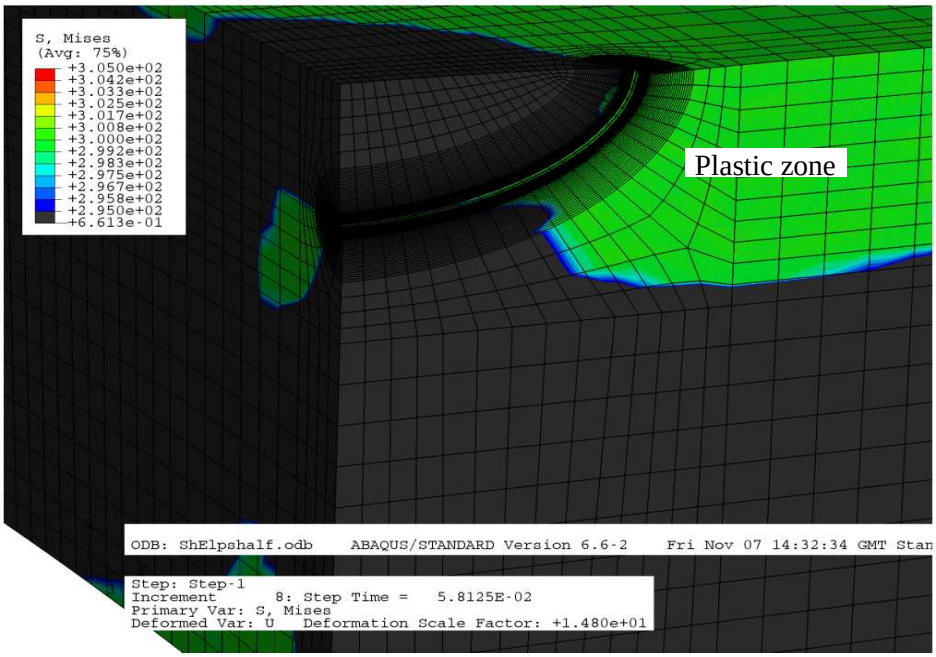

Figure 11.38: Development of the plastic zone around the crack front at $b\sigma_0/J=439$ (at the deepest point) in a shallow semi-elliptical surface crack (a/w=0.2) with an aspect ratio of a/c=0.5 in bending.

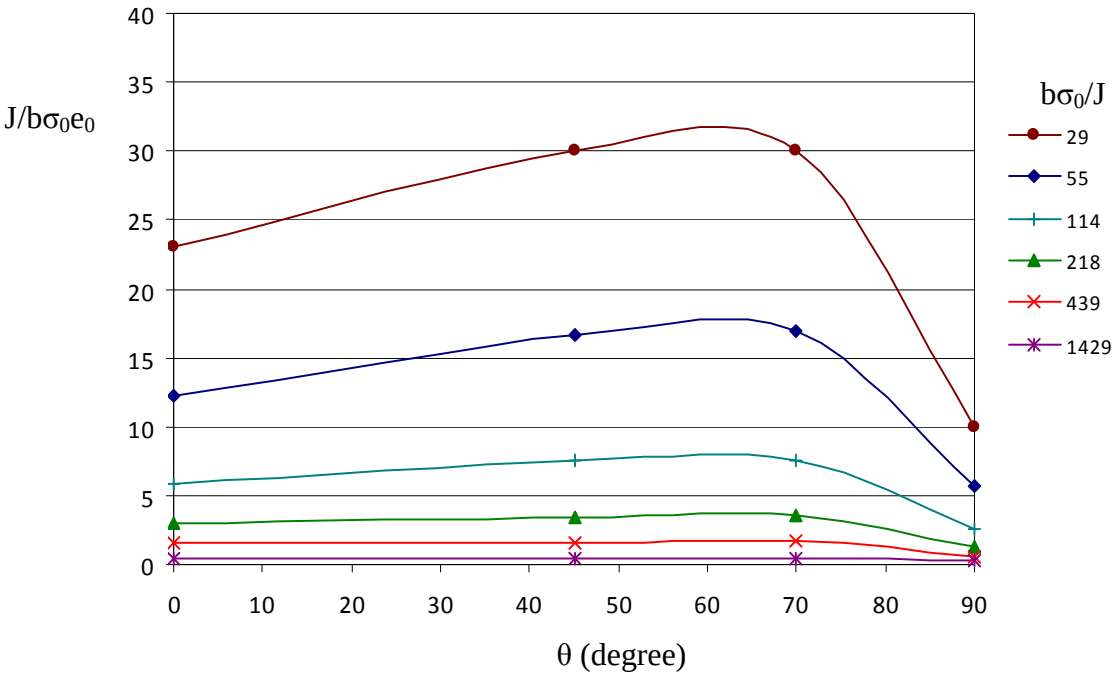

Figure 11.39: J-integral along the crack front for a shallow semi-elliptical surface crack in bending, (a/c=0.5, a/w=0.2).

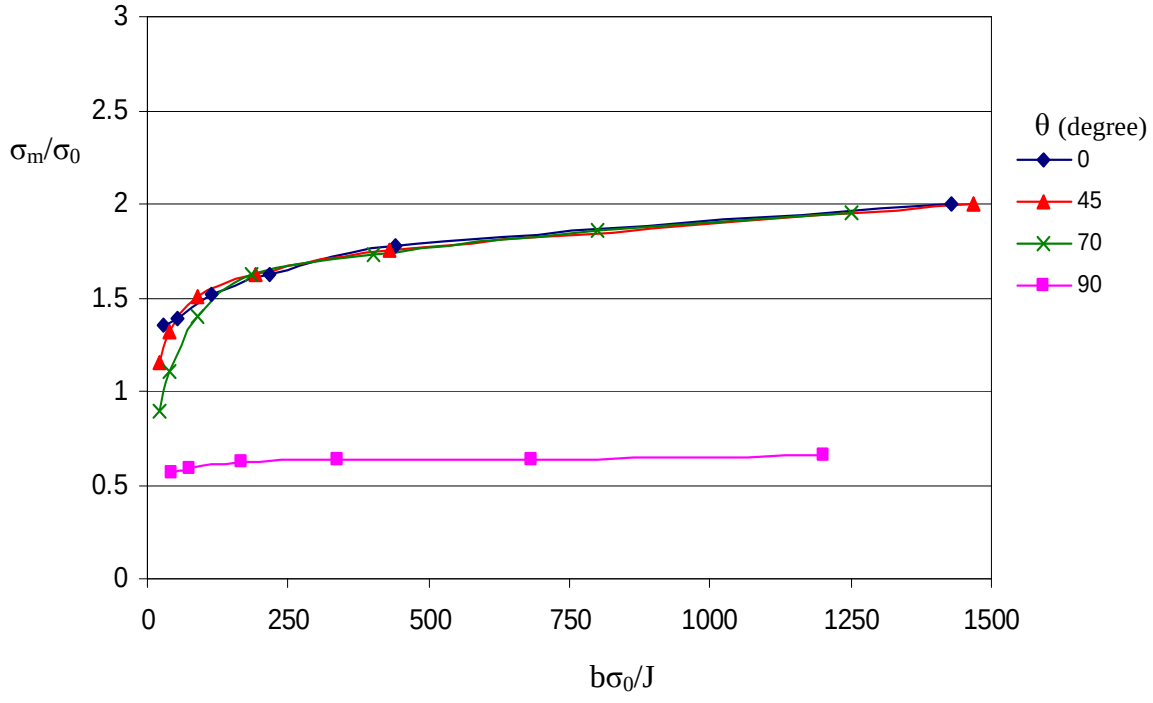

Figure 11.40: The mean stress at a distance rσ0/J=2 as a function of deformation level around the crack front for a shallow semi-elliptical surface crack in bending (a/c=0.5, a/w=0.2).

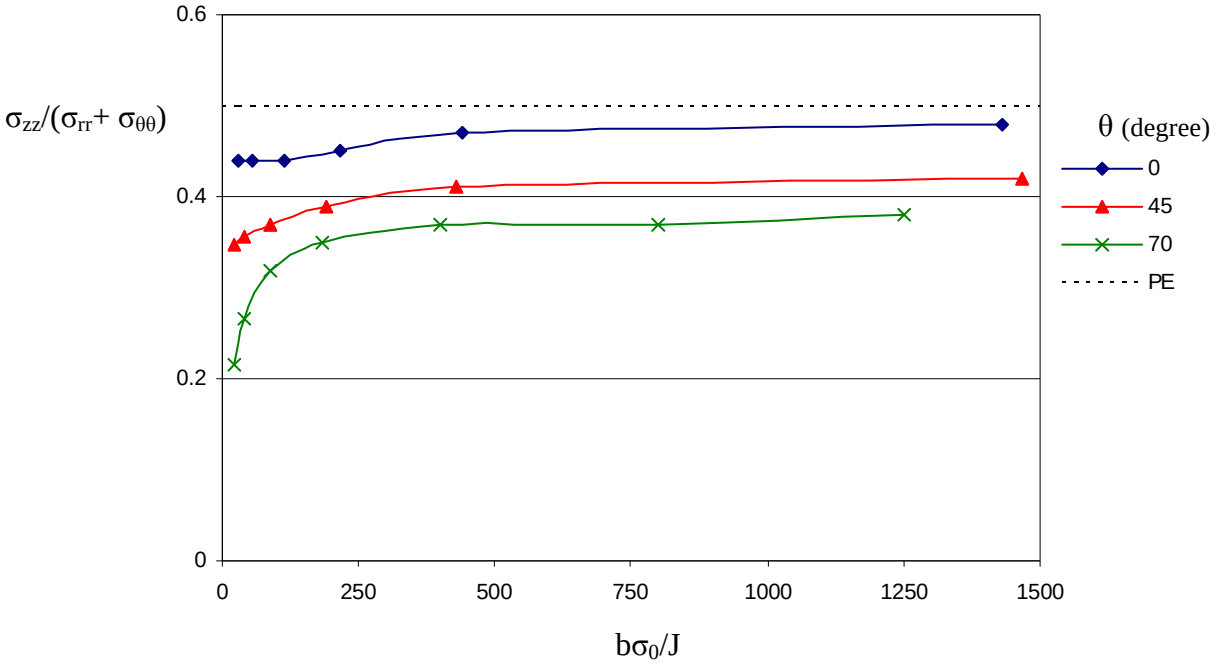

Figure 11.41: The proximity to plane strain around the crack front for a shallow semi-elliptical crack (a/c=0.5, a/w=0.2) in bending.

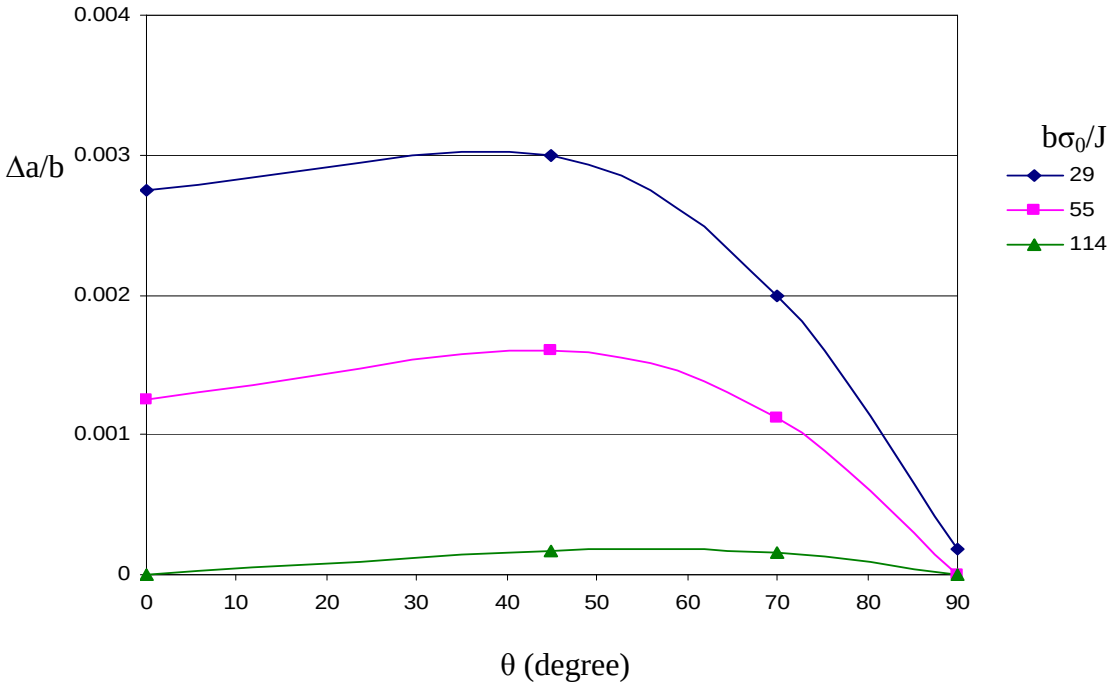

Figure 11.42: Crack growth around the crack front as a function of the parametric angle θ for a shallow semi-elliptical surface crack in bending (a/c=0.5, a/w=0.2).

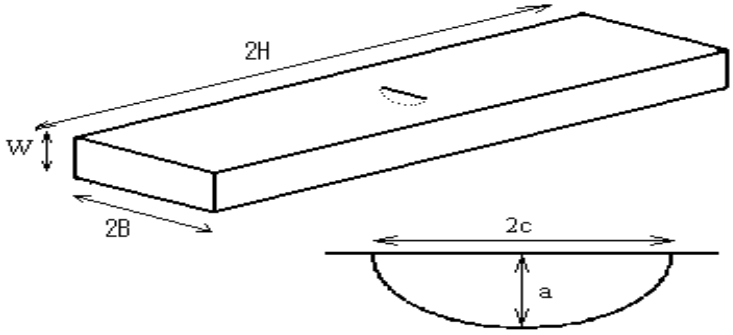

Figure 11.43: The geometry of the surface crack used in the fracture test (a/w=0.2, a/c=0.2).

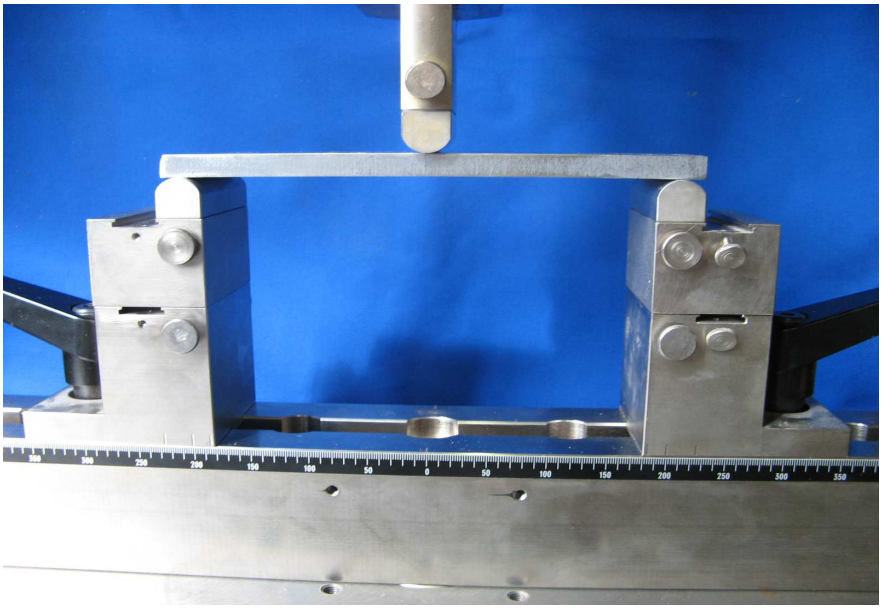

Figure 11.44: Fracture test set-up in three point bending.

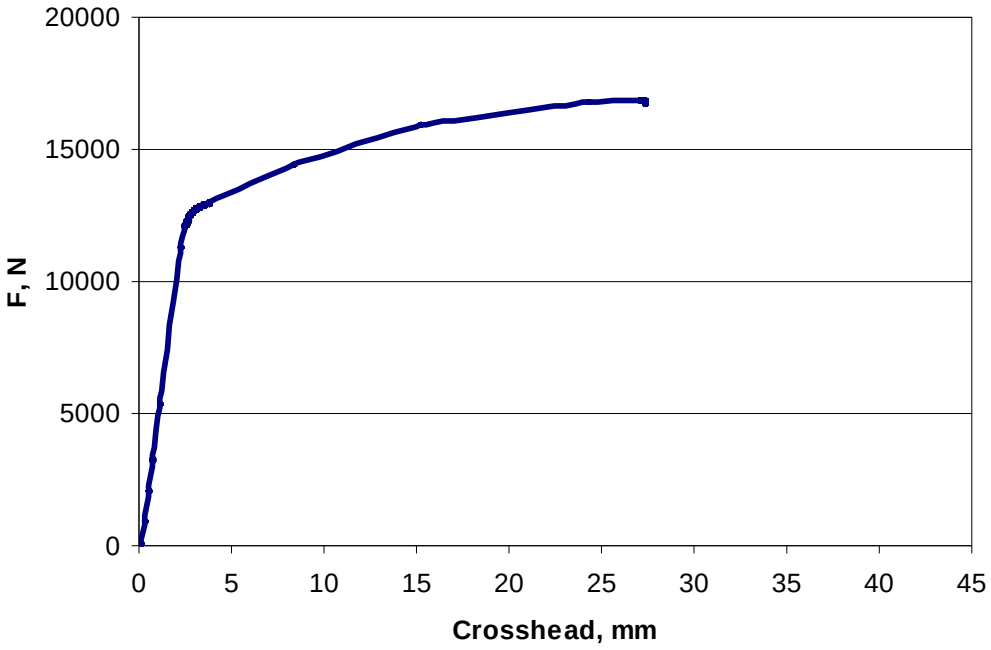

Figure 11.45: Force-crosshead displacement curve during the test for the first sample.

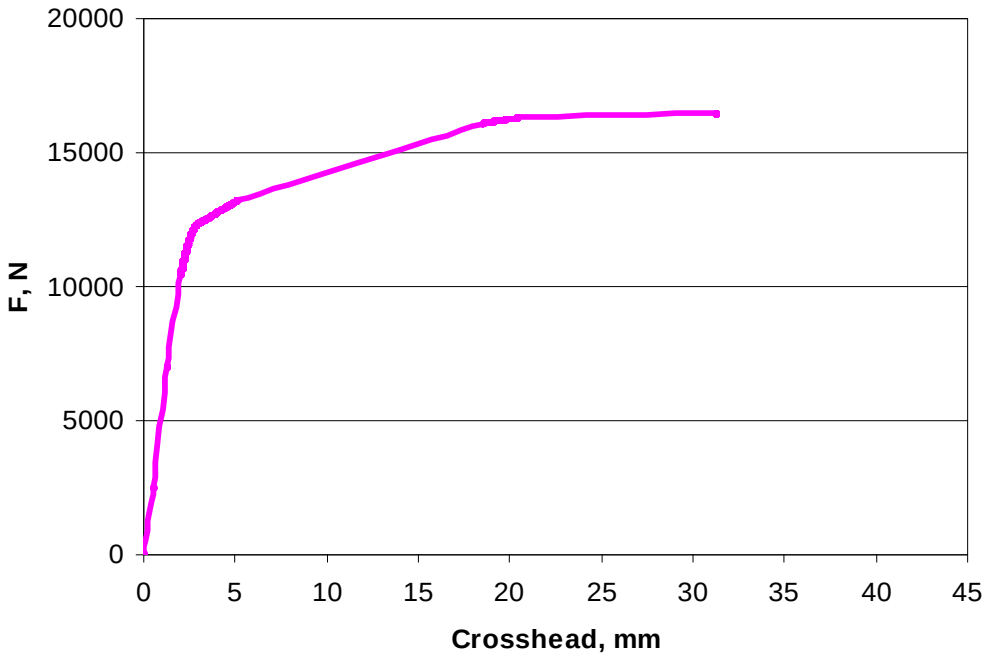

Figure 11.46: Force-crosshead displacement curve during the test for the second sample.

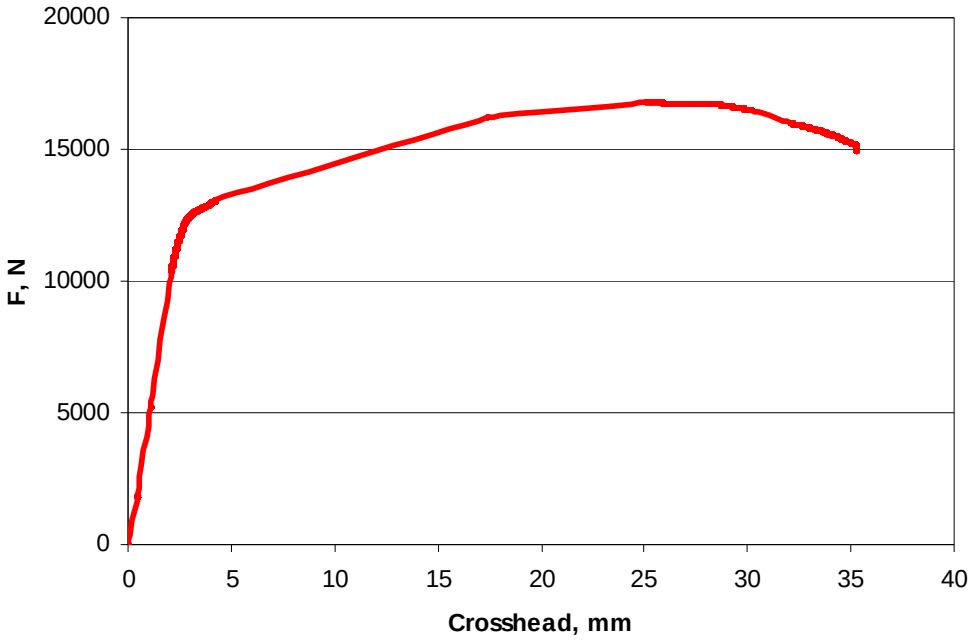

Figure 11.47: Force-crosshead displacement curve during the test for the third sample.

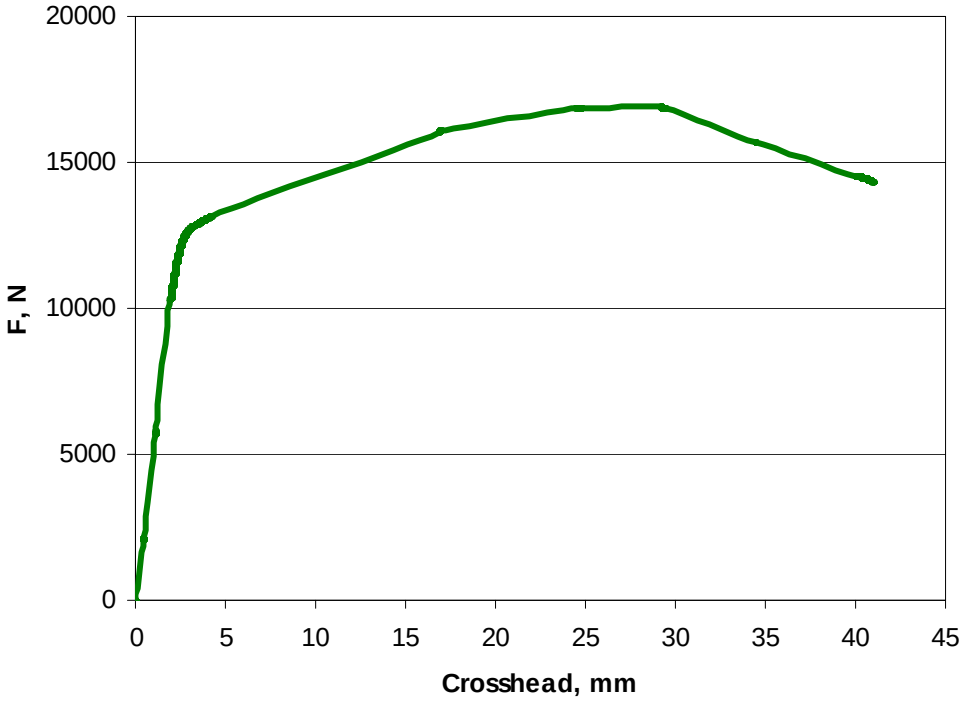

Figure 11.48: Force-crosshead displacement curve during the test for the fourth sample.

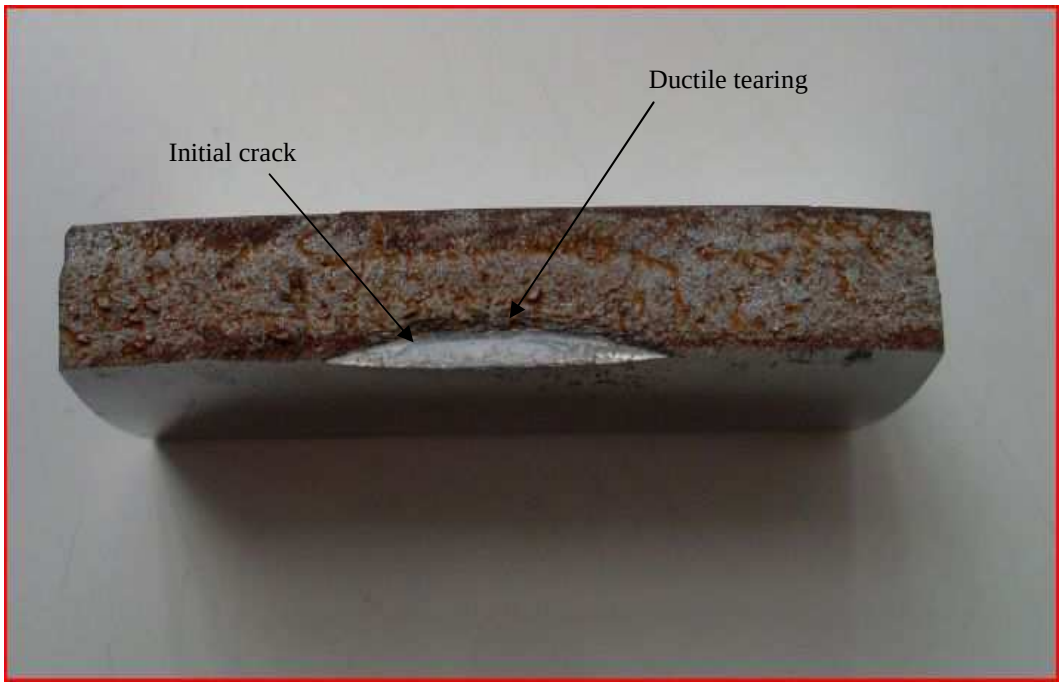

Figure 11.49: Ductile tearing for a shallow semi-elliptical surface notch under bending (sample-1).

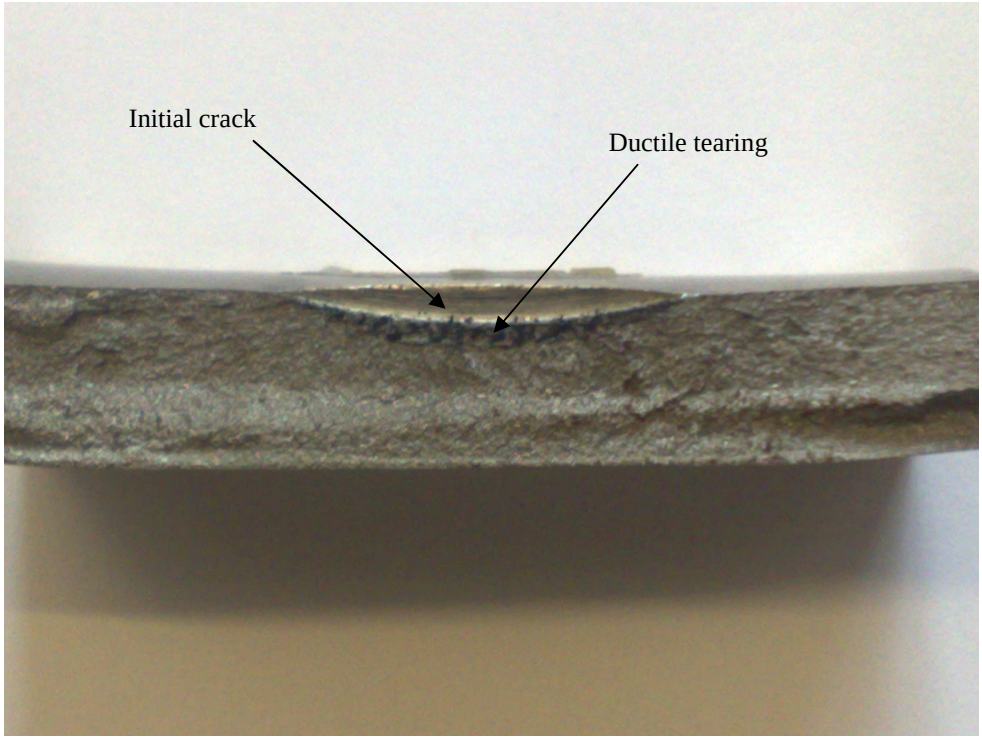

Figure 11.50: Ductile tearing for a shallow semi-elliptical surface notch under bending (sample-2).

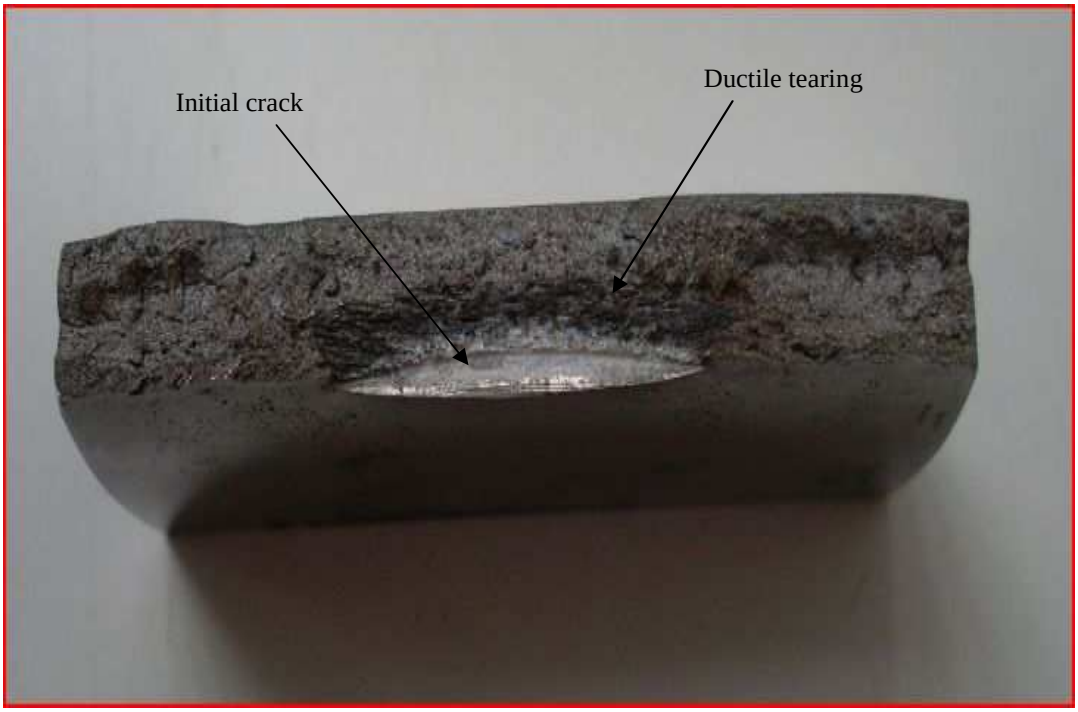

Figure 11.51: Ductile tearing for a shallow semi-elliptical surface notch at very large displacement (high deformation level) under bending (sample-3).

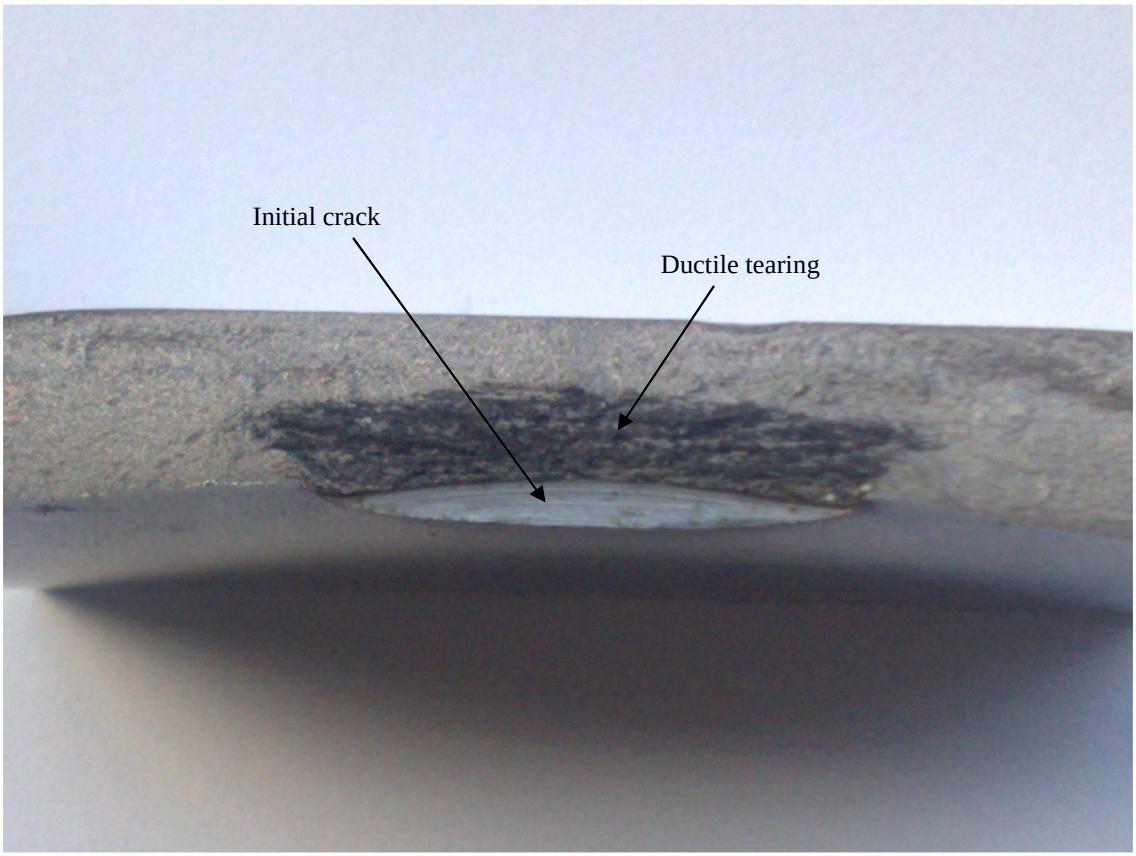

Figure 11.52: Ductile tearing for a shallow semi-elliptical surface notch at very large displacement (high deformation level) under bending (sample-4).

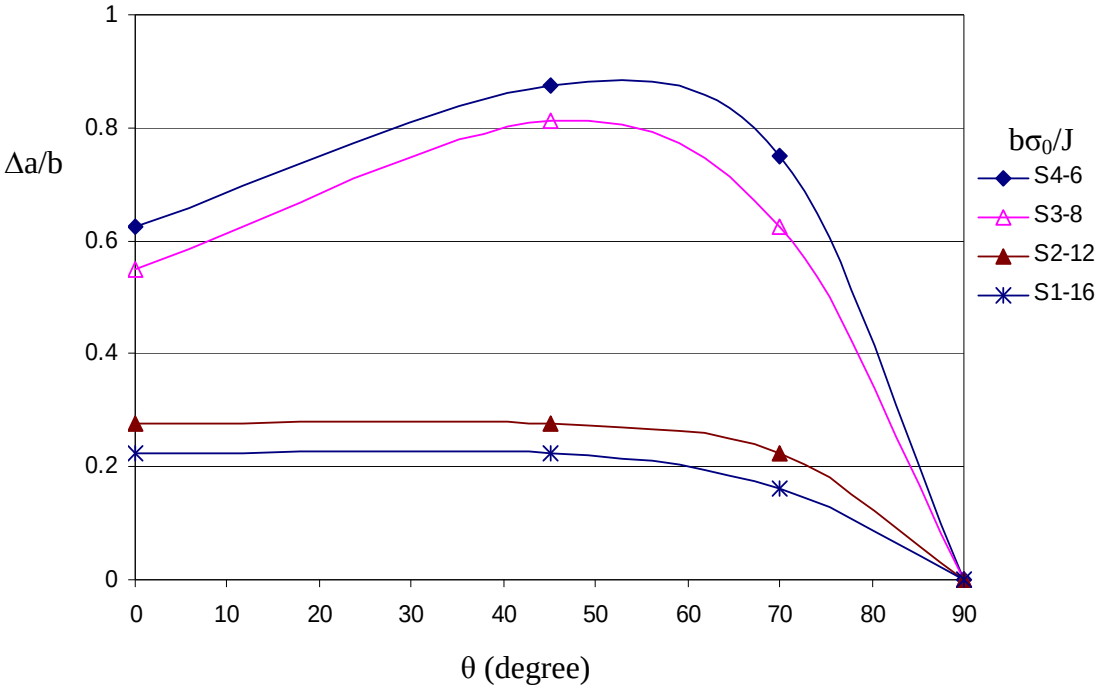

Figure 11.53: Crack growth along the crack front for the test samples.

12. Deep semi-elliptical surface cracks in tension

12.1 Introduction

This chapter presents detailed finite element analyses of semi-elliptical surface cracks subject to displacement controlled tension under elastic-plastic conditions. Collapsed three dimensional continuum hexahedral elements with reduced integration with coincident but independent nodes were used. This employs the small geometry change solution to be used. Due to symmetry only one quarter of the geometry was modelled and semmetry and displacement boundary conditions were imposed on the appropriate surfaces as shown in Figure (12.1).

The same material behaviour (non-hardening), specimen geometry and finite element models were used as in the bending calculations discussed in Chapter (10). The development of the plastic zone around the crack at both low deformation levels and in full plasticity is shown. The mean stress, J-integral and proximity to plane strain at different parametric angles were examined. Finally ductile crack extension was investigated using the model of ductile crack growth proposed in Chapter (9).

12.2 Deep semi-circular surface crack in tension (a/c=1, a/w=0.5)

12.2.1 Benchmark of the model

The stress intensity factor was benchmarked in displacement controlled tension against the results of Newman and Raju (1981) and good agreement was obtained as shown in Figure (12.2a).

Figure (12.2b) shows benchmark calculations of the T-stress associated with a semi-circular crack with Wang (2003), and compared with a two dimensional solution given by Sham (1991). The T-stress is normalised by applied stress, and plotted against the a/w ratio. The comparison is made by taking the depth ratio a/w in the two dimensional model to correspond the depth ratio a`/w in a three dimensional model where a` = a

cos(θ), as shown in the Figure (12.2b). The values of T-stress agree with Wang`s (2003) solution in the range $0.043 \leq a`/w \leq 0.5$. In the 3-D solution the T-stress was negative and consistent with Sham`s solution for the depth ratios $0.1 \leq a`/w \leq 0.5$. However near the surface the T-stress in 3-D became more negative at -1.2 and differed significantly from the 2-D solution (-0.51) (Harlin and Willis, 1988).

12.2.2 Stress fields under fully plastic condition

Figures (12.3) to (12.5) show the development of the plastic zone around the crack. The plastic zone was largest close to the surface and reduced towards the deepest point as shown in Figure (12.3). As the deformation levels increased, plasticity rapidly developed around the crack and extended to the remote boundary as shown in Figure (12.4). This contrasts with bending where the plastic zone size was smaller and confined between 45° and the surface. At a deformation level of $b\sigma_0/J \approx 39$, plasticity developed across the ligament and in most of the body as shown in Figure (12.5).

At the deepest point of the crack (θ=0) the mean stress was close to the small scale yielding solution at low deformation levels ($b\sigma_0/J = 2000$) as shown in Figure (12.6). The figure also shows the T/Q effect which was derived using the elastic T-stress (Figure 12.2) following to Karstensen (1996). It can be seen that in contained yielding, the mean stress was low because of in-plane constraint loss (negative T-stress). As plasticity increased the mean stress reduced further. Figure (12.7) shows that plane strain quantified by the constraint parameter $T_z=\sigma_{zz}/(\sigma_{rr}+\sigma_{\theta\theta})$ is maintained at both distances ($r\sigma_0/J= 0$ and 2) even in full plasticity.

Figure (12.8) shows the mean stress at a distance $r= 2J/\sigma_0$ along the crack front from the deepest point to the free surface. At low deformation levels ($b\sigma_0/J=1800$), the mean stress was close to the SSY solution over the most of the crack front except at the free surface. As deformation increased, the mean stress gradually reduced. Higher constraint levels occurred in the angular range 45°-70° than at the deepest or surface points. At the free surface $\theta = 90^\circ$ the mean stress at low deformation levels was close to the plane stress value. In full plasticity however it approached uni-axial tension (0.3). It can also be seen that the proximity to plane strain was maintained along the crack between the deepest

point and 70°, and lost towards the free surface as shown in Figure (12.9). Figure (12.10) shows the non-dimensional J-integral along the crack front as a function of the parametric angle (θ). The largest J-values were found at 45°, and J remained high even at the deepest point. This contrasts to bending when the J-integral was smaller at the deepest point and attained its largest value at 70°.

12.2.3 Determination of crack growth of a deep semi-circular surface crack a/c=1, a/w=0.5 in tension.

Using the J-integral and mean stress with the procedure described in Chapter (9) the crack extension was determined. Figure (12.11) shows the crack growth Δa as a function of the parametric angle (θ). The crack extended with the highest rate at 45°, combined with growth at the deepest point. To determine the full crack shape sequence three steps were modelled following the procedure described in Chapter (9). The results are shown in Figures (12.12), (12.13) and (12.14). The crack grew along the entire crack front with a larger rate at 45°-70° than at the deepest point. Since the level of constraint at high deformation levels was slightly higher at 45°-70° than at the deepest and surface points the maximum crack growth occurred in the range 45°-70°. However the crack continued to grow at the deepest point until it broke through the wall as shown in Figure (12.15). This contrasts to bending where the crack extended only in the width direction under the surface adopting a boat shape. The (a/c) ratio increased linearly with increasing crack depth a/w as shown in Figure (12.16). This is a different profile to crack shape under fatigue where (a/c) becomes constant at approximately one as the crack depth reaches half thickness (Scott and Thorpe, 1981). Figure (12.17) shows the development of the fracture surface area as a function of crack depth.

12.3 Deep semi-elliptical surface crack in tension (a/w=0.5, a/c=0.33)

12.3.1 Crack tip stress field

Different plastic zone profiles were observed under tension compared to bending as shown in Figure (12.18). In tension the plastic zone developed along the entire crack

front including the deepest point, while in bending it developed significantly between 45° and the surface.

For a deep semi-elliptical crack the largest values of J were located from the deepest point to 45° as shown in Figure (12.19). The results in Figure (12.20) show that the mean stress is higher from the deepest point to 70° than at the surface. Figure (12.21) shows that the level of plane strain constraint at the deepest and at the 45° segments was 0.4 close to the plane strain value (0.5).

12.3.2 Determination of crack growth of a deep semi-elliptical surface crack a/c=0.33, a/w=0.5 in tension.

The results in Figure (12.22) show the crack grows along the entire crack front with most extension at 45° and only a small amount of crack growth at the free surface, where both the J-integral and the mean stress were low. The crack shape sequence showed a uniform crack growth along the crack front until the crack broke through as shown in Figure (12.23). This is due to the uniform distribution of the J-integral and the mean stress from the deepest point to 70°. The crack shape sequence in Figure (12.24) is different to the semi-circular profile (a/c=1) as the latter showed a tendency to grow at 45°-70° as illustrated in Figure (12.15). This is also a different observation to bending when crack growth was suppressed at the deepest point and growth only occurred under the surface. Figure (12.25) shows the development of a/c as a function of crack depth, a/w.

12.3.3 Force-moment redistribution along semi-elliptical surface cracks (a/c=0.33, a/w=0.5) in tension.

Figure (12.26) shows the force and moment distribution at the deepest point (θ=0°) of a deep semi-elliptical surface crack in tension. The tensile force dominated the ligament and increased with deformation. The opening moment also increased with deformation. The opening force and opening moment caused the crack to propagate at the deepest point in contrast to the behaviour in bending. Figures (12.27) and (12.28) show the increase in force and moment with deformation at 45° and 70°, and this effect is more marked than at the deepest point. Large opening forces at 45° and 70° caused significant

crack extension at this position which agrees with the observation in the previous section where the crack grew with a higher rate at the angular range 45°-70° than at the deepest point. Figure (12.29) shows that force-moment ratio is largest at the deepest point and reduces towards the surface.

12.4 Deep semi-elliptical crack (a/w=0.5) with an aspect ratio of a/c=0.5 in tension.

Figure (12.30) confirms that the plastic zone in deep surface cracks subjected to tension develops more rapid than in bending, and that plasticity develops at the deepest point as well as the free surface.

Figure (12.31) shows the distribution of the normalised J-integral around the crack from the deepest point to the free surface. The largest value of the J-integral was located between the deepest point and 45° and J then reduced towards the free surface. This behaviour is different to that observed in bending where the J-integral was suppressed at the deepest point, in accord with the results for surface cracks with a/c=0.33.

Figure (12.32) shows the greatest mean stress occurred between 45° and 70° while small values occur at the deepest point at high deformation levels. Figure (12.33) shows the plane strain parameter is maintained at 0.4 along the crack front except at the free surface. The crack grew significantly at 45° and less at the deepest point and growth was almost suppressed at the surface as shown in Figure (12.34).

12.5 Discussion

Non uniform crack tip constraint and J-integral distribution along the crack front were observed for surface cracks under tension. However the variation of constraint and J-integral was smaller than the variation in bending. The level of constraint along the crack front was close to the SSY solution at low deformation levels ($b\sigma_0/J>1500$). The low level of mean stress in tension in contained yielding is due to the loss of in-plane constraint (T/Q). As plasticity increased ($b\sigma_0/J<300$) a further reduction in the mean

stress due to an out-of-plane effect was observed. This indicates the use of the standard fracture toughness obtained on deep bend samples for surface cracks assessment is excessively conservative. This is because surface cracks under tension show significant constraint loss near the crack tip, and the margin of safety is expected to increase accordingly.

Deep semi-circular surface cracks (a/w=0.5, a/c=1) showed a uniform distribution of mean stress and J-integral from the deepest point to 70° at low deformation levels. However as the deformation increased the maximum mean stress appeared at 45°-70°, and the maximum J-integral was at 45°. This trend is consistent with results obtained by Wang (2009) for surface cracked geometries with a/c=1 and a/w=0.6 under uniaxial tension. Crack extension is predicted to occur along the entire crack front including the deepest point most notably in the section from 45°-70°. This is also in agreement with Berg et al (2008) who observed that a significant growth was predicted to occur in the circumferential direction of a pipe containing a short surface crack. However this is slightly different from observation published by Chen et al (2005) who predicted that the maximum crack growth occurs at the deepest point. Gao et al (1998) predicted the crack grows at most at the deepest point under combined bending and tension.

For semi-elliptical surface cracks (a/c=0.5, 0.33) the mean stress at high deformation levels was greatest in the angular range 45°-70° and a slight reduction at the deepest point was observed. The J-integral maintained high values from the deepest point up to 45° and then decreased towards the free surface. The current results agree with the finding of Chen (2005) where more uniform crack growth was observed along the crack front. However current findings showed the crack extended at a relatively higher rate at 45°-70° for deep cracks with an aspect ratios a/c=0.5 and 1.

It is clear that surface cracks exhibit different behaviour under tension compared to bending. In bending crack growth was suppressed at the deepest point at approximately a/w=0.5, but the crack extended in the angular region 45°-70°. In tension, a high level of constraint was maintained between 45°-70° and the crack was predicted to grow with a larger rate in this direction compared to the deepest point. As a result the crack was

predicted to break through the wall. This contrasts the bending case where the crack extended under the surface adopting a boat shape.

An effect of the aspect ratio on the mean stress at the deepest point in tension was observed. Decreasing the value of a/c elevated the magnitude of the crack tip mean stress along the crack and significantly at the deepest point as shown in Figure (12.35), (12.36) and (12.37). This gave different crack growth profiles and caused the growth of semi-elliptical cracks to be more uniform compared to the large extension observed in the angular range 45°-70° for semi-circular cracks.

12.6 Conclusion

For semi-elliptical surface cracks both the mean stress and J-integral were geometry and load dependent. The level of constraint and the J-integral value varied along the crack front, and affected crack extension. It has been shown that crack extension is dependent on the original crack shape, type of loading. Under tension the crack was predicted to grow between the deepest point and 70°, hence the crack breaks through the thickness. This contrasts to bending where the crack grew at 45°-70°, and growth was suppressed at the deepest segment. It should also be noted that crack tip constraint and the ductile crack growth were affected by the initial aspect ratio (a/c). Semi-circular cracks (a/c=1) showed high crack tip constraint and large crack growth in the angular range 45°-70°. For semi-elliptical cracks (a/c<1), both crack tip constraint and the J-integral increased at the deepest point and as a result more growth was observed at the deepest point. It should also be noted that the boat shape predicted under uniaxial loading was less severe than that observed under bending. It was also shown that the opening force and opening moment dominated the ligament at the deepest point (θ=0°) caused crack growth at the deepest point as well as in the angular range 45°-70°.

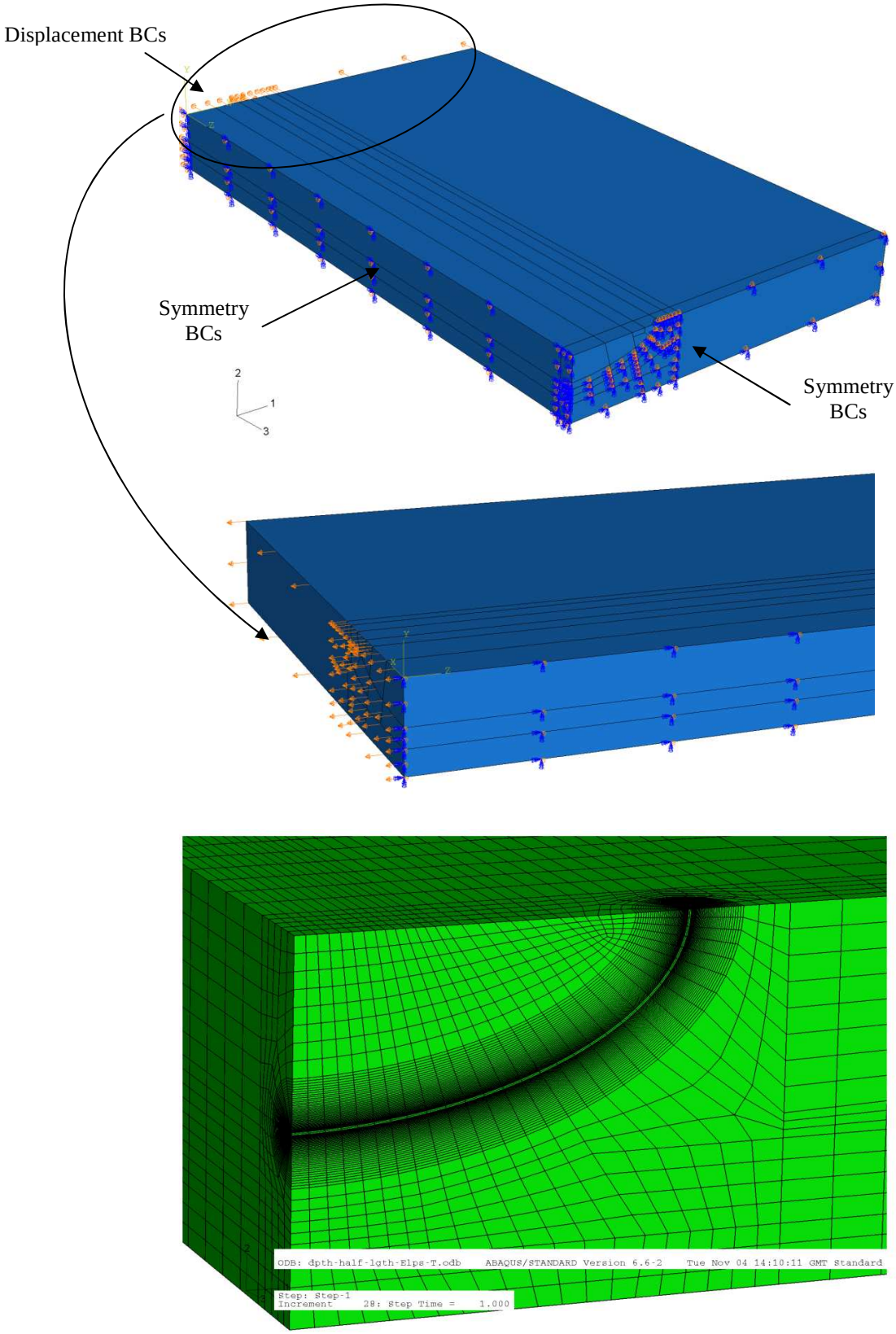

Figure 12.1: Boundary conditions and the mesh for a deep semi-elliptical surface crack.

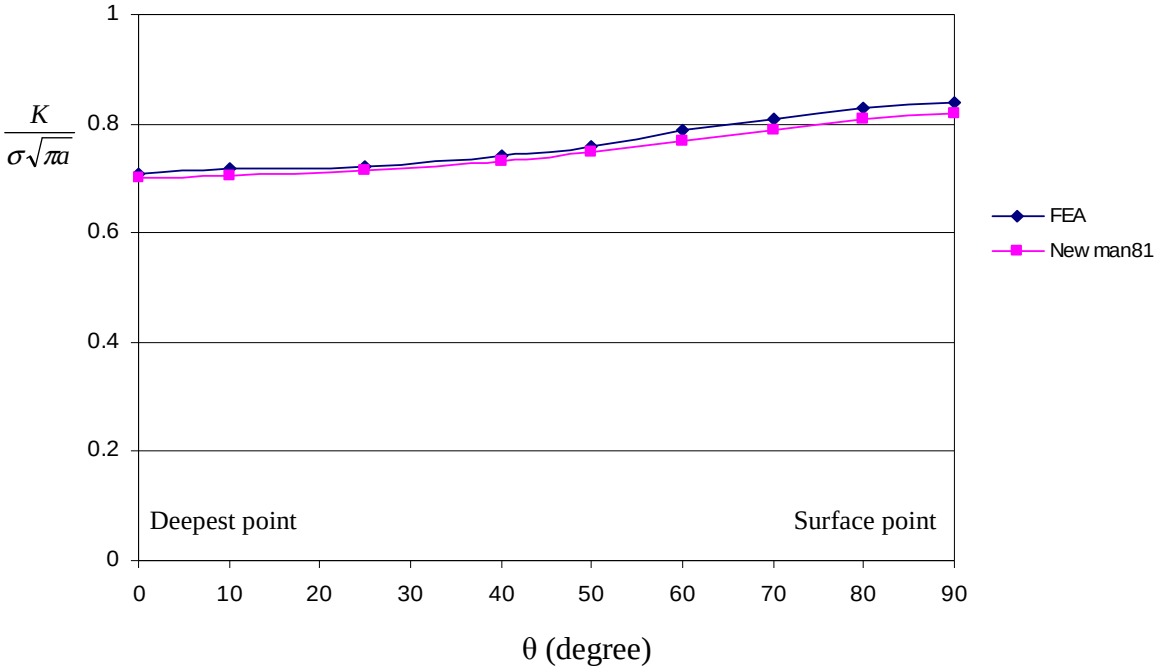

Figure 12.2a: Benchmark of stress intensity factor K in a semi-circular surface crack (a/w=0.5, a/c=1) under tension with Newman and Raju, (1981).

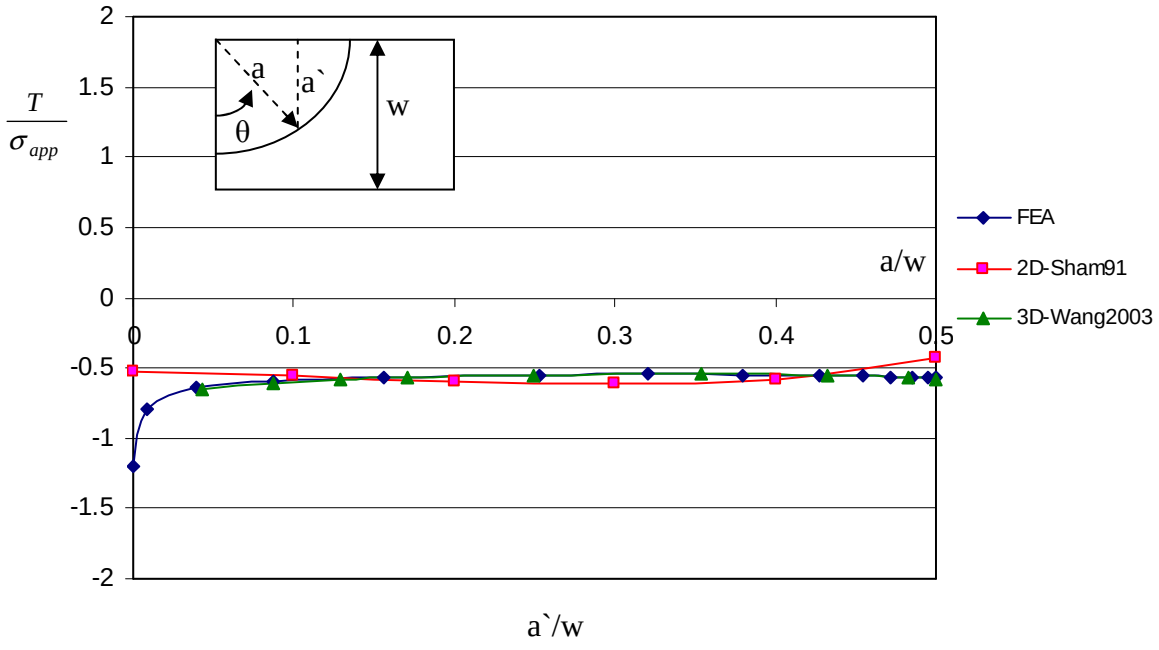

Figure 12.2b: Benchmark of the elastic T- stress in a semi-circular surface crack (a/w=0.5, a/c=1) in tension with Wang (2003), and compared with two dimensional solution (Sham, 1991).

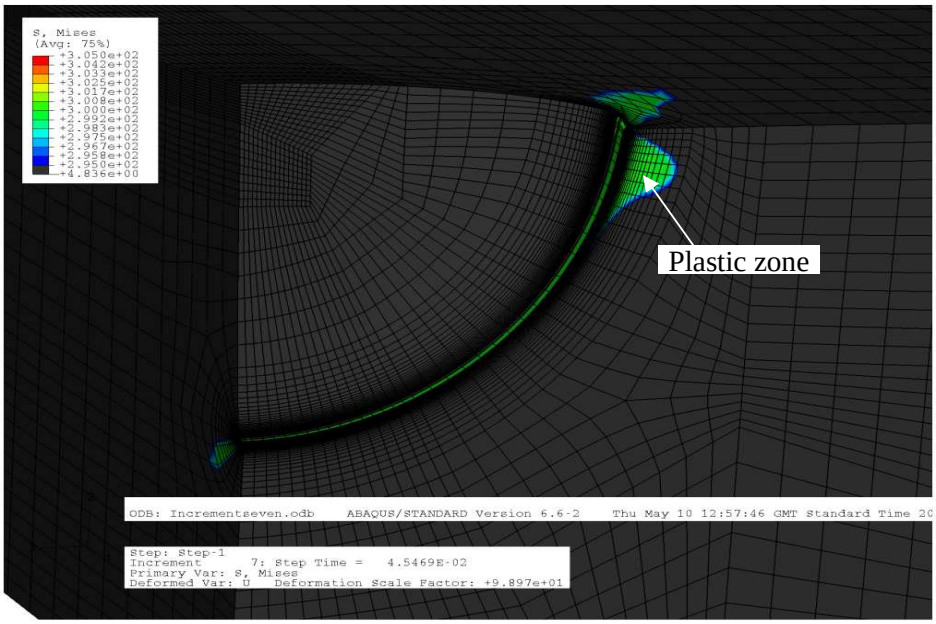

Figure 12.3: Small scale plasticity ahead of the crack at low level of deformation ($b\sigma_0/J=1050$) in a semi-circular surface crack (a/w=0.5, a/c=1) in tension.

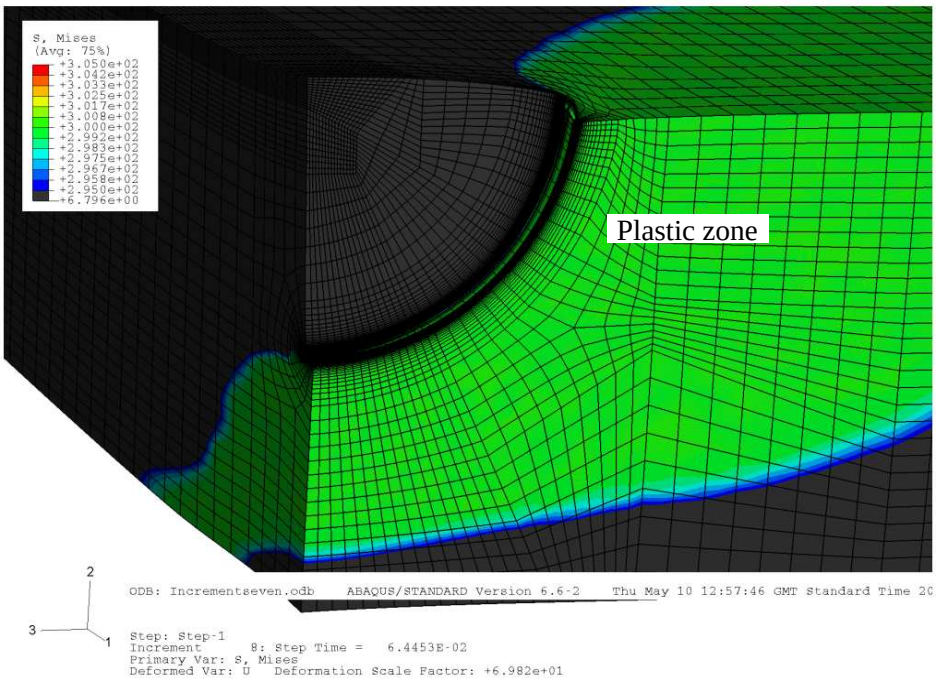

Figure 12.4: Large plasticity surrounds the crack and the whole body at $b\sigma_0/J=366$ in a semi-circular surface crack (a/w=0.5, a/c=1) in tension.

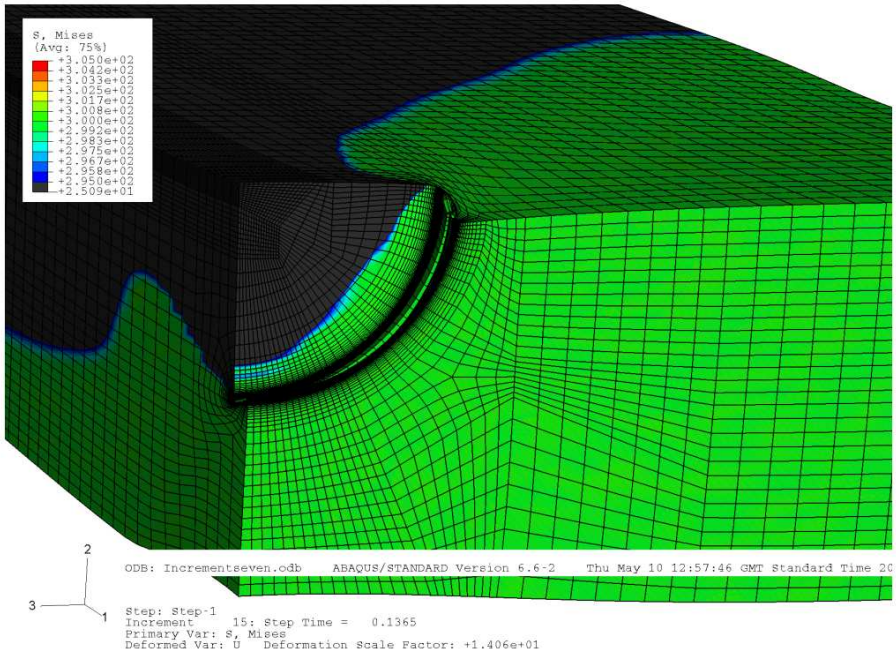

Figure 12.5: Fully plasticity at $b\sigma_0/J=39$ in a semi-circular surface crack (a/w=0.5, a/c=1) in tension.

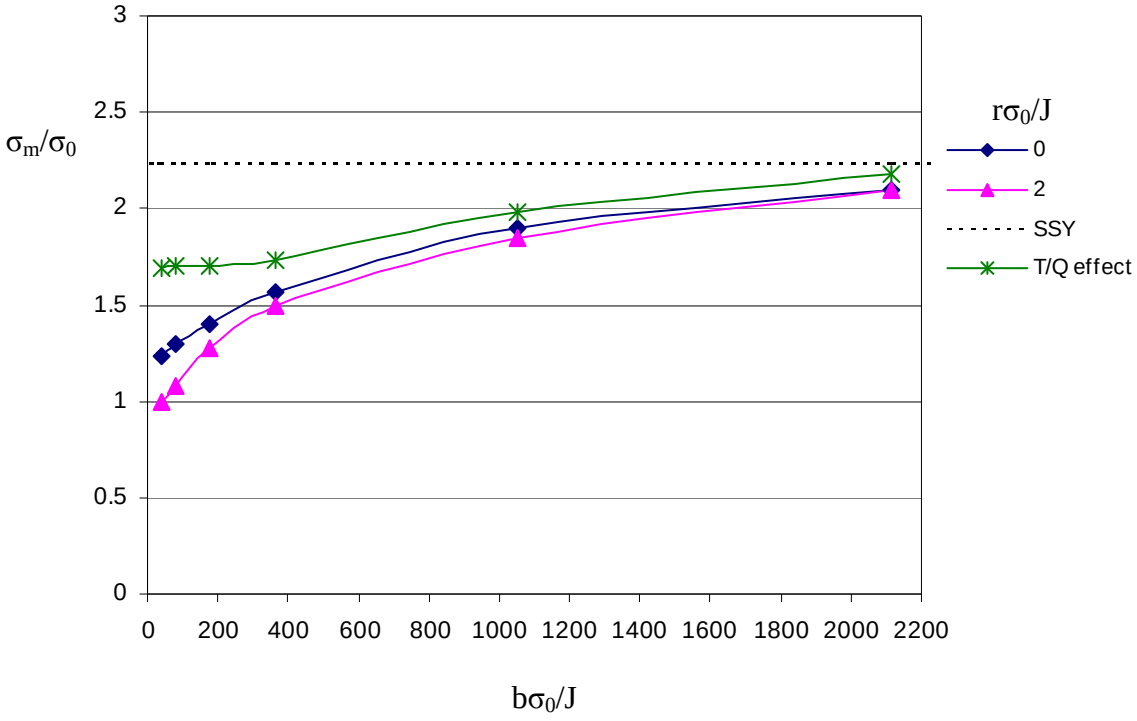

Figure 12.6: Mean stress as a function of the level of deformation at the tip (r=0) and $r\sigma_0/J=2$ at the deepest point in a semi-circular surface crack (a/w=0.5, a/c=1) in tension.

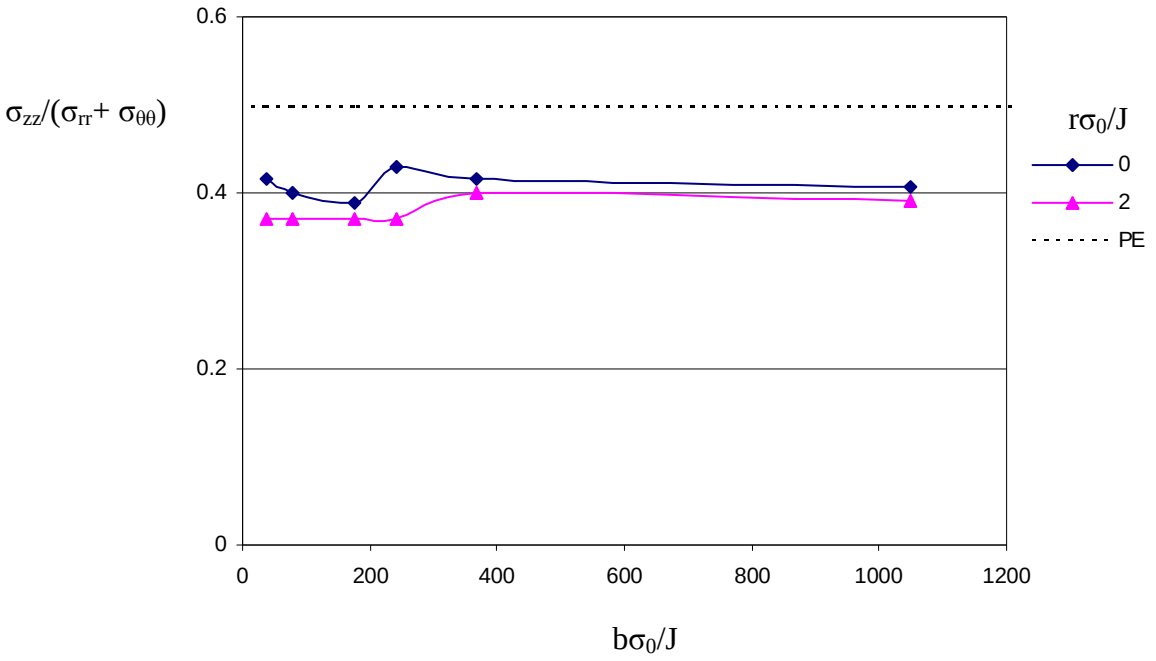

Figure 12.7: Proximity to plane strain as a function of deformation at θ=0˚ for a semi-circular surface crack (a/w=0.5, a/c=1) in tension.

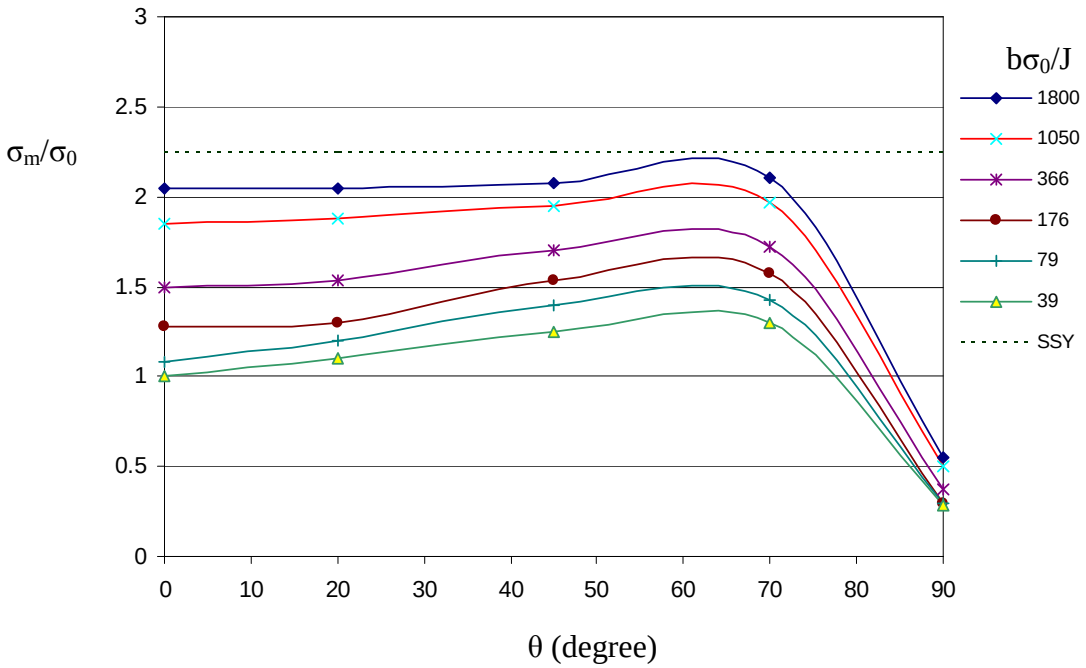

Figure 12.8: Mean stress at rσ0/J =2 as a function of the parametric angle θ along the crack front at different levels of deformation for a semi-circular surface crack (a/w=0.5, a/c=1) in tension.

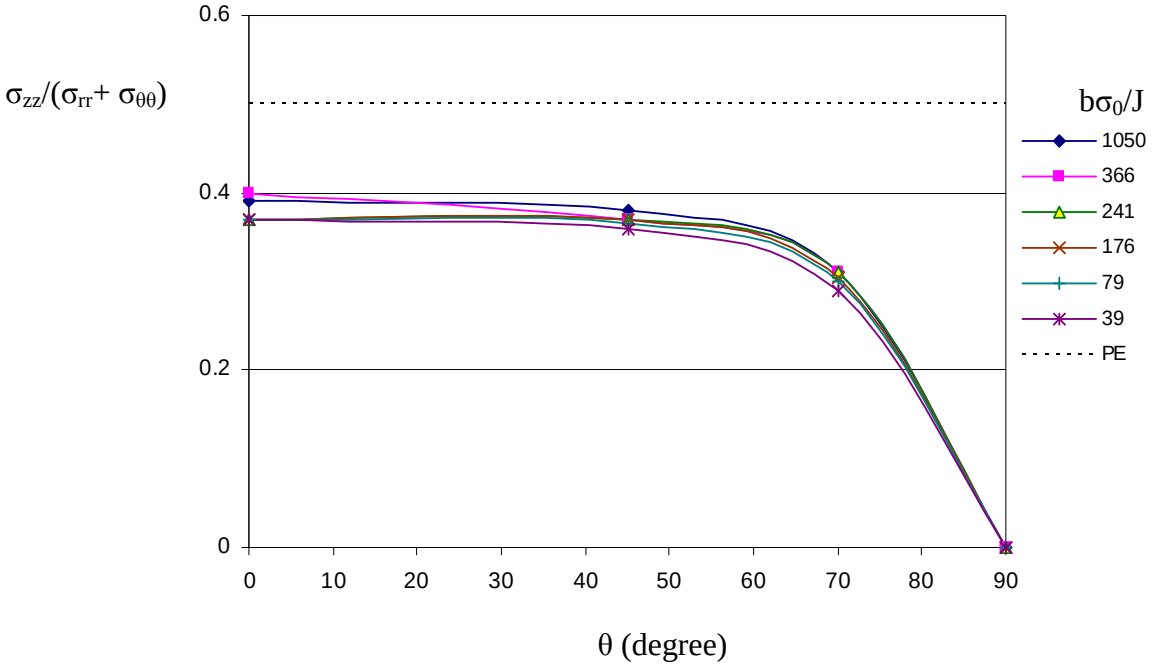

Figure 12.9: Proximity to plane strain as a function of the parametric angle (θ) along the crack in a semi-circular surface crack (a/w=0.5, a/c=1) in tension.

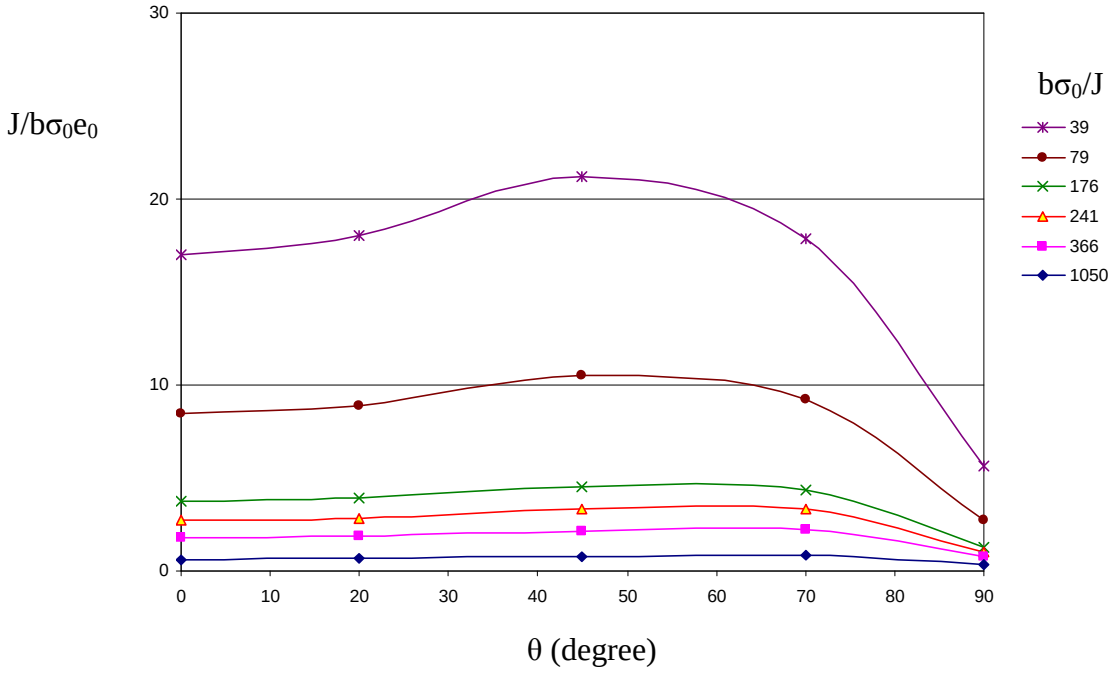

Figure 12.10: Non-dimensional J-integral along the crack front in a semi-circular surface crack (a/w=0.5, a/c=1) in tension.

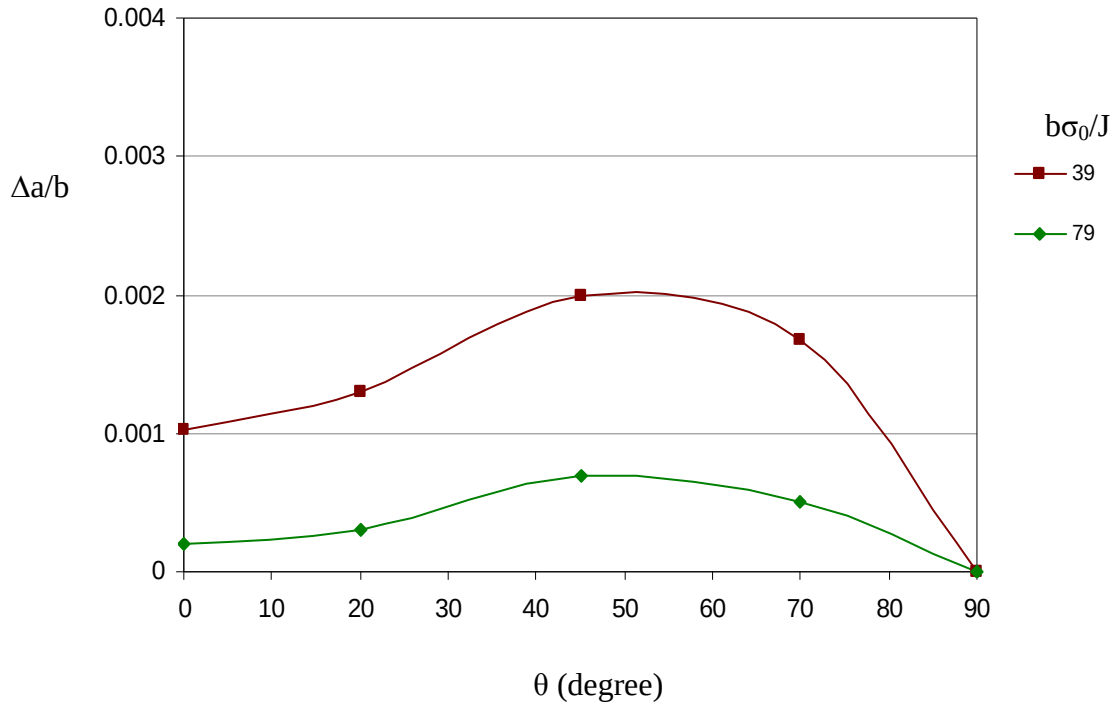

Figure 12.11: Prediction of crack growth as a function of the parametric angle (θ) from the deepest point to the free surface in a semi-circular surface crack (a/w=0.5, a/c=1) in tension from the initial shape.

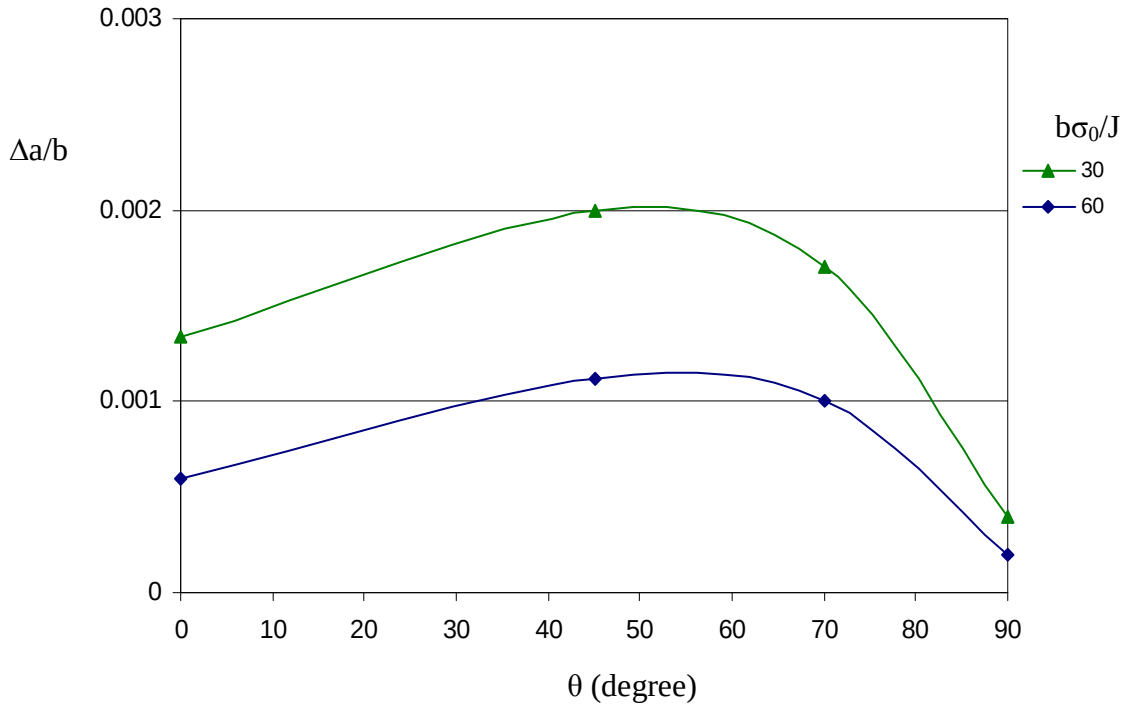

Figure 12.12: Crack extension from the 1st-step (a/w=0.65) of crack shape sequence for a deep semi-circular crack (a/w=0.5, a/c=1) under tension.

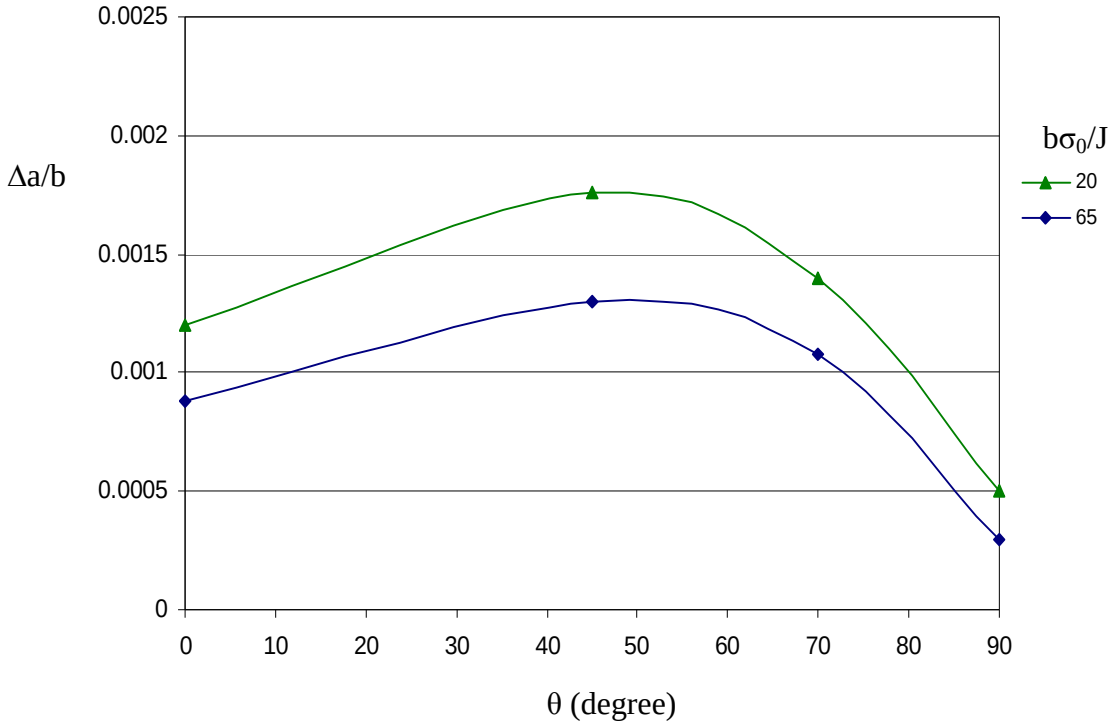

Figure 12.13: Crack extension from the 2nd-step (a/w=0.75) of crack shape sequence for a deep semi-circular crack (a/w=0.5, a/c=1) under tension.

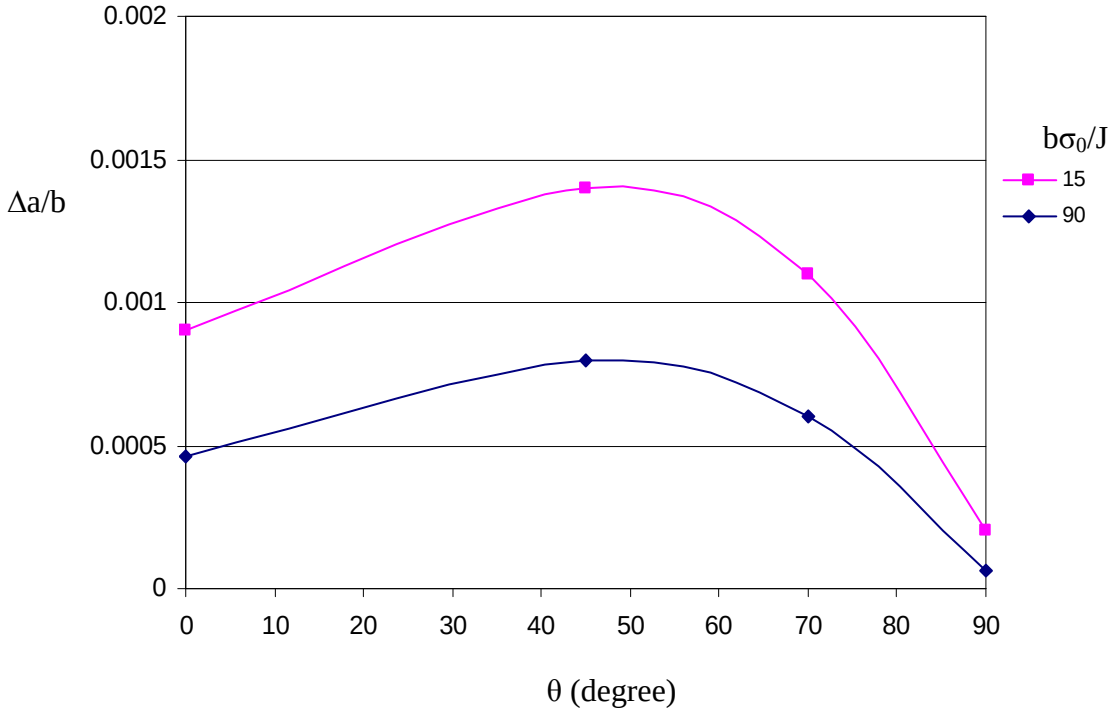

Figure 12.14: Crack extension from the 3rd-step (a/w=0.85) of crack shape sequence for a deep semi-circular crack (a/w=0.5, a/c=1) under tension.

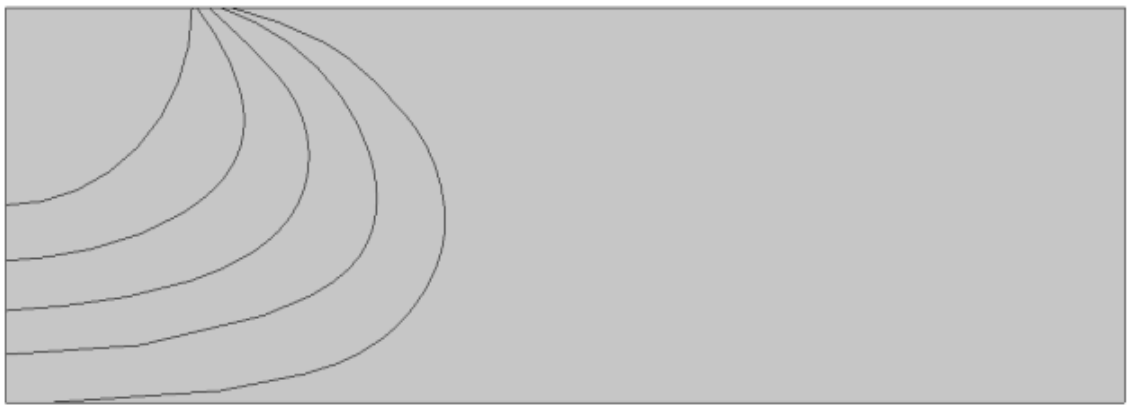

Figure 12.15: The crack shape development for a deep semi-circular surface crack (a/w=0.5, a/c=1) under ductile tearing in tension.

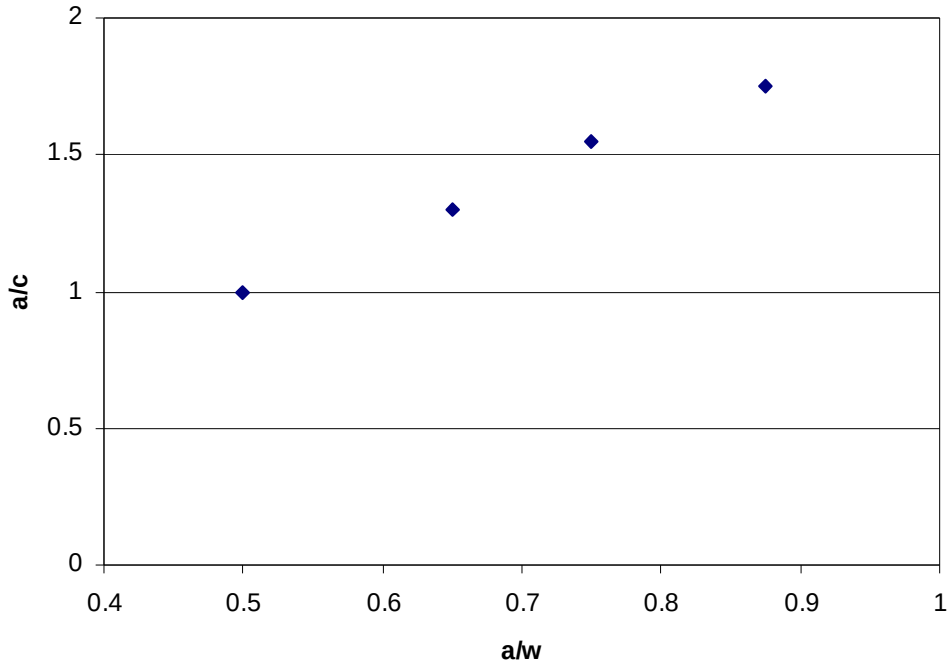

Figure 12.16: Development of the crack shape for a deep semi-circular crack (a/w=0.5, a/c=1) under tension.

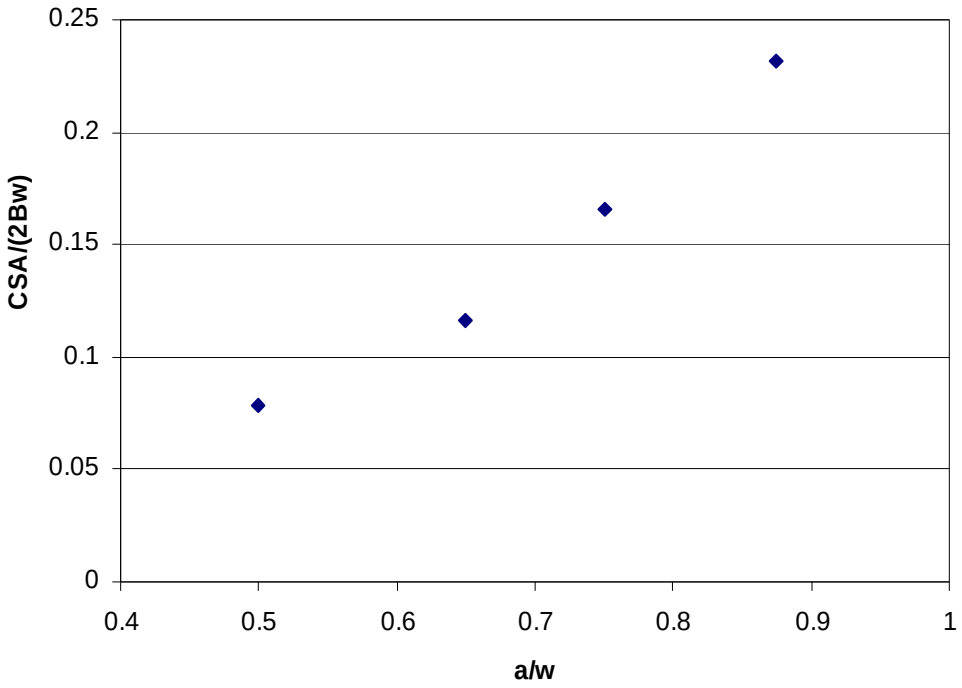

Figure 12.17: The crack surface area as a function of crack depth ratio (a/w) for a deep semi-circular crack (a/w=0.5, a/c=1) under tension.

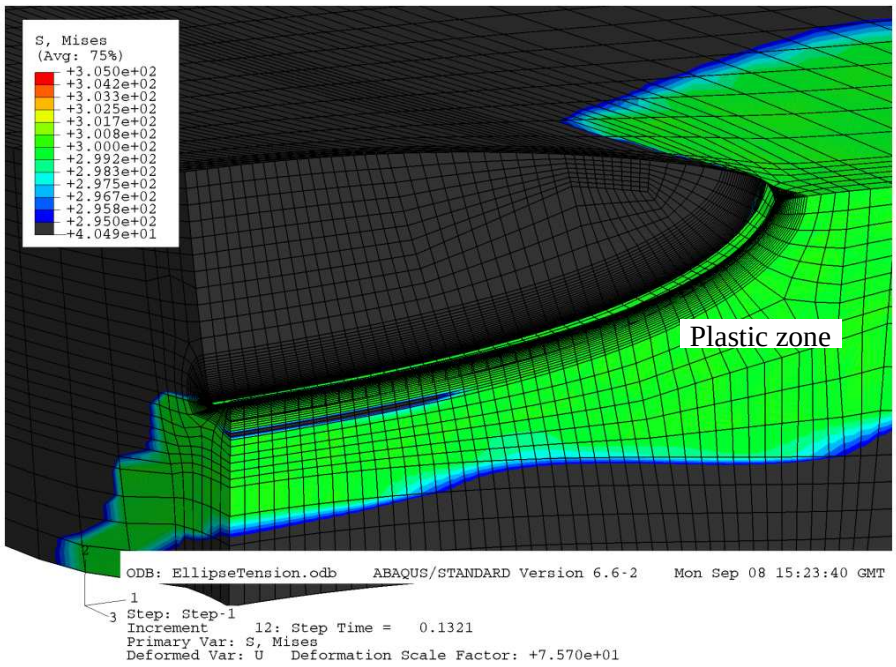

Figure 12.18: Development of the plastic zone around the crack for a deep semi-elliptical surface crack in tension, a/c=0.33, a/w=0.5.

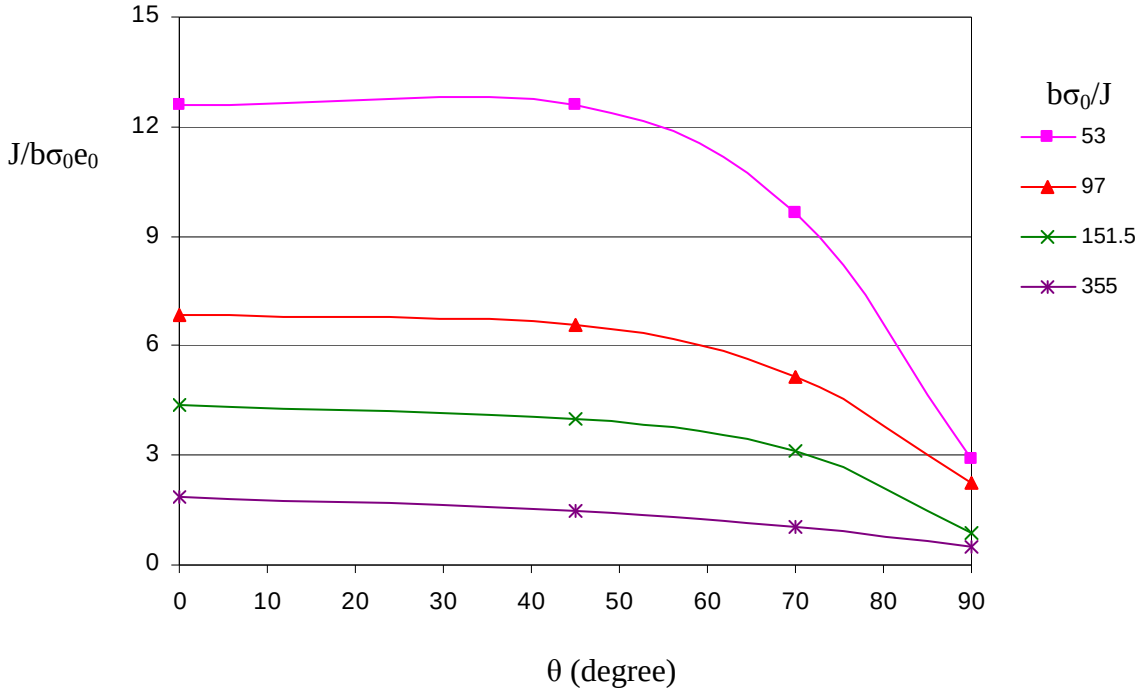

Figure 12.19: J-integral along the crack front for a deep semi-elliptical surface crack in tension, a/c=0.33, a/w=0.5.

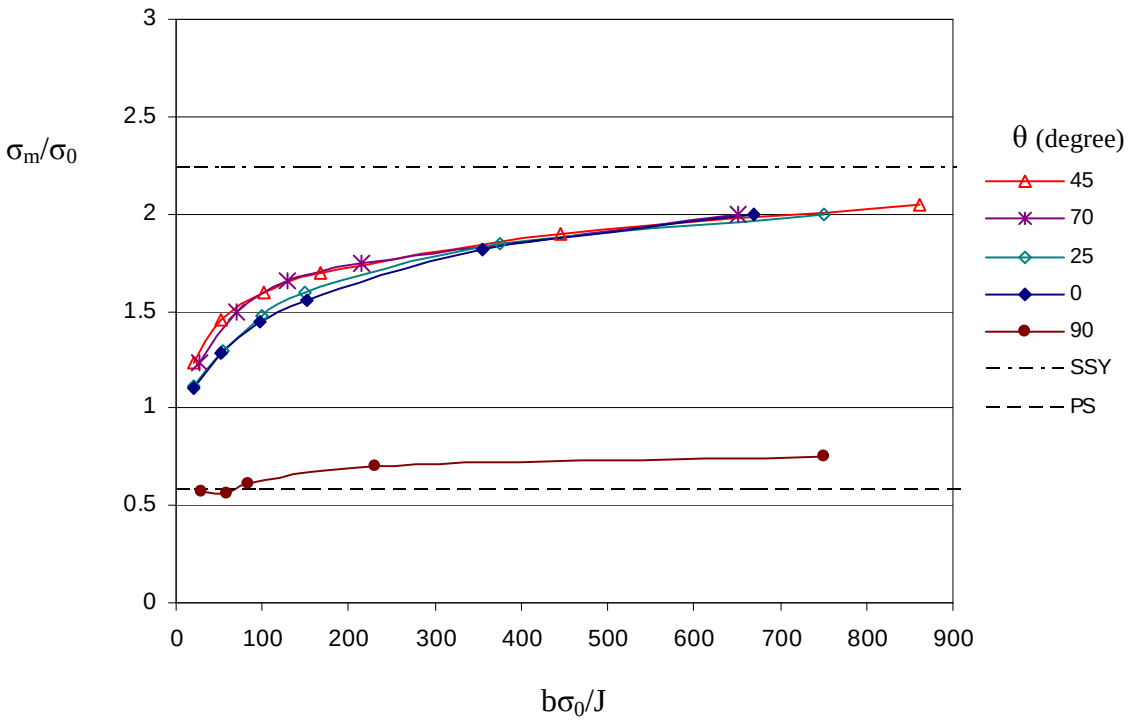

Figure 12.20: The mean stress at a distance $r\sigma_0/J=2$ as a function of deformation level along the crack for a deep semi-elliptical surface crack in tension (a/c=0.33, a/w=0.5).

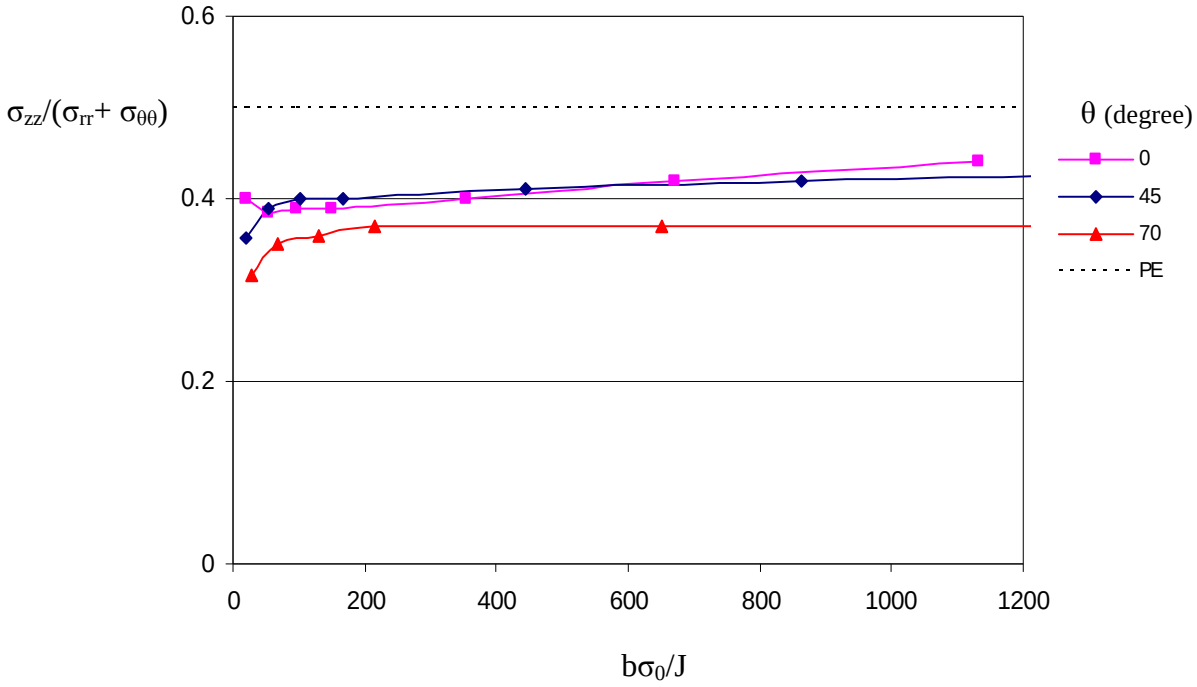

Figure 12.21: Proximity to plane strain around the crack front as a function of deformation in a deep semi-elliptical surface crack in tension, a/c=0.33, a/w=0.5.

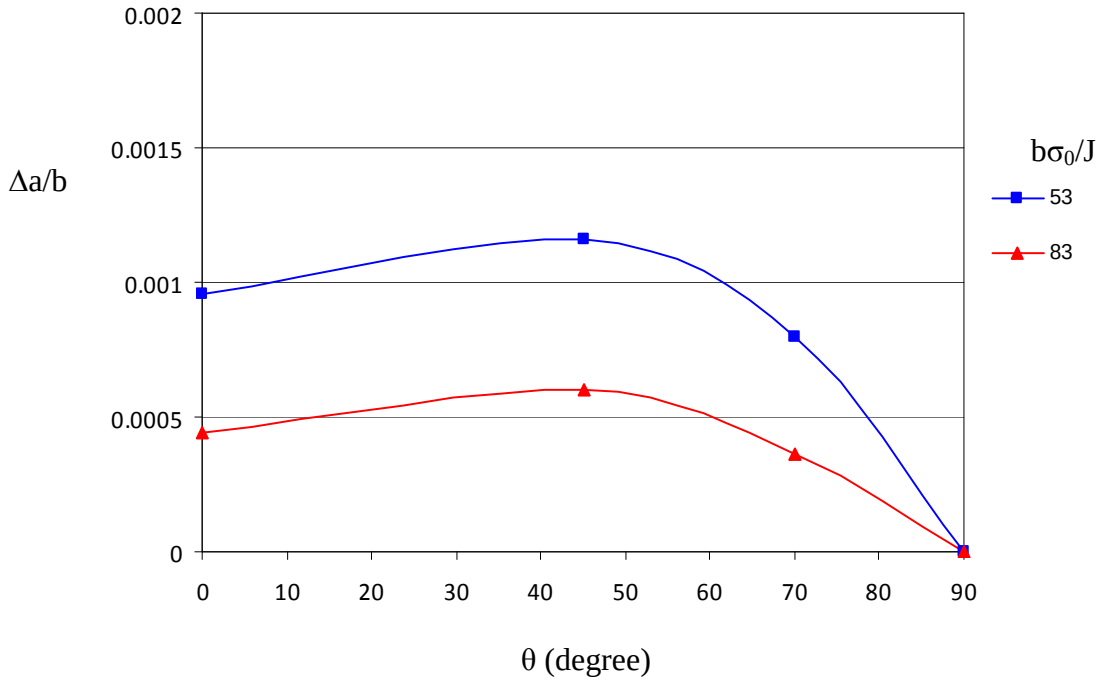

Figure 12.22: Crack growth around the crack front as a function of the parametric angle (θ) in a deep semi-elliptical surface crack in tension, a/c=0.33, a/w=0.5.

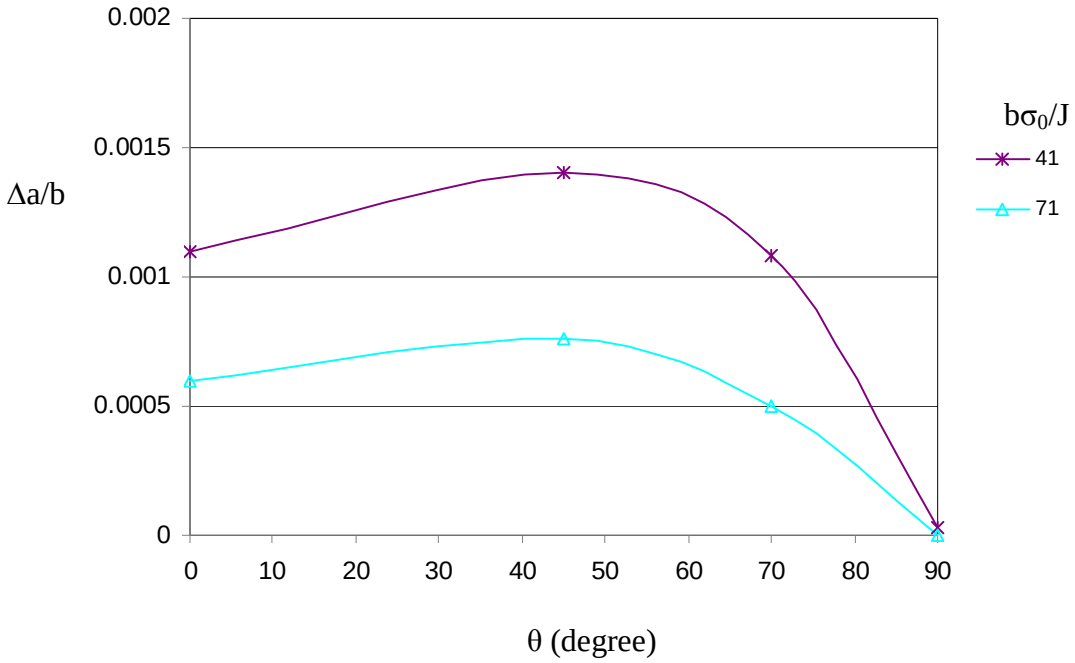

Figure 12.23: Crack growth around the crack front for the first step (a/w=0.65) of a deep semi-elliptical surface crack (a/c=0.33, a/w=0.5) in tension.

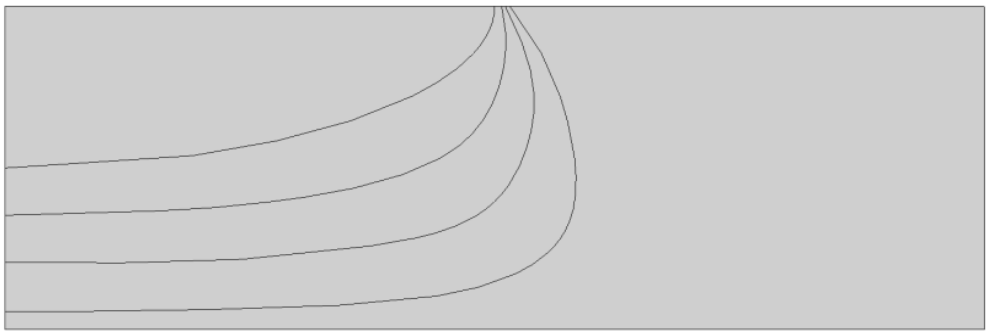

Figure 12.24: The crack shape development for a deep semi-elliptical surface crack a/c=0.33, a/w=0.5 under ductile tearing in tension.

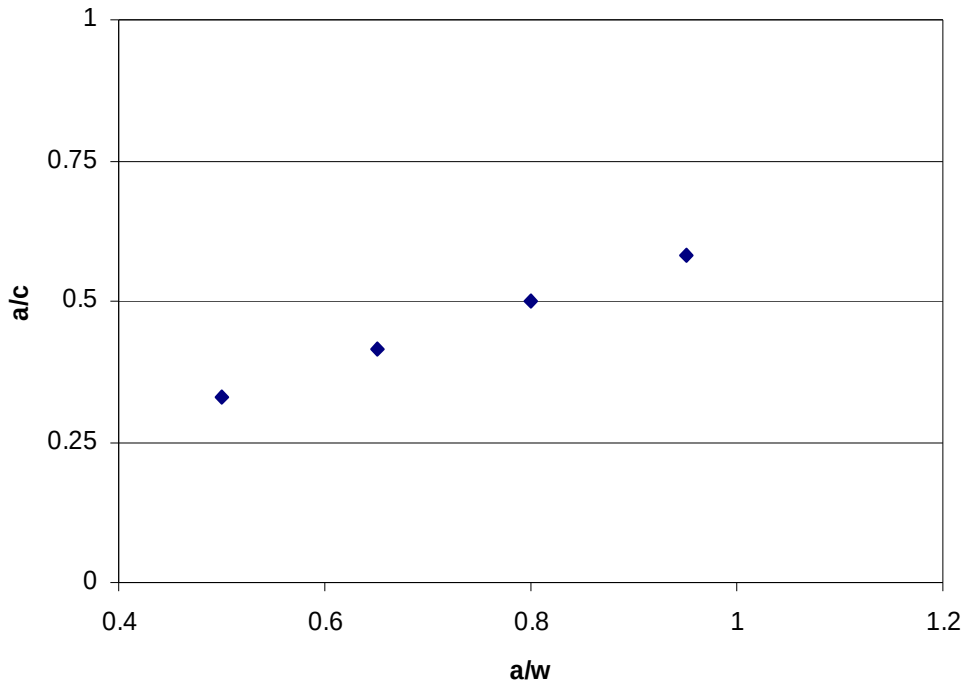

Figure 12.25: Development of the crack shape for a deep semi-elliptical crack (a/w=0.5, a/c=0.33) under tension.

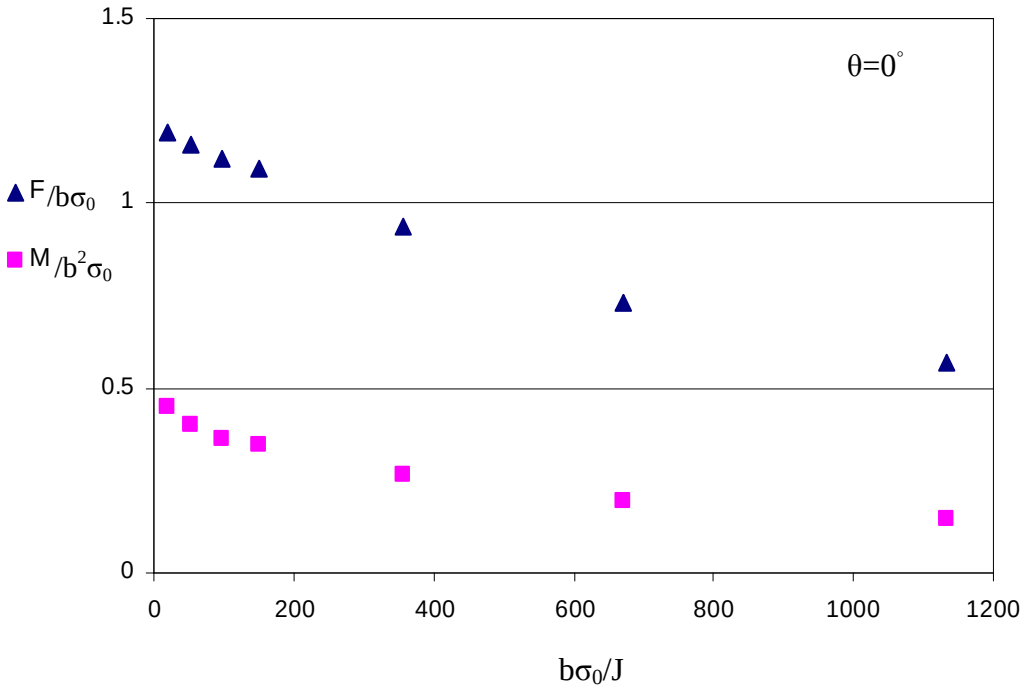

Figure 12.26: Force and moment redistribution along the uncracked ligament at the deepest point (path1) as a function of deformation in a deep semi-elliptical (a/w=0.5, a/c=0.33) surface crack in tension.

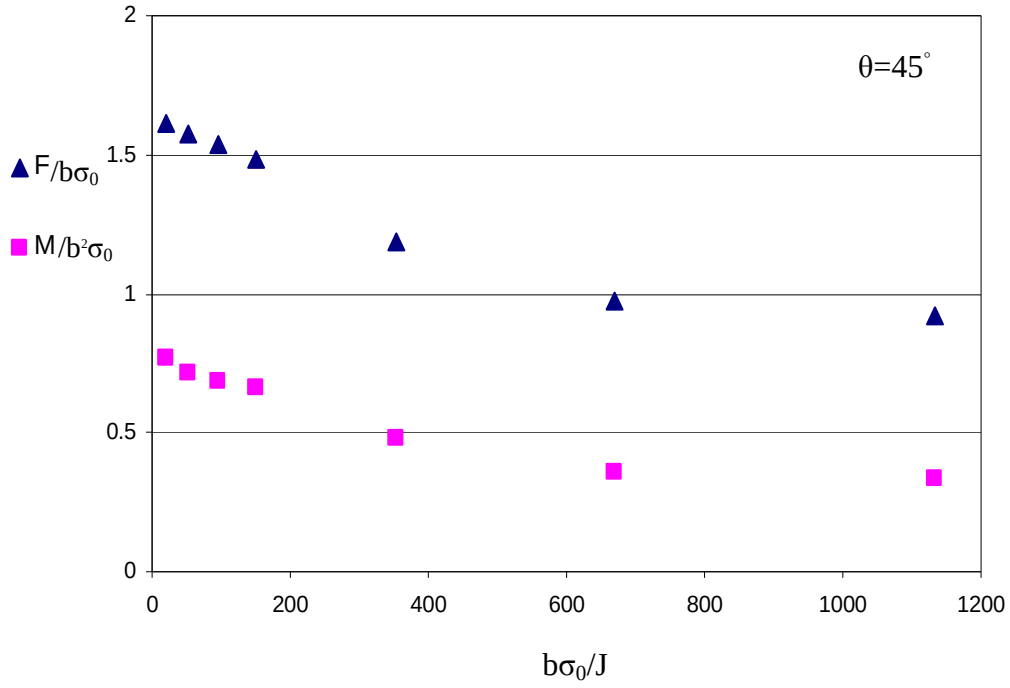

Figure 12.27: Force and moment redistribution along the uncracked ligament at 45° (path2) as a function of deformation in a deep semi-elliptical surface crack (a/w=0.5, a/c=0.33) in tension.

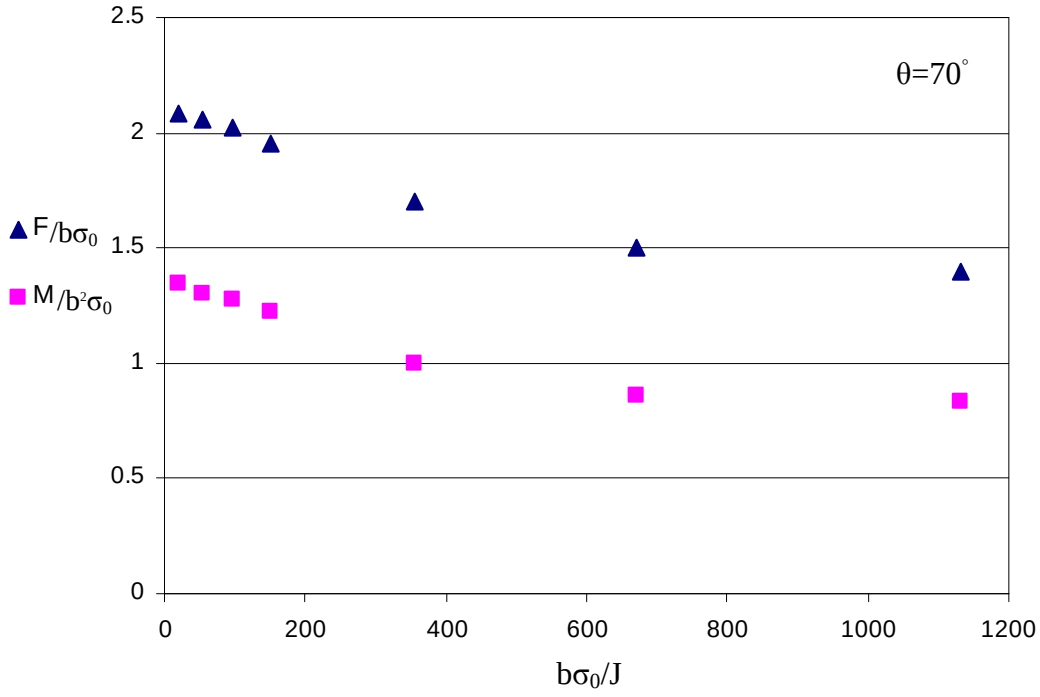

Figure 12.28: Force and moment redistribution along the uncracked ligament at 70° (path3) as a function of deformation in a deep semi-elliptical surface crack (a/w=0.5, a/c=0.33) in tension.

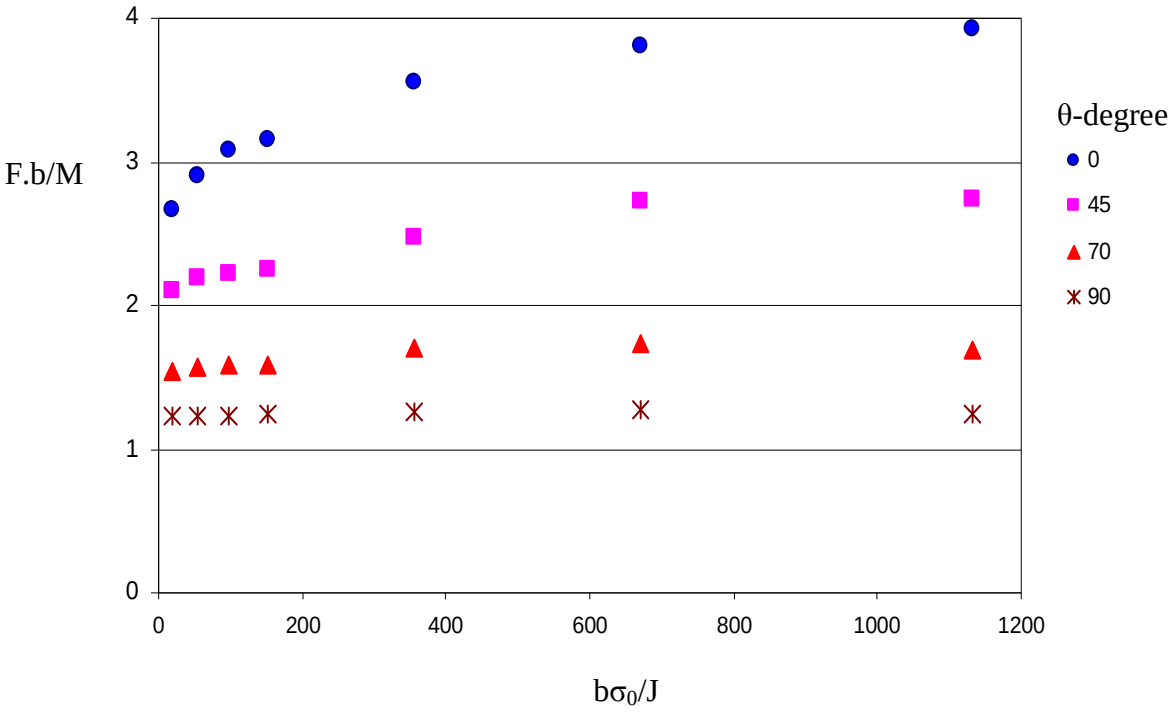

Figure 12.29: Force-moment ratio on the uncracked ligament ahead of the crack in a deep semi-elliptical surface crack (a/w=0.5, a/c=0.33) in tension.

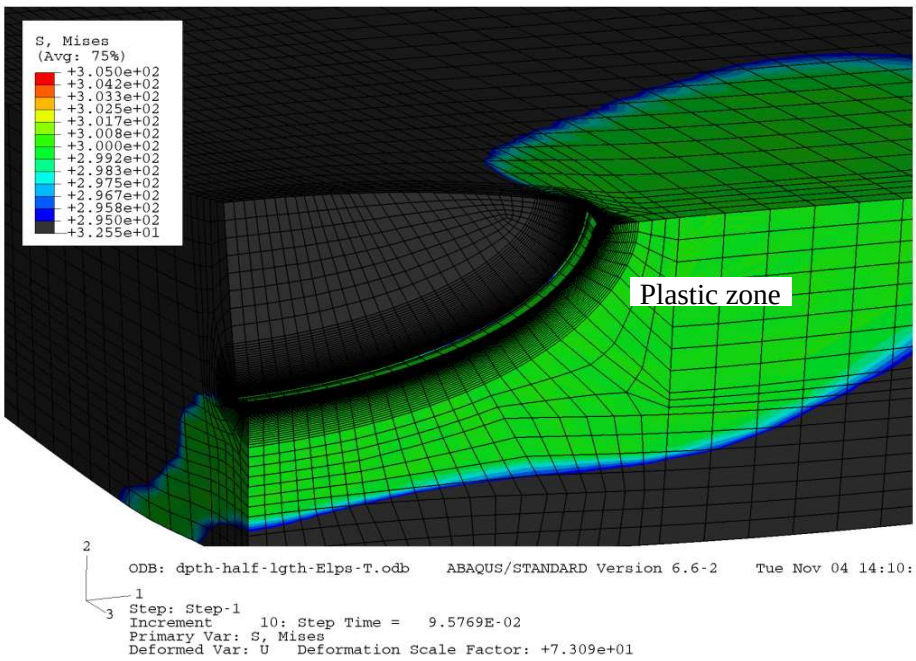

Figure 12.30: Development of the plastic zone around the crack front in a deep semi-elliptical surface crack a/w=0.5 with aspect ratio a/c=0.5 under tension.

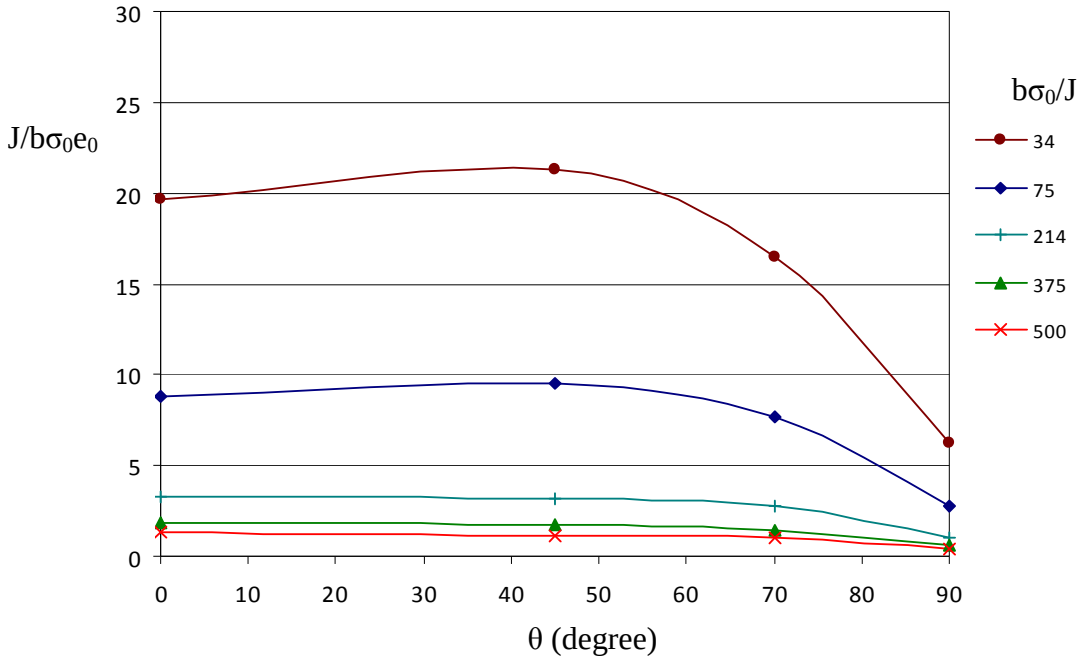

Figure 12.31: J-integral along the crack front for a deep semi-elliptical surface crack in tension (a/c=0.5, a/w=0.5).

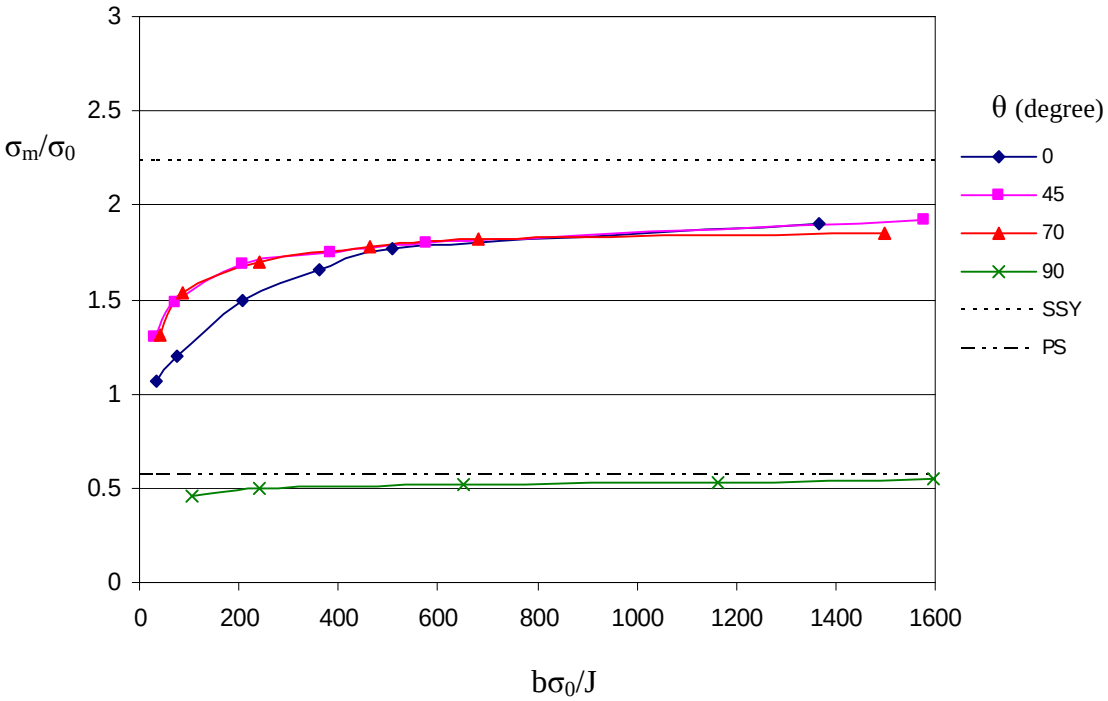

Figure 12.32: The mean stress at a distance $r\sigma_0/J = 2$ as a function of deformation level around the crack front for a deep semi-elliptical surface crack in tension (a/c=0.5, a/w=0.5).

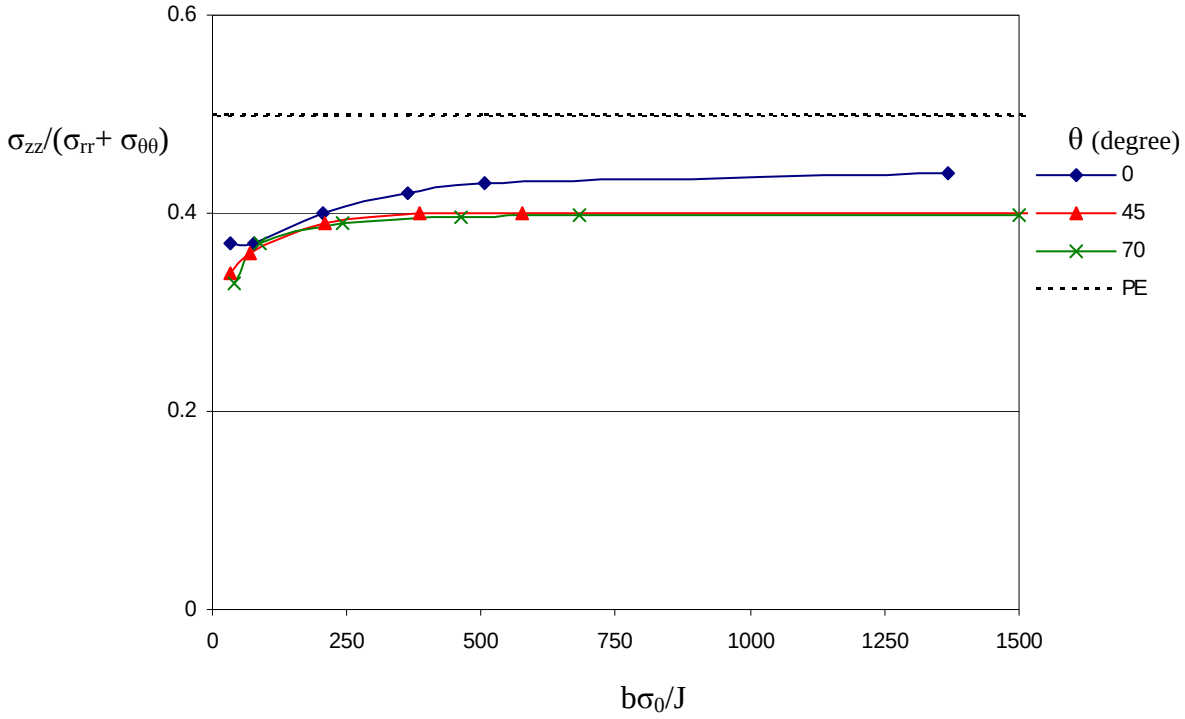

Figure 12.33: Proximity to plane strain around the crack front for a deep semi-elliptical crack a/c=0.5, a/w=0.5 in tension.

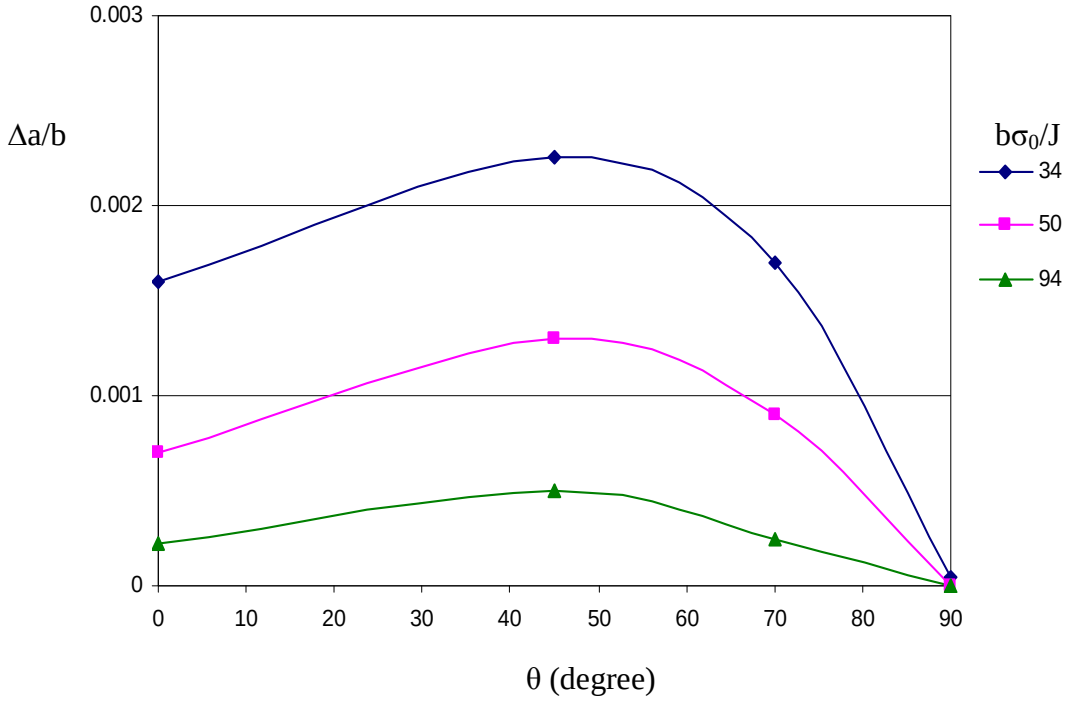

Figure 12.34: Crack growth around the crack front as a function of the parametric angle (θ) for a deep semi-elliptical surface crack in tension (a/c=0.5, a/w=0.5).

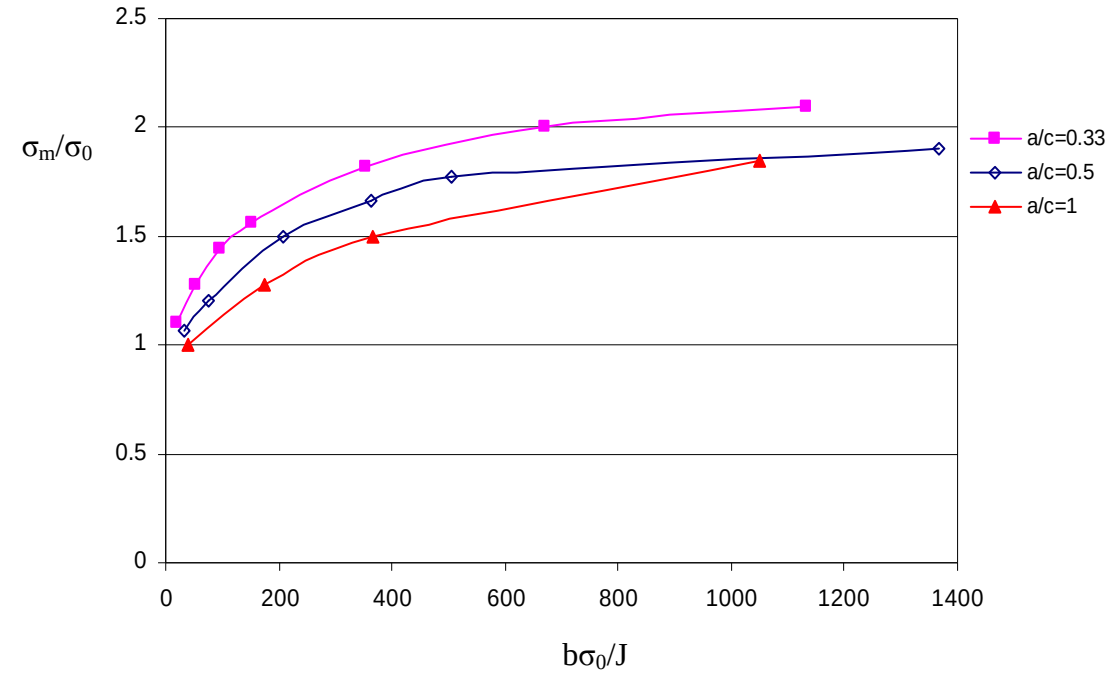

Figure 12.35: The mean stress at a distance $r\sigma_0/J$ =2 as a function of deformation level at the deepest point for a deep semi-elliptical surface crack, a/w=0.5, with different aspect ratios in tension (a/c=0.33, 0.5 and 1).

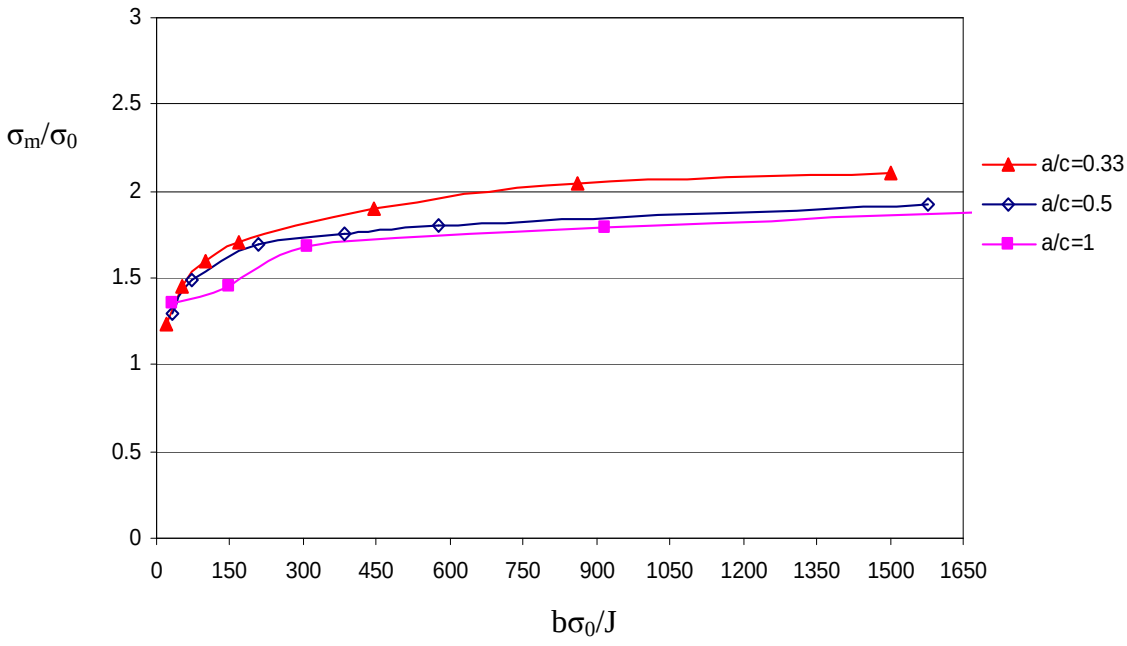

Figure 12.36: The mean stress at a distance $r\sigma_0/J$ =2 as a function of deformation level at 45° for a deep semi-elliptical surface crack, a/w=0.5, with different aspect ratios in tension (a/c=0.33, 0.5 and 1).

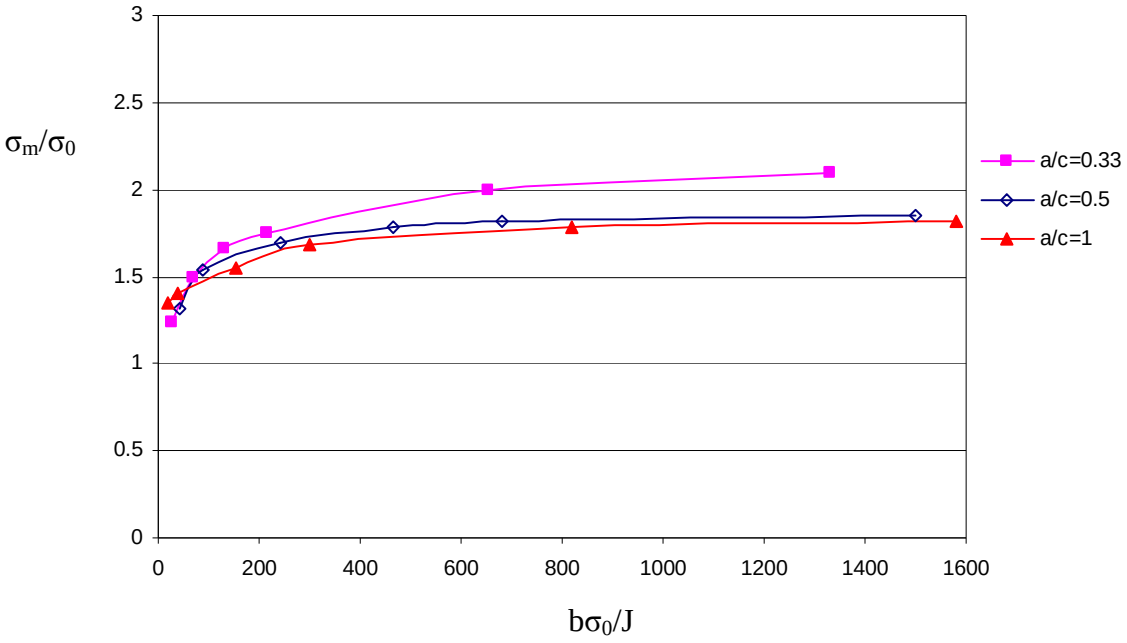

Figure 12.37: The mean stress at a distance $r\sigma_0/J = 2$ as a function of deformation level at 70° for a deep semi-elliptical surface crack, a/w=0.5, with different aspect ratios in tension. (a/c=0.33, 0.5 and 1).

13. Shallow semi-elliptical surface cracks in tension

13.1 Introduction

This chapter quantifies the constraint level and crack driving force (J-integral) for shallow surface cracks as both are necessary to determine crack growth under ductile tearing in tension. Shallow surface cracks with two different crack depths (a/w=0.1, a/c=1) and (a/w=0.2, a/c=0.5 and 0.33) in non-hardening materials were examined.

13.2 A shallow semi-circular surface crack (a/w=0.1, a/c=1.0) in tension under elastic-plastic conditions.

13.2.1 Crack tip stress field

Under tensile loading the plastic zone developed rapidly along the crack front and across the whole plate as shown in Figures (13.1) and (13.2). A uniform mean stress was observed along the crack front from the deepest point to 70°, as shown in Figure (13.3). Figure (13.4) shows that the loss of plane strain constraint occurs in a similar way between the deepest point and 70°. At low deformation levels the plane strain constraint was close to 0.4, and then collapsed in full plasticity. The variation in the J-integral around the crack is shown in Figure (13.5). The J-integral maintained a uniform value along the crack front between the deepest point and 70°, and reduced gradually towards the free surface.

13.2.2 Determination of crack growth

Figure (13.6) shows that crack extension is predicted to be uniform along the majority of the crack front so that the original semi-circular shape is largely maintained under tension. This is because of similar values of the mean stress and J-integral values in the angular region 0°-70° were observed. The development of a shallow semi-circular surface crack was uniform only for the initial step as shown in Figure (13.7). As the crack grew, high levels of constraint developed at 45° and 70° and caused a deviation from the original crack shape particularly for the second and third steps (a/w=0.3, 0.45). This profile continued until the crack broke through the plate thickness as shown in Figure (13.8).

13.3 A shallow semi-elliptical surface crack (a/w=0.2, a/c=0.3) in tension under elastic-plastic conditions.

13.3.1 Crack tip stress field

At low deformation levels the plastic zone developed in a similar way to that observed in bending as illustrated in Figure (13.9). As deformation increased the plastic zone developed more rapidly than in bending and completely engulfed the ligament as shown in Figure (13.10). The results shown in Figures (13.11) and (13.12) show that both the J-integral and the mean stress remain high at deepest point but reduce as the free surface is approached. Figure (13.13) shows the plane strain constraint at the deepest point remains constant at approximately 0.4 and collapses in full plasticity.

13.3.2 Determination of crack growth

For shallow surface cracks, the crack is predicted to grow most at the deepest point and least at the free surface as shown in Figure (13.14). Figures (13.15) to (13.18) show the evolution of the crack shape under ductile tearing. For the initial and first steps ($a/w \leq 0.3$) the crack grew at most at the deepest point as shown in Figure (13.19). However as the value of a/c increased to about 1 more growth occurred at 45°-70°, this is because both the mean stress and the J-integral were greatest at this region. The development of the crack shape can be expressed as a relationship between the a/c ratio and the crack depth as shown in Figure (13.20). Figure (13.21) shows the force-moment ratio for a/c=0.33, a/w=0.2 in tension has largest values at the deepest point and smallest values in the angular range 45°-70°.

13.4 A shallow semi-elliptical surface crack (a/w=0.2, a/c=0.5) in tension under elastic-plastic conditions.

Figure (13.22) shows the rapid development of the plastic zone along the crack front including the deepest point at deformation level of $b\sigma_0/J=923$ measured at $\theta=0°$. For shallow semi-elliptical surface cracks both the J-integral and the mean stress were largest at the deepest point and both reduced towards the free surface as shown Figures (13.23)

and (13.24). The plane strain constraint was approximately constant at 0.4 in contained yielding and reduced gradually in large scale yielding particularly in the region between 70˚-90˚as shown in Figure (13.25). The crack was predicted to grow significantly at the deepest point as shown in Figure (13.26).

13.5 Discussion

Uniform crack growth was observed around the front of shallow semi-circular surface cracks (a/w=0.1 and a/c=1) since both the constraint level and J-integral distribution did not vary over the crack front except near the free surface where plane stress conditions prevail. The uniformity of J-integral around the crack front is consistent with the results of Wang (2009) who analysed a geometry with a/w=0.2.

For shallow semi-elliptical surface cracks (a/w=0.2, a/c=0.5 and 0.33) both the J-integral and the mean stress varied along the crack front and had large values at the deepest point. This observation differs from the results by Brickstad et al (2000) who showed that the maximum J-integral occurs at 60˚measured from the deepest point. The largest crack growth was observed at the deepest point. Similar results by Berg et al. (2008) showed the crack grew at the deepest point for cracks with small values of a/c.

13.6 Conclusion

The largest mean stress and J-integral occurred at the deepest point of shallow semi-elliptical surface cracks (a/c<1) caused significant crack growth at the deepest segment, but resulted in reduced growth towards the free surface. In contrast more uniform crack tip constraint and J-integral were observed for shallow semi-circular cracks (a/c=1), and uniform growth occurred.

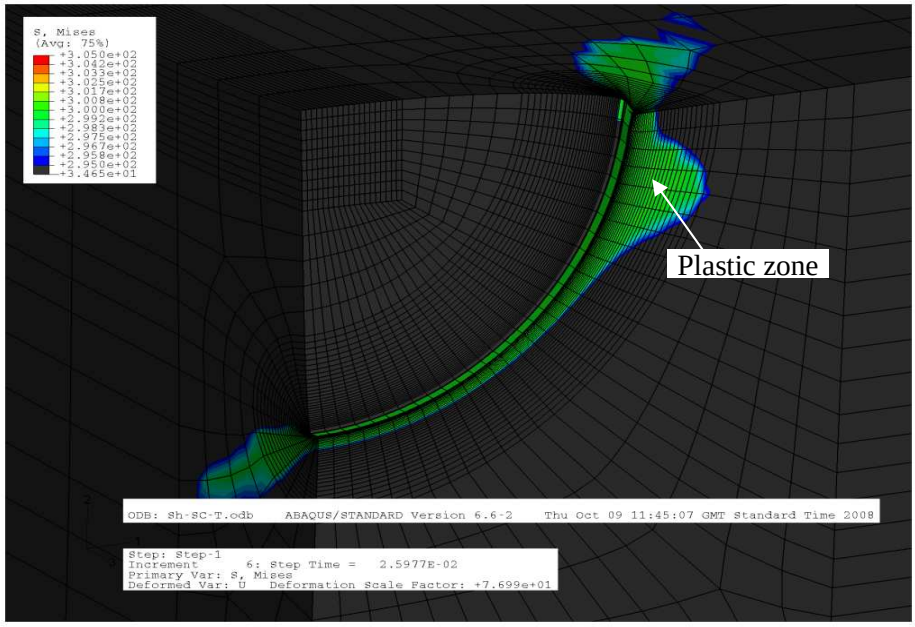

Figure 13.1: Development of the plastic zone around the crack in a shallow semi-circular crack in tension a/w=0.1, a/c=1, $b\sigma_0/J$=2500.

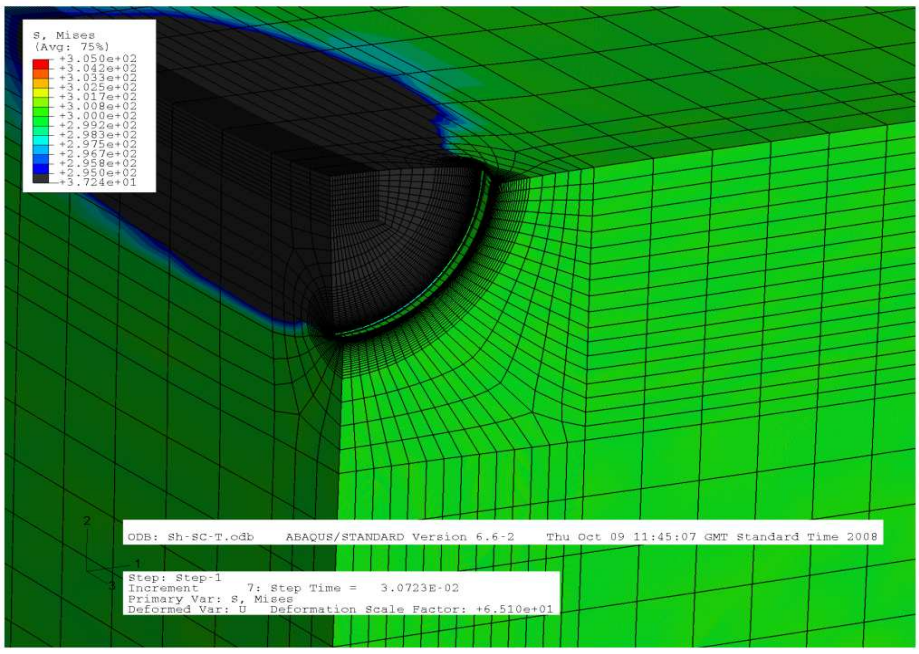

Figure 13.2: Plasticity encompasses the whole body in a shallow semi-circular crack in tension a/w=0.1, a/c=1, $b\sigma_0/J$=197.

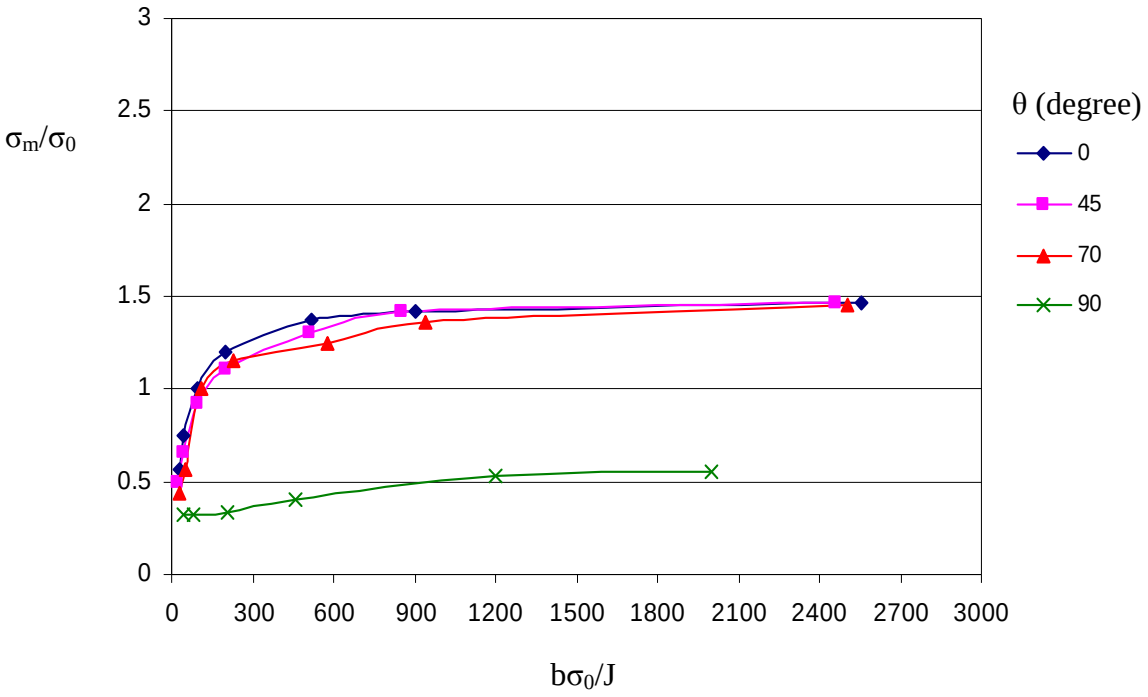

Figure 13.3: The mean stress at $r\sigma_0/J$ =2 around the crack as a function of levels of deformation for a shallow semi-circular crack (a/w=0.1, a/c=1) in tension.

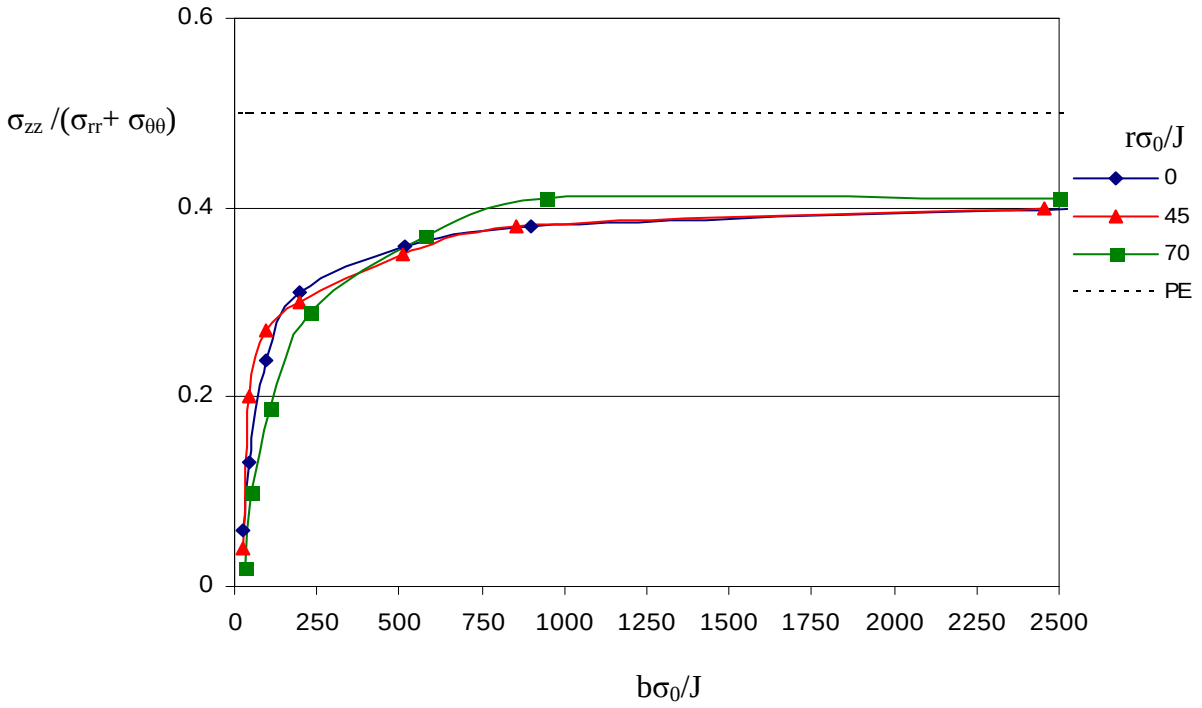

Figure 13.4: Proximity to plane strain around the crack front for a shallow semi-circular crack (a/w=0.1, a/c=1) in tension.

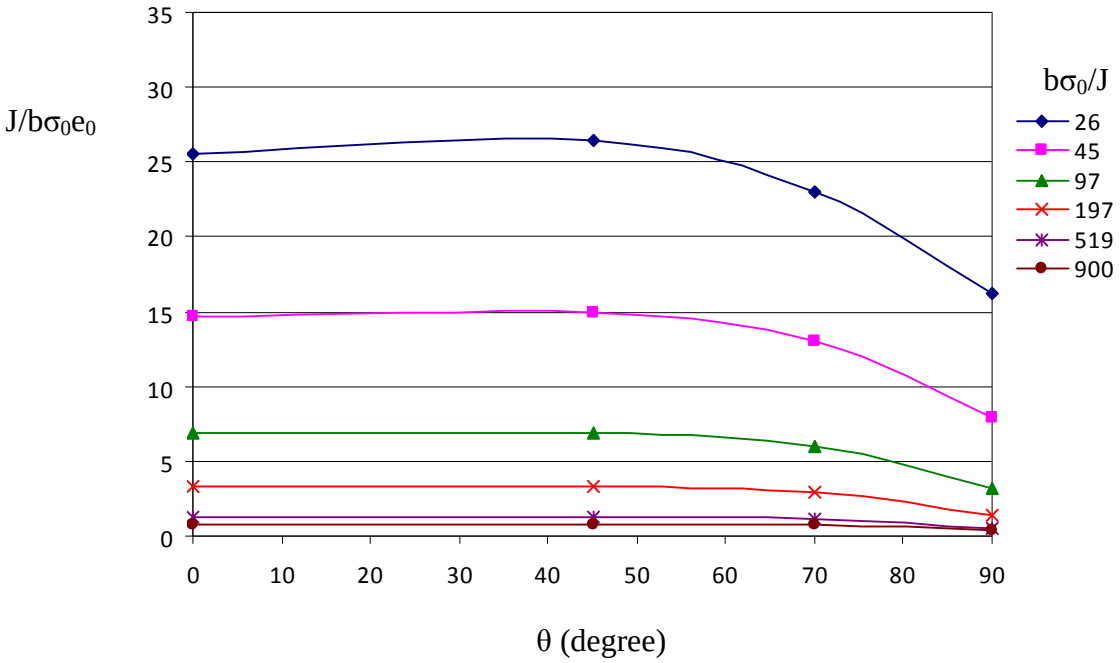

Figure 13.5: J-integral distribution along the crack front from the deepest point (θ=0˚) to the surface θ=90˚ for a shallow semi-circular crack (a/w=0.1, a/c=1) in tension.

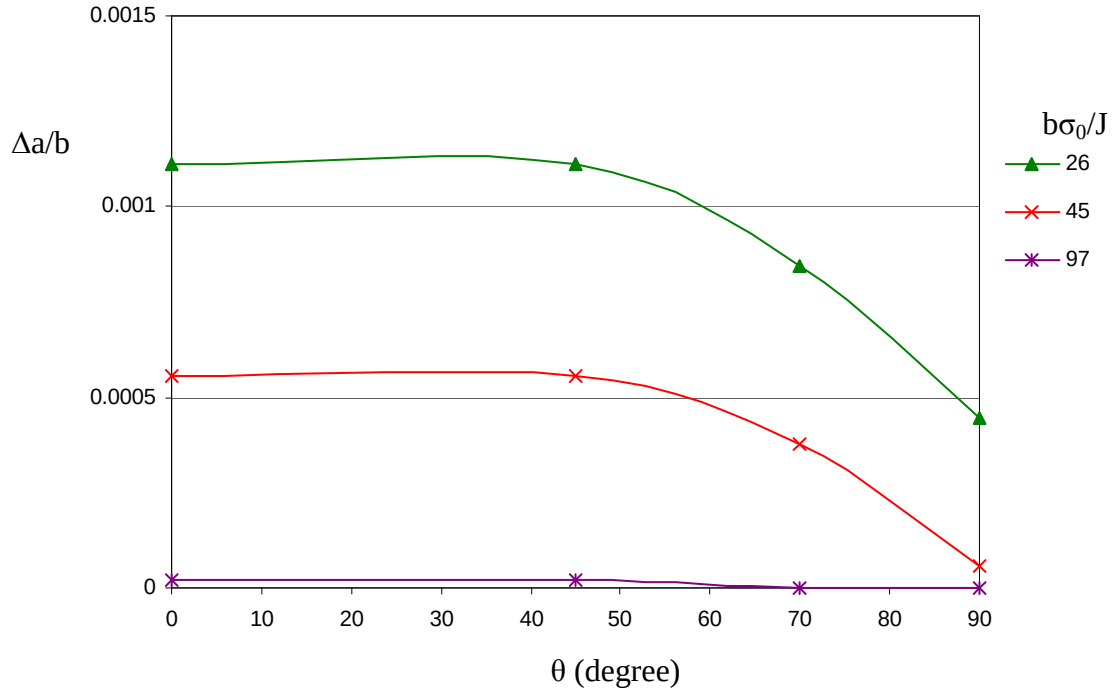

Figure 13.6: Crack growth as a function of parametric angle from the deepest point to the free surface for a shallow semi-circular crack (a/w=0.1, a/c=1) in tension.

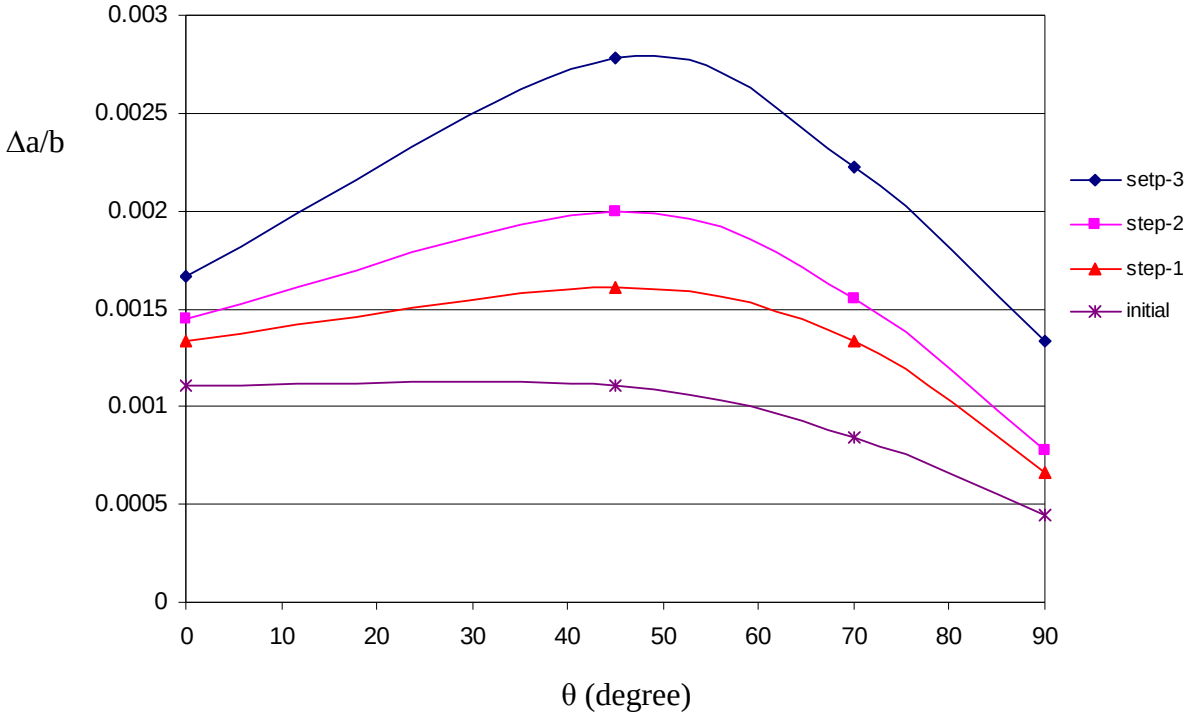

Figure 13.7: Crack growth steps as a function of the parametric angle θ for a shallow semi-circular crack in tension a/w=0.1, a/c=1.

Figure 13.8: The crack shape development for a shallow semi-circular surface crack a/c=1, a/w=0.1 under ductile tearing in tension.

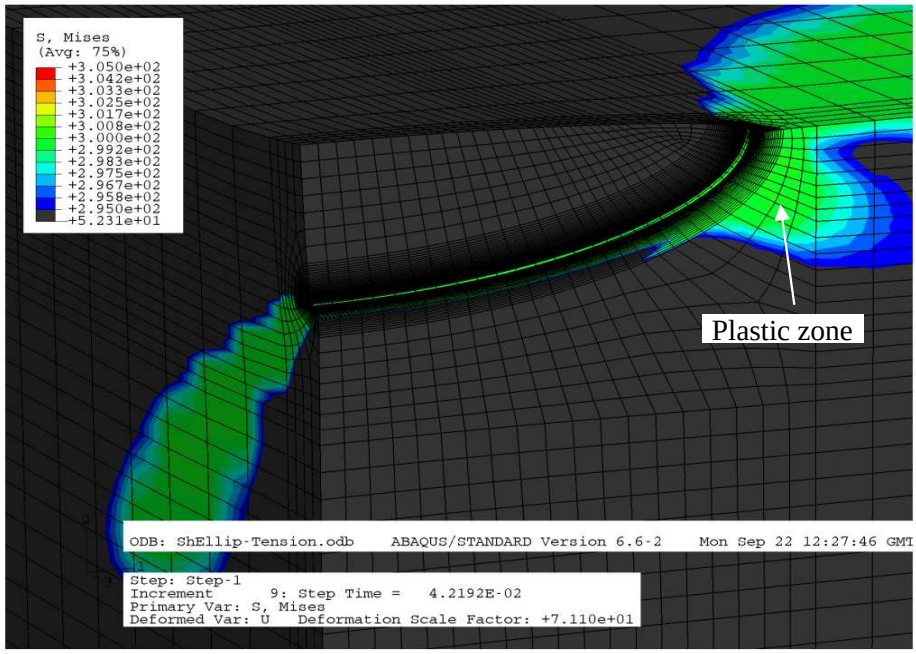

Figure 13.9: Plastic zone development around the crack in a shallow semi-elliptical crcak (a/w=0.2, a/c=0.33) in tension at $b\sigma_0/J=881$ measured at the deepest point.

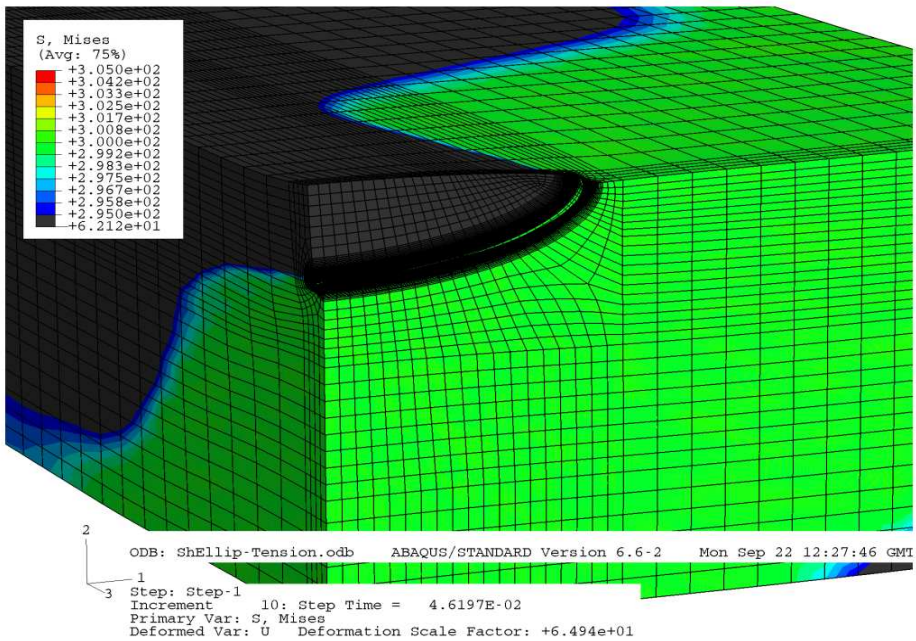

Figure 13.10: The plasticity encompases most of the plate at $b\sigma_0/J=350$ measured at $\theta=0^{\circ}$ in a shallow semi-elliptical crack (a/w=0.2, a/c=0.33) in tension.

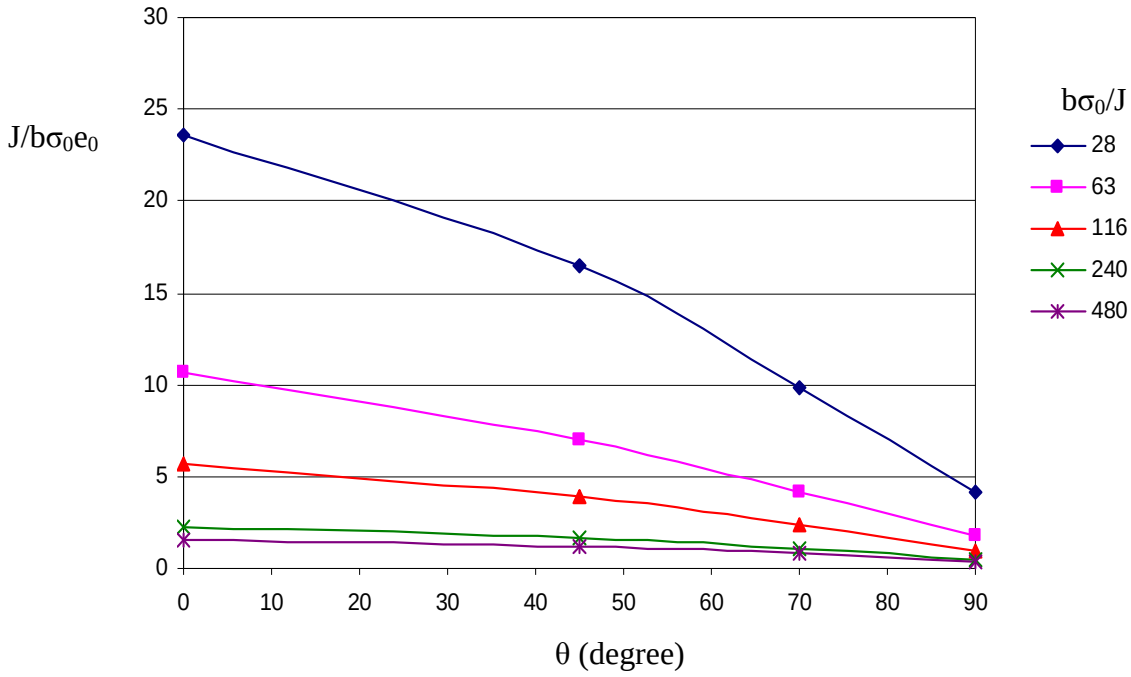

Figure 13.11: J-integral along the crack front for a shallow semi-elliptical surface crack in tension (a/w=0.2, a/c=0.33).

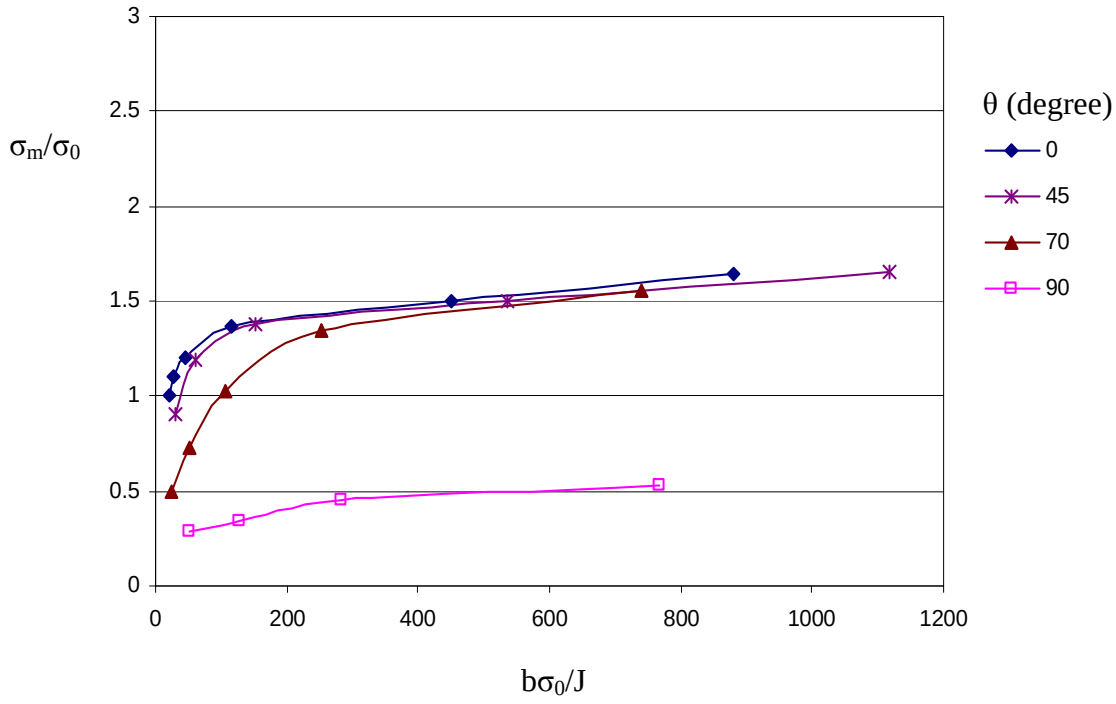

Figure 13.12: The mean stress at a distance $r\sigma_0/J = 2$ as a function of deformation level around the crack front for a shallow semi-elliptical surface crack in tension (a/c=0.33, a/w=0.2).

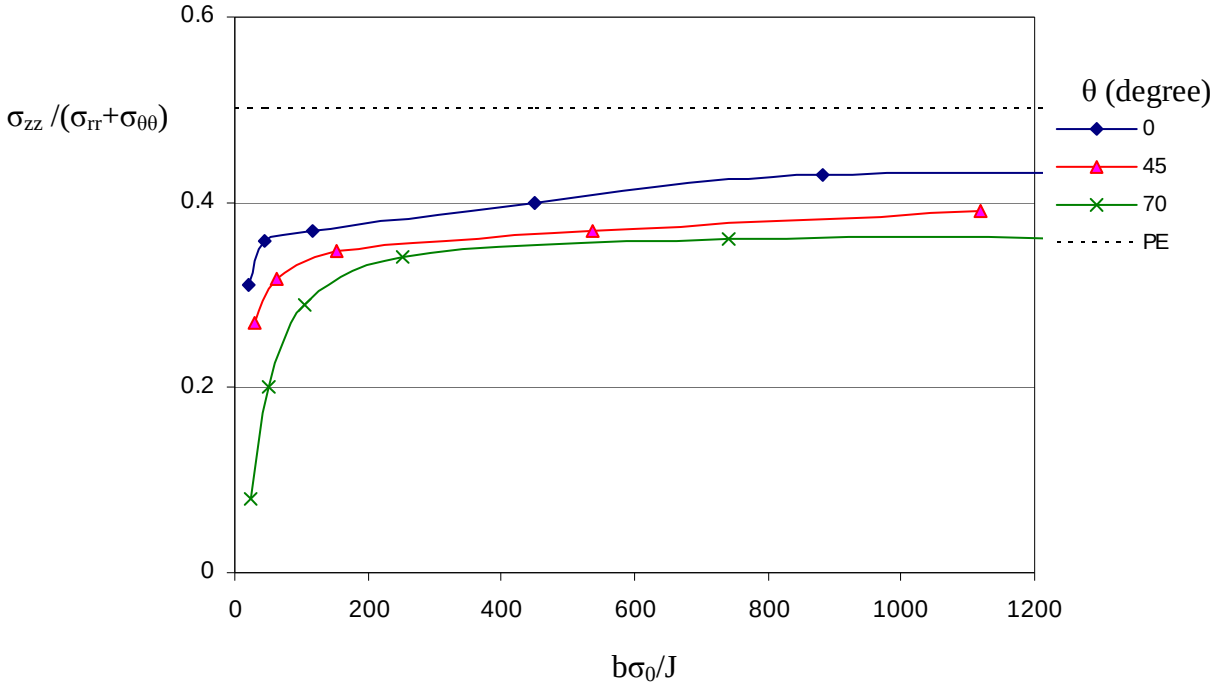

Figure 13.13: Proximity to plane strain around the crack front for a shallow semi-elliptical crack (a/w=0.2, a/c=0.33) in tension.

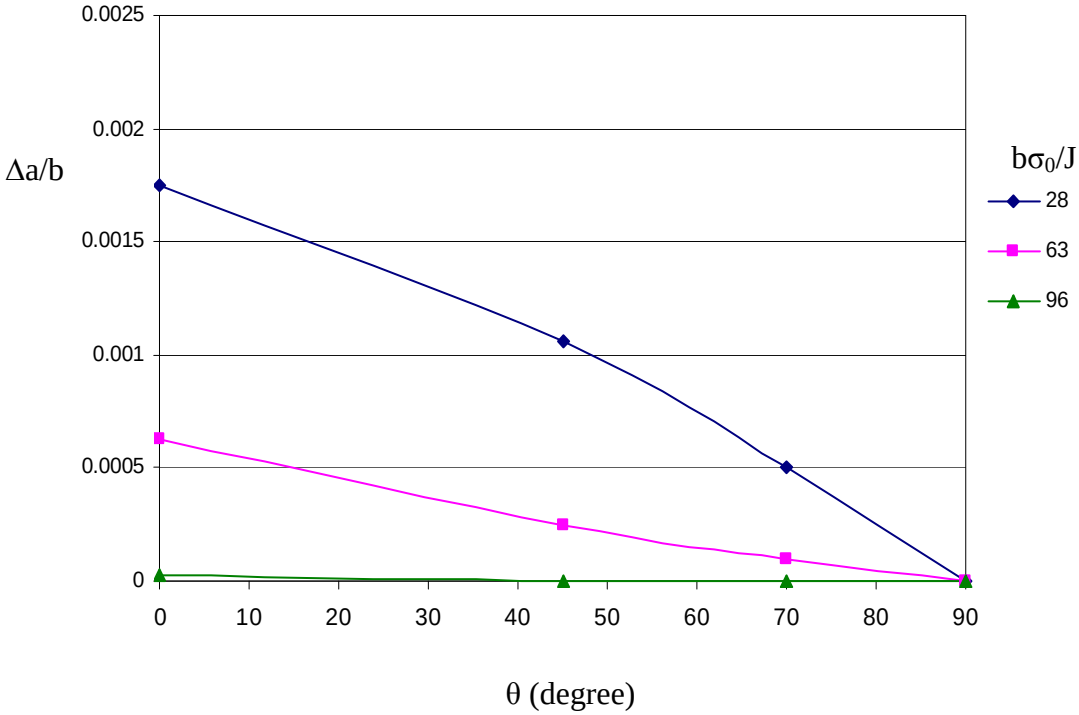

Figure 13.14: Crack growth around the crack front as a function of the parametric angle θ for a shallow semi-elliptical surface crack in tension (a/c=0.33, a/w=0.2).

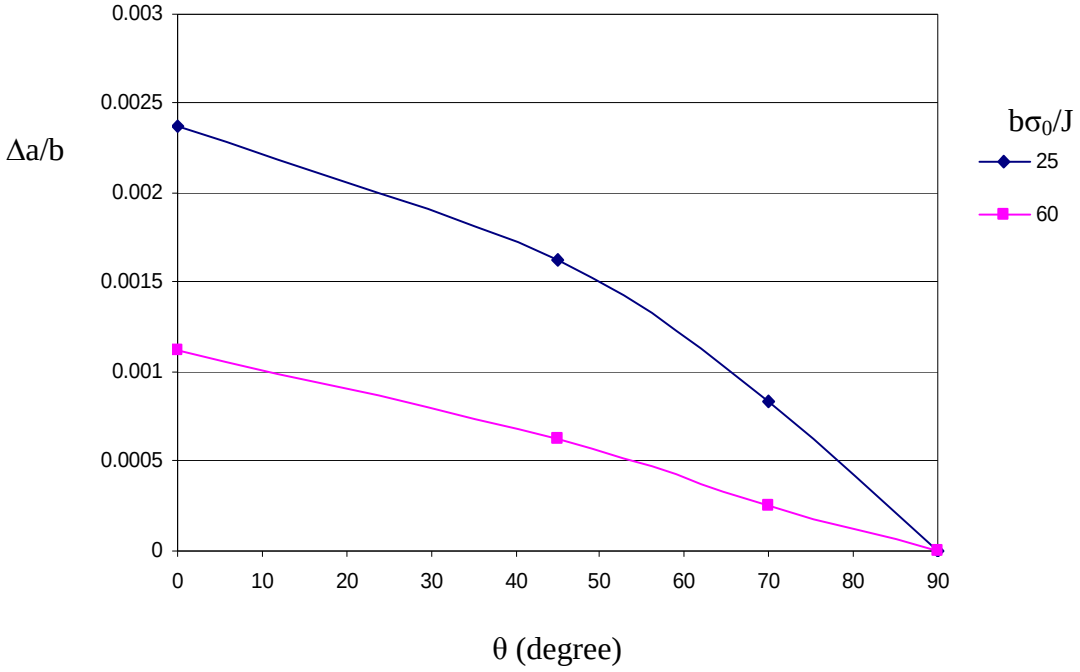

Figure 13.15: Crack growth as a function of the parametric angle θ for step-1 (a/w=0.3) in a shallow semi-elliptical surface crack (a/w=0.2, a/c=0.33) under tension.

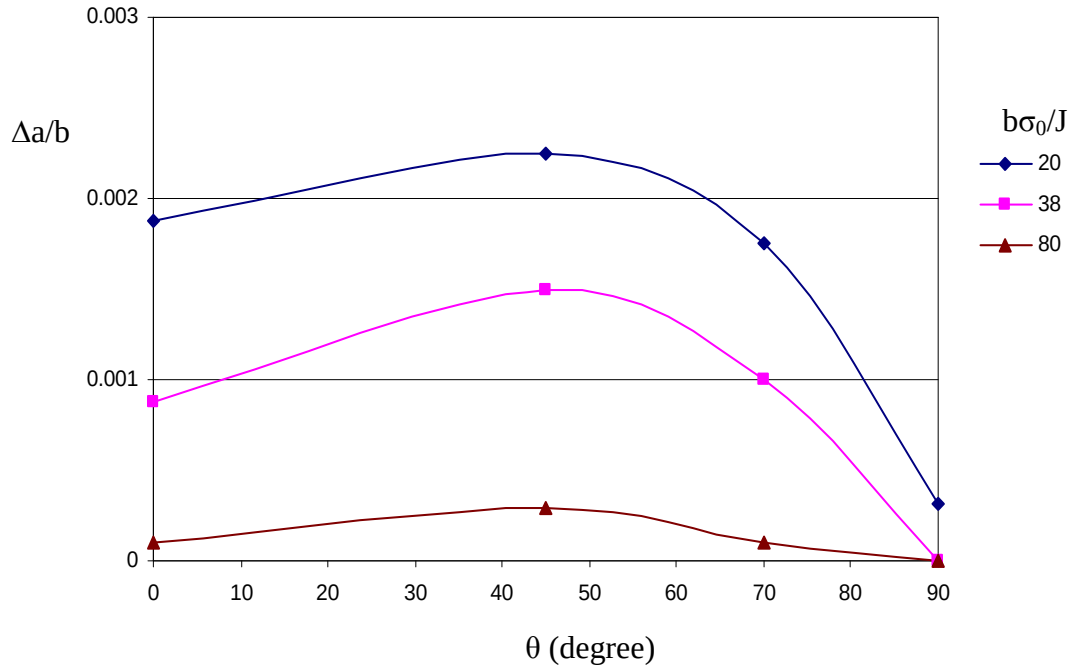

Figure 13.16: Crack growth as a function of the parametric angle θ for step-2 (a/w=0.5) in a shallow semi-elliptical surface crack (a/w=0.2, a/c=0.33) under tension.

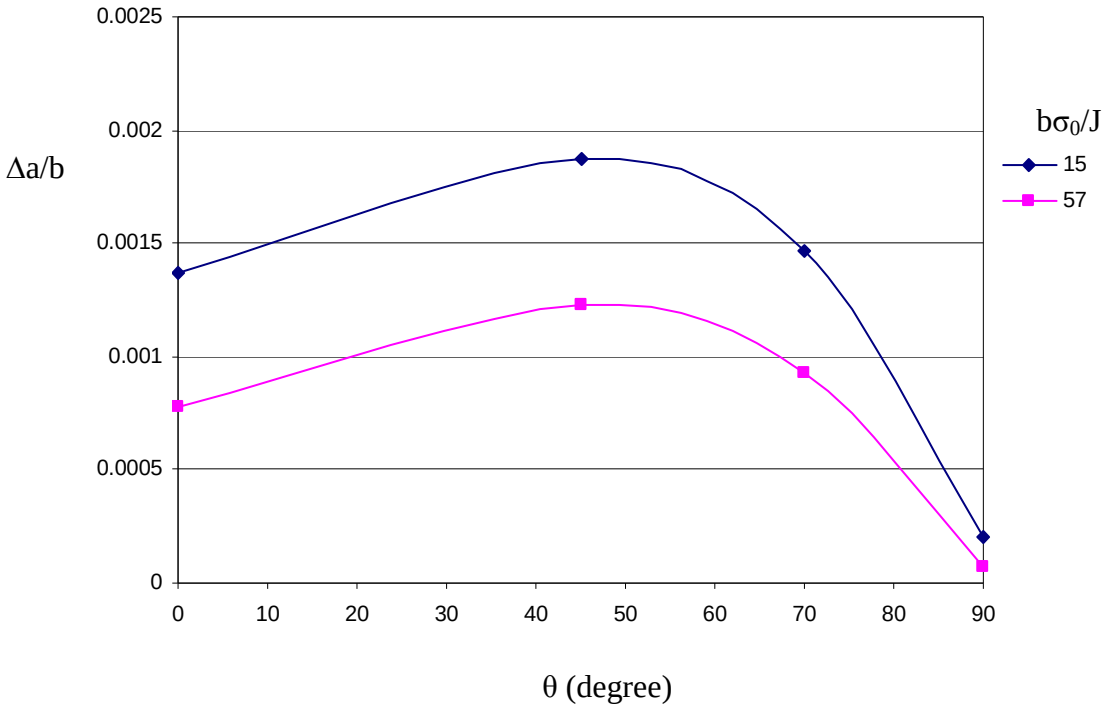

Figure 13.17: Crack growth as a function of the parametric angle θ for step-3 (a/w=0.6) in a shallow semi-elliptical surface crack (a/w=0.2, a/c=0.33) under tension.

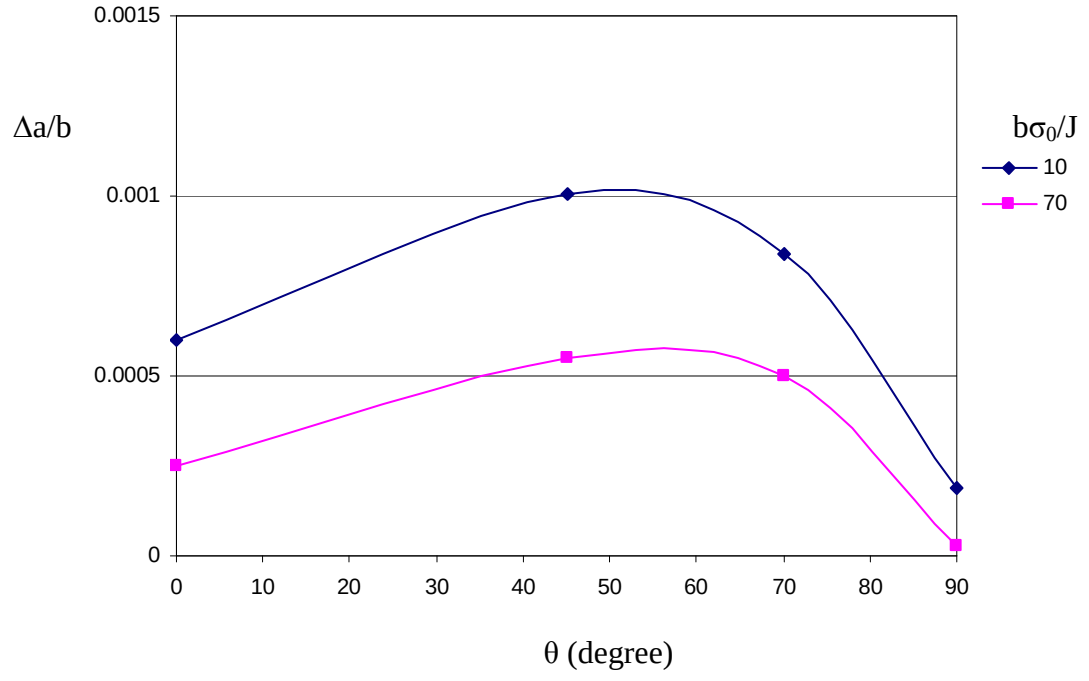

Figure 13.18: Crack growth as a function of the parametric angle θ for the step-4 (a/w=0.7) a shallow semi-elliptical surface crack (a/w=0.2, a/c=0.33) under tension.

Figure 13.19: The crack shape development in a shallow semi-elliptical surface crack (a/w=0.2, a/c=0.3) in tension.

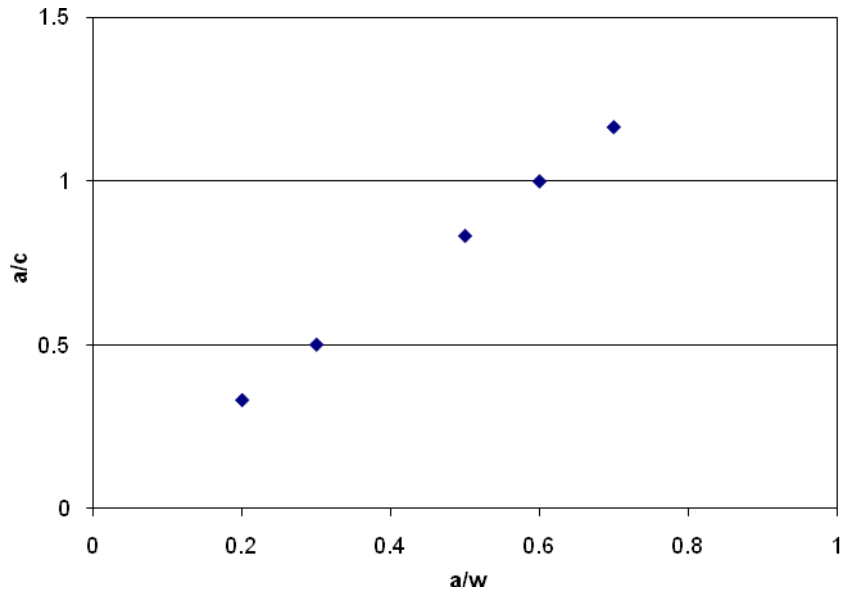

Figure 13.20: Development of the crack shape for a shallow semi-elliptical crack (a/w=0.2, a/c=0.33) under tension.

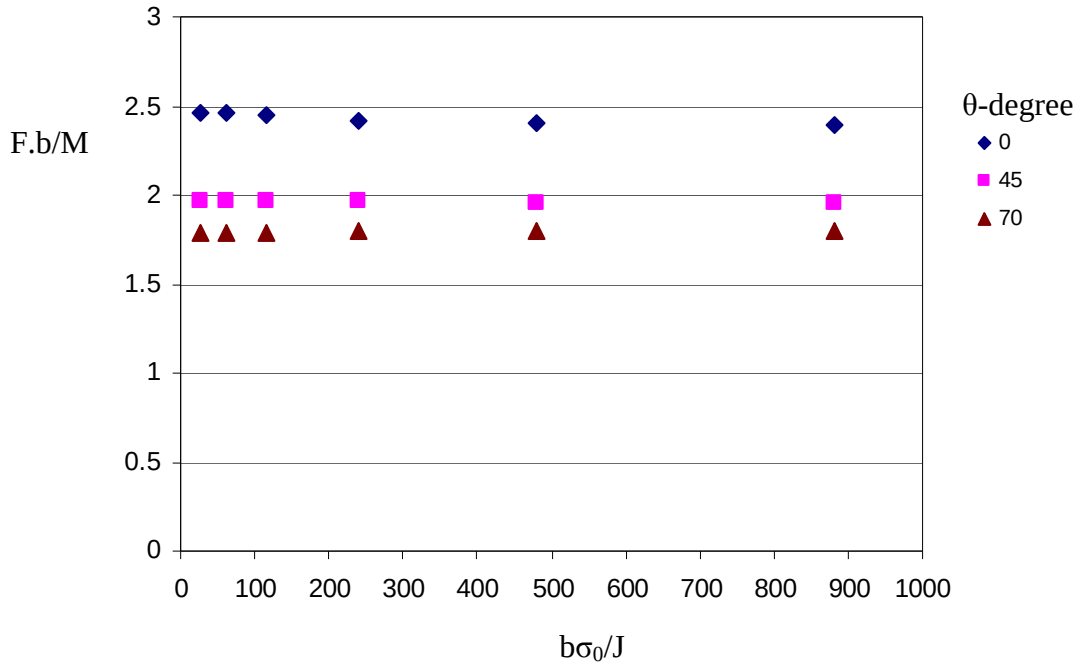

Figure 13.21: Force-moment ratio on the uncracked ligament ahead of the crack in a shallow semi-elliptical surface crack (a/w=0.2, a/c=0.33) in tension.

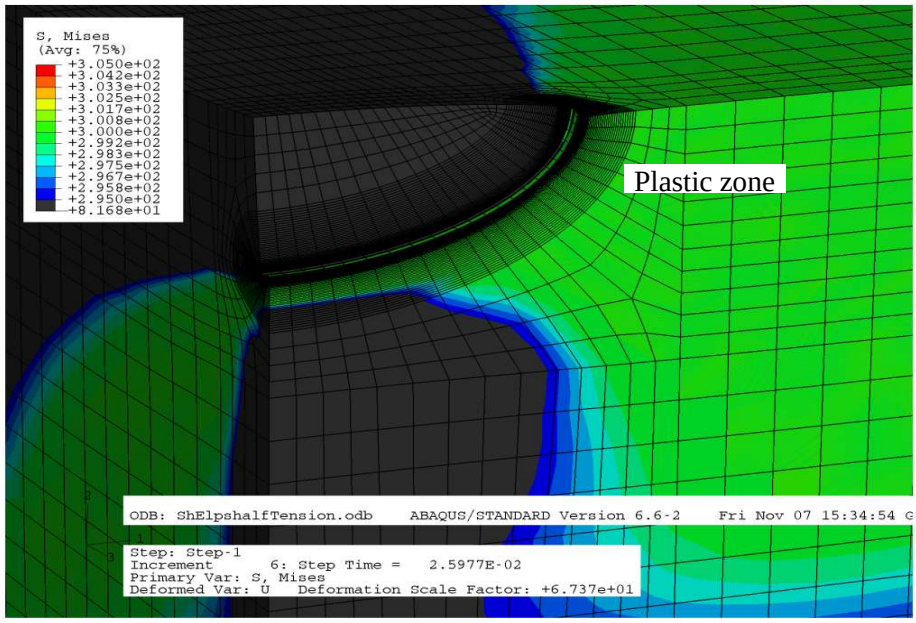

Figure 13.22: Development of the plastic zone around the crack front in a shallow semi-elliptical surface crack (a/w=0.2, a/c=0.5) in tension.

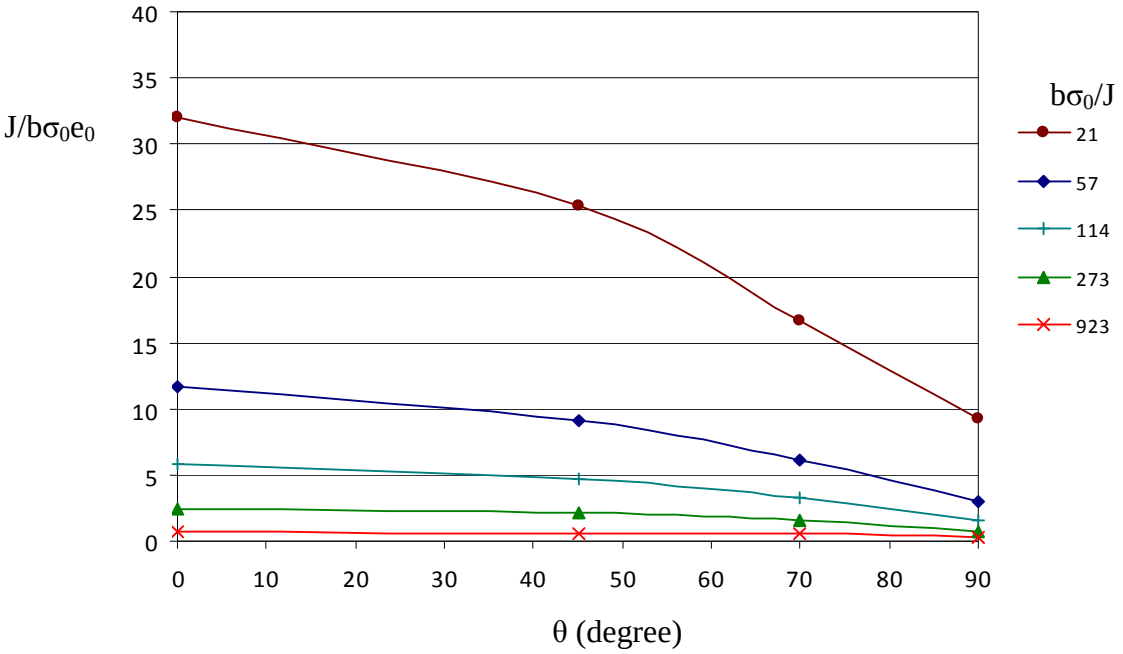

Figure 13.23: J-integral along the crack front for a shallow semi-elliptical surface crack in tension, (a/c=0.5, a/w=0.2).

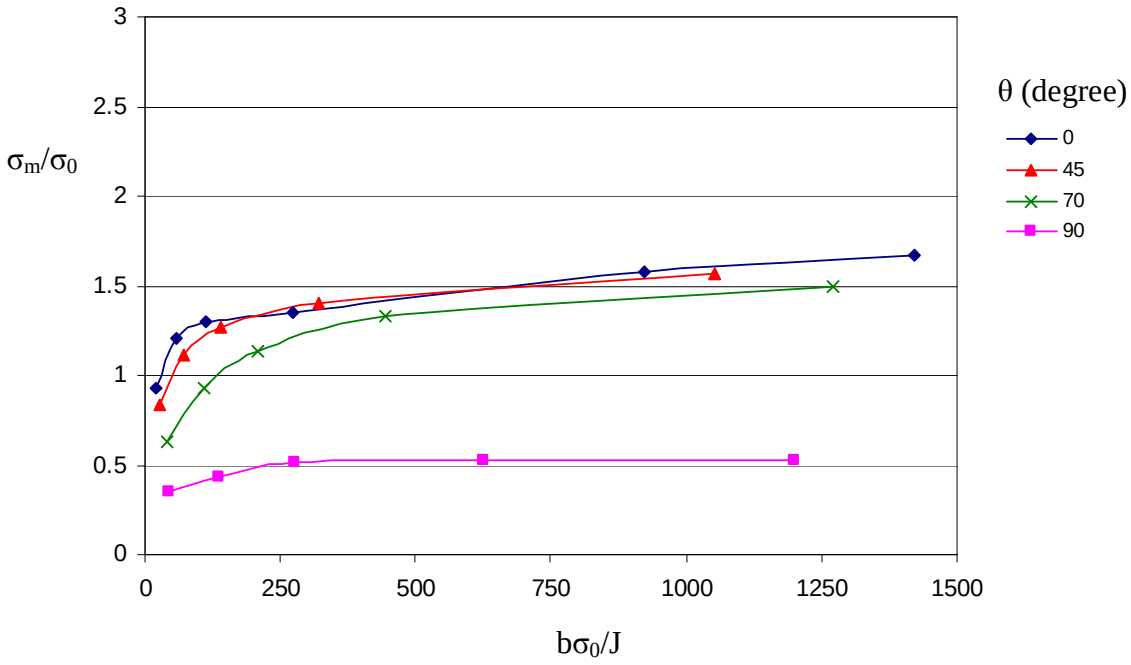

Figure 13.24: The mean stress at a distance rσ0/J =2 as a function of deformation level around the crack front for a shallow semi-elliptical surface crack in tension (a/c=0.5, a/w=0.2).

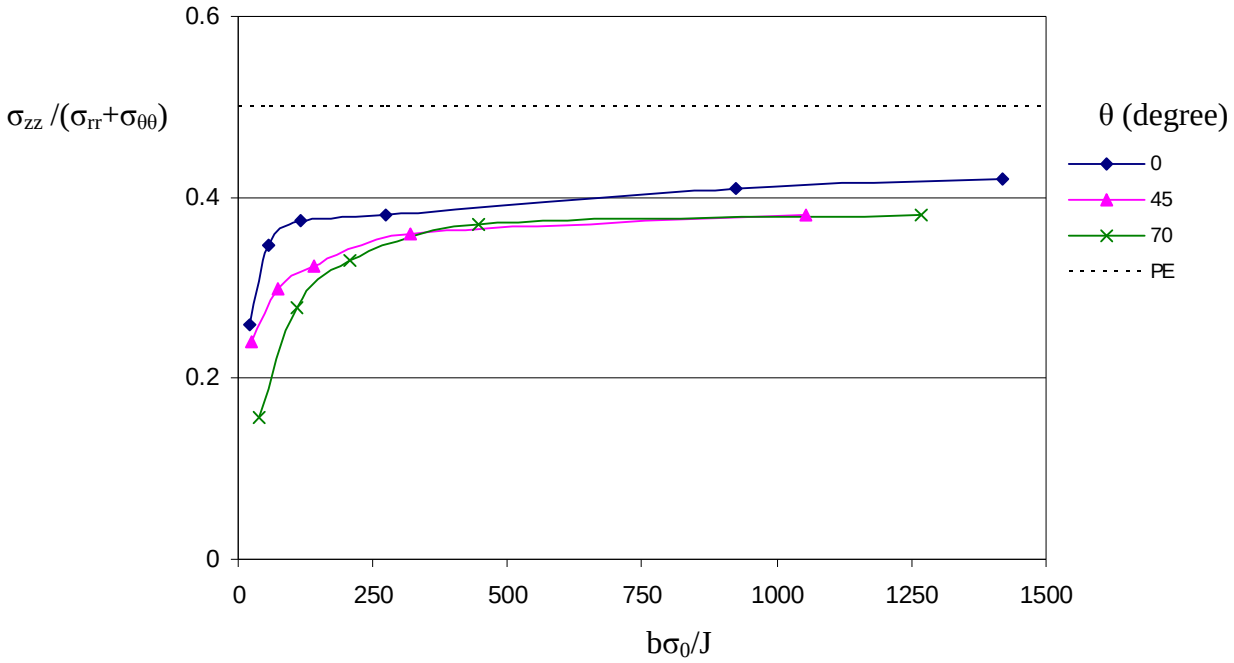

Figure 13.25: Proximity to plane strain around the crack front for a shallow semi-elliptical crack in tension. (a/c=0.5, a/w=0.2).

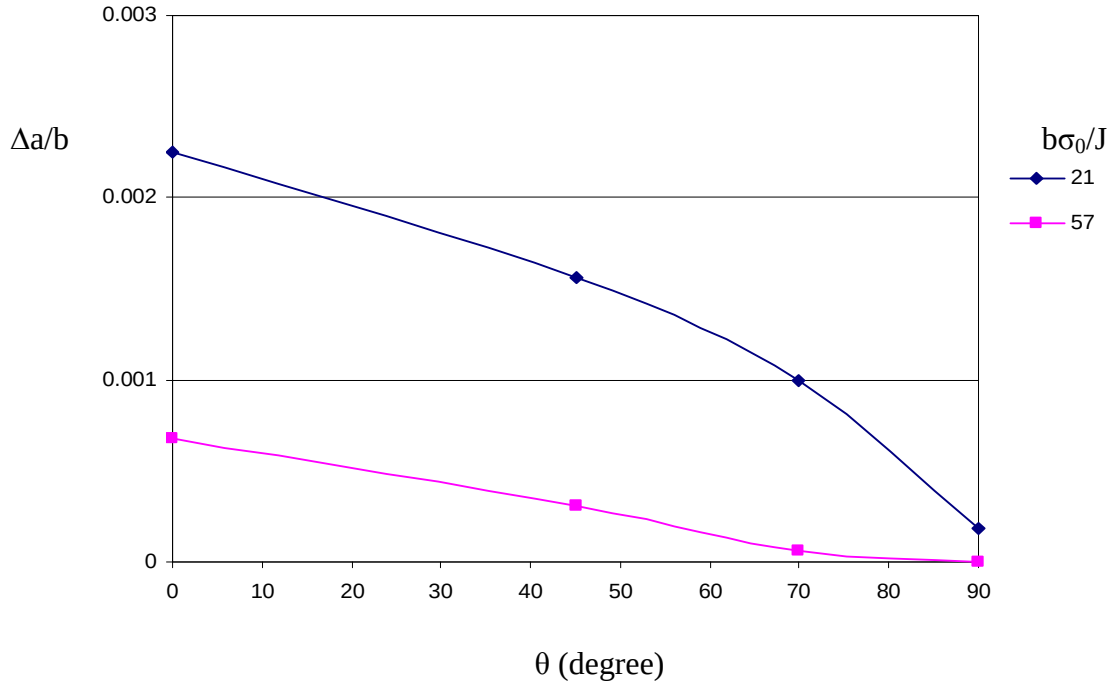

Figure 13.26: Crack growth around the crack front as a function of the parametric angle (θ) for a shallow semi-elliptical surface crack in tension (a/c=0.5, a/w=0.2).

14. Semi-elliptical surface cracks under biaxial loading

14.1 Introduction

Surface cracks in pressure vessels under internal pressure experience biaxial stress states. Under this condition (biaxiality) the crack may experience and behave in a different manner to bending or uniaxial loading. It is therefore important to investigate the effect of stress biaxiality on the elastic-plastic J-integral, mean stress and the development of ductile tearing. In this chapter deep and shallow semi-elliptical surface cracks are examined. The same FE models and material properties used for uniaxial loading were used under biaxial loading. The biaxial loading ratio was defined as $\beta=(\sigma_y/\sigma_x)_{applied}=0.5$, as shown in Figure (14.1a), and was calculated from the reaction forces in x and y directions. The displacement boundary conditions were imposed on the appropriate surfaces as shown in Figure (14.1b).

14.2 A deep semi-circular surface crack (a/w=0.5, a/c=1) under biaxial loading.

Figure (14.2) shows the mean stress along the crack front as a function of deformation. The maximum mean stress occurred at 70° and reached the plane strain HRR value ($2.39\sigma_0$). The behaviour of the mean stress under biaxial loading was different to uniaxial loading where a more uniform mean stress was observed around the crack front. The mean stress at all angles increased significantly under biaxial loading, as shown in Figures (14.3) to (14.6). However Wang (2009) showed different results for different biaxial ratio (1:1) and observed that the constraint level at the deepest point between uniaxial and biaxial loadings is the same.

Figure (14.7) shows that the proximity to plane strain increases beyond the plane strain value of (0.5) at the deepest point. The overall trend is comparable with the uniaxial loading where the value of plane strain was below 0.4 around the crack front as shown in Figure (12.9).

Figure (14.8) shows the non-uniform distribution of the J-integral along the crack front in which the maximum value occurs at 70°. This is should be compared to uniaxial loading where the J-integral distribution was more uniform along the crack front. The maximum crack growth under biaxial loading occurred at 70° where the J-integral and mean stress were maximum as shown in Figure (14.9). This can be compared to uniaxial loading where the maximum crack extension was at 45° . Figure (14.10) shows the crack develops at higher rate at 70° compared to uniaxial loading.

Figure (14.11) shows the force and moment distributions at the deepest point (θ=0) are largely independent of the deformation level. Similar results were observed for 45°-70° as shown in Figures (14.12) and (14.13), however the opening force and opening moment increased significantly at 70°. Figure (14.14) shows a similar trend to that observed in uniaxial tension in Figure (14.15) where the largest ratio was observed at the deepest point (θ=0) and the smallest ratio at 70°. Significantly, the force and moment distribution was independent of deformation.

14.3 A deep semi-elliptical surface crack (a/w=0.5, a/c=0.33) under biaxial loading.

The mean stress around the crack front for a deep semi-elliptical surface crack is shown in Figure (14.16). The maximum mean stress was located at the deepest point which is different to uniaxial loading when the maximum mean stress was located at 45° to 70°. Higher crack tip constraint levels occurred along the crack front under biaxial loading than in uniaxial loading as shown in Figures (14.17) to (14.20). The maximum J-integral occurred at the deepest point and decreased gradually towards the free surface as shown in Figure (14.21). Under uniaxial tension a uniform J-integral distribution was observed between the deepest point and 45°. The J-integral then decreased gradually at 70°, and reduced significantly at the free surface. Figure (14.22) shows that the out-of-plane parameter is largest at the deepest point and 45°. This is comparable to uniaxial loading when the proximity to plane strain was below 0.5. It was predicted that under biaxial stress states, significant crack growth would occur at the deepest point as shown in Figure (14.23), while in uniaxial tension more uniform crack growth was observed. The

crack retained a simple semi-elliptical shape with a changing aspect ratio a/c since the crack grew at the deepest point but not at the free surface, as shown in Figure (14.24).

14.4 A shallow semi-elliptical surface crack (a/w=0.2, a/c=0.33) under biaxial loading

Figure (14.25) shows higher mean stress along the crack front under biaxial loading than under uniaxial loading shown in Figure (13.12). Figure (14.26) shows that the maximum J-integral occurred at the deepest point and decreased towards the surface. Crack growth under biaxial loading was similar to uniaxial loading as the maximum crack growth occurred at the deepest point as shown in Figure (14.27).

14.5 Conclusion

It may be concluded that under biaxial loading crack extension was observed in the angular range 45°-70° compared to a more uniform crack growth in uniaxial loading for deep semi-circular surface cracks. For deep semi-elliptical surface cracks most crack extension occurred at the deepest point and a semi-elliptical shape was maintained with an increasing aspect ratio (a/c) compared to the initial crack. Shallow semi-elliptical cracks also showed similar behaviour in both uniaxial and biaxial loading.

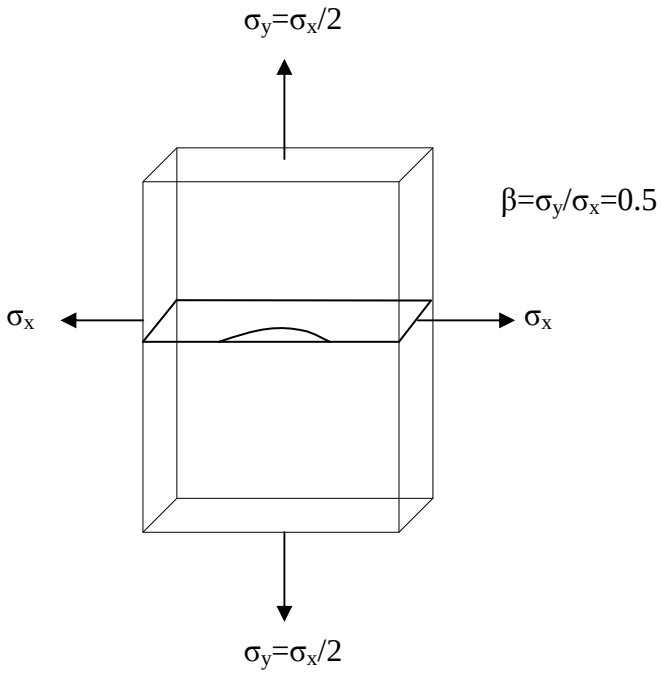

Figure 14.1a: A plate containing a surface crack under remote biaxial load.

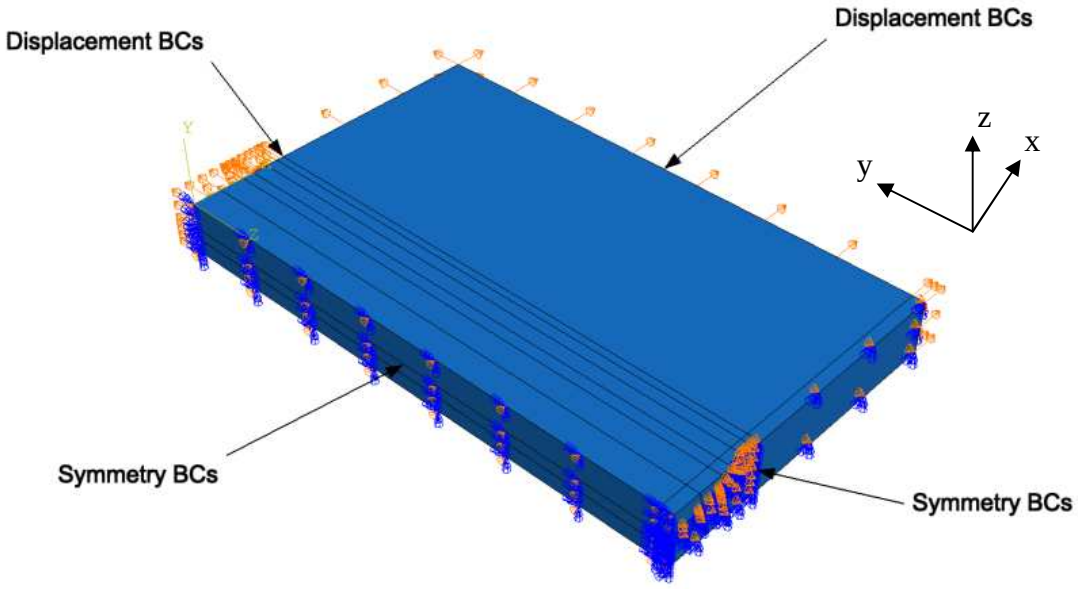

Figure 14.1b: The boundary conditions of a surface crack under biaxial loading.

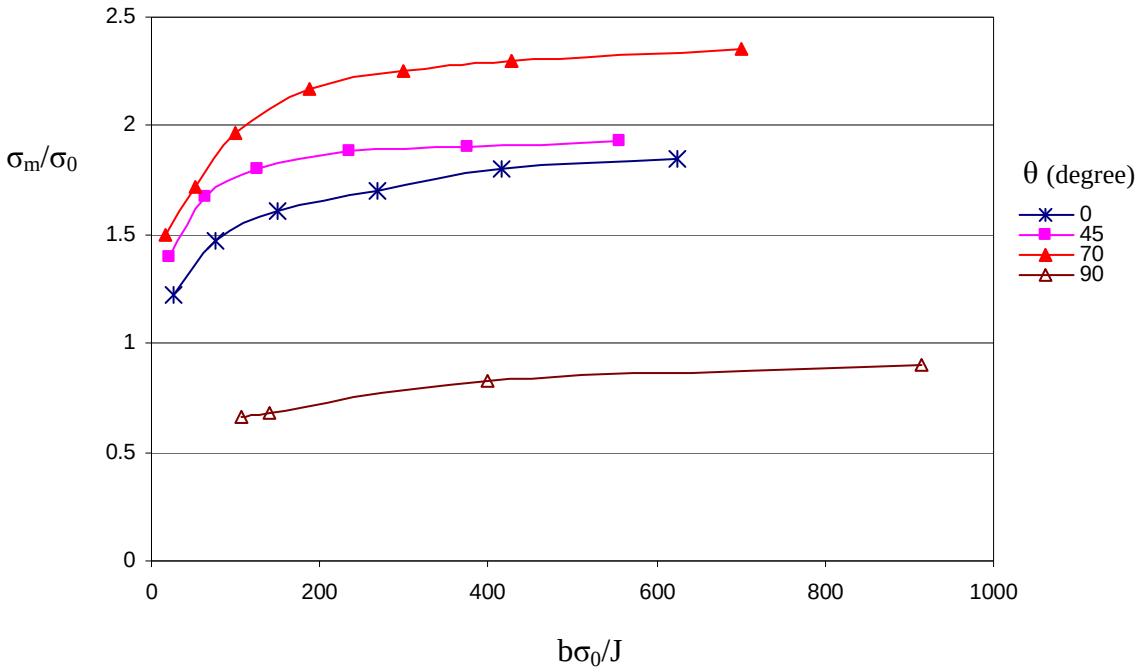

Figure 14.2: The mean stress at a distance $r\sigma_0/J=2$ as a function of deformation level along the crack for a deep semi-circular surface crack in biaxial load (a/c=1, a/w=0.5).

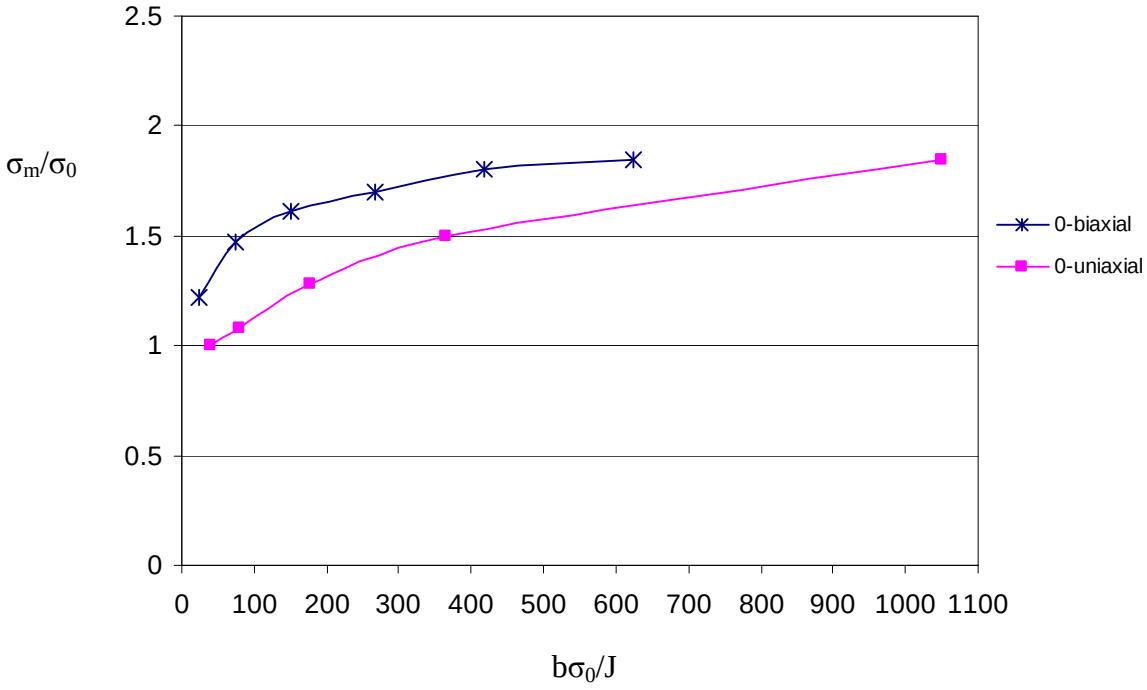

Figure 14.3: The mean stress at a distance $r\sigma_0/J=2$ as a function of deformation level at the deepest point for a deep semi-circular surface crack in uniaxial and biaxial loading (a/c=1, a/w=0.5).

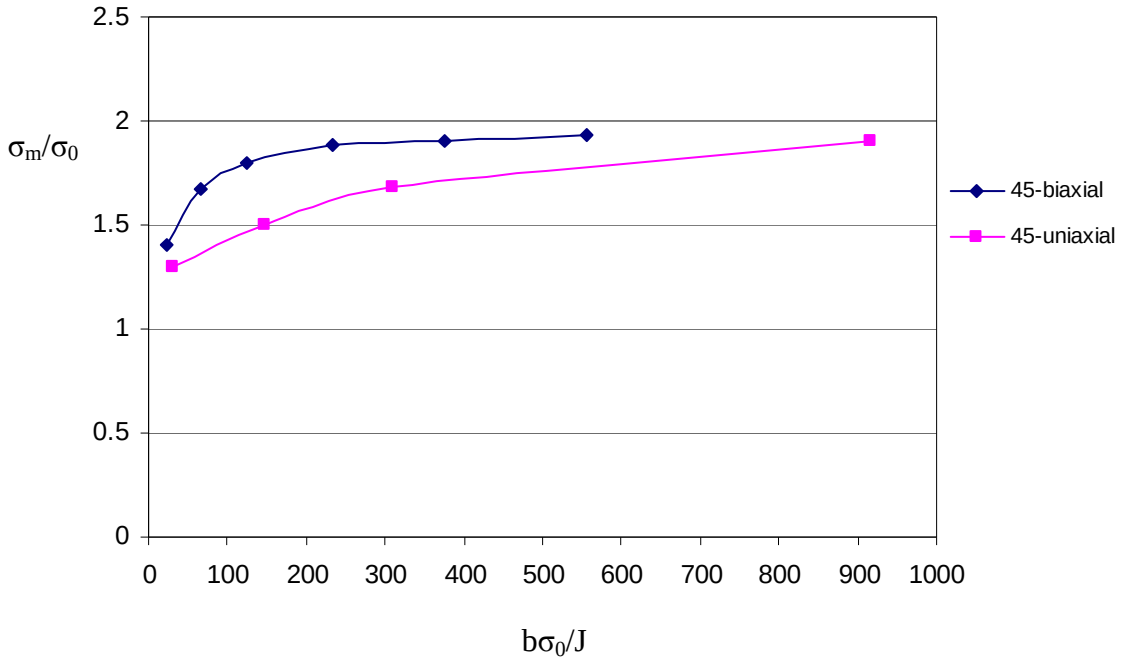

Figure 14.4: The mean stress at a distance $r\sigma_0/J=2$ as a function of deformation level at 45˚ for a deep semi-circular surface crack in uniaxial and biaxial loading (a/c=1, a/w=0.5).

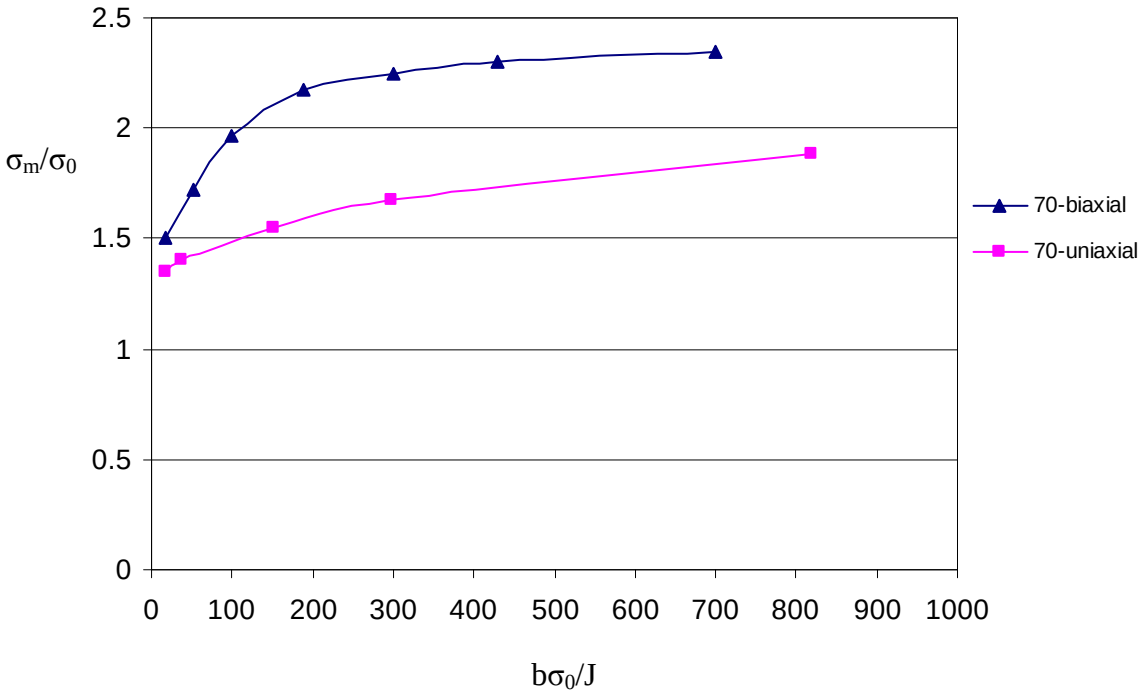

Figure 14.5: The mean stress at a distance $r\sigma_0/J=2$ as a function of deformation level at 70˚ for a deep semi-circular surface crack in uniaxial and biaxial loading (a/c=1, a/w=0.5).

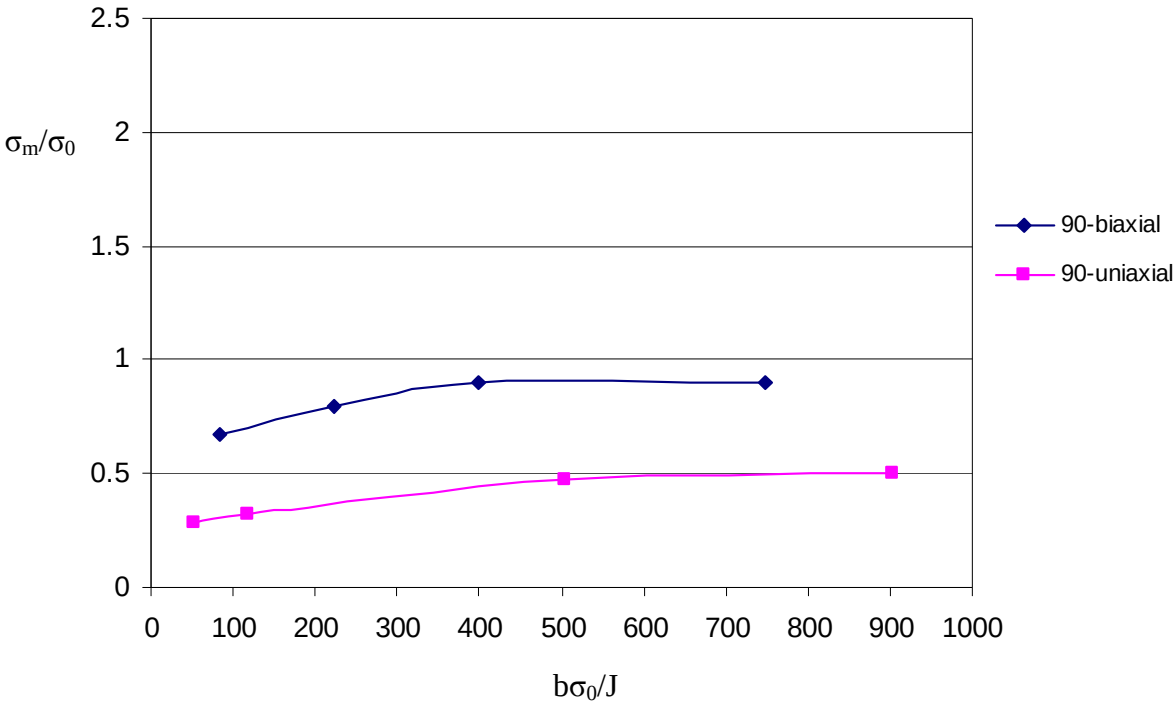

Figure 14.6: The mean stress at a distance $r\sigma_0/J=2$ as a function of deformation level at the free surface for a deep semi-circular surface crack in uniaxial and biaxial loading (a/c=1, a/w=0.5).

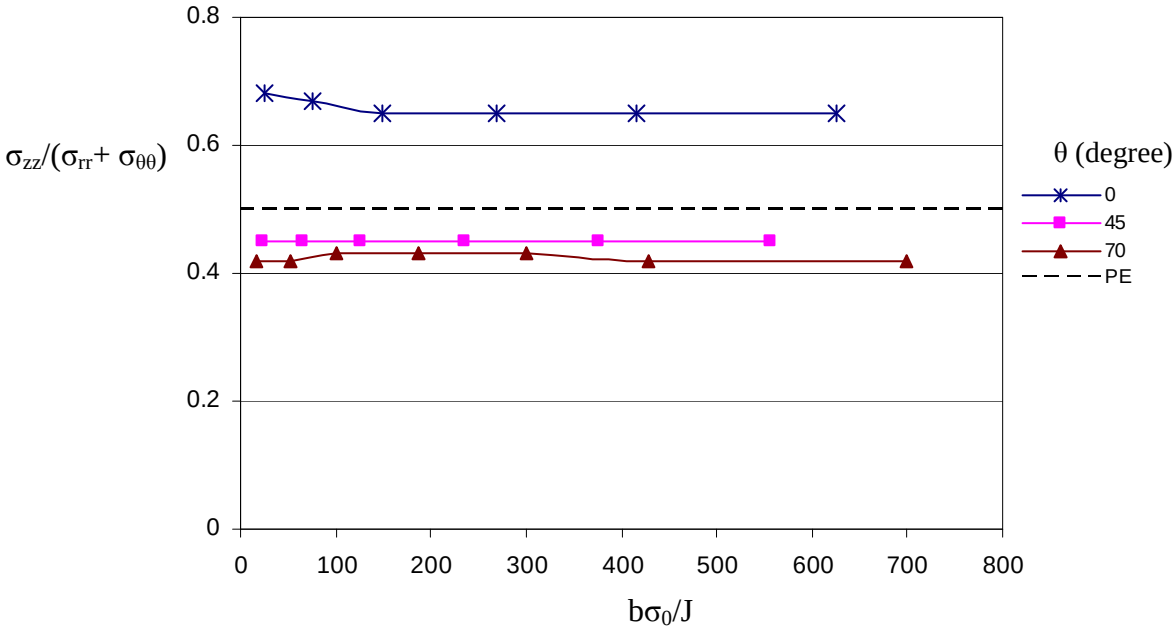

Figure 14.7: Proximity to plane strain around the crack front for a deep semi-circular surface crack a/c=1, a/w=0.5 under biaxial load.

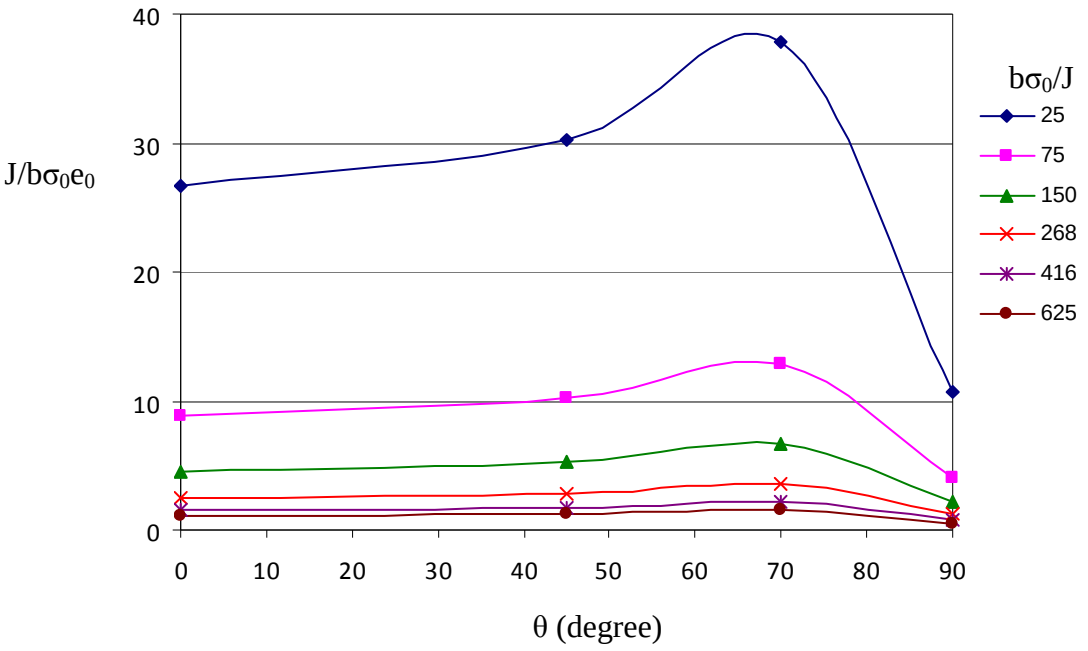

Figure 14.8: J-integral along the crack front for a deep semi- circular surface crack in biaxial load, a/c=1, a/w=0.5.

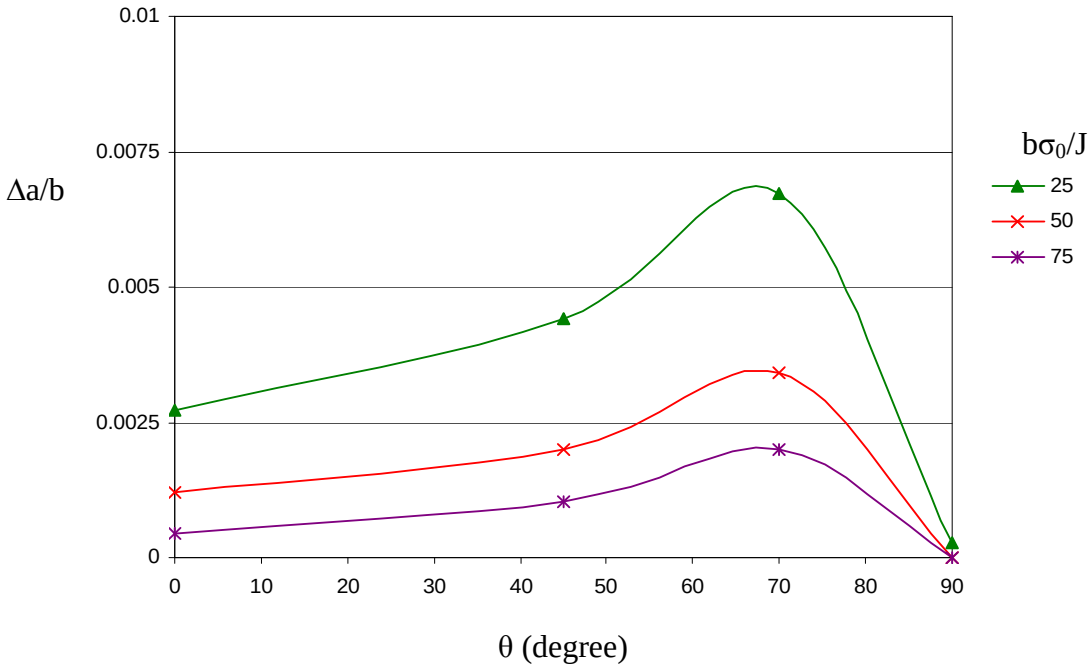

Figure 14.9: Crack growth around the crack front as a function of the parametric angle θ in a semi-circular surface crack a/c=1, a/w=0.5 under biaxial load.

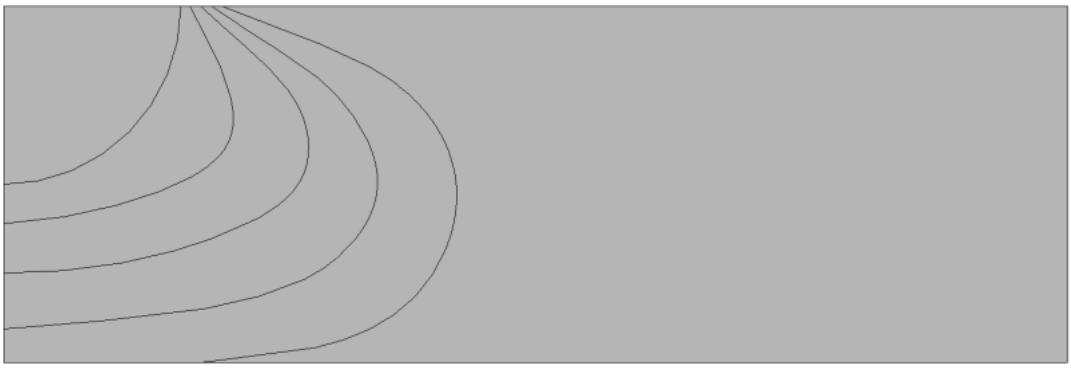

Figure 14.10: The crack shape development for a deep semi-circular surface crack (a/w=0.5, a/c=1) under ductile tearing in biaxial load.

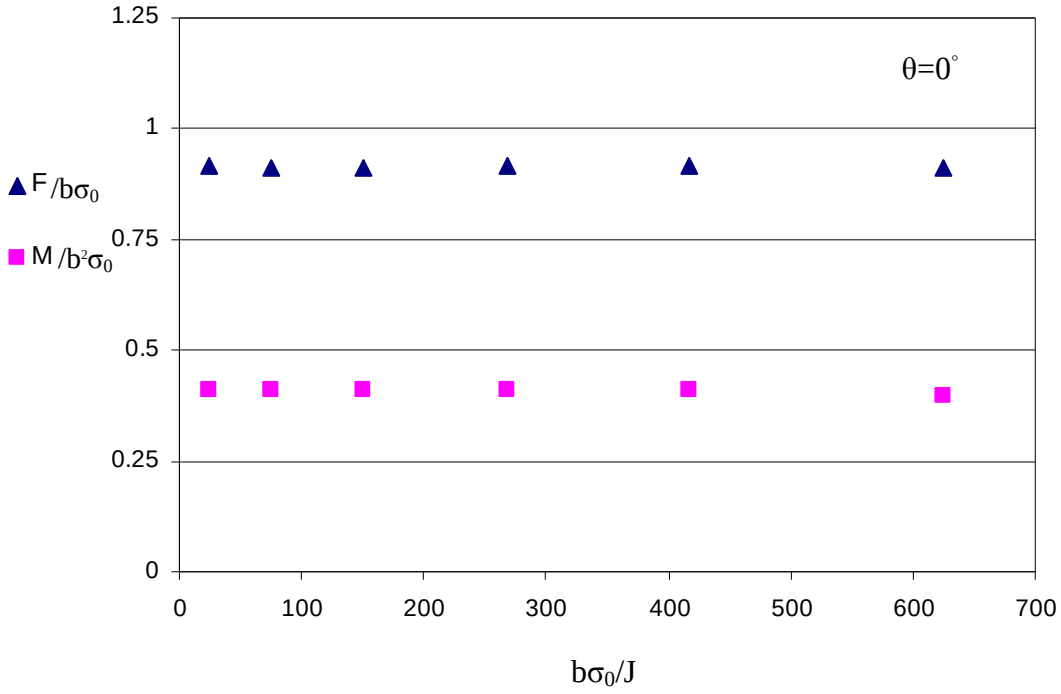

Figure 14.11: Force and moment redistribution along the uncracked ligament at the deepest point (path1) as a function of deformation in a deep semi-circular (a/w=0.5, a/c=1) surface crack under biaxial load.

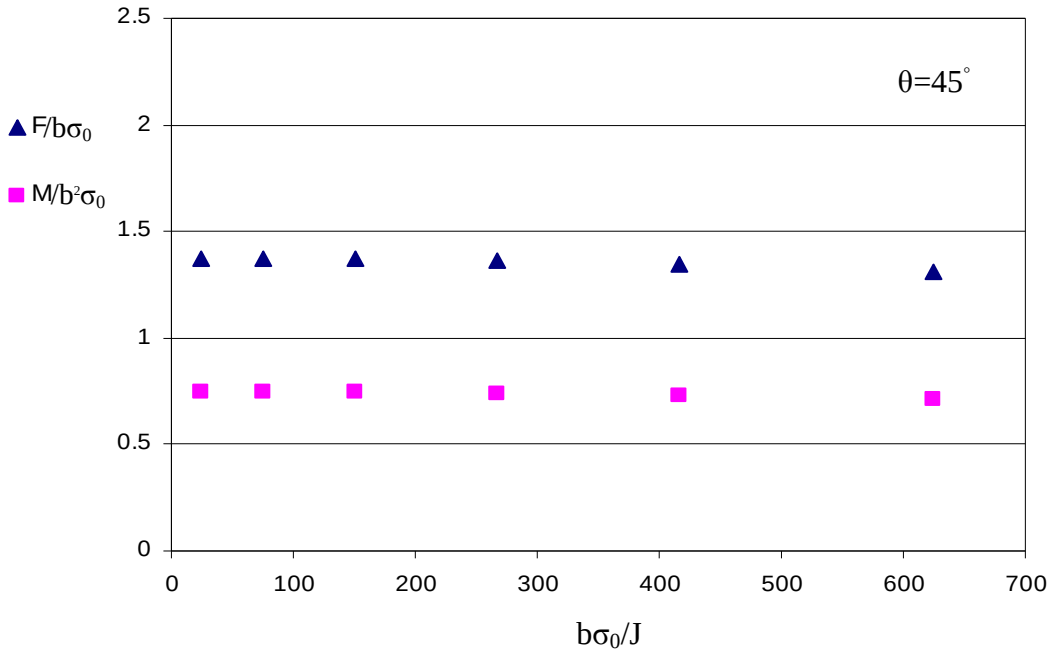

Figure 14.12: Force and moment redistribution along the uncracked ligament at 45° (path2) as a function of deformation in a deep semi-circular (a/w=0.5, a/c=1) surface crack under biaxial load.

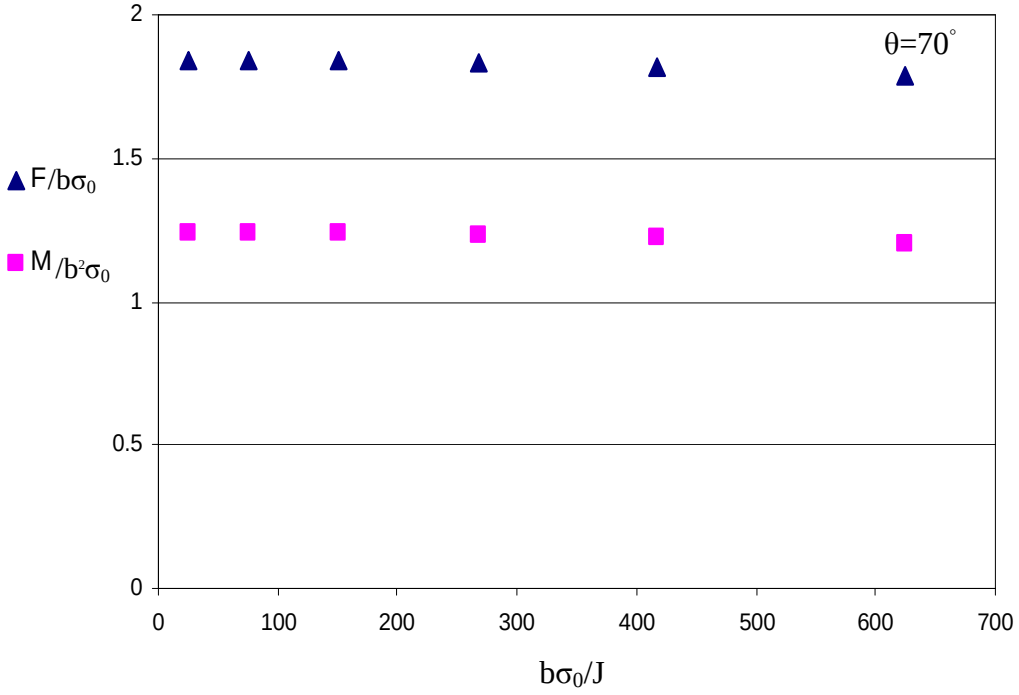

Figure 14.13: Force and moment redistribution along the uncracked ligament at 70° (path3) as a function of deformation in a deep semi-circular surface crack (a/w=0.5, a/c=1) under biaxial load.

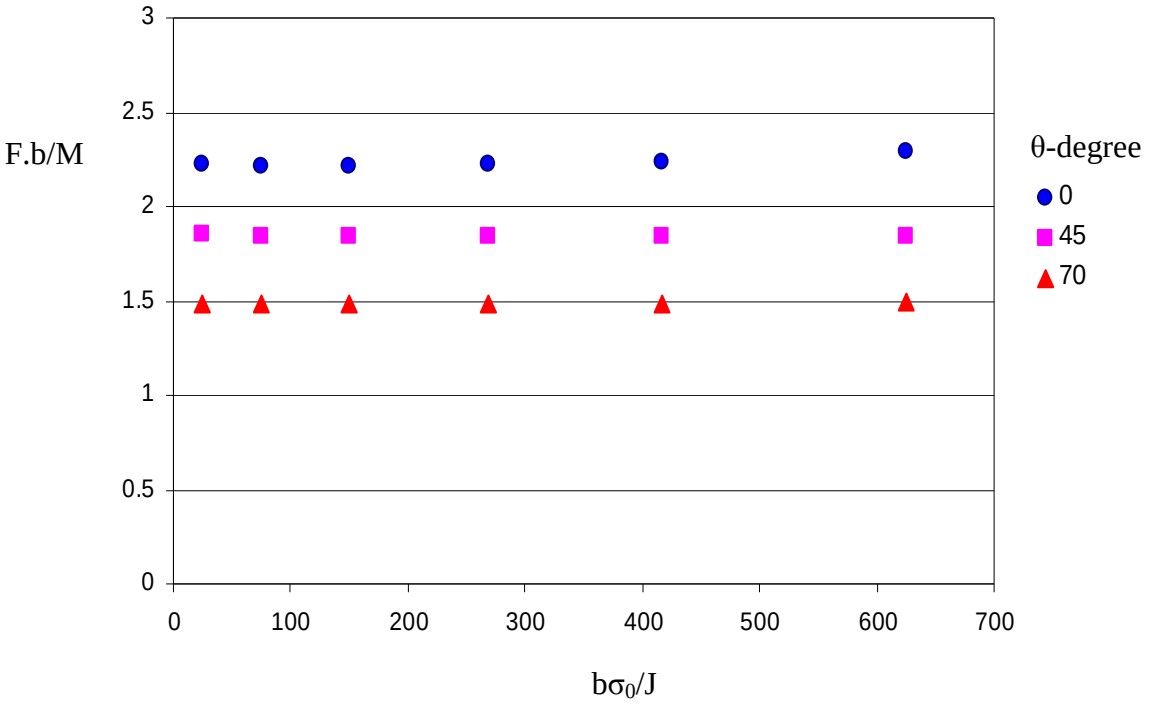

Figure 14.14: Force-moment ratio on the uncracked ligament ahead of the crack in a deep semi-circular surface crack (a/w=0.5, a/c=1) under biaxial load.

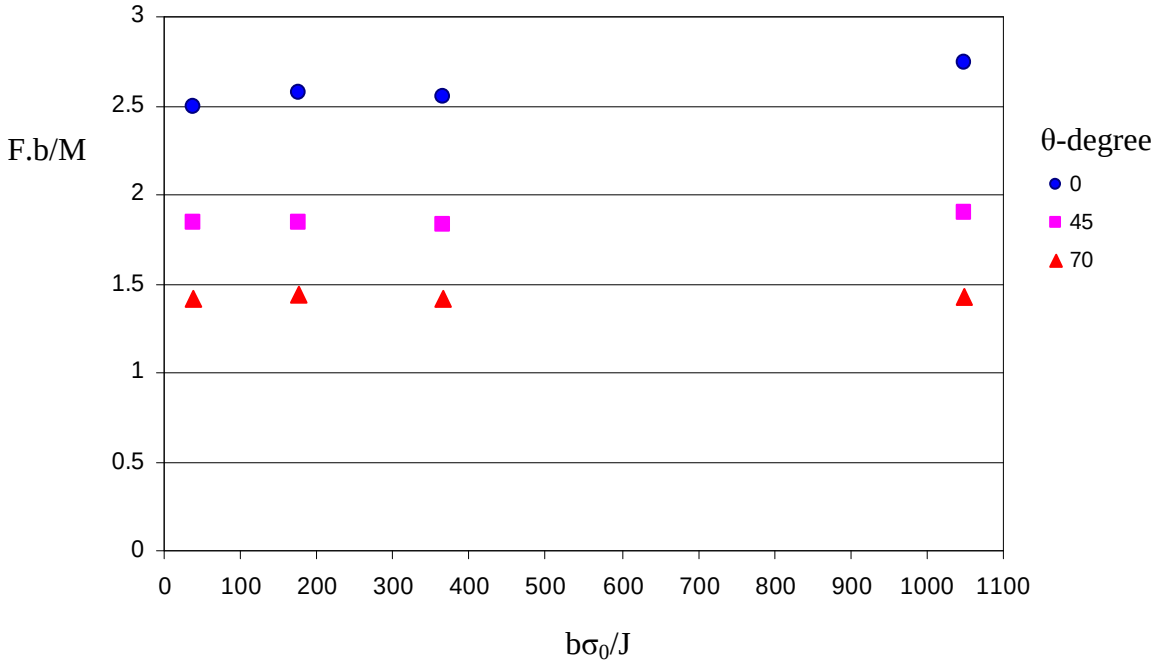

Figure 14.15: Force-moment ratio on the uncracked ligament ahead of the crack in a deep semi-circular surface crack (a/w=0.5, a/c=1) under uniaxial load.

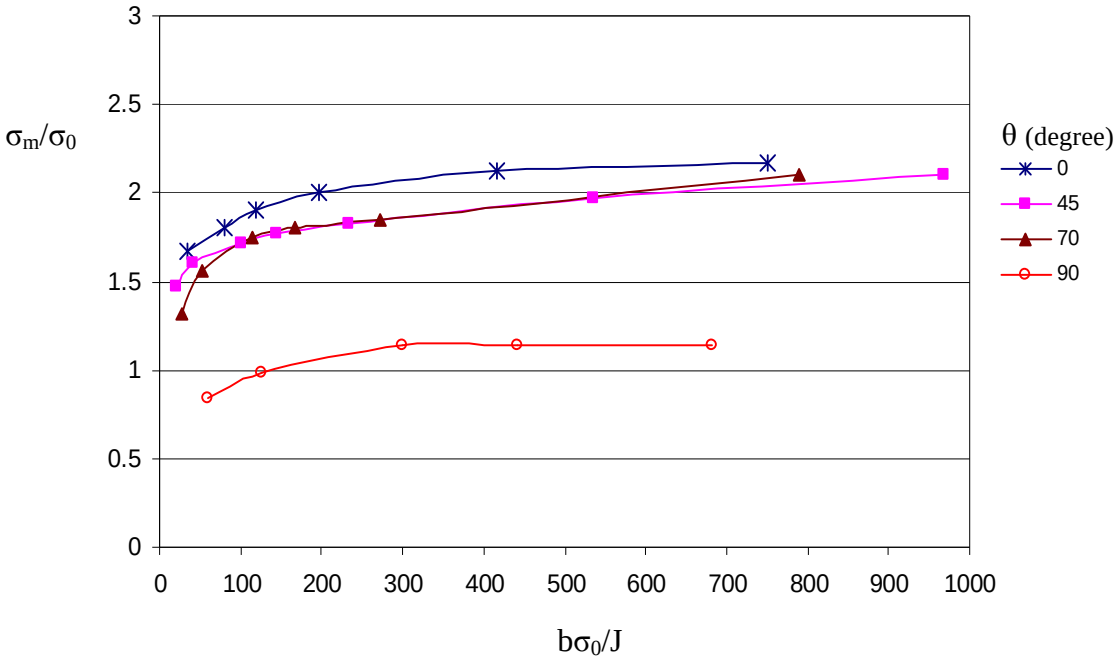

Figure 14.16: The mean stress at a distance $r\sigma_0/J=2$ as a function of deformation level along the crack for a deep semi-elliptical surface crack in biaxial load (a/c=0.33, a/w=0.5).

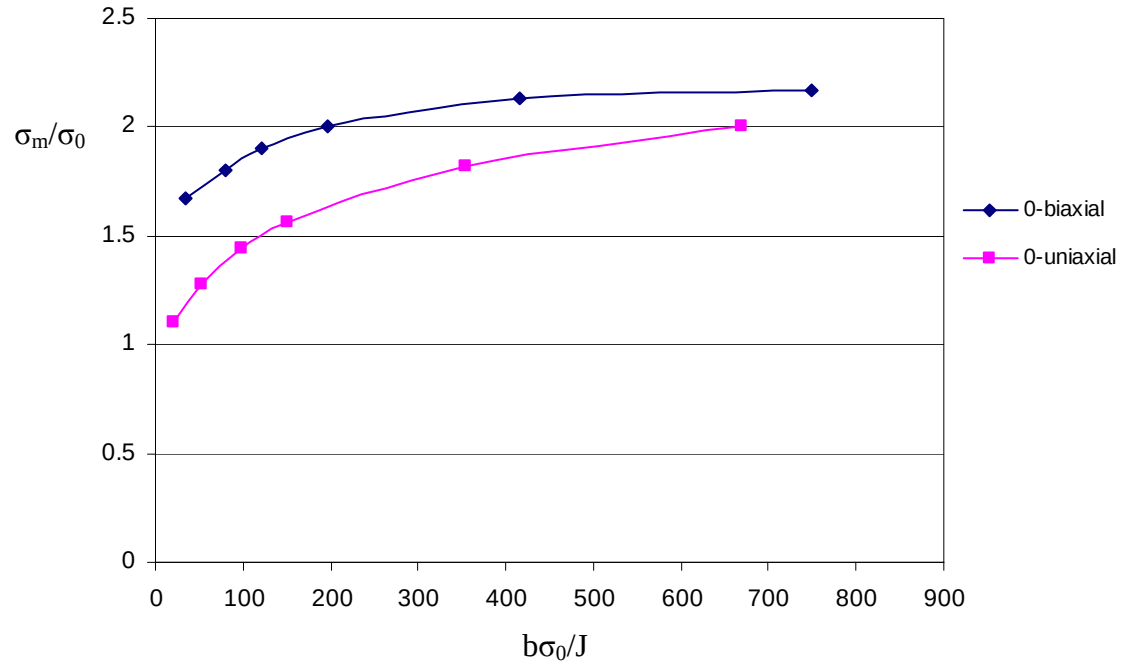

Figure 14.17: The mean stress at a distance $r\sigma_0/J=2$ as a function of deformation level at the deepest point for a deep semi-elliptical surface crack in uni-axial and biaxial loading (a/c=0.33, a/w=0.5).

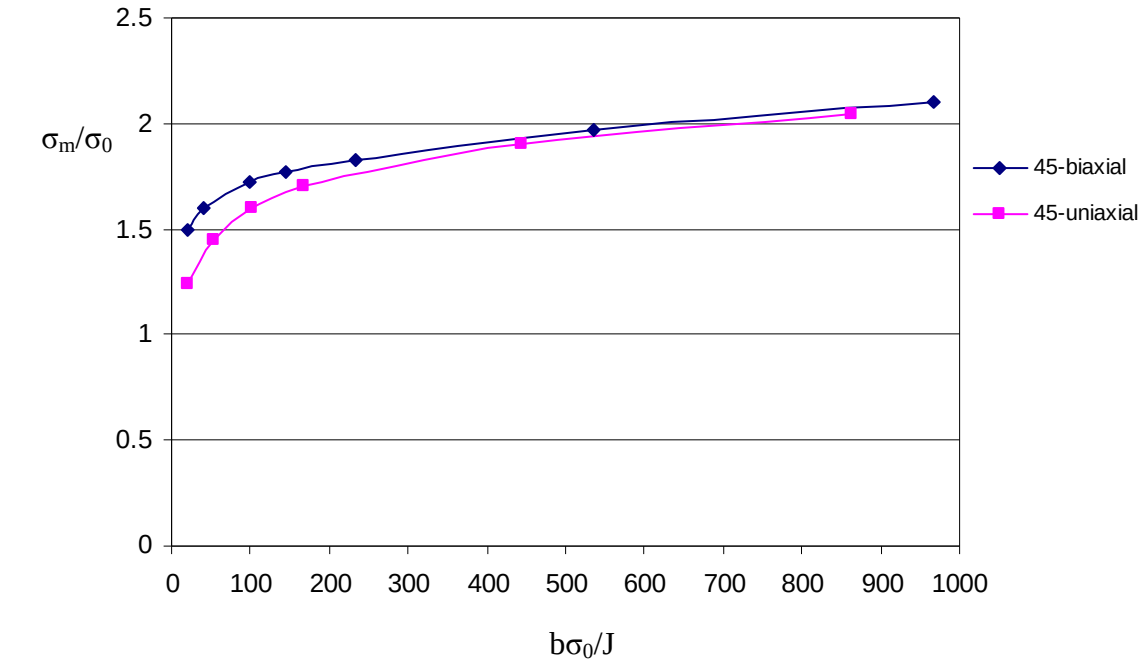

Figure 14.18: The mean stress at a distance $r\sigma_0/J=2$ as a function of deformation level at 45° for a deep semi-elliptical surface crack in uni-axial and biaxial loading (a/c=0.33, a/w=0.5).

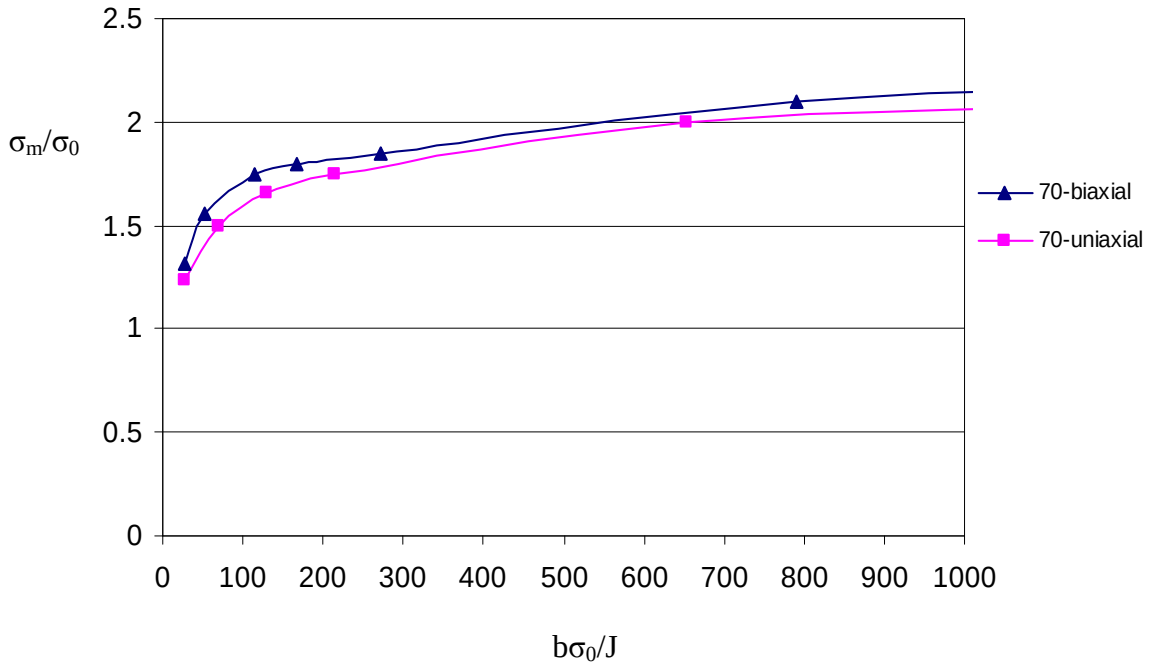

Figure 14.19: The mean stress at a distance $r\sigma_0/J=2$ as a function of deformation level at 70° for a deep semi-elliptical surface crack in uni-axial and biaxial loading (a/c=0.33, a/w=0.5).

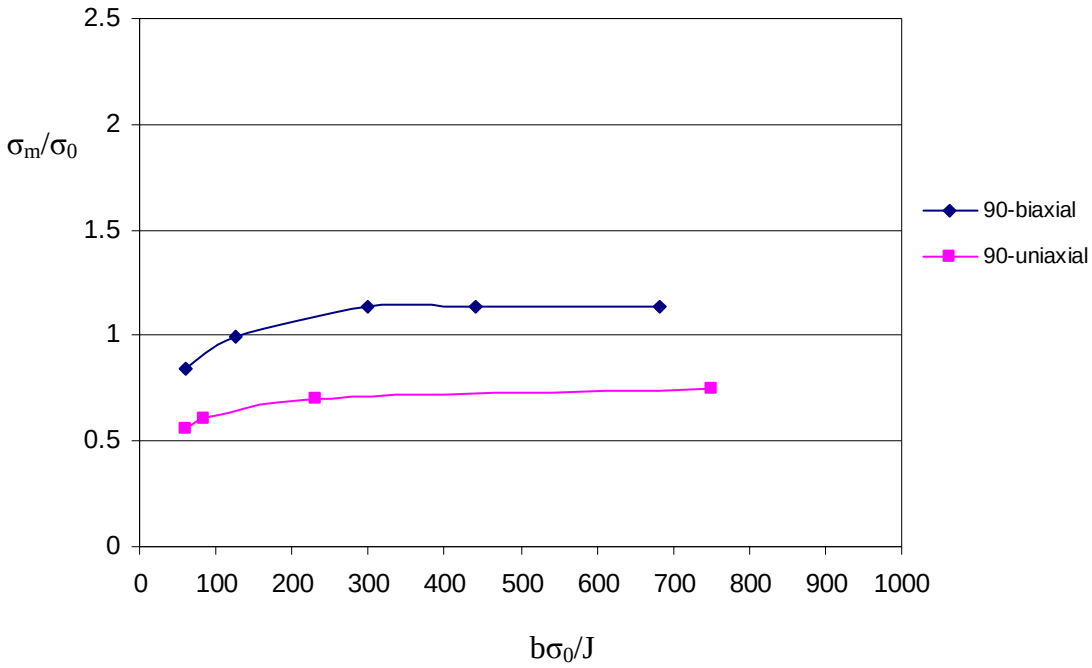

Figure 14.20: The mean stress at a distance $r\sigma_0/J=2$ as a function of deformation level at the free surface for a deep semi-elliptical surface crack in uni-axial and biaxial loading (a/c=0.33, a/w=0.5).

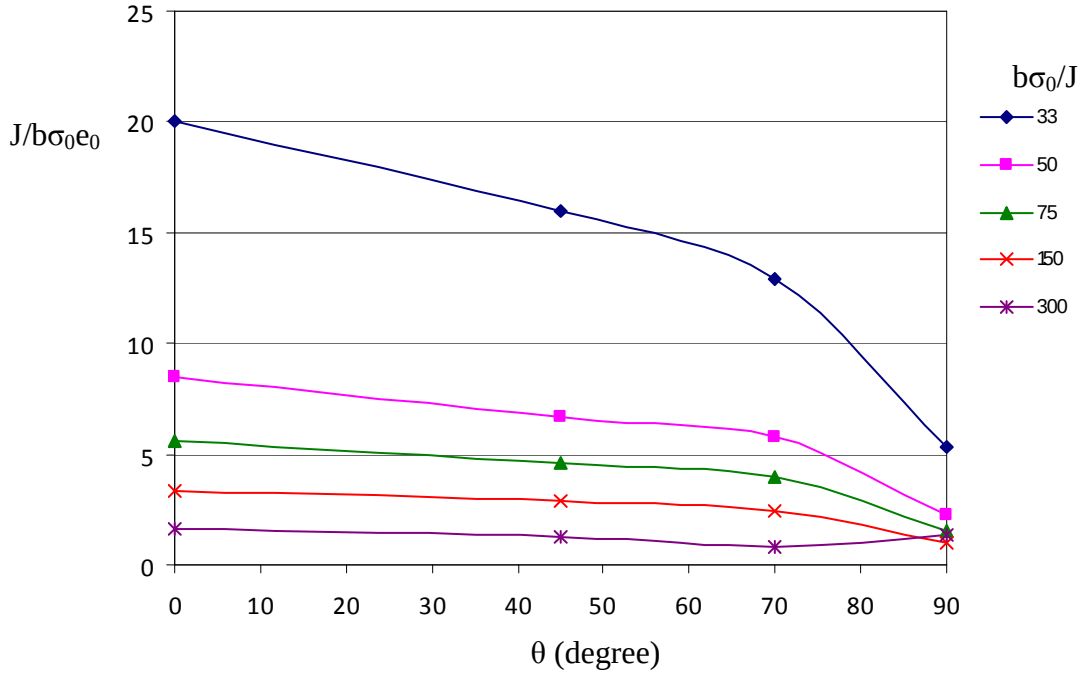

Figure 14.21: J-integral along the crack front for a deep semi-elliptical surface crack a/c=0.33, a/w=0.5 in biaxial load.

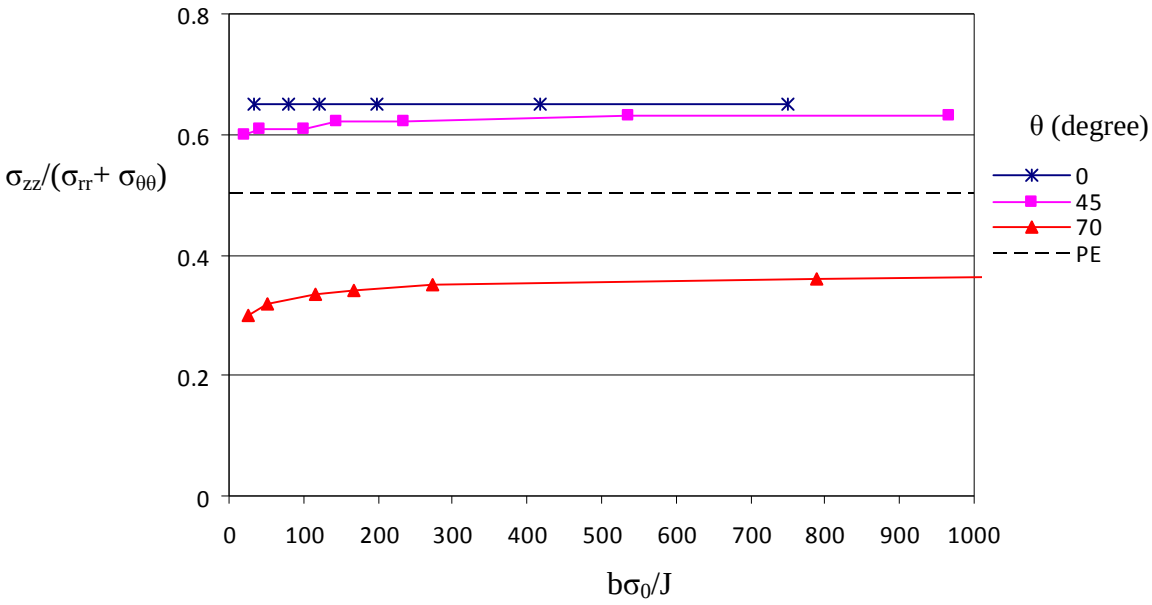

Figure 14.22: Proximity to plane strain around the crack front for a deep semi-elliptical surface crack a/c=0.33, a/w=0.5 under biaxial load.

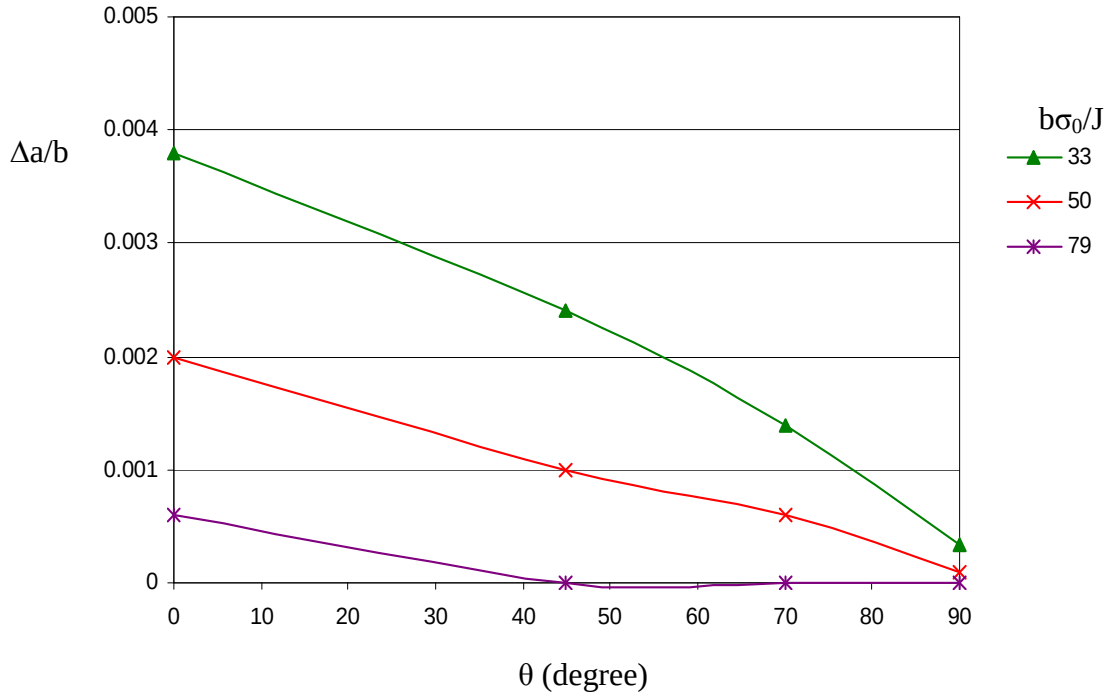

Figure 14.23: Crack growth around the crack front as a function of the parametric angle for a deep semi-elliptical surface crack a/c=0.33, a/w=0.5 under biaxial load.

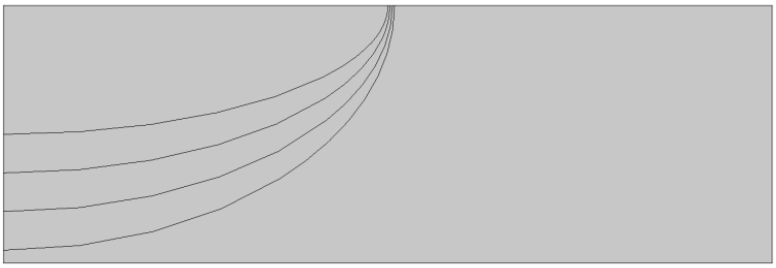

Figure 14.24: The crack shape development for a deep semi-elliptical surface crack a/c=0.33, a/w=0.5 under biaxial loading.

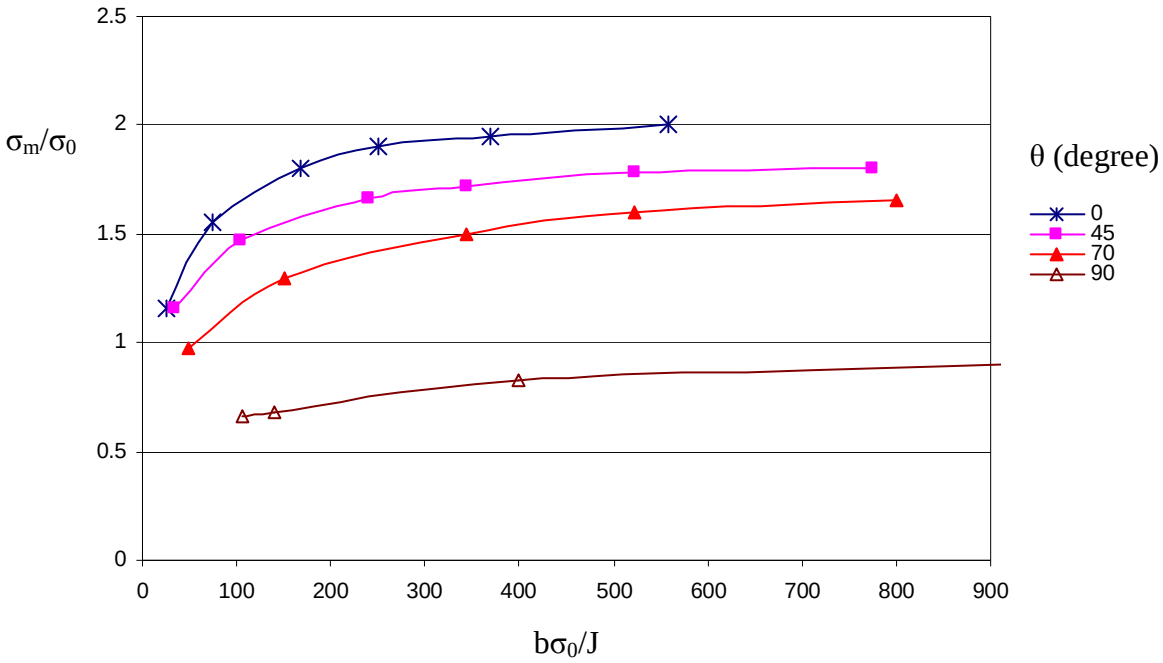

Figure 14.25: The mean stress as a function of deformation level for a shallow semi-elliptical surface crack under biaxial loading (a/c=0.33, a/w=0.2).

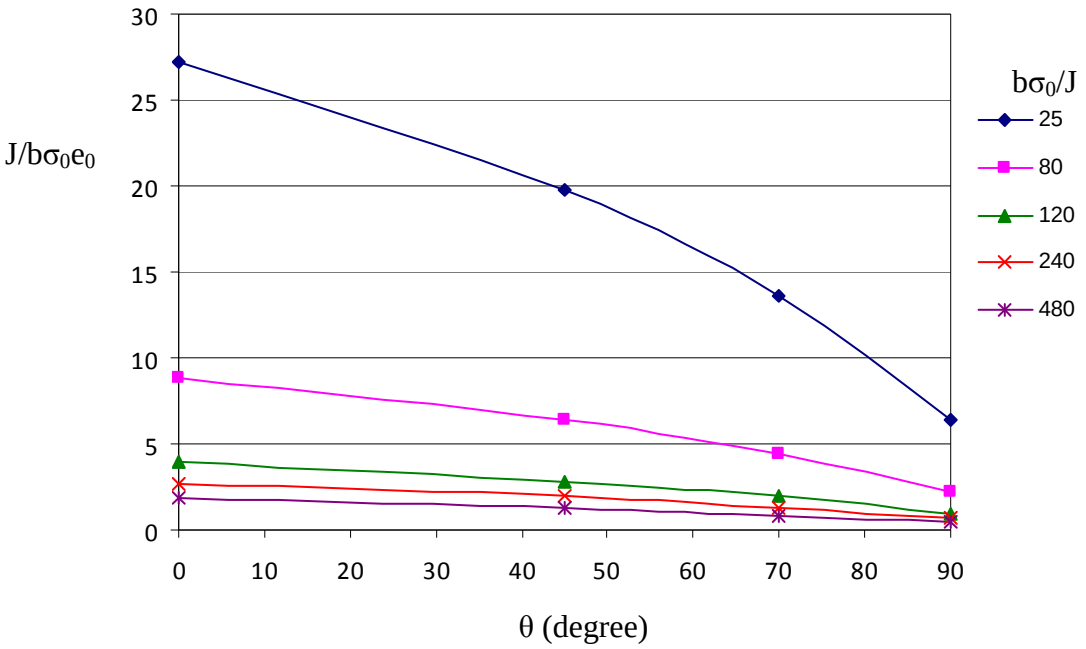

Figure 14.26: J-integral along the crack front for a shallow semi-elliptical surface crack under biaxial loading (a/w=0.2, a/c=0.33).

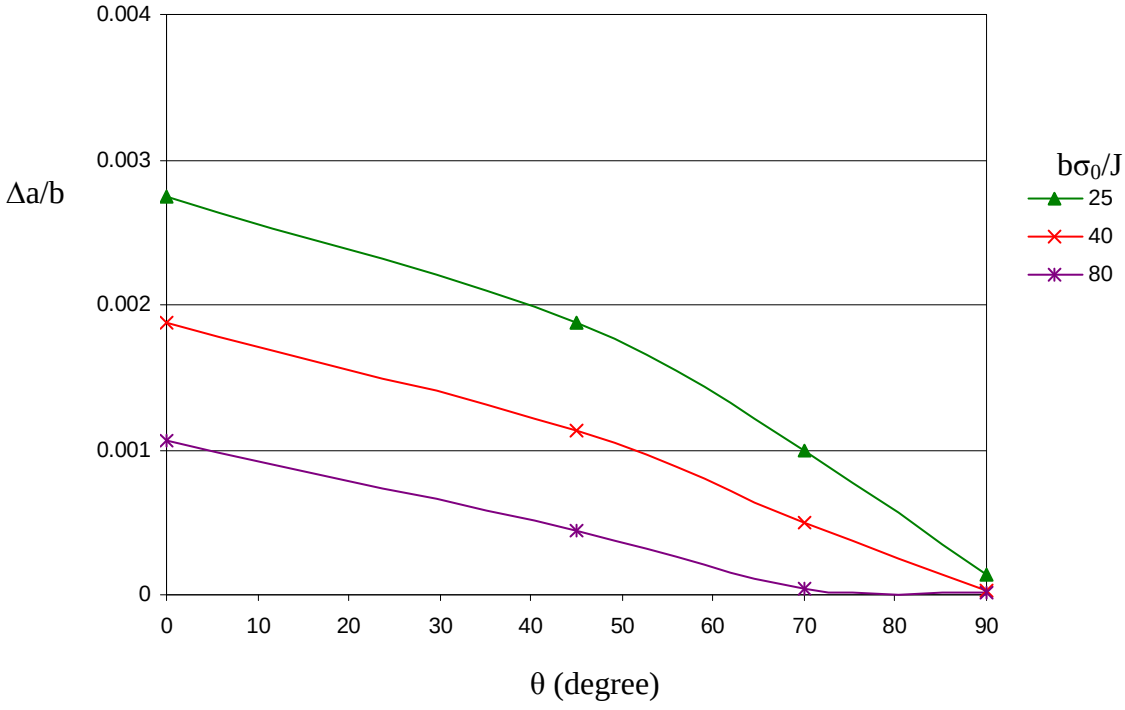

Figure 14.27: Crack growth as a function of the parametric angle (θ) for a shallow semi-elliptical surface crack (a/w=0.2, a/c=0.3) under biaxial loading.

15. Conclusions

Three-dimensional effects associated with loss of crack tip constraint have been studied in this work. The first part of the thesis focuses on edge cracked geometries. Here constraint may be lost due to in-plane (T/Q) effects, global bending and out-of-plane effects. Initially plane specimens were used to examine in-plane and out-of-plane effects. Out-of-plane constraint loss (Op) was measured at a distance $2J/\sigma_0$ at centre plane and was used to quantify the loss of the mean stress due to the thickness of a structure compared to plane strain. It was shown that deep cracks (a/w=0.5) were significantly affected by out-of-plane constraint loss, while the effect became very small in shallow cracks (a/w=0.1) as in-plane effects were dominant. The out-of-plane effect in deep cracks (a/w=0.5) became significant when the plastic zone size was significant compared to the thickness. The non-side grooved samples developed lower average mean stress across the thickness compared to side-grooved samples. This suggests lower fracture toughness may be obtained from side-grooved samples and higher toughness must be expected from non-side grooved samples.

A set of side-grooved fracture mechanics specimens were tested to examine in-plane and out-of-plane effects. Constraint loss due to the thickness effect was correlated with the increase of fracture toughness. It was shown that geometries with B/w=0.2 maintained high constraint conditions up to deformation levels of $c\sigma_0/J=50$ and low fracture toughness in which the size requirements can now be relaxed. The thinnest geometries (B/w=0.1) require more restrictions on thickness as $B\geq35J/\sigma_0$ and the ligament (c) must exceed $175J/\sigma_0$, otherwise they showed thickness dependent fracture toughness. A quantitative relation between the thickness and fracture toughness was established in a similar manner to the toughness – constraint relations developed for shallow cracks, on the basis of constraint levels in thick and thin fracture mechanics samples. The enhanced fracture toughness associated with thin geometries was included in the failure assessment diagram. The out-of-plane effect was compared to the in-plane effect, and the J-Q locus was similar to J-O_p locus.

A procedure to determine crack growth under ductile tearing conditions was developed. The procedure is based on the tearing modulus which is taken to be as a function of crack tip constraint and the J-Δa resistance curve of high and low constrained samples. The procedure combines the fracture toughness of the material J_{Ic} as well as the applied J-integral and the local constraint levels around the crack front of a surface crack. The procedure was used to determine crack growth and crack shape sequence using re-meshing to account for finite geometry changes. The procedure was applied to a wide range of surface cracks under bending, uniaxial tension and biaxial loading.

In bending, deep semi-elliptical surface cracks initially developed a highly constrained field at the deepest point but this was lost in full plasticity at approximately $b\sigma_0/J=100$. The loss of constraint at the deepest point occurred because of the loss of plane strain conditions and the closing force that affected the crack tip field. This occurred at a much lower deformation level than for the plane strain edge cracked bend bars where J-dominance is lost at $b\sigma_0/J<25$. The loss of constraint at the deepest point due to global bending effect, and low constraint at the free surface of a surface crack increased the resistance to ductile tearing at these segments. This caused the largest crack extension in the angular range 45° to 70° for semi-circular cracks (a/c=1), while for semi-elliptical cracks (a/c=0.33) growth was more pronounced at 45°. In contrast shallow semi-elliptical surface cracks tended to grow most at the deepest point, however they grew sub-surface adopting a boat shape when the crack depth reached approximately half thickness. These results limit the application of leak-before-break arguments for ductile tearing in flaw assessments. This is significant because a vastly different crack sequence develops under ductile tearing condition compared to fatigue. The crack shapes developed under LEFM conditions will therefore no longer be applicable under ductile tearing scenarios.

In tension, crack tip constraint was below the plane strain HRR level due to loss of in-plane and out-of-plane constraint. The crack extended through the thickness and this was accompanied with growth in the angular range 45°-70° for deep cracks. Shallow cracks extended at the deepest point where the maximum mean stress and J-integral were located. Under biaxial loading higher constraint levels along the crack front were observed than constraint levels under uniaxial loading. Extensive crack growth occurred in the angular range 45°-70° for semi-circular cracks; however the overall trend of the

crack growth was similar to uniaxial tension. Surface cracks under uniaxial tension or biaxial loading grew through the thickness until the breakthrough occurred where the LBB approach can be applied.

Experiments on shallow surface cracks under bending showed crack growth along the crack front with the highest rate at the deepest point. However as the crack reached approximately half thickness crack growth was suppressed at the deepest point and growth occurred beneath the surface adopting a boat shape. This is in agreement with the predictions using the procedure of chapter (9) combined with finite element modelling.

It may be concluded that the mean stress and J-integral were both geometry and load dependent, and both showed a non-uniform behaviour around the crack front at large deformation levels. Both must be taken in to account to make an accurate assessment under ductile tearing conditions. It was noted that single-parameter and two parameter characterisation are not sufficient to describe the stress field at the crack tip of the surface flaw since the stress triaxiality varies along the crack front which may not coincide with the variation of the J-integral. Non-uniform crack extension around the crack front was observed which was dependent on the original crack shape and type of loading. Under large plastic deformation current investigations showed that the original crack shape was not retained after crack growth by ductile tearing. Figure (15.1) summaries the crack shape development under ductile tearing for the geometries examined in this work in bending, tension and biaxial loadings, repectively.

Figure (15.1): Crack growth shapes: a. Crack shape sequences under bending

(a/w=0.5, a/c=1)

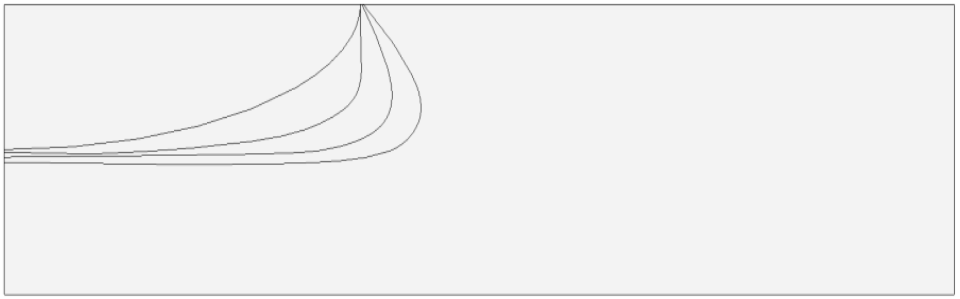

(a/w=0.5, a/c=0.33)

(a/w=0.1, a/c=1)

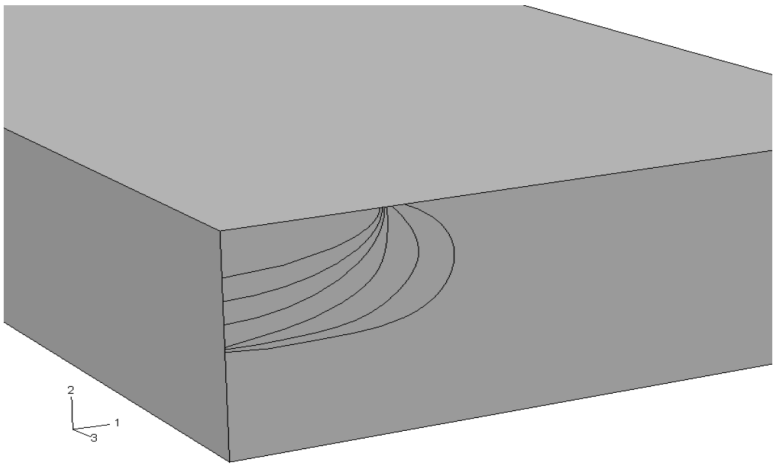

(a/w=0.2, a/c=0.33)

Continued

b. Crack shape sequence under tension

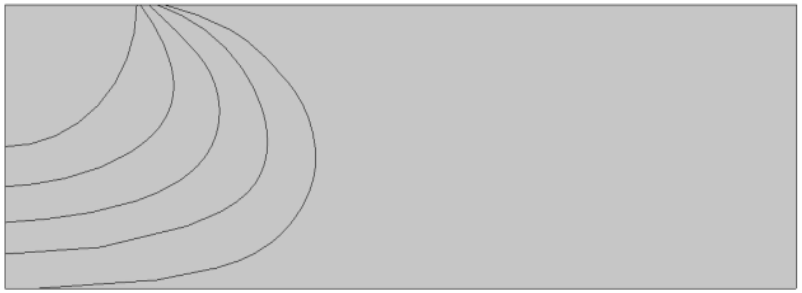

(a/w=0.5, a/c=1)

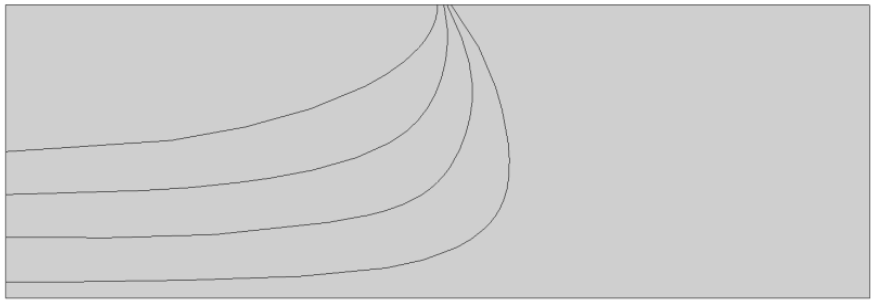

(a/c=0.33, a/w=0.5)

(a/c=1, a/w=0.1)

(a/w=0.2, a/c=0.3)

c. Crack shape sequences under biaxial loading

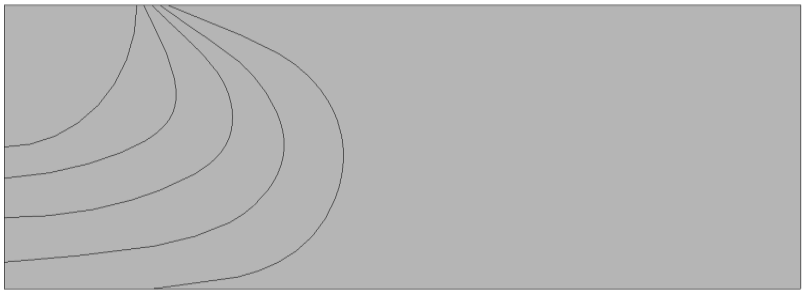

(a/w=0.5, a/c=1)

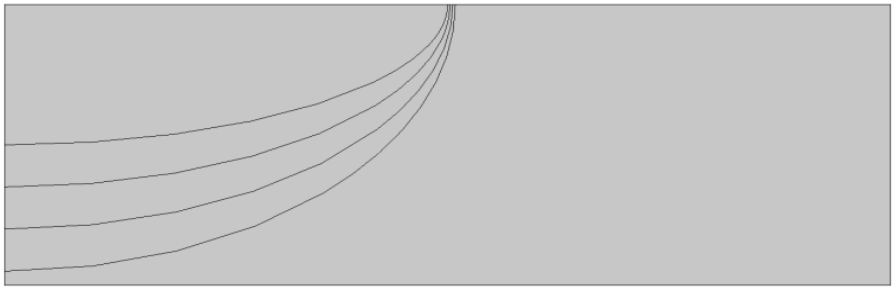

(a/c=0.33, a/w=0.5)

Ainsworth, R. and O`Dowd, N., 1995. Constraint in the failure assessment diagram approach for fracture assessment. Transaction of the ASME, Journal of Pressure Vessel Technology 117, 260-267.

Anderson, T. L., 1995. Fracture Mechanics: Fundamentals and Applications, Second Edition. Boca Raton, Florida ; London : CRC Press.

Al-Ani, A. M., and Hancock, J., 1991. J-dominance of short cracks in tension and bending. Journal of Mechanics and Physics of Solids 39, 23-43.

ASTM E399-90, 1997. Standard test method for plane-strain fracture toughness of metallic materials. American Society for Testing and Materials, 03.01, 413-443.

ASTM E1290-93, 1998. Standard test method for crack tip opening displacement (CTOD) fracture toughness measurement. American Society for Testing and Materials, 03.01, 814-823.

ASTM E1737-96, 1998. Standard test method for J-integral characterization of fracture toughness. American Society for Testing and Materials, 03.01, 957-980.

Beachem, C. D., and Yoder, G. R., 1973. Elastic-plastic fracture by homogeneous microvoid coalescence tearing along alternating shear planes. Metallurgical Transactions 4, 1145-1153.

Beardsmore, D. W., Sharples, J. K., and Madew, C. J., 2009. An analysis of the roles of J and Q in the assessment of fracture for quasi-statically extending cracks in residual stress fields. Proceedings of the ASME 2009 Pressure Vessels and Piping Division Conference. PVP2009. Prague, Czech Republic.

Berg, E., Skallerud, B., and Thaulow, C., 2008. Two-parameter fracture mechanics and circumferential crack growth in surface cracked pipelines using line-spring elements. Engineering Fracture Mechanics 75, 17-30.

Betegon, C., and Hancock, J., 1991. Two-Parameter Characterization of Elastic-Plastic Crack-Tip Fields, ASME Journal of Applied Mechanics 58, 104-110.

Bilby, B. A., Cardew, G. E., Goldthorpe, M. R., and Howard, I. C., 1986. A finite element investigation of the effects of specimen geometry on the fields of stress and strain at the tips of stationary cracks in size effects in fracture. Mechanical Engineering Publications. 37-46.

Bowen, P., Durce, S.G., and Knott, J.F., 1987. Micromechanical modeling of fracture toughness. Acta Metallurgica 35, 1735–1746.

Bricksatd, B., and Sattari-Far, I., 2000. Crack shape development for LBB applications. Engineering Fracture Mechanics 67, 625-646.

Brocks, W., and Noack, H. D., 1988. J-Integral and stresses at an inner surface flaw in a pressure vessel. International Journal of Pressure Vessels and Piping 31, 187-203.

Brocks, W., and Schmitt, W., 1995. The second parameter in J-R curves: Constraint or triaxiality, (Eds. Kirk, M. and Bakker, A.). American society for testing and materials, ASTM STP 1244. Philadelphia, 209-231.

Brocks, W., Krafka, H., Kunecke, G., and Wobst, K., 1990. Ductile crack growth of semi-elliptical surface flaws in pressure vessels. International Journal of Pressure Vessels and Piping 43, 301-316.

BS7448-91, 1991: Part 1: Method for determining of K_{Ic}, critical crack tip opening displacement (CTOD) and critical J values of fracture toughness of metallic materials. British Standard Institution, London.

BS7448-97, 1997: Part 4: Method for determination of fracture resistance curves and initiation values for stable crack extension in metallic materials. British Standard Institution, London.

Burstow, M. C., and Howard, I. C., 1996. Predicting the effects of crack tip constraint on material resistance curves using ductile damage theory. Fatigue and fracture of engineering materials and Structure 19, 641-474.

Cardew, G. E., Goldthorpe, M. R., Howard, I. C., and Kfouri, A. P., 1984. On the elastic T-stress, In fundamentals of deformation and fracture, Cambridge University Press. 465-476.

Carpinteri A., 1993. Shape change of surface cracks in round bars under cyclic axial loading. International Journal of Fatigue 15, 21-26

Chao, Y.J., Yang, S., and Sutton, M.A., 1994. On the fracture of solids characterised by one or two parameters: Theory and practice. . Journal of Mechanics and Physics of Solids, 42, 629-647.

Chao, Y.J., and Zhu, X.K., 1998. J-A_2 characterisation of the crack tip fields: extent of J-A_2 dominance and size requirements. International Journal of Fracture 89, 285-307.

Chao, Y.J., and Zhu, X.K., 2000. Constraint-modified J-R curves and its application to ductile crack growth. International Journal of Fracture 106, 135-160.

Chao, Y.J., Zhu, X.K., Kim, Y., Lar, P.S., Pechersky, M. J., and Morgan, M.J., 2004. Characterisation of crack-tip field and constraint for bending specimens under large-scale yielding, International Journal of Fracture 127, 283-302.

Chen, Y., and Lambert, S., 2005. Numerical modeling of ductile tearing for semi-elliptical surface cracks in wide plates. International Journal of Pressure Vessels and Piping 82, 417-426.

Cherepanov, G.P., 1967. Crack propagation in continuous media. International Journal of Solid Structures 4, 811-831.

Cotterell, B., Li, Q. F., Zhang, D. Z., and Mai, Y. W., 1985, On the effect of plastic constraint on ductile tearing in a structural steel. Engineering Fracture Mechanics 21, 239-244.

Curry, D. A., and Knott, J. F., 1979, Effects of microstructure on cleavage fracture toughness in mild steel. Metal Science 13, 341-345.

DeLorenzi, H. G., 1985. Energy release rate calculations by the finite element method. Engineering Fracture Mechanics 21, 129-143

Dowling, A.R., and Townley, C.H.A., 1975. The effect of defects on structural failure: A two-criteria approach. International Journal of Pressure Vessels and Piping 3, 77-107.

DeLorenzi, H. G., and Shih, C. D., 1983, 3-D Elastic-plastic investigation of fracture parameters in side-grooved compact specimen. International Journal of Fracture 21, 195-220.

Dodds, R. H., Anderson, T. L., and Kirk, M. T., 1991, A framework to correlate a/w ratio effects on elastic-plastic fracture toughness (J_c).International Journal of Fracture 48,1-22.

Drugan, W. J., Rice, J. R., and Sham, T. L., 1982. Asymptotic analysis of growing plane strain tensile cracks in elastic-ideally plastic solids. Journal of Mechanics and Physics of Solids 30, 447-473.

Du, and Hancock, J., 1991. The effect of non-singular stresses on crack tip constraint. Journal of Mechanics and Physics of Solids 39, 555-567.

Faleskog, J., 1994. An experimental and numerical investigation of ductile growth characteristics in surface cracked specimens under combined loading. International Journal of Fracture 68, 99-126.

Gao X, Faleskog, J., Shih, C. F., and Dodds, R. H., 1998. Ductile tearing in part-through cracks: Experiments and cell-model predictions. Engineering Fracture Mechanics 59, 761-777.

Ger, J. M., and Timoshenko, S. P., 1991. Mechanics of Materials, Third Edition, Chapman and Hall.

Griffith, A.A., 1921. The phenomena of rupture and flow in solids. Philosophical Transactions, series A, 221, 163-198.

Guo, W., 1995. Elasto-plastic three-dimensional crack border field-III. Fracture Parameters. Engineering Fracture Mechanics 51, 51-71.

Guo, W., and She, C., 2007. The out-of-plane constraint of mixed-mode cracks in thin elastic plates. International Journal of Solids and Structures 44, 3021-3034.

Gurson, A. L., 1977. Continuum theory of ductile rupture by void nucleation and growth: Part I-Yield criteria and flow rules for porous ductile media. Transactions of the ASME. Journal of Engineering Materials and Technology.

Hancock, J.W., and Cowling, M. J., 1980. Role of state of stress in crack-tip failure processes. Journal of Metal Science 293-304.

Hancock, J.W, Reuter, W.G., and Parks, D.M., 1993. Constraint and toughness parameterised by T. Constraint effect in fracture. ASTM STP 1171, Philadelphia, 21-40.

Harlin, G., and Willis, J. R., 1988. The influence of crack size on the ductile–brittle transition. Pro. Royal Society, London. A415, 197–226.

Hebel, J., Hohe, J., Friedmann, V., and Siegele, D., 2007. Experimental and numerical analysis of in-plane and out-of-plane crack tip constraint characterisation by secondary fracture parameters, International Journal of Fracture 146, 173-188.

Hellen, T. K., 1975. On the method of virtual crack extension. International Journal for Numerical Methods in Engineering 9, 187-207.

Hodulak, L., Kordisch H., Kunzelmann S., and Sommer E., 1978. Influence of the load level on the development of part-through cracks. International Journal of Fracture 14. 35-38.

Hutchinson, J, W., 1968a. Singular Behaviour at the end of a Tensile crack in a Hardening Material, Journal of Mechanics and Physics of Solids 16, 13-31.

Hutchinson, J, W., 1968b. Plastic stress and strain fields at a Crack Tip. Journal of Mechanics and Physics of Solids 16, 337-347.

Hutchinson, J. W., and Paris, P. C., 1979. Stability analysis of J-controlled crack growth. Elastic-plastic fracture, ASTM STP668. 37-64.

Inglis, C. E., 1913. Stresses in a plate due to the presence of cracks and sharp corners, Transactions of the Institute of the Naval Architects 55, 219-241.

Irwin, G.R., 1948. Fracture dynamics, Proceedings of the ASM symposium on fracturing of metals. Cleveland (Ohio), 147-166.

Irwin, G.R., and Kies, J. A., 1954. Critical energy rate analysis of fracture strength, Welding Journal 33, 193-198.

Irwin, G.R., Kies, J. A., and Smith, H.C., 1958. Fracture strength relative to onset and arrest of crack propagation. Proceedings of ASTM 58, 640-657.

Irwin, G.R., 1957, Analysis of stress and strain near the end of a crack traversing a plate. Journal of Applied Mechanics 24, 361-364.

Irwin, G.R., 1956. Onset of fast crack propagation in high strength steel and aluminium alloys. In: Sagamore Ordnance Materials Research Conference Proceedings, Syracuse University 2, 289-305.

Irwin, G.R., 1960. Plastic zone near a crack and fracture toughness. Proceedings of 7th Sagamore Ordnance Materials Research Conference. Syracuse University Press 4, 63-78.

Janssen, M., Zuidema, J., and Wanhill, R.J.H., 2002. Fracture mechanics. Second Edition. Delft University Press.

Joyce, J.A., and Link, R.E., 1997. Application of two parameter elastic-plastic fracture mechanics to analysis of structures. Engineering Fracture Mechanics 57, 431-446.

Karstensen, A., 1996. Constraint estimation schemes in fracture mechanics. PhD, Thesis. Faculty of Engineering, University of Glasgow.

Kfouri, A.P., 1986. Some evaluations of the elastic T-term using Eshelby`s method. International Journal of Fracture 30, 301-315.

Kim, Y.J., 2002. Experimental J estimation equations for single-edge-cracked bars in four-point bend: homogeneous and bi-material specimens. Engineering Fracture Mechanics 69, 793–811

Kim, Y-Jae., Kim, J. S., Cho, S. M., and Kim, Y-Jin., 2004, 3-D constraint effects on J testing and crack tip constraint in M(T), SE(B), SE(T) and C(T) specimens: numerical study. Engineering Fracture Mechanics 71, 1203-1218.

Kim, Y-J., Lin, G., Cornec, A., and Schwalbe, K.-H., 1996. Fully plastic crack-tip fields for plane strain shallow-cracked specimens under pure bending. International Journal of Fracture 78, 21–34.

Kim, Y., Chung, K., Kim, J., and Kim, Y-J., 2004. Effect of biaxial loads on elastic-plastic J and crack tip constraint for cracked plates: finite element study. International Journal of Fracture 130, 803-825.

Kim, Y., Zhu, X. K., and Chao, Y. J., 2001. Quantification of constraint on elastic-plastic 3D crack front by the J-A_2 three-term solution. Engineering Fracture Mechanics 68, 895-914.

Kim, Y., Chao, Y. J., and Zhu. X. K., 2003. Effect of specimen size and crack depth on 3D crack-front constraint for SENB specimens. International Journal of Solids and structures 40, 6267-6284.

Kim, Y-J. and Schwalbe, K-H., 2001. On experimental J estimation equations based on CMOD for SE(B) specimens. Journal of Testing and Evaluation. American Society for Testing and Materials 29, 67-71.

Knott, J. F. and Met. B., 1974. Fundamentals of fracture mechanics, London, Butterworth.

Kirk, M. T. and Dodds, R. H. Jr., 1993. J and CTOD estimation equations for shallow cracks in single edge notch bend specimens, Journal of Testing and Evaluation 21, 228-238.

Lam, P. S., Chao, Y. J., Zhu, X. K., Kim, Y., and Sindelar, R. L., 2003. Determination of constraint-modified J-R curves for carbon steel storage tanks. Journal of Pressure Vessel Technology 125, 136-143.

Larsson, S. G. and Carlsson, A. J., 1973. Influence of non-singular stress terms and specimen geometry on small-scale yielding at crack tips in elastic plastic material. International Journal of Fracture 21, 263-277.

Leevers, P. S. and Radon, J. C., 1982. Inherent stress biaxiality in various fracture specimen geometries. International Journal of Fracture 9, 311-325.

Li, F. Z. Shih, C. F., and Needleman, A., 1985. A comparison of methods for calculating energy release rate. Engineering Fracture Mechanics 21, 405-421.

Lin X.B., and Smith R.A., 1999. Shape evolution of surface cracks in fatigued round bars with a semicircular circumferential notch. International Journal of Fatigue 21, 965–973

Lin, X.B., and Smith, R.A., 1999. Finite element modelling of fatigue crack growth of surface cracked plates, Part II: Crack shape change. Engineering Fracture Mechanics 63, 523-540

MacLennan, I., and Hancock, J. W., 1995. Constraint-based failure assessment diagrams. Proc. Royal Society of London 451, 757-777.

McClintok, F. A., and Argon A. S., 1966. Mechanical Behaviour of Materials. Addison-Wesley Publishing Company, Inc, Reading, Massachusetts, USA.

McClintock, F.A., 1968. A criterion for ductile fracture by growth of hole, Journal of Applied Mechanics 4, 363-371.

McClintock, F. A., 1971. Plasticity aspects of fracture. In Liebowitz, H. (Ed). Fracture 3, Academic Press. London. 47-225.

McMeeking, R. M., and Parks, D. M., 1979. On criteria for J-dominance of crack-tip fields in large-scale yielding. Elastic-Plastic Fracture, ASTM STP 668, 175-194.

Mises, R., 1913. Gottinger nachrichten math. Phys. Klasse, 582.

Moussavi Zadeh, Gh., 1995. Analysis of stable crack growth of a semi-elliptical surface crack by numerical simulation. Nuclear Engineering and Design 158, 311-317.

Murakami, Y., 1987. Stress Intensity Factor Handbook, vol. I. Pergamom Press. New York.

Nakamura, T., and Parks, D.M., 1989. Antisymmetrical 3D stress field near the crack front of a thin elastic plate. International Journal of Solids and Structures 25, 1411-1426.

Nakamura, T., and Parks, D.M., 1992. Determination of elastic T-stress along 3-D crack fronts using an interaction integral. International Journal of Solids and Structures 29, 1597-1611.

Needleman, A., and Tvergaard, V., 1987. An analysis of ductile rupture of modes at a crack tip. Journal of Mechanics and Physics of Solids 35, 151-183.

Neimitz, A., 2004., Modification of dugdale model to include the work hardening and in- and out-of-plane constraints. Engineering Fracture Mechanics 71, 1585–1600.

Nevalainen, M., and Dodds, R. H., 1995. Numerical investigation of 3-D constraint effects on brittle fracture in SE(B) and C(T) specimens, International Journal of Fracture 74, 131-161.

Newman, J. C., and Bigelow, C. A., 1993. Three-dimensional elastic-plastic finite-element analysis of constraint variations in cracked bodies. Engineering Fracture Mechanics 46, 1-13.

Newman, J. C. JR., and Raju, I. S., 1981. An empirical stress-intensity factor equation for the surface crack. Engineering Fracture Mechanics 15, 185-192.

Nye, J. F., 1964. Physical properties of crystals. Second Edition, Oxford, the clarendon press.

O'Dowd, N.P., and Shih, C.F., 1991. Family of crack-tip fields characterised by a triaxiality parameter-1. Structure of fields. Journal of Mechanics and Physics of Solids 39, 989-1015.

O'Dowd, N.P., and Shih, C.F., 1992. Family of crack-tip fields characterised by a triaxiality parameter-2. Fracture applications. Journal of Mechanics and Physics of Solids 40, 939-963.

O'Dowd, N.P., and Shih, C.F., 1995. Two-parameter fracture mechanics: Theory and applications. American Society for Testing and Materials, ASTM STP1207. Philadelphia. 21-47.

Orowan, E., 1952. Fundamentals of brittle behaviour of metals. Fatigue and fracture of metals, Wiley, New York, 139-167.

Ostby, E., Thaulow, C., and Zhang, Z. L., 2007b. Numerical simulations of specimen size and mismatch effects in ductile crack growth-Part I: Tearing resistance and crack growth paths. Engineering Fracture Mechanics 74, 1770-1792.

Ostby, E., Thaulow, C., and Zhang, Z. L., 2007a. Numerical simulations of specimen size and mismatch effects in ductile crack growth-Part II: Near tip stress fields. Engineering Fracture Mechanics 74, 1793-1809.

Paris, P. C., Tada, H., Zahoor, A., and Ernst, H., 1979. The theory of instability of the tearing mode of elastic-plastic crack growth. ASTM STP 668, 5-36.

Parks, D. M., 1974. A stiffness derivative finite element technique for determination of crack tip stress intensity factors. International Journal of Fracture 10, 487-502.

Parks, D. M., 1977. The virtual crack extension method for nonlinear material behaviour. Computer methods in applied mechanics and engineering, North-Holland Publishing Company 12, 353-364.

R6, 2000. Assessment of the integrity of structures containing defects. Revision 3, British Energy Generated Ltd. Gloucester, UK.

Rice, J. R., 1968a. Mechanical analysis in the mechanics of fracture. Fracture, An advanced Treatise. H. Liebowitz. Academic Press. 2, 191-311.

Rice, J. R., 1968, A path independent integral and the approximate analysis of strain concentration at notches and cracks. ASTM Journal of Applied Mechanics 35, 379-386.

Rice, J. R., Drugan, W. J., and Sham, T. L., 1980. Elastic-plastic analysis of growing cracks. Fracture Mechanics 12th Conference. ASTM STP 700, 189-221.

Rice, J.R., and Rosengren, G. F., 1968. Plane strain deformation near a crack tip in a power law hardening material. Journal of Mechanics and Physics of Solids 16, 1-12.

Rice, J. R., 1974. Limitations to the small scale yielding approximation for crack tip plasticity. Journal of Mechanics and Physics of Solids 22, 17-26.

Rice, J.R and Tracey, D.M., 1969. On the ductile enlargement of voids in triaxial stress fields. Journal of the Mechanics and Physics of Solids 17, 201-217.

Rice, J.R., and Johnson, M.L., 1970. The role of large crack tip geometry changes in plane strain fracture. Inelastic Behaviour of Solids, McGraw-Hill, New York. 641-672.

Ritchie, R.O., Knott, J.F., and Rice, J.R., 1973. On the relationship between critical tensile stress and fracture toughness in mild steel. Journal of Mechanics and Physics of Solids 21, 395–410.

Rooke, D. P., and Cartwright, D. J., 1976. Compendium of stress intensity factors. Her Majesty`s Stationary Office, London.

Scott, P. M., and Thorpe, T. W., 1981. A critical review of crack tip stress intensity factors for semi-elliptic cracks. Fatigue of Engineering Materials and Structures 4, 291-309.

Sham, TL., 1991. The determination of the elastic T-term using higher order weight functions. International Journal of Fracture 48, 081-102.

Sharma, S. M., and Aravas, N. J., 1991. Determination of higher order terms in asymptotic elastoplastic crack tip solutions. Journal of Mechanics and Physics of Solids 39, 1043-1072.

Sherry, A. H., France, C. C., and Goldthorpe, M. R., 1995. Compendium of T-stress solutions for 2 and 3 dimensional cracked geometries. Fatigue and Fracture of Engineering Materials and Structure 18, 141-155.

Shih, C. F., 1981. Relationships between the J-integral and the crack opening displacement for stationary and extending cracks. Journal of Mechanics and Physics of Solids 29, 305-326.

Shih, C.F, and German. M.D., 1981. Requirements for a one parameter characterisation of crack tip fields by the HRR singularity. International Journal of Fracture 17, 27-43.

Shih, C.F, and German. M.D., and Kumar, V., 1981. An engineering approach for examining crack growth and stability in flawed structures. International Journal of Pressure Vessels and Piping 9, 159-196.

Shih, C. F., Moran, B., and Nakamura, T., 1986. Energy release rate along a three-dimensional crack front in a thermally stressed body. International Journal of Fracture 30, 79-102.

Smith, D. J., Swankie, T. D., Pavier, M. J., and Smith, M. C., 2008, The effect of specimen dimensions on mixed mode ductile fracture. Engineering Fracture Mechanics 75, 4394-4409.

Sreenivasan, P. R., and Mannan S.L., 2000. Plastic η-factor for three-point bend specimens: Analysis of instrumented Charpy impact test results for AISI 308 weld and AISI 316 stainless steels. International Journal of Fracture 101, 215-228.

Sumpter J. D. G., 1987. J_c determination for shallow notch welded bend specimens. Fatigue Fract. Eng. Mater. Struct. 10, 479–493.

Sumpter, J. D. G., and Hancock, J. W., 1991. Shallow crack toughness of HY80 welds. An analysis based on T-stress. International Journal of Pressure Vessels and Piping 45, 207-221.

Sumpter, J. D. G. And Turner, C. E., 1976. Method for laboratory determination of J_c. Cracks and Fracture. ASTM STP 601, 3-18

Tang, W. and Shi, Y. W., 1992. An investigation of the plastic rotational factor during loading processes for three point bend specimens. Computers & Structures 43, (4), 709-712.

Terfas, A. O., 2009. Crack tip constraint for a surface crack under fully plastic conditions. Proceedings of the ASME 2009 Pressure Vessels and Piping Division Conference. PVP2009-77371. Prague, Czech Republic.

Terfas, A. O., and Bezensek, B., 2009a. The development of a surface crack in a thick vessel under ductile tearing. Proceedings of the ASME 2009 Pressure Vessels and Piping Division Conference. PVP2009-77374. Prague, Czech Republic.

Terfas, A. O., and Bezensek, B., 2009b. The Influence of the specimen thickness on the CTOD fracture toughness. Proceedings of the 7th EUROMECH Solid Mechanics Conference. ESMC2009-398. Lisbon, Portugal.

Timoshenko, S. P., and Goodier, J. N., 1970, Theory of Elasticity, Third Edition, McGraw-Hill Book Company.

Tvegaard, V., 1981. Influence of voids on shear band instabilities under plane strain conditions. International Journal of Fracture 17, (4). 389-407.

Tvegaard, V., 1982. On localization in ductile materials containing spherical voids. International Journal of Fracture 18, (4). 237-252.

Tvegaard, V., and Needleman, A., 1984. Analysis of the cup-cone fracture in a round tensile bar. Acta Metall 32, 157-169.

Varias, A. G., and Shih, C. F., 1993. Quasi-static crack advance under a range of constraints: steady-state fields based on a characteristic length. Journal of Mechanics and Physics of Solids 41, 835-861.

Wallin, K., 1989. Fracture toughness testing in the ductile-brittle transition region. In Salarma, et al (eds). Advances in Fracture Research, Proceedings of the 7th International Conference on Fracture (ICF7), 267-276.

Wallin, K. R., 2001. K_{Ic}- A non-measure of plane strain fracture toughness. The tenth International Conference on Fracture, ICF10, Hawii.

Wang, X., 2009. Two-parameter characterization of elastic-plastic crack front fields: Surface cracked plates under tensile loading. Engineering Fracture Mechanics 76, 958-982.

Wang, Y.Y., and Parks, D.M., 1992. Evaluation of the elastic T-stress in surface cracked plates using the line spring method. International Journal of Fracture 56, 25-40.

Wang, G.Z., Chen, J.H., and Liu, G.H., 2002a. On the characteristic distance and minimum fracture toughness for cleavage fracture in a C-Mn steel. International Journal of Fracture 118, 57–76.

Wang, G.Z. Chen, J. H., and Wang, J.G., 2002b . On the measurement and physical meaning of the cleavage fracture stress in steel. International Journal of Fracture 118, 211–227.

Wang, X., 2003. Elastic T-stress solution for semi-elliptical surface crack in finite thickness plates. Engineering Fracture Mechanics 70, 731-756.

Wei, Y., and Wang, T., 1995a. Characterisation of elastic-plastic field near stationary crack tip and fracture criterion. Engineering Fracture Mechanics. 51, 547-553.

Wei, Y. and Wang, T., 1995b. Fracture criterion based on the higher order asymptotic fields. International Journal of Fracture 73, 39-50.

Wells, A. A., 1961. Unstable crack propagation in metals: Cleavage and Fast Fracture. In Proceeding of the crack propagation symposium 1. Cranfield. UK. 210-230. Paper 48.

Westergaard, H. M., 1939. Bearing Pressures and crack, Journal of Applied Mechanics 6, 49-53.

Williams, M. L., 1957. On the stress distribution at the base of a stationary crack. ASME Journal of Applied Mechanics 24, 111-114.

Wu, S-X., 1983. Plastic rotational factor and J-COD relationship of three point bend specimens. Engineering Fracture Mechanics 18, 83-95.

Wu, S-X., Cotterell, B., and Mai,Y-W., 1988. Slip-line field solutions for three-point notch-bend specimens. International Journal of Fracture 37, 13-29.

Xiao, Y-G., and Huang., G-H., 1982. On the compatibility between J-integral and crack opening displacement. Engineering Fracture Mechanics 16, 83-94.

Yamamoto, H., 1978. Conditions for shear localization in the ductile fracture of void-containing materials. International Journal of Fracture 14, 347-365.

Yang, S., Chao, Y.J., and Sutton M.A., 1993. Higher-order asymptotic fields in a power – law hardening material. Engineering Fracture Mechanics 45, 1-20.

Yuan, H., and Brocks, W., 1998. Quantification of constraint effects in elastic-plastic crack front fields. Journal of Mechanics and Physics of Solids 46, 219-241.

Zhang, Z. L., and Niemi, E., 1995. A new failure criterion for the Gurson-Tvergaard dilational constitutive model. International Journal of Fracture 70, 321-334.

Zhang, B., and Guo, W., 2005. T_z constraints of semi-elliptical surface cracks in elastic plates subjected to uniform tension loading. International Journal of Fracture 131, 173–187.

Zhang, B., and Guo, W., 2007. Three-dimensional stress state around quarter-elliptical corner cracks in elastic plates subjected to uniform tension loading. Engineering Fracture Mechanics 74, 386-398.

Zhang, D. Z., and Wang, H., 1987. On the effect of the ratio a/w on the values of δ_I and J_I in a structural steel. Engineering Fracture Mechanics 26, (2). 247-250.

Zhang, D. Z., and Zhu, S. F., 1988. Use of double clip gauge method to measure the plastic rotational factor r_p. Engineering Fracture Mechanics 31, 917-921.

Zhao, L. G., Tong, J., and Byrne, J., 2001. Stress intensity factor K and the elastic T-stress for corner cracks. International Journal of Fracture 109, 209-225.

Zhao, J., Guo, W., and She, C., 2007. The in-plane and out-of-plane stress constraint factors and K-T-T_z description of stress field near the border of a semi-elliptical surface crack. International Journal of Fatigue 29, 435-443.

Zhu, X-K., and Chao, Y.J., 1999. Characterization of constraint of fully plastic crack tip fields in non-hardening materials by three-term solution. International Journal of Solids and Structures 36, 4497-4517.

Zhu, X-K., and Chao, Y.J., 2000. Fully plastic crack-tip fields for CCP and DECP specimens under tension in non-hardening materials. International Journal of Solids and Structures 37 (4), 577–588

Zhu, X-K., and Joyce, J. A., 2007. J–Resistance curve testing of HY80 steel using SE(B) specimens and normalization method. Engineering Fracture Mechanics 74, 2263–2281.

Zhu, X-K., and Leis, B.N., 2006. Bending modified J-Q theory and crack-tip constraint quantification. International Journal of Fracture 141, 115-134.

Terfas, A. O., 2009. Crack tip constraint for a surface crack under fully plastic conditions. Proceedings of the ASME 2009 Pressure Vessels and Piping Division Conference. PVP2009-77371. Prague, Czech Republic.

Terfas, A. O., and Bezensek, B., 2009a. The development of a surface crack in a thick vessel under ductile tearing. Proceedings of the ASME 2009 Pressure Vessels and Piping Division Conference. PVP2009-77374. Prague, Czech Republic.

Terfas, A. O., and Bezensek, B., 2009b. The Influence of the specimen thickness on the CTOD fracture toughness. Proceedings of the 7th EUROMECH Solid Mechanics Conference. ESMC2009-398. Lisbon, Portugal.